

LASER COMMUNICATION EXPERIMENT

NASA-CR-132803) LASER COMMUNICATION N73-31469
EXPERIMENT. VOLUME 1: DESIGN STUDY
REPORT: SPACECRAFT TRANSCEIVER. PART
1: TRANSCEIVER (Aerojet-General Corp., Azusa, Calif.) 584/p HC #13,25 CSCL 20B G3/16 14722
Unclas

DESIGN STUDY REPORT
VOL. I PART I
SPACECRAFT TRANSCEIVER



CONTRACT NAS5-21072
REPORT NO. 4033

NASA GODDARD SPACE FLIGHT CENTER

JULY 1970

Reproduced by
NATIONAL TECHNICAL
INFORMATION SERVICE
US Department of Commerce
Springfield, VA. 22151



ELECTRONICS DIVISION - AZUSA, CALIFORNIA

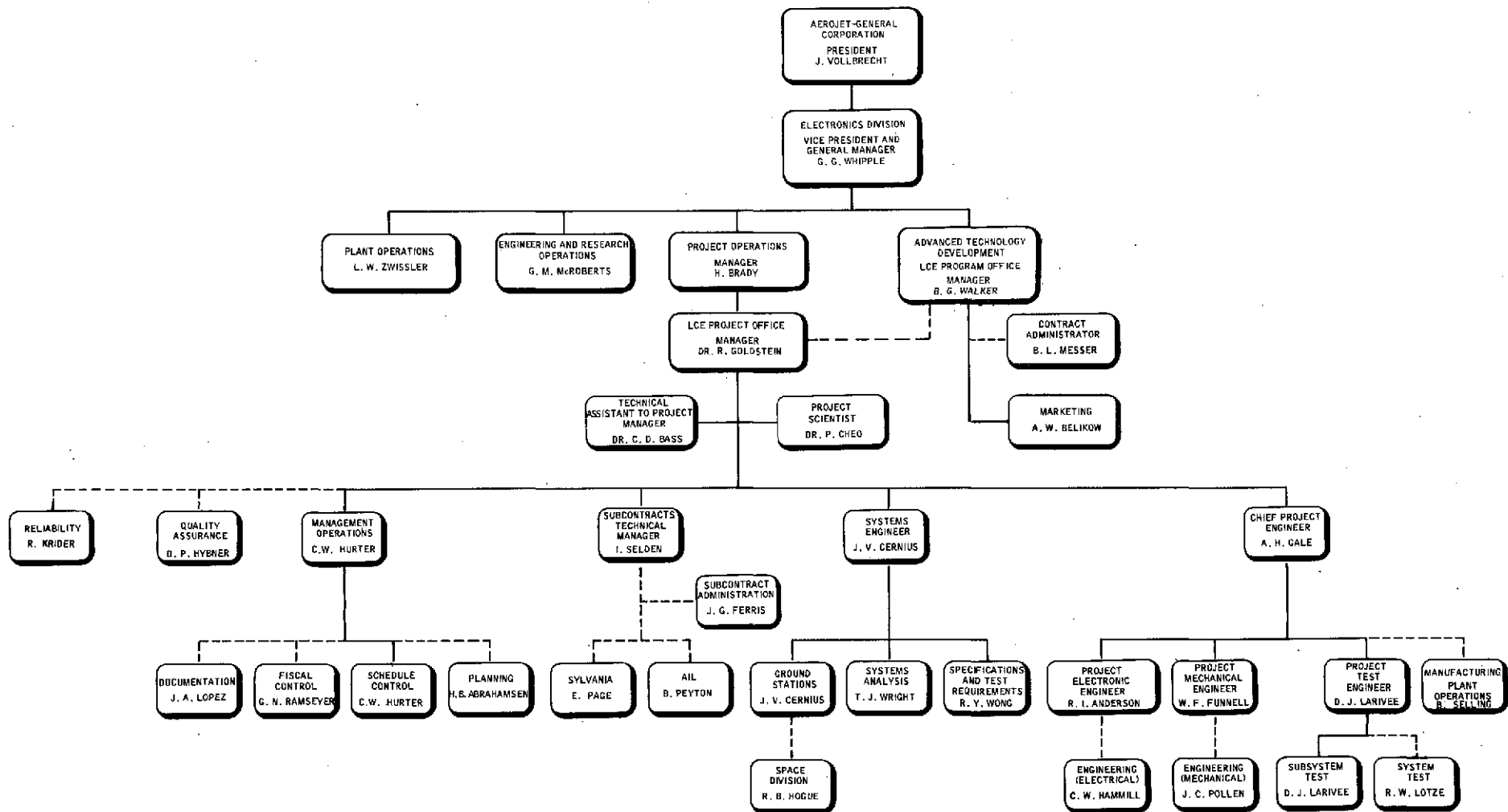
ATTENTION

AS NOTED IN THE NTIS ANNOUNCEMENT,
PORTIONS OF THIS REPORT ARE NOT LEGIBLE.
HOWEVER, IT IS THE BEST REPRODUCTION
AVAILABLE FROM THE COPY SENT TO NTIS.

FOREWORD

This report was prepared in conformance with the requirements of NASA Specification S-460-ATS-19, which is GSFC's specification pertaining to the ATS-F experiments, design study, and fabrication. Additional requirements are contained in GSFC specification S-524-P-4C, "10.6 Micron Laser Communications Systems Experiment for ATS-F." This is Part 1 of the three-part Volume I Design Study Report pertaining to the LCE spacecraft transceiver. It is a comprehensive, self-contained report of the transceiver design. Part 2 contains the appendices, while Part 3 contains the LCE design specifications.

Volume II, which will be delivered in late fall of 1970, will cover the remaining elements of the LCE, including the Operational Ground Equipment, Data Acquisition Plan, and Data Processing, Reduction, and Analysis Plan.



Laser Communications Experiment Organization

CONTRIBUTORS

The following is a list of personnel cognizant of the LCE design-study technical areas discussed in Part 1 of this report. Each primary contributor is listed by section. Figure i shows the Aerojet-General LCE organizational relationships and responsibilities.

Aerojet-General Corporation:

LCE Program Manager	B. G. Walker
LCE Project Manager	Dr. R. Goldstein
Design Study Report Manager	A. H. Gale/W. M. Kauffman
1.0 INTRODUCTION	Dr. R. Goldstein/W. M. Kauffman
2.0 SUMMARY	Dr. R. Goldstein and Staff
3.0 OBJECTIVES OF THE EXPERIMENT	B. G. Walker/Dr. R. Goldstein
4.0 SYSTEM PERFORMANCE REQUIREMENTS	J. V. Cernius
5.0 PROPOSED SYSTEM DESIGN AND ANALYSIS	
5.1 System Design and Analysis	J. V. Cernius/A. H. Gale
5.2 Subsystem Design and Analysis	
5.2.1 Optical/Mechanical Subsystem	A. H. Gale/W. F. Funnell
5.2.1.1 Optical Path Layout	Dr. C. D. Bass/T. J. Wright
5.2.1.10 Optical Train Analysis	Dr. C. D. Bass/T. J. Wright
5.2.2 Laser Subsystem	Dr. P. K. Cheo (w/Sylvania)
5.2.3 Radiation Cooler	C. B. Fischer/R. C. Coda
5.2.4 Receiver Subsystem	J. V. Cernius (w/AIL)
5.2.5 Acquisition & Tracking Subsystem	R. I. Anderson
5.2.6 Power Supply Subsystem	R. V. Hauerwaas/A. H. Gale
5.2.7 Telemetry & Command Subsystem	R. I. Anderson
5.3 Technical Areas of Continuing Development	
5.3.1 Laser Tube	Dr. P. K. Cheo (w/Sylvania)
5.3.2 Duplexer	Dr. C. D. Bass
5.3.3 Radiation Cooler	C. B. Fischer
5.4 Spacecraft/Experiment Interface	
5.4.1 Mechanical Interface	W. F. Funnell/A. H. Gale
5.4.2 Thermal Interface	C. B. Fischer/R. L. Bacharach
5.4.3 Electrical	R. I. Anderson/A. H. Gale

CONTRIBUTORS

5.4.4	EMI Requirements	S. J. Szczuka
5.4.5	Environmental Requirements	W. F. Funnell
5.5	Feasibility of Including on ATS-F	A. H. Gale
5.6	Operation Under Non-Standard Conditions	Dr. C. D. Bass
5.7	Ability of LCE to Perform Experiments	J. V. Cernius
6.0	EXPECTED LIFETIME OF THE EXPERIMENT	P. W. Stockdill
7.0	TEST PLAN	D. J. Larivee

Subcontractors:

5.2.2	Laser Subsystem	R. Reynolds Sylvania Electronic Systems Western Division
5.2.4	Receiver Subsystem	B. Peyton Airborne Instruments Laboratory

NASA:

The assistance of J. H. McElroy, GSFC Resident Engineer, in the preparation of this report is gratefully acknowledged.

CONTENTS

		<u>Page</u>
1.0	INTRODUCTION _____	1-1
2.0	SUMMARY _____	2-1
	2.1 Introduction _____	2-1
	2.2 System Concept _____	2-2
	2.3 System Description _____	2-3
	2.4 Significant Technical Achievements _____	2-5
	2.5 Report Contents _____	2-7
3.0	OBJECTIVES OF THE EXPERIMENT _____	3-1
4.0	SYSTEM REQUIREMENTS _____	4-1
5.0	PROPOSED SYSTEM DESIGN AND ANALYSIS _____	5.1-1
	5.1 System Design and Analysis _____	5.1-1
	5.1.1 System Description and Operation _____	5.1-1
	5.1.2 Subsystem Description _____	5.1.2-1
	5.1.3 Link Analysis _____	5.1.3-1
	5.1.4 Communications Analysis _____	5.1.4-1
	5.1.5 Acquisition Analysis _____	5.1.5-1
	5.1.6 Tracking Analysis _____	5.1.6-1
	5.2 Subsystem Design and Analysis _____	5.2.1-1
	5.2.1 Optical/Mechanical Subsystem _____	5.2.1-1
	5.2.2 LAser Subsystem _____	5.2.2-1
	5.2.3 Radiation Cooler _____	5.2.3-1
	5.2.4 Optical Heterodyne Receiver Subsystem _____	5.2.4-1
	5.2.5 Acquisition and Tracking Subsystem _____	5.2.5-1
	5.2.6 Power-Supply Subsystem _____	5.2.6-1
	5.2.7 Telemetry and Command Subsystem _____	5.2.7-1
	5.3 Technical Areas of Continuing Development _____	5.3.1-1
	5.3.1 Laser-Tube Development _____	5.3.1-1
	5.3.2 Duplexer _____	5.3.2-1
	5.3.3 Radiation Cooler _____	5.3.3-1

CONTENTS (cont.)

	<u>Page</u>
5.4 Spacecraft/Experiment Interface _____	5.4.1-1
5.4.1 Mechanical Interface _____	5.4.1-1
5.4.2 Thermal Interface _____	5.4.2-1
5.4.3 Electrical Interface _____	5.4.3-1
5.4.4 EMC Requirements _____	5.4.4-1
5.5 Feasibility of Including LCE System on the ATS-F Spacecraft _____	5.5-1
5.5.1 General Acceptability _____	5.5-1
5.5.2 Installation and Handling _____	5.5-1
5.5.3 Launch Environment _____	5.5-2
5.5.4 Orbital Environment _____	5.5-2
5.5.5 Cesium Ion Engine Considerations _____	5.5-3
5.6 Operation Under Non-standard Conditions _____	5.6-1
5.7 Ability of the LCE System to Perform Experiments _____	5.7-1
5.7.1 S/N Ratio as a Function of Atmospheric Parameters _____	5.7-1
5.7.2 S/N as a Function of Receiver Aperture _____	5.7-3
5.7.3 S/N Ratio as a Function of Zenith Angle _____	5.7-3
5.7.4 Space Background Noise (Sun, Stars, etc.) _____	5.7-3
5.7.5 Laser Output Power as a Function of Total Elapsed Time and Operating Time in Space Environment _____	5.7-6
5.7.6 Temperature and Noise Figure of the Mixer/Radiation Cooler as a Function of Satellite Orientation and Time of Year _____	5.7-6
5.7.7 Round-Trip and One-Way Data Compared to Reference Microwave Link _____	5.7-7
5.7.8 Laser Frequency Stability in Space Environment _____	5.7-8

CONTENTS (cont.)

	<u>Page</u>
5.7.9 Spacecraft Attitude Determination from Laser Data _____	5.7-9
5.7.10 Modes of Operation _____	5.7-10
5.7.11 Baseband Characteristics _____	5.7-10
5.7.12 S/N Ratio and Flux Densities _____	5.7-11
6.0 EXPECTED LIFETIME OF THE EXPERIMENT _____	6-1
6.1 Summary _____	6-1
6.2 Reliability Requirements _____	6-1
6.3 Reliability Predictions and Allocations _____	6-1
7.0 TEST PLAN _____	7-1
7.1 Test Flow Charts _____	7-1
7.2 Test Setups _____	7-4
7.3 Test Descriptions _____	7-6
7.4 Summary _____	7-21

Vol. I, Part 2 - APPENDIXES

Vol. I, Part 3 - ATTACHMENTS

TABLES

	<u>Table</u>
LCE Transceiver System Specifications _____	2-1
Summary of Subsystem Major Technical Characteristics _____	2-2
Key Program Test Milestones _____	2-3
LCE Design Study Report Specific-Requirements Summary _____	2-4
Transmitter Assembly Performance Requirements _____	5.1.2-1
Local Oscillator and Back-up Laser Performance Requirements _____	5.1.2-2
Optical Components Misalignment Tolerances _____	5.1.2-3
FM Video Channel Performance Requirements _____	5.1.2-4
Acquisition and Tracking Channel Performance Requirements _____	5.1.2-5
Power Supply Power Output _____	5.1.2-6
Transceiver Commands _____	5.1.2-7
Telemetry Data _____	5.1.2-8
LCE Link Analysis, Operating Mode _____	5.1.3-1
Misalignment Tolerances for Optical Components _____	5.2.1-1
System Aberrations - Telescope/Relay Lens _____	5.2.1-2
Laser Subsystem Requirements _____	5.2.2-1
Transmitter-Modulator Design Parameters _____	5.2.2-2
Values Used in Power Calculation _____	5.2.2-3
Transmitter Laser Design Summary _____	5.2.2-4
Comparison of Modulation Techniques _____	5.2.2-5
GaAs Material Properties _____	5.2.2-6
Modulator Characteristics _____	5.2.2-7
Modulator/Modulator Driver Specifications _____	5.2.2-8
Typical Thermal Control Coating Radiometric Properties _____	5.2.3-1
Points to Describe "Wine Glass" Shape _____	5.2.3-2
Radiometric Properties of Thermal Control Surfaces Which Affect the Radiator/Sunshade Design _____	5.2.3-3
Solar Shape Factor and Diffusely Reflected Solar Energy Absorbed on the Radiator vs Orbital Position _____	5.2.3-4
Temperature of Antenna and Solar Panel for Various Positions in Orbit - Solstice _____	5.2.3-5
Sunshade Solar Shape Factor Summer Solstice Orbit _____	5.2.3-6

TABLES (cont.)

	<u>Table</u>
Radiator Solar Shape Factor Summer Solstice Orbit _____	5.2.3-7
Radiator Heat Loads at 180° Orbital Position Summer Solstice _____	5.2.3-8
Sunshield Heat Loads at 180° Orbital Position Summer Solstice _____	5.2.3-9
Projected Performance at High-Temperature Limit for OHRS Flight and Ground Models _____	5.2.4-1
Power-Supply Power Output Requirements _____	5.2.6-1
Allocated and Estimated Weights _____	5.4.1-1
LCE Power Demand for Various Modes _____	5.4.3-1
Spacecraft Transceiver Telemetry Requirements _____	5.4.3-2
Spacecraft Transceiver Command Requirements _____	5.4.3-3
AM Video Channel Performance Specifications _____	5.7-1
Characteristics of Weather Instrumentation _____	5.7-2
Star Carrier-to-Noise Ratios _____	5.7-3
Key Program Test Milestones _____	7-1
Testing Index _____	7-2
LCE Transceiver Models, Test Sequence Logic _____	7-3

ILLUSTRATIONS

	<u>Figure</u>
Laser Communication Concept _____	2-1
LCE Experiment Modes _____	2-2
Laser Communication Experiment Package _____	2-3
Spacecraft Ground Link Polarization Requirements Geometry _____	2-4
LCE Block Diagram _____	5.1.1-1
LCE Optical Path Schematic _____	5.1.1-2
Variation of NEP and CNR as a Function of Mixer Temperature _____	5.1.2-1
Tracking Block Diagram (Simplified) _____	5.1.2-2
Geometry of the Nutating Tracking System _____	5.1.2-3
Head-on View of Nutating Tracking System at Range R from the Tracker _____	5.1.2-4
Telescope Blockage _____	5.1.3-1
Transmitter Blockage Configuration _____	5.1.3-2
Atmospheric Attenuation Loss vs Zenith Angle _____	5.1.3-3
Signal Loss Due to Phase Tilt vs Mixer Displacement _____	5.1.3-4
Signal Power Within a Circle of Radius R_I in the Focal Plane as a Function of R_d/F _____	5.1.3-5
LCE Communications System _____	5.1.4-1
Spectra of Uniform Distribution with Random Phase _____	5.1.4-2
Second Order Spectrum Effects _____	5.1.4-3
Transmitted Spectrum _____	5.1.4-4
Vestigial-Sideband Spectrum _____	5.1.4-5
Phase Shift vs Frequency of Output Video Amplifier _____	5.1.4-6
Acquisition Subsystem Functional Block Diagram _____	5.1.5-1
Acquisition Subsystem Performance _____	5.1.5-2
Acquisition IF Filter Characteristics _____	5.1.5-3
Tracking Subsystem Functional Block Diagram _____	5.1.6-1
Relative Signal Amplitude from Detector vs Target Off-Axis Angle _____	5.1.6-2
Relative Position of Transmitter and Receiver Beam at Time of Acquisition _____	5.1.6-3
S/N of Error Signal vs Target Off-Axis Angle _____	5.1.6-4

ILLUSTRATIONS (cont.)

	<u>Figure</u>
Error Signal, S/N, vs Target Off-Axis Angle _____	5.1.6-5
LCE Tracking Servo System _____	5.1.6-6
LCE Optical Path Schematic _____	5.2.1-1
Spacecraft Ground Link Polarization Requirements Geometry _____	5.2.1-2
Mirror Assembly - Coarse Beam _____	5.2.1-3
Telescope Breadboard Model _____	5.2.1-4
Image Motion Compensator (IMC) Breadboard Model _____	5.2.1-5
LCE Base Plate Layout Pointing Layout _____	5.2.1-6
Optical Parameters of Telescope, Deflector Mirror, Relay Lens and IMC Mirror _____	5.2.1-7
Computer-Calculated Point-Spread Function for LCE Receiver - On-Axis Beam _____	5.2.1-8
Computer Calculated Point Spread Function for LCE Receiver - 0.2° Off-Axis Beam _____	5.2.1-9
Proposed Laser Subsystem Block Diagram _____	5.2.2-1
Metal/Ceramic CO ₂ Laser Tube which Passed LCE Qualification Level Vibration Tests _____	5.2.2-2
AFC Stabilization by Heterodyne Technique _____	5.2.2-3
Heterodyne Frequency vs Time for 70-Watt Laser Beating with Stable Reference Oscillator _____	5.2.2-4
Heterodyne Frequency vs Time for 70-Watt Laser Beating with Stable Reference Oscillator with AFC _____	5.2.2-5
Gallium Arsenide Modulator Operating at Brewster's Angle _____	5.2.2-6
Electrical Characteristics of the Straight-Through and Brewster Angle Geometrics for Gallium Arsenide _____	5.2.2-7
Laser Subsystem Breadboard Electronics Package _____	5.2.2-8
Laser Subsystem Breadboard Electronics (Cover Removed) _____	5.2.2-9
Breadboard Transmitter Laser _____	5.2.2-10
Output End of Laser Transmitter Showing Expansion Optics and Wavelength Selection Optics _____	5.2.2-11
Breadboard Local Oscillator Laser Showing Removable Mirror Adjustment Jig _____	5.2.2-12
Grating Mounted on Circular Bimorph Transducer _____	5.2.2-13
Power Flow in the Transmitter Modulator Subsystem _____	5.2.2-14

ILLUSTRATIONS (cont.)

	<u>Figure</u>
Transmitter Laser Modulator Input Power and Tube Length Requirements vs Modulator Length _____	5.2.2-15
Space-Qualified Laser Tube Assembly _____	5.2.2-16
Laser Tube Fabrication Flow Chart (Sheet 1 of 3) _____	5.2.2-17
Laser Tube Fabrication Flow Chart (Sheet 2 of 3) _____	5.2.2-18
Laser Tube Fabrication Flow Chart (Sheet 3 of 3) _____	5.2.2-19
Gallium Arsenide Modulator Crystal _____	5.2.2-20
Results of Intentionally Pulling Molybdenum Electrode from GaAs Crystal _____	5.2.2-21
GaAs Modulator Crystal, Breadboard Model _____	5.2.2-22
Components of In-Cavity Modulator Assembly _____	5.2.2-23
Laser Modulator Mounted in Transmitter Assembly _____	5.2.2-24
Modulator Driver _____	5.2.2-25
Schematic, Oven Temperature Controller _____	5.2.2-26
Angular Movement of Flat Mirror _____	5.2.2-27
Angular Movement of Spherical Mirror _____	5.2.2-28
Mirror Holder _____	5.2.2-29
Doubly Clamped Bimorph with Laser Mirror Mounted _____	5.2.2-30
Measurement of Circular Bimorph Linearity of Movement, Near Rest _____	5.2.2-31
Measurement of Circular Bimorph Linearity of Movement, Large Range _____	5.2.2-32
Power-Frequency Profile Breadboard Local Oscillator Laser _____	5.2.2-33
Optical Path within Cavity _____	5.2.2-34
V-I Characteristics of Experimental Discharge Tube _____	5.2.2-35
Transmitter Search and Dither AFC Block Diagram _____	5.2.2-36
Local Oscillator Block Diagram _____	5.2.2-37
Backup Laser Control Addition to L/O Control _____	5.2.2-38
Dither Loop _____	5.2.2-39
Offset AFC Loop _____	5.2.2-40
Receiver AFC Loop _____	5.2.2-41
LCE Radiator Temperature History _____	5.2.3-1
Radiator/Sunshade Mounting System _____	5.2.3-2

ILLUSTRATIONS (cont.)

	<u>Figure</u>
LCE Radiator Temperature vs Sunshade Radiator Flange Width _____	5.2.3-3
Stacked Radiator, One-Stage Sunshade _____	5.2.3-4
Single-Stage Radiator, Two-Stage Sunshade _____	5.2.3-5
Single Radiator, Single Sunshade _____	5.2.3-6
Volume Envelope for Sunshield _____	5.2.3-7
Conical Sunshade _____	5.2.3-8
Two Methods of Scarfing Sunshade _____	5.2.3-9
ATS/FG Satellite Earth-Sun Orientation _____	5.2.3-10
Laser and Radiometer Cooler Locations and Separation Clearance Requirements _____	5.2.3-11
Sunshade - Wine Glass _____	5.2.3-12
Interface Control _____	5.2.3-13
Sketch of Radiator and Sunshield to Determine Height _____	5.2.3-14
Schematic of How Wine Glass Surface Reflects Energy _____	5.2.3-15
Wine Glass Shape _____	5.2.3-16
Wine Glass Area _____	5.2.3-17
General Configuration: Radiator Detector Housing _____	5.2.3-18
Mixer-Receiver _____	5.2.3-19
Radiator and Sunshield Temperature vs Support Temperature to Get 0.0005-in. Gap Separation _____	5.2.3-20
Relationship of Spacecraft, LCE, Detector/Mixer Sunusoidal Qualification Vibration Levels _____	5.2.3-21
LCE Sunshade Temperature History _____	5.2.3-22
Optical Heterodyne Receiver Subsystem Block Diagram _____	5.2.4-1
Region of Optimum Mixer Operation _____	5.2.4-2
Measured and Extrapolated NEP vs LO Power (Noise Measurement at 300 kHz) in Photovoltaic (Hg,Cd)Te _____	5.2.4-3
Mixer Noise Voltage vs IF Frequency in Photovoltaic (Hg,Cd)Te _____	5.2.4-4
Calculated Quantum Noise Limited Receiver Sensitivity vs Quantum Efficiency at 10.6 Microns _____	5.2.4-5
Quantum Efficiency vs Temperature in Photovoltaic (Hg,Cd)Te _____	5.2.4-6
Noise Equivalent Power vs Temperature in Photovoltaic (Hg,Cd)Te _____	5.2.4-7

ILLUSTRATIONS (cont.)

	<u>Figure</u>
Subcontract Minimum Quantum Efficiency vs Mixer Temperature _____	5.2.4-8
Quantum Efficiency vs Mixer Temperature vs PV (Hg,Cd)Te _____	5.2.4-9
Effective IF Noise Temperature vs Cable Loss _____	5.2.4-10
Detector Model A Envelope Drawing _____	5.2.4-11
Detector Model B Envelope Drawing _____	5.2.4-12
Detector Housing and Adapter Assembly Installation Control Drawing _____	5.2.4-13
Receiver Electronics Noise Factor vs First Stage Gain with Second Stage Noise Figure as a Parameter _____	5.2.4-14
Variation of Amplifier Noise Factor with IF Frequency _____	5.2.4-15
Variation of Noise Factor with Source Resistance _____	5.2.4-16
Calculated Response to 30 MHz Channel Filter (High Rejection) _____	5.2.4-17
Calculated Response of 20 MHz Channel Filter _____	5.2.4-18
Calculated Group Delay vs Frequency of Noise Filter _____	5.2.4-19
Calculated Response of 30 MHz Channel Filter Low Delay Distortion _____	5.2.4-20
Calculated Combined Group Delay vs Frequency of Noise Filter and Channel Filter _____	5.2.4-21
Calculated Response of Video Filter _____	5.2.4-22
Noise Figure of IF Preamplifier for Various Matching Conditions _____	5.2.4-23
AGC Characteristics of IF Amplifier, AGC Detector, and DC Amplifier in Closed Loop Operation _____	5.2.4-24
Measured Power Limiting Characteristics of 20 MHz Limiter _____	5.2.4-25
Frequency Response of Limiter _____	5.2.4-26
Phase Shift vs Frequency of Limiter Circuit _____	5.2.4-27
Measured Discriminator Output vs IF Frequency _____	5.2.4-28
Discriminator Output Voltage vs Frequency with Input Power as a Parameter _____	5.2.4-29
Discriminator Output Voltage vs Frequency with Load Resistance as a Parameter _____	5.2.4-30
Phase Shift vs Frequency of Video Amplifier _____	5.2.4-31
Power-Output Capability of Video Amplifier _____	5.2.4-32
Frequency Response of Tuned Audio Amplifier in Tracking Error Channel _____	5.2.4-33

ILLUSTRATIONS (cont.)

	<u>Figure</u>
Phase Detector Output Voltage vs Percent Amplitude Modulation _____	5.2.4-34
Mixer Bias Circuit Characteristics _____	5.2.4-35
Block Diagram of Acquisition Sequence _____	5.2.5-1
Block Diagram for Mirror Command System _____	5.2.5-2
Block Diagram for Coarse Pointing Mirror Motor Drive System _____	5.2.5-3
Block Diagram for Search Generator _____	5.2.5-4
Block Diagram for Center IMC Function _____	5.2.5-5
LCE Power Supply Block Diagram _____	5.2.6-1
Proposed LCE Power Supply Configuration _____	5.2.6-2
Experimental Discharge Tube with Variable Anode Position Capability _____	5.3.1-1
Anode-Cathode Voltage vs Distance _____	5.3.1-2
Experimental Discharge Tube Used to Measure Cathode Discharge Area _____	5.3.1-3
Pressure and Partial Pressure vs Time in Two Discharge Tubes _____	5.3.1-4
Life Test Program Schedule _____	5.3.1-5
Wire Grating on Dielectric Substrate _____	5.3.2-1
Wire Grating Performance at $\lambda/d = 4$ _____	5.3.2-2
Wire Grating Polarizer Performance Without $\lambda/4$ Coating _____	5.3.2-3
Transmission of a Polarizer on a Polyethylene Substrate, $a = 4.2\mu$ and $d = 10\mu$ _____	5.3.2-4
FTIR Polarizers _____	5.3.2-5
Duplexer Program Plan _____	5.3.2-6
Dummy Support Assembly Attached to Electrical Heater and Flowmeter _____	5.3.3-1
Development and Testing Schedule (Support System) _____	5.3.3-2
Test Instrumentation _____	5.3.3-3
Test Schedule _____	5.3.3-4
AGC Laser Spacecraft Interface Control Drawing _____	5.4.1-1
Atmospheric Loss vs Zenith Angle _____	5.7-1
Carrier-to-Noise Ratio vs Receiver Equivalent Noise Power _____	5.7-2

ILLUSTRATIONS (cont.)

	<u>Figure</u>
Reliability Diagram, LCE Spacecraft Transceiver _____	6-1
Reliability Diagram, Acquisition and Tracking Subsystem _____	6-2
Reliability Diagram, Optical Subsystem _____	6-3
Reliability Diagram, Laser Subsystem _____	6-4
Reliability Diagram, Receiver Subsystem _____	6-5
Reliability Diagram, Power Supply Subsystem _____	6-6
Breadboard Test Chart _____	7-1
FIM Test Flow Chart _____	7-2
Prototype Test Flow Chart _____	7-3
Flight Test Flow Chart _____	7-4
Laser Subsystem Testing at Sylvania _____	7-5
Receiver Subsystem Testing at ALL _____	7-6
Test Setup No. 1 _____	7-7
Test Setup No. 2 _____	7-8
Test Setup No. 3 _____	7-9
Test Setup No. 4 _____	7-10
Test Setup No. 5 _____	7-11

1.0 INTRODUCTION

The ATS-F Laser Communications Experiment (LCE) is the first significant step in the application of laser systems to space communications. The space-qualified laser communications system being developed in this experiment, and the data resulting from its successful deployment in space, will be applicable to the use of laser communications systems in a wide variety of manned as well as unmanned space missions, both near earth and in deep space. Particular future NASA missions which can benefit from this effort are the Tracking and Data Relay Satellite System and the Earth Resources Satellites.

The LCE had its origin in a report written in 1965 by McAvoy,¹ who pioneered the application of carbon dioxide laser systems in space. This early report showed the desirability of 10.6-micrometer (28 THz) communications systems for space communications, particularly for interplanetary missions. A more recent and direct precursor of the LCE is a report by McAvoy, et al.,² which describes in depth the feasibility of developing a 10.6-micrometer laser communications system for use in performing satellite-to-ground and satellite-to-satellite communications experiments. This report led to the decision to initiate the development of the LCE.

The LCE makes use of carbon dioxide lasers to establish simultaneous, two-way communication between the ATS-F synchronous satellite and a ground station. In addition, the LCE is designed to permit communication with a similar spacecraft transceiver proposed to be flown on ATS-G, nominally one year after the launch of ATS-F. This would be the first attempt to employ lasers for satellite-to-satellite communications.

¹McAvoy, N., "10.6 Micron Communication System" NASA TM X-524-65-461, Goddard Space Flight Center, Greenbelt, Md., Nov. 1965

²McAvoy, N., H. E. Richards, J. H. McElroy, and W. E. Richards, "10.6-Micron Laser Communications System Experiment for ATS-F and ATS-G," NASA TM S-524-68-206, Goddard Space Flight Center, Greenbelt, Md., May 1968

This Design Study Report for the LCE was prepared by the Aerojet-General Corporation under Contract NAS 5-21072. This prime contract for the LCE was awarded to Aerojet on 7 January 1970 by the NASA Goddard Space Flight Center (GSFC). Major subcontractors are Sylvania Electronic Systems for the laser subsystem and Airborne Instruments Laboratory, a Division of Cutler-Hammer, for the optical receiver subsystem.

The Aerojet prime contract covers the development and fabrication of the LCE spacecraft equipment and the LCE ground equipment necessary for the performance of the experiment. The LCE Specification GSFC-S-524-P-46, "10.6-Micron Laser Communications System Experiment for ATS-F," is used as a design basis. The deliverable hardware end items (and approximate delivery dates) consist of:

- (1) A prototype model (fall of 1971);
- (2) A flight model (late in 1971);
- (3) A flight spare model (early in 1972);
- (4) Ground equipment (late in 1971);
- (5) Two spacecraft integration test consoles (fall and winter of 1971); and,
- (6) A thermal/structural model of the spacecraft transceiver (optical transmitter and receiver, fall of 1970).

In addition, a breadboard model is being fabricated and tested to verify the concepts of the LCE design (summer of 1970), and a functional test model (a non-deliverable pre-prototype model) will be fabricated and tested to prove the performance capability and environmental integrity of the LCE system and to aid in identifying potential problems prior to fabricating the prototype model (winter of 1970-71). It is presently planned that (1) the breadboard will be refurbished for use as a ground calibration unit, (2) the FTM will be refurbished for use as the ground equipment transceiver, and (3) the prototype will be refurbished for use as a flight spare.

Major software deliverable end items under Contract NAS 5-21072 include:

- (1) This Design Study Report
- (2) A Thermal Math Computer Model (fall of 1970)
- (3) A Maintenance and Operations Manual (summer of 1971)
- (4) An Experiment Handbook (spring of 1971)
- (5) Final Report

Volume I of this report deals with the spacecraft transceiver, by far the most critical design element for the experiment. Part 1 of this volume is divided into three parts; Part 1 contains the basic design study material; Part 2 contains the results of detailed analyses and data in support of the arguments presented in Part 1; and Part 3 is a compilation of LCE design specifications prepared by Aerojet. The Operational Ground Equipment (OGE), Data Acquisition Plan, and Data Processing, Reduction, and Analysis Plan will be discussed in a second volume (to be delivered in late fall of 1970). This report complies with the Design Study Report requirements of the LCE Specification GSFC-S-524-P-4C and of the ATS-F experiments Specification GSFC-460-ATS-19, to which it refers.

At the time of the preparation of this report (July 1970) the LCE spacecraft transceiver is undergoing detailed design of the deliverable units. In addition, a nondeliverable breadboard is being constructed; fabrication of subsystems has been completed with the completion of breadboard system assembly expected by the end of July 1970 and completion of breadboard system testing during September 1970. With GSFC concurrence, a few long-lead components and parts have been ordered for a functional test model, a nondeliverable pre-prototype unit.

REPRODUCIBILITY OF THE
ORIGINAL PAGE IS POOR

2.0 SUMMARY

2.1 INTRODUCTION

The purpose of the ATS Laser Communications Experiment as stated in the system specification is to ascertain the practicality of wideband communications between the spacecraft and the ground station and between two orbiting spacecraft using the 10.6-micrometer radiation from a carbon dioxide laser, and to establish the resulting efficiency that can be effected in terms of communication bandwidth per pound on the spacecraft. In order to meet this objective, a number of experiments and measurements will be conducted on a two-way laser communication link between the ATS-F satellite and a ground station. In addition, the LCE is designed to permit communication with a similar spacecraft transceiver proposed to be flown on ATS-G, nominally one year after the launch of ATS-F. These include measurement of signal-to-noise ratio as a function of system and environmental parameters and the measurement of data quality compared to a reference microwave link, in various modes of operation.

The design report describes in detail the systems analyses, system and subsystem specifications, hardware design, design analyses and determined fabrication techniques that will result in the flight transceiver. In particular:

(1) Detailed analyses, in terms of the system requirements and required modes of operations, have been performed and have resulted in system and subsystem performance and design specifications for a transceiver which will perform the experiments necessary to achieve the required objective.

(2) Detailed analyses and trade studies of the various technical approaches for each subsystem designs have been performed.

(3) Designs of the subsystems have been made. In most cases, the detailed design must still be completed, but it is considered that the designs are at an excellent point for a meaningful review.

REPRODUCIBILITY OF THE
ORIGINAL PAGE IS POOR

(4) Detailed analyses of the designs have been performed to ensure that they meet, or can be modified to meet, the determined specifications and interface requirements and that the hardware can be fabricated. Where required, the necessary fabrication techniques and equipment are being assembled.

(5) Detailed investigations of all critical technical areas have been performed and have either (a) verified the analyses and assumptions in the system/subsystem designs and design fabrication or (b) increased the understanding to the point where the validity of the design and/or fabrication technique is proven so that the LCE requirements can be satisfied. For the latter areas, further developmental, experimental and/or analytical efforts are continuing as described herein. Final results are expected in accordance with the program schedule.

(6) A test program, which includes informal engineering functional and environmental tests and formal qualification and acceptance tests, has been detailed with the intent to uncover problem areas and to prove out the designs at the earliest possible date.

(7) All breadboard subsystems have been fabricated. Testing to date has not disclosed any major problems. Final assembly of the breadboard is being performed.

Certain critical technical areas were identified early in the program and the goal has been to resolve these technical uncertainties as soon as possible through analyses and testing. Both program planning and test planning have been directed toward the early identification of additional potential problem areas.

2.2 SYSTEM CONCEPT

A simplified block diagram illustrating the system concept is shown in Figure 2-1. The LCE transceiver, mounted on the ATS-F spacecraft operating in a synchronous orbit, will maintain two-way communication with a similar transceiver located at the ATS-F ground station. The spacecraft transmitter

will transmit FM signals on one line (P20) of the 10.6 micron CO_2 laser spectrum with N-S polarization and will receive similar signals from the ground station on another line (P16) with E-W polarization. In the spacecraft, the signal to be transmitted can be either taken from the LCE receiver output or from the spacecraft communication system. This permits operation in any of the four modes shown in Figure 2-2. In the Atmospheric Propagation mode, the unmodulated carriers of both transmitters are received at the opposite station and signal strengths can be measured. In the Two-way Laser Communication mode, the signal transmitted to the satellite will be re-transmitted back to the ground and compared with the same signal transmitted via a microwave link. In the Down-Link Laser mode, the one-way laser signal will be compared with the microwave link. In the Data Relay mode, signals received at the satellite from a low-altitude satellite on an S-band link will be relayed to the ground station via the laser link.

2.3 SYSTEM DESCRIPTION

A perspective view of the LCE spacecraft transceiver is shown in Figure 2.3 and a schematic of the spacecraft/ground station geometry is shown in Figure 2-4.

The baseplate of the experiment will be mounted on the north face of the ATS spacecraft with the beam-pointing mirror housing facing the earth. A viewing port in this earth-facing side of the spacecraft will accommodate the beam-pointing angles of $\pm 40^\circ$ E/W and $\pm 8^\circ$ N/S. This capability will permit the LCE transceiver to communicate not only with a ground based station with allowance for spacecraft attitude variations, but will also allow communication with another satellite-borne transceiver (e.g., on ATS-G). Below the coarse beam-pointing mirror is the Cassegrain telescope which functions as the optical antenna of the system. Energy received from the remote station is collected and relayed by means of the telescope and relay lens to the Image Motion Compensator (IMC) as a .78 in collimated beam. From the IMC, the received beam, is reflected from rather than transmitted through a

duplexer, due to its E-W polarization, and is focused onto the detector or optical mixer of the receiver. The IMC performs the function of tracking the remote station so that the image of the energy from this station is always maintained on the detectors. The signals for controlling the IMC are derived by nutating the image of the received beam in a very small circular pattern on the detector. This nutation produces a small amount of amplitude modulation on the received signal which is detected in the receiver subsystem and used to generate the control signals for the IMC. The detector is also illuminated by energy from a LO laser operating on the same line as the remote transmitter but offset by 30 MHz. The beating of these two optical signals produces a 30 MHz IF signal at the output of the detector. The detector depends for proper operation on being maintained at approximately 110°K. This temperature is achieved by mounting the detector in such a way as to provide thermal contact with a passive radiator which has a view to space. The radiator is mounted facing north and is surrounded by a sunshield. This will prevent any direct or reflected solar radiation or infrared radiation from other portions of the spacecraft from impinging on the radiator through any combination of a sun angle and spacecraft attitude. The IF signal from the detector is amplified and detected in the optical receiver and appears at the receiver output as a video signal which can either be fed to a spacecraft microwave link or used to modulate the laser transmitter.

In addition to providing local oscillator power for heterodyne detection of the received signal, the laser subsystem contains the transmitter and backup lasers. The transmitter laser, operating on a frequency different from that of the remote transmitter, contains within its cavity a gallium-arsenide crystal modulator which frequency modulates the transmitter with the video signal input. The transmitter output, which is polarized in the N-S direction, is processed by beam shaping optics and transmitted through the duplexer. From this point on, the transmitted and received beam share the same optical path. The transmitted beam is reflected from the IMC which, in the process of tracking the receiving station, serves to maintain

the transmitted beam also pointed at the remote station. From the IMC, the transmitted beam goes through the relay lens and the telescope and is reflected from the coarse beam pointing mirror. The backup laser can function either as a replacement for the local oscillator or the transmitter except that, when acting as a transmitter, the backup laser cannot be modulated. The laser electronics performs the startup and frequency control functions for the lasers; another electronic assembly controls the function of searching, acquiring, and tracking the remote station. A power supply for the system is also located on the baseplate near the lasers.

A summary of the system specifications pertaining to the LCE transceiver described in this report is given in Table 2-1, which also lists the relative values cited in specification GSFC-S-524-P-4C. The two areas of present concern are power and weight. The values in the GSFC specification were listed as design goals and the values in parentheses represent adjustments made after the program start, subsequent to discussions with GSFC personnel. Both power and weight reduction programs are presently under way. Several areas of potential reduction are discussed in the report.

A summary of the major technical design and performance characteristics of the LCE transceiver subsystems is given in Table 2-2.

2.4 SIGNIFICANT TECHNICAL ACHIEVEMENTS

Fabrication of all the breadboard subsystems has been completed and breadboard systems assembly is being performed. Several critical design concepts have already been verified and some of the subsystem performance parameters have been demonstrated by breadboard testing.

During acceptance testing of the laser subsystem breadboard, the following critical performance features were demonstrated:

- (a) Automatic laser startup and laser line selection
- (b) Frequency stabilization by line center dither technique
- (c) Modulator deviation sensitivity and bandwidth requirements

- (d) Local oscillator line shape and a 30-MHz offset capability
- (e) Heterodyne detection of transmitted beam
- (f) Ability of a backup laser to operate on either transmitter or local oscillator lines

Fabrication of the breadboard optical path elements, including telescope, (similar in design to the flight model and made of aluminum rather than beryllium) indicates its performance is well within specification. Preliminary testing of the breadboard acquisition and tracking subsystem has shown expected performance.

- Preliminary testing of the breadboard receiver has demonstrated
- (1) the ability to generate the necessary tracking error signals by nutating the received beam;
 - (2) adequate performance of the receiver communication functions for the LCE requirements.

Many analyses have been completed in order to define the detailed specifications for the subsystems of the LCE. Some of the more important of these are:

- (a) the optical train analysis which has specified the key performance parameters and tolerances for each optical component in the LCE;
- (b) the thermal analysis which has optimized the design of the thermal radiator and sun shield;
- (c) the acquisition analysis which has established the essential acquisition technique and determined the acquisition parameters;
- (d) the tracking analysis which has optimized the performance of the tracking loop;
- (e) the communications analysis which has optimized the transmitter and receiver communication parameters;
- (f) the link analysis which has determined and allocated gains and losses in the system such that the signal-to-noise ratio requirements of this system are satisfied.

REPRODUCIBILITY OF THE
ORIGINAL PAGE IS POOR

Each of these accomplishments has increased our confidence in the ability of the LCE to meet its objectives. Of course, there are additional milestones which must be achieved before complete confidence is established. A list of the key technical milestones and the tests at which the designs will be completely verified is given in Table 2-3. As the table indicates, the testing plan is intended to uncover problem areas and prove out designs at the earliest possible date. Of particular importance, is the use of the functional test model as a pre-prototype unit in order to minimize the possibility of the prototype failing to pass the qualification test.

Certain areas still require final resolution, although the results of analytical, experimental, and design efforts to date have created a high level of confidence that the present solutions will satisfy the LCE requirements. In particular, these include (1) the laser tube lifetime characteristics, (2) fabrication of the duplexer, and (3) design and fabrication of the radiation cooler. Final development programs, described in the reports, are continuing on an intensive level and final resolution is expected in all these areas before FTM assembly.

2.5 REPORT CONTENTS

The objectives of the experiment and the manner in which these are to be met are discussed in Section 3. A statement of the system performance requirements as outlined in the system specification follows in Section 4. In Section 5, the proposed system design is described in detail. In particular, this section includes the system description and a summary of the system analyses in Section 5.1; detailed descriptions of the subsystem requirements, design trades, designs and analyses in Section 5.2; discussions of the technical design areas in which development is still required and a description of the continuing development program in Section 5.3; detailed discussions and descriptions of the interfaces between the spacecraft and the experiment in Section 5.4; discussions relative to the feasibility of incorporating the experiment in ATS-F spacecraft in Section 5.5; while Section 5.6 discusses the

REPRODUCIBILITY OF THE
ORIGINAL PAGE IS POOR

experiment operation under non-standard conditions; and, quantitative discussions of the ability of the experiment to perform the required measurements in Section 5.7. Section 6 is a reliability discussion wherein the reliability requirements, criteria for success, and predictions relative to the probability of meeting mission requirements are discussed. The discussion shows that the LCE spacecraft transceiver is capable of meeting the reliability requirements allocated to it. Section 7 discusses the test plans for the LCE program, and includes flow diagrams and detailed test outlines for each of the hardware units. Further details of the designs and analyses are included in the Appendices (Part 2 of Volume I) and in the LCE design specifications (Part 3 of Volume I).

As stated in the introduction, this report was prepared in conformance with the requirements of NASA Specification S-460-ATS-19, GSFC's specification for ATS-F experiments, design study, and fabrication; and additional requirements contained in GSFC specification S-524-P-4C "10.6 Micron Laser Communications Systems Experiment for ATS-F." These specifications emphasized the fact that contents rather than format is the main concern. However, in order to assure that all of the requirements are covered, Table 2-4 supplies a cross-reference between the requirements of the two specifications and the sections in this report. It should be noted that all of the requirements listed have an accompanying reference to a section of this report except for those dealing with the Operational Ground Equipment (OGE), Data Acquisition Plan, and a Data Processing and Reduction Analysis plan. These requirements will be discussed in Volume II of this report.

REPRODUCIBILITY OF
ORIGINAL PAGE IS POOR

2.0 SUMMARY

There are no major modifications to this section. The status of the program at the time of termination is described in the modifications summary to Section 1.0. The systems concept is the same. Modifications to the system description, where appropriate, are presented in the modifications summary of the sections; the only items of note are the LCE power and weight, which increased to about 70 watts and 80 lbs, respectively. Additional technical achievements include: near-completion of the duplexer development, including satisfactory test data on preliminary hardware; design of a radiation cooler which appeared to meet the LCE requirements (hardware development testing was in progress); and satisfactory operation of the image motion compensator had been demonstrated. The major remaining uncertainty at the time of termination appeared to be the laser tube design and its associated lifetime; in addition, a few design concepts still required manifestation in hardware fabrication and test. On the other hand, a great increase in the understanding of laser tube design characteristics and lifetime parameters had been achieved.

In order to present an up-to-date picture of the design and analysis status at the time of termination, this report contains either (1) an additional summary at the end of each section or (2) handwritten corrections in the text of the major modifications of the data presented in those sections that were incorporated since the initial writing of this report. No attempt is made to detail the modifications nor the analysis that went into the changes, but in some cases figures are included for illustration. Further understanding and detail of the design can be obtained by review of the viewgraphs for the second LCE Design Review of 9 and 10 September 1970. In addition, a copy of the action items generated during the 5-6 August 1970 Design Review with NASA/GSFC personnel, along with the Aerojet responses, is included at the end of Part 2.

REPRODUCIBILITY OF THIS
ORIGINAL PAGE IS POOR

TABLE 2-1

LCE TRANSCEIVER SYSTEM SPECIFICATIONS

Parameter	Expected Performance	OSFC-S-524-P-4C
Transmitter Beamwidth		
(1) Operational	1 arc second	Not specified
(2) Acquisition	0.177 seconds	Not specified
Receiver Beamwidth	30 arc seconds	Not specified
Pre-Detection Carrier-to-Noise Ratio (CNR)	Not less than 23 db	Same
Post-Detection Peak Signal-to-Noise Ratio (P/N)	Not less than 33 db	23 db
Modulation	FM	Same
Peak Frequency Deviation	4 MHz	Not specified
Receiver IF Bandwidth	30 ±6 MHz	Not specified
Baseband Response		
(1) Spaceborne transceiver	30 Hz to 4.6 MHz	30 Hz to 5.0 MHz
(2) Ground transceiver	1.0 to 6.0 MHz	30 Hz to 5.0 MHz
Flux Density at Receiver Aperture	10^{-10} watts/meter ²	10^{-9} watts/meter ²
Coarse Mirror-Pointing	Range: ±40° E-W, ±20° N-S Pointing in 0.2° increments each axis	Same
Acquisition	Target Location Coverage: ±0.2° each axis Acquisition Probability: 0.9 False-Alarm Time: 1100 seconds Acquisition Time: 220 seconds	Meets intent of specification
Acquisition Tracking	Tracking Range: ±0.206° each axis Nutation Radius: 8 arc seconds	Meets intent of specification
Operational Tracking	Tracking Range: ±0.206° each axis Nutation Radius: 1.5 arc sec Tracking Accuracy: ±3 arc sec Tracking Bandwidth: 5.1 Hz Response Time: 0.11 seconds	Meets intent of specification
Prime Power	57.3 watts*	30 watts (~42 watts)†
Weight	69.6 lb*	30 lb (53.7 lb)†
Size	30 in x 24 in x 16 in plus radiation cooler shield, satisfies ATS interface requirements	Meets intent of specification
Lifetime	2000 hr in 2 years at 90% probability of success	Meets intent of specification
Environment		
(1) Temperature	Qualification -5°C to 45°C Nominal S/C LCE interface Temperature 20° to 110°C	Meets intent of specification
(2) Vibration	To withstand ATS environment specified in OSFC S-320-ATS-2A	

*Details of these values are given in Sections 5.4.4 and 5.4.3. Reduction programs are under way.

†Stated as design goals in specification. Numbers in parenthesis are adjusted values generated after program start after discussions with NASA personnel.

TABLE 2-2

SUMMARY OF SUBSYSTEM MAJOR TECHNICAL CHARACTERISTICS

Laser Subsystem

Transmitter Laser Power Output:	650 mw at end of 2-year life
LO Laser Power Output:	85 mw at end of 2-year life
Back-Up Laser Power Output:	650 mw at end of 2-year life
Laser Output Beam Characteristic:	3.0 \pm 0.12 mm beam diameter between $(\frac{1}{e})^2$ relative power levels, diffraction limited, collimated beam
Laser Tube Type:	3-electrode, coaxial, metal-ceramic tube
Transmitter Laser Length:	12.5 in.
Back-Up Laser Length:	10 in.
LO Laser Length:	9 in. long
Laser Tube Key Material:	BeO, Kovar
Operating Lines:	P(20) and P(16)
Modulator:	In-cavity GaAs electro-optic modulator
Peak Frequency Deviation:	4 MHz

Opto-Mechanical Subsystem

Telescope Type:	Cassegrain concentric
Telescope Power:	10x
Telescope Primary:	7.75 in.
Transmitter Beamwidth (Operate):	12 $\overline{\text{sec}}$ between 3 db points
Transmitter Beamwidth (Acquisition):	.178 degrees between 3 db points
Receiver Beamwidth:	30 $\overline{\text{sec}}$ between 3 db points
Duplexer:	Wire grid polarizer on Ge substrate
IMC:	Piezoelectric driven mirrors in two orthogonal axes, up to 2° off-axis motion
Nutator:	Piezoelectric driven mirror in two orthogonal axes, to circularly nutate the received beam at 100 Hz rate
Received Signal Airy Disk Diameter:	.17 mm
LO Airy Disk Diameter:	.64 mm between $(\frac{1}{e})^2$ of power points

Optical Heterodyne Receiver Subsystem

NEP:	1×10^{-19} watts/Hz (95-108°K); 1.5×10^{-1} watts/Hz (125°K with a design goal of 10-
Mixer Diameter:	0.2 mm
IF Bandwidth:	30 \pm 6 MHz
Automatic Gain Control Dynamic Range:	12 db
Output Video Level:	1 volt peak-to-peak \pm 0.5 db

TABLE 2-2 (cont.)

Acquisition and Tracking Subsystem

Target Location Coverage:	+0.2" each axis
Acquisition Probability:	0.9
False Alarm Time:	1100 sec
Acquisition Time:	220 sec
Receiver Beam Scan Pattern	
Consecutive Line Displacement:	11.6 arc sec
Line Rate:	1.72 sec/line
Acquisition Tracking	
Tracking Range:	+208° each axis
Nutation Radius:	8 arc sec
Operational Tracking	
Tracking Accuracy:	+3 arc sec
Tracking Bandwidth:	5.1 Hz
Response Time:	0.11 sec
Nutation Radius:	1.5 arc sec

High Voltage and Low Voltage Power Supply

Transmitter Laser Starting and Operating Power:	2000 V
Back-Up Laser Starting and Operating Power:	2000 V
LO Laser Starting and Operating Power:	800 V
Nutator, IMC, and Cavity End-Mirror Tuner Power Supply:	225 V
Low Voltage Power Supply:	+12 V, + 5 V

Command and Telemetry

Number of Commands:	33 commands; 4 of these commands will consist of a series of pulses
Number of Analog Telemetry Channels:	31 channels, max bandwidth 10 Hz
Number of Digital Telemetry Channels:	2 channels
Wideband Telemetry Channels:	1 channel, 10 KHz bandwidth

Thermal and Radiation Cooler Subsystem

Mixer Temperature Range:	110 \pm 15°K { summer solstice 114°K, +10° un- winter solstice 98°K (certainty)
Maximum Electronic Component Temperature:	60°K at highest spacecraft LCE inter- face temperature

KEY PROGRAM TEST MILESTONES

ITEM	DESCRIPTION
Breadboard Testing	Verifies the validity of the design concepts and determines the parameters for use in further optimization of system design. System level testing in conjunction with approval of the design report, will serve as the basis for FTM assembly. Several functional design concepts will be verified during subsystem level testing.
Functional Test Model Testing	Serves to prove the performance capability, environmental integrity, and interface compatibility of the LCE transceiver and to aid in early identification of potential problems that may prevent the prototype from passing qualification tests. The FTM will be fabricated as close to the flight-model design as is possible at that stage of development. System level testing will be the basis for prototype and flight model assembly. Several function and environmental design concepts will be verified during subsystem-assembly level testing.
Prototype Testing	Qualifies the flight model design. Several of the subsystems will be qualified before system assembly.

FUNCTION	TESTING PERIOD
<u>Laser Startup and Stabilization</u> Demonstrate startup operation and automatic line selection	Breadboard Subsystem*/System Tests
Demonstrate Amplitude and frequency stability	Breadboard* (Invar baseplate) and FTM Subsystem/System Tests (CERVIT baseplate)
<u>Acquisition and Tracking</u> Demonstrate DM and nutator performance	Breadboard Subsystem*/System Tests
Demonstrate course pointing mirror performance	FTM Subsystem/System Tests
Demonstrate acquisition and tracking subsystem performance	Breadboard System Tests
<u>Communications</u> Achieve required transmitter and local oscillator power output	FTM Subsystem/System Tests
Determine transmitted and received antenna patterns	Breadboard and FTM System Tests (Telescope design changed from Breadboard to FTM)
Demonstrate modulator performance	Breadboard* and FTM Subsystem/System Tests (Modulator design may change from Breadboard to FTM)
Demonstrate receiver sensitivity	FTM Subsystem/System Tests
Demonstrate receiver performance	Breadboard System Tests
<u>Radiation Cooler Performance & Environmental Effects</u> Demonstrate Ability to Withstand Vibration	Development Tests on Structural Model of Radiation Cooler and during FTM System Tests
Demonstrate Cooling Performance in Thermal Vacuum	Development Tests on Structural Model (comparison to predicted values for rough sunshield surface) and during FTM Subsystem Tests
<u>Laser Performance & Environmental/Life Effects</u> Achieve required transmitter, local oscillator, and backup laser efficiencies	FTM Subsystem/System Tests
Achieve 2000 hours life on ceramic laser tube	Basic Laser Tube Life Test Program performed in conjunction with FTM development
Demonstrate experimentally lifetime reliability of flight configured Laser tubes	Extended Laser Tube Life Test Program (proposed) performed in conjunction with FTM development and completed prior to Prototype System delivery
Demonstrate ability of Laser tubes to withstand vibration	Breadboard development tests*, Basic Laser Tube Life Test Program and FTM System Tests
<u>Mirror Performance and Environmental Effects</u> Demonstrate ability of mirror to withstand vibration	Development tests performed in conjunction with FTM development and during FTM Subsystem/System Tests
Achieve required MEP over operating temperature range	Development tests performed in conjunction with FTM and prototype development and during Prototype Subsystem/System Tests.
<u>Additional Environmental/Life Effects</u> Demonstrate ability to maintain alignment	FTM Subsystem/System Tests
Demonstrate coarse pointing mirror assembly ability to withstand vibration and vacuum life performance	Assembly qualification level and life tests to be performed in conjunction with FTM development and completed prior to Prototype Subsystem delivery

*Completed

Table 2-3

Report No. 4033, Vol. I, Part I

Report No. 4033, Vol. I, Part 1

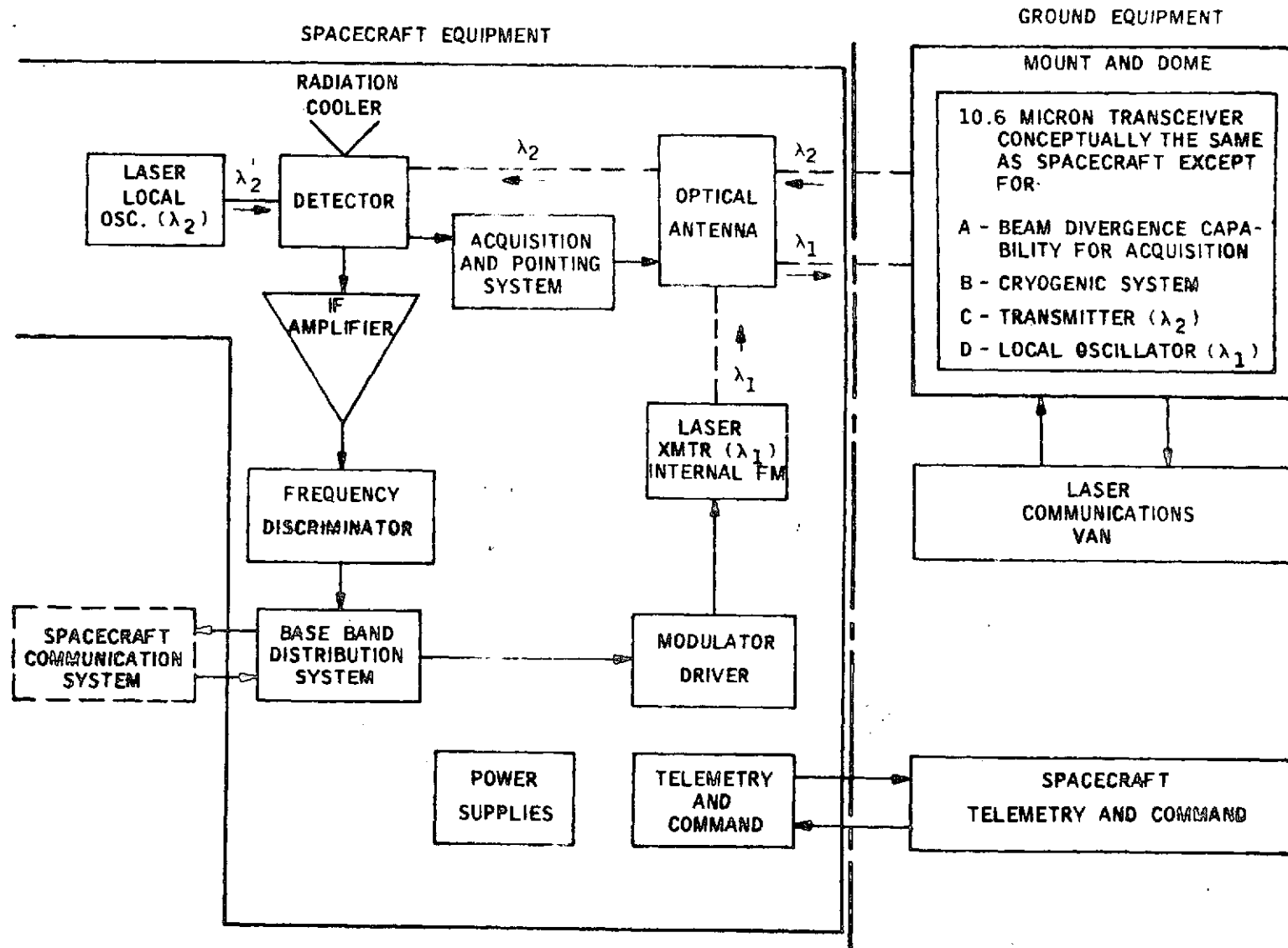
TABLE 2-4

LCE DESIGN STUDY REPORT SPECIFIC-REQUIREMENTS SUMMARY

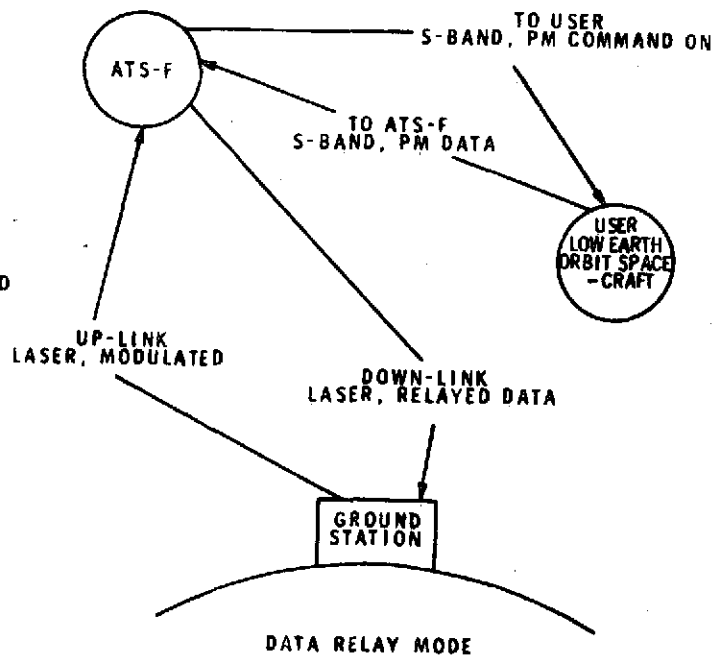
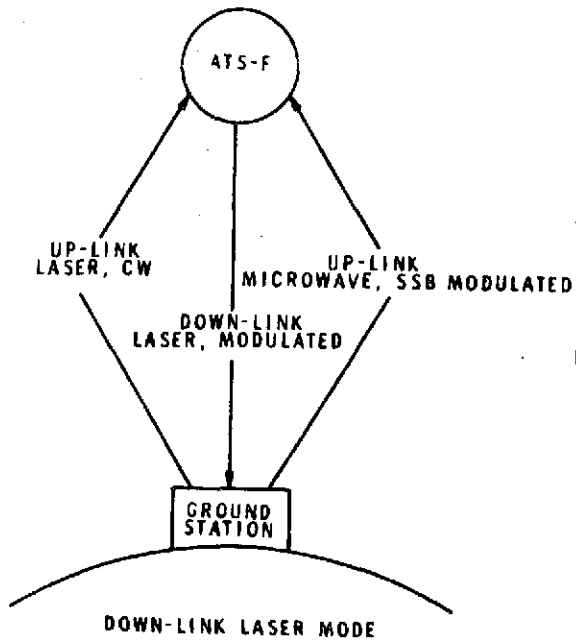
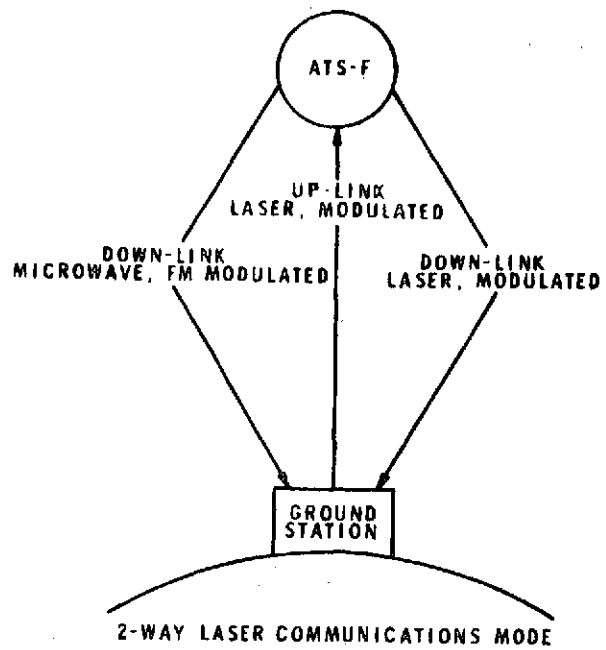
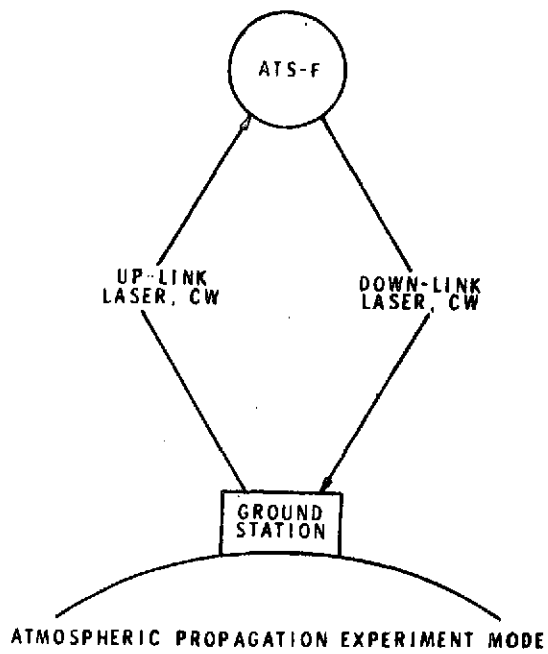
Specific Requirements		Results	
GFSC Spec./Sect.	Description	Detailed in Sec.	Comments
S-460-ATS-19/ 3.1	Define experiment objectives	3.0	Based on GFSC-S-24-P-4C
3.2	Discuss ability of experiment to meet its objectives	5.7	
3.3	Discuss feasibility & practicality of including experiment into the ATS-F S/C	5.5	
3.4	Describe operation of the experiment	5.1.2	
3.5	Describe portions of experiment requiring significant development	5.3	Includes laser tube, dup er and radiation cooler
3.6	Recommend any special ground equipments	---	In Vol. II
3.7	Describe interface between S/C and experiment	5.4	
3.8	State expected lifetime of the experiment	6.0	
3.9	Outline the Test Plan for qualifying experiment for flight	7.0	
3.10	Outline a Data Acquisition Plan	---	In Vol. II
3.11	Outline a Data Processing, Reduction & Analysis Plan	---	In Vol. II
3.12	Discuss expected achievements under non-standard flight conditions	5.6	
3.13	Attach definitive specification of experiment	Book II	
S-524-P-4C/ 6.1	Optical design, with analysis of tolerances, error budget & focusing misadjustments	5.2.1	
6.2	Thermal analysis of temp., gradients, & delivered load at S/C interface	5.4.2	
6.3	Detailed weight & power budget		
6.4	Design drawings & specifications with latter covering the system and sub-systems	Book II	Specifications for OGS, Integration, etc. in Vol. II

Table 2-4

Figure 2-1

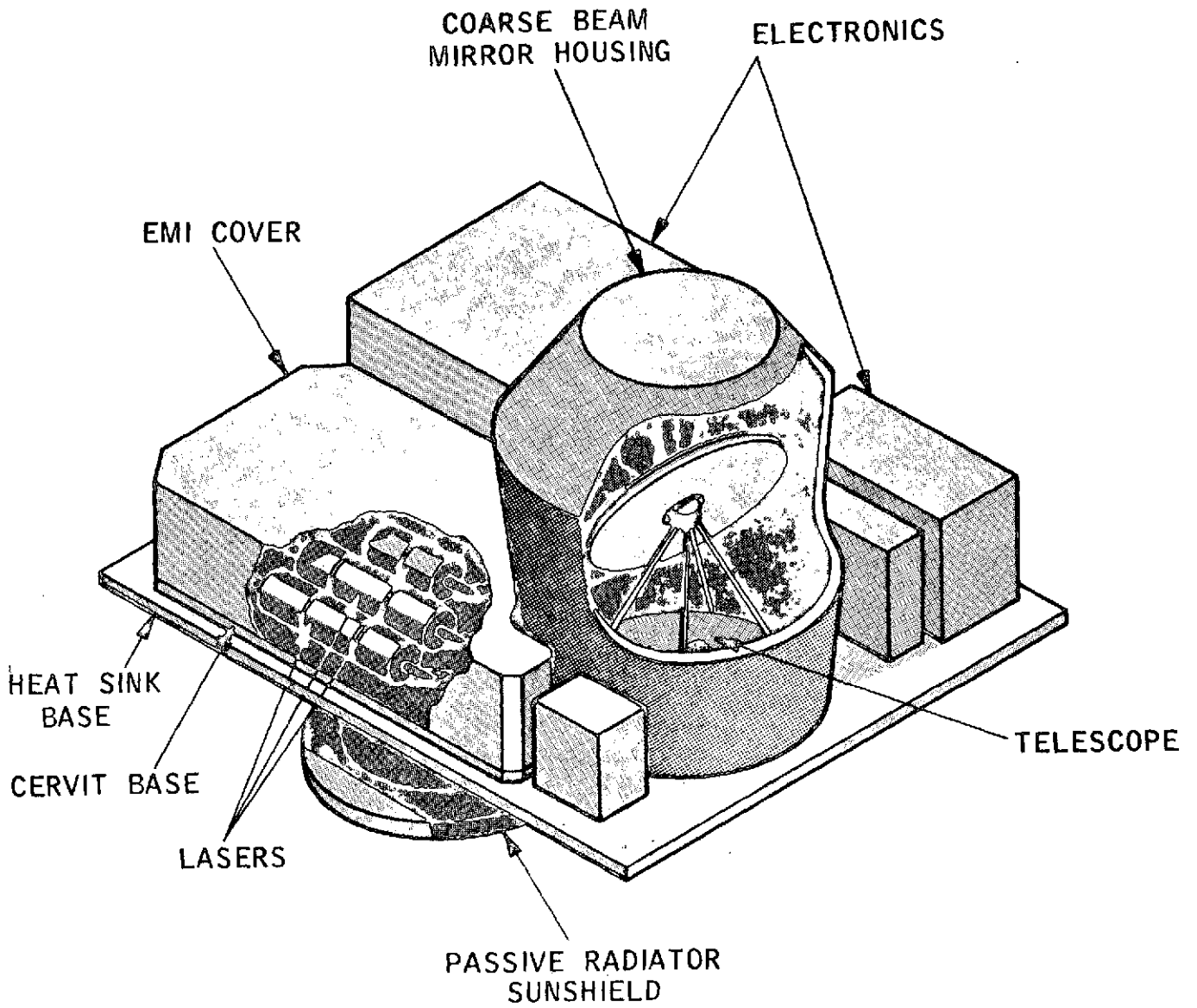


LASER COMMUNICATION CONCEPT



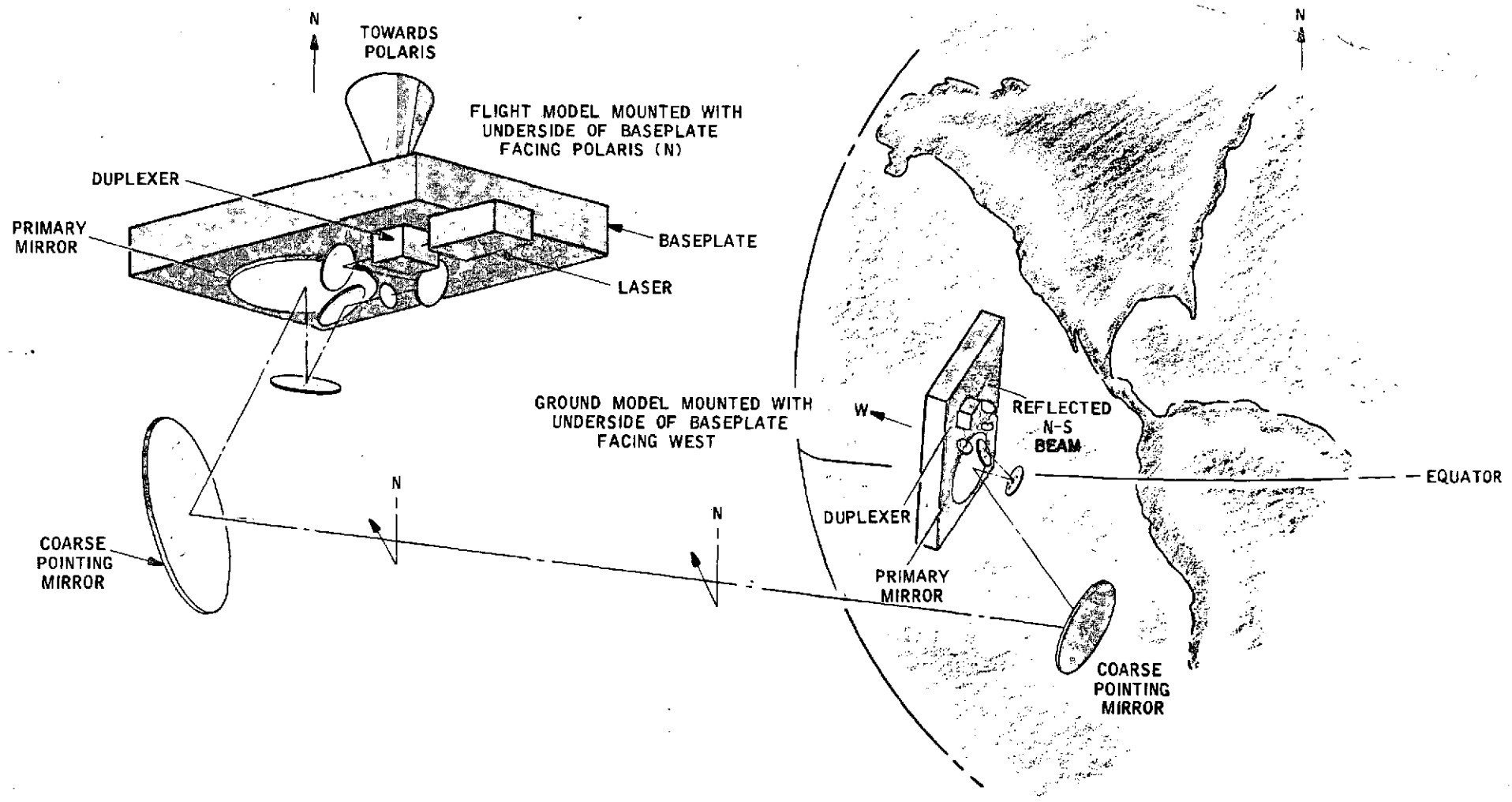
LCE EXPERIMENT MODES

Figure 2-2



LASER COMMUNICATION EXPERIMENT PACKAGE

Figure 2-3



SPACECRAFT/GROUND LINK POLARIZATION REQUIREMENTS GEOMETRY

3.0 OBJECTIVES OF THE EXPERIMENT

3.0 OBJECTIVES OF THE EXPERIMENT

The fundamental objective of the Laser Communications Experiment is to ascertain the practicality of wideband optical communications between a spacecraft and a ground station, and between two orbiting spacecraft using the 10.6-micrometer radiation from a carbon-dioxide laser, and to establish the resulting efficiency that can be effected in terms of communication bandwidth per pound and per watt on the spacecraft.

The objective will be achieved in two phases. These will entail:

- (a) Designing, fabricating and ground testing of the space and ground equipment for spacecraft-to-ground and spacecraft-to-spacecraft communication links; and,
- (b) Performing experiments, tests, and measurements with the deployed hardware.

The design, fabrication and testing phase will lead to a greatly increased understanding of the practicality of spacecraft wideband optical communications. In particular, this phase will:

- (a) Establish the analytical trades between the required system/subsystem characteristics and the system performance;
- (b) Establish the physical parameters; such as size, weight, and power, as a function of potential system performance and the available trades between these parameters;
- (c) Establish equipment and procedures for "hands-off" startup, acquisition, tracking and operation of spaceborne optical communication system;
- (d) Establish design parameters for long life of components required in a spaceborne optical communications system;
- (e) Establish design parameters for the equipment to survive launch; and,

- (f) Establish design data in relatively new developmental areas such as radiation cooling, laser tube characteristics, line selection mechanisms, and modulators.

The second phase involving data gathering after deployment of the equipment, will result in actual performance parameters for a spaceborne optical communications system. In particular, after deployment of ATS-F, this phase will:

- (a) Verify the design and ground test data on all items in the preceding paragraph;
- (b) Measure the parameters required to determine the practicality and potential quality of wideband optical communications between a spacecraft and ground station;

and, after the ATS-G is deployed, this phase will:

- (c) Verify ability for space-to-space acquisition and operation of an optical communications system;
- (d) Establish the link performance without atmospheric attenuation; and,
- (e) Provide data on S/N and other performance parameters as a function of zenith angle over a wider range of zenith angles than is attainable with only ATS-F deployed.

The data gathering, during the second phase, will include, as a minimum, the following tests:

1. S/N as a function of atmospheric parameters;
2. S/N as a function of receiver aperture (Note: This objective is being met by a separate ground station which is not being developed by Aerojet);
3. S/N as a function of zenith angle;
4. Space background noise (sun, stars, etc.);

5. Laser power output as a function of total elapsed time and operating time in the space environment;
6. Temperature and noise figure of the mixer/radiation cooler as a function of satellite orientation and time of year;
7. Round-trip and one-way data quality compared to a reference microwave link;
8. Laser frequency stability in the space environment; and,
9. Spacecraft attitude determination from laser data.

It should be noted that these are not the only measurements that are expected to be taken during the course of the experiment. Further discussions will be presented in Volume II of the Design Study Report.

The manner in which each of the experiments noted as numbers (1) through (9) above will be performed with the LCE equipment described in the present report, is discussed in Section 5.7, along with the expected quantitative results.

4.0 SYSTEM PERFORMANCE REQUIREMENTS

4.0 SYSTEM REQUIREMENTS

The system requirements cited in GSFC-S-524-P-46, "10.6 Micron Laser Communications Experiment for ATS-F" require that the LCE be:

- a. Compatible with the ATS-F spacecraft;
- b. Able to operate in certain communication modes; and,
- c. Able to meet functional and performance specifications.

The interface with the ATS-F spacecraft is defined in GSFC-S-460-ATS-38 (ATS F & G 1900) "ATS-F Experiment Interface Specification." In addition, the design must be able to pass the tests defined in GSFC-S-320-ATS-2B, "ATS-F and G Environmental Test Specifications for Components and Experiments" and in accordance with other applicable documents listed in GSFC-S-524-P-46.

The LCE must be able to operate in: (1) Atmospheric Propagation Experiment Mode, (2) Two-Way Laser Communications Mode, (3) Down-Link Laser Mode, and (4) Data Relay Mode. Operations in these modes is illustrated in Figure 2-2.

The LCE must be able to meet functional and performance specifications in accordance with GSFC-S-524-P-46. A summary of these specifications is given in Table 2-1, along with the expected values for the LCE transceiver described in this report.

The AGC systems specification for the LCE can be found in Part 3 of this report.

5.0 PROPOSED SYSTEM DESIGN AND ANALYSIS

In order to meet the objectives of the experiment and fulfill the system performance requirements, a rigorous analysis and design effort was performed. This resulted in a transceiver design which satisfies the requirements as stated in GSFC-S-524-P-4C, "10.6-Micron Laser Communications System Experiment for ATS-F," dated January 1969. The details of the design and analysis are presented here. Specifically, Section 5.1 deals with the system description and provides a summary of the system analysis; Section 5.2 describes the design and analysis of the subsystems; technical areas wherein development is continuing are defined in Section 5.3, which includes a description of the development programs; details relative to the spacecraft/experiment interface are given in Section 5.4; the feasibility of including the experiment on the ATS-F spacecraft is discussed in Section 5.5; LCE operation under non-standard conditions is described in Section 5.6; and the ability of the LCE to meet the objectives of the experiment noted in the GSFC specification is assessed in Section 5.7. Details of the analysis and design are included in the appendices which comprise Part 2 of this report volume.

5.1 SYSTEM DESIGN AND ANALYSIS

The system and subsystem, along with their operation, are described, as is the manner in which they combine to perform the required system functions. In addition, the analyses performed (link, communications, acquisition, and tracking) as the basis for determining the required system and subsystem performance characteristics are described and the results summarized.

5.1.1 System Description and Operation

The LCE transceiver (Figure 5.1.1-1) is comprised of laser subsystem, optical/mechanical subsystem, optical heterodyne receiver, acquisition and tracking subsystem, high- and low-voltage power supplies, command and telemetry subsystem, and thermal and radiation cooler subsystems. In addition, associated with the ground model is an up-converter/down-converter subsystem (not shown on the block diagram). A summary of the system specifications is given in Table 5.1.1-1. As a complete system the transceiver is designed to:

Report No. 4033, Vol. I, Part 1

- a. Place itself on operational status upon command, within one-half hour;
- b. Acquire and establish a two-way communications link between a ground station and a synchronous satellite under the following conditions:
 1. Satellite attitude uncertainty of $\pm 0.2^\circ$ along each axis
 2. Satellite maximum roll rate of $0.001^\circ/\text{sec}$.
- c. Provide a simultaneous two-way communications link using an FM 10.6-micron carrier having an information bandwidth capability of 5 MHz (low distortion) and a pre-detection CNR and post-detection peak signal-to-noise ratio of at least 23 db;
- d. Track the received energy at angular rates up to $0.01^\circ/\text{sec}$; and,
- e. Provide the telemetry data required for operating the transceiver and accomplishing the experimental objectives.

The features of the seven major LCE subsystems noted above are combined to provide a transceiver which performs these functions. The performance functions of the subsystems summarized below are described in detail in Sections 5.1.2 and 5.2.

(a) Laser Subsystem.- Three lasers with their associated control loops comprise the laser subsystem. The laser transmitter generates frequency modulated carriers at 10.6 microns. The laser local oscillator generates the reference signal to be heterodyned with the received signal to produce an instantaneous IF signal at 30 ± 4 MHz. In addition to being used as a backup transmitter (without FM modulation) or backup local oscillator, the backup laser is used in conjunction with the transmitter or local oscillator to permit system self-check.

(b) Optical/Mechanical Subsystem.- In performing the required coupling and beam shaping functions the optical/mechanical subsystem:

- (1) Couples the transmitter output to the telescope;
- (2) Separates the transmitted and received beams to permit operation with one telescope;

- (3) Provides a means for tracking the angle of the received beam for pointing the transmitter beam;
- (4) Couples the transmitter output to the coarse mirror by by-passing the telescope in order to facilitate acquisition;
- (5) Performs functions (1) through (4) when the backup laser is used;
- (6) Couples the received energy (collected by telescope aperture) and focuses it on the receiver mixer;
- (7) Couples the local oscillator power and combines it with the receiver signal to provide the required illumination of the mixer;
- (8) Performs function (5) when backup laser is used;
- (9) Couples and combines the transmitter and backup laser power to the mixer for self-checking and FM noise measurement;
- (10) Couples and combines the local oscillator and backup laser power to the mixer for self-checking and FM noise measurement; and
- (11) Extracts fraction (1 percent) of laser power output for power measurement and identification of laser operating line.

(c) Optical Heterodyne Receiver Subsystem.- This subsystem mixes the received FM carrier with the local oscillator signal using a (Hg-Cd)Te photovoltaic mixer resulting in an instantaneous intermediate frequency of 30 ± 4 MHz. The receiver IF bandwidth is 30 ± 6 MHz. Outputs of the receiver include:

- (1) Video Signals
- (2) Tracking Error Signals
- (3) Automatic Frequency Control Signals
- (4) Acquisition Pulses
- (5) Acquisition Confirm Pulses

(d) Acquisition and Tracking.- The required control signals generated by this subsystem sequence the acquisition, and provide the acquisition receiver scan pattern and the acquisition operational nutation driving voltages. The angle-of-arrival tracking servo loop performs the acquisition and operational tracking functions.

(e) High Voltage and Low Voltage Power Supplies.- The power required to operate the laser and the low voltages required to operate the transceiver are provided by this unit. Redundant high-voltage power supplies are provided for greater reliability by the transmitter and local oscillator.

(f) Command and Telemetry Subsystem.- Commands from the spacecraft are coupled and shaped as necessary by this subsystem for distribution within the transceiver. The telemetry section couples various telemetry outputs and shapes them as necessary to be compatible with the LCE-S/C telemetry interface.

(g) Thermal and Radiation Cooler Subsystem.- The radiation cooler maintains the receiver mixer temperature at $110 \pm 15^{\circ}\text{K}$. The thermal subsystem maintains the required temperature gradients to meet the laser and optical alignment requirements and maintains the electronic components at the required temperatures.

A perspective view of the LCE transceiver package is shown in Section 2.0 and a schematic of the optical path in the transceiver is given in Figure 5.1.1-2. The baseplate of the experiment equipment mounts on the north face of the ATS spacecraft with the beam pointing mirror housing facing the earth. A viewing port in this earth facing side of the spacecraft will accommodate the beam pointing angles of $\pm 40^{\circ}$ E/W and $\pm 8^{\circ}$ N/S. This capability will permit the LCE transceiver to communicate not only with a ground based station, with allowance for spacecraft attitude variations, but will also allow communication with another satellite borne transceiver (e.g., another ATS satellite). Below the coarse beam pointing mirror is the Cassegrain telescope which functions as the optical antenna of the system. Energy received from the remote station is collected and relayed by means of the telescope and relay lens to the Image Motion Compensator (IMC) as a 0.78-in.-dia collimated beam. From the IMC, the received beam is

focused onto the detector or optical mixer. The IMC performs the function of tracking the remote station so that the image of the energy from this station is always maintained on the detectors. The signals for controlling the IMC are derived by nutating the image of the received beam in a very small circular pattern on the detector. This nutation produces a small amount of amplitude modulation on the received signal which is detected in the receiver subsystem and used to generate the control signals for the IMC. The detector is also illuminated by energy from a local oscillator laser operating on the same line as the remote transmitter but offset by 30 MHz. The beating of these two optical signals produces a 30 MHz intermediate frequency (IF) signal at the output of the detector. The detector depends for proper operation on being maintained at approximately 110°K . This temperature is achieved by mounting the detector in such a way as to ensure good thermal contact with a passive radiator which has a view to space. The radiator, which is mounted facing north, is surrounded by a sunshield. This prevents any direct or reflected solar radiation or infrared radiation from other portions of the spacecraft from impinging on the radiator through any combination of sun angle and spacecraft attitude. The IF signal from the detector is amplified and detected in the optical receiver and appears at the receiver output as a video signal which can either be fed to a spacecraft microwave link or used to modulate the laser transmitter.

In addition to providing local oscillator power for heterodyne detection of the received signal, the laser subsystem contains the transmitter and backup lasers. The transmitter laser, operating on a frequency which is different from that of the remote transmitter, contains within its cavity a gallium-arsenide (GaAs) crystal modulator which frequency modulates the transmitter with the video signal input. The transmitter output, after being processed by beam-shaping optics, is transmitted through the duplexer. From this point on, the transmitted and received beam share the same optical path. The transmitted beam is reflected from the IMC which, in the process of tracking the receiving station, serves to maintain the transmitted beam also pointed at the remote station. From the IMC, the transmitted beam goes through the relay lens and the telescope and is reflected from the coarse beam pointing mirror. The backup laser can function either as a replacement for the local oscillator or the transmitter except that, when acting as a transmitter, the backup laser cannot be modulated.

Before the communication functions can be accomplished, two other operations must be performed. The first is the start-up and stabilization of the transmitter and local oscillator (LO) laser, while the second is the search acquisition and tracking of the remote station. Start-up is initiated by applying the necessary high voltage to the laser tubes to start and maintain the discharge. Approximately 30 min. is required to attain thermal equilibrium, at which time frequency stabilization of the lasers can begin. This is accomplished by varying the effective length of the optical cavity by means of a piezoelectric tuning device. This device, which is capable of covering the complete free-spectral range of the laser cavity, is scanned through this range until an output is detected on the line-selecting power meter. At that time, the frequency search is stopped and the laser is stabilized on the center of the selected line. To maintain the laser frequency on the center of the line, the piezoelectric tuning (PZT) device is "dithered" a small amount (corresponding to a change in laser frequency of ± 300 KHz) and the resulting slight changes in laser power output, as indicated by the power meter, are fed back through a control loop. The LO frequency is stabilized in the same manner as the transmitter frequency except that, once stabilized, the LO frequency is offset (by offsetting the PZT) by 30 MHz from the line center. At this time the search and acquisition functions can begin.

The first step in performing the search and acquisition functions is to command the coarse beam pointing mirror to point at the remote station. Although the resolution of the coarse beam pointing mirror is 0.02° , uncertainties in spacecraft attitude determination may cause errors in the direction of the beam pointing mirror as great as 0.2° . Therefore a flip mirror is used to divert the transmitted beam from its normal path and broaden it so as to illuminate, although at a lower intensity, the entire uncertainty area of $0.2 \times 0.2^\circ$. The IMC is then commanded to scan the field of view of the receiver in a $0.2^\circ \times 0.2^\circ$ 128-line raster pattern. When the receiver detects the signal from the remote station, the scanning operation is stopped, acquisition is confirmed, and the system automatically is placed in the tracking mode. The transmitted beam is then returned to its normal diameter and the local oscillator is locked to a fixed offset from the received frequency. The communication system is now ready for use.

5.1.1.2 Systems Operations

The four LCE operating modes or phases are: (1) Start-up, (2) Acquisition, (3) Operation, and (4) Backup Operations. These are summarized as follows.

5.1.1.2.1 Start-Up Phase

The time allocated for the start-up phase is one-half hour. That time is used to bring the transceiver to operational status which is necessary in order to initiate acquisition and subsequent operational phases of the experiment. The following specific actions will take place:

- a. Commands will be sent to turn on the low voltage power supplies.
- b. Commands will be sent to turn on the transmitter and local oscillator laser high-voltage power supplies. The high voltage will be applied to the laser tubes in two steps. First, from 3000 to 5000 volts (starting voltage) will be applied to the tubes. As soon as the laser tubes start to operate, this voltage will drop automatically to the nominal operating level of 1500 to 2000 volts.
- c. Commands will be sent to set the acquisition pulse threshold and acquisition confirm threshold levels.
- d. At the same time, the transmitter assembly and the local oscillator assembly will automatically initiate the search for the appropriate laser operating line by:
 1. Sweeping the laser cavities over a $\lambda/2$ interval until the correct operating lines are identified, at which time, the line search will cease; and,
 2. Locating the maximum power point on the power-frequency profile by dithering the cavity length and comparing the phase of the resulting laser power amplitude modulation with the dither driving voltage. At the peak of the power-frequency profile, the error signal will be zero.

- e. The following telemetry data will be reviewed:
1. Power supply status
 2. Laser power
 3. Mixer element and modulator crystal temperature
 4. Receiver Automatic Gain Control (AGC) voltage
 5. Mixer bias current
 6. Image Motion Compensator (IMC) and nutator position voltages.

f. The spacecraft ephemeris data will be obtained and the position of the coarse mirror at the time of the acquisition sequence will be determined.

At the completion of these steps, the transceiver will be ready to initiate the acquisition phase.

5.1.1.2.2 Acquisition Phase

During acquisition, the transmitter beams of both stations will be broadened and the receivers of both stations will be spatially scanned simultaneously. Both receivers will be scanned in a rectangular search pattern, with scan retrace at the end of each horizontal scan line. The transmitter beams will be expanded from the 3-db beamwidth of 0.0033° for normal operation to 0.177° for acquisition. Receivers of both stations will scan spatially to cover a horizontal and vertical search angle of $\pm 0.206^{\circ}$. The values of the expanded transmitter beamwidth and search angle are selected to optimize the acquisition probability for a target uncertainty angle of $\pm 0.2^{\circ}$. Methods used to select these values are described in Appendix B. To compensate for the relative rolling motion of the scanning beam with respect to the target (relative rolling rates up to $0.001^{\circ}/\text{sec}$), each scan line is overlapped about 60%. With a receiver beam, which has a 3-db beamwidth of 30 arc, 128 scanning lines are needed to cover the required search angle. The following specific steps will be performed during the acquisition phase:

a. The optimum coarse mirror pointing position for acquisition will be determined and commands to position the mirror will be transmitted.

b. The telemetry data will be used to verify that Step (a) has taken place.

c. The optimum values of the acquisition and acquisition-confirm signal threshold levels will be determined. Command signals necessary to set the threshold detectors to the proper threshold levels will be transmitted.

d. Acquisition search will be initiated by:

1. Offsetting the LO frequency 30 ± 1.1 MHz below the laser line peak-power frequency position;

2. Causing the transmitter beam to expand and illuminate the coarse pointing mirror directly (bypassing the telescope);

3. Inhibiting the nutator drive; and,

4. Starting the receiver-beam search pattern.

e. When the receiver beam intersects the transmitter beam, an acquisition signal will be generated to stop the scanning. To compensate for the time delay between target detection and execution of the acquisition signal, a fixed biased voltage is applied to the horizontal scan generator thereby properly positioning the receiver beam.

f. The acquisition tracking operation will be initiated by:

1. Turning on the north-south and east-west axis nutating driving voltages. Driving voltage amplitudes are set to produce the proper radius of nutation;

2. Turning on a third nutating driving voltage to generate an acquisition-confirm signal; and,

3. Verifying the presence of the acquisition-confirm signal to indicate that the transmitter beam has been acquired and that the tracking subsystem is tracking the transmitter beam.

g. In absence of the acquisition-confirm signal, the system will be returned to the search mode to complete the scan frame.

h. After a prescribed time sufficient for both receivers to acquire their respective transmitter beams, the following steps are to be performed:

1. The transmitter beam is narrowed to 0.0033° .
2. Using the Image Motion Compensator (IMC) driving voltages as reference, the coarse pointing mirror is slowly driven in a direction to bring the target position within 0.06° of the telescope axis.

5.1.1.2.3 Operation Phase

At the initiation of the operation phase, the following actions will take place:

a. The nutator driving voltages will be switched to their normal tracking amplitudes, permitting tighter angular tracking (within ± 4 arc sec). The target will always be kept within $\pm 0.06^\circ$ of the telescope axis, since the coarse mirror position will be stepped to keep the target within this angular cone,

b. Communication and atmospheric experimentation involves several operational variations utilizing the basic techniques already described are available for use in the various LCE experiment modes. These include:

1. Laser up/laser down link
2. Laser up/microwave down link
3. Microwave up/laser down link
4. Simultaneous laser up/microwave down and microwave up/laser down operation.

5.1.1.2.4 Backup Operations

Several backup operation modes are available:

Report No. 4033, Vol. I, Part 1

a. Self-check mode. In this mode, the backup laser and the transmitter laser or backup laser and the local oscillator laser will be mixed within the transceiver. The receiver output signal telemetered to earth will be highly diagnostic as to the operational status of the laser.

b. If either the transmitter laser or oscillator laser fail, the backup laser can be used in their place. However, the backup laser does not have FM capability. Acting as transmitter, it will permit establishment of the two-way link, performance of the atmospheric experiment, and the laser up/microwave down communications link.

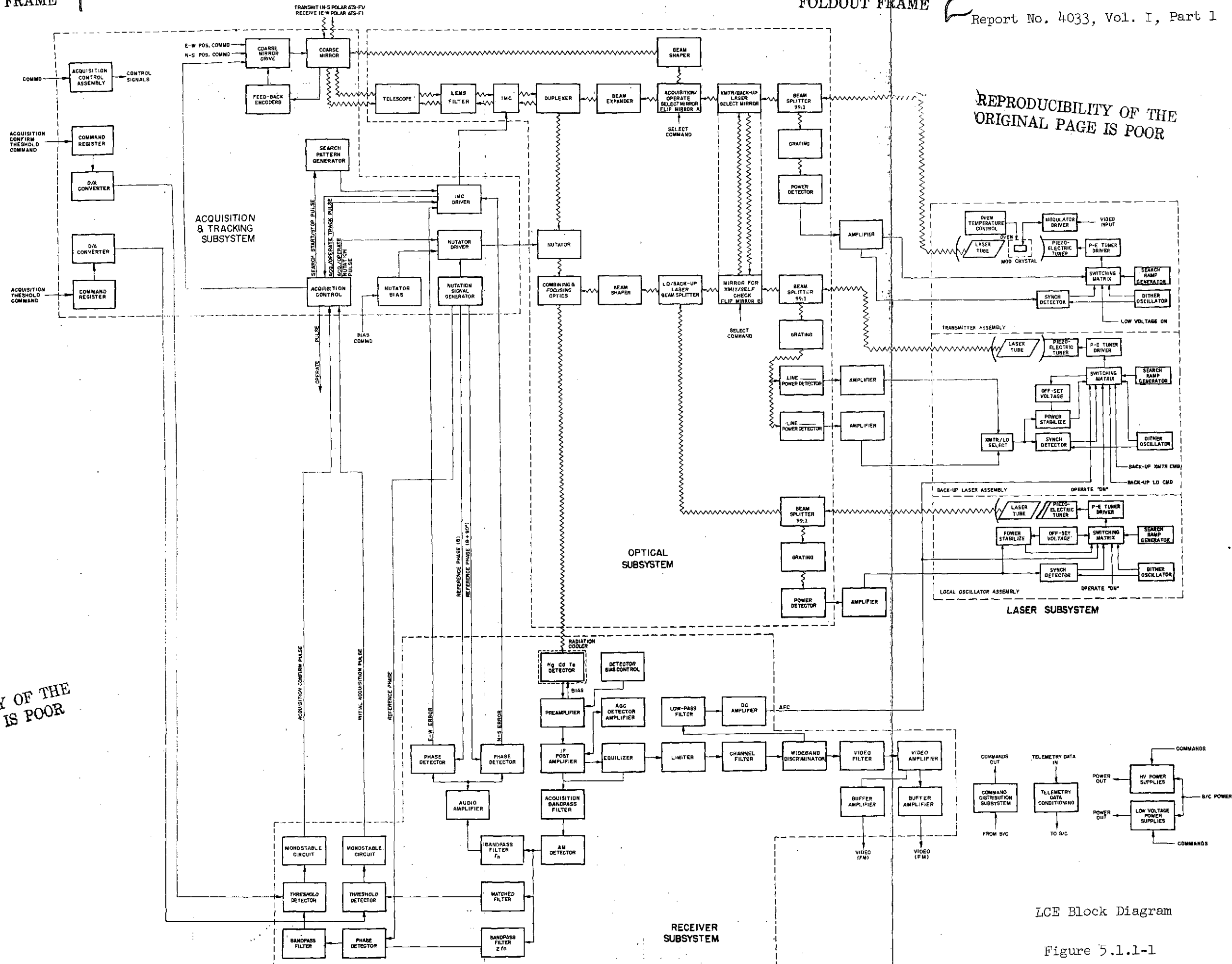
UNIT	CHARACTERISTIC	REQUIREMENT
OVERALL SYSTEM	OPERATING MODES BASEBAND CHARACTERISTICS FLUX DENSITY S/N RATIO	OPERATE PER GFSC-S-524-P-4C FIGURE 2-5 MODES: ATMOSPHERIC PROPAGATION EXPER., 2-WAY LASER COMMUNICATION DOWNLINK LASER, DATA RELAY ADEQUATE FREQUENCY RESPONSE OVER 30 Hz TO ≤ 5 MHz FOR HIGH-QUALITY TV AND MULTIPLE TELEPHONY MINIMUM AT EARTH FROM ATS-F OF 10^{-9} w/m ² CW MINIMUM PREDETECTION AND POST-DETECTION CARRIER-TO-NOISE RATIO OF 23 dB WITHIN A 10. MHz BANDWIDTH COMMUNICATION AND DATA RELAY MODES
SPACECRAFT SYSTEM (DESIGN GOALS)	PRIME POWER CONSUMPTION TOTAL WEIGHT SIZE ENVIRONMENT RFI LIFETIME	≤ 53 W FOR ANY OPERATING MODE ≤ 30 LB FOR COMPLETE EXPERIMENT PACKAGE ≤ 5600 INCHES ³ (~17 x 22 x 15 INCHES) TOTAL AS SPECIFIED IN ATS-F ENVIRONMENT TEST (S-520-ATS-2) AND INTERFACE (S-460-ATS-38) SPECIFICATIONS LIST ALL SOURCES > 0 dBm AT $f > 1$ kHz; RIPPLE FEEDBACK TO PAYLOAD-REGULATOR < 150 mV; 2000 HOURS ACTIVE, SPREAD UNIFORMLY OVER 2 YEARS, W/90% PROBABILITY
OPTICAL/MECHANICAL SUBSYSTEM	BEAM POINTING: FAILURE POSITIONING UNOBSTRUCTED COVERAGE COMMAND POSITIONING ACQUISITION AUTOTRACK SUN REJECTION OPTICAL ALIGNMENT	AUTOMATIC RETURN TO ON-AXIS S/C POSITION UPON ANY POINTING MODE FAILURE OVER $\pm 8^{\circ}$ N-S, $\pm 40^{\circ}$ E-W FROM EARTH-VIEWING AXIS WITHIN $\pm 0.02^{\circ}$ ANYWHERE IN COVERAGE REGION SEARCH $\pm 0.2^{\circ}$ ANYWHERE IN COVERAGE REGION, ACQUIRE IN ≤ 60 SECONDS; $\pm 1.0^{\circ}$ IN MINIMUM TIME HOLD/TRANSCIVE/RECEIVE BEAMS ALIGNED UNDER S/C MAXIMUM ANGULAR VELOCITIES AND ACCELERATION RECEIVER OPERATE WHILE SUN WITHIN FIELD OF VIEW MAINTAIN SETTINGS AND AIRY DISC SIZE THROUGH ENVIRONMENTS, MAXIMUM RECEIVER LOSS ≤ 1 dB
LASER SUBSYSTEM	POWER OUTPUTS (FOR LTH AND LO) EFFECT OF LO POWER ON RECEIVER S/N FREQUENCY AND AMPLITUDE STABILITY TRANSMIT/RECEIVE ISOLATION	COMPATIBLE WITH SYSTEM PERFORMANCE REQUIREMENTS S/N NOT DEGRADED BY LOW POWER, EVEN WITH SUN IN FIELD OF VIEW AFTER 30-MINUTE WARMUP, MUST NOT LIMIT COMMUNICATION SYSTEM PERFORMANCE SUFFICIENT FOR SIMULTANEOUS TRANSMIT/RECEIVE TO PERFORMANCE SPECIFICATION LEVEL
RADIATION COOLER/MIXER CONVERTER SUBSYSTEM	SENSITIVITY FREQUENCY RESPONSE RADIATION COOLER	RECEIVER NOISE FIGURE APPROACHING 2×10^{-20} w/Hz OF BANDWIDTH, EVEN WITH SUN IN FIELD OF VIEW DATA-CHANNEL MIXER FLAT TO ≥ 30 MHz; ERROR SENSOR COMPATIBLE w/SERVO LOOP MAINTAIN DETECTOR AT REQUIRED TEMPERATURE THROUGH SEASONAL SUN/SATELLITE ANGLE CHANGES
SIGNAL PROCESSING SUBSYSTEM	BASEBAND DISTRIBUTION	ABILITY TO ACCEPT AND DISTRIBUTE INPUT SIGNALS FROM VARIOUS DEMODULATORS
TELEMETRY AND COMMAND SUBSYSTEM	SYSTEM COMPATIBILITY TELEMETRY COMMAND	PER INTERFACE SPECIFICATION S-460-ATS-38 (ATS F & G 1900) SATISFACTORY PERFORMANCE FOR APPROVED S/C OUTPUTS AND FUNCTIONS SATISFACTORY RESPONSE TO APPROVED S/C COMMANDS FOR ALL OPERATIONAL MODES
POWER SUPPLY SUBSYSTEM	SYSTEM COMPATIBILITY	PER INTERFACE SPECIFICATION; MONITOR INPUT AND OUTPUT VOLTAGES AND POWER

Table 5.1.1-1

LCE FUNCTIONAL AND PERFORMANCE REQUIREMENTS SUMMARY

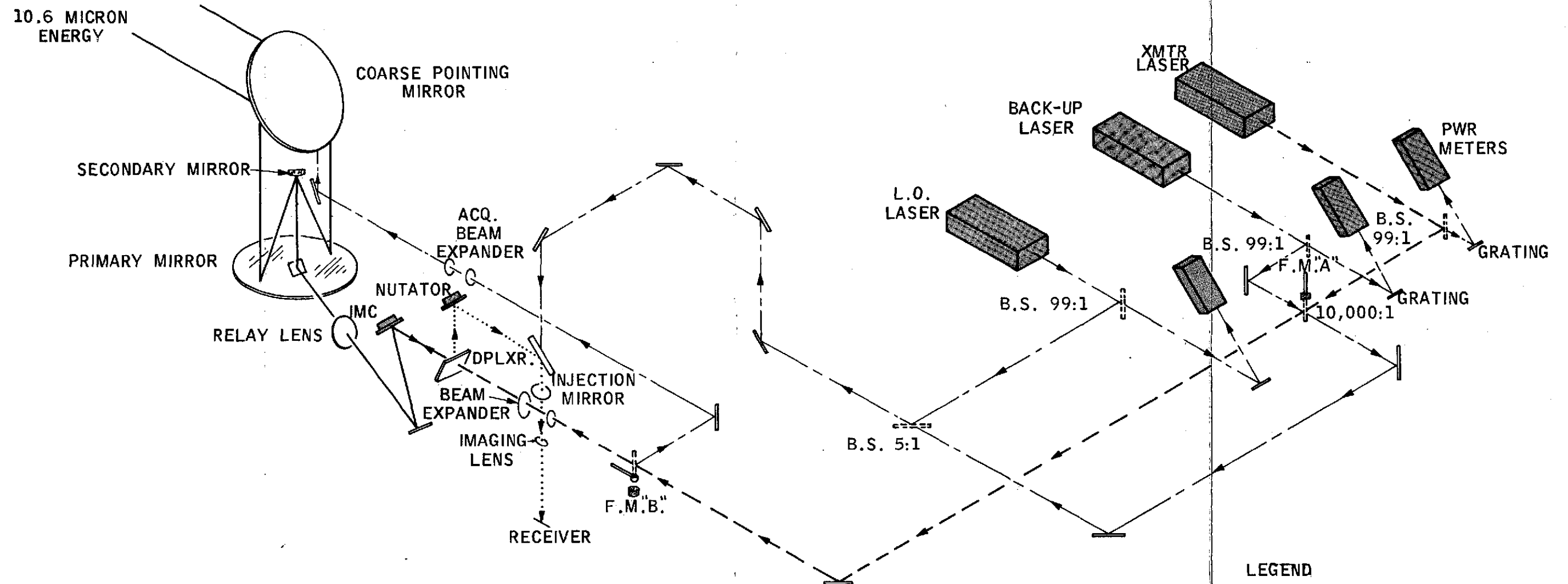
REPRODUCIBILITY OF THE ORIGINAL PAGE IS POOR

REPRODUCIBILITY OF THE ORIGINAL PAGE IS POOR



LCE Block Diagram

Figure 5.1.1-1



LEGEND

- TRANSMIT AND RECEIVE
- TRANSMIT
- RECEIVE
- SECONDARY PATHS

B.S. = BEAM SPLITTER, RATIO OF REFLECTANCE: TRANSMITTANCE
 F.M. = FLIP MIRROR, RATIO OF REFLECTANCE: TRANSMITTANCE

LCE OPTICAL PATH SCHEMATIC

5.1.2 Subsystem Description

The functional operations and a brief description of the seven subsystems that comprise the LCE transceiver are presented below. Details relative to the subsystem designs and analyses are presented in Section 5.2.

5.1.2.1 Laser Subsystem

The laser subsystem consists of the transmitter, local oscillator and backup assemblies. The transmitter assembly generates the frequency modulated, 10.6 micron carrier. The modulation is accomplished by using an in-cavity GaAs crystal placed between two electrodes since the index of refraction of the crystal is a function of the electric field in the crystal. Therefore, by making the potential difference between the electrodes a function of the baseband signal, the carrier will be frequency modulated. The modulator driver amplifies the baseband signal to give the required amplitude for the peak frequency deviation of 4.0 MHz. As designed, the modulator sensitivity is 1.86×10^{-2} MHz/volt.

The index of refraction of GaAs is also a function of temperature. To reduce its sensitivity to temperature variation, the modulator will be mounted in an oven and kept at a temperature of $50 \pm 1^\circ\text{C}$.

The output of the transmitter laser is a carrier signal having an instantaneous frequency of $2.83 \times 10^{13} \pm 4.0 \times 10^6$ Hz. Spatially, it is a collimated, diffraction-limited beam having a 3-mm dia. Gaussian intensity distribution between the $(\frac{1}{e})^2$ relative power levels.

The control electronics of the transmitter laser will:

- a. Place the transmitter laser into an operational status by:
 1. Searching for the correct operating line. (P-20 for flight transmitter and P-16 for ground transmitter); and,
 2. Locating the peak of the laser power-frequency profile.

b. Track the laser power output and continuously reposition its operating point on the peak of the power-frequency profile.

This function is performed by mounting one cavity end mirror on a piezo-electric mount and subjecting the piezo-electric mount to an electric field which causes it to either expand or contract thereby varying the effective laser cavity length. The range of the piezo-electric tuner is at least 6 microns thereby permitting search over one complete laser output profile. Over the operating temperature range, the laser cavity length will change over several ($\Delta \lambda = \frac{10.6}{2}$) micron increments. However, it has been experimentally proven that the laser output is repeatable over several $\Delta \lambda$ increments. Therefore, as the piezo-electric drive reaches one extreme of its tracking range, it will backstep one $\Delta \lambda$ increment and continue tracking the peak of the power-frequency profile of the correct operating line.

The initial search for the proper operating line is achieved by applying the output of the search ramp generator to drive the piezo-electric tuner. At the same time, the output of the transmitter tube is sampled by the 99:1 beamsplitter. This fraction of the transmitter power is then coupled by means of a grating to an infrared power meter. The geometric arrangement between the power meter and the grating is such that only the wavelength of the correct laser operating line will illuminate the power meter (15:1 rejection of adjacent lines).

Once the proper line is identified, the search will cease and line dither will be initiated at a rate of 75 Hz and an amplitude of ± 300 KHz. At the peak of the power-frequency profile, this will superimpose a power amplitude modulation of 0.01 percent. (This is the minimum slope position.) As the dithering center slides along the power-frequency profile, the dithering phase will be compared with the driving signal phase deriving an error signal which will always seek the peak of the power-frequency profile corresponding to the zero error position, within ± 100 KHz.

The function of the local oscillator assembly is to generate the required power to illuminate the mixer of the optical heterodyne receiver. Sufficient power must be generated to cause the local oscillator power to be the dominant noise source (shot noise). The local oscillator will operate at a point of its power-frequency profile 30 MHz below the peak such that when this power is mixed with the received signal, the output of the mixer will have an instantaneous frequency in the range of 30 ± 4 MHz. The control loops of the local oscillator are essentially the same as discussed in the preceding paragraph; however, in addition, after the peak of the power-frequency is selected, it is offset 30 MHz below the peak and kept there within ± 1.6 MHz until the acquisition of the far-distant transmitter is completed. At that time, a frequency error signal is received from the optical heterodyne receiver which is proportional to the frequency difference between the received and local oscillator frequency, zero error corresponding to 30 MHz. The local oscillator then tracks the error signal with an accuracy of ± 50 KHz.

The last assembly of the laser subsystem is the back-up laser which:

- a. Operates on the transmitter laser line which it serves as a back-up transmitter; however, not having the frequency modulation capability, it serves as a beacon which makes possible two-station tracking and is used to perform atmospheric transmission experiments.
- b. Operates on the local oscillator line at 30 MHz below the peak, serving as a back-up for the local oscillator.
- c. Is used to perform self-checking tasks while operating at the transmitter line less 30 MHz. Combining the transmitter and the back-up lasers in this mode, the receiver mixer will produce a signal which will be a good measure of the operational status of the transmitter and of the space FM noise spectrum (of course, it will require telemetering this data to earth).

- d. Can be operated at the peak of the local oscillator line also for self-checking purposes. Combining the two beams (LO and back-up in this mode) will produce the same data as discussed under Item c.

The technical characteristics of the laser subsystem are summarized in Tables 5.1.2-1 and -2.

5.1.2.2

Optical/Mechanical Subsystem

The Optical/Mechanical Subsystem must:

1. Accept the outputs of the lasers and couple these outputs, after suitable shaping and processing as required by various modes of operation, either to the telescope, coarse mirror, or the receiver mixer element;
2. Couple the telescope collected energy to the receiver mixer after properly focusing this energy;
3. Provide means to include in the optical train an Image Motion Compensation (IMC) Assembly and a nutator assembly in order to accomplish energy angular tracking;
4. Extract a small portion of each laser beam energy and via a grating (which selects only the energy when the laser is operating on the proper line) focus it on a power meter to measure the laser power output; and,
5. Hold the optical path and laser subsystem component alignment to within the tolerances listed in Table 5.1.2-3.

The layout of the optical subsystem is designed to minimize the number of optical components and their complexity while accommodating the above mentioned requirements.

The components of the opto-mechanical subsystem include the telescope, telescope output collimating lens, duplexer, beam expander, image motion compensator, and nutator assemblies, received signal and local oscillator combining and focusing optics, beamsplitters, flip mirrors, mirrors, gratings, filter, window, and lens required to focus laser power on the infrared thermistor detectors for measuring power output. In particular, the duplexer separates the transmitted and received beams by reflecting the received signal of spatial polarization, 0, and passing the transmitted beam of spatial polarization $(\theta + \frac{\pi}{2})$. The Image Motion Compensator (IMC) provides the means to steer the transmitter and receiver optical axes using two orthogonally placed mirrors whose angular position is controlled by the tracking subsystem. The nutator being identical to the IMC rotates the receiver optical axes causing the received carrier, whose phase and amplitude are functions of the received energy angular position with respect to the LCE reference axes, to be amplitude modulated. The received signal and local oscillator combining and focusing optics combine beams such that the two phase fronts are parallel and are properly focused on the mixer element.

The key structural components required for proper alignment are the CERVIT baseplate, the beryllium baseplate, on which the telescope is mounted, and various mounts supporting the optical components. The mounts are designed to permit adjustment of the optical component positions, but include locking provisions to assure that the settings survive launch environments.

The four optical subsystem configurations or modes (normal, backup, acquisition, and self-check) are summarized as follows:

(The optical layout schematic of the optical subsystem is shown in Figure 5.1.1-2).

Normal Operating Mode.- In this mode, the laser transmitter output is coupled to the telescope and the received energy is combined with the local oscillator power.

Acquisition Mode.- In this mode, the transmitter laser output bypasses the telescope illuminating directly the coarse mirror and its output beam is expanded to cover the target location angle of uncertainty. The receiver field of view of scanned until the target is acquired.

Backup Operating Mode.- If either transmitter or local oscillator lasers fail, the backup laser can be used to operate in the normal and acquisition modes.

Self-Check Mode.- In this mode, the backup laser power is combined with transmitter or local oscillator power to be heterodyned in the optical receiver. The output of the receiver will be telemetered to earth to provide good data or operational status of the transceiver.

5.1.2.3 Optical Heterodyne Receiver Subsystem

The optical heterodyne receiver subsystem consists of the mixer assembly, preamplifier, and processing electronics assembly. Functionally, it accepts the combined received/local oscillator power, mixer it in the mixer element (photovoltaic, back-biased, (Hg,Cd) Te diode) with the resulting signal output at an intermediate instantaneous frequency of 30 MHz \pm 4 MHz.

The output of the mixer is amplified in a preamplifier to provide a nominal 26-db gain. The nominally 10^{-19} watts/Hz noise equivalent power (NEP) measured at the output of the preamplifier will vary as a function of mixer element temperature as shown in Figure 5.1.2-1. The output of the preamplifier will be processed in several channels to produce the transmitted baseband signal, the AFC error signal, the quadrature tracking error signals both for acquisition and normal operational modes, the acquisition pulse, and the acquisition confirm pulse.

The FM receiver channel consists of the post-amplifier, automatic gain control (AGC), equalizer, limiter, channel filter, wideband discriminator, video filter, video and buffer amplifier stages. The functional highlights of the FM receiver channel are summarized in Table 5.1.2-4.

The automatic frequency control (AFC) error-signal channel consists of a lowpass filter and a d-c amplification stage. Its output will have the following characteristics:

- a. Zero error voltage at 30.0 ± 0.1 MHz
- b. Bandwidth of 0.1 Hz to 10.0 KHz and 3 db with fall-off of 6 db/active.
- c. Slope of:
 - 1) At least -5 to + 5 volts from 29.5 to 30.5 MHz
 - 2) Between -5 to -13 volts from 29.5 to 27.5 MHz
 - 3) Between +5 to +13 volts from 30.5 to 32.5 MHz

Strictly for automatic frequency control purposes, this channel has a wider bandwidth than required. However, the output of this channel also constitutes an important telemetry point and will provide data relative to the spaceborne laser FM noise spectral distribution.

The tracking channel consists of the bandpass filter, audio amplifier and two phase-detectors generating the east-west and north-south tracking error signals.

The acquisition pulse channel consists of the matched filter, threshold detector and a monostable circuit which will shape the acquisition pulse. During acquisition, the two stations (ground and spacecraft) will go through a programmed search sequence to find each other.

The uncertainty in the attitude of the spacecraft, which will cause the flight transceiver transmitter and receiver optical axes to be at any angle within an aperture $0.4^\circ \times 0.4^\circ$, makes this necessary. The problem is further complicated by the spacecraft rolling rate of up to $0.001^\circ/\text{sec}$. This is a very dynamic situation considering that the operating transmitter beam width is 0.0039° between the 3-db points and received beam width is 0.0038° between the 3-db points. The details of the acquisition phase are given in Section 5.1.2. However, as far as the receiver subsystem is concerned, at the time the receiver beam is sweeping past the angular position coincident with the ground - spacecraft line-of-sight (within ± 5.8 arc sec.) a signal will be received having a signal-to-noise ratio at the output of the preamplifier as low as -19 db peak. The function of the acquisition channel is to extract this signal with a probability of detection of 90% and average time between false alarms of 1100 seconds.

The acquisition pulse will cause the acquisition nutation to be initiated to start tracking the received energy. Presence of the tracking error signal will indicate that indeed the acquisition pulse was caused by the received energy. Such conformation is required since there is a finite probability for noise to trigger the acquisition pulse. However, there is also a finite probability that at the beginning of the acquisition tracking, the target is at zero tracking error position. Therefore, to ensure the presence of an acquisition, a confirm signal will be superimposed on one of the nutation driving voltages of double the Nutation Frequency.

The resultant $2 f_n$ amplitude modulation will always be on the carrier if the target is within field of view of the receiver beam and its presence will confirm bona fide acquisition.

The acquisition-confirm channel differs from the tracking channel only in that it is centered at double the nutation frequency, f_n . A monostable circuit at the output shapes the acquisition confirm channel.

Table 5.1.2-5 summarizes the operating requirements of the tracking, acquisition pulse, and acquisition confirm channels.

5.1.2.4

Acquisition and Tracking Subsystem

The acquisition and tracking subsystem must perform several key functions in order to acquire the far distant station and then track in angle the incoming energy. The major functions entail:

- a. Providing the required electronics to position the coarse mirror such that the optical axis of the telescope intersects the nominal position of the far-distant station within $\pm 0.02^\circ$ over an angular aperture of $30^\circ \times 16^\circ$;
- b. Providing the required receiver beam sweep such that the angle of uncertainty ($0.4^\circ \times 0.4^\circ$) of the far-distant station is covered during acquisition;
- c. Tracking the received energy and positioning coarse mirror upon acquiring the far-distant station, such that the optical axis of the telescope intersects (within $\pm 0.05^\circ$) the far distance station;
- d. Switching to operational tracking, at the completion of acquisition phase, to track within ± 4 arc sec at tracking rates up to $0.01^\circ/\text{sec}$.

The coarse mirror is positioned by comparing digitally (for two axes) its position with the required position. As long as there is a difference, appropriate driving voltages will be generated to reduce the position error to zero. Following two sources generate the required mirror position information:

- a. Transmit commands designate the position of the coarse pointing mirror. This position will be entered in the elevation and azimuth "Required Position" registers. This mode of positioning will be used at the beginning of acquisition phase to position coarse mirror such that the optical axis of the flight telescope intersects (within $\pm 0.02^\circ$) the ground station nominal position (or vice versa) which is the center of the $0.4^\circ \times 0.4^\circ$ angular uncertainty aperture.
- b. During acquisition and normal tracking, the average angular position of the IMC will indicate whether the target is close to (in angle) or is off from the telescope optical axis. Optimum operation is obtained when the target is within an angle $\pm 0.06^\circ$ of the telescope axis. Therefore, the IMC mirror position voltages will serve as error voltages (after analog to digital conversion) to position the coarse mirror for centering the target.

The tracking function encompasses elements of the optical, receiver, and acquisition and tracking subsystem. Figure 5.1.1-2 shows the simplified block diagram of the tracking system (one-axis tracking).

Briefly, it operates as follows. If the nutator and IMC mirrors are positioned at their nominal positions, the principal ray emanating from the center of the detector will emerge parallel and concentric with the optical axis of the telescope. The nutating (oscillating) is now initiated at $\pm \Delta \theta_q$ degrees at frequency f_n . This will cause the principal ray to scan up and down $\pm \Delta \theta_q / X$ degrees with respect to the telescope axis where X is the power of the telescope. Since there are two such systems, azimuth and elevation, and the nutation drives are displaced 90° in phase, the resulting motion of the principal ray is circular around the axis of nutation (which is concentric with the telescope axis, so far). Now, if the IMC mirror moves from its nominal angular position by $\Delta \theta_r$ degrees, it will cause the axis of rotation to be displaced $\Delta \theta_r / X$ from the optical axis of the telescope. If there is a target, P, as shown in Figure 5.1.2-2, the nutation of the receiving beam will cause corresponding amplitude modulation of the received carrier.

The more exact target, axis of nutation, and received optical beam relative orientation are shown in Figure 5.1.2-3 and 5.1.2-4.

The tracking servo subassembly demodulates this amplitude modulation envelope, compares it with the two quadrature nutator driving voltages in the phase detectors generating the target position error voltages. The servo subsystem always tries to position the IMC mirror such that the error voltages are zero which corresponds to the axis of rotation intersecting the target (within ± 4 arc sec.).

5.1.2.5 Power Supply Subsystem

The High Voltage and Low Voltage Power Supply Subsystem generates the power and voltages (Table 5.1.2-6) required to operate the transceiver.

5.1.2.6 Command and Telemetry Subsystem

The Command and Telemetry Subsystem couples and shapes the spacecraft commands as required by specific transceiver circuits. Also, it conditions as necessary the telemetry data generated at various functional points of the transceiver to be compatible with the spacecraft requirements. Tables 5.1.2-7 and -8 list the commands and telemetry points.

5.1.2.7 Thermal and Radiation Cooler Subsystem

The thermal and radiation cooler subsystem provides the required thermal control and structural support required to survive launch, transit, and injection environment. In synchronous orbit it provides:

- a. Radiative cooling of the mixer at $110 \pm 15^{\circ}\text{K}$;
- b. Electronic component temperatures not to exceed 60°C at the highest transceiver/spacecraft interface temperature ($+ 35^{\circ}\text{C}$); and,
- c. Thermal gradients in the telescope spider not to exceed 10°C between the three legs.

In addition to the above subsystem, an up-translator and down-translator subsystem is used only with the ground station. It translates the baseband signal to be transmitted from 30 Hz - 4.6 MHz band to 1.4 - 6.0 MHz plus a vestige of lower sideband from 1.0 to 1.4 MHz. A corresponding down-translation is performed on the received signal. The primary reason for the baseband frequency shift is the need to bypass the GaAs in-cavity modulator resonances which occur in the frequency region from 100 KHz to 1.0 MHz, depending on the crystal dimensions. Therefore, spectral components of the baseband signal in the vicinity of the crystal

resonant frequencies will produce carrier frequency deviations out of proportion with the response to all other baseband spectral components, resulting in a distorted signal.

The up-translation and down-translation stages each consist of couple conversion, thereby retaining low spectral component to high spectral component amplitude relationship.

TABLE 5.1.2-1

TRANSMITTER ASSEMBLY PERFORMANCE REQUIREMENTS

Transmitter Assembly Performance

<u>Characteristic</u>													
(1) <u>Power Output, minimum</u> (At the output of the laser cavity)	650 mw at line center at 25°C												
(2) <u>Mode</u>	TEM ₀₀												
(3) <u>Polarization</u>	Linear with electric field perpendicular to the baseplate ± 2°												
(4) <u>Output power beam width</u> (at output of cavity end mirror)	3.0 ± 0.12 millimeters (mm) beam diameter between (0.367) ² relative power levels, diffraction limited, collimated beam												
(5) <u>Operating lines</u> Flight Model Ground Model	P 20 P 16												
(6) <u>Operating line width</u>	Compatible with the video transmission requirements												
(7) <u>Power frequency profile</u>	Compatible with stabilization requirements of the assembly												
(8) <u>Operating frequency</u>	Line center frequency + 100 KHz over a time period of 10 to 100 seconds at a dither frequency of 75 ± 5 Hz with peak-to-peak frequency deviation not to exceed ± 300 KHz.												
(9) <u>Frequency stability</u> 0.1 Hz to 5 Hz 5 Hz to 800 KHz 800 KHz to 6.0 MHz	100 KHz rms 50 KHz rms deviation 2.7 KHz rms deviation (exclusive of dither modulation).												
(10) <u>Amplitude stability</u>	2% rms at line center over a bandwidth of 5 to 45 Hz												
(11) <u>Modulation characteristics (FM)</u> Deviation capability Modulation sense Input frequency bandwidth Baseband amplitude - Frequency characteristics	Provide deviation of up to ± 4.0 MHz Increase in carrier frequency deviation for increase in positive potential. 1 MHz to 6.0 MHz												
	<table border="1" style="margin-left: auto; margin-right: auto;"> <thead> <tr> <th>Reference Frequency</th> <th>Design Goal</th> <th>Minimum Acceptable</th> </tr> </thead> <tbody> <tr> <td>1.025 MHz</td> <td>0 db</td> <td>0 db</td> </tr> <tr> <td>1.0 to 1.840 MHz</td> <td>± 0.1 db</td> <td>± 0.25 db</td> </tr> <tr> <td>1.840 to 6.0 MHz</td> <td>± 0.2 db</td> <td>± 0.4 db</td> </tr> </tbody> </table>	Reference Frequency	Design Goal	Minimum Acceptable	1.025 MHz	0 db	0 db	1.0 to 1.840 MHz	± 0.1 db	± 0.25 db	1.840 to 6.0 MHz	± 0.2 db	± 0.4 db
Reference Frequency	Design Goal	Minimum Acceptable											
1.025 MHz	0 db	0 db											
1.0 to 1.840 MHz	± 0.1 db	± 0.25 db											
1.840 to 6.0 MHz	± 0.2 db	± 0.4 db											
	8.0 MHz/volt input												
(12) <u>Modulator/Driver Sensitivity</u> <u>Modulator/Driver Sensitivity Stability</u> (MHz deviation/volt input)	Within ± 0.1 db during environmental stresses for one operating period, (24 hours or less)												
(13) <u>Modulator/Driver group delay over 6.0 MHz bandwidth output, maximum</u>	+ 0.2 ns/MHz slope 0.04 ns/MHz ² parabolic 0.6 ns peak-to-peak ripple												
(14) <u>Modulator linearity (Derivative method), maximum</u>	2% for center 90 percent of * MHz band 1% over 75 percent of bandwidth												
(15) <u>Amplitude of the synchronizing signal</u>	Synchronizing pulses shall be between 0.27 and 0.31 volts												
(16) <u>Noise</u> Periodic noise (ratio of P-P picture signal amplitude to the P-P noise amplitude) Power Supply Hum..... (Including the fundamental frequency and low harmonics) Single frequency noise between 1 KHz and 2 MHz..... Single-frequency noise between 2 and 6 MHz.....	38 db min. 62 db min. 46 db min.												

* To be added at a later date.

Table 5.1.2-1

Report No. 4033, Vol. I, Part 1

TABLE 5.1.2-2

LOCAL OSCILLATOR AND BACK-UP LASER PERFORMANCE REQUIREMENTS

	Local Oscillator	Line Center Operation	Back up Laser
			Line Center -30 MHz Operation
(1) <u>Power Output, Minimum</u> (At the output of the laser cavity)	85 mw at line center minus 30 MHz at 25°C	650 mw at line center at 25°C	500 mw at line center minus 30 MHz at 25°C
(2) <u>Mode</u>	TEM ₀₀	TEM ₀₀	TEM ₀₀
(3) <u>Polarization</u>	Linear with electric field perpendicular to the baseplate ± 2°	Linear with electric field perpendicular to the baseplate ± 2°	Linear with electric field perpendicular to the baseplate ± 2°
(4) <u>Output Power Beam Width</u> (At output of the cavity end mirror)	3.0 ± 0.12 millimeters (±) beam diameter between (0.367) ² relative power levels, diffraction limited, collimated beam	3.0 ± 0.12 millimeters (mm) beam diameter between (0.367) ² relative power levels, diffraction limited collimated beam	3.0 ± 0.12 millimeters (mm) beam diameter between (0.367) ² relative power levels, diffraction limited, collimated beam.
(5) <u>Operating Lines</u>			
Flight Model Operating	P 16	P 20	P 16
Ground Model Operating	P 20	P 16	P 20
Flight Model Test	P 16	P 16	P 20
Ground Model Test	P 20	P 20	P 16
(6) <u>Oscillator Power/frequency profile</u>	Compatible with stabilization requirements of the assembly	Compatible with stabilization requirements of the assembly	Compatible with stabilization requirements of the assembly
(7) <u>Operating Frequency</u>	30 ± 0.05 MHz below received signal frequency	Line center frequency ± 100 KHz over a time period of 10 to 100 seconds at a dither frequency of 75 ± 5 Hz with peak-to-peak frequency deviation not to exceed ± 300 KHz	30 ± 0.05 MHz below received signal frequency
(8) <u>Frequency uncertainty during acquisition</u>	30 ± 1.1 MHz below line center with additional drift not to exceed 0.5 MHz over a 5 minute period	Line center frequency ± 100 KHz over a bandwidth of 0.1 to 1.0 MHz	30 ± 1.1 MHz below line center with additional drift not to exceed ± 0.5 MHz over a 5 minute period
(9) <u>Frequency Stability</u>			
0.1 Hz to 5 Hz	100 KHz rms deviation	100 KHz rms deviation	100 KHz rms deviation
5 Hz to 800 KHz	50 KHz rms deviation	50 KHz rms deviation (Exclusive of Dither Modulation)	50 KHz rms deviation
800 KHz to 6.0 MHz	2.7 KHz rms deviation	2.7 KHz rms deviation	2.7 KHz rms deviation
(10) <u>Amplitude Stability</u>	0.3 % rms over band width from 5 to 45 Hz Design goal is 0.1% rms	2% rms at the line center over a bandwidth of 5 to 45 Hz.	0.3% rms over band width from 5 to 45 Hz Design goal is 0.1% rms.
(11) <u>AFC Cavity/Mirror Variation, minimum, (piezo electric tuner)</u>	6 microns	6 microns	6 microns

Table 5.1.2-2

Report No. 4033, Vol. I, Part 1

TABLE 5.1.2-3

OPTICAL COMPONENTS MISALIGNMENT TOLERANCES

<u>Component</u>	<u>Random Misalignment Tolerance (sec)</u>	<u>Temperature Misalignment Tolerance (sec)</u>
Flat Laser End Mirror	15	4
Modulator	50	4
Laser Tube	50	4
Curved End Mirror	15	4
Reflecting Mirrors	15	4
Beam Expander	15	4
Duplexer	100	20
IMC	370	20
Reflecting Mirrors	370	20
Filter Relay Lens	370	20
Nutator	370	20
Imaging Lens	370	20

Table 5.1.2-3

TABLE 5.1.2-4

FM VIDEO CHANNEL PERFORMANCE REQUIREMENTS

(1) <u>Receiver Video Output:</u> (2 required)			
(a) Level over 1 MHz to 6 MHz			1 volt peak-to-peak \pm 0.5 db
(b) Impedance over 1 MHz to 6 MHz			75 ohms, unbalanced, with minimum return loss of 20 db
(2) <u>Preamplifier</u>			
(a) Bandwidth			30 \pm 6 MHz, consistent with video distortion and noise requirements
(b) Input saturation			-40 dbm or greater at the input to the mixer assembly
(3) <u>Demodulation Characteristics</u>			
(a) Demodulation sense (at video output)			Increase in positive potential for increase in carrier frequency deviation
(b) Instantaneous bandwidth			Consistent with the video distortion and noise requirements specified herein
(c) Center frequency			30 MHz
(d) Output sensitivity over -72 dbm to -56 dbm carrier input power levels at mixer window at any frequency from 26.0 to 34.0 MHz			Constant within \pm 0.3 db
(e) Baseband amplitude - frequency characteristics			
	<u>Reference</u>	<u>Design Goal</u>	<u>Minimum Acceptable</u>
	Frequency		
	1.025 MHz	0 db	0 db
	1.0 to 1.840 MHz	\pm 0.1 db	\pm 0.25 db
	1.840 to 6.0 MHz	\pm 0.2 db	\pm 0.4 db
			\pm 0.7 n sec/MHz slope
			0.5 n sec/MHz ² parabolic
			6.0 n sec peak-to-peak ripple
			A carrier deviation of \pm 4.0 MHz shall produce a 1 volt \pm 0.5 db peak-to-peak output signal
(f) Group delay over 12 MHz bandwidth			
(g) Demodulation Amplitude			
(4) <u>Video Distortion and Noise</u>			
(a) Amplitude of the synchronizing signal			Synchronizing pulses shall be 0.29 \pm 0.02 volts
(b) Periodic noise (ratio of P-P picture signal amplitude to the P-P noise amplitude)			
1. Power Supply Rum.....			38 db min.
(Including the fundamental frequency and low harmonics)			
2. Single frequency noise between 1 KHz and 2 MHz.....			62 db min.
3. Single-frequency noise between 2 and 6 MHz.....			46 db min.
(5) <u>Automatic Gain Control</u>			
(a) Recovery time (for instantaneous carrier power level changes up to 41 db with respect to Carrier to Noise Ratio (C/N) of -18 db to -6 db)			Receiver automatic gain control shall set the output power to its nominal level \pm 1 db within 0.2 seconds and pass amplitude modulation
(b) Telemetry output of the ATC			0 to 5 volts corresponding to a carrier dynamic range of -72 dbm to -56 dbm with an output impedance of 1000 ohm or less. The bandwidth of the telemetry channel shall be 10 Hz at the 3 db points.

Table 5.1.2-4

Report No. 4033, Vol. I, Part I

TABLE 5.1.2-5

ACQUISITION AND TRACKING CHANNEL PERFORMANCE REQUIREMENTS

- (1) Acquisition
- (a) Input: -18 db minimum^{1/}
- (b) Output:
1. Amplitude: 3.8 ± 1.4 volts
 2. Pulse Width: 50 ± 10 milliseconds
 3. Rise and Fall Time: 1 millisecond, maximum
- (2) Acquisition Tracking
- (a) Input: -19 db to -7db and 1.5% amplitude modulated^{2/}
-23 db to -11db and 40% amplitude modulated^{2/}
- (b) Output: 0 ± 0.1 volt corresponding to -19 db to -7db 1.5% modulated input, minimum, peak-to-peak with a linear signal of ± 5 volts corresponding to -23db 40% modulated input.
- (3) 2 f_n (Acquisition) Signal
- (a) Input: -19 db to -7db and 15% amplitude modulated^{2/}
-23 db to -11db and 70% amplitude modulated^{2/}
- (b) Output: 3.8 ± 1.4 volts
- (4) Operational Tracking
- (a) Input Signal: 23 db and 1.0% amplitude modulated^{2/}
19 db and 15% amplitude modulated^{2/}
- (b) Output Signal: 0 ± 0.1 volt corresponding to 23 db, 1.0% modulated input, minimum, peak-to-peak with a linear signal of ± 5 volts corresponding to 19 db, 15% modulated input

^{1/} Peak carrier power/rms noise ratio with Gussian shaped signal

^{2/} Minimum average carrier power/rms noise ratio.

TABLE 5.1.2-6 POWER SUPPLY POWER OUTPUT

	LASER TRANSMITTER H.V. CURRENT REGULATOR	LASER I.O. H.V. CURRENT REGULATOR	BACKUP LASER H.V. CURRENT REGULATOR	MODULATOR & IMC DRIVER POWER SUPPLY	LOW VOLTAGE POWER SUPPLY	
					±12V	+ 5V
1.) OPERATING CURRENT ^{8/} (Milliamperes, DC)	4 ± 0.2 ^{1/}	5 ± 0.25 ^{1/}	4 ± 0.2 ^{1/}	25	100 to 235 ^{10/}	1500 to 2500
2.) OPERATING VOLTAGE ^{8/} (Volts, DC)	2000 ± 100 ^{1/}	800 ± 50 ^{1/}	2000 ± 100 ^{1/}	225 ± 3.4 ^{1/}	±12±0.225 ^{1/}	5 ± 0.25 ^{1/}
3.) STARTING VOLTAGE (Volts)	5000 ± * ^{1/}	2600 ± * ^{1/}	5000 ± * ^{1/}	-	-	-
4.) RIPPLE CURRENT (Max.) (6.5 Hz to 50 Hz) (50 Hz to 1 KHz) (1 KHz to 10 KHz)	0.5% rms 1% rms 3% rms	0.08% rms 1% rms 3% rms	0.08% rms 1% rms 3% rms	- - -	- - -	- - -
5.) RIPPLE VOLTAGE (Max.) (Millivolts P-P) (Millivolts RMS)	- -	- -	- -	150 50	15 2	300 100
6.) LOAD/LINE REGULATION ^{3/} (Milliamperes, DC) ^{2/} (Millivolts, DC) (5 Hz to 50 KHz)	0.2 ^{3/}	0.0625 ^{4/}	0.2 ^{5/}	3400 ^{6/}	225 ^{6/}	250 ^{11/}
7.) EFFICIENCY ^{7/}						
8.) TEMPERATURE COEFFICIENT (0° to 140°F)	.5%/°C	.5%/°C	.5%/°C	.1%/°C	.1%/°C	.1%/°C

Table 5.1.2-6

^{1/} Initial Tolerance

* To be added later

^{2/} Line Change ± 7%.

^{3/} Load change resulting in a 400-volt change in output voltage.

^{4/} Load change resulting in a 100-volt change in output voltage.

^{5/} Load change resulting in a 150-volt change in output voltage.

^{6/} Load ΔI of 50%.

^{7/} Overall efficiency shall be greater than 70% from 50% of full load to maximum rated load.

^{8/} To each of the tubes two anodes.

^{9/} Load impedance variation of ± 20%.

^{10/} Current required from each 12V source

^{11/} Load ΔI of 30%

* To be added at a later date

NOTE: Cathodes of the Laser tubes shall be operated near ground potential.

TABLE 5.1.2-7

TRANSCEIVER COMMANDS

(a) Power Supply Subsystem.-

<u>Command</u>	<u>Function</u>
(1) Transmitter Laser High voltage No. 1	On
(2) Transmitter Laser High voltage No. 1	OFF
(3) Transmitter Laser High voltage No. 2	On
(4) Transmitter Laser High voltage No. 2	OFF
(5) Transmitter Laser High voltage Nos. 1 & 2	Adjust current
(6) Local oscillator Laser High voltage No. 1	On
(7) Local oscillator Laser High voltage No. 1	Off
(8) Local oscillator Laser High voltage No. 2	On
(9) Local oscillator Laser High voltage No. 2	Off
(10) Local oscillator Laser High voltage Nos. 1 & 2	Adjust current
(11) Backup Laser High voltage No. 1	On
(12) Backup Laser High voltage No. 1	Off
(13) Backup Laser High voltage No. 2	On
(14) Backup Laser High voltage No. 2	Off
(15) Backup Laser High voltage Nos. 1 & 2	Adjust current
(16) Low voltage converter	On
(17) Low voltage converter	Off

(b) Laser Subsystem.-

(1) Backup Laser line (P-16) select	Select
(2) Backup Laser line center offset (P-16)	Offset
(3) Backup Laser line (P-20) select	Select
(4) Backup Laser line center offset (P-20)	Offset
(5) Modulator, video input Nos. 1 & 2	Select

TABLE 5.1.2-7
TRANSCEIVER COMMANDS

(c) Acquisition and Tracking Subsystem.-

(1) Nutator Bias Adjust (Beam Alignment)

	<u>Function</u>
a. Command, North-South axis (one pulse)	Counter reset
b. Command, North-South axis (series of pulses)	Counter input
c. Command, North-South axis (one pulse)	Execute
d. Command, East-West axis (one pulse)	Counter reset
e. Command, East-West axis (series of pulses)	Counter input
f. Command, East-West axis (one pulse)	Execute

(2) Acquisition threshold

a. Command (one pulse)	Counter reset
b. Command (series of pulses)	Counter input
c. Command (one pulse)	Execute

(3) Acquisition Confirm Threshold

a. Command (one pulse)	Counter reset
b. Command (series of pulses)	Counter input
c. Command (one pulse)	Execute

(4) Acquisition Control

a. Initiate search	Initiate
b. Inhibit search	Inhibit
c. Center IMC	Initiate
d. Initiate normal tracking	Initiate

(5) Spare discrete commands

- a. *
- b. *
- c. *
- d. *

* To be added at a later date

TABLE 5.1.2-8

TELEMETRY DATA

Power Supply Subsystem.-

<u>Function</u>	<u>Level</u>	<u>Accuracy</u> ¹	<u>Bandwidth</u>
(a) Transmitter Laser current	0 to 5 V	+ 2%	1 Hz
(b) Transmitter Laser voltage	0 to 5 V	+ 5%	"
(c) Local oscillator Laser current	0 to 5 V	+ 2%	"
(d) Local oscillator Laser voltage	0 to 5 V	+ 5%	"
(e) Backup Laser current	0 to 5 V	+ 2%	"
(f) Backup Laser voltage	0 to 5 V	+ 5%	"

Optical/Mechanical Subsystem.-

(a) Transmitter Laser power output	0 to 5 V	+ 1%	0.1 Hz
(b) Local oscillator Laser power output	0 to 5 V	+ 2%	"
(c) Back-up Laser power output(A) ²	0 to 5 V	+ 2%	"
(d) Back-up Laser power output(B) ³	0 to 5 V	+ 2%	"
(e) ICE baseplate temperature	0 to 5 V	+ 2%	"
(f) Radiation cooler temperature	0 to 5 V	+ 2%	"
(g) Sun shield temperature	0 to 5 V	+ 2%	"

3.1.4.1.3

(a) Local oscillator Laser tuner voltage:	0 to 5 V	+ 2%	10 Hz
(b) Transmitter Laser tuner voltage	0 to 5 V	+ 2%	10 Hz
(c) Backup Laser tuner voltage	0 to 5 V	+ 2%	10 Hz
(d) Modulator current	0 to 5 V	+ 2%	0.1 Hz
(e) Modulator oven temperatures	0 to 5 V	+ 2%	0.1 Hz

3.1.4.1.4 Receiver Subsystem.-

(a) Receiver AGC voltage	0 to 5 V	+ 1%	10 Hz
(b) Mixer bias current ⁴	0 to 5 V	+ 2%	0.1 Hz
(c) AFC Error output	0 to 5V	+ 2%	10 K Hz

1. Accuracy applies from 25% of full scale to 75% of full scale.
2. Back-up Laser in L.O. mode (P 16 line)
3. Back-up Laser in XMTR mode (P 20 line)
4. Accuracy applies from 10% of full scale to 50% of full scale.

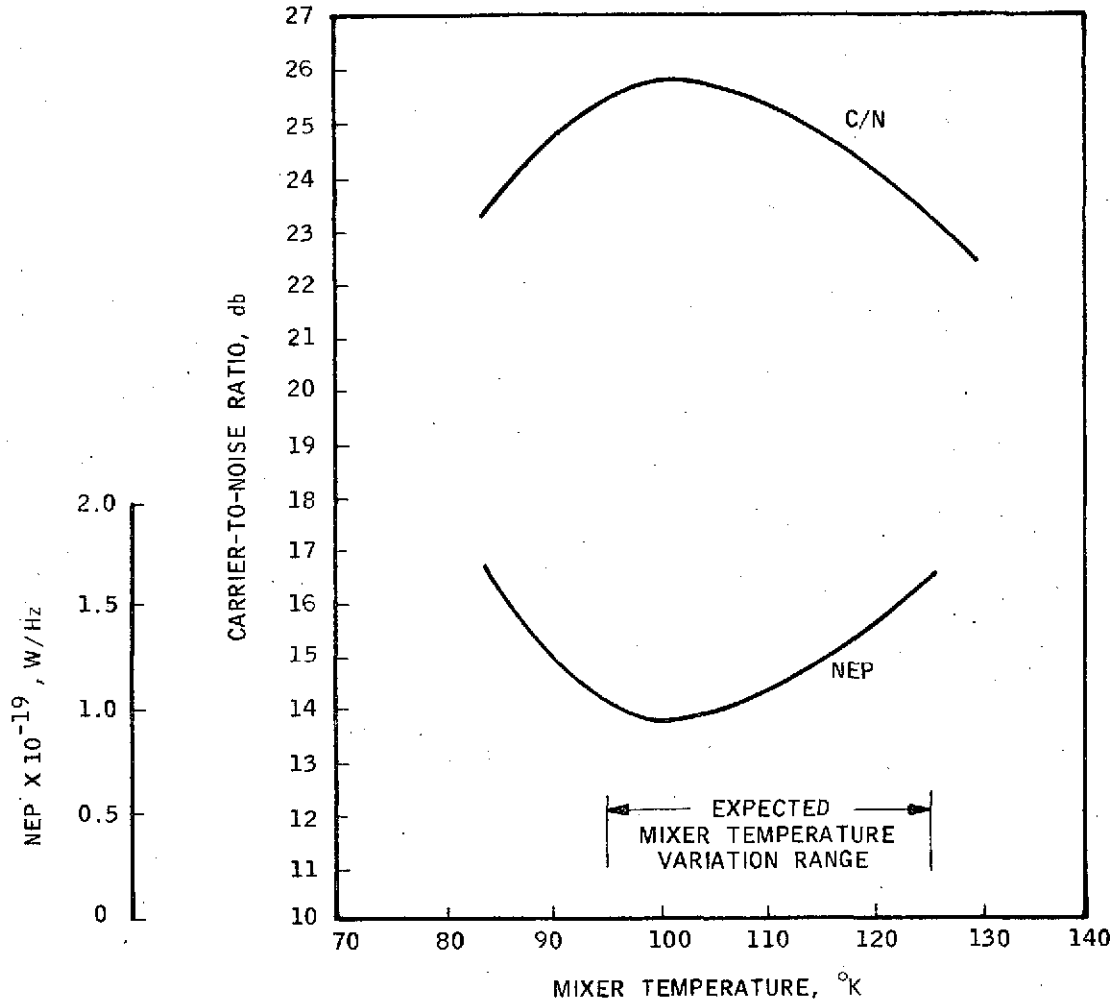
TABLE 5.1.2-8

TELEMETRY DATA

Acquisition and Tracking Subsystem.-

<u>Function</u>	<u>Level</u>	<u>Accuracy</u> ¹	<u>Bandwidth</u>
(a) Coarse pointing mirror-position (North-South)	0 to 5 V	±1%	2 Hz
(b) Coarse pointing mirror-position (East-West)	0 to 5 V	↑ ↓	2 Hz
(c) Image motion compensation position (North-South)	0 to 5 V		5 Hz
(d) Image motion compensator position (East-West)	0 to 5 V		5 Hz
(e) Acquisition threshold voltage	0 to 5 V		0.1 Hz
(f) Acquisition confirm threshold voltage	0 to 5 V		0.1 Hz
(g) Nutator bias voltage, (North-South)	0 to 5 V		0.1 Hz
(h) Nutation bias voltage, (East-West)	0 to 5 V		0.1 Hz

<u>Function</u>	<u>Bits</u>	<u>Bit Rate</u>
(i) Coarse pointing mirror position (East-West)	12	128 bps
(j) Coarse pointing mirror position (North-South)	10	128 bps



VARIATION OF NEP AND CNR AS A FUNCTION OF MIXER TEMPERATURE

Figure 5.1.2-1

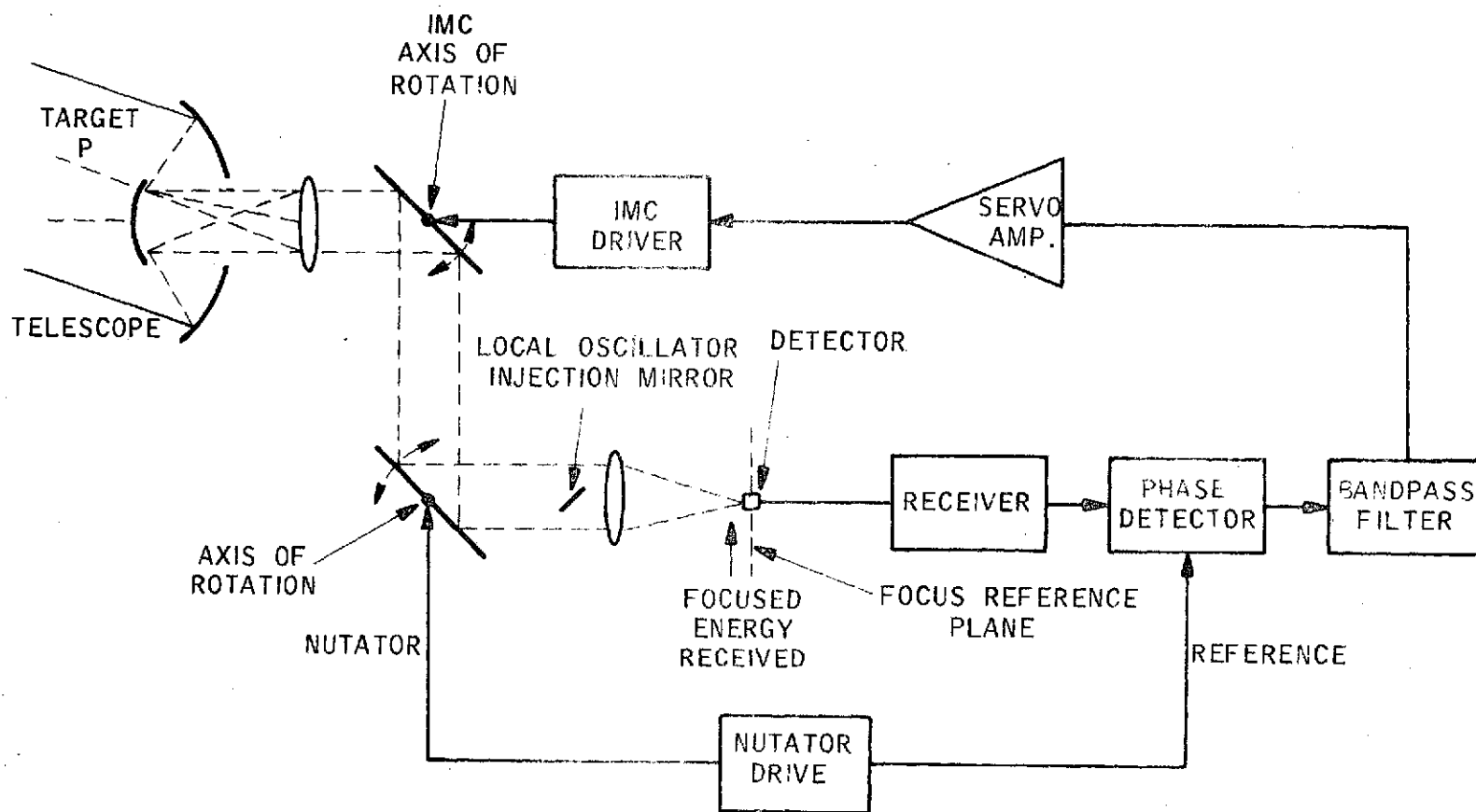
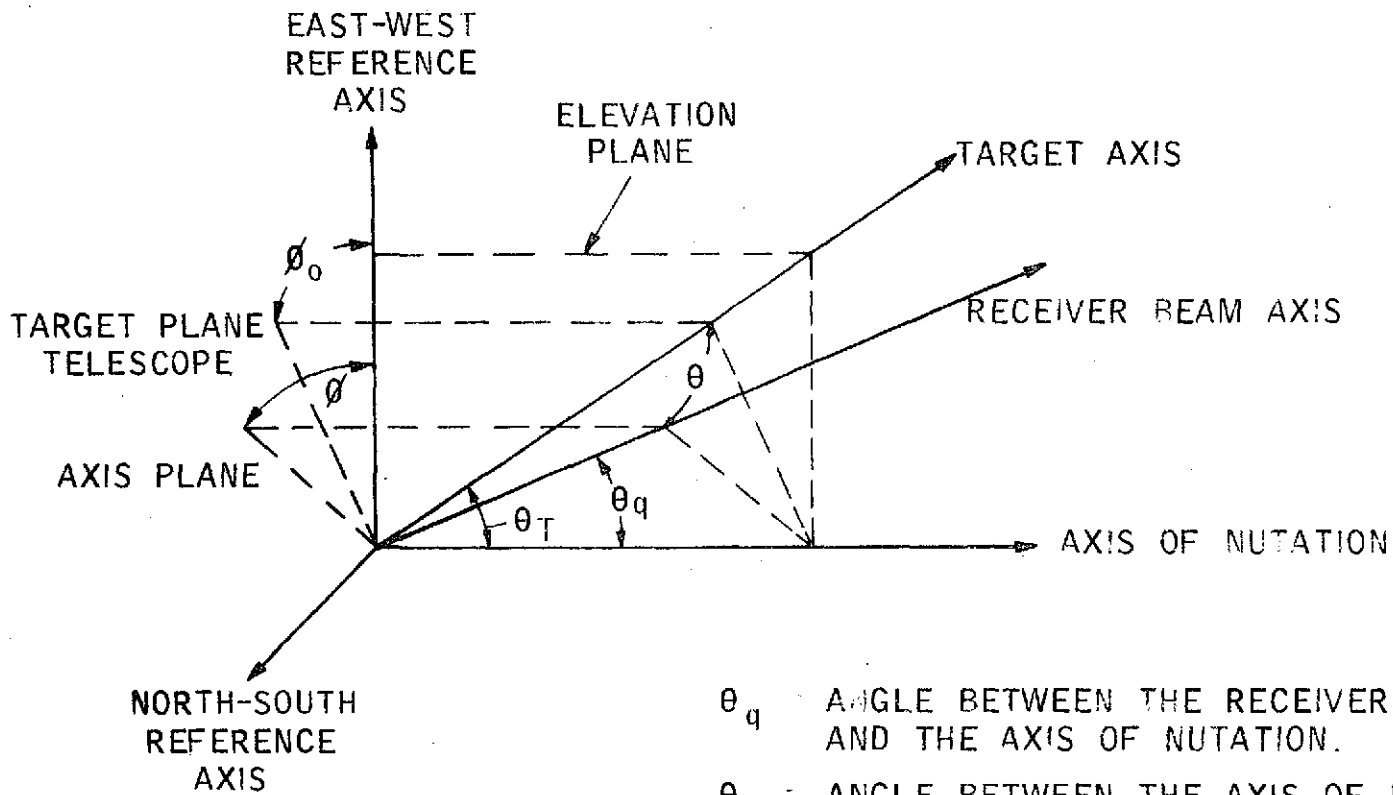


Figure 5.1.2-2

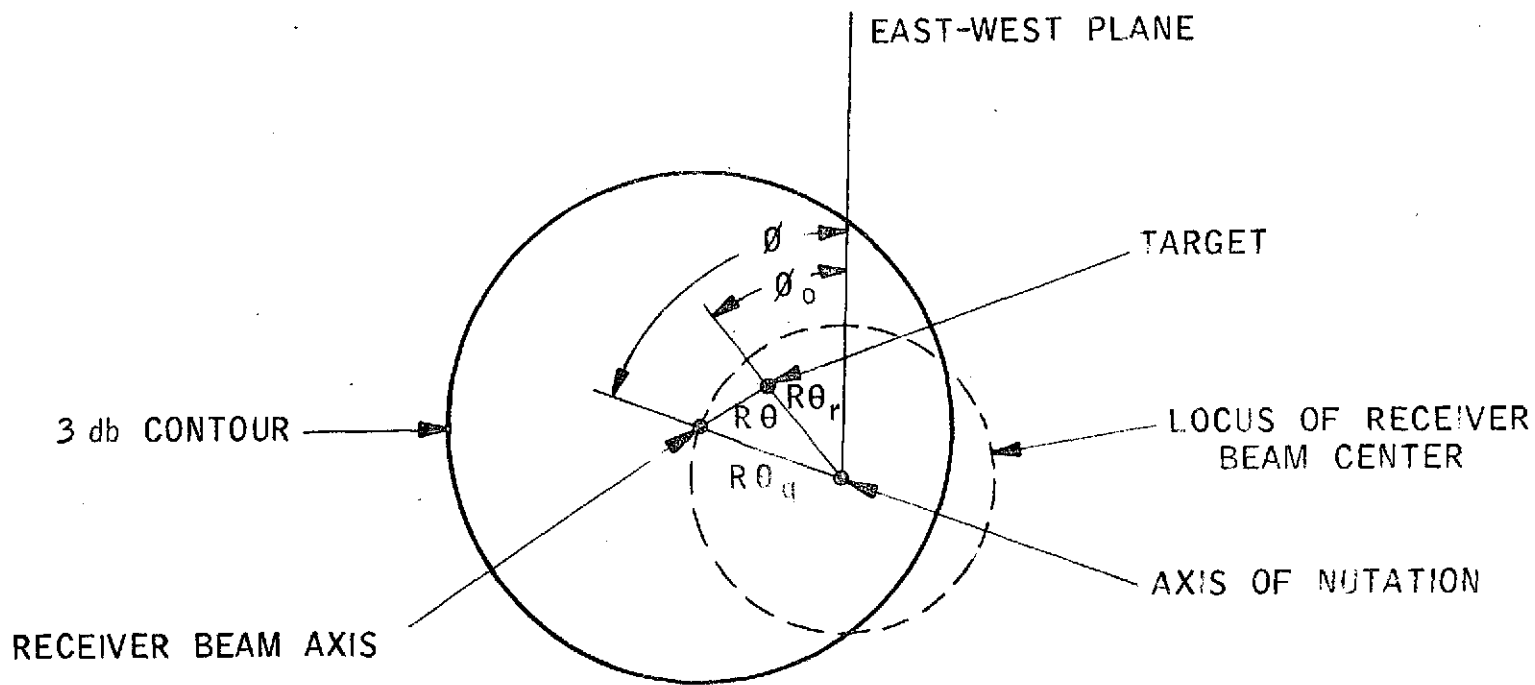
TRACKING BLOCK DIAGRAM (SIMPLIFIED)



- θ_q = ANGLE BETWEEN THE RECEIVER BEAM AXIS AND THE AXIS OF NUTATION.
- θ_T = ANGLE BETWEEN THE AXIS OF NUTATION AND THE TARGET AXIS.
- θ = ANGLE BETWEEN THE TARGET AXIS AND RECEIVER BEAM AXIS.
- ϕ = ROTATION ANGLE OF THE RECEIVER BEAM AXIS WITH RESPECT TO EAST-WEST REFERENCE AXIS.
- ϕ_0 = ANGLE BETWEEN THE TARGET AXIS AND THE EAST-WEST REFERENCE AXIS.

GEOMETRY OF THE NUTATING TRACKING SYSTEM

Figure 5.1.2-3



HEAD-ON VIEW OF NUTATING TRACKING SYSTEM
AT RANGE R FROM TRACKER

Figure 5.1.2-4

5.1.3 Link Analysis

This analysis sums and explains all of the power gains and losses from transmitter laser to the receiver heterodyne signal output from the pre-amplifier. The expressions for each gain or loss are stated in dbm, which allows total carrier-to-noise output from the link to be computed by adding up the positive and negative described terms.

The link analysis will consider the following cases:

a. At the beginning of the experiment, at maximum operating-temperature and minimum operating-temperature laser output, and mirror reflectivities of 99% and other nominal losses as described, both for operate and for acquisition cases.

b. At the end of the experiment, at maximum and minimum operating temperature laser output and all other losses as described above.

Results of this analysis are listed in Table 5.1.3-1, which includes the gains or losses associated with each contributing item in the LCE link. These items are discussed individually in the following subsections, arranged in the same order as listed in the table.

5.1.3.1 Transmitter Output (Item 1)

The value of transmitter laser output power varies according to operating temperature and age. These values are given by the laser subcontractor and are included in the laser specifications.

The range of operating temperatures of the LCE is specified as $25 \pm 10^{\circ}\text{C}$. Accordingly, the following values of laser output power have been given:

Beginning of experiment		
Minimum temperature (15°C)	790 mw	(29.0 dbm)
Maximum temperature (35°C)	650 mw	(28.1 dbm)
End of experiment (2 years)		
Minimum temperature (15°C)	710 mw	(28.5 dbm)
Maximum temperature (35°C)	550 mw	(27.5 dbm)

5.1.3.2 Transmitter Optical Coupling Losses (Item 2)

The transmitter optical coupling losses consist of the losses resulting from the mirror and lens surfaces, the beam splitter, the duplexer, and the filter, but exclude blockage loss. These losses are summarized below. The total transmitter optical coupling losses are found by adding the losses of all the components. Thus, the total loss is -1.8 db.

7 mirror surfaces at .99 ea	=	-.29 db
1 beam splitter (.97)(.99)	=	-.18 db
4 lens surfaces .99 ea	=	-.17 db
Duplexer .85	=	-.71 db
Filter .90	=	-.46 db
		<hr/>
Total loss		-1.8 db

5.1.3.3 Blockage Losses (Items 3 and 10)

Because of the structure of the telescope, there will be signal losses due to the shadow of the frame, the secondary mirror, and the acquisition beam mirror. The blockage area is shown in Figure 5.1.3-1, where the central blocking radius (due to the secondary mirror) is 0.73 in. and the primary radius is 3.875 in. Since the received signal will be a uniform beam, the blockage loss is proportional to the shadowed area. The transmitted beam will have a Gaussian distribution, and so the blockage loss must be found by integrating the power distribution over the shadowed area.

The receiver blockage calculation can be separated into three calculations: for the central blockage area, the spider blockage area, and the acquisition beam mirror area. The central blockage area is only the area of the circular-type region in the center with the rectangular region attached to it.

The circular-type area is the secondary mirror retainer as viewed by a beam traveling to the primary mirror and the rectangular region is the retainer as viewed by the beam incident on the coarse mirror from an outside source. This area is 2.24 in.². An effective radius is found from this area by computing the radius of the circle which has an area of 2.24 in.². The effective radius is .845 in. or 21.45 mm.

The spider blockage area is computed by adding the areas of the six legs. A_3 and A_4 are due to the blockage by the legs after the signal is reflected from the coarse mirror and is transmitted to the primary mirror. The width of the shadow is $1/4$ in., the width of the legs. A_2 is due to blockage by the legs when the beam is incident on the coarse mirror. In this case, the signal is at an angle of 45° to both the $1/4$ -in. and the $3/8$ -in. sides of the legs. This gives an effective width of $(3/8 + 1/4) \cos 45^\circ = .442$ in. When the width times the length of each of the legs is multiplied and the results are added together, the spider blockage area is calculated to be 5.51 in.^2 .

The acquisition beam mirror blockage area is the area of the shadow of the mirror. The shadow is a circle of radius 0.197 in., which gives an area of $.12 \text{ in.}^2$.

To find the total power loss in db, the blockage area divided by the total signal area is subtracted from 1. This gives an effective power ratio of 0.833 which is $-.79$ db blockage loss.

The transmitter blockage calculation can be analyzed in the same manner that the receiver blockage calculation was analyzed. The central blockage area was assumed to be a circle with a radius equal to the effective radius. The blockage loss was computed with a computer program using the equation given in the Optical Train Analysis section. This central blocking loss was found to be -1.00 db.

The calculation of the spider blockage loss was calculated by assuming the configuration in Figure 5.1.3-2. The combined spider blockage area is equal to the sum of the widths of the legs, which is 1.884 in., times the distance between the effective radius and the primary radius, which is 3.03 in. The amplitude distribution is $E(r) = E_0 e^{-\frac{r^2}{2\sigma^2}}$ where E_0 is 5.58 and σ is 1.82 in. The power is equal to the integral of the intensity distribution over the area. This is approximated by summing the intensity times the area of bands which are separated by $.505$ in. The blocked power is found to be 47.6 mw, which is $-.33$ db.

The acquisition beam mirror loss is approximated by using a point at the center of the circle and by multiplying the power at that point by the area. This value turns out to be negligible when compared with the other losses.

The total transmitter power loss is computed by adding the losses from each area. The total loss is equal to -1.33 db.

Calculations of blockage losses:

Telescope blockage

$$\text{Blockage area for } R_p = 3.875''$$

$$R_b = .73''$$

$$A_1 \text{ Central Blockage Area} = 2.24 \text{ in.}^2$$

$$R_b = \text{effective circle radius} = \sqrt{\frac{A_1}{\pi}} = .845 \text{ in. (21.45 mm)}$$

Spider blockage area

$$A_2 = \frac{46 \text{ in.}}{16} \times .442 \text{ in.} = 1.270 \text{ in.}^2$$

$$A_3 = \frac{46}{16} \times 1/4 = .719 \text{ in.}^2$$

$$A_4 = \frac{49}{16} \times 1/4 = .766 \text{ in.}^2$$

$$A_{\text{total}} = 2A_2 + 2A_3 + 2A_4 = 2.540 + 1.438 + 1.532 \text{ in.}^2 \\ = 5.51 \text{ in.}^2$$

Acquisition beam mirror blockage area

$$\text{Area} = \pi(.197)^2 = .12 \text{ in.}^2$$

Receiver blockage loss

$$\frac{P_r}{P_o} = 1 - \frac{2.24 + 5.51 + .12}{\pi(3.875)^2} = 1 - .167 = .833 \text{ or } -.79 \text{ db}$$

Transmitter blockage loss

$$\text{Central blockage loss} = -1.00 \text{ db}$$

Spider loss (P_2)

Let $P_0 = 650$ mw (reference)

The amplitude distribution is:

$$E(r) = E_0 e^{-\frac{r^2}{2\sigma^2}}$$

where $E_0 = \frac{1}{\sigma} \sqrt{\frac{P_0}{2\pi}}$

$$\sigma = 46.13/25.4 = 1.82 \text{ in.}$$

$$\begin{aligned} \therefore E(r) &= \frac{10.15}{1.82} e^{-\frac{r^2}{2(1.82)^2}} \\ &= 5.58 e^{-\frac{r^2}{6.60}} \end{aligned}$$

$$P_2 = \int_A E^2(r) dA \approx \sum_{i=.845}^{3.875} E^2(r_i) dA(r_i)$$

with $dr = .505$ in.

$$= 47.6 \text{ mw}$$

Then $\frac{P_T}{P_0} = 1 - \frac{P_2}{P_0} = 1 - \frac{47.6}{650} = 1 - .073 = .927$ or $-.33$ db

Acquisition beam mirror loss

$$P_3 = \int_A E^2(r) da \approx E^2(3.678) \times \pi(.197)^2$$

$$= .063 \text{ mw}$$

$$\frac{P_t}{P_0} = 1 - \frac{.063}{650} \approx 1.00$$
 or 0 db

Total transmitter blockage loss = $-1.00 - .33 = -1.33$ db

5.1.3.4 Transmitter Telescope Gain (Item 4)

Telescope gain is defined by

$$G_T = \frac{I(\theta)(4\pi R^2)}{P_T} = \frac{I(\theta)(4\pi R^2)}{\eta_T P_O}$$

where

G_T = transmitter telescope gain

R = distance to receiver (refer to next paragraph for this calculation)

$I(\theta)$ = far field off-axis intensity

P_T = transmitted power

η_T = ratio of transmitted power to telescope input power

P_O = input power to telescope

From section 5.2.1.10 of the Optical Train Analysis, the far field on-axis calculation of $I(0)/P_O$ is derived as

$$\frac{I(0)}{P_O} = \frac{4 \sigma_I^2 K^2}{2 \pi R^2} \left[\exp\left(\frac{-R_b^2}{4 \sigma_I^2}\right) - \exp\left(\frac{-R_p^2}{4 \sigma_I^2}\right) \right]^2$$

where

R_p = primary mirror radius = 3.875 in.

R_b = secondary mirror blockage radius = .845 in.

σ_I = transmitter beam sigma = 1.81 in.

$K = 2\pi/\lambda$

Thus, G_T is found to be 2.9579×10^9 , or 94.71 db.

5.1.3.5 Free Space Loss, Zenith Angle = 30° (Item 5)

The free space loss was computed for a distance R between a synchronous satellite and a point on earth having a 30° zenith angle. The formula for free space loss is derived in paragraph 5.1.3.9, where the relationship between transmitter and receiver telescope gains and isotropic free space loss is shown. The calculated value of free space loss is converted into db using the equation below.

$$F = \frac{\lambda^2}{4 \pi R^2}$$

R is derived from the equation

$$R = \sqrt{D^2 \sin^2 \alpha + h^2 + 2hD}$$

where

D = radius of the earth (6.37×10^6 meters)

α = elevation angle (60°)

h = synchronous altitude (3.8×10^4 km)

5.1.3.6 Atmospheric Attenuation Loss (Item 6)

Figure 5.1.3-3 gives the atmospheric attenuation loss as a function of the zenith angle, defined as the angle between the slant range and the line connecting the center of the earth and the ground station.

The atmosphere's attenuation loss computation is based on the Aerojet-Anding Atmospheric Transmission Program (ATMO) for 10.6 microns using the Air Force Cambridge Research Laboratory mid-latitude atmospheric model (AFCRL). ATMO is based on a 45-km atmospheric layer and calculates atmospheric attenuation in the slant-range due to molecular absorption by CO_2 , H_2O , and O_3 and due to absorption and scattering by aerosols.

ATMO is based on D. A. Anding's work Band-Model Methods for Computing Atmospheric Slant-Path Molecular Absorption (1967). The pressure, temperature, and water-vapor content as a function of altitude are based on Humidity Up to the Mesopause (1968) by Sissenwine, Grantham and Salmela, while the CO_2 content is based on the Lockheed value, 300 parts per million. An approximation to mie scattering is based on Etterman's A Model of a Clear Standard Atmosphere for Attenuation in the Visible Region and Infrared Windows (1963). The AFCRL model atmosphere is derived from measurements taken at 45° north latitude and an average of all longitudes.

5.1.3.7 Receiver Nutation Axis Transmitter Optical Axis Misalignment Loss (Item 7)

The optical axis misalignment covers a decrease in received power in proportion to the angle from the transmitter optical axis. The power

decrease versus angle is shown in the transmitter field-of-view intensity curve in section 5.2.1.10. From specifications, the transmitter and receiver optical axes will be within $3 \widehat{\text{sec}}$. The intensity loss from the given figure shows $-.70 \text{ db}$.

5.1.3.8 Tracking Error Loss (Item 8)

The sensitivity of the nutator/IMC servo loop in tracking the received beam determines the ability of the system to aim the telescope optical axis at the center of the transmitted power envelope. The transmitter field of view is illustrated in section 5.2.1.10. The nutator external telescope noise half angle is specified as $1.5 \widehat{\text{sec}}$. Then from the given figure, the intensity loss from peak-on-axis intensity is -0.3 db .

5.1.3.9 Receiver Gain (Item 9)

The receiver telescope gain differs from the transmitter telescope gain since the intensity distribution of the beam on the receiver primary is uniform instead of Gaussian. The total attenuation of the path from transmitter to receiver can then be expressed as the ratio of received power to transmitter power.

$$\frac{P_R}{P_T} = G_R G_T F = \frac{I(\theta) 4\pi r^2}{P_T}$$

where

G_R = receiver gain

G_T = transmitter gain (from para. 5.1.3.4)

F = free space loss (from para. 5.1.3.4)

r = receiver radius (3.875 in.)

As defined in paragraphs 5.1.3.4 and 5.1.3.5

$$G_T = \frac{I(\theta)(4\pi R^2)}{P_T}$$

$$F = \frac{\lambda^2}{4\pi R^2}$$

Substituting these into the first equation gives the formula for receiver gain.

$$G_R = \left(\frac{2\pi r}{\lambda} \right)^2$$

Substituting the values into these gives

$$G_R = 3.404 \times 10^9 \text{ or } 95.31 \text{ db}$$

5.1.3.10 Receiver Blockage Losses (Item 10)

Refer to paragraph 5.1.3.3 for the analysis of receiver and transmitter telescope blockage losses.

5.1.3.11 Receiver Optical Coupling Losses (Item 11)

The coupling losses consist of the losses due to the mirror and lens surfaces, the duplexer, and the filter, but excluding blockage loss. These losses are listed in the following table.

8 mirror surfaces at .99 ea.	=	-.33 db
6 lens surfaces at .99 ea.	=	-.27 db
Duplexer	.85	= -.71 db
Filter	.90	= -.46 db
		-1.8 db
	Total Loss	

5.1.3.12 Phase Misalignment Loss (Item 12)

The misalignment of the phase planes of the received signal and the local oscillator beams focused on the mixer is a result of any angular tilt between the optical axes of the two beams at the mixer and of the total effect of all plane wavefront distortions caused by aberrations in the flatness or the designed curvature of optical components in the optical train. To discuss the effect of these separately - first, the angular tilt between axes has been reduced to the angular compensation by the nutator to correct for lateral movement of the mixer from its aligned position. For an alignment tolerance of 0.015 in., the tilt angle is found by taking the arctangent of the displacement to imaging lens focal length.

$$\theta = \tan^{-1} (0.005/5.0) \approx 1 \text{ mrad}$$

The corresponding loss is less than 0.1 db, based on the phase tilt loss analysis.

The second loss contribution from distortion of the receiver beam and local oscillator beam plane wavefronts is found from the design tolerance specifications. The following tolerances are listed as the limiting production:

Receiver path	
Telescope optics	$\lambda/10$
Receiver path to mixer	$\lambda/10$
Local oscillator path	$\lambda/10$

The maximum distortion between the two wavefront planes is the root-mean-square of the three independent variances. Assuming also a worst-case estimate that the distortion is a plane tilt of this value, $1.73 \lambda/10$; the loss is computed as follows:

$$\frac{P_{\text{tilt}}}{P_o} = \left[\frac{\sin \left| \frac{2\pi}{\lambda} R_d \sin \left[\tan^{-1} \left(\frac{1.73\lambda}{2.0} \right) \right] \right|}{\frac{2\pi}{\lambda} R_d \left(\frac{1.73\lambda}{2.0} \right)} \right]^2$$

$$= .905$$

In db loss, this is -0.43 db, as shown also in Figure 5.1.3-4 for signal loss due to phase tilt versus mixer displacement.

5.1.3.13 Power Loss at Mixer Imaging Lens/Airy Disk Mismatch (Item 13)

The Airy disk loss is expressed as a function of the ratio of mixer radius to focal length of the received signal imaging lens. The optimum focal length for $r_d = 0.1$ mm is shown in Figure 5.1.3-5 to be at the maximum value of the ratio of power in the focused signal Airy disk to total imaged signal power. This maximum power ratio of .72 is for a focal length of 160 mm.

Since the receiver field of view is too narrow ($23 \widehat{\text{sec}}$) for the tracking electronics, the focal length was chosen at the sub-optimal value of 130 mm, which results in an increased field of view ($30 \widehat{\text{sec}}$) and a slight

decrease in signal power on the mixer to .70. This mismatch loss in db is increased from an optimal value of -1.43 db to -1.55 db. Refer to paragraph 5.2.1.2 of the Optical Train Analysis for a discussion of this tradeoff loss.

5.1.3.14 Mixer/Local Oscillator Airy Disk Mismatch Loss (Item 14)

The amount of mismatch between the mixer and center of the local oscillator power Airy disk that is focused on the mixer focal plane is dependent on the lateral tolerance designed into the mixer radiator mounts. The thermal and mechanical design of the radiator requires that the mixer and its radiator mount be supported on the LCE baseplate by thermal resistive pads. As a result, some lateral shift of the mixer is expected after pre-launch alignment, caused by the shock and vibration of the launch and the change to space environment. The limiting constraint in the design tolerance is the permissible mismatch between local oscillator Airy disk and the mixer. The discussion of the alignment tolerances is in para. 6.4.5.4.8. Based on a maximum movement of 0.015 in., the resulting increase in mixer noise is shown to be -0.1 db.

5.1.3.15 Noise Power (Item 15)

The noise power is the product of Noise Equivalent Power in watts/Hz and the receiver bandwidth (12 MHz). The Noise Equivalent Power is defined as the signal-to-noise ratio of unity at the output of the OHRS pre-amplifier. Therefore, it includes the mixer shot noise, background noise, mixer intrinsic noise, bias current noise, and preamplifier front-end noise contributions. The NEP is a function of the mixer temperature. The variation of expected NEP as a function of expected mixer temperature is shown on Figure 5.1.2-1. Mixer boules grown specifically for the LCE program may result in improved NEP in the expected mixer temperature range. The resulting CNR is also shown on this figure.

5.1.3.16 Carrier-to-Noise Ratio

The carrier-to-noise ratio for each case considered is the summation of all the gains and losses of the link. The heterodyned mixer output, when the units are locked on and tracking, will have the given carrier-to-noise ratio signal input to the IF amplifier.

5.1.3.17 Acquisition Carrier-to-Noise Ratio

The on-axis signal-to-noise ratio for the acquisition mode is computed by subtracting from the carrier-to-noise ratio the difference between antenna gains and transmitter blockage losses through the telescope normal operating mode and the direct path to the coarse pointing mirror in the acquisition mode. This difference in gains and losses is given in para. 6.4.5.5, Acquisition Signal Path Optimization, where an analysis is made of the acquisition field of view and on-axis intensity. A single difference value is subtracted in all four cases, since the change in transmitter laser power is already included in the C/N ratio values.

As shown in the analysis, the drop in on-axis intensity is the result of spreading the half angle to the 3-db power point to 0.178 degrees. Two small additions are gained, however, by the loss of central blockage. First, the power blocked by the secondary mirror in the center of the Gaussian distributed beam is now transmitted. Second, the additional dispersion of the beam by the central blockage is removed so that the beam diameter from the acquisition beam expander becomes the diffraction limiting aperture. Hence, the total difference between the on-axis intensities is the sum of these gain and loss changes in the acquisition beam path. The receiver of course still uses the telescope for receiving the transmitted acquisition beam. For instance, at the beginning of the experiment at minimum operating temperature, the acquisition carrier-to-noise ratio is -4.1 db, after subtracting 29.6 db from the carrier-to-noise ratio.

CG

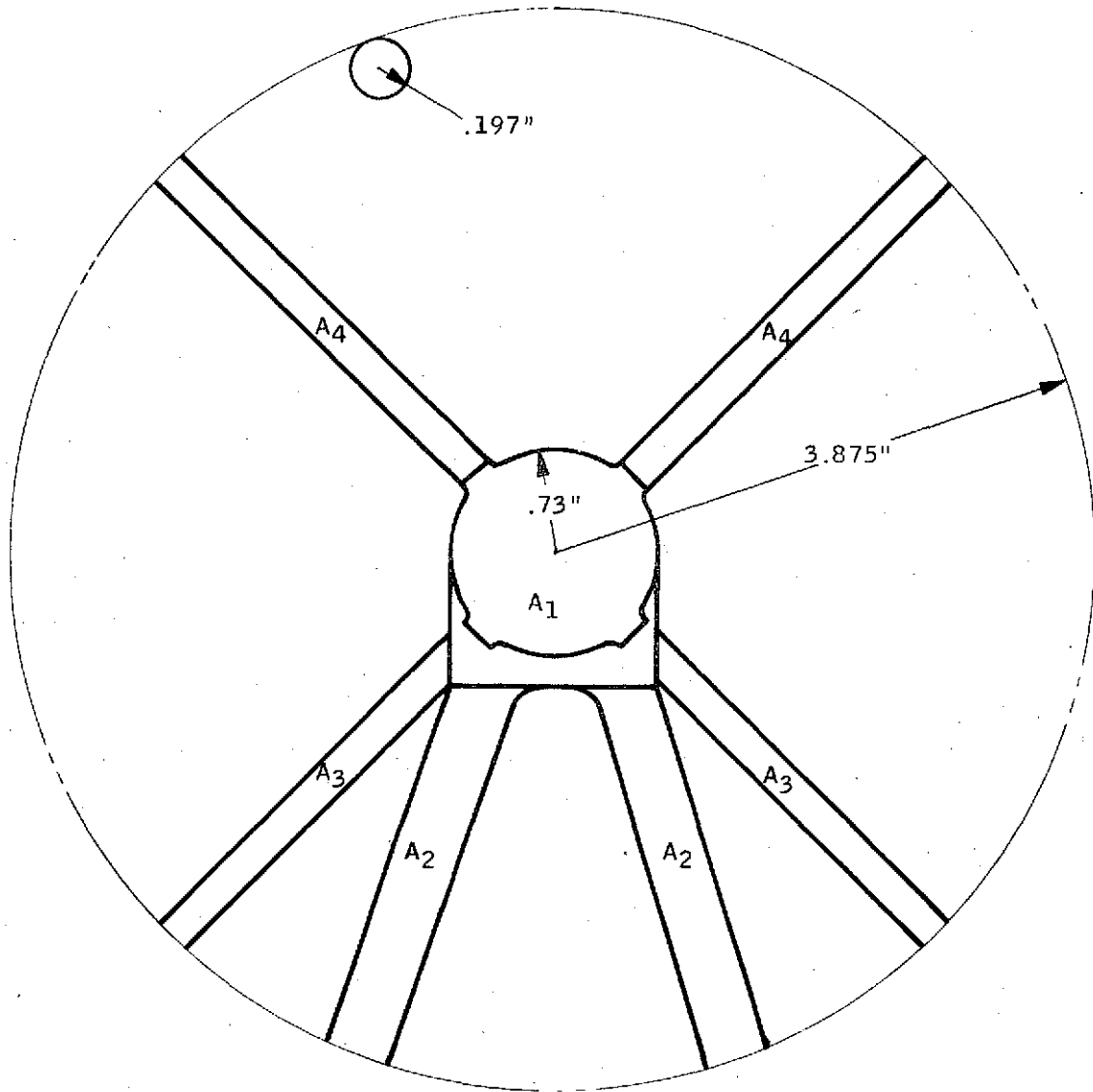
TABLE 5.1.3-1

LCE LINK ANALYSIS, OPERATING MODE

	Beginning of Experiment		End of Experiment (2 Years)	
	Min. Operating Temp. (15°C)	Max. Operating Temp. (35°C)	Min. Operating Temp. (15°C)	Max. Operating Temp. (35°C)
1. Transmitter Output	29.0 dbm	28.1 dbm	28.5 dbm	27.5 dbm
2. Transmitter Optical Coupling Loss	-1.8	-1.8	-1.8	-1.8
3. Blockage & Truncation Loss at XMIR (Radius Primary = 98.42, X 10-Power Telescope)	-1.3	-1.3	-1.3	-1.3
4. Transmitter Telescope Gain (Optimum Gaussian Intensity Distribution on the Primary)	+94.7	+94.7	+94.7	+94.7
5. Free-Space Loss (Synch, Alt., 30° Zenith Angle)	-272.7	-272.7	-272.7	-272.7
6. Atmospheric Attenuation Loss	-1.2	-1.2	-1.2	-1.2
7. Receiver Nutation Axis/Transmitter Optical Axis Misalignment Loss	-.7	-.7	-.7	-.7
8. Tracking Error Loss	-.3	-.3	-.3	-.3
9. Receiver Gain (Uniform Intensity Dist. on the Primary)	+95.3	+95.3	+95.3	+95.3
10. Receiver Blockage Loss	-.8	-.8	-.8	-.8
11. Receiver Optical Coupling Losses	-1.8	-1.8	-1.8	-1.8
12. Phase Misalignment Loss	-.4	-.4	-.4	-.4
13. Power Loss at Mixer Imaging Lens/Airy Disk Mismatch	-1.6	-1.6	-1.6	-1.6
14. Mixer Local Oscillator Airy Disk Mismatch Loss	-.1	-.1	-.1	-.1
15. Noise Power (NEP = 10^{-19} w/Hz, Noise Bandwidth = 12 MHz) (with mixer temperature = 96 to 106°K)	+89.2	+89.2	+89.2	+89.2
16. Carrier/Noise Ratio (db)	25.5	24.6	25.2	24.2
17. Acquisition Carrier/Noise Ratio (29.6 db below C/N ratio)	-4.1	-4.9	-4.4	-5.4

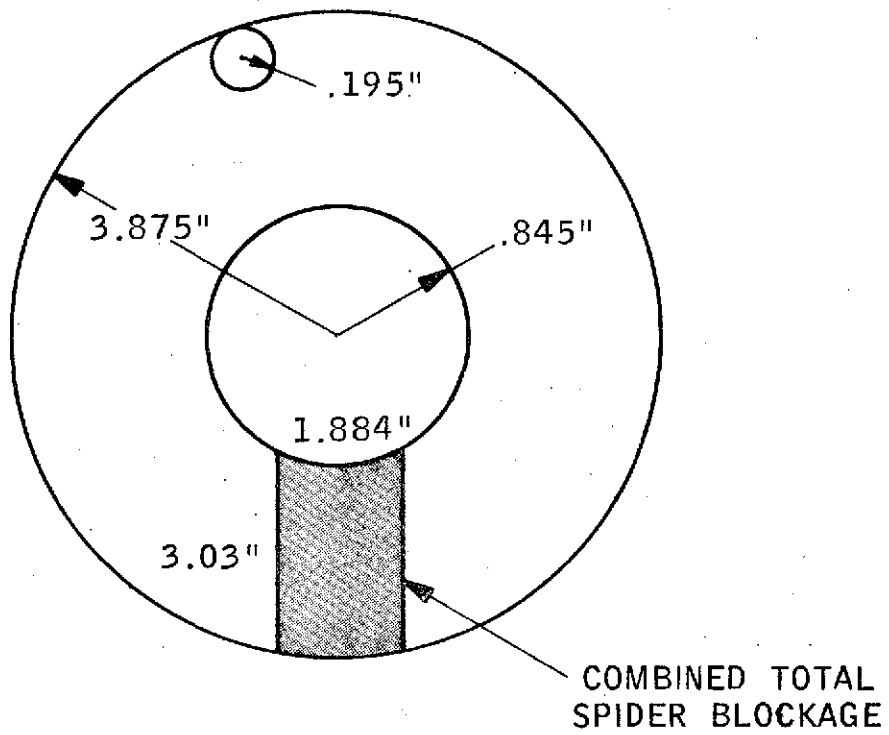
Table 5.1.3-1

Report No. 4033, Vol. I, Part I



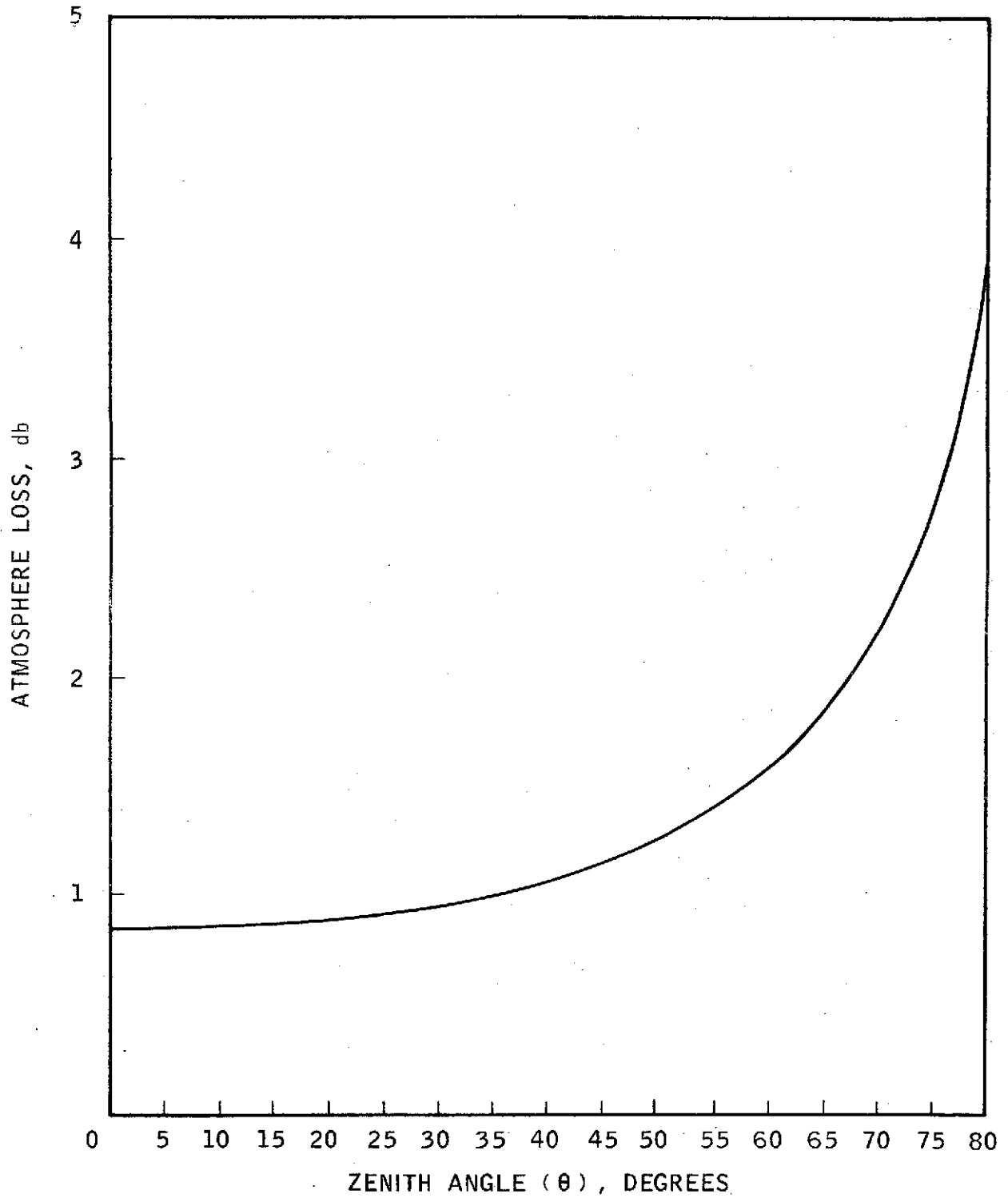
TELESCOPE BLOCKAGE

Figure 5.1.3-1



TRANSMITTER BLOCKAGE CONFIGURATION

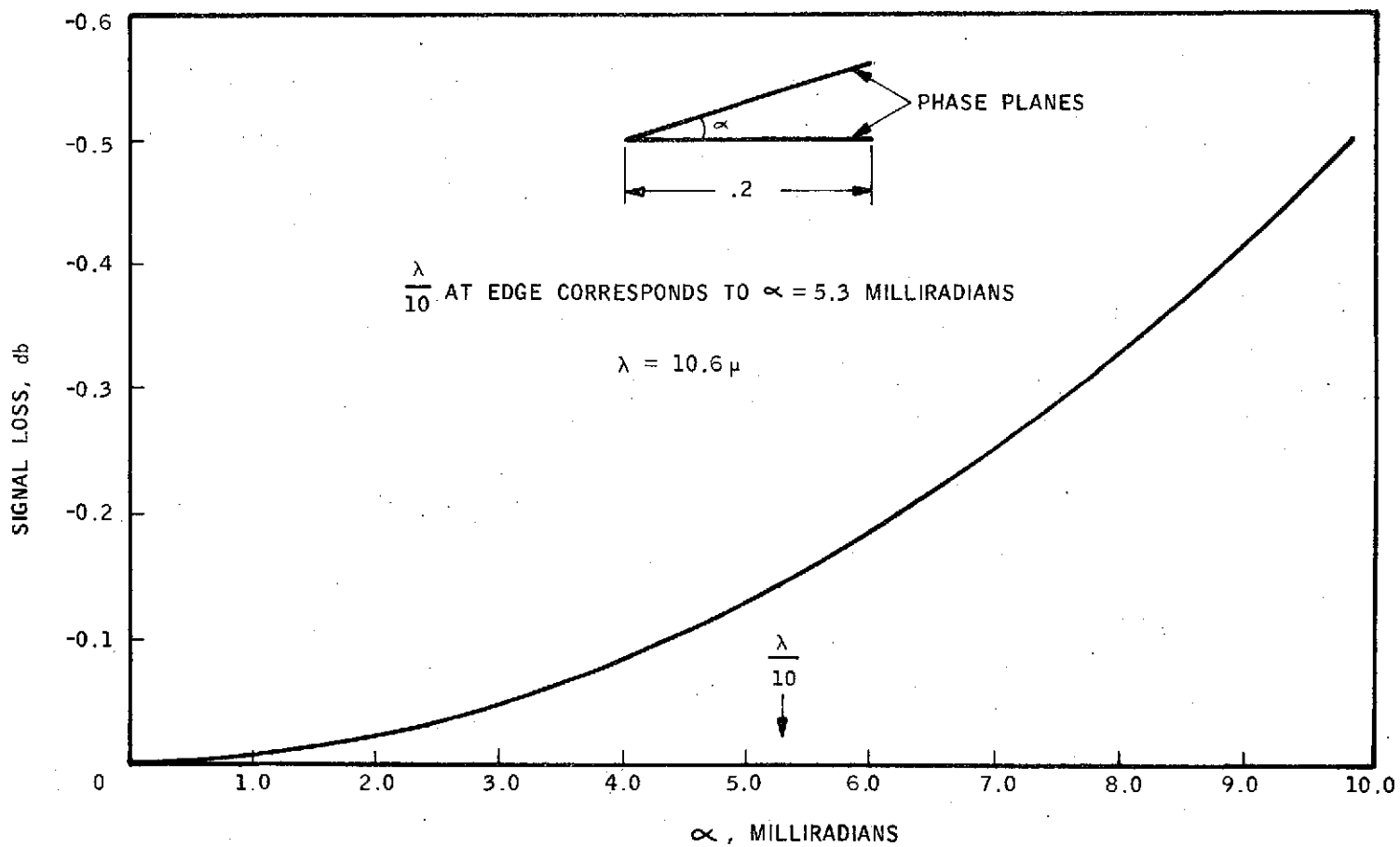
Figure 5.1.3-2



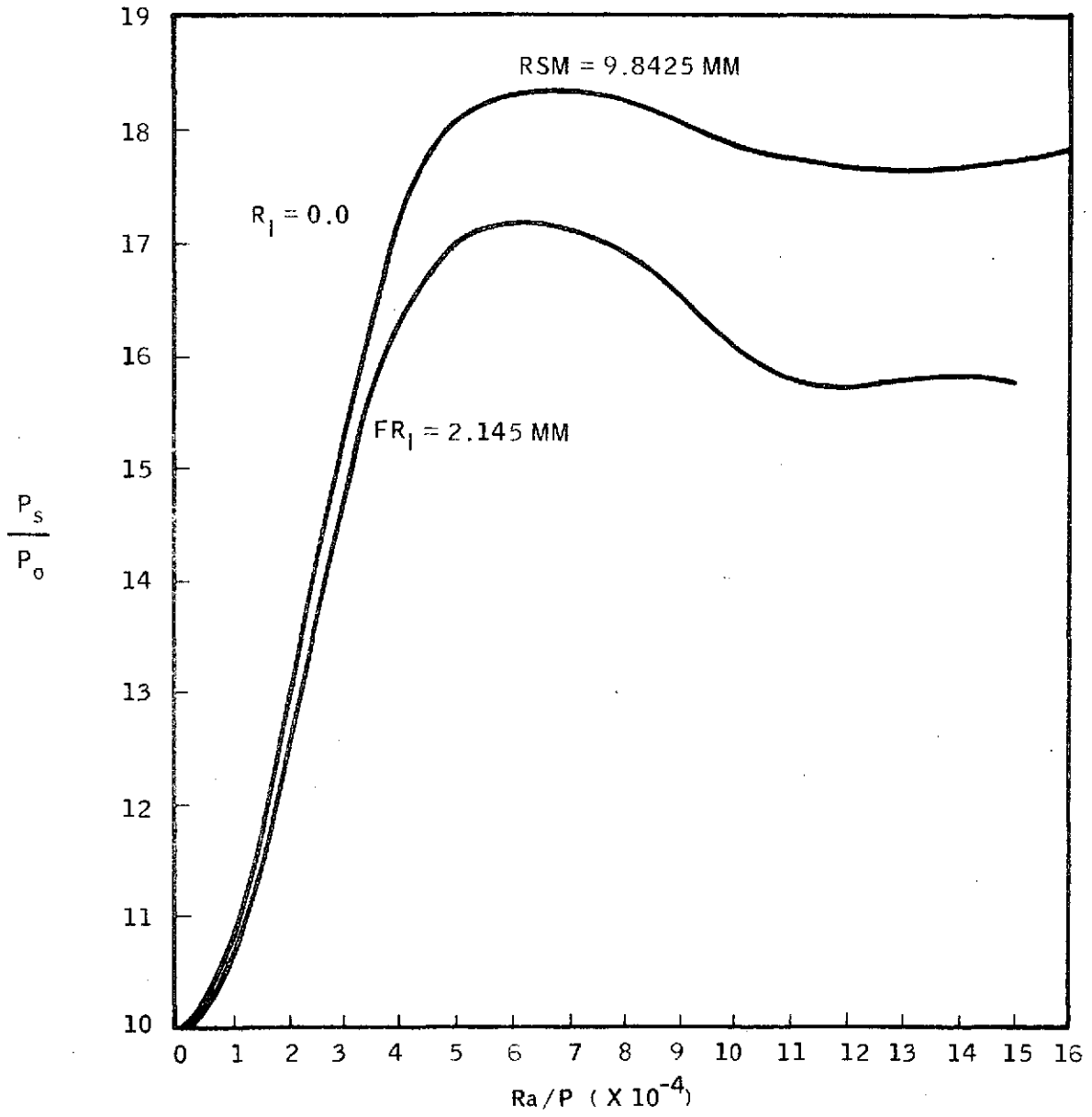
ATMOSPHERE LOSS VS ZENITH ANGLE

Figure 5.1.3-3

Figure 5.1.3-4



SIGNAL LOSS DUE TO PHASE TILT VS MIXER DISPLACEMENT



SIGNAL POWER WITHIN A CIRCLE OF RADIUS R_1 IN THE FOCAL PLANE AS A FUNCTION OF Ra/P

Figure 5.1.3-5

5.1.4 Communications Analysis

An in-depth analysis of the LCE communications link has been performed in order to determine the appropriate system requirements. A summary of the results is presented below. Details of the analysis are given in Appendix A.

The communications block diagram is shown in Figure 5.1.4-1. The vestigial sideband up-translator shifts the baseband spectrum from the 30-Hz-to-4.6-MHz range to 1.4 to 6.0 MHz, with an added "vestige" of the lower sideband of 0.4 MHz. The frequency up-conversion is used in order to bypass the GaAs modulator piezoelectric resonances, which fall in the frequency region from 100 to 900 kHz and which produce signal distortion (for details, see Appendix A).

The FM modulator is designed to produce a peak frequency deviation of 4 MHz. The resulting spectral distribution of the FM carrier, assuming the baseband of uniform spectral distribution and random phase, is shown in Figure 5.1.4-2. The ratio of second-order spectrum to first-order peak is given in Figure 5.1.4-2. It can be seen that the ratio at $f_c \pm 6$ MHz is -26 db. The carrier spectral distribution for a black-and-white television baseband is shown in Figure 5.1.4-4. As shown, the spectral components are down - 20db at $f_c \pm 4$ MHz. Based on these spectral analyses it is evident that the low index frequency modulation is taking place at peak frequency deviations up to 4 MHz. Further, computation of the effective modulation index for a TV baseband signal at peak frequency deviation of 4 MHz results in a $\beta = 0.465$ which substantiates the above conclusion. Therefore, the receiver IF bandwidth of 12 MHz has been specified centered at 30 MHz (see 5.2.4-1 for IF center-frequency selection, and Appendix A for other detailed computations).

The receiver IF filter characteristics are chosen to give a signal-to-distortion ratio of +33 db, or larger (for details, see Appendix A). The limiter has a flat frequency characteristic between 24 and 36 MHz, a power compression ratio of 10, and an AM to PM conversion factor of 1.5 °/db. The discriminator linearity is within 3% at $f_c \pm 6$ MHz.

The characteristic of the vestigial filter is shown in Figure 5.1.4-5. To meet the signal-to-distortion ratio of 27 db, the odd symmetry of the filter within the $f_o \pm 0.2$ MHz is specified at ± 0.1 db. (For other details, see Appendix A.)

The output video amplifier has essentially a flat response between 1.0 and 6.0 MHz and a linear phase characteristic as shown in Figure 5.1.4-6.

For the LCE Communications System described in preceding paragraphs the post detection peak signal-to-rms noise is given by

$$\frac{P}{N} = \frac{6}{1 + 3 \left(\frac{f_o}{B_v} \right)^2} \left(\frac{f_d}{B_v} \right)^2 \left(\frac{C}{N} \right)_{RF} \left(\frac{B_{IF}}{B_v} \right)$$

when $P =$ Peak signal power

$N =$ Rms noise power

$f_o =$ 1.4 MHz

$B_v =$ Video bandwidth = 4.6 MHz

$F_D =$ Peak frequency deviation

$\left(\frac{C}{N} \right)_{RF} =$ Predetection carrier-to-noise ratio of 23 db

$B_{IF} =$ Bandwidth of the IF of 12 MHz

The peak signal-to-rms noise is computed to be 32.7 db. (For detailed derivation of P/N equation, see Appendix A).

In summary, the following error budget results for the communications link (See Appendix A):

<u>Error Source</u>	<u>Signal to Distortion</u>
Random noise	32.7 db ($f_D = 4$ MHz)
Transmission deviations	33.0 db
Phase effects, 36 db	
Amplitude effect, 33.6 db	
Modulator/demodulator linearity	36.0 db
Vestigial filters	27.0 db
Vestigial phase tracking error	<u>36.0 db</u>
Total	26.7 db

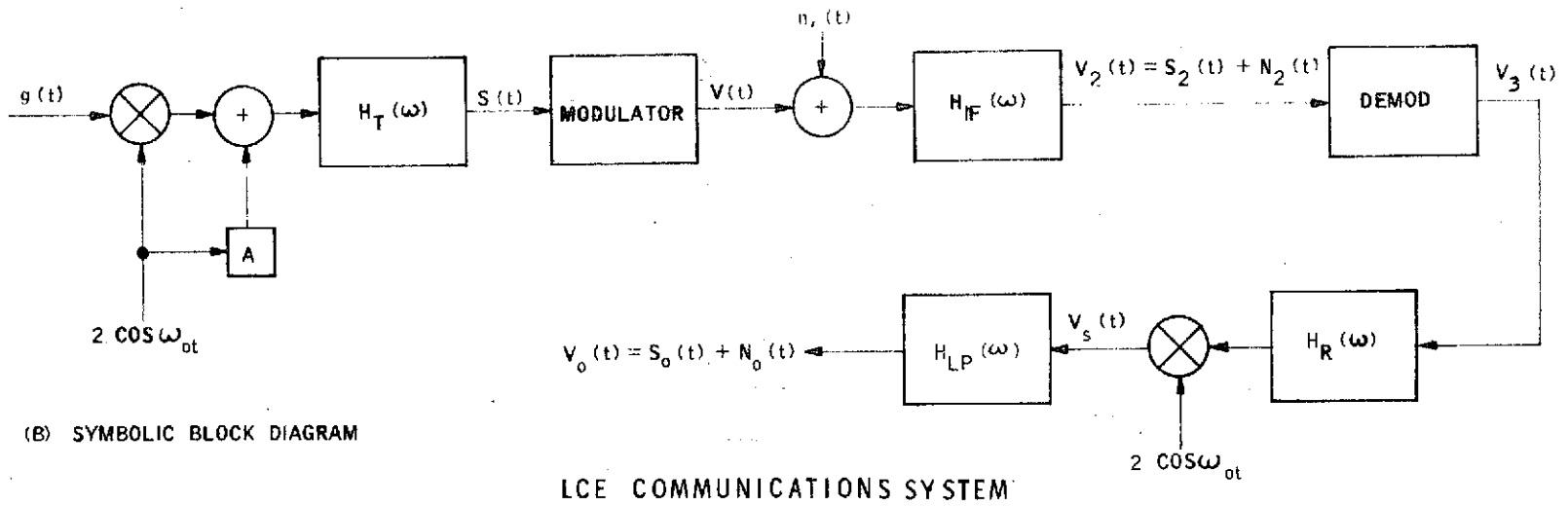
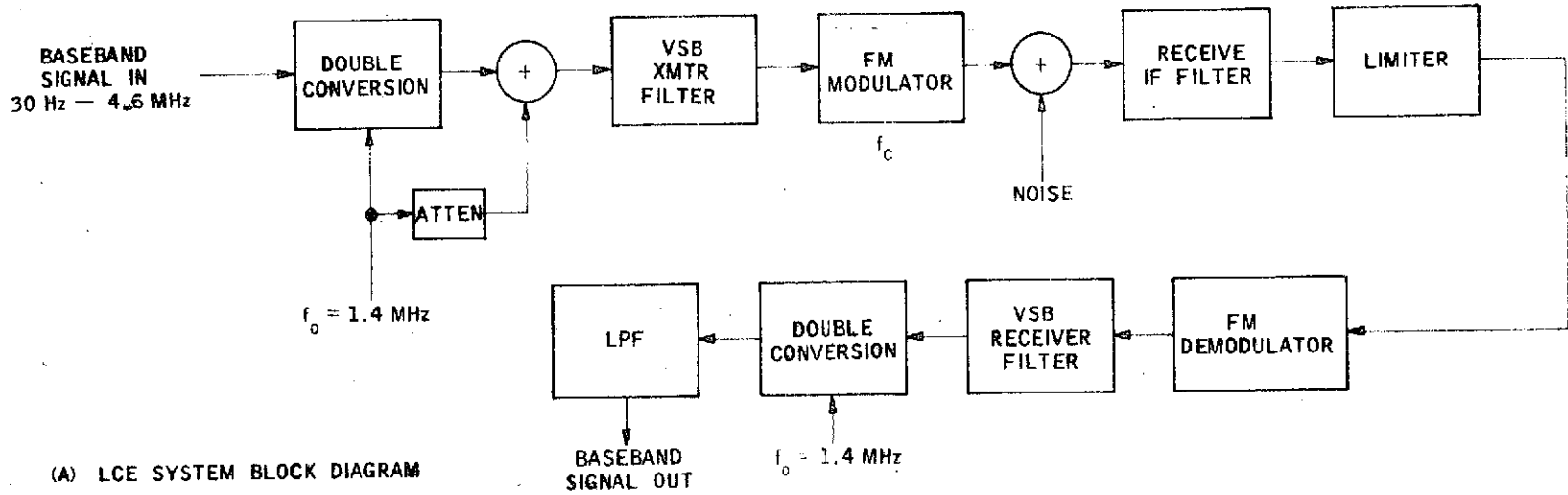
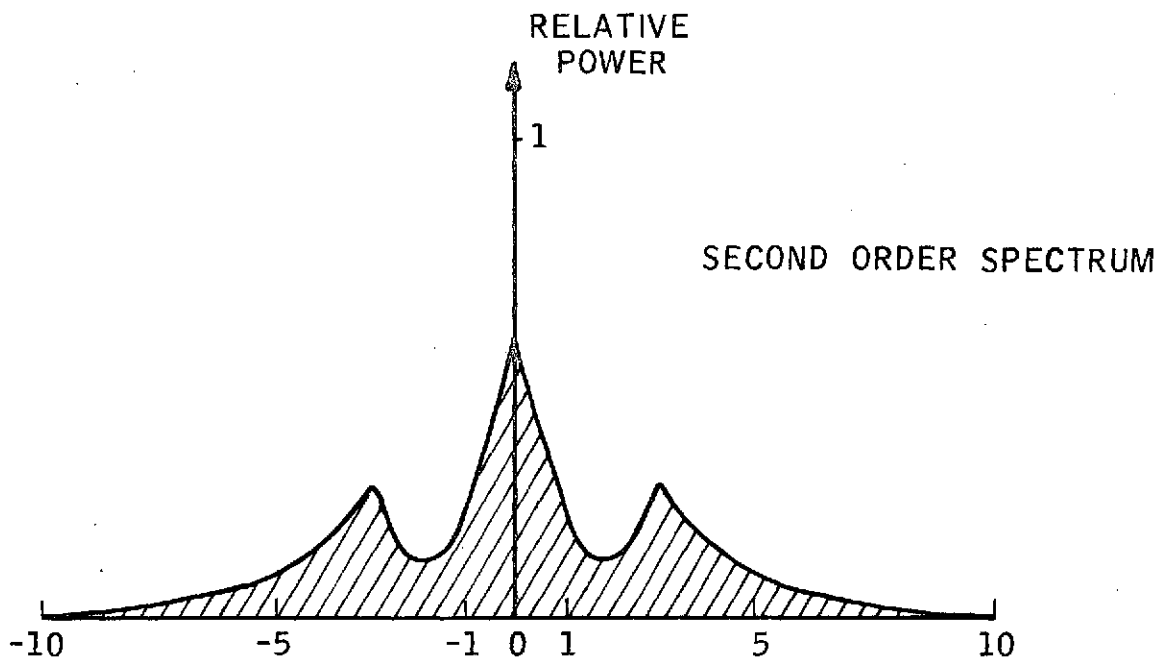
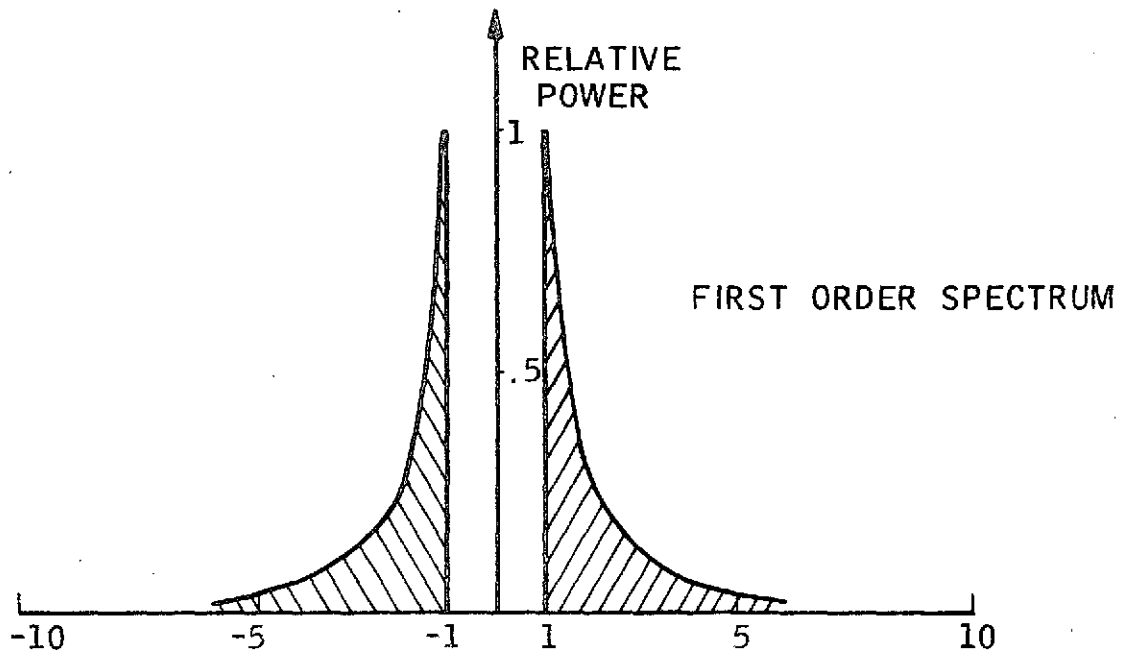
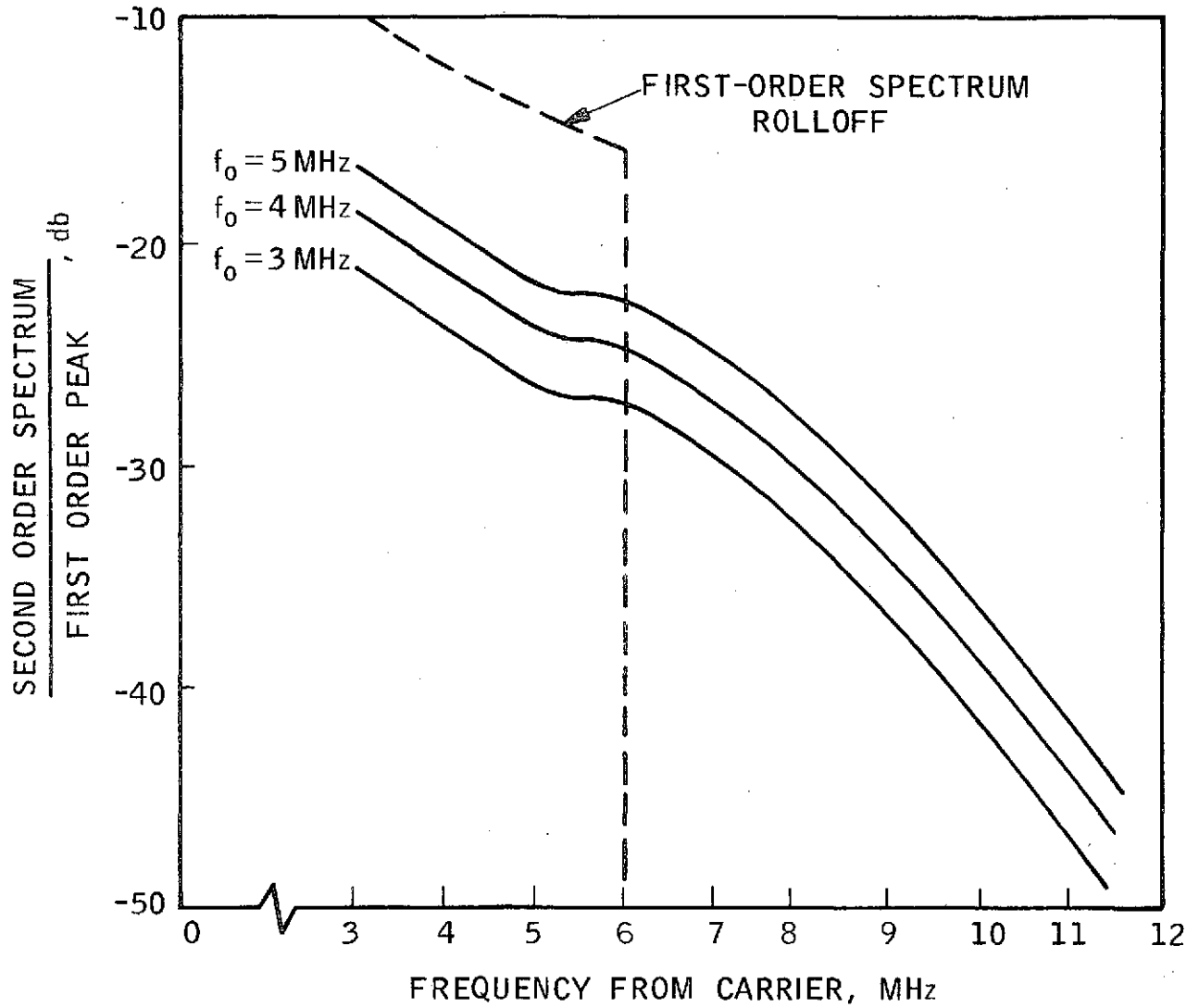


Figure 5.1.4-1



SPECTRA OF $\psi_{\theta}(f)$ ASSUMING $\psi(f)$ TO BE UNIFORM

Figure 5.1.4-2



SECOND ORDER SPECTRUM EFFECTS

Figure 5.1.4-3

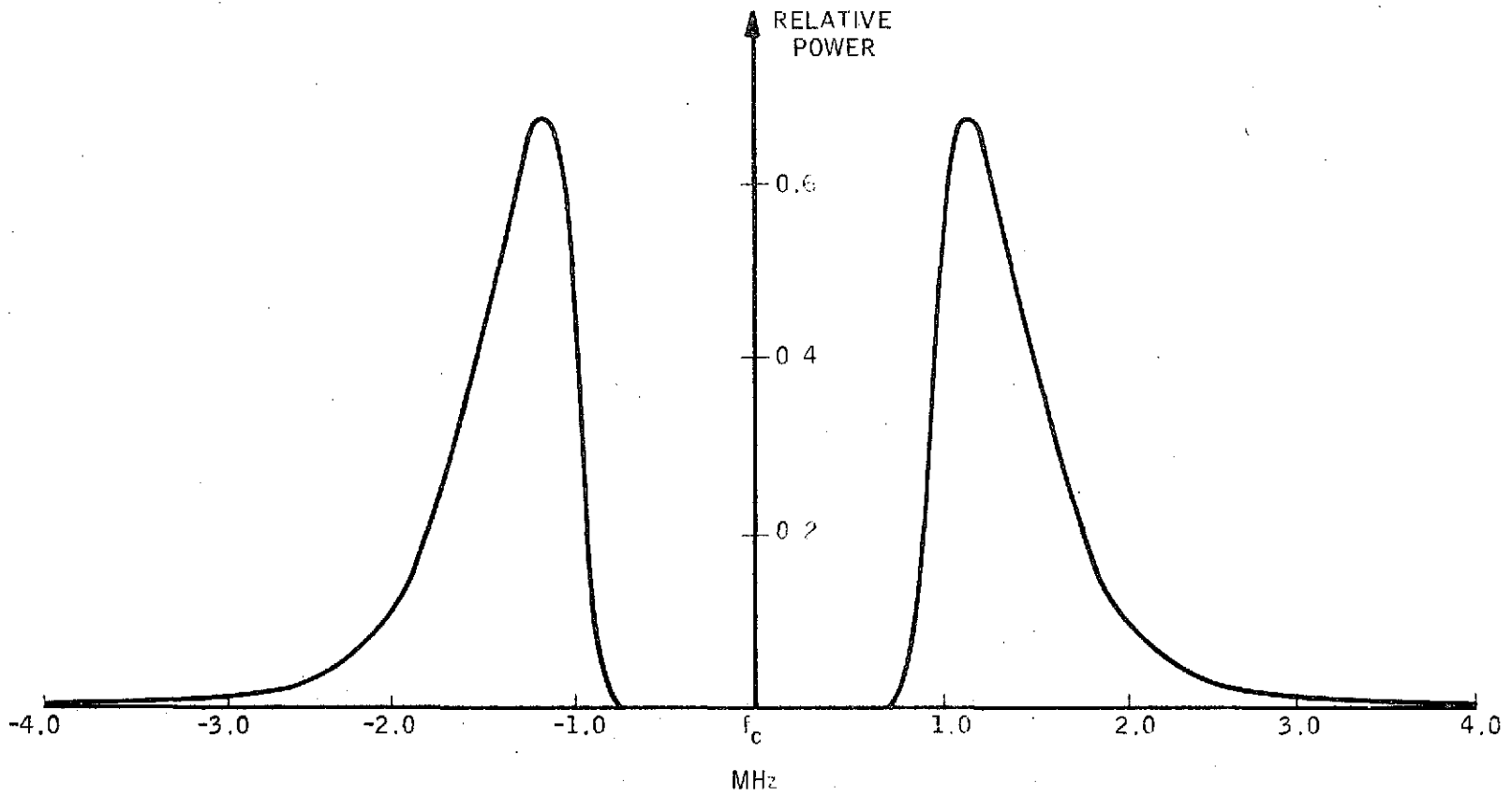
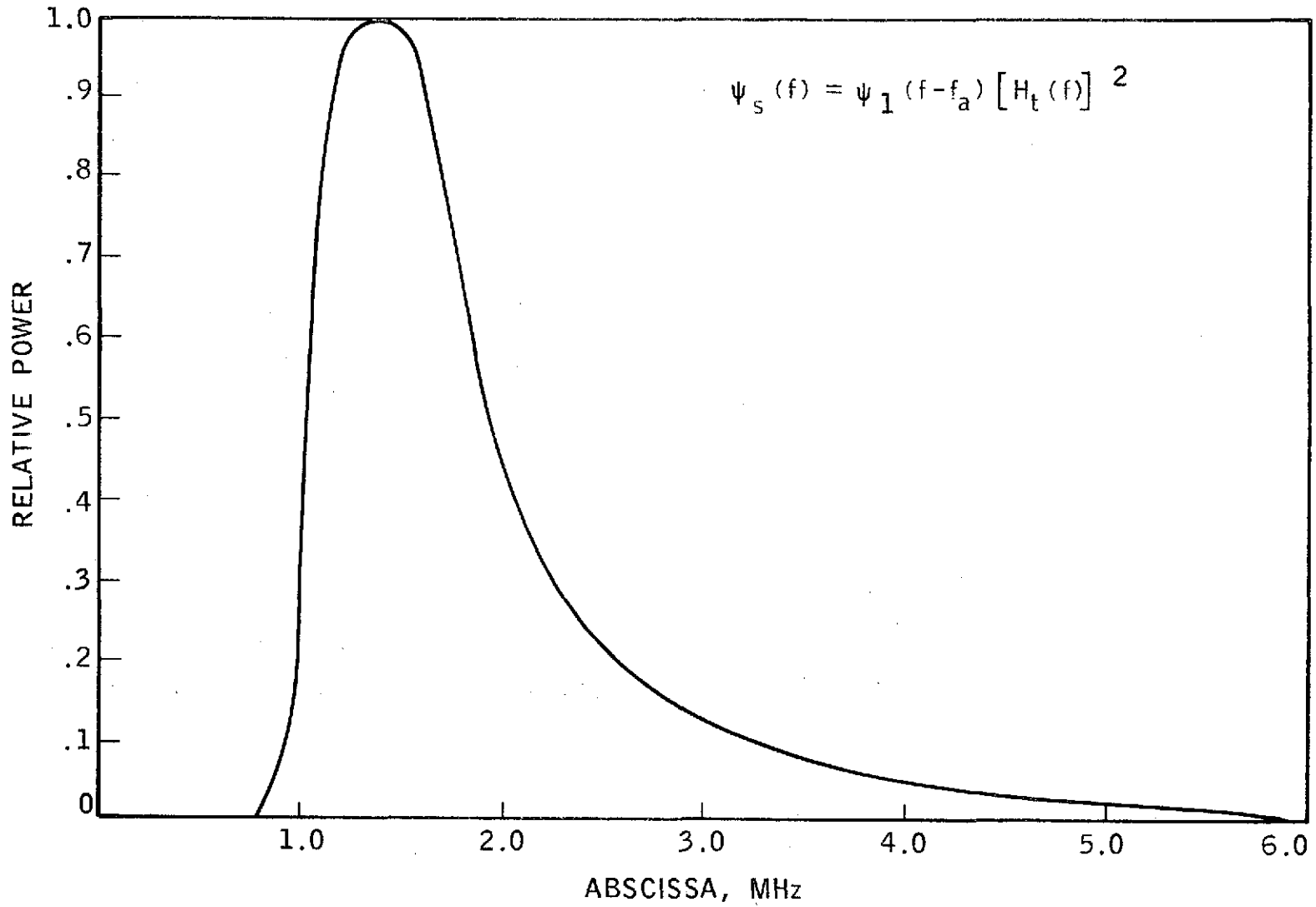


Figure 5.1.4-4

TRANSMITTED SPECTRUM



VESTIGIAL SIDEBAND SPECTRUM

Figure 5.1.4-5

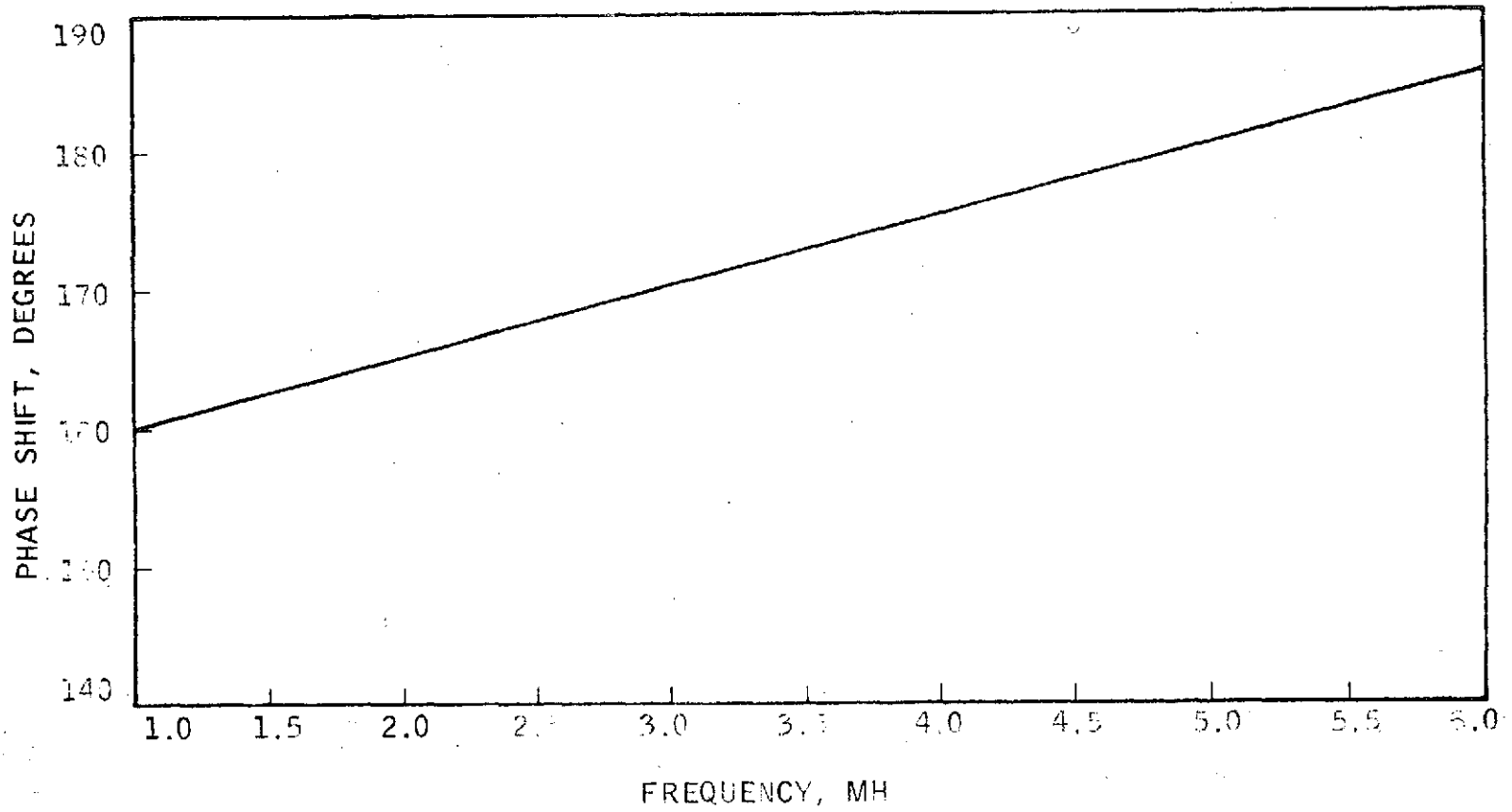


Figure 5.1.4-6

PHASE SHIFT VS FREQUENCY OF VIDEO AMPLIFIER

5.1.5 Acquisition Analysis

A two-station spatial scan technique is incorporated in the acquisition of the transmitter beam of one station by the receiver of the other station. The transmitter beams of both stations are broadened and the receivers of both stations are spatially scanned simultaneously. Both receivers are scanned in a rectangular search pattern, with the scan retrace at the end of each horizontal scan line. Acquisition is considered completed when both receivers have acquired their respective transmitter beams, and the acquisition and tracking subsystems are tracking the transmitter beams.

System design analyses have been made to establish the various system design parameters. With the design parameters established, system performances were analyzed by taking into consideration the following major parameters:

- Target-location uncertainty
- Spacecraft drift rate
- Local oscillator stability
- Background noise
- Acquisition probability
- False-alarm probability
- Carrier-to-noise ratio
- Signal-to-noise ratio
- IF filter bandwidth
- Post-detection filter bandwidth
- Transmitter beamwidth expansion
- Search angle
- Acquisition time
- Design margin

5.1.5.1 System Performance Summary

A functional block diagram of the acquisition subsystem is shown in Figure 5.1.5-1. The values of the various system parameters were selected to optimize the acquisition probability and signal-to-noise of the acquisition signal. The methods used in the evaluation of system performance and in selecting the values of the various system parameters are summarized in the subsequent sections. Further details of the method and analyses are presented in Appendix B.

Figure 5.1.5-2 shows the performance of the system in terms of acquisition time as a function of the spacecraft roll rate, with the local oscillator stability as a parameter. Conditions under which the curves are generated are specified in the same figure. Since the amplitude stability of the local oscillator is a critical parameter in determining acquisition time, this parameter is used in generating the curves. The curves indicated for a given value of local oscillator stability, acquisition time decreases as the spacecraft roll rate decreases. By specifying the local oscillator stability of 0.3 percent (the present design goal), and a maximum spacecraft roll rate of 0.001 degree/second, the acquisition time is determined to be 220 seconds.

The system performance is summarized as follows:

Target location uncertainty	+ 0.2 degrees
Acquisition probability	0.9
False-alarm time	1100 sec (one/five-scan frame)
Acquisition time	220 sec
Design S/N margin	5.6 db (4.9 db, including filter losses)

To accomplish the performance objectives, the following operation conditions and system design parameters are specified:

Maximum spacecraft drift rate	0.001 deg/sec
Local oscillator amplitude stability	0.3% (5-45 Hz)
Carrier-to-noise ratio at IF filter output	-15.4 db
IF filter noise equivalent bandwidth	8.5 MHz
Post-detection filter bandwidth	2 to 14 Hz
Expanded transmitter beamwidth	0.177 degree
Receiver beamwidth	30 arc-sec
Search angle	± 0.208 degree
Search time	220 seconds per scan frame

5.1.5.2 Received Signal-to-Noise Ratio at Time of Acquisition

During acquisition, the transmitters of both stations are broadened and the receivers of both stations are spatially scanned simultaneously. The transmitter and receiver beamwidths and the search scanning rate are such that the energy received at the time of acquisition has a carrier-to-noise ratio of $\frac{C}{N}$ at the IF filter output. The dwell time for a position in the scan is t_p . Analysis in Appendix B indicated the post-detection signal-to-noise ratio of the acquisition signal is given as:

$$\frac{S}{N} = \left(\frac{C}{N}\right) \frac{1}{\left[\frac{1}{B_I t_p} + \alpha^2 + \left(\frac{\sigma_b}{N}\right)^2\right]^{1/2}} \quad (5.1.5-1)$$

where

- $\frac{S}{N}$ = Signal-to-noise ratio of the acquisition signal
- $\frac{C}{N}$ = Carrier-to-noise ratio at the IF filter output
- B_I = Equivalent noise bandwidth of the IF filter
- B_a = Post-detection or acquisition signal bandwidth
- α = Local oscillator power output fluctuation
- $\frac{\sigma_b}{N}$ = Received background noise
- t_p = Scan dwell time, or $1/2 B_a$

The scan dwell time, t_p , as a function of the various system parameters has derived in the Appendix B as:

$$t_p = \frac{\sqrt{2\pi \rho T_f \delta B_o^2}}{2\theta_\gamma (2\theta_\gamma + \dot{\theta} t_f)} \quad (5.1.5.2)$$

where

ρ = Active fraction of the search scan line

T_f = Acquisition time or frame time

δ = Scan line overlap

B_o = Angle defining the receiver beamwidth

θ_γ = Search angle

$\dot{\theta}$ = Spacecraft roll rate

If α_o is the percent of local oscillator output power fluctuation in the bandwidth of Δf , the local oscillator output power variation falling in the acquisition signal bandwidth, B_a , is:

$$\alpha = \frac{\alpha_o B_a}{\Delta f} \quad (5.1.5-3)$$

Substituting Equation (-3) into Equation (-1):

$$\frac{S}{N} = \frac{C}{N} \frac{1}{\left[\frac{1}{B_I t_p} + \left(\frac{\alpha_o B_a}{\Delta f} \right)^2 + \left(\frac{\sigma_b}{N} \right)^2 \right]^{1/2}} \quad (5.1.5-4)$$

5.1.5.3 Selection of IF filter Bandwidth

Equation (5.1.5-4) indicated that to optimize the signal-to-noise ratio of the acquisition signal, the IF bandwidth B_I should be made as small as allowable by the frequency uncertainty between the transmitter of one station and the local oscillator of the other station. To determine worst-case frequency uncertainty, the four following factors have been taken into consideration:

- Transmitter frequency uncertainty
- Local oscillator frequency uncertainty
- Local oscillator dithering frequency deviation
- Doppler shift

During the acquisition period, communication between the two stations has not yet established. Therefore, the transmitter frequency of one station and the local oscillator frequency of the other station are controlled independently. The local oscillator performs a frequency dithering to locate its center-line frequency. The dithering amplitude produces a frequency deviation about its center line. An additional frequency uncertainty is produced when the local oscillator frequency is offset from its center line. Analysis in Appendix B indicated that with the various factors taken into consideration, an IF bandwidth of ± 2.0 MHz is required. The IF transfer characteristic $H(W)$ is

$$H(W) = \frac{KS^n}{(S-W_1)^n(S-W_2)^n}$$

K = Filter constant

$W_1 = 2\pi f_1$, $W_2 = 2\pi f_2$

f_1 = Filter lower cutoff frequency

f_2 = Filter upper cutoff frequency

n = Number of filter poles

The characteristics of a filter with $n=4$ are shown on Figure 5.1.5-3. This filter provides an attenuation of not more than 0.5 db at the frequency of ± 2.0 MHz.

The equivalent noise bandwidth of the filter, B_I , is

$$B_I = \frac{\int_{-\infty}^{\infty} |H(W)|^2 dw}{|H(W)|^2}$$

A value of $B_I = 8.5$ MHz is obtained by numerical integration of the filter characteristics shown in Figure 5.1.5-3.

5.1.5.4 Optimization of Received Power

Equation (5.1.5-4) indicated that to optimize the signal-to-noise ratio of the acquisition signal, the carrier-to-noise ratio of the received energy $\frac{C}{N}$ at the time of acquisition must be optimized. To maximize $\frac{C}{N}$, the three following design parameters have been taken into consideration:

- Expansion of transmitter beamwidth
- Search angle
- Scan line overlap

Detailed analysis in Appendix B indicates that the optimum width of the expanded transmitter beam for maximum received energy is obtained by setting the target uncertainty angle, θ_1 , equal to the angle θ_0 . The angle θ_0 must satisfy the following relationship:

$$P(\theta_0) = \frac{P(0)}{e} \tag{5.1.5-5}$$

$$\theta_1 = \theta_0 \tag{5.1.5-6}$$

where

$P(\theta_0)$ = Expanded transmitter power density at the angle θ_0

$P(0)$ = On-axis power density (peak power density) of the expanded beam

$\pm\theta_1$ = Target uncertainty angle

Equation (5.1.5-5) shows that power density at θ_0 is down $\frac{1}{e}$, or -4.36 db from the on-axis peak.

During acquisition, the receiver beams of both stations are scanning in a rectangular pattern with scan retrace at the end of each horizontal scan line. To compensate for the motion of the target, a certain amount of overlapping

of the scan line is required. Detailed analysis in Appendix B indicated that the optimum amount of overlapping is achieved when the overlapping angle, γ_m , satisfies the following relationship:

$$G(\gamma_m) = \frac{G(0)}{(e)^{0.25}} \quad (5.1.5-7)$$

$$\gamma_m = \delta\beta_0 \quad (5.1.5-8)$$

where

$G(\gamma_m)$ = Receiver gain at the angle of γ_m

$G(0)$ = Receiver on-axis power gain (peak power gain)

γ_m = Overlapping angle

δ = Overlap

β_0 = Angle defines the receiver beamwidth

Equation (5.1.5-7) shows at the point of optimum overlapping that the receiver gain is down $(e)^{-0.25}$ or 1.0 db from the peak. Equations (5.1.5-5) and (5.1.5-7) show that the maximum received energy is $\frac{1}{e.e^{0.25}}$ or -5.36 db down from the on-axis power density of the expanded transmitter peak. If P_t is the carrier power on the peak of the narrow transmitter beam which has a beamwidth of θ_t , the carrier power P for the expanded transmitter beam θ is

$$P = \frac{KP_t (\theta_t)^2}{e.e^{0.25} (\theta)^2} \quad (5.1.5-9)$$

$$P = \frac{0.285 KP_t (\theta_t)^2}{e^2}$$

K as a constant accounts for difference in transmission efficiency of the narrow and expanded beam optical paths. Since P is related to $\frac{C}{N}$ by the relationship:

$$P = \left(\frac{C}{N}\right) (NEP) (B_I)$$

$$P \propto \frac{C}{N}$$

Equation (5.1.5-9) becomes

$$\frac{C}{N} = \frac{0.285 K \left(\frac{C}{N}\right)_t (\theta_t)^2}{\theta^2} \quad (5.1.5-10)$$

5.1.5.5 Further Considerations of Expanded Transmitter Beamwidth, Search Angle and Target Uncertainty Angle

Results of the analysis in section 5.1.5.4 indicated that the received carrier energy, $\frac{C}{N}$, and the signal-to-noise of the acquisition signal, $\frac{S}{N}$, are optimized when the target uncertainty angle, θ_1 , is made equal to the search scanning angle, θ_γ . The transmitter beam is expanded to an amount equal to search angle.

During acquisition, transmitter beams of both stations are expanded and receiver beams of both stations scan. Since acquisition depends on having both receivers cover the transmitter of other stations, advantage is achieved by making the transmitter beam smaller than the scan angle. Let the transmitter beam, θ_o , decrease by a factor α_s .

$$\theta = \theta_1 \alpha_s \quad (5.1.5-11)$$

θ_1 = Target uncertainty angle (3σ) associated with a standard deviation of θ_p

To obtain an optimum value for α_s , analysis has been made in Appendix B in determining the effects of α_s on the acquisition probability under the three following mutually exclusive conditions for acquisition:

Both transmitters are pointing within θ_o

Transmitter 1 is pointed with θ_o and Transmitter 2 is pointed between θ_o and θ_γ

Transmitter 2 is pointed within θ_o and Transmitter 1 is pointed between θ_o and θ_γ

The acquisition probability, P_A , was determined to be:

$$P_A = \left[1 - \exp\left(-\frac{\theta_1^2 \alpha_s^2}{2\theta_p^2}\right) \right] \left[1 + \exp\left(-\frac{\theta_1^2 \alpha_s^2}{2\theta_p^2}\right) - 2 \exp\left(-\frac{\theta_1^2}{2\theta_p \alpha_s^4}\right) \right] \quad (5.1.5-12)$$

The value of P_A in Equation (5.1.5-12) is maximized if $\alpha_s = 0.8$, as shown in Appendix B. Equation (5.1.5-11) becomes:

$$\theta_o = \alpha_s \theta_1 = 0.8 \theta_1 \quad (5.1.5-13)$$

The optimum value of the search angle, θ_γ , for optimizing P_A was found to be:

$$\theta_\gamma = \frac{\theta_1}{\alpha_s} = 1.56 \theta_1 \quad (5.1.5-14)$$

Acquisition probability is optimized when the expanded transmitter beam is 0.8 times the target uncertainty angle, and the search angle is 1.56 times the target uncertainty angle.

5.1.5.6 Background Noise

From Equation (5.1.5-4), the signal-to-noise ratio of the acquisition signal is optimized when the background noise $\frac{\sigma_b}{N}$ is made as small as possible. Major factors in determining the value of $\frac{\sigma_b}{N}$ are:

5.1.5.6.1 Self-emitted Energy Fluctuation From Earth

Earth background energy is received by the detector as the receiver beam is scanned across the earth. The amount of energy received, according to analysis made in Appendix B, is:

$$\frac{\sigma_b}{N} = \frac{EC_2 d^3 \Delta T}{2\lambda c(\text{NEP}) T^2} \quad (5.1.5-15)$$

where

- $\frac{\sigma_b}{N}$ = Background energy from Earth
- E = Radiant emittance of Earth, watt/m²
- C₂ = 1.14 x 10⁴ micron °K
- d = Radiation wavelength, meters
- c = Speed of light, meters/sec
- NEP = Receiver NEP, watt/Hz
- λ = Radiation wavelength, microns
- T = Average temperature of Earth, °K
- dT = Variation in temperature, °K

5.1.5.6.2 Direct Solar Energy

Solar energy is received by the detector when the sun is in the scan angle. The received energy fluctuates from zero to E as the receiver beam scans from the dark background to the bright solar disk.

The received energy fluctuation, according to the analysis in Appendix B, is:

$$\frac{\sigma_b}{N} = \frac{E d^2}{2c(NEP)} \quad (5.1.5-16)$$

- $\frac{\sigma_b}{N}$ = Background energy from the sun
- E = Radiant emittance of the sun, watts/m²
- d = Radiation wavelength, meters
- c = Speed of light, meters/sec
- NEP = Receiver NEP, watt/Hz

Numerical evaluation of Equation (5.1.5-16) indicated that $\frac{\sigma_b}{N} = 0.218$. Acquisition in the presence of such high background energy reduces the acquisition probability to a low value. Therefore, it is not considered to be practical to acquire a target in presence of direct sunlight. Once the target is acquired elsewhere, the tracking subsystem is capable of tracking the target in presence of the sun.

5.1.5.7 Acquisition Probability, False Alarm Probability and Threshold Level

Acquisition is based on establishing a threshold level at the output of the subsystem. If either the noise alone or the acquisition signal plus noise exceeds the threshold level, the transmitter beam is

said to have acquired. Therefore, the threshold-to-noise ratio determines the false-alarm probability and the required signal-to-noise ratio on the acquisition signal determines the acquisition probability at a given false alarm probability. The following relationships were established, based on an analysis which is presented in Appendix B:

$$\frac{V_T}{N} = (2 \ln 5T_f B_a)^{1/2} \quad (5.1.5-17)$$

where

V_T = threshold level

N = RMS noise

T_f = Acquisition time

B_a = Acquisition signal bandwidth

$$P_d = \frac{1}{2} \left(1 - \operatorname{erf} \frac{V_T - S}{N} \right) + \frac{\exp \left[- \frac{(V_T - S)^{1/2}}{2N^2} \right]}{2 \sqrt{2\pi} \left(\frac{S}{N} \right)} \left[1 - \frac{V_T - S}{4S} + \frac{1 + (V_T - S)^2/N^2}{8 \left(\frac{S}{N} \right)^2} - \dots \right] \quad (5.1.5-18)$$

where

S = Acquisition signal amplitude

$\frac{S}{N}$ = Required signal-to-noise ratio of the acquisition signal to produce an acquisition probability P_d with the threshold set at V_T volts

$$P_s = P_A \cdot P_d \quad (5.1.5-19)$$

where

P_s = Acquisition probability of the subsystem

P_A = Acquisition probability given by Equation (5.1.5-12)

P_d = Acquisition probability given by Equation (5.1.5-18)

5.1.5.8 Acquisition Subsystem Design

The results of the design analysis are used to design the subsystem. The following represents a summary of the detailed design described in Appendix B.

5.1.5.8.1 Expanded Transmitter Beamwidth

For a target uncertainty angle of ± 0.2 degree (3σ number), the standard deviation θ_p is $\frac{0.2}{3} = 0.0667$ degree ($1 - \sigma$ number). Equation (5.1.5-12) indicated that for $P_A = 0.91$, a ratio of $\frac{\theta_1}{\theta_p} = 2$ is required

Therefore:

$$\theta_1 = 2\theta_p = 2(0.0667)$$

$$\theta_1 = 0.133 \text{ degree}$$

From Equation 5.1.5(13)

$$\theta_o = \alpha_s \theta_1 = 0.8\theta_1$$

$$= 0.8(0.133)$$

$$= 0.106 \text{ degree}$$

The half-power beamwidth of the expanded transmitter beam, $\pm \theta$, is related to θ_o by:

$$\theta = 0.833 \theta_o$$

$$= 0.833 \alpha_s \theta_1$$

$$= 0.833(0.8) (0.133)$$

$$= .0885 \text{ degree}$$

The half-power beamwidth of the expanded transmitter beam is $2\theta = 0.177$ degree.

5.1.5.8.2 Search Angle

From Equation (5.1.5-14)

$$\begin{aligned}\theta_{\gamma} &= \frac{\theta_1}{\alpha_s^2} \\ &= (1.56)(0.133) \\ &= 0.208 \text{ degree}\end{aligned}$$

Total search angle is $2\theta_{\gamma} = 0.416$ degree

5.1.5.8.3

Signal-to-noise Ratio of Acquisition Signal

From Equations (5.1.5-2), (4), (10) and (15)

$$\frac{S}{N} = \left(\frac{C}{N} \right) \frac{1}{\left[\frac{1}{B_I t_p} + \left(\frac{\alpha_o B_a}{\Delta f} \right)^2 + \left(\frac{\sigma_b^2}{N} \right) \right]^{1/2}} \quad (5.1.5-20)$$

$$\frac{C}{N} = \frac{0.285 K \left(\frac{C}{N} \right)_t (\theta_t)^2}{\theta^2} \quad (5.1.5-21)$$

$$t_p = \frac{\sqrt{2\pi p T_f} \delta \beta_o^2}{2\theta_{\gamma} (2\theta_{\gamma} + \theta T_f)} \quad (5.1.5-22)$$

$$B_a = \frac{1}{2 t_p} \quad (5.1.5-23)$$

$$\frac{\sigma_b}{N} = \frac{E C_2 d^3 \Delta T}{2 \lambda c (NE) T^2} \quad (5.1.5-24)$$

The proper numerical values for various parameters are established in Appendix B. With these values substituted, Equations (5.1.4-20) (21), (22), (23), and (24) become:

$$\frac{S}{N} = 13.1 \quad (5.1.5-25)$$

$$\frac{C}{N} = 2.87 \times 10^{-2} \quad (5.1.5-26)$$

$$t_p = 3.29 \times 10^{-2} \text{ second} \quad (5.1.5-27)$$

$$B_a = 15.2 \text{ Hz} \quad (5.1.5-28)$$

$$\frac{\sigma_b}{N} = 2.7 \times 10^{-4} \quad (5.1.5-29)$$

5.1.5.8.4 Acquisition Probability, Threshold Level and Design $\frac{S}{N}$ Margin

From Equation (5.1.5-17)

$$\frac{V_T}{N} = (2 \ln 5 T_f B_a)^{1/2}$$

Let

$$T_f = 220 \text{ sec, acquisition time}$$

$$B_a = 15.2 \text{ Hz, equivalent acquisition bandwidth}$$

$$\frac{V_T}{N} \text{ becomes}$$

$$\frac{V_T}{N} = 4.4$$

To produce an average time between false alarms of one per five scan frames, or 1100 seconds, the threshold required is 4.4 times the rms noise voltage of the subsystem.

For

$$P_d = 0.99$$

99% probability of
acquiring the signal

$$P_{fa} = \frac{1}{5 T_f B_a} = 6 \times 10^{-5}$$

False-alarm probability for
 $5 T_f = 1100$ sec and $B_a = 15.2$ Hz

The signal-to-noise ratio required to satisfy the established values of P_d and P_{fa} according to Equation 5.1.5(18) is

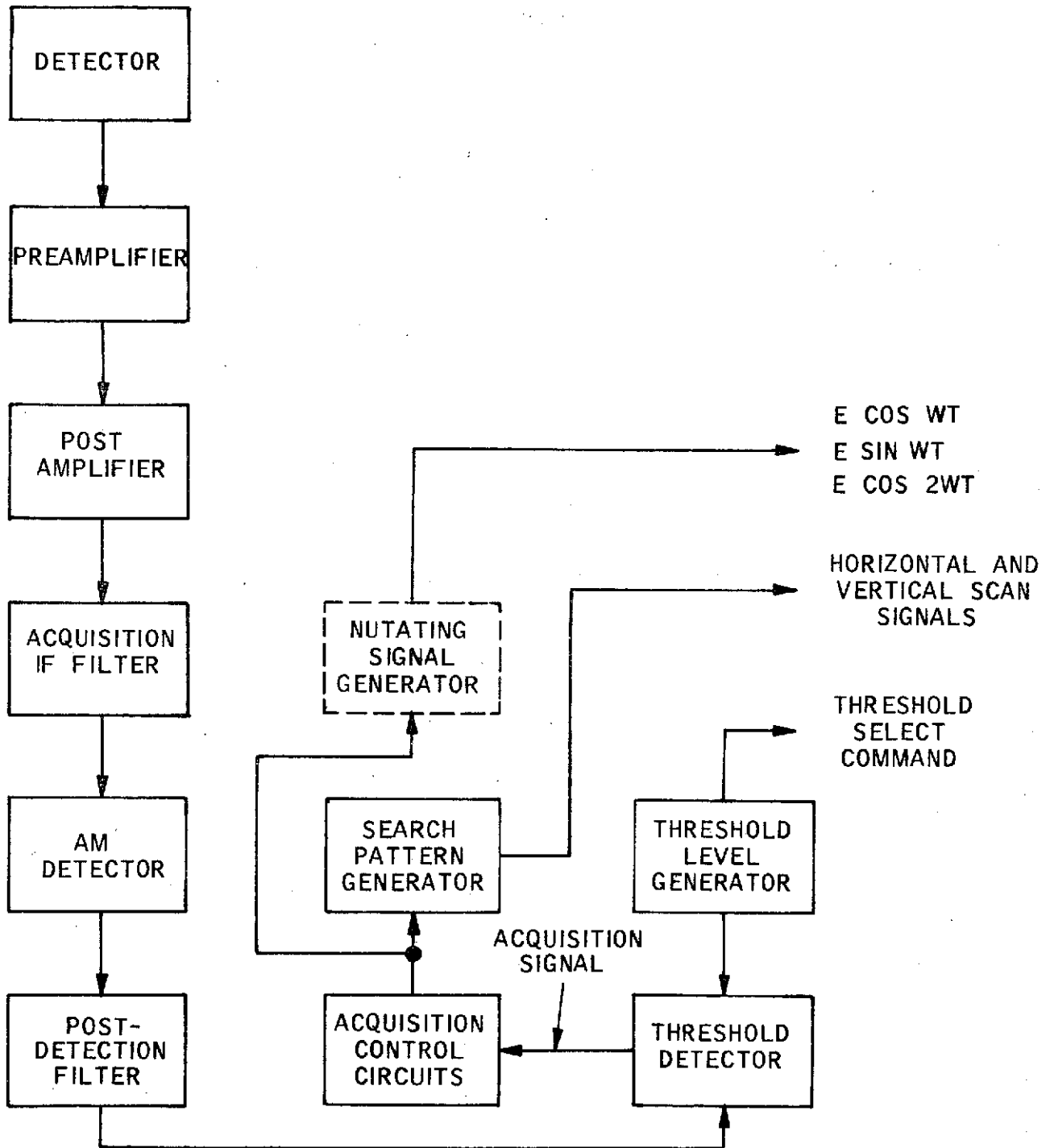
$$\frac{S}{N} = 6.9 \tag{5.1.5.30}$$

Comparing Equation (5.1.5-25) and (5.1.5-30), the acquisition subsystem has a design margin of 5.6 db. With the acquisition signal filter attenuation taken into consideration, the design margin reduced to 4.9 db.

From Equation (5.1.5-19),

$$\begin{aligned} P_s &= P_A \cdot P_d \\ &= (.91)(.99) \\ &= 0.9 \end{aligned}$$

The subsystem has an overall acquisition probability of 0.9.

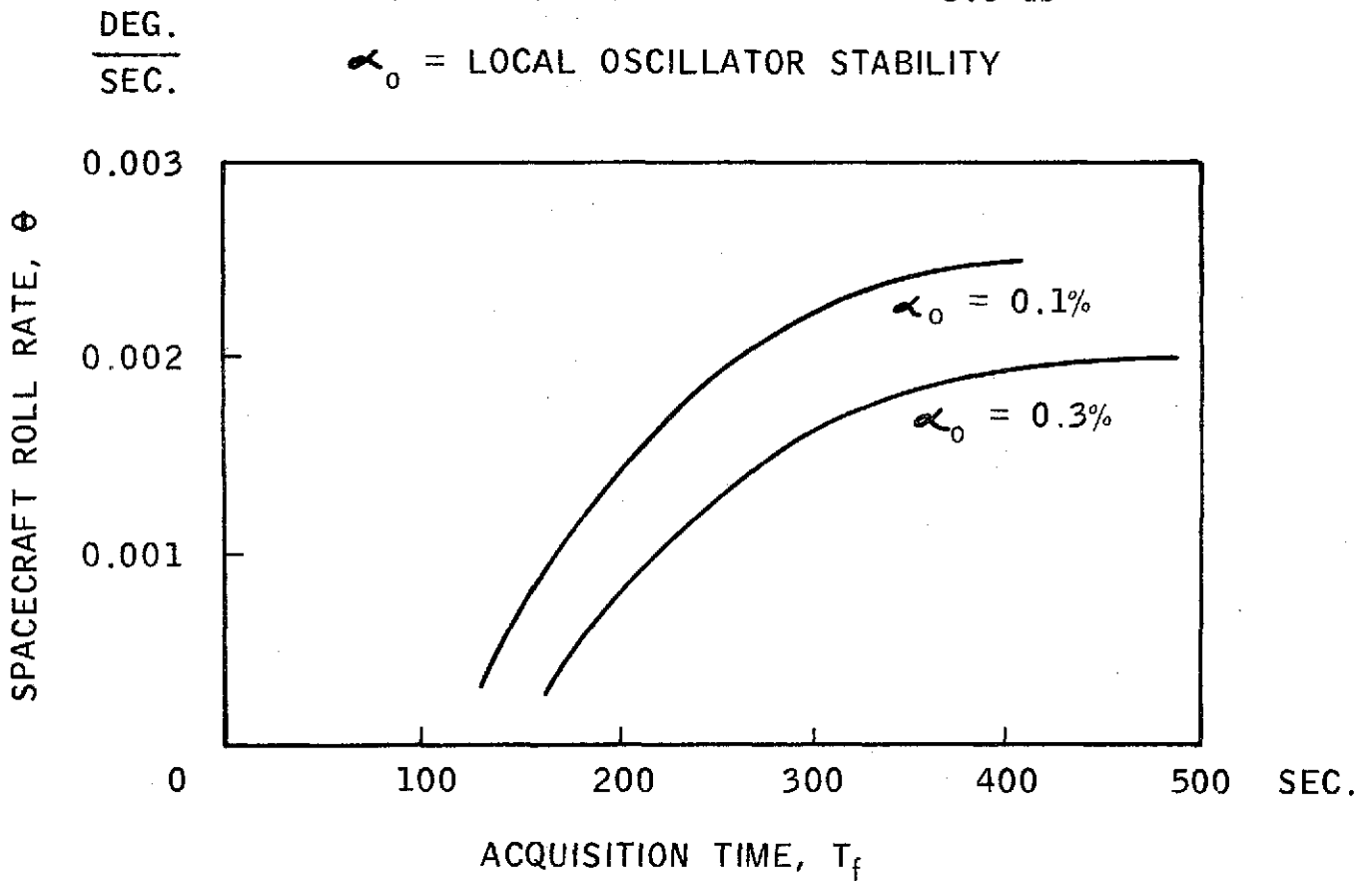


ACQUISITION SUBSYSTEM FUNCTIONAL
BLOCK DIAGRAM

Figure 5.1.5.1

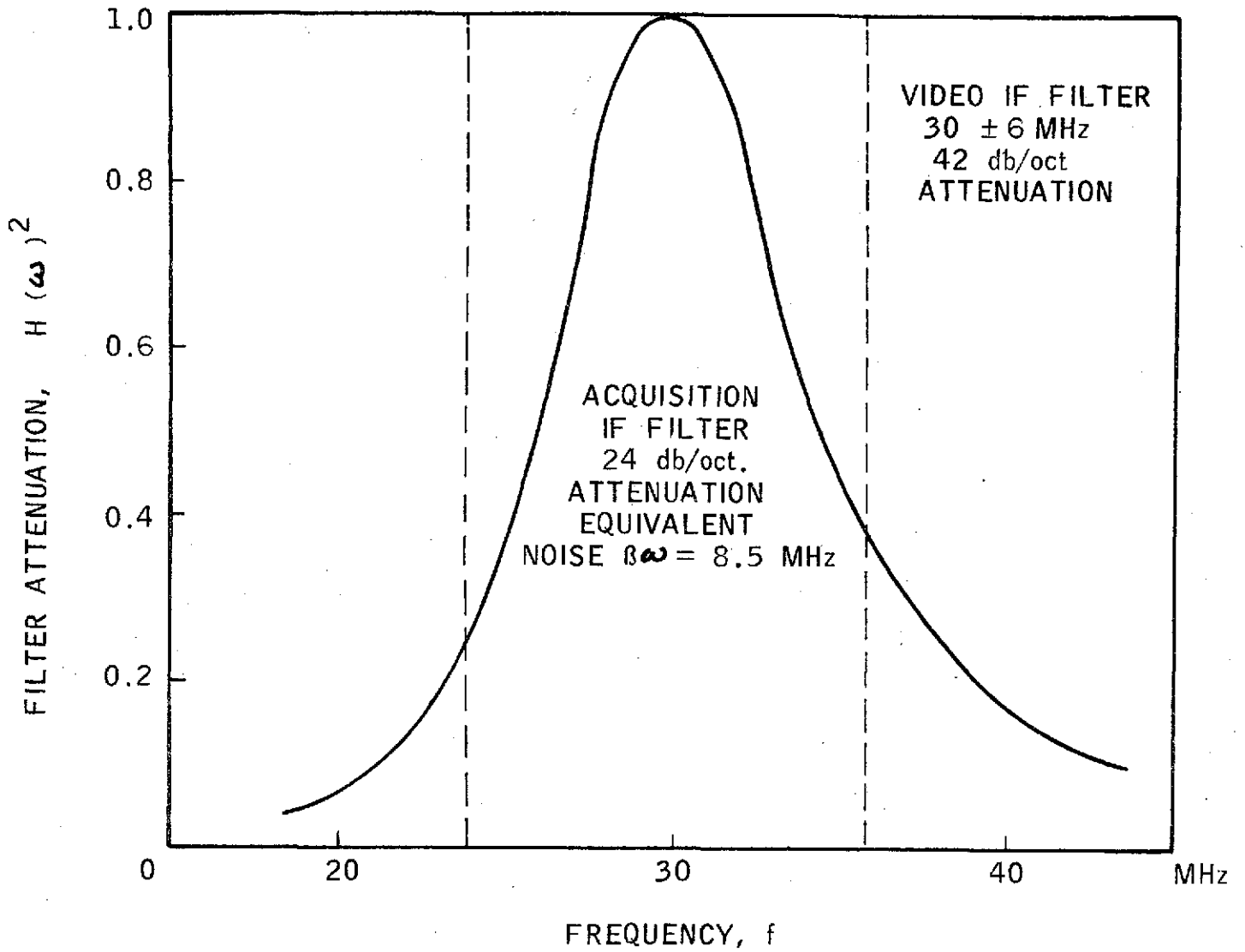
TARGET UNCERTAINTY ANGLE: ± 0.2 DEG.
ACQUISITION PROBABILITY: 0.9
FALSE ALARM TIME: 1100 SEC.
DESIGN MARGIN: 5.6 db

α_0 = LOCAL OSCILLATOR STABILITY



ACQUISITION SUBSYSTEM PERFORMANCE

Figure 5.1.5-2



ACQUISITION IF FILTER CHARACTERISTICS

5.1.6 Tracking Analysis

To compensate for spacecraft motion and to maintain the proper optical alignment between the transmitter of one station and the receiver of another, target tracking is to be performed by both stations. A functional block diagram of the tracking subsystem is shown in Figure 5.1.6-1. The subsystem performs a position sampling by rotating the received beam over the detector. When the received beam is not centered on the detector, the IF carrier signal is amplitude-modulated, and the phase and depth of the modulation indicate the direction and magnitude of misalignment. North-south and east-west axis error signals are generated by detecting the AM signal from the IF carrier, and by phase-detecting the AM signal using the two nutation-drive signals as reference. The two error signals are then utilized to actuate and control the servo system to center the received beam on the detector.

The tracking subsystem has two modes of operation:

- Acquisition tracking
- Operational tracking

To maintain pointing during acquisition after only one station has acquired the other station, acquisition tracking is performed. Since the transmitter beam is expanded, the beam's power density is low. The radius of nutation for acquisition tracking must be large enough to produce a tracking error signal of sufficiently high signal-to-noise ratio to control the servo system. An acquisition-confirm signal is produced during acquisition tracking; this signal is used to verify that the transmitter beam has been acquired and that the subsystem is tracking the beam. In the absence of the acquisition-confirm signal, the subsystem reverts to the search mode of operation. The acquisition-confirm signal is generated by driving the nutator with an additional signal which has a frequency approximately twice the tracking nutating frequency. This driving signal will apply to one axis of nutation. The acquisition-confirm signal is synchronously detected from the IF carrier, using the new nutator drive signal as reference.

Electronics employed in the acquisition tracking is also utilized for operational tracking. To compensate for the difference in the received power density during acquisition and normal operation, both the radius nutation and the amplification of the error signal are decreased for normal operation.

System design analyses have been made to establish the various system design parameters. With the design parameters established, system performances were analyzed with the following major parameters taken into consideration:

- Spacecraft roll rate
- Radius of nutation
- Nutating frequency
- Carrier-to-noise ratio
- Tracking-error signal-to-noise ratio
- Tracking subsystem bandwidth
- Tracking error
- Carrier attenuation at maximum tracking error
- Acquisition tracking confirm capability
- Acquisition-confirm signal-to-noise ratio

5.1.6.1 System Performance Summary

The values of the various system parameters were selected to achieve good tracking accuracy, and to minimize the amount of hardware required to implement the system. The methods used in the evaluation of system performance and in selecting the values of the various system parameters are summarized in the subsequent sections. Further details of the methods and analyses are in Appendix B. The system performance is summarized as follows:

Tracking	± 3.0 arc-sec
Carrier attenuation at maximum tracking error	- 0.9 db
Tracking range	± 0.208 degree
Acquisition-confirm signal S/N margin	6.1 db

To accomplish the performance objectives, the following operating conditions and system design parameters are specified:

Maximum spacecraft drift rate	0.001 deg/sec
Acquisition tracking nutating radius	8 arc-sec
Normal tracking nutating radius	1.5 arc-sec
Acquisition confirm signal nutating radius	8 arc-sec
Tracking subsystem bandwidth	5.12 Hz
Tracking subsystem response time	0.112 sec
Acquisition confirm signal bandwidth	1.0 Hz

5.1.6.2 Tracking Signal-to-Noise Ratio

The signal-to-noise ratio of the tracking error signal, as derived in Appendix B, is:

$$\frac{S}{N} = \frac{\left(\frac{C}{N}\right) [E(\theta)] [M(\theta)] [K(\gamma)]}{\left[\frac{2\beta_a}{\beta_I} + \left(\frac{\alpha_o \beta_a}{\Delta f}\right)^2 + \left(\frac{\sigma_b}{N}\right)^2\right]^{1/2}} \quad (5.1.6-1)$$

where

- $\frac{C}{N}$ = carrier-to-noise ratio at the IF output
- $E(\theta)$ = carrier attenuation as a function of target off-axis angle, θ
- $M(\theta)$ = percent of error signal modulation as a function of target off-axis angle, θ
- $K(\gamma)$ = on-axis carrier attenuation as a function of radius of nutation
- β_I = equivalent noise bandwidth of IF filter
- β_a = tracking subsystem bandwidth
- α_o = local oscillator output power fluctuations in bandwidths of Δf

$$\frac{\sigma_b^2}{N^2} = \text{rms fluctuation of background noise from earth}$$

The relative signal amplitude from the detector as a function of target off-axis angle θ is shown in Figure 5.1.6-2. The curve is obtained by numerical integration of the Gaussian receiver beam on a 32-arc-sec round detector with a uniform local oscillator energy across the detector surface. For a given radius of nutation, γ , the error signal modulation $M(\theta)$ at various off-axis angles, θ , can be determined from Figure 5.1.6-2. This is done by finding the maximum signal amplitude, E_{\max} , the minimum signal amplitude, E_{\min} , and the carrier level, $E(\theta)$, at each of the various angles, θ . Then $M(\theta)$ can be calculated by the following equation:

$$M(\theta) = \frac{E_{\max} - E_{\min}}{2} \frac{1}{E(\theta)} \quad (5.1.6-2)$$

During acquisition, the transmitter beam is expanded from 12 arc-sec, or .00333 degree, to 0.177 degree. If the on-axis power density of the narrow transmitter beam is assumed to be 23.7 db and if acquisition occurs at 5.36 db below the on-axis power density of the expanded transmitter beam (as shown in Figure 5.1.6-3), the carrier-to-noise ratio is:

$$\begin{aligned} \frac{C}{N} &= 23.7 - 10 \log \left(\frac{.177}{.00333} \right)^2 - 5.36 \\ &= -16.21 \text{ db or } 2.39 \times 10^{-2} \end{aligned} \quad (5.1.6-3)$$

A beam expander is used to form the expanded beam, thus bypassing the primary mirror and eliminating beam blockage by the secondary mirror. To account for the difference in transmission efficiency of the two optical paths, a constant, $K = 1.2$, is introduced into Equation (5.1.6-3):

$$\begin{aligned} \frac{C}{N} &= (2.39 \times 10^{-2})(1.2) \\ &= 2.87 \times 10^{-2} \end{aligned} \quad (5.1.6-4)$$

The proper numerical values of the various design parameters indicated in Equation (5.1.6-1) are established in Appendix B. With these values substituted, Equation (5.1.6-1) becomes:

$$\frac{S}{N} = 24.4 [E(\theta)] [M(\theta)] [K(\gamma)] \quad (5.1.6-5)$$

Equation (5.1.6-5) is used to calculate the $\frac{S}{N}$ of the error signal as a function of the target off-axis angle θ at various values of nutation radius. Figure 5.1.6-4 shows curves of $\frac{S}{N}$ as a function of θ for nutational radii of 6 and 8 arc-sec. Acquisition tracking with a nutation radius of 8 arc-sec provides a maximum signal-to-noise ratio of 6.8 when the target is displaced 14 arc-sec from the center of the detector. At the displacement of 1.5 arc-sec, the signal-to-noise ratio is 1.0. This indicates the servo system inactive zone of ± 1.5 arc-sec, within which no correction is provided.

For operational tracking, the radius of nutation is reduced to 1.5 arc-sec. The signal-to-noise ratio as a function of the target off-axis angle θ can be calculated by Equation (5.1.6-1), with $\frac{C}{N}$ representing the narrow transmitter beam carrier-to-noise ratio at the IF output. Figure 5.1.6-5 shows curve of the normalized $\frac{S}{N}$ as a function of θ for $\gamma = 1.5$ arc-sec.

5.1.6.3 Acquisition-Confirm Signal

During acquisition, the acquisition-confirm signal is used to verify that the transmitter beam is acquired and the subsystem is tracking the beam. The signal is generated by driving the nutator with a signal which has a frequency which is twice the tracking-nutating frequency. This signal will apply to one axis of nutator. The signal-to-noise ratio of the acquisition-confirm signal can be calculated, using Equation (5.1.6-1). For a radius of nutation of 8 arc-sec, the various design parameters (as calculated in Appendix B) have the following numerical values:

$$K(\gamma) = 0.8 \quad (5.1.6-6)$$

$$E(\theta) = 0.8 \quad (5.1.6-7)$$

$$M(\theta) = 0.362 \quad (5.1.6-8)$$

With the proper values substituted into Equation (5.1.6-1), the signal-to-noise ratio of the acquisition-confirm signal was found to be:

$$\frac{S}{N} = 11.8 \quad (5.1.6-9)$$

The signal-to-noise ratio required to achieve a detection probability of $P_d = 0.98$, and a false-alarm time of one per five search frames, or 1100 seconds, was calculated using Equation (5.1.5-18) and was found to have a value of:

$$\frac{S}{N} = 5.9 \quad (5.1.6-10)$$

Comparing Equations (5.1.6-9) and (5.1.6-10), the acquisition-confirm signal has an $\frac{S}{N}$ margin of 6.1 db.

5.1.6.4 Tracking Servo System

The north-south and east-west axis error signals are used to activate and control the servo system to center the receiver beam on the detector. The servo system is shown in Figure 5.1.6-6. Detailed analysis of the servo system is presented in Appendix B. To provide the servo system with a suitable damping factor for stable operation, an inner-loop feedback assembly is incorporated. This feedback assembly is used to compensate for the relatively low damping provided by the bimorph driving assembly. In the inner loop, $G_3(S)$ represents the bimorph driver and $G_4(S)$ is the transfer characteristic of the bimorph assembly. A feedback bimorph acting as a transducer is represented as $H_1(S)$; this bimorph is attached to the driving bimorph. The transfer characteristics of a feedback amplifier with frequency compensation filter are represented by $H_2(S)$. The design parameters were selected to provide the inner loop with a 5-Hz filter breakpoint.

In the outer loop, $G_1(S)$ represents the transfer functions of the AM detector and error signal phase detector; $G_2(S)$ represents the compensation amplifier at the output of the phase detector. The design parameters were selected to provide the servo system with system bandwidth of 5.12 Hz and a system damping factor of 0.5.

The performance of the tracking subsystem is summarized as follows.

5.1.6.4.1 Tracking Error, θ_e

$$\theta_e = \theta + \theta_1 + \theta_2$$

θ = Tracking error resulting from target motion

$$\theta = 0.5 \text{ arc-sec}$$

θ_1 = Tracking error due to noise, offset and drift of the subsystem's electronics

$$\theta_1 = 1.5 \text{ arc-sec}$$

θ_2 = Optical and mechanical misalignment

$$\theta_2 = 1.0 \text{ arc-sec}$$

$$\begin{aligned} \theta_e &= 0.5 + 1.5 + 1.0 \\ &= 3 \text{ arc-sec} \end{aligned}$$

5.1.6.4.2 Carrier Signal, $E(\theta)$ at Maximum Tracking Error

Figure 5.1.6-2 indicates that, with a radius of nutation, γ , of 1.5 arc-sec and target displacement of 3 arc-sec from the center of the detector, the carrier signal is $E(\theta) = 0.95$, or -0.2 db. The attenuation due to 3-arc-sec misalignment of the receiver and transmitter beams is 0.7 db, according to the optical-link analysis in section 5.1.3 of Vol. I, Part 1. Therefore, the carrier-signal attenuation at maximum tracking error is 0.9 db.

5.1.6.4.3 Subsystem Tracking Bandwidth

$$\begin{aligned} f &= \frac{\omega}{2\pi} = \frac{32.2}{2\pi} \\ &= 5.12 \text{ Hz} \end{aligned}$$

5.1.6.4.4 Response Time

Rise time, t_r , in response to a unit-step input is:

$$\theta_o = \left[1 + (1 - \delta^2)^{-1/2} \exp(-\delta\omega t) \sin \beta t \right]$$

$$\theta_o = (1 + 1.16 e^{-16t} \sin 28t)$$

$$\theta_o = \left[1 + 1.16 e^{-16t} \sin 2\pi (4.45) t \right]$$

$$t_r = 1/2 \text{ cycle of } 4.45 \text{ Hz}$$

$$t_r = 1/2 \frac{1}{4.45}$$

$$t_r = 0.112 \text{ sec}$$

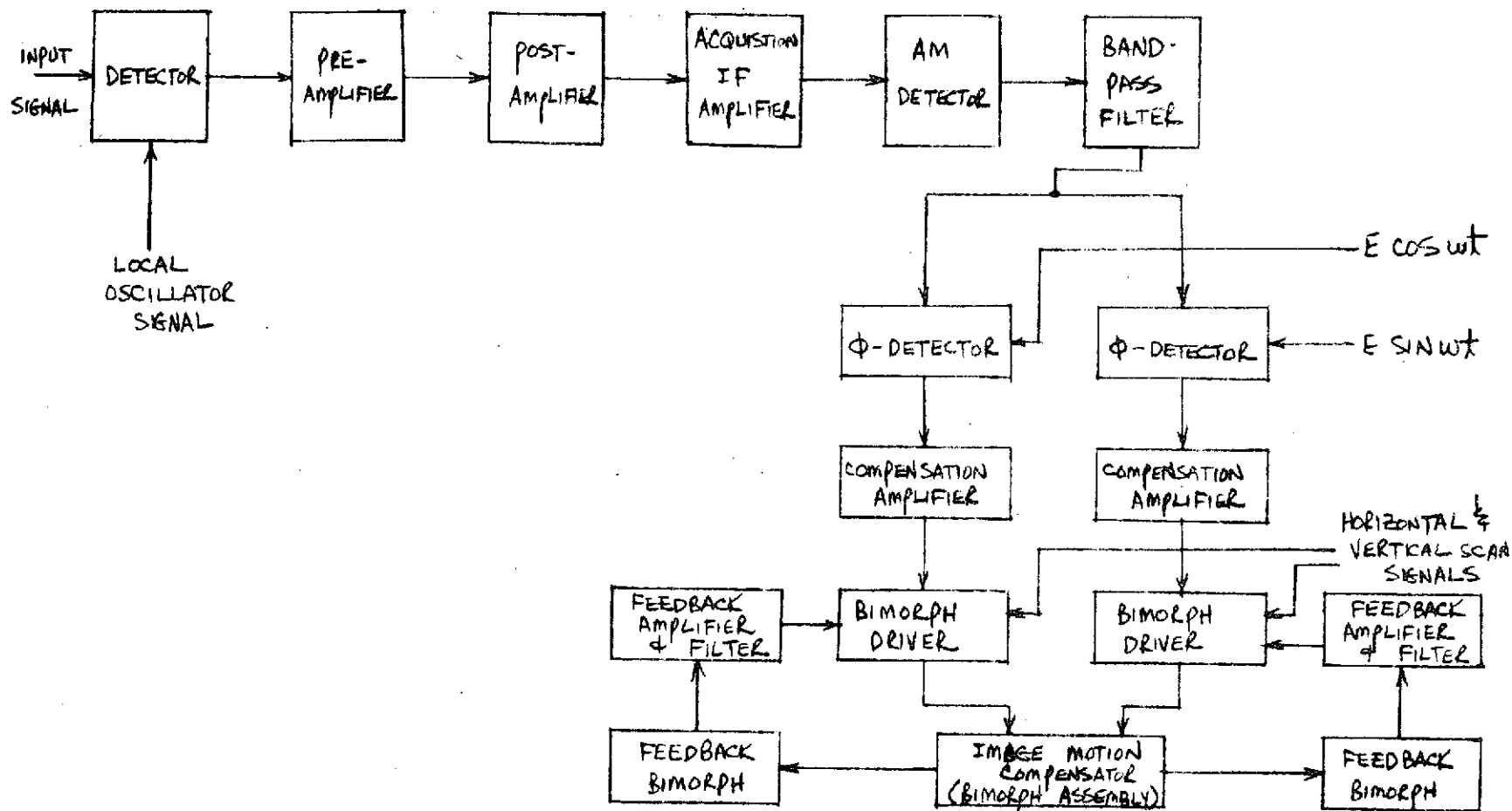
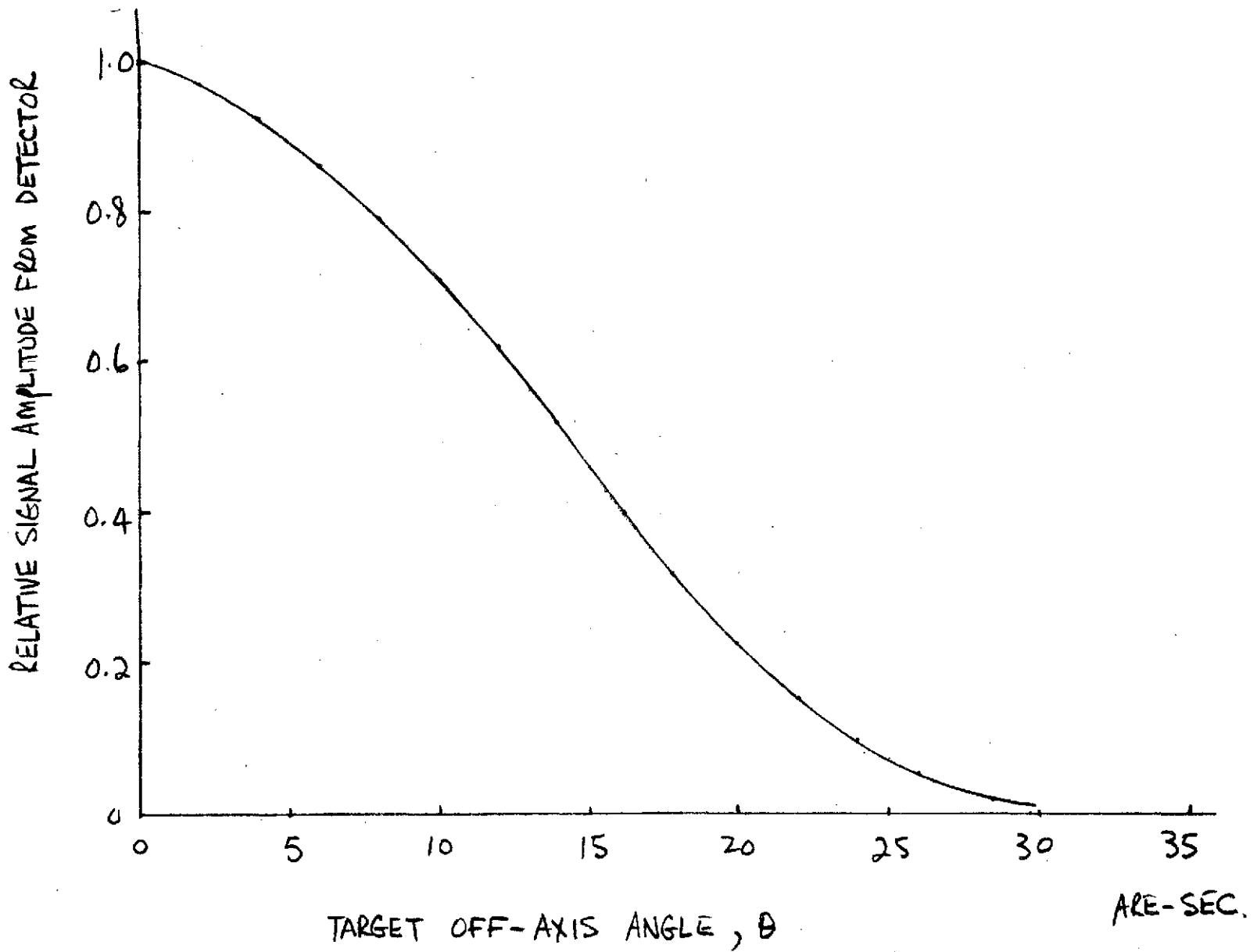


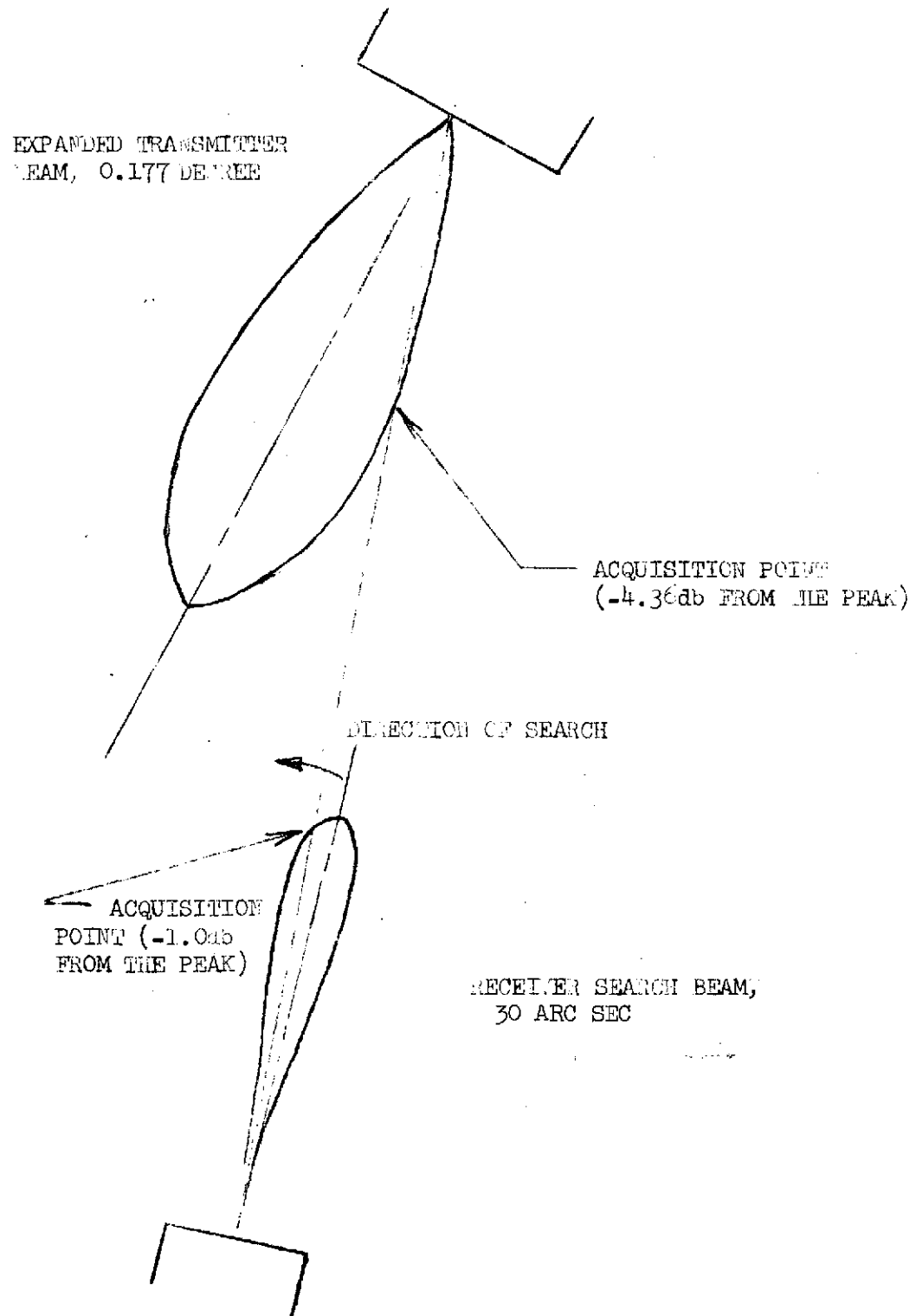
Figure 5.1.6-1

Tracking Subsystem Functional Block Diagram



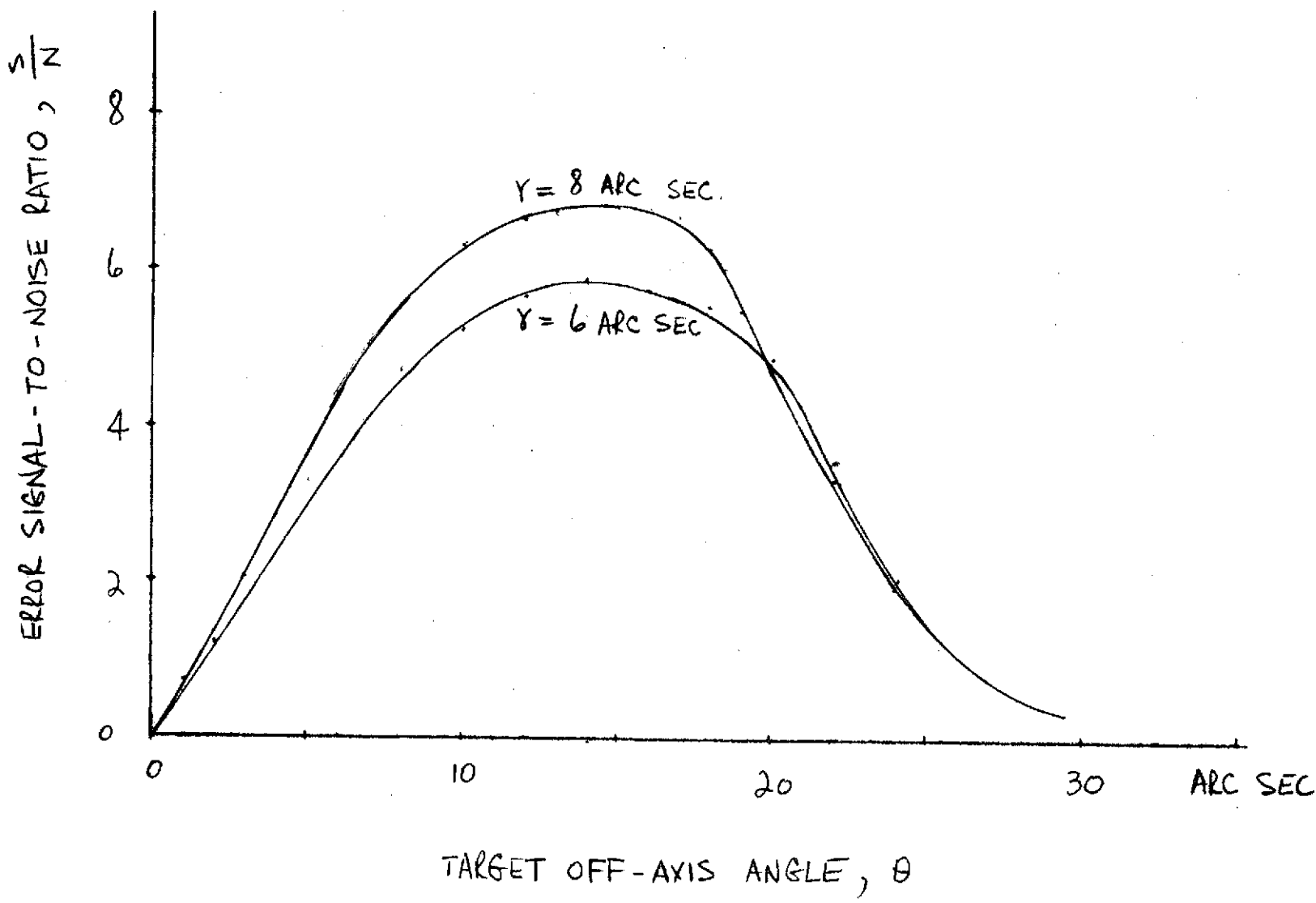
Relative Signal Amplitude from Detector vs Target Off-axis Angle

Figure 5.1.6-2



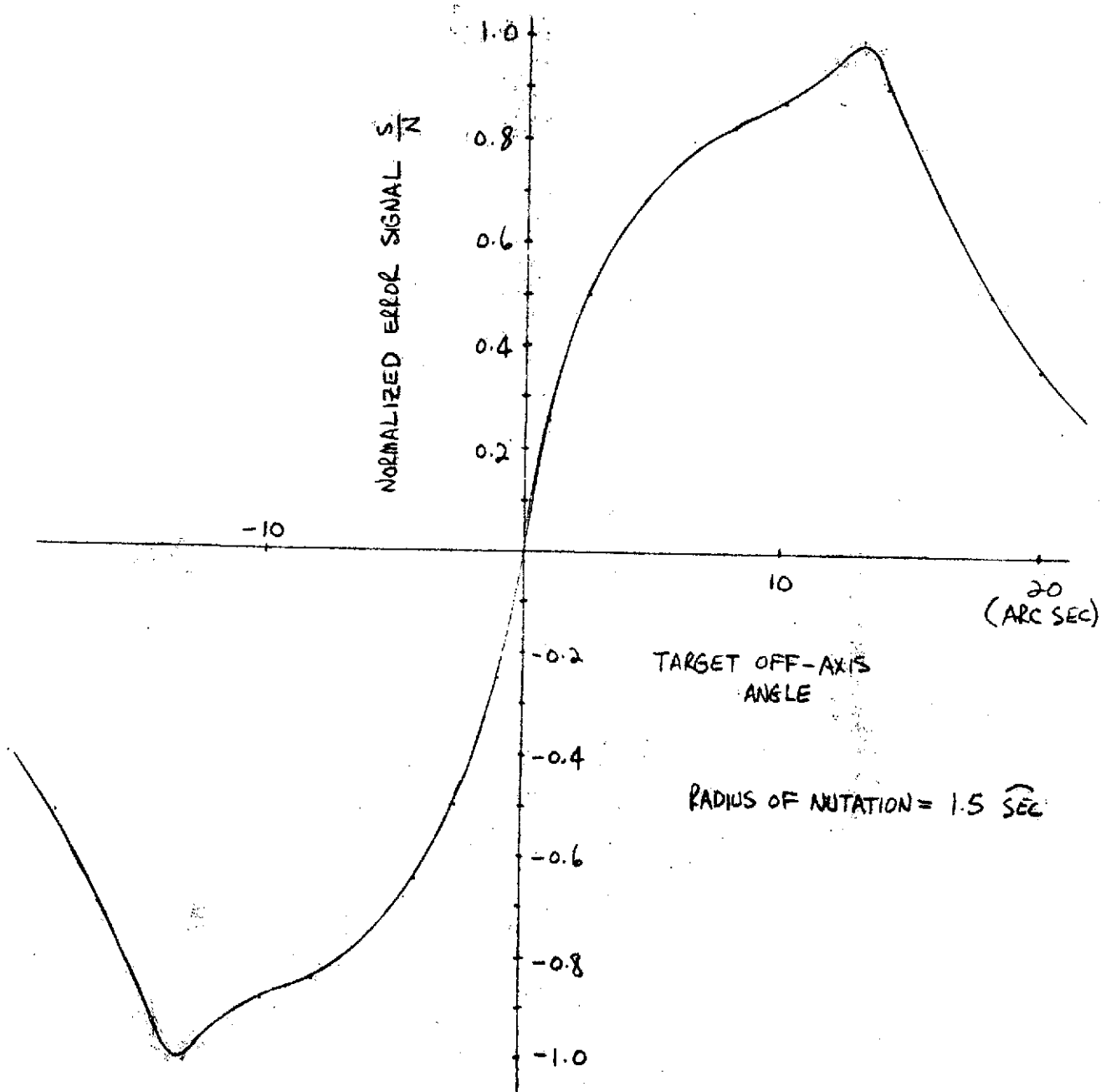
Relative Position of Transmitter and Receiver Beam at Time of Acquisition

Figure 5.1.6-3



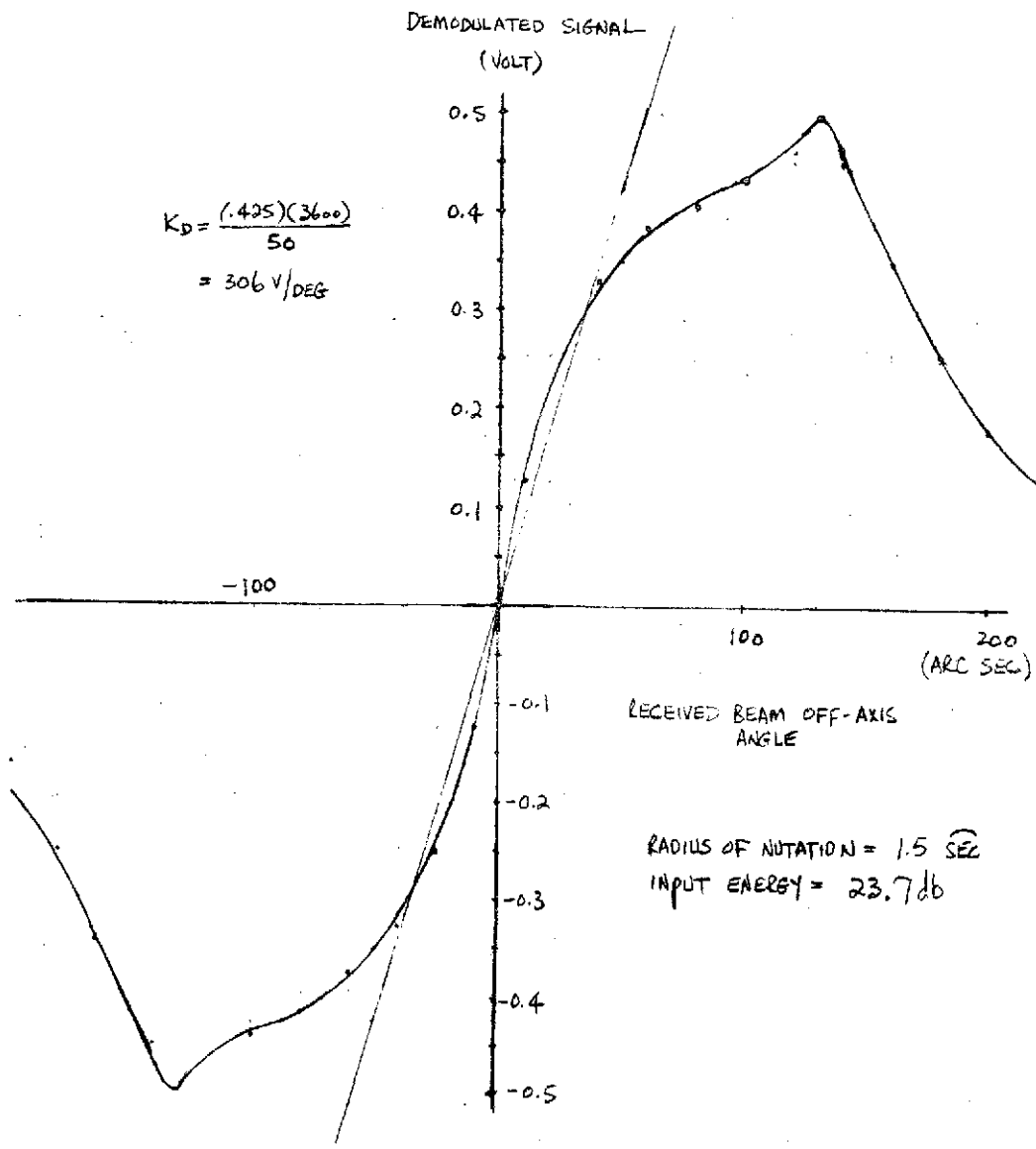
S/N of Error Signal vs Target Off-axis Angle

Figure 5.1.6-4



Error Signal, S/N, vs Target Off-axis Angle

Figure 5.1.6-2



LCE Tracking Servo System

Figure 5.1.6-6

5.2.2 Laser Subsystem

5.2.2.1 General Discussion

This section describes in detail the functional characteristics, requirements, design trades, and analyses of the laser subsystem. The present design was formulated from analyses generated early in the program and was modified by results recently obtained from the testing of the breadboard laser subsystem. Although the design concepts have now been finalized, and the basic approach toward achieving the laser-subsystem requirements has been fixed, some design details have not been frozen. These areas are discussed extensively.

The design of laser subsystem components is discussed in detail following several subsections that briefly describe the functional characteristics of, and requirements placed upon, the laser subsystem. Several of the more critical technical areas of concern - e.g., laser life, line-signature repeatability, laser frequency stabilization, and modulation techniques, which have required early evaluation in order to demonstrate system feasibility - are discussed briefly in Section 5.2.2.4.

In the ensuing discussions an attempt has been made to condense the subject matter as much as possible by summarizing analytical results rather than giving detailed calculations. The more extensive formulations and details of the experimental results are appended.

5.2.2.2 Functional Characteristics

Succeeding paragraphs describe in general terms the design philosophy and general tradeoff considerations and present the functional characteristics of the laser portion of the optical communication system. They develop, without going into specific detail, the approach required for the LCE and the techniques to be used for the laser subsystem.

The function of the laser subsystem is to generate the required optical beams for the communication system. The transmitter laser beam can be modulated by one of several techniques and can then be passed through appropriate optics for transmission. In many types of systems, as in the LCE,

heterodyne techniques are used in the receiver, requiring that a local oscillator (LO) laser be used that can operate at the appropriate optical frequency. By heterodyne techniques, the signal-to-noise ratio of the communication band can be enhanced with increasing LO power to the point where the dominant noise in the receiver system is generated from the LO beam (see Section 5.2.4). Further increase in LO power beyond this point will no longer be beneficial.

To achieve good heterodyne efficiencies, the LO beam must be matched in its spatial distribution and in its frequency with the incoming laser beam at the mixer, which is located in the receiver subsystem. The LO frequency is adjusted relative to the incoming transmitter frequency (which contains information sidebands) so that the heterodyne beat frequency generated at the square-law mixer falls into a convenient region for amplification by conventional electronic techniques. The heterodyne beat frequency [intermediate frequency (IF)] must be chosen high enough to permit the information-sideband content of the transmitted beam to be amplified without distortion but must be low enough so that available mixers can respond. In addition, as will be seen later, the LO laser may limit the upper end of intermediate frequency, due to its finite frequency-tuning capability. Early laser designs demonstrated that the local oscillator would not allow an IF greater than about 20 MHz, thus creating major difficulties in receiver-electronics design. A new approach to the LO laser design has shown that an IF of more than 50 MHz can be easily obtained allowing bandwidths of 10 MHz or greater, depending on the capabilities of existing mixers. For the LCE, an IF of 30 MHz has been chosen that appears to be near optimum for the required bandwidths (12 MHz) and the presently available components.

To achieve the 30-MHz IF, the local oscillator must be operated at a frequency that is 30 MHz above or below the incoming transmitter-carrier frequency (near 3×10^7 MHz). Fortunately, this small relative difference can be obtained accurately by a simple adjustment of the laser.

The laser frequency of a longitudinal mode is determined by

$$f = q \frac{c}{2L}$$

where q is the number of half-wavelengths of light between the laser mirrors, C is the velocity of light, and L is the distance between mirrors. By adjusting L by a small amount (usually by an electromechanical transducer), the laser frequency can be controlled. For lasers of the size needed on the LCE, the tuning sensitivity is about 120 MHz/micron. A mirror adjustment of about 2500 Angstroms is therefore required to obtain the desired LO offset frequency.

Several modulation techniques are available for use with heterodyne types of communication systems; for propagation through the atmosphere, however, a definite advantage exists for a frequency-modulation (FM) scheme. The atmosphere can cause large power fades and a low frequency modulation (≤ 1 kHz) in the received beam, due to scintillation effects. By using an FM format, the power fluctuations at the IF can be removed by conventional limiting circuits so that the detected signal remains at a constant amplitude.

To achieve a frequency-modulated beam from a laser, a technique must be used that effectively causes a change in laser-cavity length (see above formula). The movement of a laser cavity end mirror can achieve frequency modulation but is limited in available bandwidth to less than 1 MHz, due to mechanical resonances. By introducing in the laser an electro-optic modulator whose optical length can be varied with the application of an external voltage, the effective length of the laser cavity can be varied at high rates. With the modulator placed inside the laser cavity, the laser light passes through the modulator material and experiences a very large change in effective optical length, thus allowing large modulation depths to be obtained at relatively low modulator power (for detailed analysis, see Section 5.2.2.4.4).

This technique of in-cavity modulation is the most efficient one now known that is capable of meeting LCE requirements. Unfortunately, the introduction of a material with finite optical absorption into the laser cavity can cause a substantial drop in laser efficiency. The best material now available for this purpose (single-crystal gallium arsenide) exhibits a loss of about 0.7 to 1.2% per centimeter. Even though this loss is small compared with most optical materials, it can still have a major effect on the power of a very short

laser. For the crystal lengths required to achieve the modulation depths for the LCE laser, power-output reductions of up to a factor of 2 are typical. Detailed tradeoff analyses (not done prior to the LCE program) have been conducted with regard to the required prime power for both the laser tube and modulator as a function of tube dimensions and modulator dimensions. The results are covered in later sections.

A Laser-frequency-stability degradation is always observed when more optical materials are introduced into the laser cavity. In this case gallium arsenide exhibits a rather large change of index of refraction with temperature that directly relates to a change in laser frequency with temperature. In addition, the structure on which the laser mirrors are mounted can expand or contract with temperature, creating slow frequency changes with temperature. By differentiating the above expression it becomes clear that

$$\frac{\Delta f}{f} = - \frac{\Delta L}{L}$$

where L is the optical distance between laser mirrors.

To determine the temperature stability of the laser, all the materials used in the laser must be analyzed as to their thermal characteristics. By far the major contributor to long-term drift (see Section 5.2.2.4.3) is the gallium arsenide crystal. Over the expected operating-temperature range, the change in laser optical length due to the modulator will be too large to allow continuous laser operation within the required frequency range for a heterodyne system. Frequency control of the laser is therefore required; analysis indicates that it cannot be obtained by thermal-compensation techniques alone and some sort of automatic electronic frequency control is required. Using an established technique called "dither" stabilization (described in Section 5.2.2.4.3), the desired degree of laser stability can be obtained. More detailed analysis (see Section 5.2.2.4.3) shows, however, that the range of control required by the electromechanical transducer used in the laser is too large to be practical if the drift due to the modulator is to be compensated over the full temperature range that is expected. The modulator will therefore be enclosed in an oven that will be temperature-controlled to an accuracy of $\pm 1^{\circ}\text{C}$, which is adequate to keep the transducer within its operating range.

Report No. 4033, Vol. I, Part 1

The backup laser assembly is available in case of failure of the LO tube. Although it does not contain a modulator, it can provide limited transmitter functions (if required) by operating on either the outgoing transmitter wavelength or the incoming transmitter wavelength. Because of its dual capacity, the backup laser will have capabilities for assisting in the important experiment of determining the short-term stability of lasers in space by heterodyning with the LO laser. It can also be heterodyned with the transmitter laser to test the modulator and receiver prior to acquisition.

To achieve the 30-MHz offset in either the LO laser or the backup laser, the piezoelectric tuner can be moved a predetermined distance by the addition of a fixed, calibrated voltage. Because the acquisition scheme requires the detection of a heterodyne signal, the LO-laser frequency stability after offset must be very good during the acquisition period or the beat signal will not fall into the IF of the receiver. It has been determined that the frequency drift of the LO laser will be too large (due to thermal effects) to ensure that the LO frequency will remain close enough to the 30-MHz offset until acquisition is achieved if the laser is allowed to run open loop. A simple frequency control scheme has therefore been designed and tested (see Section 5.2.2.6) to stabilize the laser power at the 30-MHz offset frequency. The scheme will allow adequate frequency control of the laser for at least 5 minutes with the present circuitry. Longer periods can also be easily achieved.

After acquisition, the LO frequency will be locked to the incoming frequency at the 30-MHz IF by means of an AFC loop that uses receiver-subsystem electronics. The LO-laser subsystem electronics will then be disabled.

5.2.2.3 Laser Subsystem Requirements

Table 5.2.2-1 gives the major laser subsystem specifications required to meet the overall LCE requirements. They summarize the results of analyses applied to the LCE in various sections of this report, and are to be met during the required life of the experiment (2000 operating hours). Although none of these specifications is individually difficult to meet, the major problem in laser subsystem design is to meet them all simultaneously in the operating

environment with a minimum of weight and prime power. To ensure that the specifications can be met, several important areas related to the final design had to be investigated in order to ensure compatibility and feasibility within the LCE requirements. These areas are as follows:

- Laser tube life
- Laser efficiency
- Modulator losses and birefringence
- Modulator-driver design and power required
- Frequency stability during LO acquisition
- LO efficiency with internal grating
- 30-MHz offset in both lines from backup laser
- Optimum subsystem design compromises because of unavailability of qualified parts
- Transmitter-frequency stability during normal operation
- Mechanical stability of cavity
- Line-center shift with tube life
- Modulator operation inside laser cavity
- Reproducibility of line signatures.

All of these investigations involving demonstration of subsystem and LCE feasibility have been completed with positive results. They are discussed in Section 5.2.2.4. Some of the remaining areas (involving detailed tradeoff studies to arrive at an optimum design in terms of minimum weight, power, and availability of high-reliability components and described subsequently) are nearing completion.

5.2.2.4 Feasibility Studies

Several basic considerations - tube life, laser signature, laser frequency stabilization, and laser modulation techniques - are of significant importance and to a large extent determine the success of the Laser Communication Experiment. Consequently, they have been treated theoretically and/or experimentally. Pertinent information on these topics is introduced first, to serve as a guideline to the design of the laser subsystem.

5.2.2.4.1 Laser Tube Life

Before the LCE program was initiated, and even in the early months of the program, long tube life was considered to be one of the most critical problems. The combined effects of the development efforts in the LCE program and a separate NASA program (NAS 12-2021) conducted in parallel by Sylvania have relieved the criticality of this area and have substantiated the early confidence that this problem would be solved. Sylvania has demonstrated a ceramic laser tube with an operating life in excess of 1000 hours. Techniques involving ceramic-to-ceramic, ceramic-to-metal, and ceramic-to-GaAs seals have been well established. In addition, mechanisms responsible for the reduction of laser tube life have already been extensively investigated. Assuming good tube-fabrication and processing techniques, the life-limiting factors for the CO₂ laser are (a) gas removal by pumping effects, and (b) chemical changes in gas constituents. These two basic factors are intimately related to the cathode design. Briefly, the CO₂ molecule in the plasma tube discharge dissociates into carbon monoxide and oxygen, reaching an equilibrium concentration suitable for laser operation. If the oxygen is slowly removed by chemical reactions with the laser tube materials (such as the cathode), or the CO₂ and other gases are slowly pumped from the system by sputtering from the cathode, laser power will slowly drop because of a loss of CO₂ gas.

The three most important techniques that have permitted long life in the CO₂ laser were first developed by Witteman,* who proposed the use of nonreactive platinum cathodes and of water vapor in the gas mixture, and Carbone,** who proposed the use of heated nickel cathodes. Although the platinum cathode has a high sputtering rate, it is chemically inert and does not chemically remove oxygen from the discharge. The addition of water vapor to the gas mixture

* W. J. Witteman, "High Power Outputs and Long Lifetimes of Sealed-Off CO₂ Lasers," Appl. Phys. Letters, 11, 337 (1967).

** R. J. Carbone, "Continuous Operation of a Long-Lived CO₂ Laser Tube," IEEE J. Quantum Electronics, Vol. QE-4, No. 102 (1968).

reduced the CO_2 dissociation rate, thus providing less free oxygen to the system. The nickel cathode has a comparatively low sputtering rate and has low chemical activity in the CO_2 discharge when heated to between 250 and 300°C.

Experiments with small platinum-electrode laser tubes fabricated at Sylvania indicated that their life is limited to only about 500 hours, because of the high sputtering rate of platinum, which migrates onto the Brewster window even at a 15-cm distance from the cathode. Sputtering also occurs with the nickel cathode, but at a much slower rate. For this reason, the LCE laser tubes are designed with the cathode located at tube center (three-electrode configuration).

To reduce the sputtering rate, it was experimentally found in the LCE cathode study program (see Section 5.3.1) that (a) the cathode must be operated at an elevated temperature (e.g., $T \geq 250^\circ\text{C}$), and (b) the cathode surface must be made large enough to avoid over-filling (i.e., the available cathode area must be as large as, or larger than, the natural emission area).

The current density for a normal glow gas discharge is given by*

$$J_N = \frac{1.84 B^3 K_p P^3}{V_N}$$

where B is the ratio of the electric field, E, to the gas pressure, P ($E/P \approx 254$ volts/cm-torr), $K_p = 20 \text{ cm}^2/\text{V-sec}$, $P = 30$ torr, and $V_N = 365$ volts. This equation gives a current-density value of 4 ma/cm^2 , consistent with the experimental measurements (see Section 5.3.1).

For an operating current of 10 ma, the surface area must be so chosen that the emission corresponds to a current density of 4 ma/cm^2 for the tube pressure that yields maximum tube efficiency. It was also found, however, that the cathode area covered by a normal glow discharge increases with decreasing gas pressure. This implies that a slightly larger cathode with a surface greater

* J. D. Cobine, Gaseous Conductors, Dover Publishing Company, 1941, p. 225.

than 2.5 cm^2 must be used to avoid a higher sputtering rate near the end of tube life, when the gas pressure will be somewhat lower. These results contribute significant insight for the design of a long-life CO_2 laser tube.

All the design principles developed in the earlier tubes are directly applicable to the metal-ceramic space-qualified tube now being developed. For example, an early prototype tube (which was sealed off over 3 years ago but was not often operated) has shown no deterioration in its output-power capability. The tube uses Kovar, stainless steel, Pyrex, epoxy, copper, and various other materials of construction. Except for BeO , all the fabrication materials to be used in the space-qualified laser have been proven with regard to shelf life.

In another experiment, a CO_2 laser tube (constructed with water-cooled quartz tubing and an externally heated nickel cathode) has recently passes the 10,000-hour mark. Information particularly useful to the LCE program is the design of the cathode. The outer surface of the hollow nickel cathode was not exposed to the laser mixture and is not in contact with the CO_2 gas. This has led to a conclusion that the outer cathode surface must be of inert material, such as platinum, whereas the inner emission surface should still be nickel.

Sylvania has had considerable experience in the fabrication of ceramic CO_2 Laser tubes. In addition to the two metal-ceramic tubes used in the breadboard, Sylvania has built two metal-ceramic CO_2 tubes (similar to the flight configuration) under Contract NAS 12-2021 for NASA-ERC. They use self-heated nickel cathodes and the life of each tube has exceeded 1000 hours. A tube such as that shown in Figure 5.2.2-2 also passed a laboratory vibrational test in April 1970 at the qualification test level for the LCE program.

Major significance must be attributed to that successful test. It demonstrates that the fundamental design will be adequate for the LCE and that the fabrication techniques (involving brazing of the ceramic, soldering of the Brewster windows, and welding of the metal parts) are satisfactory. With this successful environmental test, greater confidence can be placed in the final tube design form, allowing more rapid design finalization for related components and interfaces.

Although the LCE-laser-tube lifetime requirement has not yet been demonstrated (this is the purpose of the expanded life test program now waiting for NASA approval) considerations such as those described above indicate that the basic design is sound and will provide lifetime exceeding 2000 hours. In addition, the mechanical design and fabrication approaches appear to be satisfactory, to ensure operation at the specified level after the launch.

5.2.2.4.2 Laser Line Shape and Signature

In the design of the local oscillator and backup lasers, it is important to know the effects of various operating parameters (such as gas pressure, discharge current, and gas temperature) on laser line shape and laser signature.* To obtain this information, Aerojet established a task force team in February 1970, consisting of technical personnel from NASA, Case-Western Reserve University, RCA Canada, and Aerojet. This effort has generated considerable theoretical and experimental data (see Appendix E). The apparatus required for these experiments typically consists of a stable and tunable CO₂ laser, whose operating parameters (such as gas pressure, discharge current, and cavity length) can be varied over a wide range. A spectrometer is also needed to identify laser transitions.

Results compiled by the task force indicated that the CO₂ laser lines P(16) and P(20) of the 10.6-micron transition compete so effectively, relative to all other transitions in the same band, that these two lines can be relied on to oscillate over a very wide gain curve and under a wide range of operating conditions. As an example, an identical laser signature has been obtained by Claspy and Pao at Case-Western Reserve over a pressure/current range varied from 10 to 26 torr and 5 to 11 ma (see Appendix E). Another interesting observation is that the laser signature changes drastically, both in line shape and identification of transitions, as the laser cavity length

* Laser signature is defined as the sequence of CO₂ laser lines as the cavity length of a laser is varied over distance of $\lambda/2$, where λ is the laser wavelength.

is varied over a wide range ($L_0 + 200$ microns). However, P(16) and P(20) lines survive reasonably well under these conditions. On the basis of these results it was recommended that P(16) and P(20) lines of the 10.6-micron band be used in the LCE laser subsystem.

The effects of partial gas pressure, particularly of CO_2 and He, on laser signature, were also brought into question. An investigation was conducted by McElroy and Walker at NASA (see Appendix E). Their results indicated that the laser signature remained the same as the partial gas pressures for CO_2 varied from 5 to 16.7% and for He varied from 66.6 to 80%. A similar conclusion was reached on the effects of discharge current, consistent with results mentioned previously. A change of cooling-water temperature from 5°C to 20°C produces only a shift of the signature but no significant change in shape (see Appendix E). It was observed that higher transverse modes and instabilities in the laser exert more influence on laser signature than do the operating parameters of the laser. Similar measurements were made at RCA Canada (see Appendix E) with a CO_2 laser consisting of one spherical ($R = 42$ cm) and one flat mirror, separated at a distance of 41 cm, and a water-cooled quartz tube (8-mm ID). The gases used were CO_2 (13.7%), N_2 (21.9%), and He (64.4%) at a total pressure of 28 torr. The tube was operated at a discharge current of 6 ma. The results show that the P(18) line is the broadest, and its shape remains the same as the cavity length is varied over $3\lambda/2$, which appears to be in contradiction with the results of other experimenters.

Work on computer calculation of the CO_2 laser signature was conducted by Schiffner (see Appendix E). Its purpose was (a) to find cavity spacings for which a certain transition is clearly separated from adjacent ones, and (b) to determine the total length of travel required in order to go from one well defined transition to another - e.g. P(20) \longrightarrow P(16). His results indicate that the signature repeats itself with minor changes over many half-wavelength intervals, conforming reasonably well with the observations. For a cavity length near 50 cm, there exist several good cavity spacings for which linewidths greater than 60 MHz can be obtained. The total length of travel

from the P(20) transition to P(16) is approximately 1 micron, which is within the capability of the piezoelectric transducer.

These data are extremely useful for backup-laser design, because this laser will be required to operate on both P(16) and P(20). The present design calls for a cavity length of approximately 25 cm, which is a good choice in terms of being able to obtain both lines easily. It also appears that a 30-MHz offset may also be obtainable for both wavelengths without the use of an in-cavity grating at this spacing. This capability is presently being explored experimentally.

5.2.2.4.3 Laser Frequency Stabilization

The frequency stability of the transmitter and LO lasers will be of prime importance to the success of the LCE. Before the communication channel is acquired, it is important that the transmitter and LO lasers be capable of maintaining a precisely known difference frequency so that searching operations are minimized. This requires that both oscillators be independently stable in an absolute sense. After the channel has been acquired, it is necessary to actively control the LO laser frequency at 30 MHz from the transmitted frequency so that the required IF remains constant during any communication period. It is also necessary during this period to actively control the transmitter laser frequency to prevent it from drifting off its operating line. When the channel is open, it will also be important to maintain reasonably good short-term frequency stability so that FM noise in the channel is kept to a minimum. As has been shown (see Appendix E), the use of baseband conversion tremendously reduces the problems in this regard and, for example, allows continuous use of FM stabilization on the transmitter laser.

Before the channel is acquired, the lasers will be operating independently and their frequency difference will not be measurable. It will therefore, be very important during the acquisition period to maintain the ground transmitter and spacecraft local oscillator at precisely separated frequencies so that it will not be necessary to search over a large frequency range during the acquisition phase.

To achieve a high degree of frequency stability during acquisition, both the ground transmitter and the spacecraft local oscillator will be electronically calibrated to the center of the gain line on which they are oscillating. This will be done by means of a dither-stabilization technique developed specifically for application to the CO₂ laser (see Appendix F for a detailed discussion). The technique involves sinusoidal tuning of the laser cavity at a low audio rate, thus producing an FM-to-AM conversion in the laser output. The error signal is then used to indicate laser-frequency offset from the line center to a feedback control loop for frequency stabilization. Laser frequency can be stabilized by this technique to within ± 100 kHz of the line center of molecular resonance, provided that the center frequency of the line does not vary in time. Early analysis indicates that a shift in center frequency will not occur. Measurements have been made by Mocker,* who observed no change in the center frequency of the CO₂ laser gain curve as a function of pressure. However, recent measurements by Freed and Javan** indicate a possible change, with time, in the center frequency of the resonance line. Preliminary results indicate that the change is not very large (~ 0.1 MHz torr). More accurate measurements will be made to determine the magnitude and cause of this effect. Based on the 0.1 MHz torr value, the maximum change of no more than 0.5 MHz is expected during the lifetime of the laser. This amount of shift will not degrade the performance of the acquisition cycle.

After the spacecraft local oscillator and ground transmitter have been frequency-calibrated to line center by the FM technique, a command is given to the LO laser that causes an offset in its frequency by 30 ± 1.1 MHz from the line center. This is accomplished by moving the piezoelectric transducer to a new position that corresponds to the 30-MHz offset.

* M. W. Mocker, "Pressure and Current Dependence Shifts in Frequency of Oscillation of the CO₂ Laser," Appl. Phys. Letters, 12, 20 (1968).

** C. Freed and A. Javan, "Standing Wave Saturation Resonance Stabilization of CO₂ Lasers," paper presented at 1970 Device Research Conference, 29 June - 2 July 1970, Seattle, Washington.

Several factors can, however, affect the ability of the local oscillator to remain at the 30-MHz offset during acquisition. Changes in the oscillation frequency of laser sources can be attributed in part to changes in the optical length of the oscillator cavity and to changes in refractive index in the medium as given by

$$\frac{\Delta\nu}{\nu} = \frac{\Delta n}{n} + \frac{\Delta L}{L}$$

In addition, as pointed out by Mocker, a frequency shift (of the order of 0.5 to 1 MHz/ma) is expected as a result of the change in refractive index. A well regulated power supply is therefore required to eliminate this fluctuation. On the other hand, by using materials having a very low thermal-expansion coefficient (such as Invar or Cervit), long-term stabilities (of the order of minutes) of 10 kHz have been demonstrated at a number of laboratories (Lincoln Laboratory, Honeywell, Sylvania, etc.) Very good temperature stability is required however, to achieve these stabilities. Other contributors to laser thermal drifts are window, mirrors, PZT, etc. Calculations (see Appendix F) show that laser-component temperature variations must be kept to $\pm 1.4 \times 10^{-3}$ °C/minute in order to meet LCE stability requirements. This value is so low that it appears impossible for the local oscillator to remain within the 1.1-MHz band around 30 MHz during acquisition without an electronic control loop assist. To compensate for this small temperature variation, an active electronic control is provided by comparing the LO power at the 30-MHz offset with a reference voltage (see paragraph 5.2.2.6.1). A piezoelectric transducer capable of one free spectral-range movement is adequate for this purpose.

As soon as the 30-MHz IF signal is present in the receiver, the local oscillator will be automatically switched to the AFC mode to maintain the 30-MHz IF. This is accomplished by producing a d-c signal in the IF bandwidth which will be used to switch the local oscillator from the "offset" mode into the AFC mode (see discussion of receiver subsystem).

Local-oscillator AFC is implemented as follows: The output beam from the LO laser is combined with the incoming signal at a beam splitter. The beam is then directed to a high-speed photodetector to produce a heterodyne beat signal; this signal, in turn, is fed to the frequency discriminator with its center frequency at 30 MHz. The output of the discriminator is a d-c signal proportional to the difference between the beat-signal frequency and 30 MHz. If this d-c output is suitably amplified and fed back with proper phase to the cavity tuner of the LO laser, this laser may then be frequency-locked to a constant 30-MHz offset from the incoming transmitter-laser frequency. Figure 5.2.2-3 illustrates this technique, which is often referred to as the AFC (automatic-frequency-control) technique.

Sylvania has recently used the AFC technique to stabilize the output of a 70-watt CO₂ laser by AFC-locking it to a small, stable, 1-watt oscillator. Results from this experiment show that this is indeed a very powerful technique. Figure 5.2.2-4 plots the frequency fluctuations of the 70-watt laser before AFC stabilization, and Figure 5.2.2-5 shows frequency fluctuations with respect to the reference laser after AFC stabilization. The results indicate that long-term stabilities of at least 1 part in 10⁹ (30 kHz) with respect to the reference laser are highly feasible.

5.2.2.4.4 Modulator Technique

5.2.2.4.4.1 Power Considerations

Frequency modulation of the 10.6-micron transmitter, using an electro-optic modulator, has been chosen for the LCE. For this application, GaAs is considered to be the most practical material in terms of low optical loss, frequency response, and availability of good optical-quality single crystals. Other infrared electro-optical materials (e.g., CdTe) have been demonstrated* to yield a factor-of-4 improvement in performance as compared with the GaAs modulator, but techniques of producing a good-optical-quality CdTe single crystal in a size useful for this experiment remain to be developed.

* J. E. Kiefer and A. Yariv, Appl. Phys. Letters, 15 (1969).

GaAs is hard and nonhygroscopic and has reasonable thermal conductivity. It can be grown into a fairly large single-crystal boule size (7 cm in length) with little or no strain. The boule can easily be cut and polished flat to 1/10 wave of visible light, for good performance in modulation applications.

The power $P_{\pi/2}$ required to drive a linear E-O modulator, in order to produce a change of phase by $\pi/2$ for a given modulation bandwidth B, is given by**

$$P_{\pi/2} = \epsilon_0 \epsilon B \frac{t^2 \lambda^2}{2 l n^3 r^2}$$

where ϵ_0 and ϵ are respectively free-space permittivity and dielectric constant, t and l are the width and length of a rectangular rod, λ is the laser wavelength, n is the refractive index, and r is the electro-optical coefficient. For a typical-crystal-size (3 by 3 by 50-mm) GaAs modulator, the foregoing equation yields a value greater than 100 watts/MHz for a change of phase by $\pi/2$. External modulation is therefore impractical for the LCE.

Intracavity modulation of a CO₂ laser using a GaAs crystal can greatly reduce the power consumption by as much as 2 orders of magnitude. When the modulator is placed inside the laser cavity, the change in index n of the GaAs crystal, upon application of an applied voltage V, is given by

$$\Delta n = \frac{n^3 r V}{2 t}$$

where t is the thickness of the crystal between electrodes, and other symbols have their usual meaning. When laser radiation passes through this crystal, the change of index corresponds to a change in optical cavity length, ΔL , as given by

$$\Delta L = \Delta n L_c$$

where L_c is the length of the crystal. The change in length produces a deviation in the laser output frequency, f, given by

* I. P. Kaminow and E. H. Turner, Proc. I.E.E.E., 54, 1374 (1966).

$$\frac{\Delta f}{f} = - \frac{\Delta L}{L}$$

where f is the optical frequency of the laser and L is the cavity length. Upon combining these equations, the expression for the frequency deviation as a function of the applied voltage and geometric dimensions of the modulator is given by

$$\Delta f = \frac{f n^3 r V L_c}{2t [L + (n-1) L_c]}$$

For a laser-cavity length of 30 cm, a maximum drive voltage of ± 210 volts, and a modulator thickness of 3 mm, this equation shows that a frequency deviation of $\Delta f = \pm 4.0$ MHz can be obtained with a modulator length slightly in excess of 2 cm.

Laboratory experience at Sylvania with a CO_2 communication link using an internal modulator has demonstrated that the specified frequency deviation can be obtained with a modulator 3 cm long at a drive voltage of approximately ± 210 volts. It is most desirable to keep the modulator below ± 200 volts so that readily available high-frequency transistors can be used in the modulator driver.

5.2.2.4.4.2 Optical Losses

Two kinds of optical losses are introduced when a GaAs modulator is placed inside the modulator laser cavity: Fresnel reflections at the crystals faces and absorption losses in the bulk crystal. The high index of refraction of GaAs will cause substantial reflections from its faces unless corrective measures are taken. For light normally incident on the uncoated crystal face, the reflectivity is $R = (n-1)^2 / (n+1)^2 = 0.29$. Reduction of this reflectivity requires either antireflection coatings or faces cut at the Brewster angle. Antireflection coatings have recently become commercially available for GaAs and can reduce the reflection at one face to a level of about 1%. To date, however, the repeatability from coating to coating has not been good and several attempts are usually required to obtain the 1% value. A carefully cut Brewster angle will reduce the reflection loss well below 1%.

Optical absorption losses in the crystal are also important, and should be minimal in order to maintain the maximum laser power output. Several measurements of the optical-absorption coefficient of semi-insulating GaAs have been reported. Comly, et al.* obtained an absorption of $0.006 \pm 0.002/\text{cm}$ using a calorimetric measurement. However, most other published results indicate that a more usual value of 0.011 should be expected. Efforts must be made to obtain a crystal with the best material quality for the transmitter laser.

5.2.2.4.4.3 Brewster Angle Design

Measures must be taken to reduce reflection at the GaAs surface when the modulator crystal is inserted in the cavity. Antireflection coatings are available for use with the linear configuration that reduce the reflectivity per surface to 1% or less. While losses of this magnitude can be tolerated, the still lower reflectivities obtainable through the Brewster-angle configuration are highly desirable for maximum laser efficiency. In addition, Sylvania has found that coating manufacturers often must try several times before obtaining a coating with less than 1% reflectivity, thus sharply increasing the coating cost.

For these reasons, the Brewster-angle configuration is proposed here. The modulator will be placed inside the cavity at the angle shown in Figure 5.2.2-6. When the modulator is placed inside the cavity, the beam becomes enlarged in one direction inside the modulator crystal and will be elliptical, with one major axis a factor of 3.44 longer than the other. Clearly, the modulator crystal must also be larger in order to accommodate the enlarged beam, and will now be 3 mm by 10.5 mm by 3 cm.

The electrical properties of two possible Brewster-angle configurations are compared with the linear configuration in Figure 5.2.2-7. If the electrodes are applied to the narrow sides of the modulator, the capacitance is decreased by a factor of 3.44, and the resistance, drive voltage, and drive

* J. Comly, E. Garmire, and A. Yariv, "Infrared Absorption at 10.6 Microns in GaAs," J. Applied Phys., Vol. 38, pp. 4091 to 4092 (1967).

power are increased by a factor of 3.44. If the electrodes are applied to the broad sides of the modulator, the drive voltage remains fixed, the resistance decreases by a factor of 3.44, and the capacitance and drive power are increased by a factor of 3.44. Because the critical parameter in the modulator drive is the required voltage, application of the electrodes to the broad faces of the modulator is clearly the most desirable approach and is being used. In practice, the modulator-driver power will not have to be increased by the full factor of 3.44, because half of the capacitance (3pf) associated with the modulator was expected to be stray capacitance. Although the modulator capacitance increases from 3 pf to 10.5 pf, the total capacitance is thus expected to increase only from 6 pf to 13.5 pf; the critical drive voltage therefore remains the same.

The use of a Brewster-angle modulator also requires an altered crystal configuration. The light incident on the modulator must be polarized along one of the induced electro-optic axes to obtain the desired optical-path-length change, and it must be polarized in the plane of incidence (the plane of the paper in Figure 5.2.2-6) in order that there be no reflection. To accomplish this arrangement, the broad faces of the modulator will be (001) planes. Light will be incident on a (110) plane. It will travel in the (110) direction and will be polarized in the ($\bar{1}\bar{1}0$) direction. The narrow faces of the modulator will be (001) planes. With this arrangement, all conditions are satisfied, and the induced index change is that previously used.

5.2.2.4.5 Laser Subsystem Breadboard

The breadboard model of the laser subsystem was recently completed and delivered to Aerojet. Figures 5.2.2-8 through 5.2.2-13 provide views of the transmitter laser assembly, LO laser assembly, and electronics assembly. No backup laser assembly was required for the breadboard model. The purpose of the breadboard model is to demonstrate the functional characteristics of the laser subsystem and to check the feasibility of the various approaches taken in the design. It has indeed fulfilled its purpose. Present efforts on this model involve detailed studies of operational characteristics in an attempt to determine where improvements could be made for the next unit.

In particular, the breadboard model demonstrated the following:

- a. In-cavity modulation using a GaAs modulator is possible. The modulation index and frequency response are as expected from theoretical considerations.
- b. Closed-loop operation of the lasers (to obtain good frequency stability) is indeed possible for all the lasers during any operational period of the communication link. Line-center dither stabilization and stabilization at the 30-MHz offset in the local oscillator were demonstrated.
- c. Operation on the required laser wavelengths was demonstrated.
- d. Operation of the local oscillator with an internal grating was demonstrated.
- e. TEM₀₀ mode operation was demonstrated in both the LO and transmitter lasers.
- f. The required amplitude stability was demonstrated for the local oscillator and the transmitter, even for the case when the former is operating at the offset frequency of 30 MHz.
- g. The Brewster-angle-modulator configuration removed problems of modulator etalon effect. This has now eliminated difficulties of wavelength hopping in the transmitter.
- h. The thermal characteristics of the modulator and laser tubes were as expected on the basis of earlier calculations.
- i. Effects of modulator losses on the laser output power were greater than originally expected, but appear to correspond well to a new model of the transmitter laser recently developed (see Section 5.2.2.5). Greater power input to the transmitter laser will be needed in order to meet the power-output requirements in future units. This same theoretical model now predicts that an increase in LO prime power will also be required. The backup laser will not need an increase in power, because it will contain no loss elements. The desirability of lower-loss modulator crystals is apparent from these results.

- j. Actual measurements of the variations in laser-output-power to cavity-component misalignment are close to the amount expected from theoretical considerations. The cavity components must remain aligned to angular tolerances of a fraction of a milliradian (see paragraph 5.2.2.5.4) in order to result in negligible power loss.
- k. Thermal-lensing effects in the modulator do not appear to be a problem in the present modulator design.

It should be emphasized that no major attempt was made to develop an optimum system for the breadboard. Experimental data (variation of tube gain and saturation parameter as a function of current, bore diameter, pressure, tube length, etc.) are required for such an optimization. Many of the measurements have now been made although a few remain incomplete. Analytical formulations are nearing completion (see Appendix G) that will allow computer optimization of the laser-modulator dimensions as well as the LO and backup laser dimensions. Unfortunately, not all the formulations were completed in time to include in this report.

The breadboard system is now serving an important role in evaluating the design parameters to be implemented in future models.

5.2.2.5 Transmitter Laser

The transmitter laser assembly consists of a metal-ceramic laser tube, a Brewster-angle GaAs modulator, cavity mirrors, and a piezoelectric transducer. The design is based on tradeoff studies involving laser gain, beam size and mode volume, and diffraction and absorption losses in various in-cavity components, and has been modified by results recently obtained from the testing of the breadboard laser subsystem. Detailed analyses and descriptions are presented below for each component.

5.2.2.5.1 Transmitter Laser Design Analysis

5.2.2.5.1.1 General Considerations

The design of an optimized transmitter laser involves a number of considerations that are not required in the design of the LO and backup lasers used in the LCE system. Specifically, the transmitter laser makes use

of two active components: (a) the plasma tube, and (b) an intracavity electro-optical phase modulator that produces FM on the transmitter output. The transmitter laser tube and the amplifier that drives the modulator crystal will consume more prime power than any other elements in the LCE system. This, together with the fact that the power requirements for the tube and modulator are strongly interrelated, makes it essential that the transmitter design be optimized on the basis of the minimum prime power required for the two elements combined.

The relationship between tube and modulator power is readily observed by noting that increased modulator-crystal length reduces the voltage required by the modulator (for a given modulation depth) and hence reduces its power requirements. However, increased optical absorption in the cavity dictates that the laser must supply higher gain and will therefore need higher excitation power. A best configuration that minimizes the total power required by the transmitter-modulator subsystem is the subject of the ensuing design analysis.

5.2.2.5.1.2 Input-Power Minimization

The basic elements of the transmitter-modulator subsystem that must be considered in minimizing the total power requirement are shown schematically in Figure 5.2.2-14. The total power input required is the sum of the tube and modulator powers:

$$P = P_T + P_M \quad (5.2.2-1)$$

This quantity must be minimized, subject to the constraint that the laser power output, P_o , be 700 mw (to ensure that the specified 650-mw output will be met over the tube lifetime). Design parameters and variables used in this section are summarized for convenience in Table 5.2.2-2.

5.2.2.5.1.3 Laser Tube Power

The power input required by the laser-tube power supply is given by

$$P_T = K_L V_T I_T \quad (5.2.2-2)$$

where K_1 is the efficiency of the power supply that provides a tube voltage of V_T and a current I_T . Empirical data obtained for a large number of CO_2 laser tubes indicates the following relationships to be valid over the fairly small range of bore diameters considered here:

$$V_T = \frac{106 L_T}{D} \text{ volts} \quad (5.2.2-3a)$$

$$I_T = 31 \times 10^{-3} D^2 \text{ amp} \quad (5.2.2-3b)$$

where D is the tube diameter measured in cm and L_T is the tube length in cm. Thus, the power required for the laser plasma tube is

$$P_T = 3.3 L_T D K_1 \text{ watts} \quad (5.2.2-4)$$

5.2.2.5.1.4 Modulator Power

Quasi-static analysis shows that the peak frequency deviation when the optical length, L_c , of a laser cavity is modulated is given by

$$\Delta f_{\text{peak}} = \frac{f \Delta n_{c, \text{peak}}}{L_c} \quad (5.2.2-5)$$

where f is the laser oscillation frequency. For the present case, in which this length modulation is produced by modulation of the crystal index of refraction, n ,

$$\Delta L_c = L_M \Delta n \quad (5.2.2-6)$$

where L_M is the crystal length. For the modulator orientation chosen, Δn is given by*

$$\Delta n = \frac{1}{2} n^3 r_{41} \frac{V_M}{a} \quad (5.2.2-7)$$

where the electrical field is expressed as the modulator voltage, V_M , divided by the distance between electrodes. In this particular case, the distance a also corresponds to the dimension, a , of the square optical aperture formed by the modulator. Combining Equations (5.2.2-5), (-6), and (-7) and solving for the peak modulation voltage required,

*S. Namba, "Electro-Optical Effect of Zincblende," J. Optical Soc. Am., 51, p. 76 (1961).

$$V_{M, \text{peak}} = \frac{2a\Delta f_{\text{peak}}}{f n^3 r_{41}} \left(\frac{L_c}{L_M} \right) \quad (5.2.2-8)$$

The power required for the modulator, P_M , will be

$$P_M = P_Q + K_2 2 \pi f_m C V_{M, \text{peak}}^2 \quad (5.2.2-9)$$

where P_Q is the quiescent power required by the modulator and K_2 is the slope efficiency of the driver. Both these factors will depend greatly on the type of driver used (i.e., Class A or Class B) and the type of coupling to the load. The particular value of f_m is chosen so as to correspond approximately to a weighted center of the information-power-density spectrum. It remains to write Equation (5.2.2-9) in geometric terms (i.e., modulator length and aperture) wherever possible. The modulator capacitance may be shown to be

$$C = C_S + \frac{\epsilon_0 \epsilon_r L_M \times 10^{-2}}{\tan(90 - \theta_B)} \quad (5.2.2-10)$$

where ϵ_0 is the permittivity of free space, ϵ_r is the dielectric constant of GaAs (= 11), θ_B is Brewster's angle in GaAs, and C_S is the stray capacitance.

The expression for the total power input to the transmitter laser may now be written as the sum of P_T and P_M :

$$P = 3.3 L_T D K_1 + P_Q + K_2 2\pi f_m C V_M^2 \quad (5.2.2-11)$$

with C and V_M given by Equations (5.2.2-9) and (-10).

5.2.2.5.1.5 Optical Cavity

In order to determine an optimum configuration, values for the geometric terms L_T , L_M , and D may be chosen from the set of L_T , L_M , and D that yields a laser power output of 0.7 watt. These values are obtained by an analysis, using the equation for laser power output developed in Appendix G. The present design uses a tube bore diameter of 0.4 cm. This value was chosen because the optical mode diameter must be kept reasonably constant along the length of the laser tube in order to make efficient use of the

discharge volume. This dictates that the radius of curvature of the spherical output mirror must be significantly larger than the separation between mirrors, and the mode size that results from this curvature dictates that the bore diameter must be 0.4 cm. An analysis by Li^{*} that was used in computing diffraction losses for the IO and backup lasers cannot be used directly for the transmitter laser, because the modulator makes the limiting aperture different at each end of the cavity. The radius of curvature of the mirror is therefore chosen so that a modulator of 3-mm cross section and a tube of 0.4-cm diameter will intercept the mode at the same intensity point of the cavity mode. This will be true if the radius of curvature is 50 cm. Estimating the diffraction loss by the amount of energy vignettted by the tube and modulator, a 1 to 2% loss is calculated for the TEM₀₀ mode. Work is currently underway to accurately determine this loss. The mirror radius used in the breadboard transmitter laser is 50 cm, giving a beam diameter at the output mirror of 2.8 cm, 1/e² power points. (Section 5.2.2.6.2.4 gives beam-diameter equations.)

Because the beam inside the optical cavity enters and exits from the modulator crystal at Brewster's angle, some astigmatism occurs that makes the mode shape slightly elliptical.** The ellipticity, however, is very small; the difference in the beam diameters in the sagittal and tangential planes at the output mirror is 2% of the diameter.

Significant departures from the breadboard cavity and tube dimensions are not expected in the final design, except for tube length. Extra space presently in the cavity will allow an increase in tube length to achieve full rated output power without a significant increase in cavity length. Other slight changes may be made as indicated by refinements in the design analysis (see Appendix G) indicating that the laser tube length must increase with increasing modulator length as shown in Figure 5.2.2-15. Using Equation (5.2.2-11), the input power, P, is computed and plotted in Figure 5.2.2-15 as a function of modulator length based on the GaAs material on hand having an absorption loss of 1.2%/cm. Values used in this computation are given in Table 5.2.2-3.

* T. Li, BSTJ, Vol. 45, p. 917 (1965).

** G. A. Massey and A. E. Siegman, Applied Optics, Vol. I, p. 975 (1969); and D. C. Hanna, IEEE J. Quantum Electronics, Vol. QE-5, p. 483 (1969).

To obtain a 4.0-MHz peak frequency deviation requires 180 volts (peak) across the 3-cm-long modulator in the breadboard transmitter laser. The data in Figure 5.2.2-15 indicate that the modulator length should be reduced from the present 3 cm to 1.4 cm, to minimize the total transmitter-power input. However, this requires an increase in modulator-drive voltage to 386 volts peak. Currently available space-qualified transistors do not allow the design of a 1 to 6-MHz, low-distortion, modulator driver capable of supplying this voltage; therefore, the use of such a short modulator crystal cannot be considered.

Fortunately, total-power-input dependence on modulator length in the region of the minimum is reasonably flat toward the longer modulator lengths. For this reason a modulator length of 2.0 cm and a tube length of 20 cm have been chosen. This results in a 1-watt power penalty above the minimum obtainable but allows a conveniently short tube (20 cm between anodes). The modulator voltage is now reduced to 270 volts peak. It should be emphasized that the results of Figure 5.2.2-15 represent the worst possible case as far as input power consumption is concerned. Both theoretical and experimental investigations are in progress to minimize the power requirement. It is expected that by using an absorption-loss value of 0.007 cm^{-1} , the transmitter power requirement for the LCE program can be satisfied.

The capabilities of the modulator driver have a very large impact on transmitter-laser-modulator design. Much emphasis is being placed on development of the modulator driver, and significant improvements in this area in subsequent weeks are expected to allow further improvement as regards transmitter power requirements. Some small variations in transmitter-modulator geometry may occur as a result, but Table 5.2.2-4 summarizes essentially the final design.

In summary, it is imperative that modulator material with an extremely low absorption coefficient be used in order to reduce transmitter power to a value that will allow the overall power budget to be met. Cadmium telluride or low-loss GaAs are the two candidates that appear to offer a solution. These possibilities are being investigated. Optical absorption measurements are being made on both CdTe (supplied by NASA) and Fe-doped GaAs materials (supplied by Mr. D. High, Research Department, Monsanto Company).

5.2.2.5.2 Laser Tube

5.2.2.5.2.1 Tube Design and Processing

Although a few design parameters [e.g., cathode surface gas-reservoir volume, fractional increase in CO_2 content (see Section 5.3.1)] are still being determined, the basic, ceramic, laser tube design is well defined. The design is based on the following set of major parameters:

- a. The tube must be sufficiently long to provide enough gain for 625-mw minimum output power at the end of 2000 accumulated hours of operation.
- b. The tube must operate with conduction cooling.
- c. It must operate with a heated cathode.
- d. It must provide TEM_{00} power only.
- e. The output beam must be polarized.
- f. The tube must have a long operating life.
- g. It must be bakeable.
- h. It must be rugged enough to withstand liftoff conditions.
- i. It must be capable of operating in a vacuum environment.
- j. It should have as high an operating efficiency as possible.

Figure 5.2.2-16 presents a detailed assembly drawing for the tube configuration that appears to most closely satisfy the foregoing requirements. The tube is of metal-ceramic construction, to achieve the desired degree of ruggedness. It has circular geometry with a 4.0-mm diameter bore made from beryllium oxide. Four 1/4-in.-thick BeO fins are located along the tube bore, approximately equally spaced. BeO ceramic was chosen because of its very high coefficient of thermal conductivity and light weight. The outside shell, made from nickel-plated, thin-walled Kovar, serves as a rigidizing structure as well as the vacuum envelope. The spaces between

the BeO fins are used as gas ballast, necessary for increased life, and have a volume of about 150 cc, which is approximately 80 times the active volume.

The heat-transfer characteristics of this design are highly satisfactory: Thermal calculations indicate that the temperature rise from the outside surface of the tube to the hottest spot in the bore (outside the cathode area) would be less than 4°C , even for tube dissipations as high as 15 watts. Subsequent tests on mockup structures have verified this value. The bore temperature will therefore never exceed about 44°C during operation when the baseplate temperature is at its maximum specified value of 40°C .

For maximum tube efficiency, the laser employs a coaxial electrode structure rather than electrodes in side arms. The Kovar pieces at each end of the laser tube will serve as anodes, while the cathode will be the platinum-clad nickel cylinder in the center of the tube. For long life the cathode must be heated to at least 250°C during operation (see Section 5.3.1 on laser tube life tests). To achieve this without requiring additional external heat, the cathode has been isolated from the BeO bore by insulating sections of alumina ceramic.

The cathode surface area is also an important tube-design parameter. For an optimum gas mixture in the tube and for a given cathode material, an optimum cathode surface area can be determined (see Section 5.3.1). An optimum current density of about 4.0 ma/cm^2 has been experimentally determined for the transmitter laser. This corresponds to a cathode surface area of about 2.5 cm^2 if a 10-ma discharge current is used. To provide the electrical connection to the cathode, as well as additional support, four thin wires of stainless steel run between the cathode and the outside surface of the tube. The wires are terminated on insulating ceramic tubing so that the cathode may be operated somewhat above ground potential if required. Measurements show that this structure will be sufficiently self-heating to allow cathode temperatures somewhat higher than 250°C .

The advantages of a two-anode, single-cathode approach over a single-cathode, single-anode approach are that (a) sputtered material from

the cathode is kept farther from the laser windows, (b) the total tube voltage is approximately halved, and (c) greater power is dissipated at the cathode, because twice the current is being drawn, enabling the cathode to be self-heated.

The GaAs Brewster windows will be attached to the end Kovar assemblies by metal-soldering techniques, allowing rugged ultra-high-vacuum seals. The window assemblies (which will be prepared independent of the tube) will then be oriented and heliarc-welded to the tube at the appropriate point in the fabrication cycle.

The total length of the tube (11.3 in. from window to window) has been chosen to give enough gain to provide 725 milliwatts of initial output power (with modulator) at the high heat-sink temperature of 40°C. At the low heat-sink temperature of 15°C, the power output will be approximately 700 mw. The input power vs tube length calculations are made in Section 5.2.2.5.1, in conjunction with optical design.

The tube is approximately 1-3/4 in. in diameter and will weigh about 3/4 lb.

Based on life test data, it appears that the tube should employ a gas mixture of H₂, Xe, N₂, CO₂, and He. The exact partial pressure for each gas mixture will be determined at the end of the life test program. The N₂ and He are used with CO₂ to obtain high gain and power output. The Xe is added to reduce the starting and operating voltage, and the H₂ to increase tube life by reducing the CO₂ dissociation rate. No automatic pumpout and refill procedures in space are planned for this laser. The tube will be permanently sealed during the processing cycle and will not require further attention.

Tests of similar small lasers have shown that the lifetime goals will be met with this approach. Partial pressures of 7 torr for CO₂, 7 torr for N₂, 15 torr for He, 1 torr for Xe, and 0.1 torr for H₂ are used for the 4-mm-diameter ceramic tube in the breadboard model. In addition to cathode material, emissive surface area, gas mixtures, and gas-reservoir volume, tube processing is an important consideration for long life. Before filling

with gas mixtures, each tube assembly is pumped down to a pressure between 1×10^{-6} and 1×10^{-7} mm Hg and a leakage rate not greater than 1×10^{-9} atm-cc/sec.

5.2.2.5.2.2 Fabrication Plan for LCE Laser Tubes

A preliminary but detailed fabrication plan has been completed for the laser tubes to be constructed for the LCE (see Figures 5.2.2-17, -18, and -19). After receipt and inspection, parts for the laser tubes are filed in a high-relative-humidity storage area. The parts are pulled from storage as required for processing and fabrication of the tube. The finished assemblies are returned to storage until they are required for assembly into the laser subsystem.

5.2.2.5.3 Modulator

The configuration chosen for the LCE employs a GaAs electro-optical phase modulator inside the transmitter laser cavity. In this configuration, the modulator produces changes in optical-cavity phase length in proportion to some applied electrical signal, which then produces corresponding changes in the oscillation frequency of the laser (i.e., frequency-modulated output). This format provides several important advantages in the present application as compared with other types of modulation. Table 5.2.2-5 summarizes the relative merits of several of the other possible methods.

A suitable intracavity modulator should be designed to minimize the losses presented to the transmitter laser, because very small amounts of loss produce large changes in power output. In addition, the modulator must produce minimum perturbation in such areas as transmitter-laser-cavity alignment and cavity-length stability even with large changes in ambient temperature. The modulator must be designed to minimize the power required to produce the required electro-optical phase modulation. The modulator crystal alone is essentially a passive element, and the choice of optimum crystal design depends heavily on interactions with the laser and the modulator-driver electronics. Section 5.2.2.5.3.1 presents an analysis that yields a more or less optimum crystal geometry based on the properties of GaAs material (see Table 5.2.2-6). These properties are discussed in greater detail in succeeding paragraphs, and details on modulator design, construction, and testing are presented.

5.2.2.5.3.1 Modulator Design Considerations

Most publications on electro-optical modulators have dealt with amplitude modulation outside the laser cavity.* For this application, the electro-optical crystal is normally placed between crossed polarizers, and for optimum performance the largest possible rotation of the plane of polarization is sought. It has been shown that the maximum amplitude modulation

* F. Sterzer, D. Blattner, and S. Minter, J. Optical Soc. Am., 54, 62, (1964); and S. Namba, J. Optical Soc. Am., 51, 76 (1961).

is obtained from a cubic crystal with $\bar{4}3m$ symmetry when the crystal is cut so that the light is propagated in a $(\bar{1}10)$ direction and the electric field is applied in the $(\bar{1}10)$ direction. In this case, the direction of polarization of the incident light bisects the angle between two induced crystal axes.

This design is well known as is the proof that it provides optimum amplitude modulation. The proof is not directly applicable to a modulator that is to be used inside the laser cavity. In this case, the interest is not in the maximum angular rotation of the plane of polarization of the incident light, but in the maximum obtainable change in the optical length of the crystal. Indeed, there can be no rotation if the laser is to operate properly. Hence, the direction of polarization inside the laser cavity must be parallel to the direction of one of the induced axes in the crystal. In order to obtain optimum performance of an intracavity modulator, it is therefore necessary to consider only the question of what configuration will yield the maximum index change along any of the induced principal axes in the material.

The question of the maximum change of index is treated in passing by Sterzer, et al.* The induced principal indices are given by

$$n_{z'} = n_o + \frac{r_{41}|E|n_o^3}{\sqrt{3}} \cos\left(\frac{\theta}{3}\right)$$

$$n_{x'} = n_o + \frac{r_{41}|E|n_o^3}{\sqrt{3}} \cos\left(\frac{\theta}{3} + 120\right)$$

$$n_{y'} = n_o + \frac{r_{41}|E|n_o^3}{\sqrt{3}} \cos\left(\frac{\theta}{3} + 240\right)$$

* Op. cit.

where the angle θ is related to the applied field E , by

$$\cos \theta = \frac{(27)^{1/2} E_1 E_2 E_3}{|E|^3}$$

The only assumption is that the crystal is cubic, with $\bar{4}3m$ symmetry. It is clear from these expressions that the maximum change of index is obtained when the electric field is chosen so that $\theta = 0$. It is also clear that, to obtain this result, the field must be applied in a (111) direction. The field vector is then

$$E = E \frac{1}{\sqrt{3}}, \frac{1}{\sqrt{3}}, \frac{1}{\sqrt{3}}$$

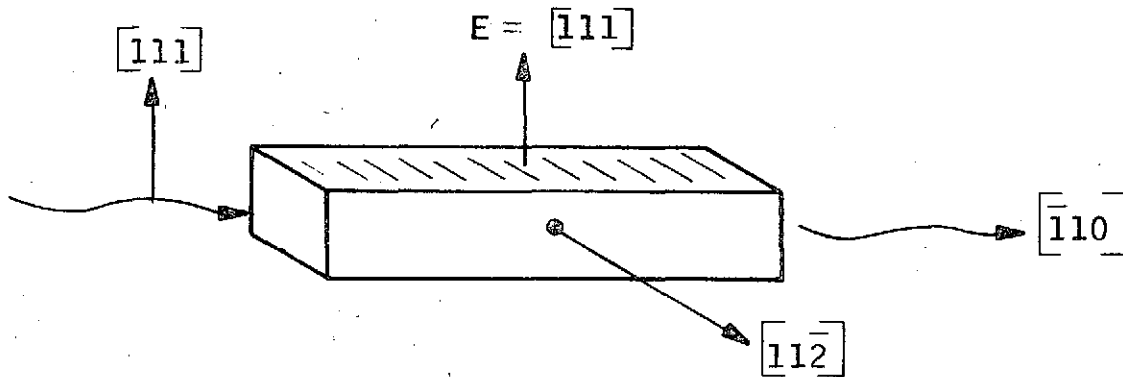
For this field direction, the changes of index and the directions of the induced axes are

$$\Delta n_{x'} = \frac{n_o^3 r_{41} E_o}{2\sqrt{3}}, \quad x' = (11\bar{2})$$

$$\Delta n_{y'} = \frac{n_o^3 r_{41} E_o}{2\sqrt{3}}, \quad y' = (\bar{1}10)$$

$$\Delta n_{z'} = \frac{n_o^3 r_{41} E_o}{\sqrt{3}}, \quad z' = (111)$$

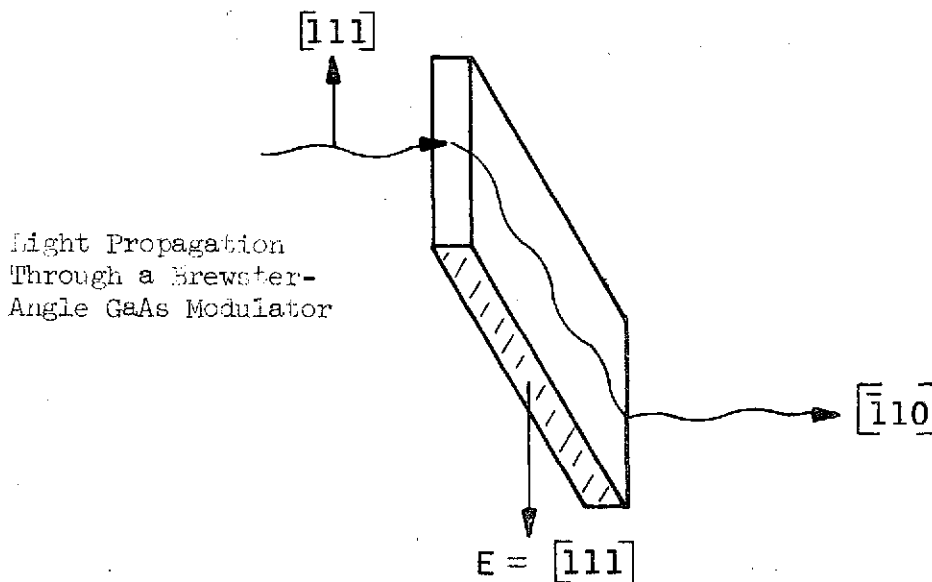
Thus to obtain a modulator with the maximum possible index change, the incident light must be polarized in the direction of the applied field. A suitable configuration is sketched at the top of the next page,



Light Propagation Through a Linear GaAs Modulator

The light propagates in the $(\bar{1}10)$ direction, and the field is applied in the (111) direction.

In order to use this modulator inside the laser cavity, Fresnel reflections at the crystal faces must be avoided. This may be done either by antireflection coating of the two surfaces or by tilting the crystal so that the light is incident at Brewster's angle. Tilting has been chosen, to avoid optical losses and possible life problems with antireflection coatings. When the Brewster-angle technique is employed, the direction of polarization of the incident light must unfortunately remain in the plane of incidence, and the crystal must be made wider in one direction in order to accommodate the refracted beam. Thus, the Brewster-angle configuration for maximum index change is as sketched below.



Light Propagation Through a Brewster-Angle GaAs Modulator

In this case the modulator crystal is in the direction in which the field is to be applied. Obtaining the required field will therefore require that the drive voltage be increased by a factor of 3.

The increase in drive voltage needed for the Brewster-angle configuration can be avoided if the field can be applied at right angles to the direction of polarization of the incident light. This cannot be done if the maximum index change is required. However, a cut is available that allows the field and polarization directions to be at right angles, and produces an index change only 5% less than the maximum obtainable in a $\sqrt{3}$ m crystal.

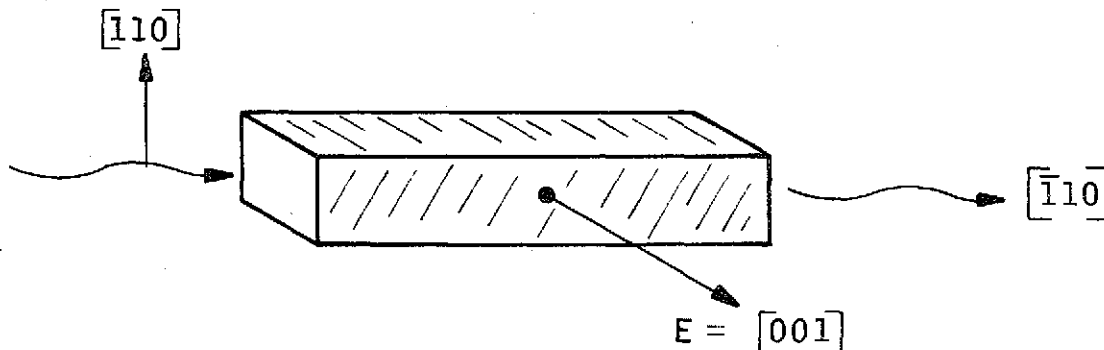
If the field is applied in the (001) direction, the following index changes occur for corresponding induced axes:

$$\Delta n_{x'} = -\frac{n_o^3 r_{41} E_o}{2}, \quad x' = (110)$$

$$\Delta n_{y'} = \frac{n_o^3 r_{41} E_o}{2}, \quad y' = (\bar{1}10)$$

$$\Delta n_{z'} = 0, \quad z' = (001)$$

To obtain a modulator with this index change, the light may be polarized in the (110) direction, with the direction of propagation in the ($\bar{1}10$) direction. The configuration is as follows:



Light Propagation Through a Linear GaAs Modulator

The modification of this structure into the Brewster-angle configuration does not require an increase in the applied drive voltage.

In summary, an intracavity modulator requires the maximum index change rather than the maximum rotation of the incident plane of polarization as in an amplitude modulator. For crystals with $\bar{4}3m$ symmetry, the maximum index change is

$$\Delta n = \left(\frac{1}{\sqrt{3}} \right) r_{41} n_o^3 |E| = 0.578 r_{41} n_o^3 |E|$$

where $|E|$ is the magnitude of the applied field, n_o is the zero field index, and r_{41} is the electro-optical coefficient. This index change is obtained when the field is applied in the (111) direction and when the incident light is polarized in the direction of the field and is propagating along the (110) direction. In the Brewster-angle configuration, this crystal cut unfortunately requires an increase in the applied voltage by a factor of 3 over the voltage required by the in-line configuration. To avoid this potential disadvantage, the directions of the polarization and the applied field must be at right angles. Such a cut is available with an index change of only 15% less than the maximum obtainable. The field is in the (001) direction; the light is polarized in the (110) direction and propagates in the (110) direction. The obtainable index change is

$$\Delta n = \frac{1}{2} r_{41} n_o^3 |E|$$

Several of the more important material properties for GaAs are shown in Table 5.2.2-6.

5.2.2.5.3.2 Crystal Geometry

Because of the large index of refraction of GaAs ($n = 3.30$ at 10.6 microns and 300°K), the refracted beam inside the Brewster-angle modulator is very slight elliptical. In order to present a 0.3 by 0.3-cm optical aperture to the laser cavity, the width of the crystal must be equal to W (see Figure 5.2.2-20, which summarizes the geometric properties of the modulator crystal).

The optimum modulator length has been chosen at 2 cm, based on a tradeoff analysis for the transmitter laser.

5.2.2.5.3.3 Crystal Fabrication

The techniques involved in crystal fabrication include semiconductor-material preparation and cutting, high-quality optical-surface finishing, metal-semiconductor cleaning, and soldering. A significant development during the breadboard phase of the program has been the demonstration of a reliable technique for rugged attachment of the electrodes. A nickel film is deposited on the GaAs crystal blank and is diffused into the surface. Molybdenum electrodes are then soldered to the nickel layer with an indium-base solder. Figure 5.2.2-21 shows the results of the intentional destruction of a sample soldered by this technique; the contact held and material was pulled from the bulk crystal.

5.2.2.5.3.4 Modulator Characteristics and Assembly

Table 5.2.2-7 summarizes important modulator characteristics, Figures 5.2.2-22, -23, and -24 present photographs of the breadboard modulator crystal, the modulator assembly, and the complete modulator unit installed in the transmitter laser.

5.2.2.5.3.5 Modulator Driver and Modulator-Oven Temperature Control

In order to provide the required index of modulation, the 2-cm modulator must be driven with a peak emf of 270 volts. The modulation frequencies are in the band between 1 and 6 MHz, and the gain must be flat within ± 0.1 db between 1.0 and 1.84 MHz, and within ± 0.2 db to 6 MHz. Other specifications are given in Table 5.2.2-8.

Because of the gain, the flatness is required to be less than 2% over the bandwidth. Because of the linearity requirements, it becomes necessary to use negative feedback to stabilize the gain and linearity to accommodate tolerances in component parameters and changes in component values over the frequency range that are due to aging, environmental conditions, etc.

It is also important to use the minimum power from the prime power source consistent with fulfilling the operating specifications. This suggests Class B operation on the output stage, so that the efficiency is maximized and that the power drawn is proportional to the power required. The modulator-driver-circuit output stage shown in Figure 5.2.2-25 is operated Class B. Each high-voltage string is biased near cutoff, so that a drive on the bases of Q1 and Q2 will change the capacitance of the modulator alternately positive and negative. The feedback can be generated by taking the difference between the currents sampled in the emitters of the driving transistors.

The advantage of this circuit is that the supply voltage need be only slightly larger than the required peak voltage and, hence, the quiescent power may be minimized.

The oven-temperature controller is shown schematically in Figure 5.2.2-26. The thermistor is placed in a bridge circuit formed by the R1, R2, R3, and R4 resistors, which drive the inputs to the operational amplifier operated as a comparator. The operational-amplifier output switches Q1 and Q2 on or off, depending on whether the temperature is below or above the set temperature. The oven heater is connected between the collector of Q2 and the 28-volt supply.

The modulator will be clamped by boron nitride and shielded with aluminum housing. Boron nitride was selected because it has a low dielectric constant, low density, and good thermal conductivity. The temperature of the modulator will be maintained to $\pm 1^{\circ}\text{C}$ in order to limit cavity-length tuning to less than one free spectral range.

The oven controller has been designed and successfully tested. When the modulator is operated at a controlled temperature of 70°C , the total input power to the controller will be a maximum of about 2 watts at the lowest heat-sink temperature of 10°C .

5.2.2.5.4 Optical Design5.2.2.5.4.1 Alignment Tolerance Requirements

Experiments have been performed in order to determine the alignment tolerances of the various laser components. Both the flat and spherical transmitter mirrors were tilted by a known amount about their horizontal and vertical axes. Figures 5.2.2-27 and -28 plot the resulting decrease in laser output power as a function of angular tilt for the flat and spherical mirrors. The angular misalignment of the spherical mirror at a 3-db power loss is ± 1.16 mrad for movement about the vertical axis and ± 1.05 mrad for movement about the horizontal. The corresponding angles for the flat mirror are ± 1.50 and ± 1.38 mrad.

The tolerance on the lateral displacement of the tube and modulator can be inferred from the angular misalignment, θ_s , of a spherical mirror having radius of curvature R . When the spherical mirror is tilted, the beam is laterally displaced rather than being tilted, as is the case for angular movement of the flat mirror. The lateral beam displacement, d , is given by $d = R \theta_s$. A lateral displacement of the beam is identical to a lateral displacement of the tube and modulator, assuming that the power drop is due to vignetting by the tube and modulator. The lateral displacement corresponding to a 50-cm radius-of-curvature mirror being tilted ± 1.16 mrad is ± 0.58 mm, while that corresponding to ± 1.05 mrad is ± 0.525 mm. These displacements correspond to a 3-db loss of power.

The angular tolerance of the tube can be estimated by noting that the worst case occurs when the tube is pivoted about its end near the flat mirror. This angular displacement produces a maximum laser-tube effect on the laser beam. If the tube is 10.3 in. long, as is the case expected for the final lasers, the angular displacement producing the same effect as a lateral displacement of 0.55 mm is $\frac{(0.55)}{(10.3)(25.4)} = 2.1$ mrad.

5.2.2.5.4.2 Mirror Mount and Transducer Considerations

The type of mirror mount that would satisfy the requirements of the LCE program should be capable of being adjusted in the field, should be lightweight, and should be very rigid against vibrational effects.

To achieve the required mechanical isolation against vibration, the individual elements of the structure must be designed with geometries and methods of support that do not have low-frequency transverse resonances. The basic design approach is to eliminate all thin-plate and weak-cantilever structures that have low-frequency transverse resonances. The joints between the various components of the structure, especially in the area of the mirror mounts, have been designed to have large-area contacts in order to keep the spring constant of the joint at a high level.

It is expected that the vibrational environment around the laser after it is in the spacecraft environment may be improved sufficiently to increase the short-term stability of the laser by orders of magnitude. To test the laser satisfactorily, however, it will be necessary to obtain a high degree of stability in the laboratory.

Figure 5.2.2-29 shows the mirror holder. In this case, the non-output mirror is attached to a piezoelectric bimorph transducer, which in turn is rigidly held to a rotatable "ball." When the ball clamp is loosened, the ball can be rotated with an external adjustment jig, and can then be tightly clamped to the frame. The main advantage is the large area contact on the ball with positive clamping. The output mirror will be mounted on a thermally compensating standoff in order to reduce the effects of temperature changes.

With the removal of all etalon-type components from the laser cavity, the limits on the allowable temperature variations in the modulator are determined only by the extent to which they can be tracked out by the piezoelectric transducer; i.e., the maximum-attainable transducer movement will eventually set the level of temperature control required.

Analysis subsequently verified by experimental tests shows that a bimorph-configuration piezoelectric transducer will provide movement of more than 15 microns (three free spectral ranges) while still exhibiting a high fundamental resonant frequency. This movement is about a factor of 3 larger than for the conventional stack-of-plates type of transducer.

A "bimorph" or "bender" transducer is a piezoelectric device made from two, thin, plate-shaped, transducer elements bonded together in such a manner that one expands when the other contracts in length. This provides a bending motion when one end of the transducer is allowed to remain unconstrained, as is the case for the image-motion compensators to be used in the LCE optical system.

If the bender is clamped at both ends, with a mirror mounted in the center of the bender (as shown in Figure 5.2.2-30), the mirror can be translated without tilting. Either a linear bimorph clamped at both ends or a circular bimorph clamped around its periphery can be used for this application. Clamping a circular bimorph entirely around its edge, however, will reduce its travel by a factor of about 3.5 as compared with the travel that can be obtained from a linear bimorph with a length equal to the circular-bimorph diameter.

Figure 5.2.2-30 shows a doubly clamped bimorph with laser mirror mounted.

Tradeoff analysis involving size limitations in the laser package, maximum voltages, mounting configurations, and environmental-stress levels indicates that a circular bimorph with the following characteristics will be most suitable:

Diameter	1.0 in.
Thickness	0.020 in.
Maximum safe voltage	200 volts
Normal voltage range	0 to 150 volts (below arc-over point at critical pressure)
Normal displacement	0 to 15 microns
Unloaded resonant frequency	3.6 kHz
Resonant frequency with mirror	2.5 kHz (above environmental-test spectra)

A stress/deflection analysis has been conducted to determine the structural behavior of piezoceramic bimorph configurations under the qualification, vibration test, and operational environments. It was found that all the stress levels were very low and the unit will operate with a margin of safety of 1.8. Such bimorph structures have been tested at Sylvania and found to operate according to the foregoing analysis.

The linearity of the circular bimorphs has been measured (see Figures 5.2.2-31 and -32). As expected, they show excellent linearity around the static position. At higher voltages, when the device has moved over a 10-micron distance, the deviation from linearity is about 13%. This nonlinearity will not be a problem, because the laser will be operating in the closed-loop mode at all times. The sensitivity of the transducer (microns/volt) is very close to that expected.

Short-term aging effects were studied by measuring the sensitivity and total movement of a transducer after it had set for 2 weeks with 150 volts applied. No noticeable change in either quantity was observed.

5.2.2.6 Local Oscillator and Backup Lasers

5.2.2.6.1 Laser Cavity

The design of the local oscillator and the backup laser tubes is similar to that of the transmitter laser tube. In both cases, a three-electrode, BeO, ceramic-metal tube is employed (see Figure 5.2.2-16). Because these tubes

are required to operate at somewhat lower output power than the transmitter laser, the input power will be proportionally less. To reduce the total power input, the cathode-to-anode electrode distance is reduced, thus lowering the operating voltage while keeping the discharge current at the same level as that of the transmitter laser. In this way the cathode temperature will be maintained at the required level ($\geq 250^{\circ}\text{C}$) in order to obtain long life. The basic ceramic-metal tube structure has been discussed earlier in this section and is therefore omitted here.

The primary differences in the optical cavities of the three lasers are that the LO and backup lasers do not contain a modulator and that one mirror of the LO laser is replaced by a grating, as discussed in Section 5.2.2.6.2.3.

5.2.2.6.2 Local Oscillator Laser

5.2.2.6.2.1 Cavity Losses

The total cavity loss is the sum of the diffraction loss occurring at the ends of the tube and the losses at the end mirror and grating. The coupling loss, caused by removing some of the intercavity power as useful power out, is considered separately.

The diffraction loss is a function of the mirror separation, mirror radius of curvature, and tube bore. These parameters are chosen so that the loss for the TEM_{∞} mode is kept low, while the loss for the TEM_{10} mode is high enough to prevent it from lasing. Li* has generated plots for diffraction loss vs Fresnel number and g factor. The Fresnel number is defined as $N = a^2/\lambda L$, where a is the limiting aperture at each mirror, λ is the mirror separation. The g factor is defined as $g = 1 - (L/R)$, where R is the radius of curvature of the spherical mirror. A further constraint on the radius of curvature and mirror separation is the requirement on output-beam size, w , where w is defined as the radius of the Gaussian beam at which the intensity has fallen to $1/e^2$ of its peak value. The dependence of w on R and L is discussed in Section 5.2.2.6.2.4.

* T. Li, B.S.T.J., 45, 917 (1965).

The following geometrical parameters were selected by an iterative process to yield a diffraction loss of 0.5% for the TEM_{00} mode while that for the TEM_{10} mode is 6%:

$$a = 2 \text{ mm}$$

$$R = 50 \text{ cm}$$

$$L = 9 \text{ in.}$$

As will be shown, these values yield the proper beam diameter while providing low TEM_{00} mode loss and high enough TEM_{10} loss.

The loss due to scattering and absorption at the end mirror is taken to be 0.8%. The loss at the grating is 4%.

5.2.2.6.2.2 Tube Length

The required length of the discharge tube depends on the available gain in the tube, the saturation intensity, the cavity losses, and the required power output. The tube diameter is taken as 4 mm for reason discussed in the preceding section. For this tube diameter, the saturation intensity, I_s , as deduced from experimental observations on small-bore tubes, is 250 watts/cm². The required power out is 30 mw at 30 MHz from line center, and the beam radius, w , is 1.24 mm (as shown in Section 5.2.2.6.2.4) for the radius of curvature and cavity length discussed above.

The average output intensity, I_o , defined as $P_o/\pi w^2$, is therefore 2.07 watts/cm². From Rigrod's analysis,* discussed in Appendix G, the value of the product of small signal gain, g_o , and active discharge length, L_A , corresponding to $I_o/I_s = 0.0083$ is $g_o L_A = 0.09$ for a total cavity loss of 0.053. Rigrod's analysis shows a corresponding optimum mirror transmission of 4%. This transmission can be achieved from either of two coupling schemes. One involves the usual output coupling through the partially transmitting spherical mirror; the other involves the coupling from the grating at the zero-th order. Preliminary laboratory tests show that the latter approach is not only feasible but will improve laser efficiency.

* W. Rigrod, J. Applied Phys., 36, 2487 (1965).

Because $g_0 L$ is 0.09, the active discharge length is about 7 cm for a small signal gain, g_0 , of 0.012 cm^{-1} , a value obtained from measurements performed on 4-mm-bore-diameter tubes.

5.2.2.6.2.3 30-MHz Offset

A diffraction grating is used in the LO laser to maintain a greater oscillation line width on a single laser line so that a 30-MHz offset from the oscillation-line center can be reliably achieved. Without a diffraction grating, a large frequency offset from the oscillation-line center can cause the laser oscillation to switch from one vibration-rotation transition to another. This is possible because there is extremely high competition among various vibration-rotation transitions in a CO_2 gas discharge via collisions so that the gain of some other lines can easily exceed the operating line at the offset position.

The line shape and line width have been measured for the bread-board LO laser. The results are shown in Figure 5.2.2-33. The full width at half maximum power point is approximately 90 MHz. From that figure it is evident that a 30-MHz offset can easily be achieved at a small increase in the prime power needed to overcome the grating loss.

5.2.2.6.2.4 Beam Properties

According to Kogelnik and Li,* a beam of radial intensity $I = I_0 \exp(-2r^2/w^2)$ will have a w parameter at a distance z from the beam waist, w_0 , of

$$w^2 = w_0^2 \left[1 + \frac{(\lambda z)^2}{(\pi w_0^2)^2} \right]$$

and a radius of curvature, R , as given by

$$R = z \left[1 + \left(\frac{\pi w_0^2}{2z} \right)^2 \right]$$

If $z = L$, the cavity length, R , is the radius of curvature of the cavity mirror when the opposite mirror is a flat. Thus, the radius of curvature of the cavity mirror determines w_0 , which in turn determines w at any distance from the beam waist (located at the flat cavity mirror).

* H. Kogelnik and T. Li, Proc. IEEE, 54, 1312 (1966).

With the output-mirror radius of curvature and the cavity length given previously, $w = 1.24$ mm for the LO laser. Here, w is the radius of the output beam to the $1/e^2$ intensity point. The output beam, taken from the spherical mirror, will be recollimated by shaping the outer surface of this mirror. This technique has been verified in the laboratory on the breadboard laser system.

5.2.2.6.2.5 Beam Shift

It is important to note that if the Brewster windows are anti-parallel, the laser-mirror alignment must be changed for operation in a vacuum as opposed to operation in air. If the windows are parallel, the beam is translated laterally within the cavity. In this case, no realignment is required, but allowance must be made in tube and modulator dimensions to assure that no vignetting occurs. The beam displacement in either case is due to index-of-refraction variation between air and a vacuum. If the windows are parallel and at a Brewster angle set for air, the lateral displacement of the beam at the curved mirror is zero. With reference to Figure 5.2.2-34 for geometrical definitions,

$$x_1 = -t \frac{\cos 2 \theta_B}{\sin \theta_B}$$

$$x_2 = x_1 - \left(\frac{n_1}{n_2} - 1 \right) n_g L + \frac{L \Delta \theta}{1 + n_g \Delta \theta}$$

$$x_3 = x_2 + x_1$$

$$\Delta \theta = n_g \Delta n$$

where Δn is the difference in index of air and vacuum. If $L = 18.5$ cm and $t = 0.05$ in., $n_g = 3.3$, then $x_1 = 1.10$, $x_2 = 0.94$, and $x_3 = 2.04$ mm if the system is in air. If the system is in a vacuum, x_2 and x_3 are increased by 0.165 mm. Because this variation occurs at the flat mirror end of the cavity, where the beam is much smaller than the tube diameter, little or no significant effect is expected to be observed in the LO and backup lasers. In the

transmitter laser, however, the modulator will cause some vignetting of the beam unless its cross section is sufficiently large. In one direction the modulator will be made approximately 0.2 mm larger than required in order to operate satisfactorily in both air and a vacuum.

5.2.2.6.2.6 Input Power

Experimental results in life testing of laser tubes indicate that about 5 ma of current is required in each leg of the discharge tube to provide enough cathode heating to maintain tube life. Figure 5.2.2-35 plots tube voltage as a function of tube current for various anode-cathode displacements. It corresponds to one-half of the discharge tube and indicates that the required power for a 3.5-cm discharge (the length required for the LO tube) is approximately 5 watts, or 10 watts for the entire discharge tube. An analysis currently in progress indicates that the total input power may be reduced by decreasing the tube current and using an external cathode heater.

5.2.2.6.3 Backup Laser

5.2.2.6.3.1 Cavity Design

The backup and LO lasers are very similar in construction, except that the backup laser lacks the internal grating of the LO laser. The analysis leading to the backup design is identical to that of the LO laser, and only the results will be presented here. A 7-cm active discharge in a 4-mm diameter tube will produce the required 650 mw of output power. The spherical-mirror radius of curvature is 107 cm, and there is a 10-in. separation between the spherical output mirror and the totally reflecting flat mirror. The power required by such a tube is 10 watts. The collimated-output-beam radius is 1.42 mm to the $1/e^2$ intensity point. This has been demonstrated in an experiment with the breadboard LO laser.

5.2.2.6.3.2 Wavelength Selection

The backup laser must operate on two P-transitions upon command, in order to facilitate its use as a transmitter or a local oscillator. To accomplish this, the flat mirror will be mounted on a piezoelectric transducer

that will translate the mirror. The resulting change in cavity length will allow the required wavelength to be selected.

A further requirement is that a 30-MHz offset from line center be obtained at each of the two P-transition wavelengths. The problem encountered here is that the laser may shift to another wavelength when the cavity length is tuned from line-center operation. Gerhard Schiffner has shown that the proper choice of total cavity length will eliminate this problem. Therefore, the total cavity length may change by 1 or 2 mm, with wavelength selection being accomplished by additional fine length tuning of about 1 micron.

5.2.2.7 Laser Subsystem Electronics

The frequency of the three lasers in the modes required for laser functions is controlled by the AFC electronics for the laser subsystem. The transmitter laser uses the AFC electronics to search for the proper wavelength and, upon acquisition, to lock to the line center and remain locked.

The local oscillator uses the electronics to search for the proper wavelength and, upon acquisition, to lock offset from line center by 30 MHz and to remain locked there until commanded to lock to the discriminator output of the receiver subsystem. In this mode, the local oscillator will track the transmitted signal with the specific 30-MHz offset.

The backup laser uses the electronics to provide either of the two functions - the transmitter AFC and the local oscillator AFC - upon receipt of the proper command. In addition, the backup laser electronics must be capable of selecting either wavelength, which is accomplished by selecting the output beam from the appropriate power detector illuminated from the proper diffraction grating.

Succeeding paragraphs discuss the block diagrams of the AFC electronics and explain the operation of the unit.

Figure 5.2.2-36 presents a block diagram for the transmitter AFC system. Operation is initiated by the application of low-voltage power. With no power returning from the power detector, the output from the threshold circuit is a NOT THRESHOLD, which throws the FET switch (shown schematically

as a single-pole, two-throw switch) to connect the search oscillator into the integrator. The search oscillator has a square-wave output that becomes a triangular wave when passed through the integrator. The triangular wave is amplified in the tuner driver and is applied to the bender bimorph, which tunes the laser cavity. The entire range of the bender bimorph is swept out once per second, searching for power returning from the power detector. When the cavity is the proper length to produce power at the selected wavelength, the power detector will deliver a voltage that will trigger the threshold circuit. This action will throw the FET switches into position for dither stabilization.

A dither oscillator is operating at about 75 Hz and is fed to the input to the tuner driver; the laser is frequency-modulated at this dither rate. The output of the power detector will be amplitude-modulated at the dither rate by slope-detection on the power-profile curve of the laser operating line. By detecting the amplitude modulation in synchronism with the dither frequency, a discriminator-like curve is generated that has a zero at the line center. Thus, an error signal is generated that will drive the tuner so that the laser is operating on line center.

The transmitter will continue to operate on line center, provided power is sensed on the power detector. Any interruption of power will cause the system to revert to the search mode until power is again sensed.

A level-sensing and inhibit circuit is shown. Its purpose is to inhibit locking to a power profile that is only partially present within the range of the tuner driver. For instance, if the first power sensed is from a profile that centered at a voltage beyond the capability of the tuner driver, the dither-stabilization error will require the voltage to be increased up to the limit of the driver. At that point the system will be locked without having found line center. With the level sensing and inhibit circuit, the threshold is inhibited from looking at the power profile on the extreme limits of the tuner driver range, and, when a lock is accomplished, a lock on line center is assured.

Figure 5.2.2-37 presents the local oscillator block diagram. Operation is again initiated by the application of low-voltage power to the circuits and the initial operation is identical to that of the transmitter. However, after the laser has been dither-stabilized to the line center and a preset time delay has expired, the system is locked to make the power output equal to a reference value that has just previously been determined. The reference power is determined by measuring the power at line center at the time the system is dither-stabilized and by reducing the voltage analog of the peak power by an offset voltage. The voltage difference is then held in a digital sample-and-hold circuit and provides the analog of the reference power to which the system will be locked. The output power is then held to this value until an OPERATE "ON" level command is received. This command switches the integrator input to the output of the receiver-subsystem discriminator, and the local oscillator will be slaved to the frequency of the received transmitter with the desired 30-MHz offset.

An analysis of the errors introduced by drifts and offsets in the LO offset method is presented below.

The power-frequency profile is assumed to have a characteristic shape defined by

$$V = V_m \frac{1 - 4f^2}{(\Delta f_{osc})^2}$$

where $\Delta f_{osc} \approx 90$ MHz. It is also assumed that the shape of the profile is preserved under aging effects, loss of gas pressure, etc. The slope at the IF offset frequency will thus remain essentially constant. The slope at the offset frequency is given by

$$\left| \frac{dv}{df} \right| = V_m \frac{8f}{(\Delta f_{osc})^2} \Big|_{f = f_{IF}}$$

Using $V_m = 2.5$ volts, $f_{IF} = 30$ MHz, and $\Delta f_{osc} = 90$ MHz,

$$\left| \frac{dv}{df} \right| = 74 \text{ mv/MHz}$$

Analysis of a measured power profile indicates the slope to be slightly less than this value. To be conservative, the measurement value (approximately 50 mv/MHz) will be used.

As an arbitrary breakdown, assume two-thirds of the budget for the laser and one-third for electronics.

The allowable fixed-frequency error is

$$1.1 \text{ MHz} \times 50 \text{ mv/MHz} = 55 \text{ mv}; \text{ electronics } 18 \text{ mv}$$

The allowable drift is

$$0.5 \text{ MHz} \times 50 \text{ mv/MHz} = 25 \text{ mv}; \text{ electronics } 9 \text{ mv}$$

The identified sources for the fixed-frequency error are as follows:

Measurement of V_{in}

Value of offset voltage, V_d

Quantizing error in sample-and-hold circuit

Offset voltage in integrator

Finite loop gain.

The open-loop gain will be designed to be nearly 10^4 so that the error caused by finite loop gain will be negligible.

The offset voltage in the integrator will have a maximum of 5 mv, with a typical value of 1 mv.

The seven-bit sample-and-hold circuit will have a maximum quantizing error of about 6 mv, considering that the voltage to be sampled is about 1.5 volts. In addition to the quantizing error of the sample-and-hold circuit, the comparator will have an offset error that may be as high as 5 mv. However, it is important to note that the offset errors in the comparator and in the integrator are not random errors but are attributed to the tolerance of components. Once the components are selected, these errors may be compensated by adjusting the value of V_d .

The offset voltage, V_d , may be held to 0.5% or about 3 mv.

Time will be required to permit the accurate measurement of V_m . To hold to 4 mv, at least 17 millisecc is required.

The total initial offset budget, considering offset errors in the operational amplifier than can be compensated, is thus

	<u>Budget, mv</u>
Quantizing error	6
V_d	3
Measurement of V_m	4
	<hr style="width: 10%; margin: 0 auto;"/>
	13

which is well within the requirement.

The sources of drift during the 300-second period one identified in the electronics are (a) offset voltage drift in the integrator, (b) power detector/amplifier drift, and (c) sample-and-hold drift.

Again as an arbitrary breakdown, each of the three sources of drift is budgeted at one-third of the allowable drift of 9 mv. Each of these items is therefore assigned a 3-mv drift within a 300-second period.

The backup laser must be capable of assuming either the role of the transmitter or that of the local oscillator. To do this, the functions shown in Figure 5.2.2-38 are added to the local oscillator - e.g., selection of the proper power-detector output to allow locking on either line and also to be able to lock on line center or offset. This is accomplished by inhibiting the time delay following the threshold in the transmit mode. With the delayed threshold inhibited, the LO offset sequence is interrupted and the system will remain locked in the dither-stabilized mode.

Figures 5.2.2-39, -40, and -41 provide block diagrams for the feedback loops and show the particular transfer functions.

TABLE 5.2.2-1

LASER SUBSYSTEM REQUIREMENTS

			Backup Laser	
	Transmitter	LO	Transmitter	LO
Power output	650 mw	80 mw	650 mw	500 mw
Mode	TEM _∞	TEM _∞	TEM _∞	TEM _∞
Polarization	Linear	Linear	Linear	Linear
Transition	P(20), 10.6 microns	P(16), 10 microns	P(20)	P(16)
Operating frequency	+100 kHz from line center	30 ± 0.05 MHz from line center	+100 kHz from line center	30 ± 0.05 MHz from line center
Offset accuracy	--	±1.1 MHz	--	±1.1 MHz
Frequency stability				
0.1 to 5 Hz	100 kHz, rms	100 kHz, rms	100 kHz, rms	100 kHz, rms
5 to 800 kHz	50 kHz, rms	50 kHz, rms	50 kHz, rms	50 kHz, rms
800 kHz to 6 MHz	2.7 kHz, rms	2.7 kHz, rms	2.7 kHz, rms	2.7 kHz, rms
Amplitude stability	2%, rms	0.3%, rms	2%, rms	0.3%, rms
PZT travel	15 microns	6 microns	6 microns	6 microns
Frequency modulation bandwidth	1 to 6 MHz			
Modulator-driver in- put stability (24 hours)	±0.1 db			
Linearity	1% over 75% of bandwidth			

TABLE 5.2.2-2

TRANSMITTER-MODULATOR DESIGN PARAMETERS

<u>Symbol</u>	<u>Definition</u>
a	Modulator-aperture size
C	Total modulator capacitance
C _c	Modulator-crystal capacitance
C _s	Stray modulator capacitance
D	Bore diameter of tube
f	Laser oscillation frequency $\cong 2.8 \times 10^{13}$ Hz
f _m	Modulation frequency
Δf_{peak}	Peak-frequency deviation at FM on transmitter output (4.0 MHz maximum)
J _T	Tube current
K ₁	Efficiency factor for tube power supply
K ₂	Efficiency factor for modulator driver
L _C	Laser-cavity length
L _M	Modulator-crystal length
L _T	Active length of tube
n	Refractive index of modulator crystal = 3.3 for GaAs
V _M	Modulator voltage
V _T	Tube voltage
V ₄₁	Electro-optic coefficient = 1.6×10^{-10} cm/volt for GaAs

TABLE 5.2.2-3

VALUES USED IN POWER CALCULATION

Tube diameter	0.4 cm
Modulator aperture	0.3 cm
Modulator loss	0.012 per cm
Modulation frequency	1.5 MHz
Modulator quiescent power	1.5 watts
Stray modulator capacitance	7 pf
Modulator-driver efficiency	64%
Tube-power-supply efficiency	100%

TABLE 5.2.2-4

TRANSMITTER LASER DESIGN SUMMARY

Power output (TEM ₀₀ mode)	0.70 watt (max)
Active length of tube	20 cm
Bore diameter of tube	0.4 cm
Modulator-crystal length	2.0 cm
Modulator absorption loss	1.4%
Modulator aperture	0.3 cm (square)
Tube, power input	26 watts, 2.6 kv, 10 ma
Modulator, power input	6.5 watts
Ballast volume	150 cc
Polarization	Linearly polarized with GaAs Brewster-angle windows
Output-beam shape	Round, 2.8 mm in diameter
Electrode configuration	Heated nickel cathode, two anodes

TABLE 5.2.2-5

COMPARISON OF MODULATION TECHNIQUES

Technique	Notes
Amplitude modulation	<p>Sacrifices available carrier power whether internal or external</p> <p>Large signal-level changes because of power fades in atmospheric path</p>
Phase modulation (external electro-optic phase modulator)	<p>Requires that receiver local oscillator be phase-coherent with carrier oscillator, which is difficult at optical frequencies</p> <p>Very large modulator fields required to produce significant phase-modulation depth</p>
Frequency modulation (internal electro-optic phase modulator)	<p>Makes use of heterodyne detection with easily achieved AFC of local oscillators</p> <p>Moderate electrical fields produce large modulation depth</p> <p>Sacrifice in available carrier power easily made up in reduced modulator-drive power required</p>

TABLE 5.2.2-6

GaAs MATERIAL PROPERTIES

Property	Value
Mechanical	
Density	5.3 g/cm ³
Young's modulus	12.3 x 10 ⁶ psi
Etch-pit density	8.3 x 10 ⁴ cm ⁻²
Thermal	
Melting temperature	1240°C
Thermal conductivity	0.0885 cal/sec-cm-°C at 300°K
Linear expansion coefficient	6 x 10 ⁻⁶ /°C
Specific heat	0.064 cal/cm-°C
Electrical	
Resistivity	7.9 - 7.6 x 10 ⁷ ohm-cm
Optical	
Refractive index	3.30 at 10.6 microns at 300°K
Electro-optical coefficient (γ_{41})	1.6 x 10 ⁻¹⁰ cm/volt

TABLE 5.2.2-7

MODULATOR CHARACTERISTICS

Modulation depth	4.0 MHz for 270-volt peak
Temperature tuning effect	300 MHz/°C
Modulator-crystal capacitance	6.5 pf

TABLE 5.2.2-8

MODULATOR/MODULATOR DRIVER SPECIFICATIONS

Output voltage	270 volts peak		
Load impedance	10 M Ω and 20 pf		
Input voltage	1 volt \pm 0.5 db		
Power input			
Quiescent	2.75 watts		
Maximum	6.15 watts		
Input impedance	75 ohms		
Gain stability	\pm 0.1 db for 24 hours		
Return loss	>30 db		
Overall modulator/driver response	4-MHz/volt input		
Frequency response	1 to 5.3 MHz		
	<u>Reference Frequency</u>	<u>Design Goal</u>	<u>Minimum</u>
	1.025 MHz	0 db	0 db
	1.0 to 1.840 MHz	\pm 0.1 db	\pm 0.25 db
1.840 to 5.3 MHz	\pm 0.2 db	\pm 0.4 db	
Group delay	\pm 0.2 ns/MHz slope		
	0.04 ns/MHz ² parabolic		
	0.6 ns peak-to-peak ripple		
Modulator linearity	2% for center 90% of bandwidth		
	1% over 75% of bandwidth		
Nonlinearity distortion of synchronizing signal	Synchronizing pulses between 0.25 and 0.30 volt (measured at a point of 0-db insertion gain)		

TABLE 5.2.2-8 (cont.)

Noise

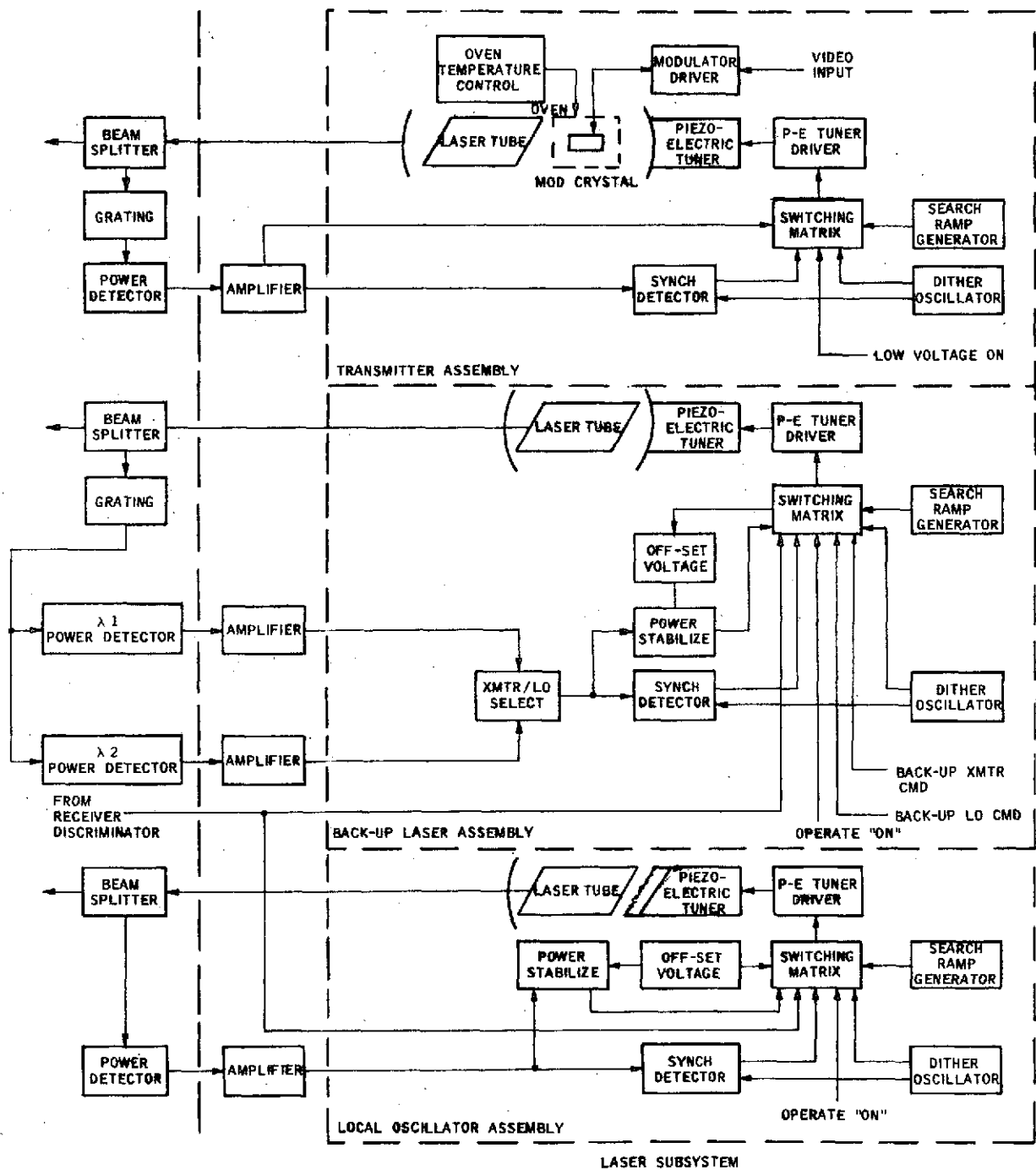
Periodic noise (ratio of peak-to-peak picture signal amplitude to peak-to-peak noise amplitude)

Power-supply hum (including fundamental frequency and low harmonics) 38 db

Single-frequency noise between 1 kHz and 2 MHz 62 db

Single-frequency noise between 2 and 5 MHz 46 db

Input command Gate on/off (0 \pm 0.5 volt to 5 \pm 0.5 volt)
 Size 3 x 3 x 2 in.
 Weight 10 oz



PROPOSED LASER SUBSYSTEM BLOCK DIAGRAM

Figure 5.2.2-1

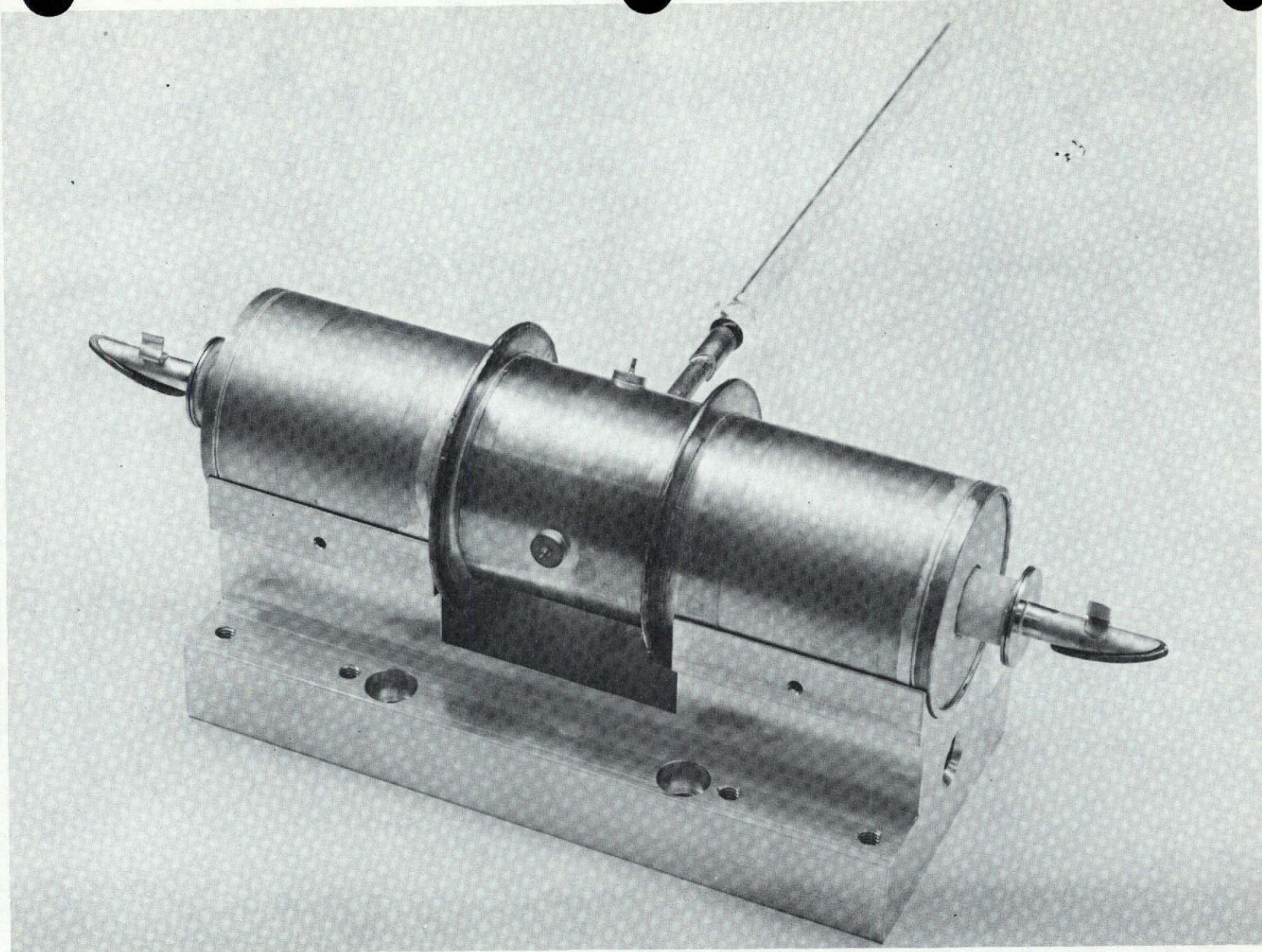
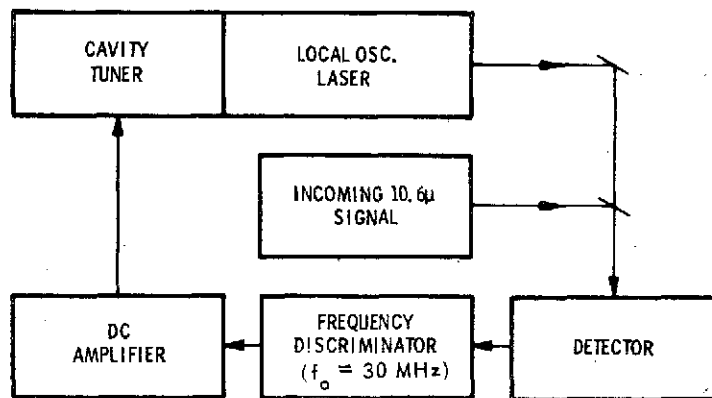


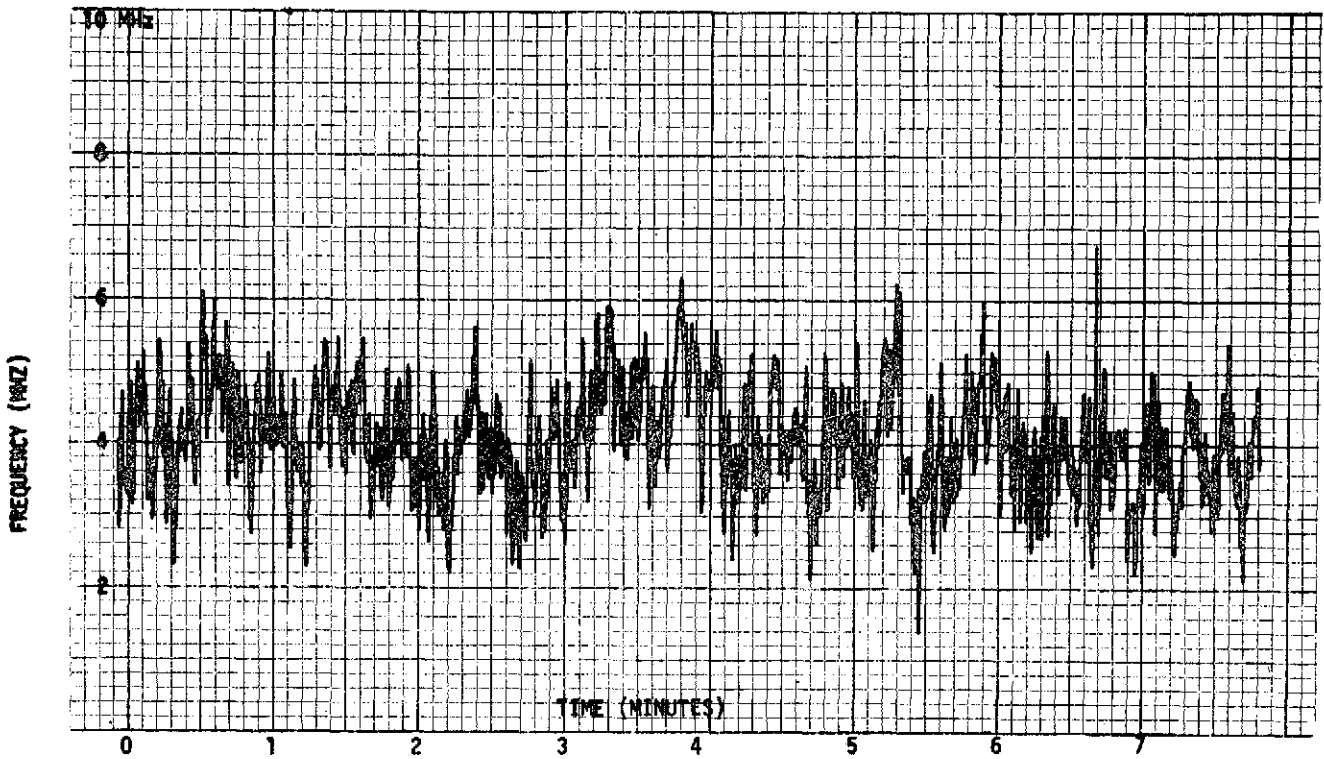
Figure 5.2.2-2

Metal-Ceramic CO₂ Laser Tube which Passed LCE
Qualified Level Vibration Tests



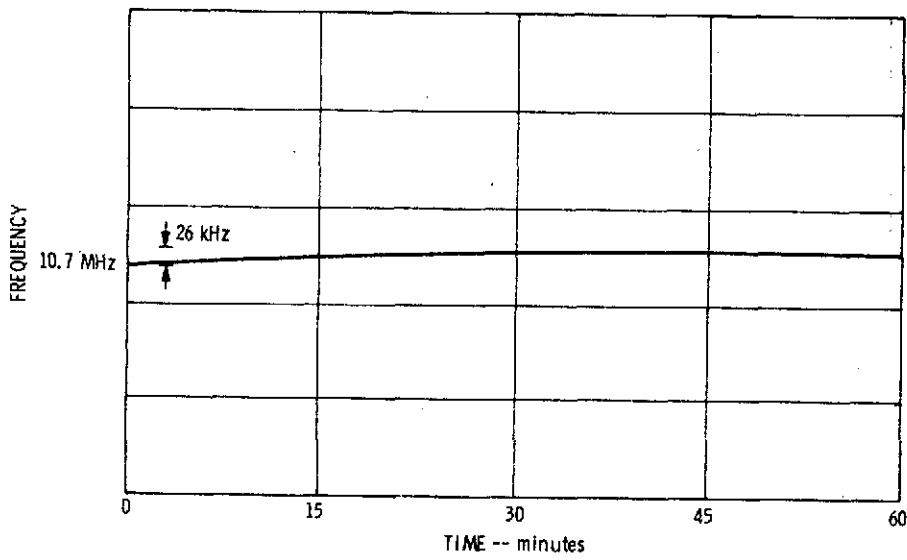
AFC Stabilization by Heterodyne Technique

Figure 5.2.2-3



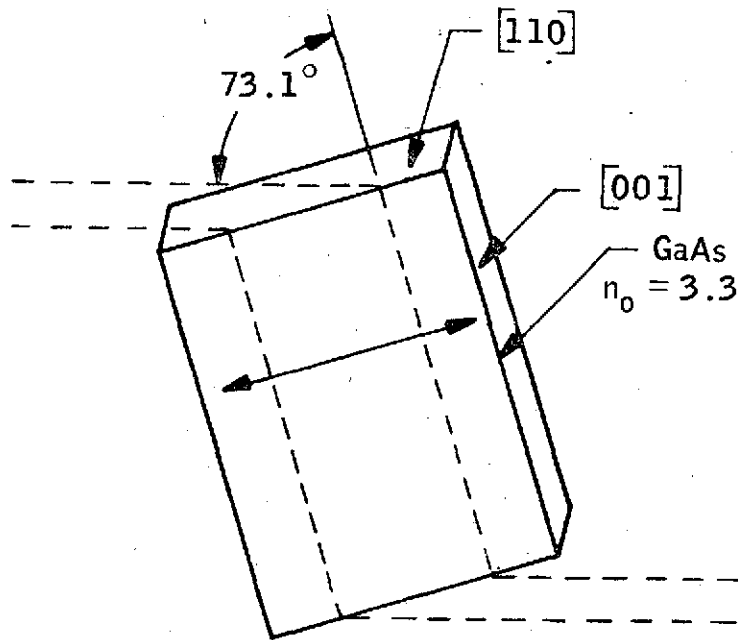
Heterodyne Frequency Versus Time for 70-Watt Laser
Beating with Stable Reference Oscillator

Figure 5.2.2-4



Heterodyne Frequency Versus Time for 70-Watt Laser
Beating with Stable Reference Oscillator with AFC

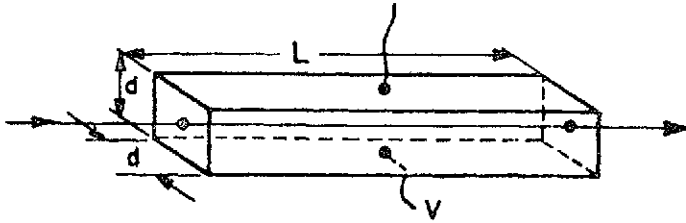
Figure 5.2.2-5



GALLIUM ARSENIDE MODULATOR
OPERATING AT BREWSTER'S ANGLE

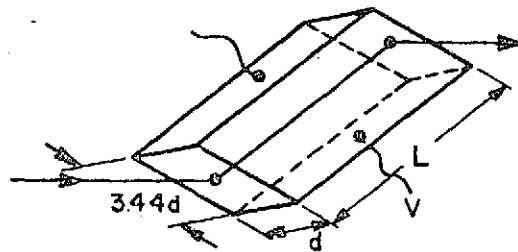
Figure 5.2.2-6

**CASE 1 STRAIGHT-THROUGH MODULATOR WITH
ANTIREFLECTION COATED ENDS**



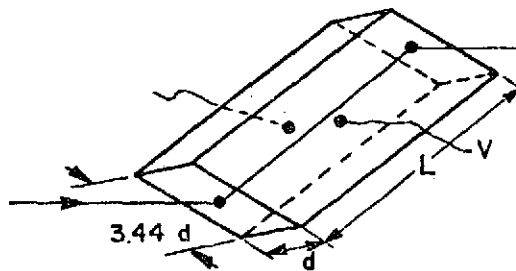
CAPACITANCE = C
DRIVE VOLTAGE = V
DRIVE POWER = P

CASE 2 BREWSTER ANGLE MODULATOR (HIGH VOLTAGE)



CAPACITANCE = C / 3.44
DRIVE VOLTAGE = 3.44 V
DRIVE POWER = 3.44 P

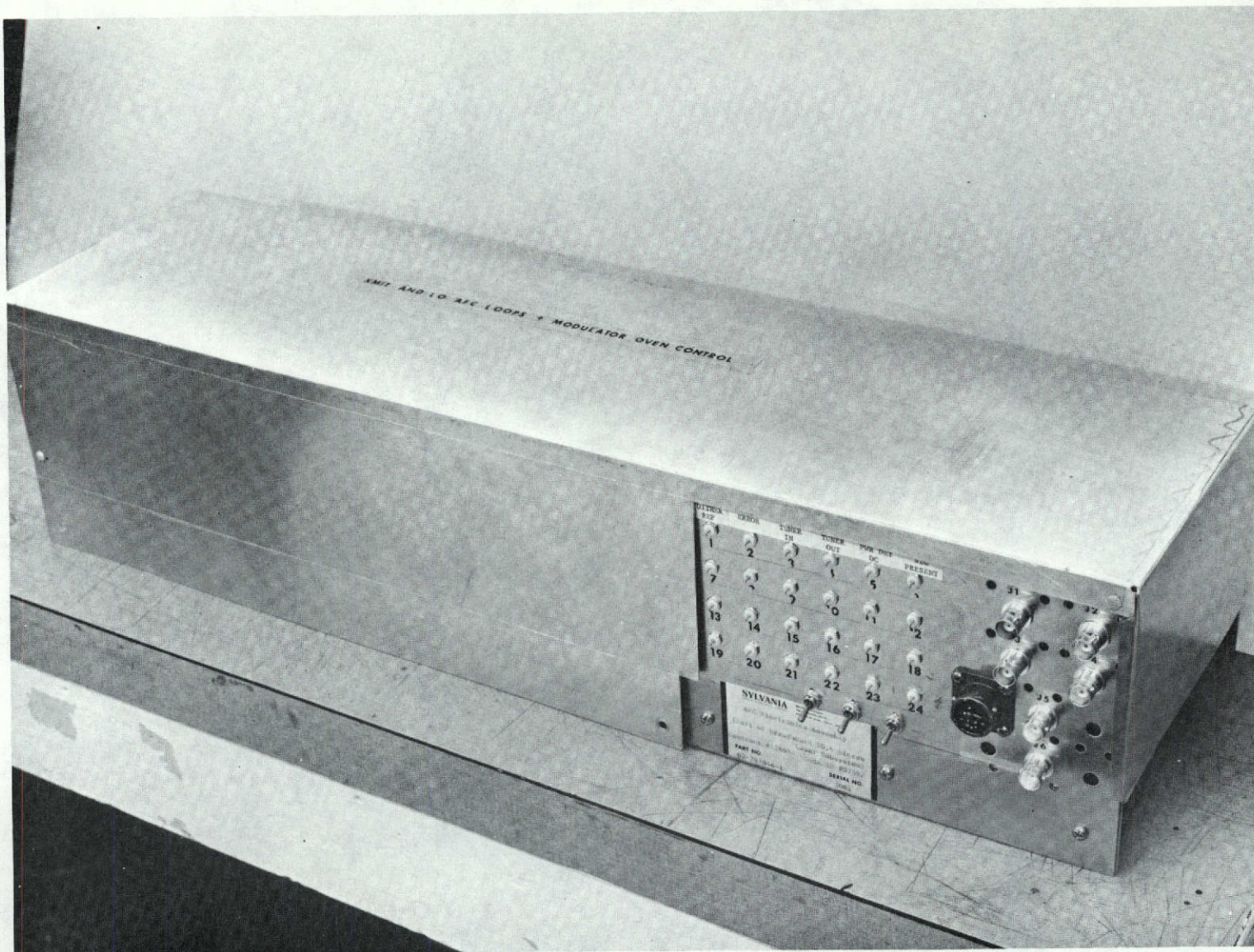
CASE 3 BREWSTER ANGLE MODULATOR (HIGH CAPACITANCE)



CAPACITANCE = 3.44 C
DRIVE VOLTAGE = V
DRIVE POWER = 3.44 P

Electrical Characteristics of the Straight-Through and
Brewster Angle Geometries for Gallium Arsenide

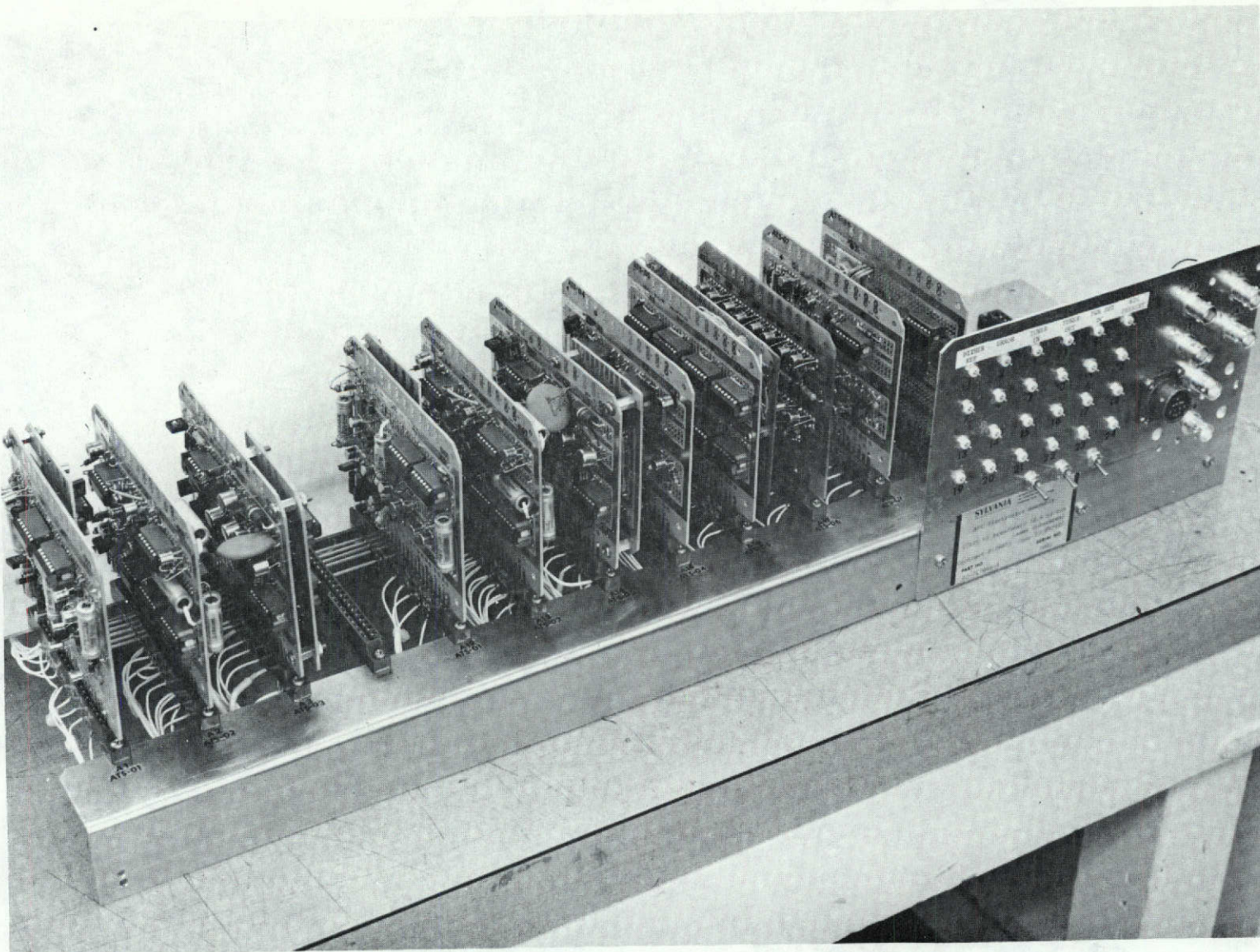
Figure 5.2.2-7



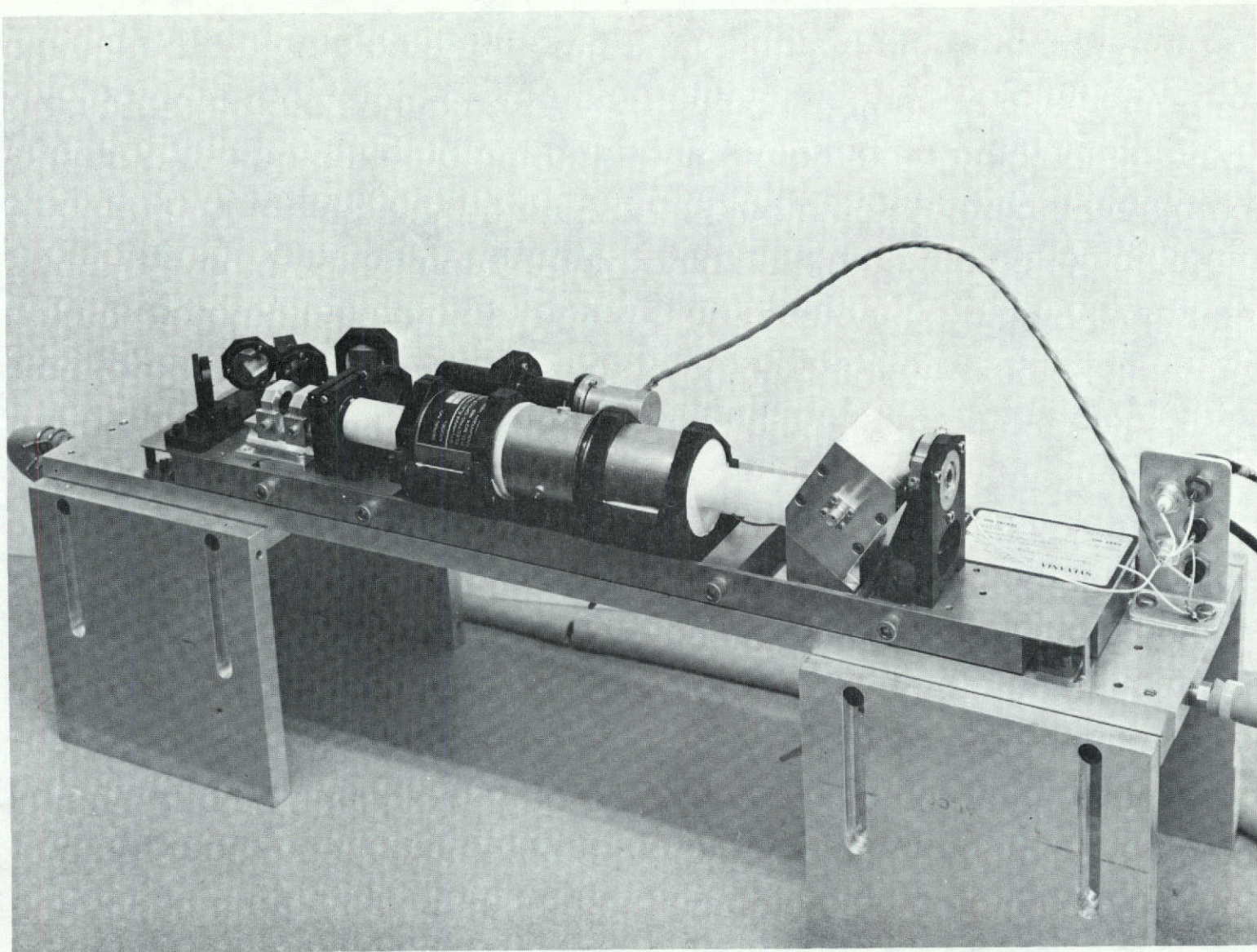
Laser Subsystem Breadboard Electronics Package

Figure 5.2.2-8

Figure 5.2.2-9



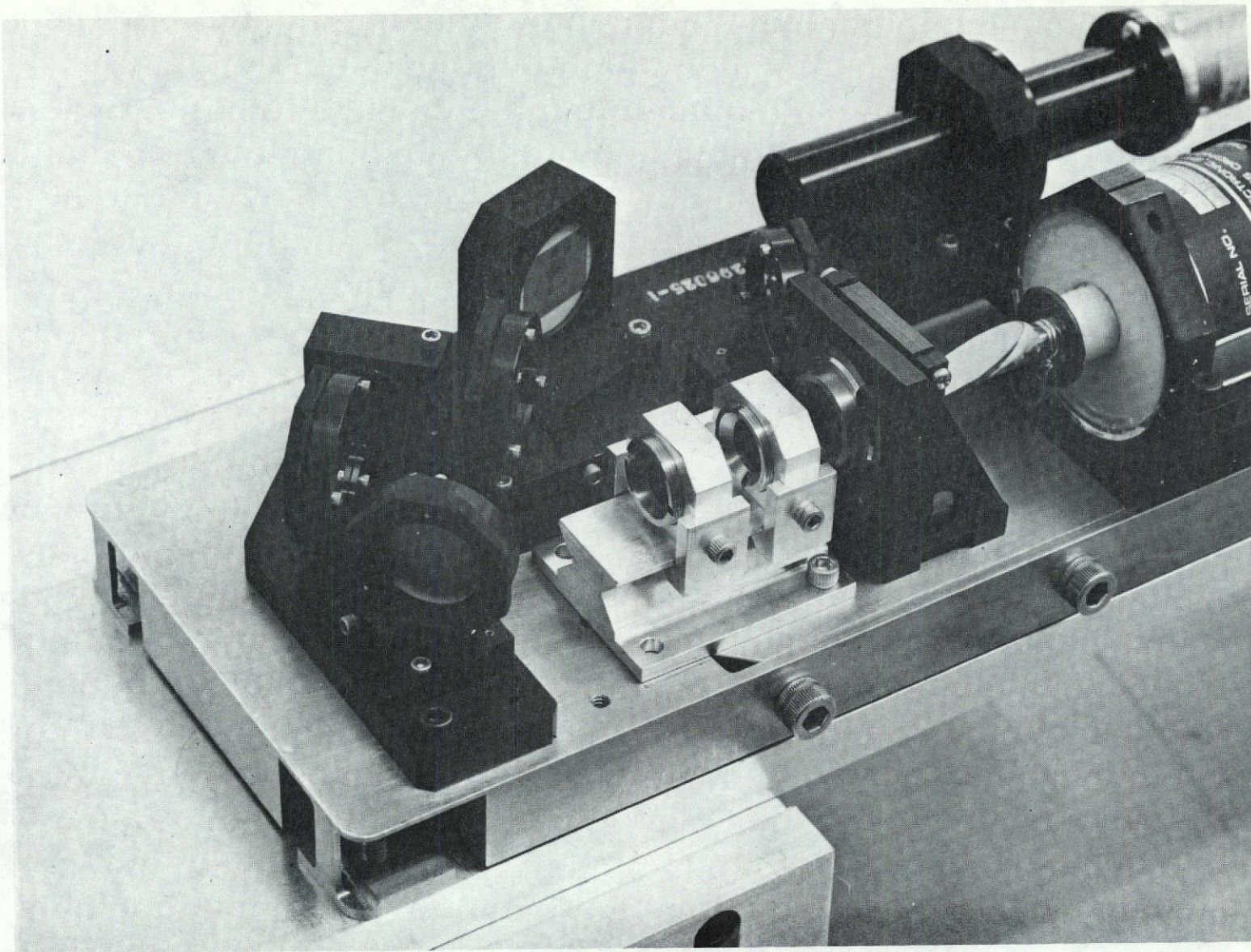
Laser Subsystem Breadboard Electronics (Cover Removed)



Breadboard Transmitter Laser

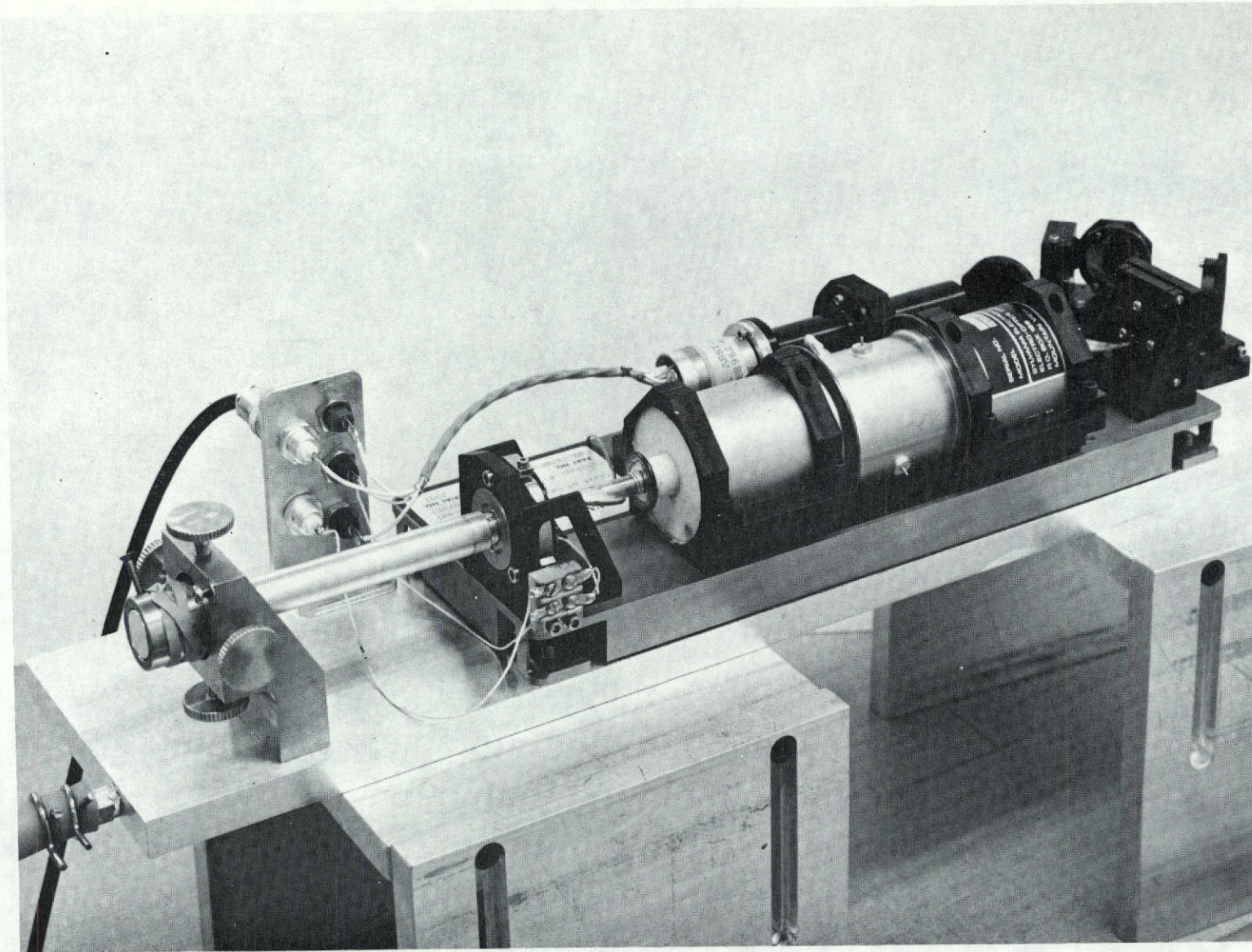
Figure 5.2.2-10

Figure 5.2.2-11



Output End of Transmitter Laser Showing Expansion Optics and Wavelength Selection Optics

Figure 5.2.2-12



Breadboard Local Oscillator Laser Showing Removeable Mirror Adjustment Jig

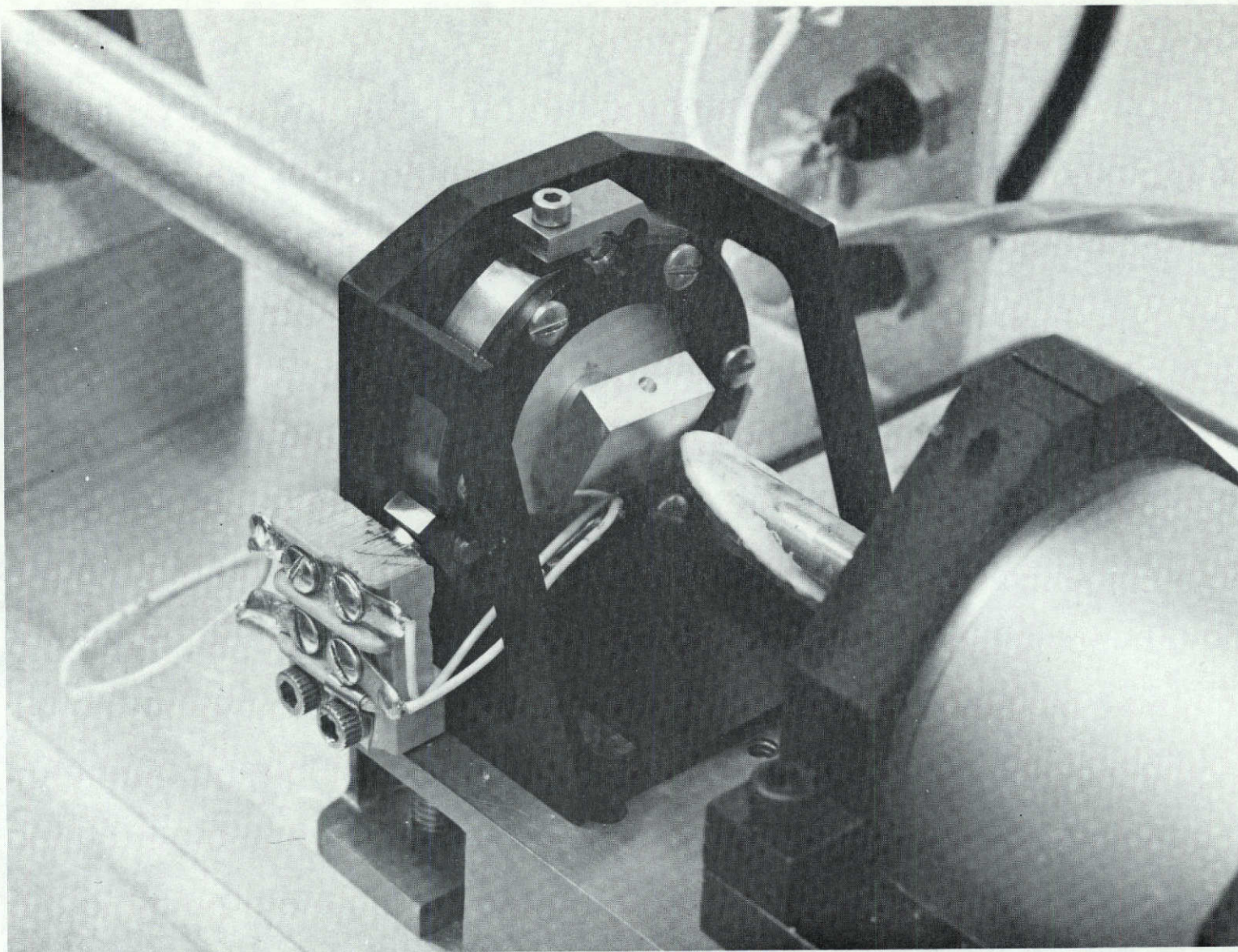
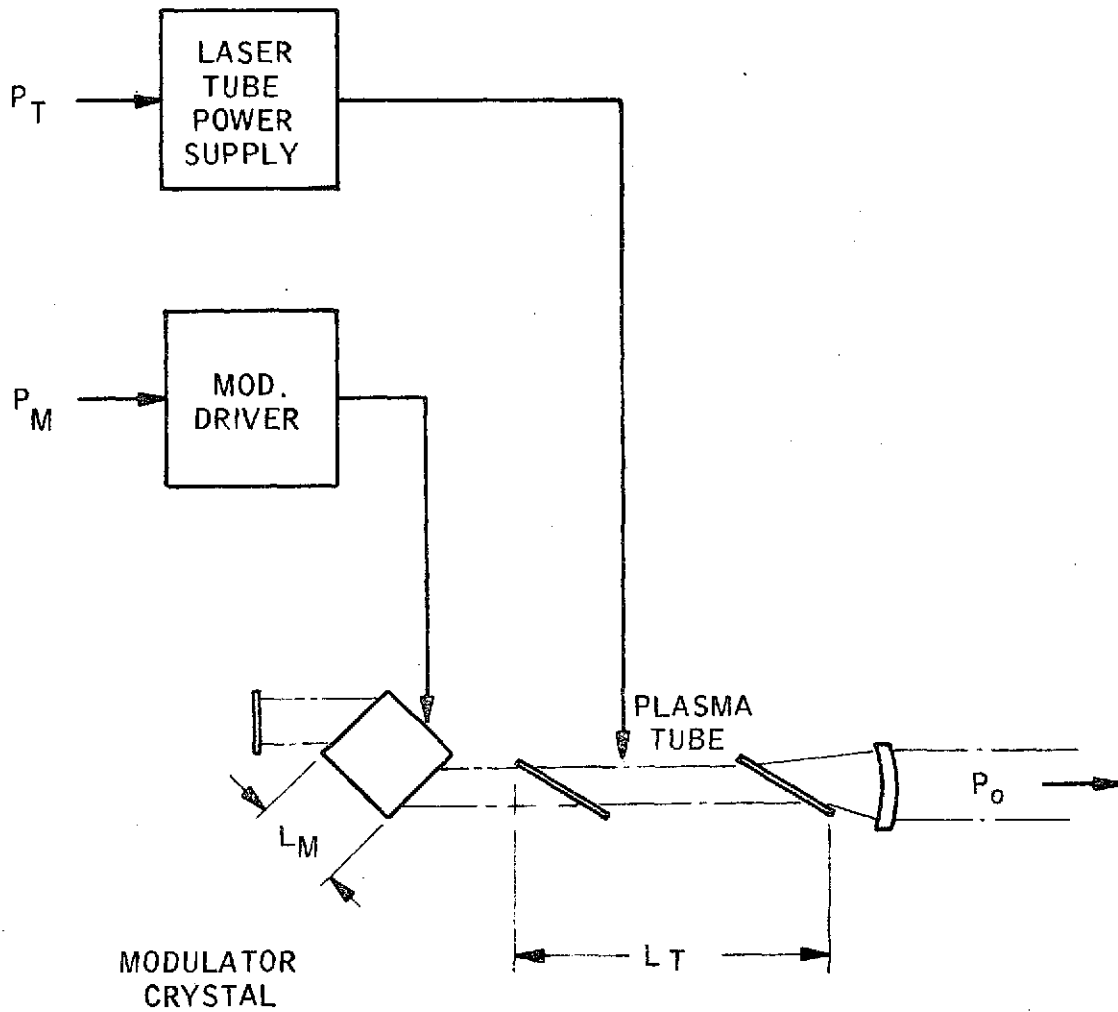


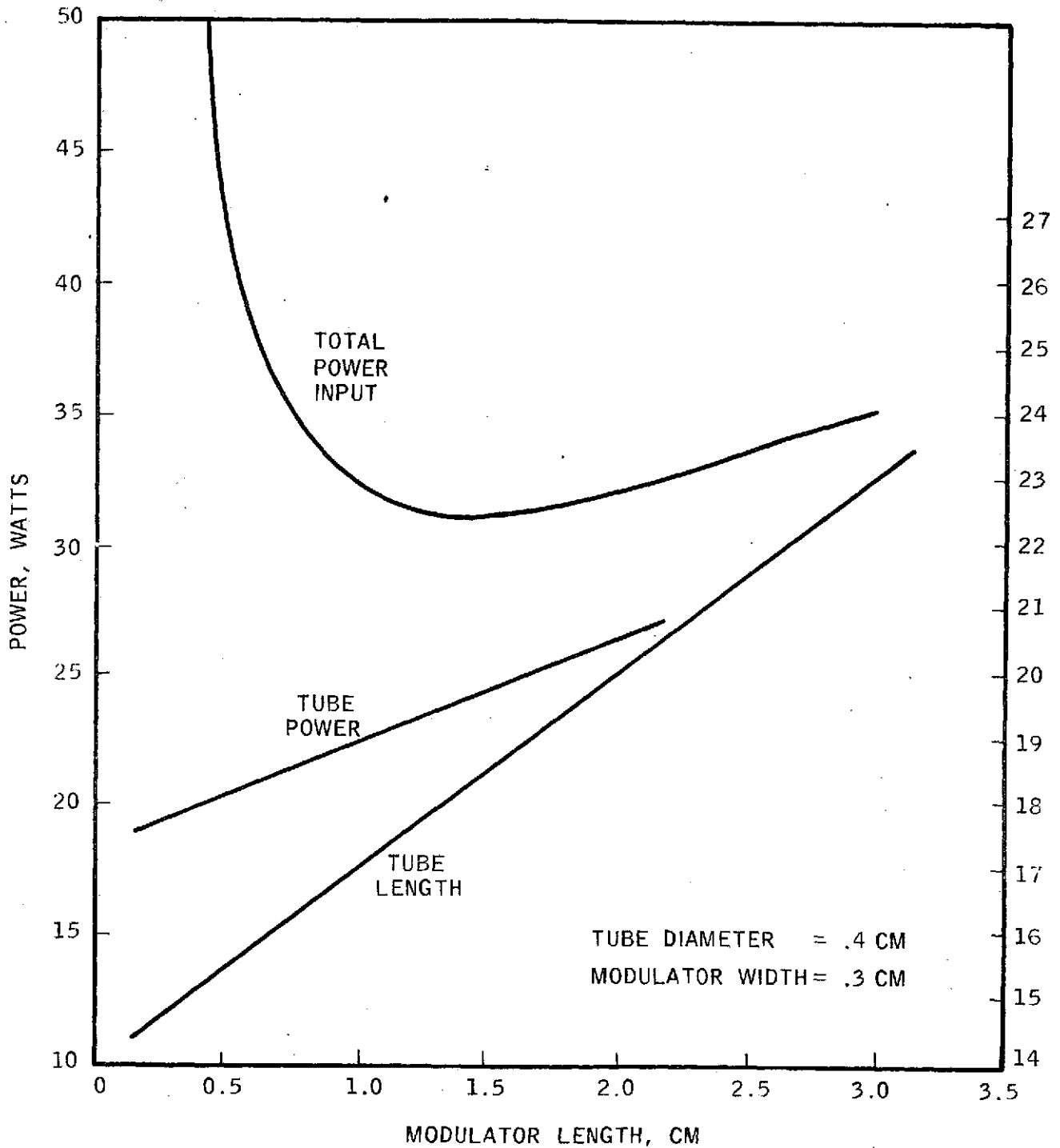
Figure 5.2.2-13

Local Oscillator Grating Mount Showing Internal Grating
Mounted on Circular Bimorph Transducer



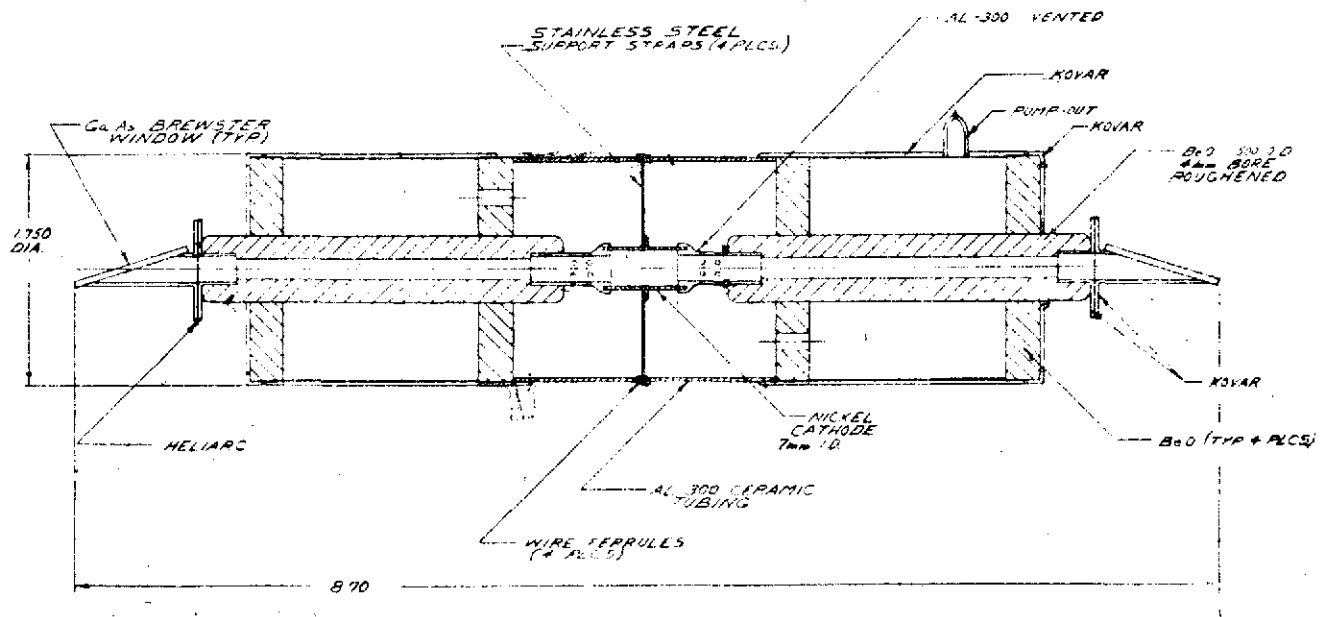
POWER FLOW IN THE TRANSMITTER
MODULATOR SUBSYSTEM

Figure 5.2.2-14



TRANSMITTER LASER - MODULATOR INPUT POWER AND
TUBE LENGTH VS MODULATOR LENGTH

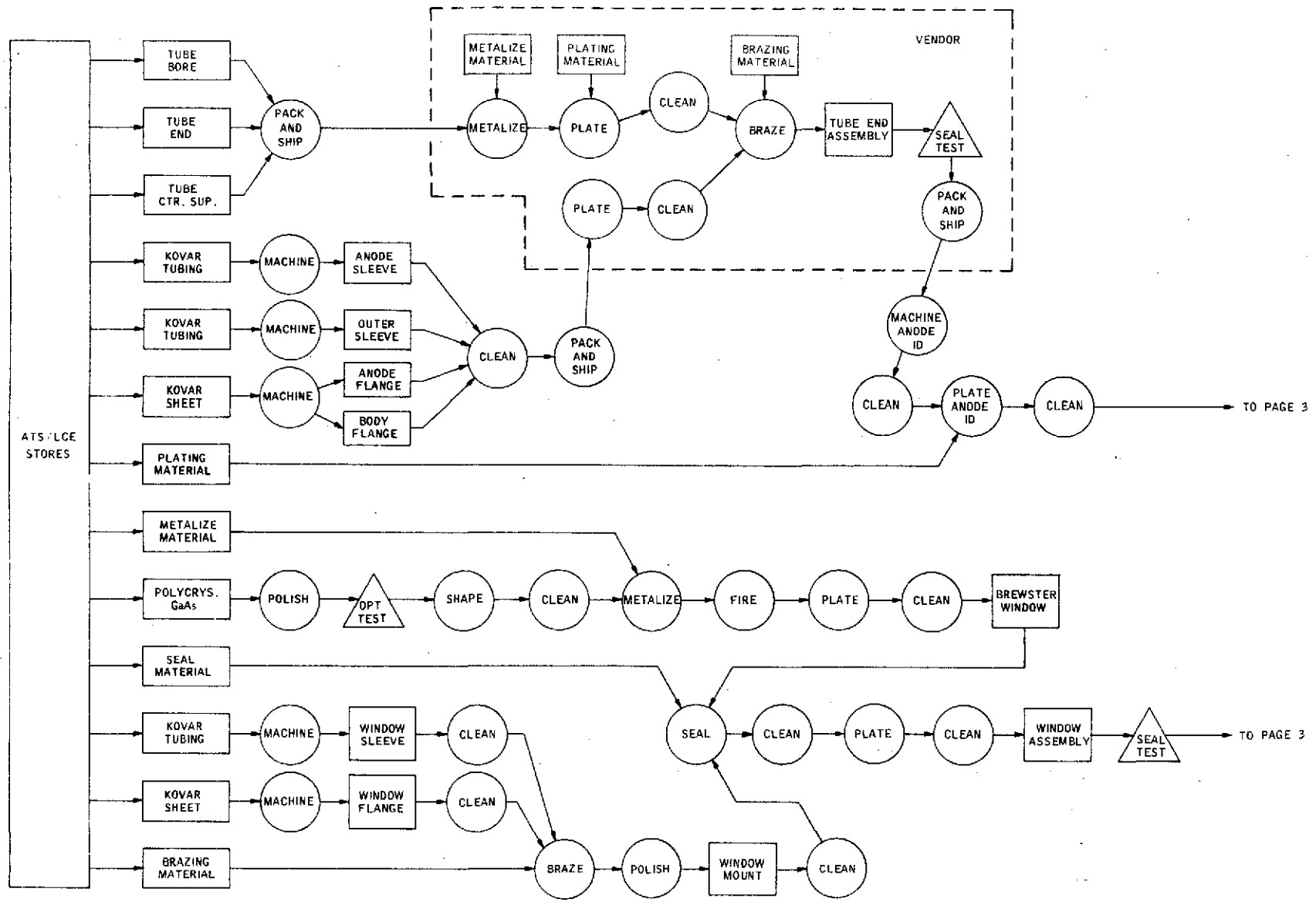
Figure 5-2-2-15



Space-Qualified Laser Tube Assembly

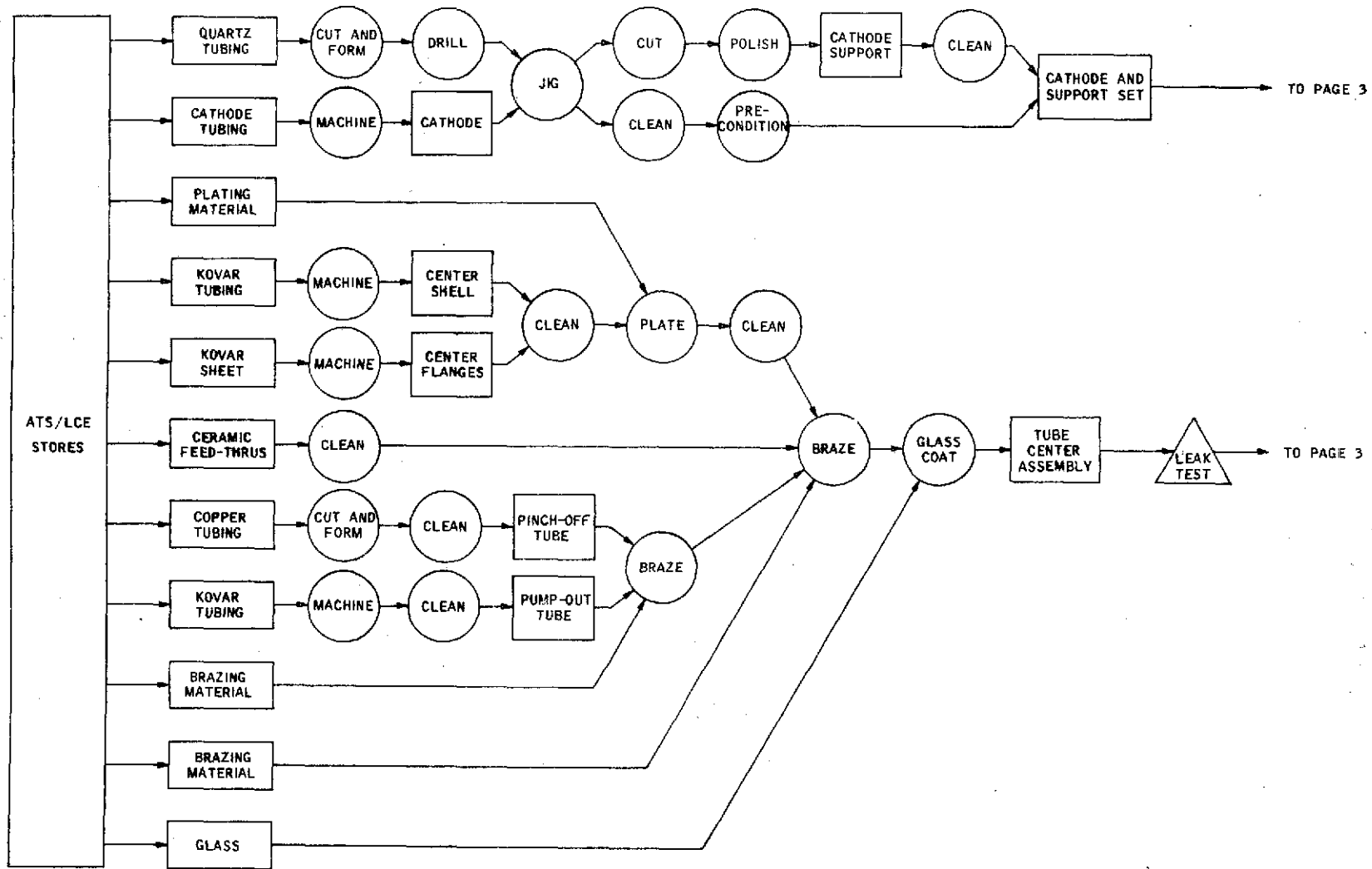
Figure 5.2.2-16

Figure 5-2-2-17

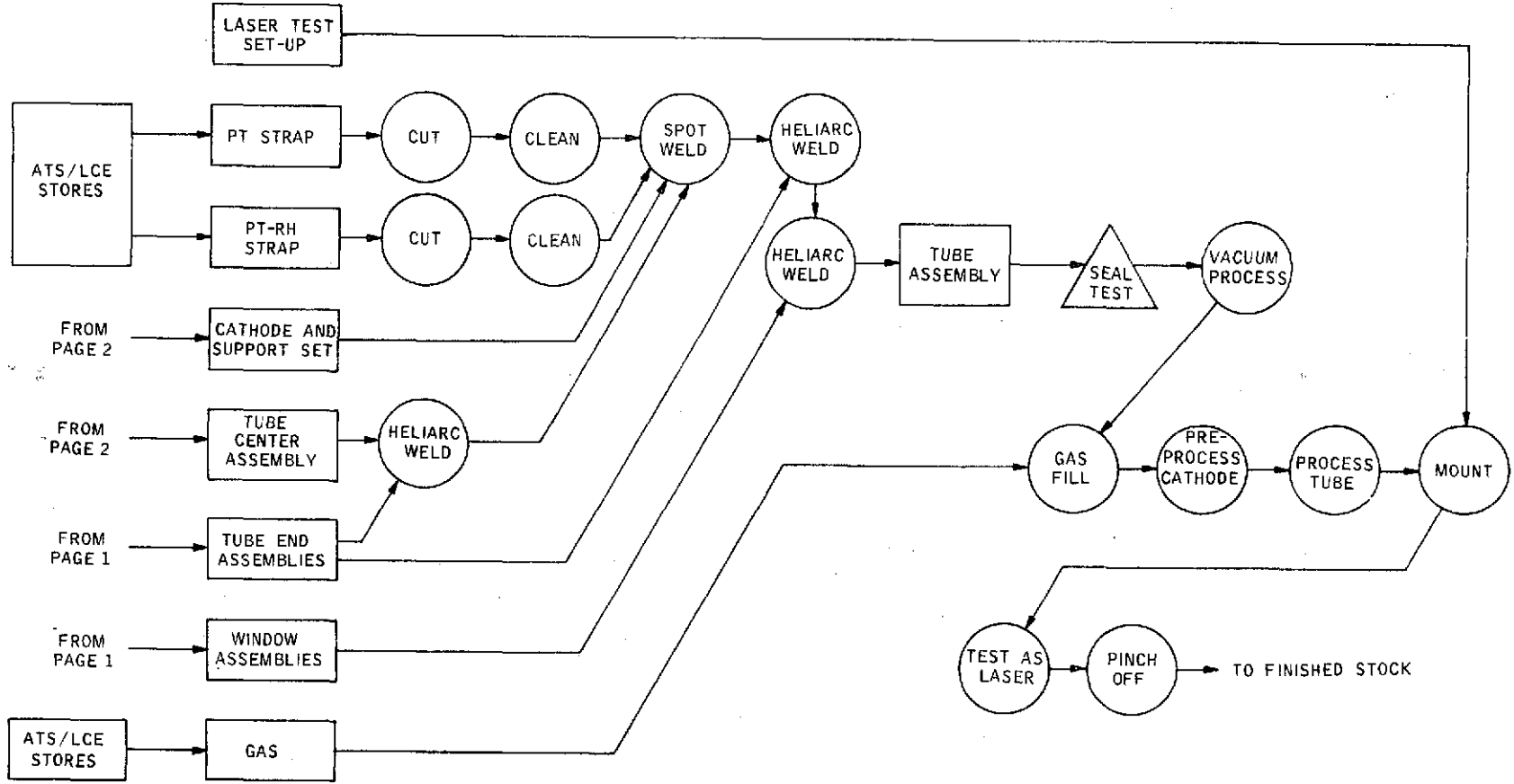


LASER TUBE FABRICATION FLOW CHART (PRELIMINARY)

Figure 5-2-2-18

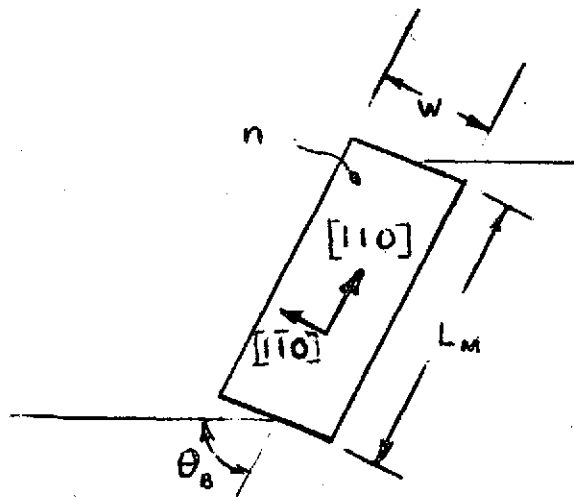


LASER TUBE FABRICATION FLOW CHART (PRELIMINARY)



LASER TUBE FABRICATION FLOW CHART (PRELIMINARY)

Figure 5.2.2-19

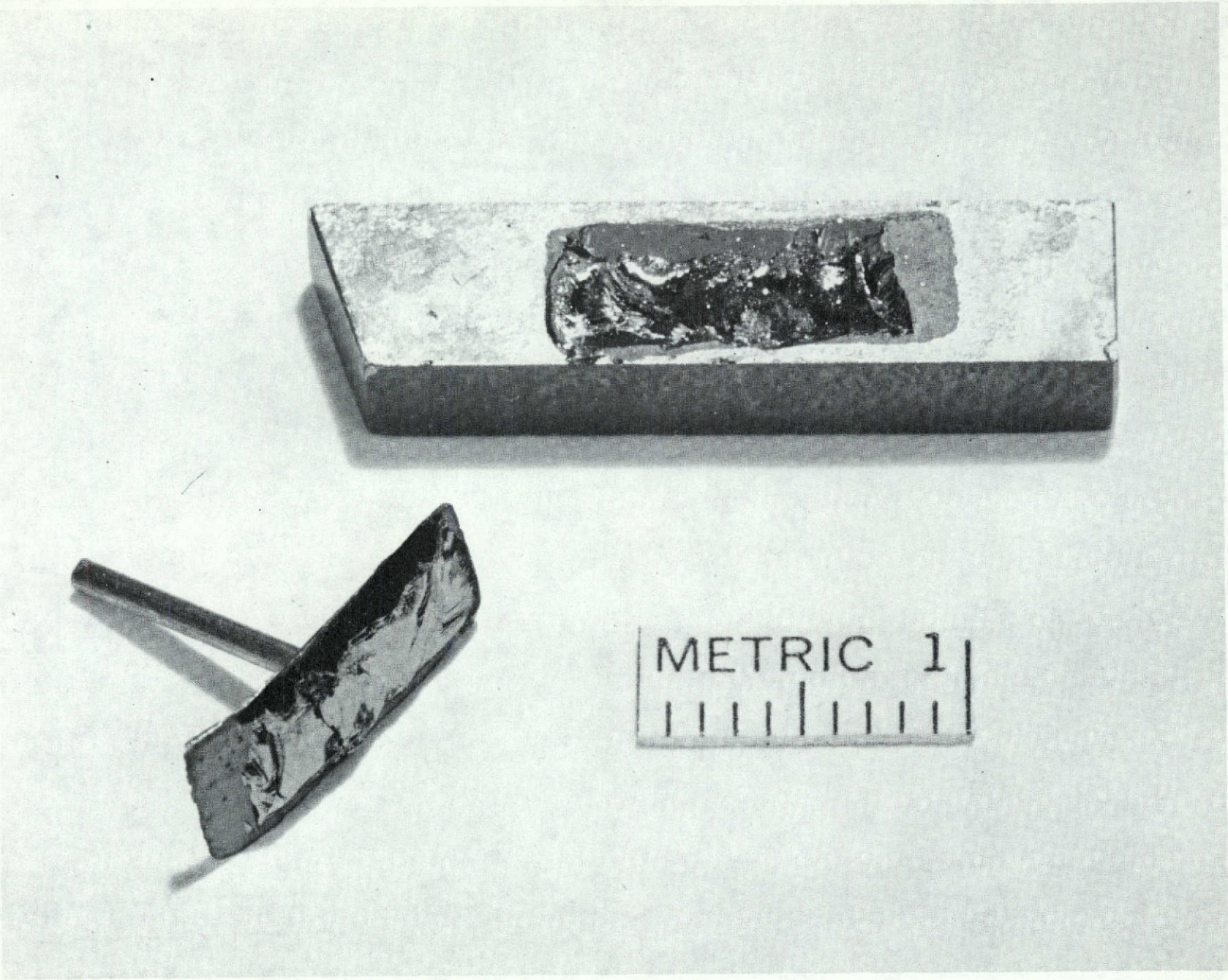


$$n = 3.3$$

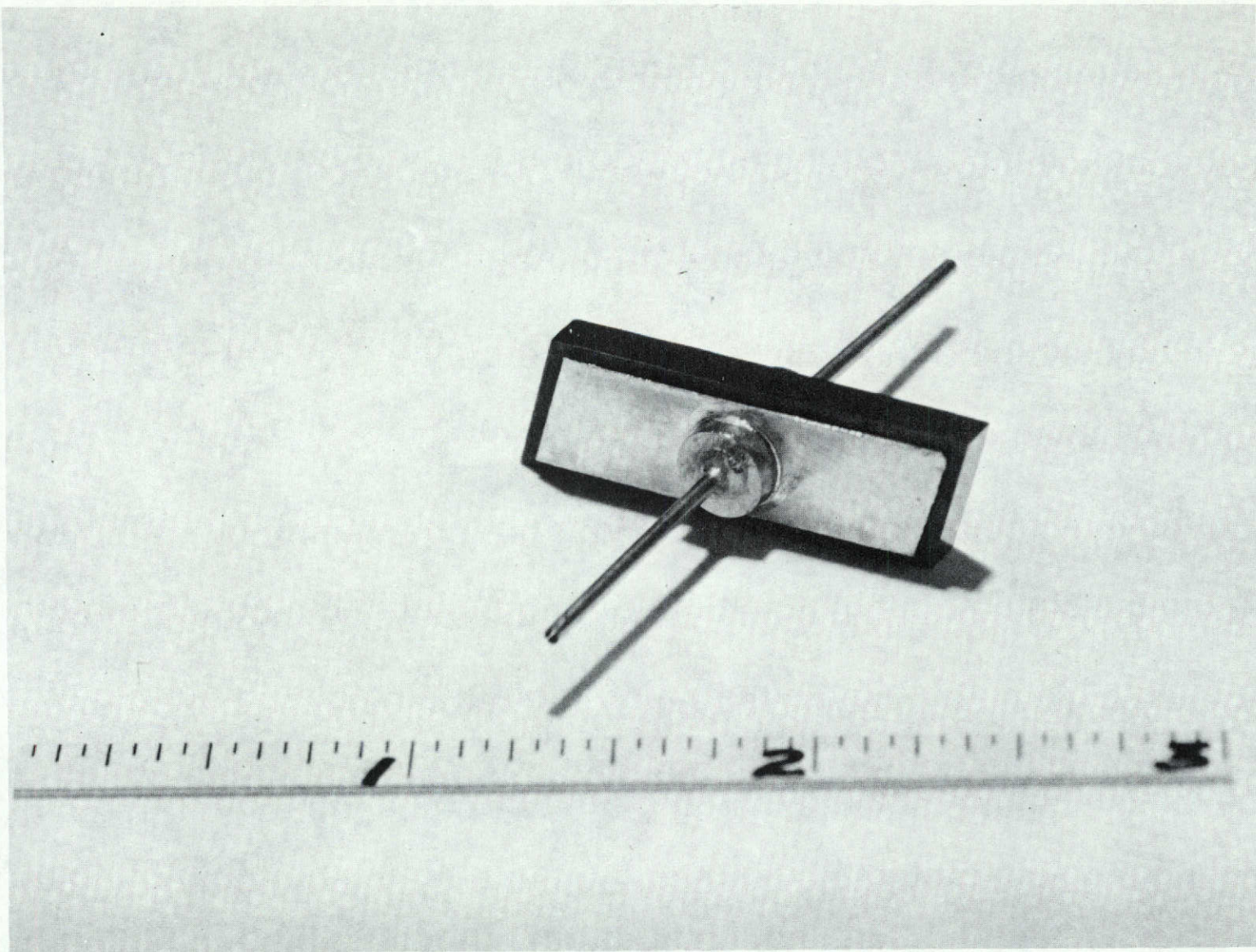
$$\theta_B = 73.15^\circ$$

Gallium Arsenide Modulator Crystal

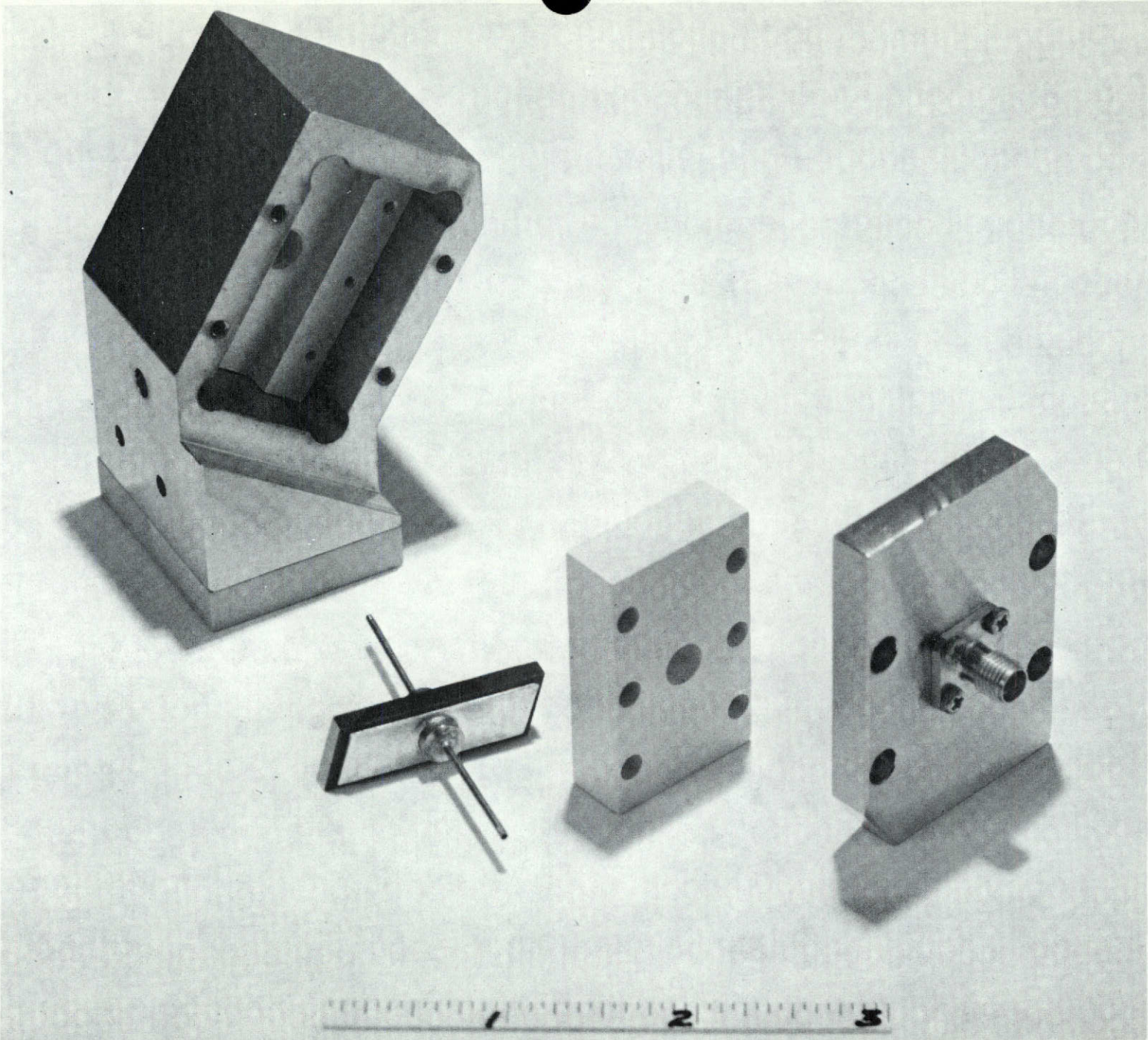
Figure 5.2.2-20



Results of Intentionally Pulling Molybdenum Electrode from GaAs Crystal

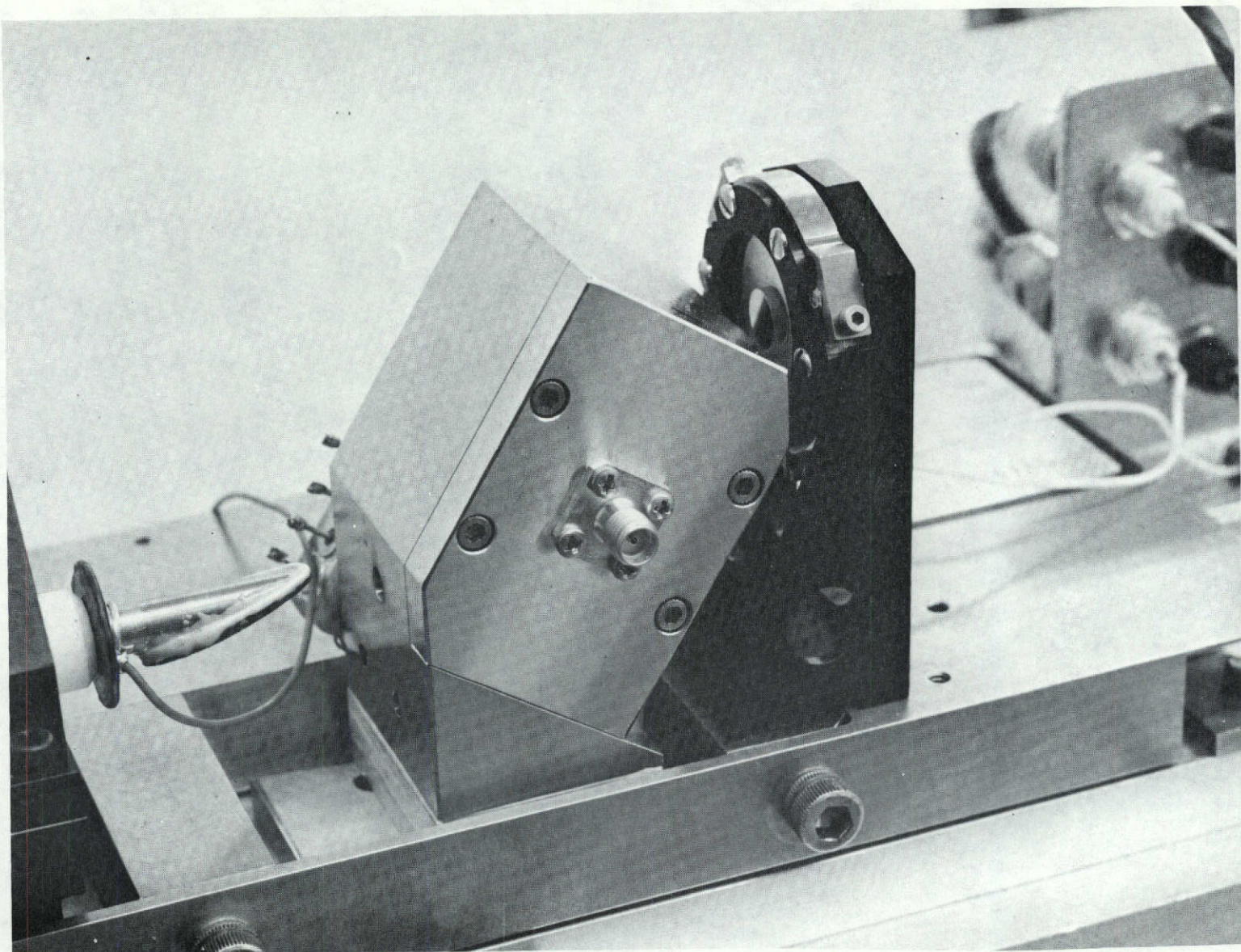


GaAs Modulator Crystal, Breadboard Model



Components of In-Cavity Modulator Assembly

Figure 5.2.2-23



Laser Modulator Mounted in Transmitter Assembly

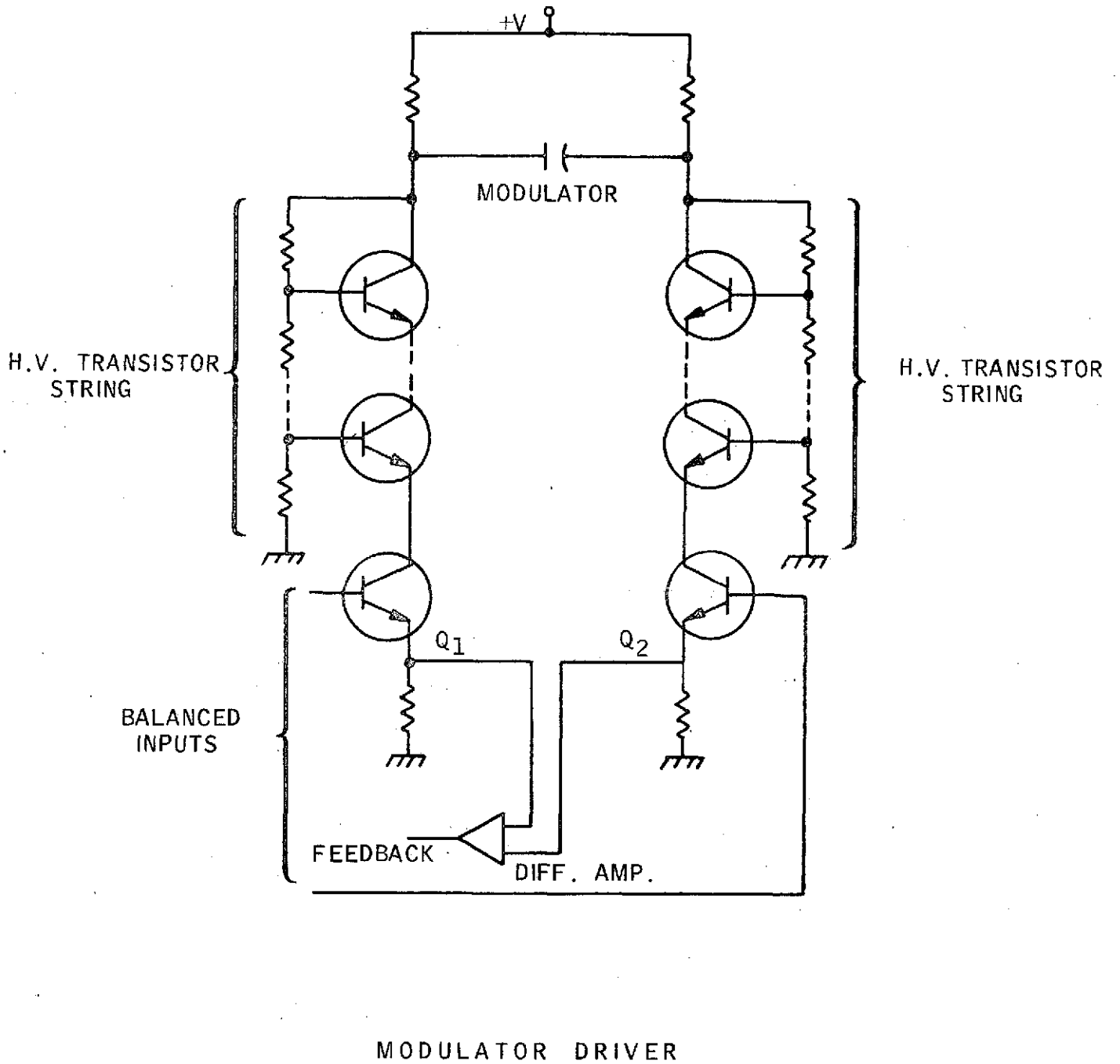


Figure 5.2.2-25

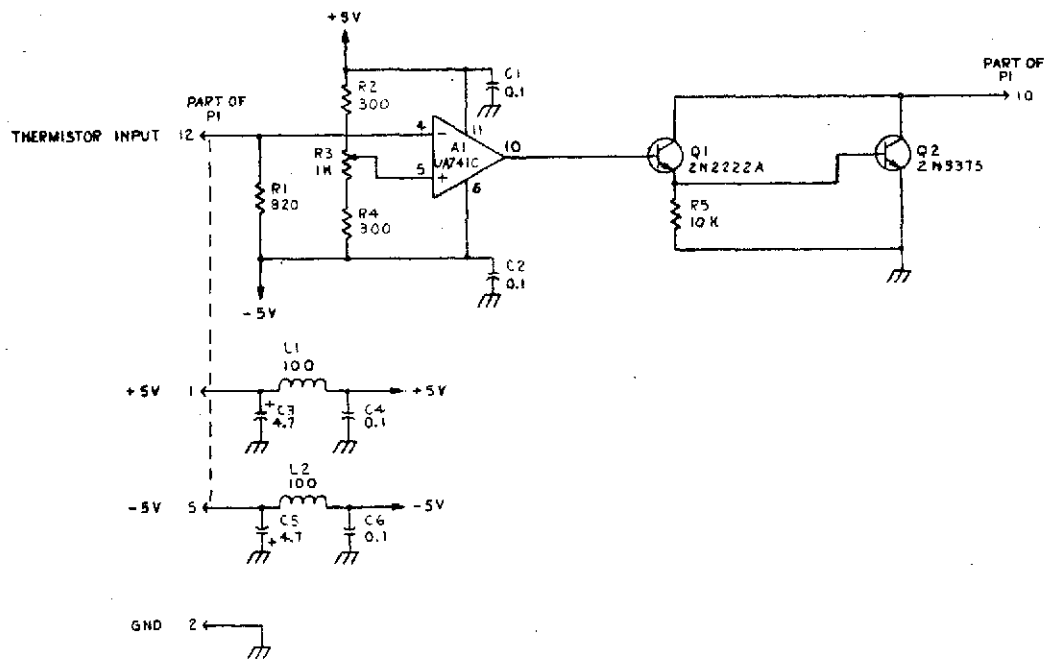


Figure 5.2.2-26

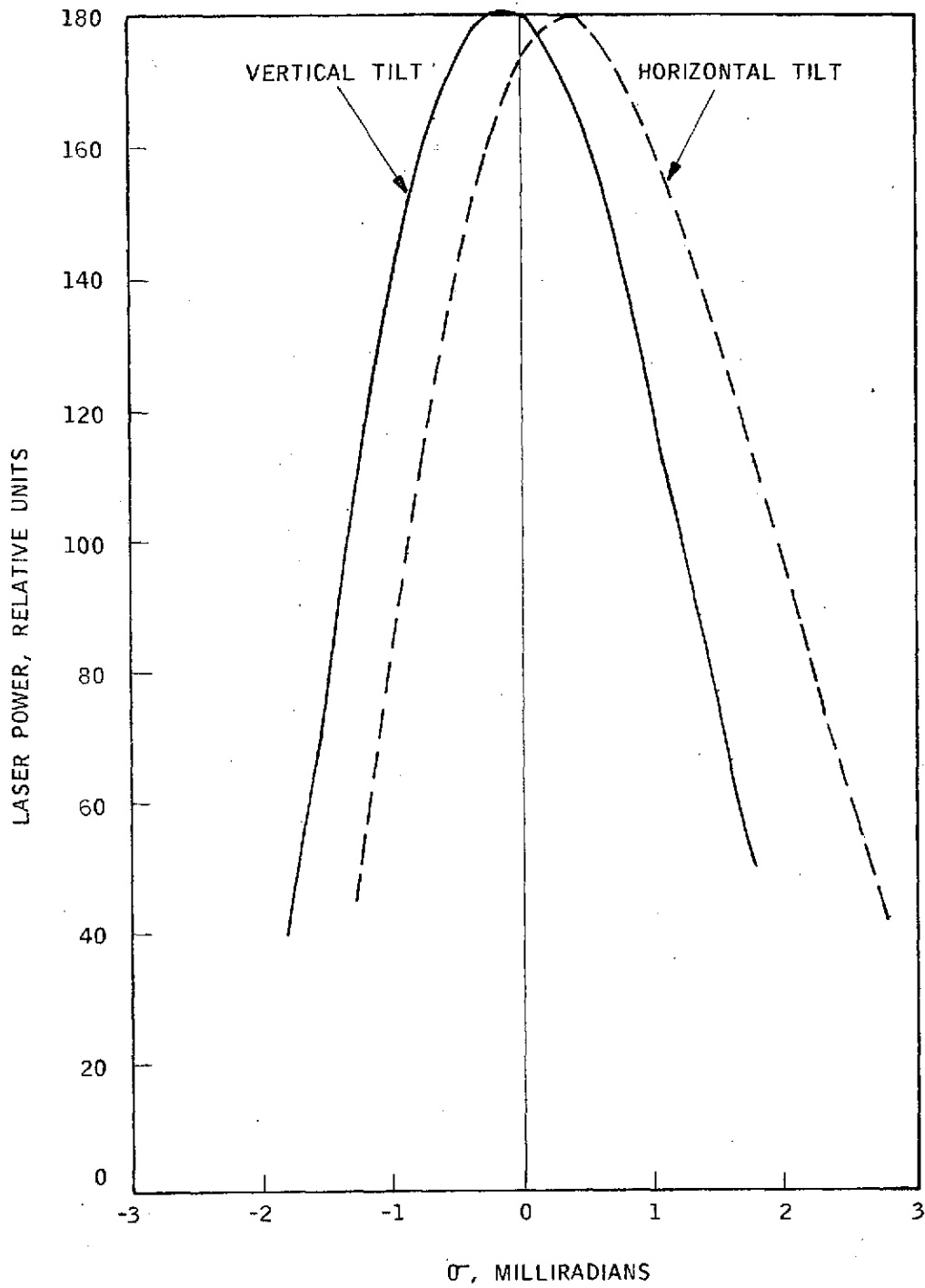
NOTES-UNLESS OTHERWISE SPECIFIED:

1. PARTIAL REFERENCE DESIGNATIONS ARE SHOWN: FOR COMPLETE DESIGNATION PREFIX WITH UNIT NO. AND ASSEMBLY DESIGNATIONS.
2. RESISTANCE VALUES IN OHMS
3. CAPACITANCE VALUES IN UF
4. UNUSED PINS NOT SHOWN

HIGHEST REFERENCE DESIGNATIONS			
A1	C6	L2	Q2
R5			
REFERENCE DESIGNATIONS NOT USED			

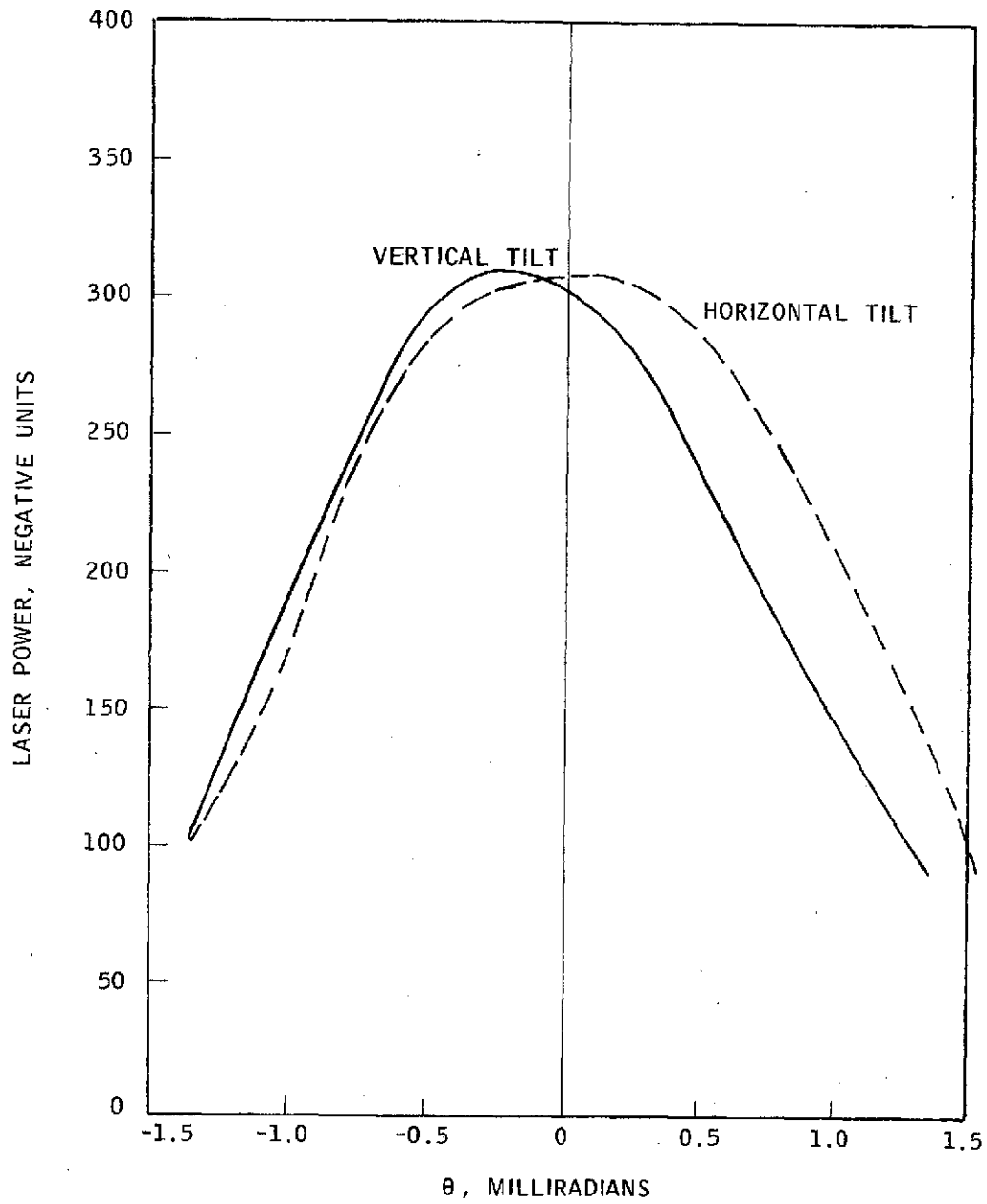
-1 AS SHOWN

QTY PER DRAWING	REV	CODE	PART OR IDENTIFYING NO.	SYLVANIA PART NO.	DESCRIPTION OR IDENTIFICATION	ITEM NO.																																																								
PARTS LIST																																																														
REV. B—RENDER ITEM—FOR PROCUREMENT OR PART NUMBER SEE SPECIFICATION CONTROL OR SOURCE CONTROL DRAWING																																																														
<table border="1"> <tr> <td>APPLICABLE DOCUMENTS</td> <td>UNLESS OTHERWISE SPECIFIED DIMENSIONS ARE IN INCHES</td> <td colspan="2">CONTRACT NO.</td> <td colspan="3">SYLVANIA ELECTRONIC SYSTEMS DIVISION OF SYLVANIA ELECTRIC PRODUCTS INC MCMURRAY VIEW, CALIFORNIA</td> </tr> <tr> <td></td> <td>TOLERANCE</td> <td>DATE</td> <td>DATE</td> <td colspan="3">SCHEMATIC DIAGRAM</td> </tr> <tr> <td></td> <td>FRACTIONS =</td> <td>APPROVED</td> <td>DATE</td> <td colspan="3">MODULATOR</td> </tr> <tr> <td></td> <td>DIMENSIONAL =</td> <td>APPROVED</td> <td>DATE</td> <td colspan="3">OVEN TEMP CONTROL</td> </tr> <tr> <td></td> <td>2 PLACE =</td> <td>APPROVED</td> <td>DATE</td> <td colspan="3">3222-202-231</td> </tr> <tr> <td></td> <td>3 PLACE =</td> <td>APPROVED</td> <td>DATE</td> <td colspan="3">SIZE CODE IDENT. NO. SYLVANIA NO.</td> </tr> <tr> <td>FINISH</td> <td>MATERIAL</td> <td>RELEASE APP'D BY</td> <td></td> <td>D</td> <td>07397</td> <td>00-787040</td> </tr> <tr> <td>TEXT CHANGE NO.</td> <td>MODEL</td> <td></td> <td></td> <td></td> <td></td> <td></td> </tr> </table>							APPLICABLE DOCUMENTS	UNLESS OTHERWISE SPECIFIED DIMENSIONS ARE IN INCHES	CONTRACT NO.		SYLVANIA ELECTRONIC SYSTEMS DIVISION OF SYLVANIA ELECTRIC PRODUCTS INC MCMURRAY VIEW, CALIFORNIA				TOLERANCE	DATE	DATE	SCHEMATIC DIAGRAM				FRACTIONS =	APPROVED	DATE	MODULATOR				DIMENSIONAL =	APPROVED	DATE	OVEN TEMP CONTROL				2 PLACE =	APPROVED	DATE	3222-202-231				3 PLACE =	APPROVED	DATE	SIZE CODE IDENT. NO. SYLVANIA NO.			FINISH	MATERIAL	RELEASE APP'D BY		D	07397	00-787040	TEXT CHANGE NO.	MODEL					
APPLICABLE DOCUMENTS	UNLESS OTHERWISE SPECIFIED DIMENSIONS ARE IN INCHES	CONTRACT NO.		SYLVANIA ELECTRONIC SYSTEMS DIVISION OF SYLVANIA ELECTRIC PRODUCTS INC MCMURRAY VIEW, CALIFORNIA																																																										
	TOLERANCE	DATE	DATE	SCHEMATIC DIAGRAM																																																										
	FRACTIONS =	APPROVED	DATE	MODULATOR																																																										
	DIMENSIONAL =	APPROVED	DATE	OVEN TEMP CONTROL																																																										
	2 PLACE =	APPROVED	DATE	3222-202-231																																																										
	3 PLACE =	APPROVED	DATE	SIZE CODE IDENT. NO. SYLVANIA NO.																																																										
FINISH	MATERIAL	RELEASE APP'D BY		D	07397	00-787040																																																								
TEXT CHANGE NO.	MODEL																																																													

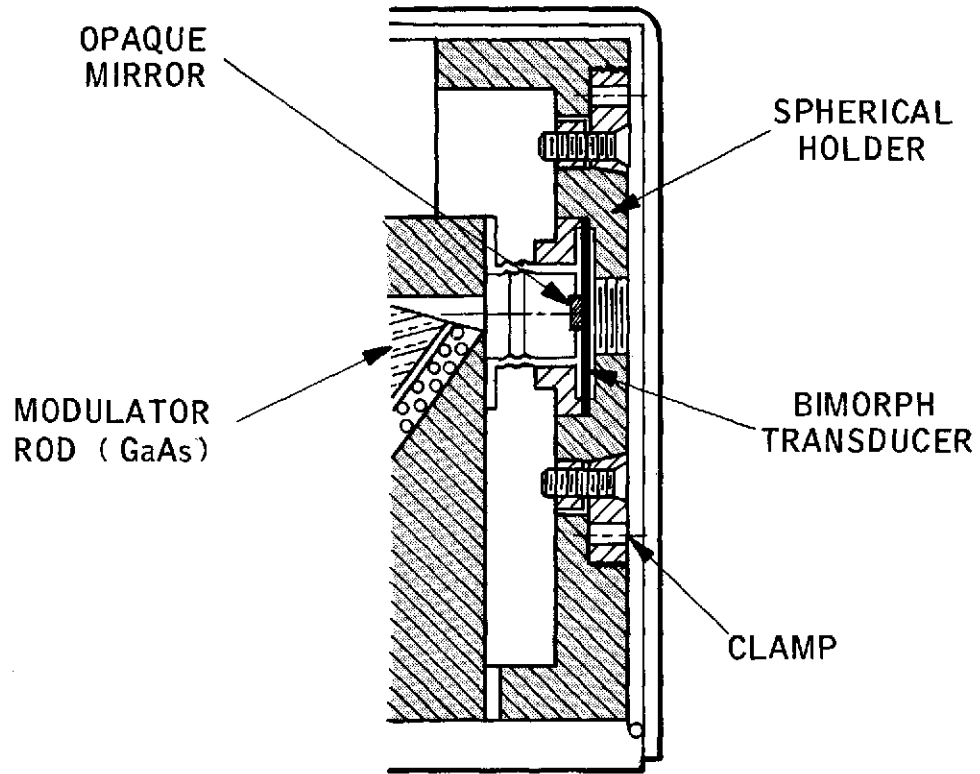


ANGULAR MOVEMENT OF FLAT MIRROR

Figure 5.2.2-27

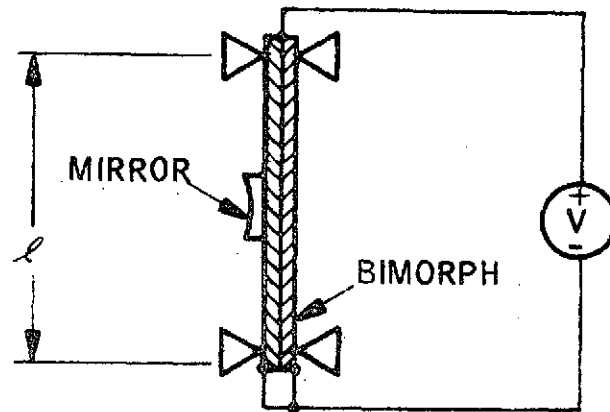


ANGULAR MOVEMENT OF SPHERICAL MIRROR



MIRROR HOLDER

Figure 5.2.2-29



DOUBLY CLAMPED BIMORPH
WITH LASER MIRROR MOUNTED

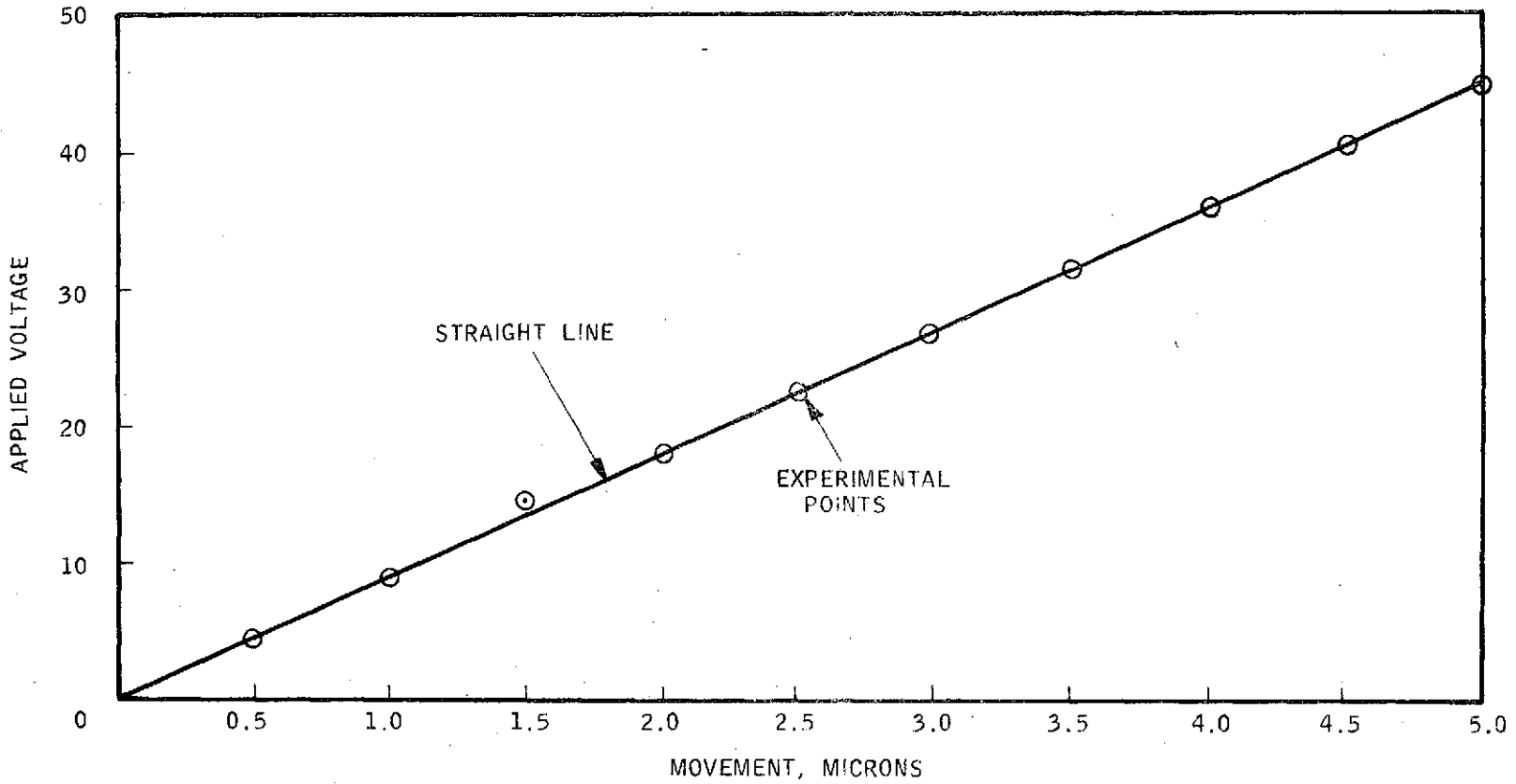


Figure 5.2.2-31

MEASUREMENT OF CIRCULAR SIMORPH LINEARITY OF MOVEMENT
WITH APPLIED VOLTAGE OVER NARROW RANGE NEAR REST POSITION

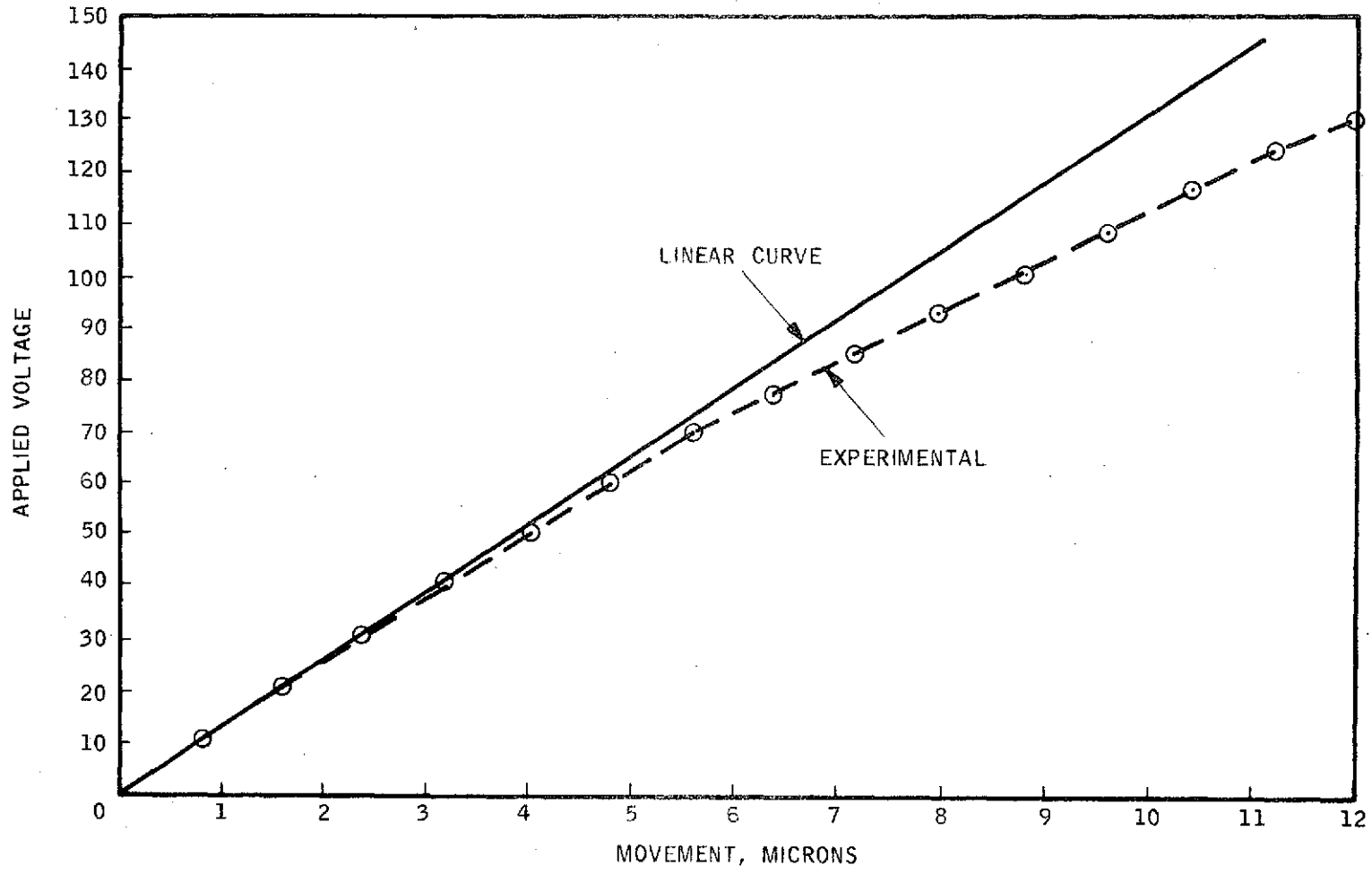
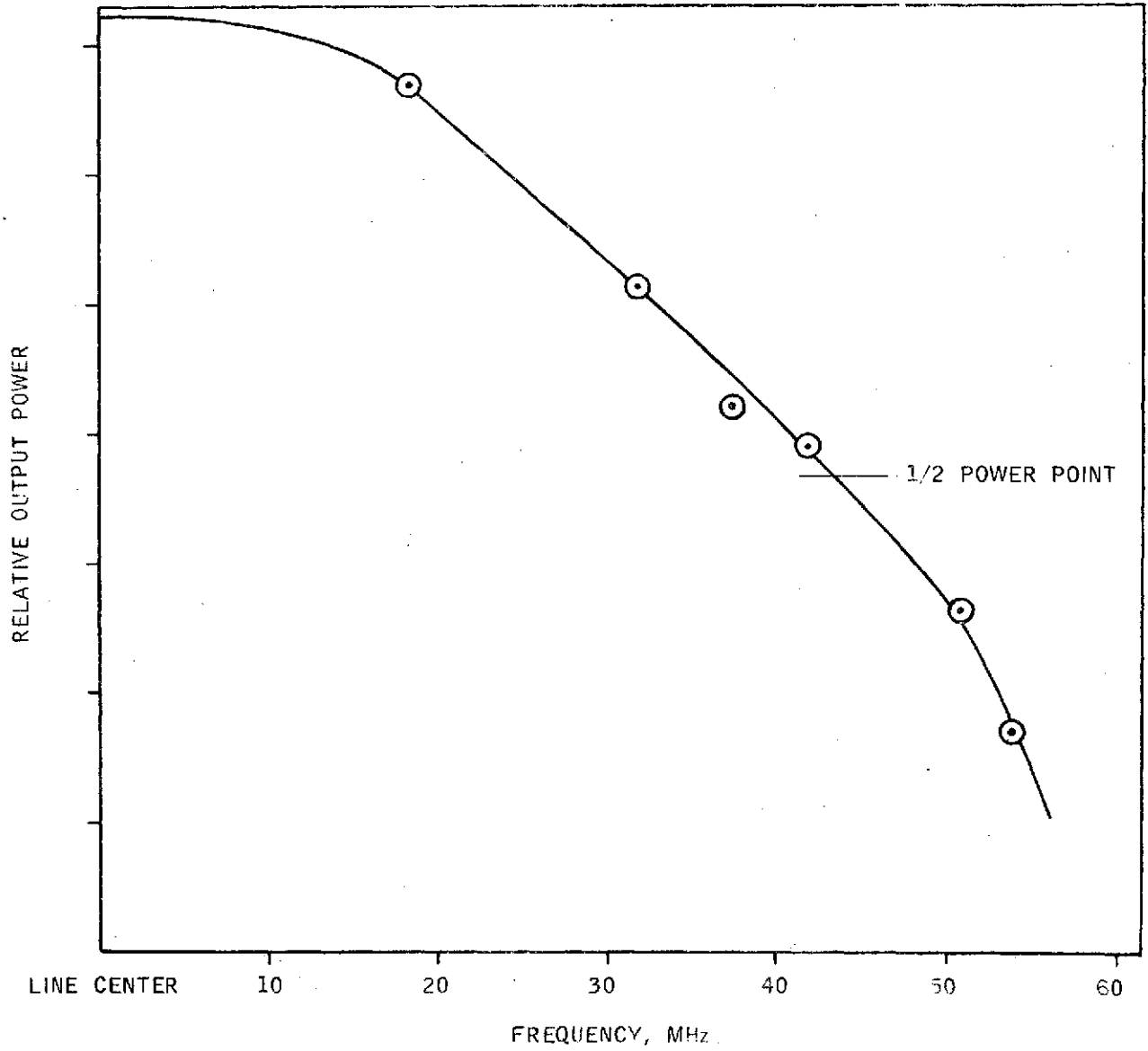


Figure 5.2.2-32

MEASUREMENT OF CIRCULAR BIMORPH LINEARITY OF MOVEMENT
WITH APPLIED VOLTAGE OVER LARGE RANGE



POWER-FREQUENCY PROFILE BREADBOARD LOCAL-OSCILLATOR LASER

Figure 5.2.2-33

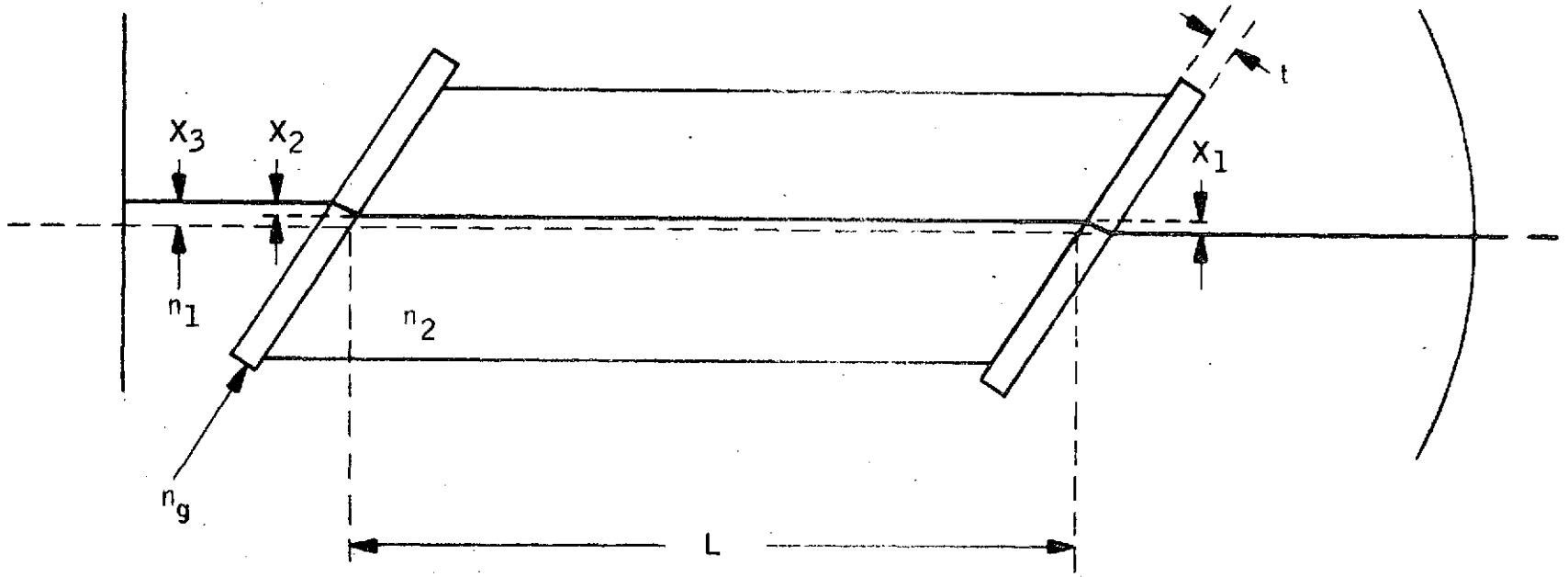


Figure 5.2.2-34

OPTICAL PATH WITHIN CAVITY

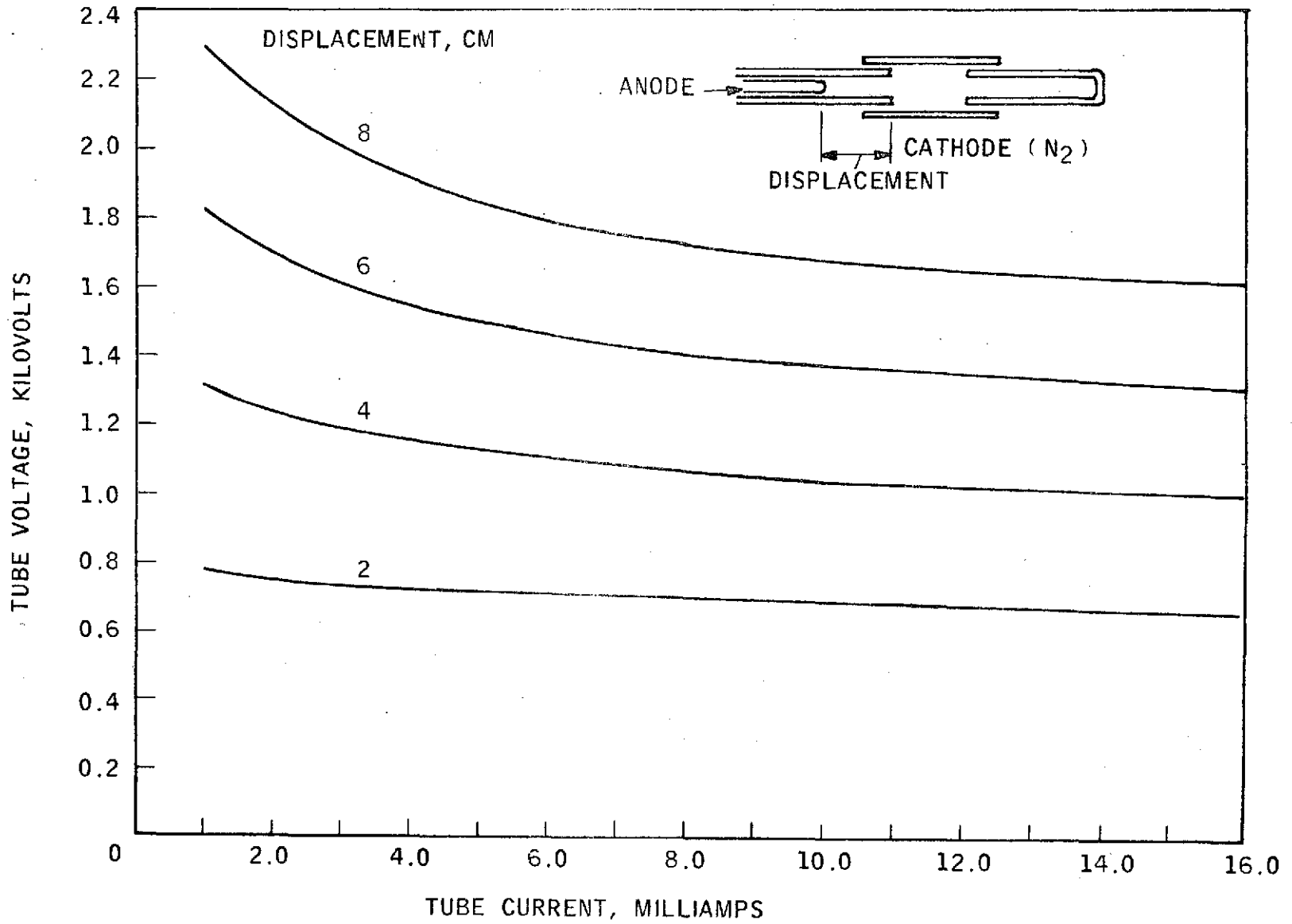


Figure 5.2.2-35

EXPERIMENTAL DISCHARGE TUBE V-I CHARACTERISTICS

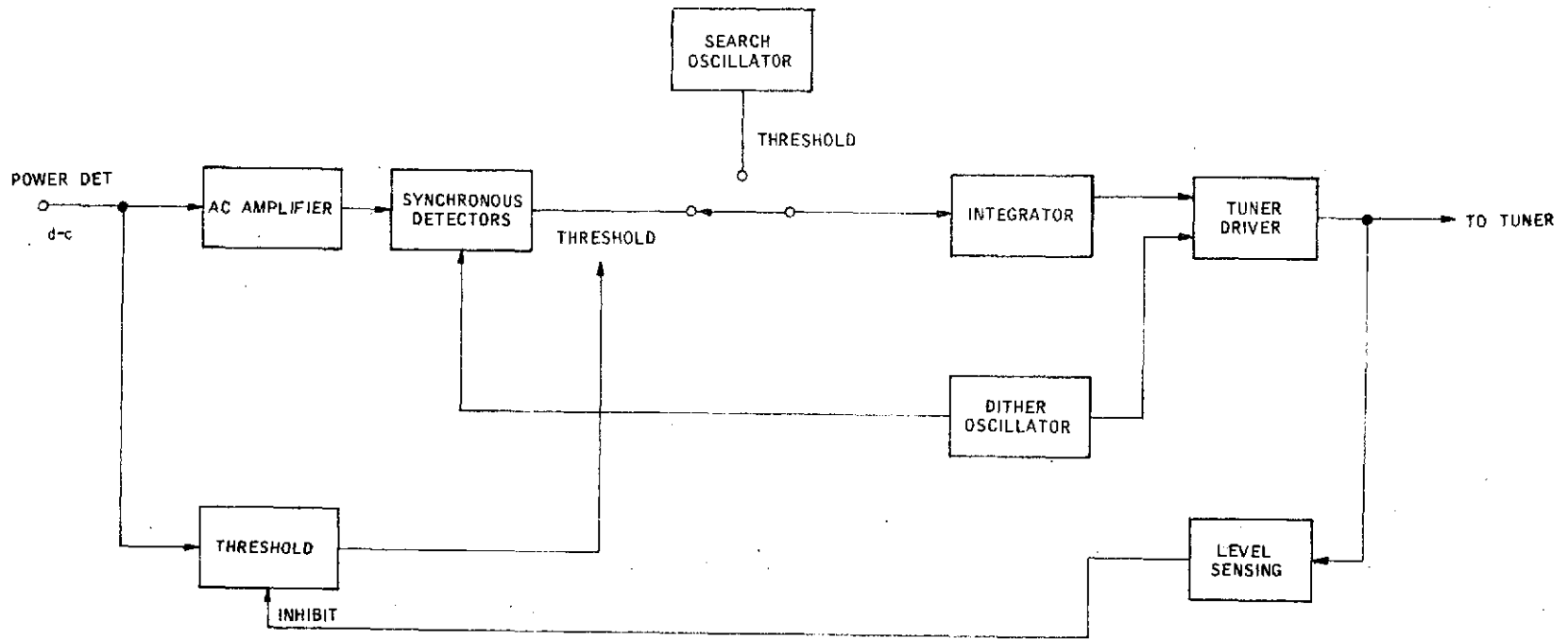
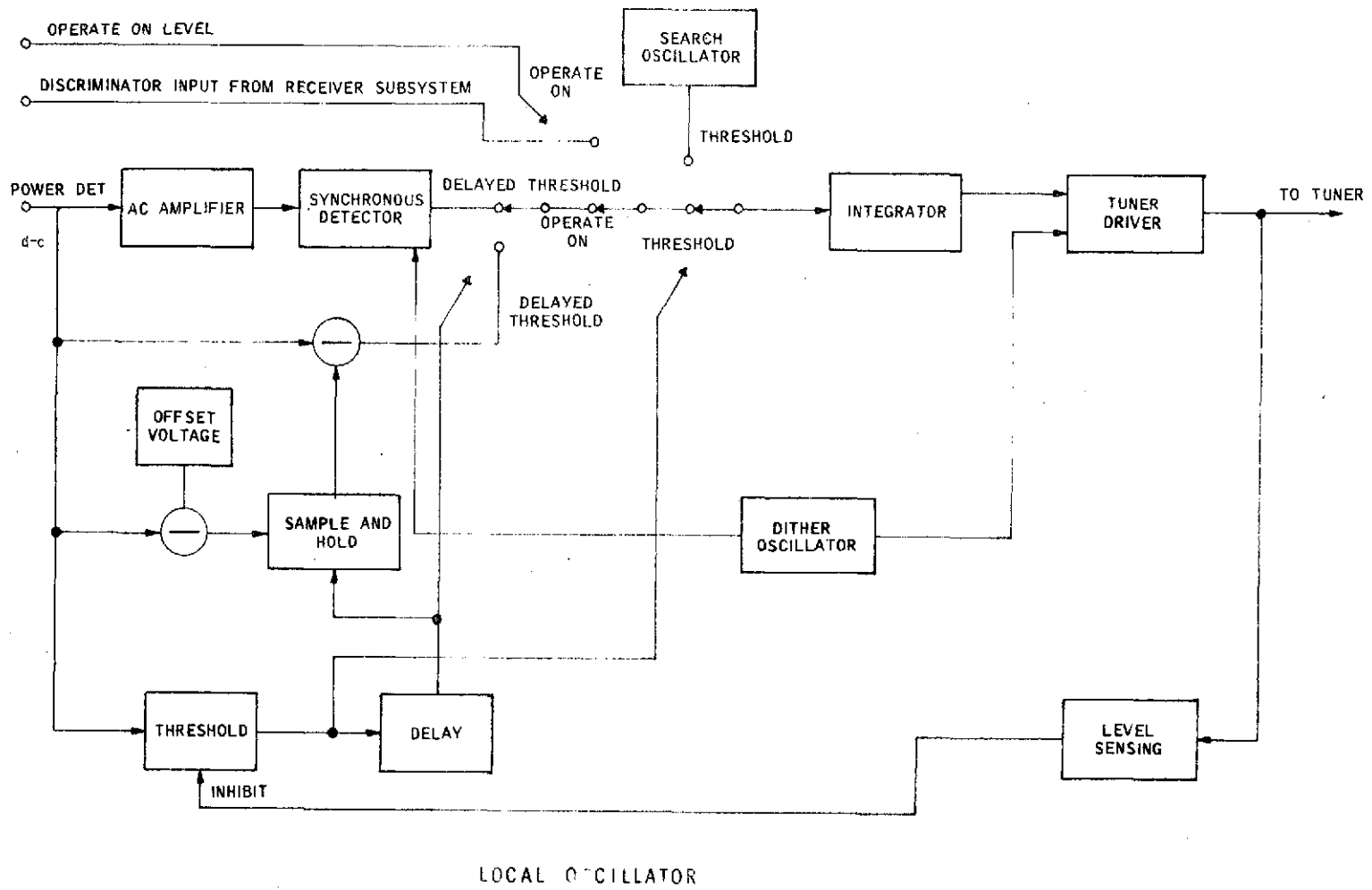
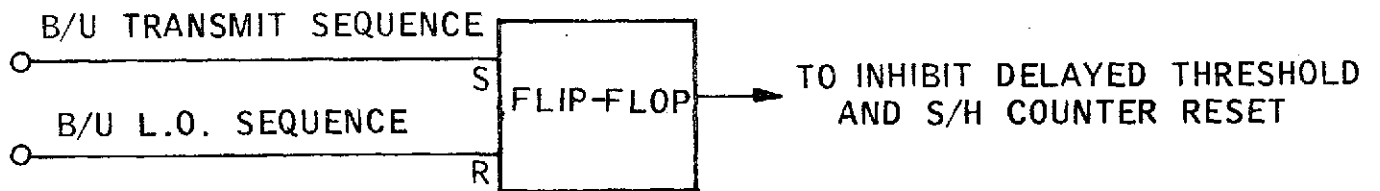
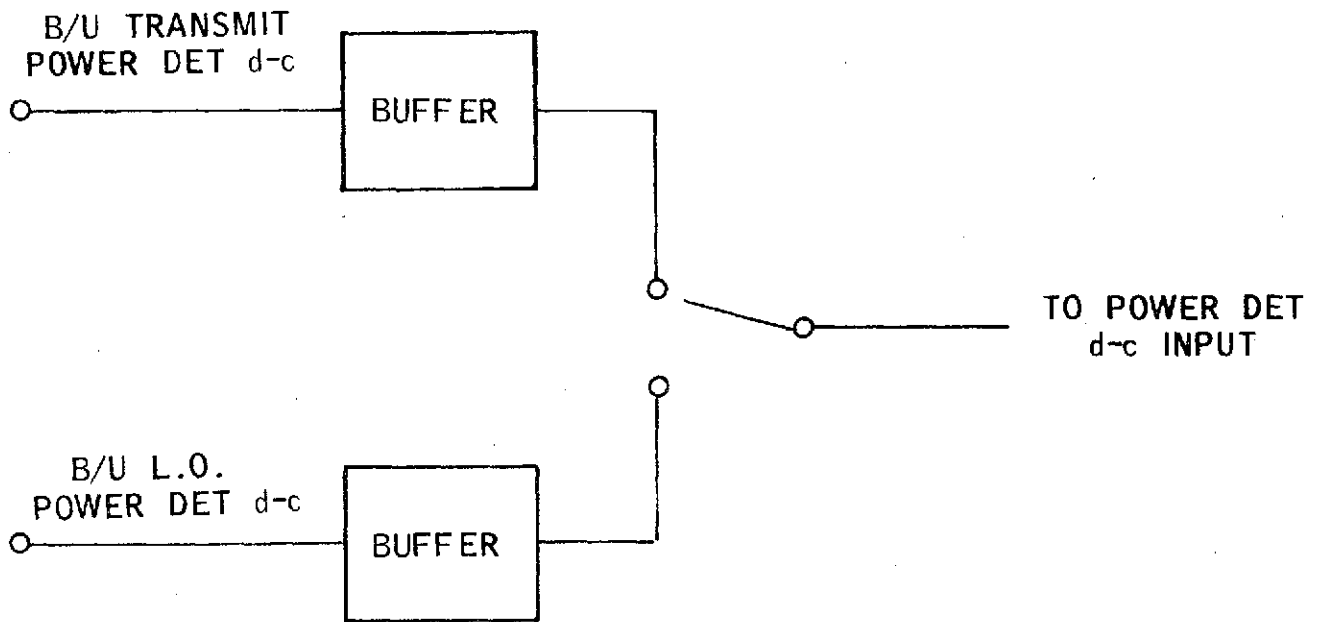


Figure 5.2.2-36

TRANSMITTER SEARCH AND DITHER AFC

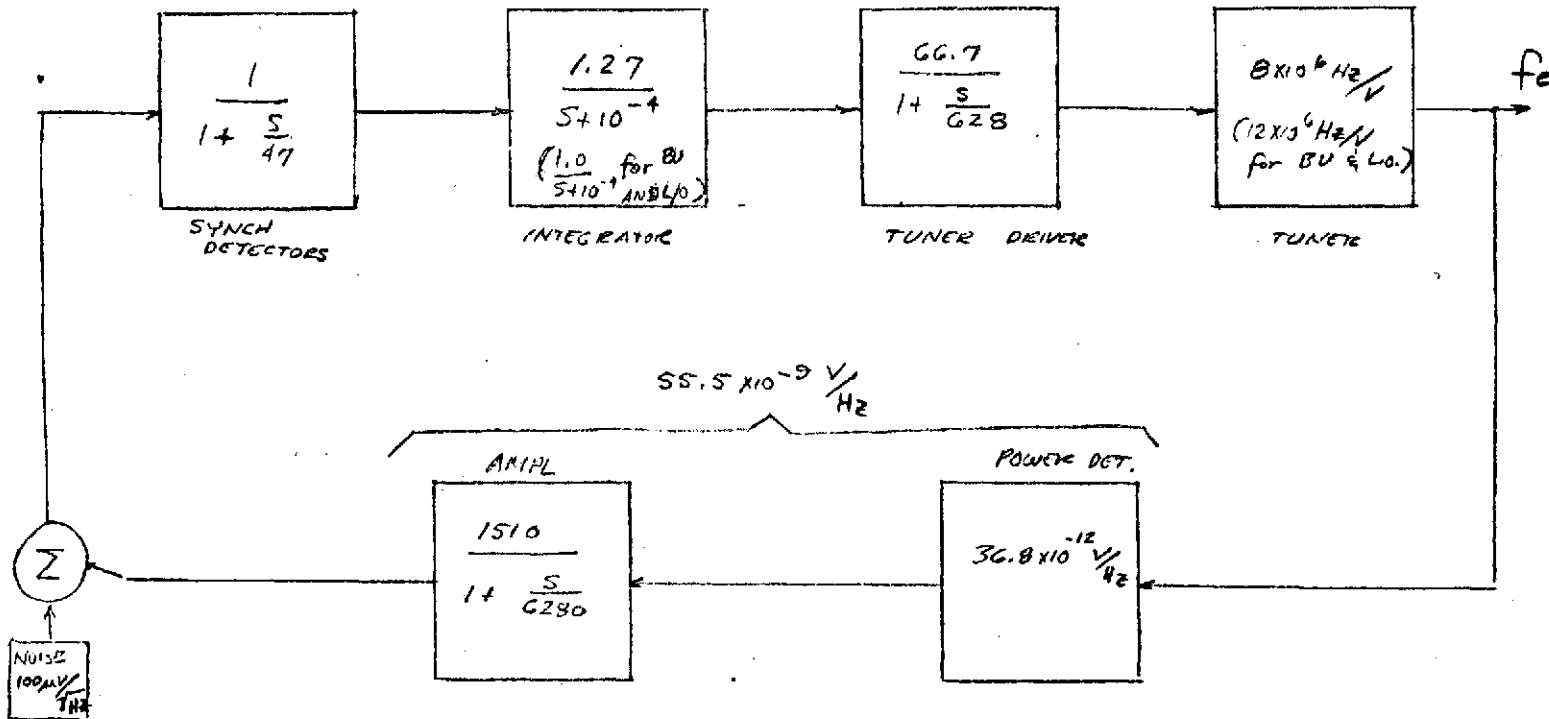
Figure 5.2.2-37





ACK-UP LASER CONTROL ADDITION TO L/O CONTROL

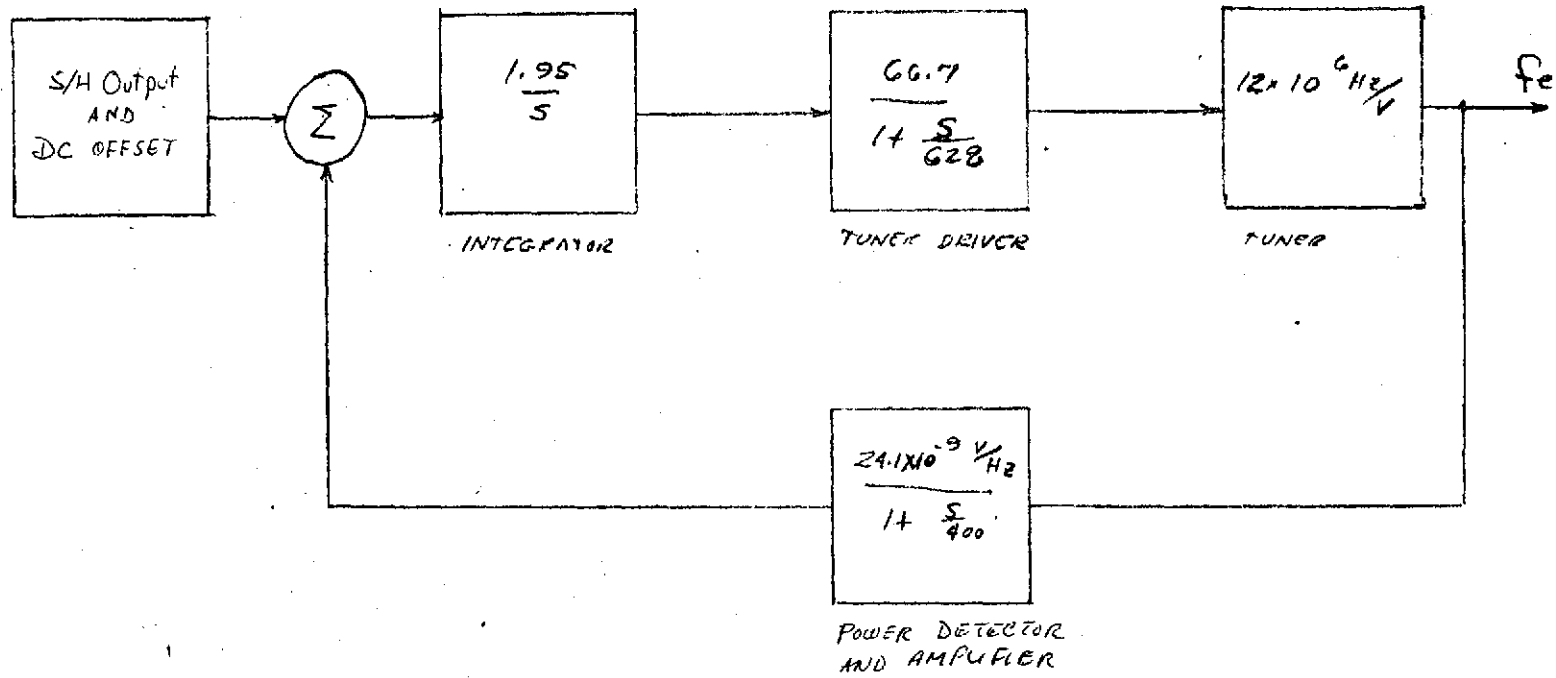
Figure 5.2.2-38



$$K = \frac{37.6}{5 \left(1 + \frac{s}{47}\right) \left(1 + \frac{s}{628}\right) \left(1 + \frac{s}{6280}\right)}$$

Dither Loop

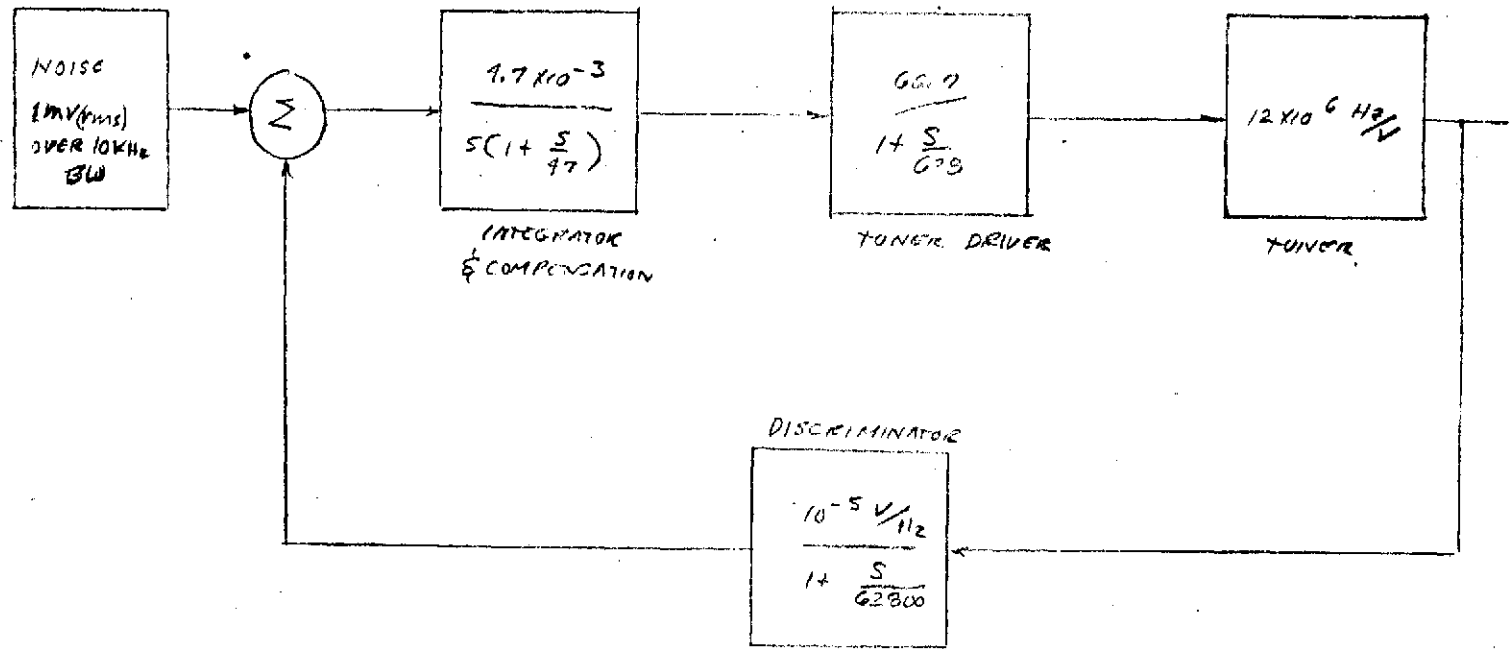
Figure 5.2.2-39



$$K = \frac{37.6}{s(1 + \frac{s}{400})(1 + \frac{s}{628})}$$

Offset AFC Loop

Figure 5.2.2-40



$$K = \frac{37.6}{\left(1 + \frac{s}{628}\right) \left(1 + \frac{s}{50}\right) s}$$

Receiver AFC Loop

Figure 5.2.2-41

5.2.3 Radiation Cooler

The discussion of the radiation cooler that follows: (a) provides a general description of the cooler; (b) discusses the requirements imposed on this assembly; (c) highlights all the trade studies that led to the proposed design; and (d) presents a detailed discussion of that design in terms of meeting the requirements.

The mixer detector of the LCE must be cooled to approximately 100°K to ensure proper and reliable performance of the experiment. This low temperature must be maintained in a geosynchronous satellite space environment for a period of at least 2 years. This length of time, coupled with power, vibration, reliability, and weight considerations associated with the LCE, precludes the use of closed-cycle, open-cycle, or mechanical coolers and leaves only a passive cooler as the possible mechanism for cooling the mixer.

In designing a passive radiator, the attempt is made to minimize heat inputs to the radiator, and to maximize heat transfer from the radiator to space. Sources of heat that must be considered include:

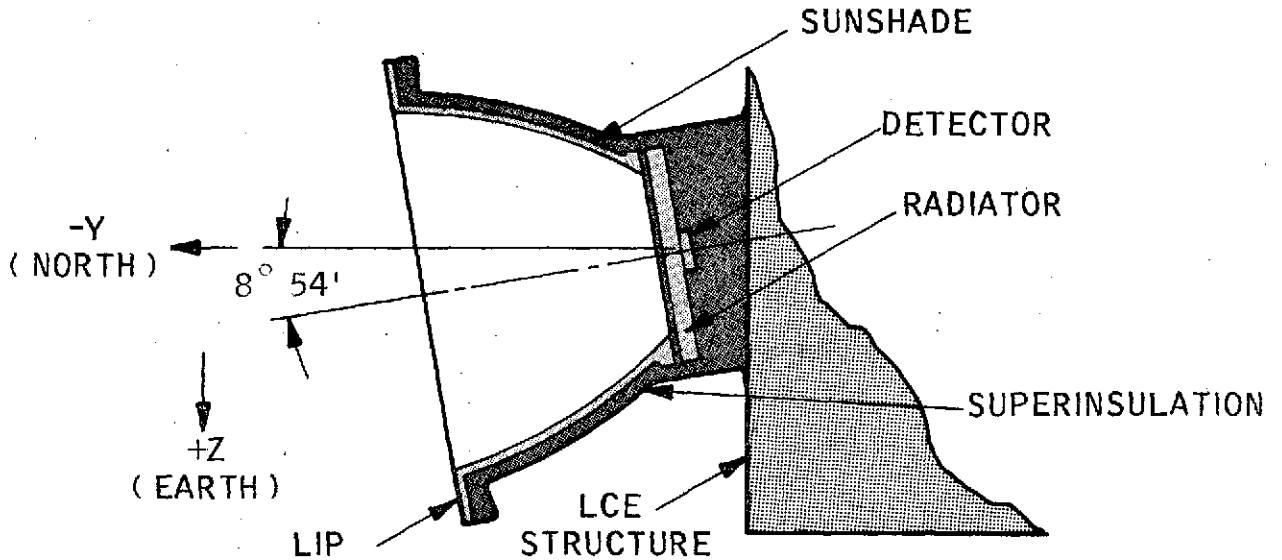
- Direct and reflected solar energy
- Earthshine and albedo
- Heat conducted through
 - Insulation barriers
 - Electrical wires
 - Supports
- Infrared radiation from
 - Protective sunshade
 - LCE
 - ATS

The proposed radiation cooler design meets all the requirements outlined in Paragraph 5.3.2.1. The predicted temperature cycle of the radiation cooler during the year is presented in Figure 5.2.3-1, the extremes are 98°K during winter solstice and 116°K during summer solstice. The uncertainties associated with these temperature predictions are $\pm 10^{\circ}\text{K}$. These

uncertainties account for inaccuracies in the analytic techniques, inaccuracies in available information on thermophysical properties used to construct the radiation cooler, a lack of precision in the environment's definition, etc. Detailed trade studies were conducted prior to the selection of the proposed design. These trade studies have indicated that this design is an optimum for the LCE. Although the cooler did not meet the initial design goal of $100 \pm 5^{\circ}\text{K}$, it comes closest to fulfilling this requirement. Because the design goal was not reached, the specification to SAT on the flight mixer assembly units had to be changed. The implications of this change for the system are described in other sections of the report. If the volume constraints placed upon the radiation cooler were lessened, then it would be possible to lower the temperature and more closely approach the original design goal. No other passive radiation cooler type can come as close to meeting the design goal. An additional advantage of this cooler is that the sunshade can be removed without altering the alignment of the detector and radiator. This facilitates integration of the LCE into the ATS spacecraft. Many of the design features associated with the radiator cooler are essentially state of the art. An extensive development program is underway to ensure that the proposed design is successfully transformed into successful hardware. Work to date indicates that this transformation can be successfully completed at Aerojet within the schedule constraints of the program. The details of this program are presented in Section 5.3.3.

The cooling system proposed for use on the LCE is presented in Figure 5.2.3-2. Before going into the details of the requirements, analysis, and design, a brief description of the radiator cooler is given below.

The radiator and sunshade are individually attached to the LCE by low-conductance ball/spring mechanisms. The radiator, sunshade, and sunshade radiator flange, or lip, are all symmetric about one axis and are all backed by super-insulation:

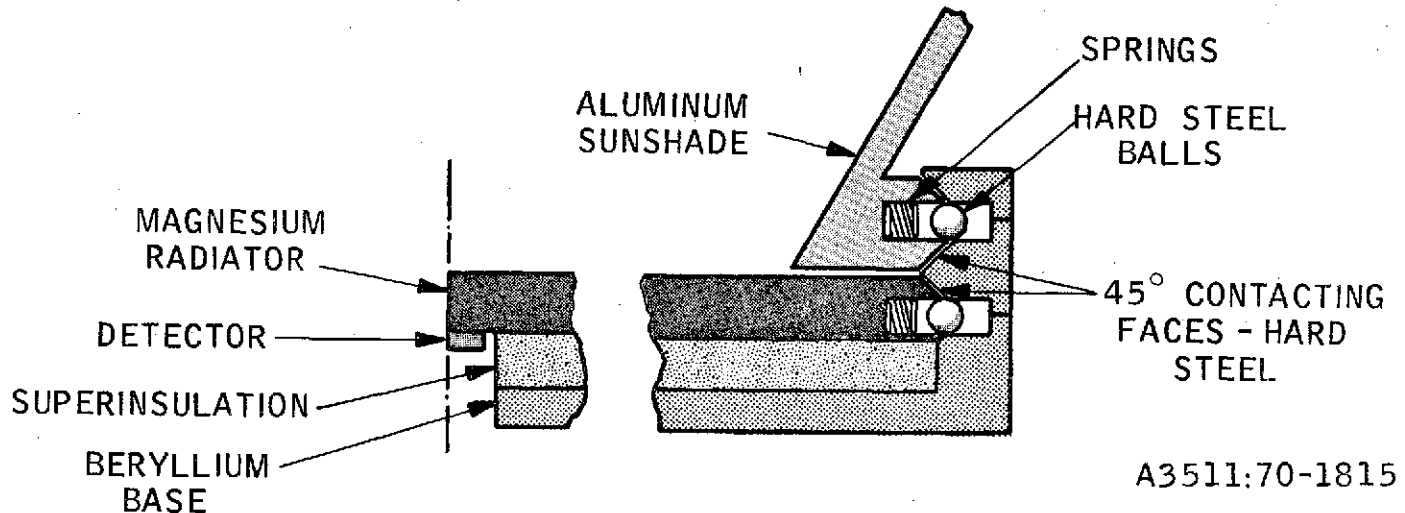


The detector is attached to the back of the radiator. The radiator's front face has a view to space and the sunshade. The radiator is a flat disc, the radiating diameter of which is 6.4 in. and the axis of which points 8 degrees 54 minutes of arc down, toward the +Z axis (earthward) from the -Y axis (north). The sunshade is an ogival surface of revolution with a constant radius of curvature of 23.384 in. in any plane of the axis. The sunshade's diameter, where it meets the lip, is 9.56 in. The axial length of the sunshade is 7.362 in. The sunshade radiator flange or lip is a flat surface of revolution, the inner diameter of which is the same as the outer diameter of the sunshade, and the outer diameter of which is 15.56 in.

Figure 5.2.3-3 presents the maximum and minimum temperatures of the radiator as a function of the width of the sunshade lip for the two orbital extremes, the summer and winter solstices. Volume limitation imposed by the ATS spacecraft design constraints precludes having a lip the width of which is much in excess of 3 in.

The exposed surfaces of the radiator and lip are covered with second-surface mirrors. The sunshade's exposed surface is vacuum-deposited aluminum over electroless nickel which is applied to an aluminum structure 0.090 in. thick.

A description of the mounting system follows:



The radiator and sunshade are each attached separately to an outer ring. At the temperature associated with vehicle launch, 300°K , the radiator and sunshade are each in tight mechanical contact with the mating ring along their 45° slopes. This provides mechanical support to withstand the loads associated with launch. Once in orbit, the sunshade and radiator cool down considerably and contract inwardly, away from the support ring. They are each then held accurately in place by three hard-steel ball/spring sets that provide sufficient load carrying capability to handle orbital maneuvers, yet allow only a small heat flow. They are designed to maintain detector alignment within the required tolerances for efficient operation.

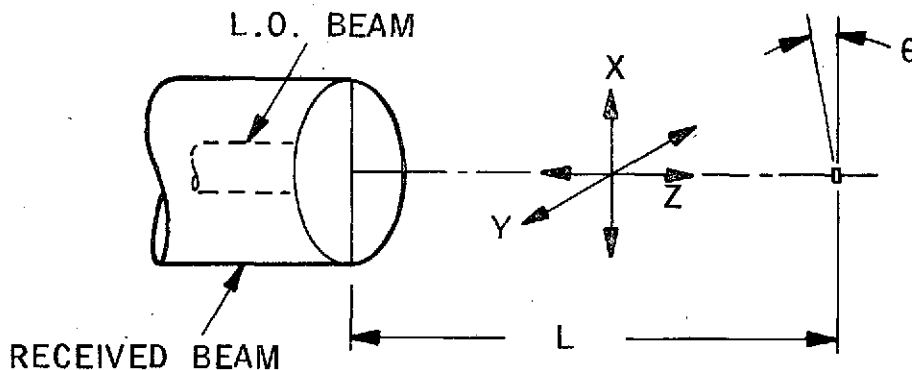
5.2.3.1 Requirements

The following is a listing of requirements for the radiation cooler:

1. The LCE passive radiation cooler will be designed to keep the temperature of the receiver detector within the temperature range of $110 \pm 15^{\circ}\text{K}$ throughout the entire first 2-year period of on-station operation
2. The passive radiator will be designed such that sunlight can impinge normally on the radiator for a sufficient period of time such that steady-state temperatures are achieved.

During this time, the maximum temperature of the radiator shall not be sufficient to cause damage to the receiver detector

3. The radiation cooler must not exceed the volume envelope presented in Figure 5.2.3-4
4. The radiation cooler will be designed to have minimal weight. As a design goal, the weight will be less than 5.5 lbm
5. The design will facilitate integration of the LCE with the ATS spacecraft. In particular, it must be possible to install the LCE without disturbing the alignment of the mixer detector
6. The radiation cooler and sunshade will be designed to survive the radiation and accelerate environments presented in NASA Specification S320-ATS-2B. Both sinusoidal and random vibration must be considered.
7. The radiator will provide a mounting surface for the AIL mixer assembly
8. The alignment requirements for the detector and imaging optics are presented below



Assume the Local Oscillator and received signal beams are combined as shown above

	<u>Detector-Mixer</u>
Δx	± 0.005 inch
Δy	± 0.005 inch
Δz	± 0.010 inch
$\Delta \theta$	$\pm 2^\circ$

ΔL (Distance between optics and detector) - ± 0.010

* $\Delta \theta$ of the imaging optics is dependent on the length L and Δz of the detector-mixer.

To meet these requirements, a detailed analytical design, and development program was initiated. Details of that program are summarized in the following pages.

5.2.3.2 Trade Studies

5.2.3.2.1 Cooler Types

At the beginning of the LCE Program, Aerojet initiated a detailed investigation of all passive radiation coolers which might be used to cool the mixer/detector. Work performed during the proposal and on other Aerojet contracts had indicated that power and reliability considerations precluded the use of active refrigerators to obtain the required temperature of approximately 100°K. To begin the investigation, the Aerojet technical library conducted a detailed survey to gather all literature, both classified and unclassified, that had been written on the subject of radiation coolers (see references 5.2.3-1 through -12). This survey indicated that most of the work on radiation coolers had been done by the following four companies:

- a. Arthur D. Little (ADL), Cambridge, Massachusetts
- b. Philco-Ford, Palo Alto, California
- c. Hughes, Santa Barbara Research Center (SBRC), California
- d. IIT Industrial Laboratories, Fort Wayne, Indiana.

After scrutinizing the literature, members of the Aerojet technical staff contacted the above mentioned companies to solicit their advice and opinions. In all instances, the assistance that these companies provided was beyond that initially anticipated. Aerojet wishes to acknowledge this help and to openly thank all the contributors.

This background, coupled with Aerojet's own extensive experience in the analysis of radiation coolers, provided the bases from which the candidates for the trade study were selected. These candidates were:

- Stacked radiator - single sunshade (Figure 5.2.3-5)
- Single radiator stage - multiple sunshades (Figure 5.2.3-6)
- Single radiator, single sunshade (Figure 5.2.3-7)

Parameters that could be varied in each of the above designs were the size of the radiator, the shape and size of the sunshades, the tilt angle with respect to the spacecraft, the sunshade cone angle, and the thermal control coatings.

The first configuration that was examined in detail after the contract award date was a stacked radiator with a single sunshade. This was essentially the concept presented in the Aerojet proposal. As stated in the proposal, Aerojet had analyzed and tested a portion of this design and the results appeared to be quite favorable. During the testing, the effect of the sun on the cooler's performance was not empirically determined because facilities which are adequate for this type of testing are not available anywhere in the United States. The fact that the values for solar input were not checked again during the proposal, either by analysis or test, proved to be quite critical, since a calculation error was made. Appendix I presents an internal Aerojet memorandum that discusses the analysis of the proposal design subsequent to the program start date. As indicated in the analysis, the performance of the proposed design was quite sensitive to changes in the specularity of the sunshade's inner coating. However, to a large degree, the problem of specularity could be alleviated by using second-surface mirrors on the outside surface of the radiator. The proposed design, as modified by subsequent design analysis (Figure 5.2.3-5), still had problems that made further investigation of alternate designs attractive. Some of these problems are itemized below:

- a. Mounting second surface mirrors on a radiator stack would be exceedingly difficult
- b. Alignment of the detector would be quite difficult
- c. IR input from the sunshade was significant enough to negate the advantages of a radiator stack. There was essentially only a 1°K or 2°K temperature difference between each radiator stage
- d. The volume required by this system was larger than that allotted by NASA at interface meetings held in February 1970
- e. The maximum radiator temperature for a design which had (i) second-surface mirrors on the radiator, (ii) 98% specularity for the sunshade coating, (iii) a second surface mirror cooled sunshade, and (iv) two radiator stages were 112°K. This was far in excess of the Aerojet design goal of 90°K. Aerojet hoped to obtain this design goal so that there would be a good margin of safety in the design and so that heaters could be incorporated to control the temperature of the mixer detector to a value of 100 ±5°K

On 22 January 1970, a member of the Aerojet Thermal Design Group visited Philco-Ford, Palo Alto to discuss in detail their work on a 77°K passive radiator. A summary of this meeting is presented in Appendix J. Subsequently, Aerojet began a detailed analysis of a radiation cooler with one radiator stage and two sunshades. This configuration is presented in Figure 5.2.3.6. The advantages of the two sunshade configurations are:

a. The inner sunshade blocks a large portion of the solar energy which is diffusely reflected from the outer sunshade. The system is designed so that direct solar irradiation of the inner sunshade is impossible. Therefore, the need for a high degree of specularity on the inner surface of the sunshades is reduced. A coating the specularity of which is as low as 90% would be quite acceptable with the double sunshade design.

b. A major source of heat input to a radiator which has a single sunshade is direct infrared radiation from the sunshade. Because the inner surface of the sunshade is a polished metal which acts as a solar absorber ($\alpha_s/\epsilon \geq 3$), the sunshade's temperature can get as high as 261°K. At this temperature, approximately 40% of the total heat input to the radiator arrives via direct radiation from the sunshade. With a double-sunshade design, this heat input can be reduced significantly. The inner sunshade can have its own radiator to cool it. The inner sunshade is designed to block IR radiation from the warm outer sunshade. Therefore, the total heat input to the radiator is reduced significantly. With this design, a maximum radiator temperature as low as 100°K can be achieved. However, there was a volume design constraint imposed by the ATS Program Office that precluded use of this design. This constraint stated that the portion of the radiation cooler assembly that extended outside of the package must entirely fit within the envelope presented in Figure 5.2.3-4. When this constraint was placed on the double sunshade configuration all of its advantages disappeared. The height of the inner sunshade became so small that its benefits were negligible. This design when placed in the allowable volume had a maximum detector temperature of 114°K. This led to the investigation of a radiator design that was based on the concept of a single-radiator stage and a single sunshade.

Figure 5.2.3-7 presents a schematic of the final configuration analyzed - the single-stage radiator with one sunshade. A detailed drawing of

this design is shown in Section 5.2.3.4.1.3-3. There are many design variables which can be altered to achieve an optimum design. Some of these variables include:

- Sunshades size and shape
- Type and location of thermal control coatings
- Position of the LO optics
- Type of supports for the radiator and sunshade

The results of the analyses performed in each of the above-mentioned areas will be discussed briefly below:

5.2.3.2.2 Sunshade Geometry

The purpose of the sunshade is to prevent solar energy from impinging on the surface of the radiator. It is also to prevent thermal energy (either reflected solar or emitted infrared) coming from the ATS solar panels and antenna from impinging on the radiator. It was determined quite early in this effort that the optimum shape for the radiator would be a surface of revolution. It was believed that this design could be more readily fabricated than one that employed flat plates, or that had corners, which could possibly act as radiation traps. In addition, an analysis of the orbit plane, altitude, and satellite dynamics indicated that a surface of revolution would be preferred due to symmetry. The first shape considered was a conical sunshade. Figure 5.2.3-8 presents the two limiting design approaches for a sunshade of this type. In Shade A, the meridional solar ray is reflected back on itself. In Shade B, this ray is reflected horizontally. This latter design will have a smaller envelope than the one presented as Shade A.

A detailed heat balance of the radiation cooler with the two-bounce sunshade presented in Figure 5.2.3-8 indicated that 49% of the total energy transferred to the radiator arrived via infrared radiation from the sunshade. It was obvious that there were three ways to reduce this heat input:

- Lower the emittance of the sunshade coating
- Lower the temperature of the sunshade
- Reduce the emitting area of the sunshade

The first two items will be discussed in a later section of this report; the third item, reducing the emitting area, which bears directly on the sunshade's size, shape, and contour will be dealt with here. When considering the requirements for the sunshade, it is obvious from a thermal design standpoint that the full frustum of a right circular cone is not needed. As a minimum, the cone could be scarfed, as shown in Figure 5.2.3-9a, to reduce the radiation area. However, even this design can be improved upon, since there remains a significant amount of area that can be removed and still meet the requirements imposed on the sunshade. Aerojet thermal design personnel wrote a computer program to determine the shape of a conical sunshade which had minimal surface area. That design is presented in Figure 5.2.3-9b. Analytically, this design was far superior to the full-cone design, since its radiator temperature remained within the range of 95°K to 108°K , while the full cone had a radiator the temperature of which was in the range of 98°K to 114°K . Because of the aforementioned volume constraints placed on the radiator assembly by the ATS Contractor, the conical sunshade could not be designed to meet the requirement of successful performance when the spacecraft was slewed $\pm 10^{\circ}$. The previously discussed conical sunshades were designed to function when the slew angle of the ATS was $\pm 1^{\circ}$. This was a serious disadvantage with the conical design. Its principal advantage was that manufacturing facilities are more familiar with constructing conical surfaces of revolution than other surfaces. One exception to this rule was the shaped conical sunshade. The polishing of such a sunshade would have been extremely difficult. Further analysis of the sunshade, aimed at finding the shape that would provide optimum performance, led to the proposed design. A detailed discussion of the wineglass sunshade is presented in a subsequent section of this report.

5.2.3.2.3 Thermal Control Coatings

A detailed coating investigation was conducted to determine the optimum coating for the inside surface of the sunshade. The requirements for the coating were that it be highly specular ($\gamma \geq 98\%$), have a low total hemispherical emittance ($\epsilon \leq 0.05$) and a low solar absorptance ($\alpha_s \leq 0.16$). The coatings investigated include gold, silver, enhanced silver, and aluminum. Of these coatings, aluminum was selected because it met all of the above criteria and test and flight data on this coating's behavior in the natural

environment of a synchronous satellite far exceeded the data available for the other coatings. Documents referred to in this literature search included References 5.2.3-13 through -24. Table 5.2.3-1 presents values of solar absorptance and emittance for the candidates. The discussion below summarizes advantages and disadvantages associated with each candidate:

Gold

Gold coatings have been used extensively on space vehicles. The coating is extremely stable and, when placed on a properly prepared substrate, will provide the required specularly. However, a review of Table 5.2.3-1 will indicate that the solar absorptance of this coating exceeds that of any of the remaining candidates and, indeed, is out of the specified range. Therefore, gold was dropped as a candidate.

Silver

From a review of Table 5.2.3-1, it is evident that, next to enhanced silver, pure silver is the second choice for the sunshade coating. However, silver quickly tarnishes, and the values of α_s and ϵ for the degraded coating are unacceptable.

Enhanced Silver

The most attractive coating from the standpoint of α_s and ϵ is enhanced silver. However, there is no data on how this coating will perform in the space environment of a geosynchronous satellite. Because the radiator must maintain the temperature of the mixer detector at, or near, 100°K for a minimum of 2 years, the stability and reliability of the thermal control coating must be not only well understood but also high. There is insufficient data on enhanced silver to allow one to select it as the prime candidate coating for use on the LCE. An extensive combined-effects test program would have to be conducted before this coating could be recommended for use in the design of the LCE. This test program would require at least 4 months of actual test time and at least \$100,000. If this coating were used instead of aluminum (the prime candidate) in the proposed design, then the radiator's temperature would be in the range of 96° to 110°K rather than 98° to 116°K .

Aluminum

The prime candidate for the coating on the inside of the sunshade is aluminum. Details on the application procedure are outlined in a subsequent section of this report. The aluminum cannot be covered with either a MgF or an SiO protective coating, since these coatings will increase the emittance (ϵ) beyond acceptable limits. Therefore, the sunshade cannot be readily cleaned if water or volatiles condense on the coating. The only cleaning that can be done is to remove particulate contamination by blowing dry air or nitrogen gas across the surface.

To lower the temperature of the sunshade, a decision had to be made on what thermal coatings should be used and where they should be applied. It was obvious that the temperature control coatings would consist of a combination of multi-layer or superinsulation, and second-surface mirrors. For the first iteration, second-surface mirrors were placed over the entire outside surface of the sunshade. This proved unattractive for at least the following two reasons:

- The sunshade's external surface would have to be multi-faceted, since second-surface mirrors can only be mounted on a flat surface. This would increase the weight, manufacturing complexity, and cost of the sunshade
- The IR exchange between the north wall of the ATS and the sunshade was excessive when this design was considered. Because of this high heat input to the sunshade, its temperature was excessively high

The second and final design for the thermal control coating scheme for the exterior of the sunshade uses superinsulation to isolate the sunshade from the ATS and the LCE. A radiator flange or lip is placed at the outer edge of the sunshade. This flange is covered with second-surface mirrors. These mirrors are extremely stable in space and they have the required thermo-physical properties: low solar absorptance ($\alpha_s \leq 0.06$) and high infrared emittance ($\epsilon \geq 0.77$).

Further details on the thermal control system of the proposed design are presented in a subsequent section of this report.

5.2.3.2.4 Position of Local-Oscillator Imaging Optics

Of critical concern early in the design of the radiator was the question of whether or not to support the local-oscillator (LO) imaging optics on the radiator. The answer to this question was, of course, tied quite closely to the problem of detector alignment and radiator support. There were obvious advantages to mounting the imaging optics on the radiator, including:

- The requirements for alignment of the detector relative to the LO beam would be alleviated. With this design, the optics would be fixed relative to the detector and any movement of the radiator would move the detector/optics combination through a collimated beam from the LO. This beam would be of sufficient diameter so that it filled the optics aperture at all times
- Because the optics and detector were mounted closely together the ability to position these elements relative to one another would be facilitated

However, there were important disadvantages which more than counterbalanced the above advantages. Two principal disadvantages of mounting the imaging optics on the radiator are increased heat load and the impact on support design. The heat load cannot be held to manageable levels with warm imaging optics. Even with a cold lens, an additional 10 mw of radiant input to the lens from the surrounding warm surfaces can be expected. This is a substantial fraction of the 130-mw total being dissipated by the radiator and would result in a 2°K increase in radiator temperature.

To mount the imaging lens from the radiator requires it to be cantilevered off of the detector/mixer mount. This increases the moments at the radiator supports during launch, and requires a more massive support mechanism, resulting in higher heat loads to the radiator during initial cooldown.

To make a final decision on whether or not to support the optics from the radiator, a detailed review was made of the alignment requirements. A description of the positional tolerances to be employed during the design of the detector-mixer and its imaging optics are given in the requirements, in Section 5.2.3.1.

With this information, the decision was made to mount the imaging optics separately from the radiator. This decision was based on calculations of expected movements of detector/mixer and imaging optics, and of allowable positional tolerances to ensure acceptable focus.

5.2.3.2.5 Radiator and Sunshade Supports

The trade study to determine the optimum support scheme for the radiator and sunshade is still in progress. A discussion of this effort is provided in Section 5.3.3.1 of this report. Of primary concern with this design is the fact that it is highly desirable to mount the sunshade and radiator separately. All of the systems presently under consideration at Aerojet allow the removal and installation of the sunshade without disturbing the radiator's alignment. Because of the size of the LCE transceiver, and the size of the installation port of the ATS Spacecraft, it would be impossible to install the LCE while the sunshade was mounted. If the radiator was attached to the sunshade, then the entire assembly would have to be removed prior to mating the LCE with the ATS. The radiator/sunshade would then have to be accurately aligned with the LCE on the spacecraft. This would be extremely difficult, if not impossible, since it would require that the detector be cooled to operating temperature and that the signal output level from the detector be used as a measure of alignment. It is much more attractive to align the detector to the optical system at Aerojet and not alter it subsequently.

An additional advantage of a design which allows mounting the sunshade and radiator separately is that, once the electrical connections between the preamplifier and detector, temperature sensor, and its electronics, etc., have been made and checked out, they need never be broken. Mounting the radiator to the sunshade would force the disconnection of the electrical connections each time the radiator assembly was removed.

5.2.3.3 Computer Programs Utilized in the Analysis

Two computer programs are available at Aerojet to perform the thermal analysis of the LCE radiator/sunshade: the Monte Carlo program, and the steady-state program.

5.2.3.3.1 Monte Carlo Program

Monte Carlo is a technique by which radiant shape factors from one surface to another can be determined and interreflections between a group of surfaces can be calculated. It is the most powerful tool available for accurately simulating a problem involving radiant exchange between several surfaces and space.

The technique consists of choosing one surface as an emitter. From points on this surface, rays are emitted. Each ray is followed through the system to determine which surface it strikes first. The ray is then either reflected back into the system or absorbed, depending upon the reflectance of the surface. Continuing in this way, each ray is followed through the system until it is finally absorbed. Specific points and directions of emission or reflection, and the absorption or reflection of a ray are determined by the selection of random numbers weighted by the properties of the surface involved.

A computer program exists at Aerojet to accomplish this calculation, and the final output of the program is a list of blackbody shape factors from the emitter to every other surface, as well as absorption factors for each surface. Options to the program allow both specular and diffuse surfaces to be used, provide biasing advantages to speed the computations, and give the capability of incorporating rotating surfaces.

Another important option provides a means of determining solar shape factors to each surface by introducing an artificial sun. The $1/2^\circ$ divergence angle for the sun's rays can be included, so that it is not necessary to assume that the sun is a point source.

This program is used as a preliminary step to calculations in orbit. It is an important first step in the analysis because with it, an accurate representation of reflected and interreflected external, as well as self-emitted energy, is possible. The effects of spectral surfaces can be included, as well as partial diffuseness of primarily specular surfaces. With the small loads and low temperature involved in the proposed passive radiator, small increases in energy flow can result in large errors in predicted radiator temperature, thus making the Monte Carlo determination of radiant interchange factors essential.

The Monte Carlo program was developed in-house with Aerojet funds and is considered to be a unique proprietary tool.

5.2.3.3.2 Steady-State Program (503S)

This program evaluates the steady-state temperature and heat fluxes for a thermal network consisting of isothermal nodes. The Gaussian reduction solution technique (matrix triangulation) is employed for the simultaneous equation solution. This program handles heat flow via conduction, radiation, convection, and mass transfer, along with external and internal heat generation.

5.2.3.4 Proposed Design

5.2.3.4.1 Preliminary Mechanical Design

5.2.3.4.1.1 Radiator Design

The radiator is a 6.4-in.-dia circular plate covered with back-surface mirrors. This is the largest size radiator which, when combined with the required sunshade, fits within the available envelope.

Back-surface mirrors cover the radiator surface to provide a low-solar-absorptance ($\alpha_s \leq .06$), high-infrared-emittance ($\epsilon \geq 0.8$) surface. This minimizes the amount of solar energy which is diffusely reflected from the sunshade and absorbed on the radiator, while still maintaining the high heat-radiating properties needed for an efficient radiator.

The detector/mixer subassembly is mounted at the center of the radiator.

5.2.3.4.1.2 AIL Interface

A boss at the center of the radiator provides the mounting surface for the detector/mixer subassembly. Surface finish and flatness of the mating surfaces are important to minimize the temperature difference across the joint.

Two major sources of heat input to the subassembly are conduction along the coaxial lead and radiation from the local-oscillator beam. Lead conduction is minimized by proper selection of lead material and length. Beam radiation is minimized by coating the germanium window to admit energy only in a narrow bandpass centered at 10.6 microns and by reflecting a major part of the energy that enters the detector housing back out the window.

5.2.3.4.1.3 Sunshade Design

A sunshade is required around the radiator because the radiator is on the north face of a satellite in a geo-synchronous equatorial orbit (Figure 5.2.3-10). Its position on the spacecraft is shown in Figure 5.2.3-11 (this is a copy of G.E. Dwg. SK-56177-102). Sunlight directly illuminates the north face from the vernal to the autumnal equinox. Even though the solar absorptance of the radiator is low, radiator temperatures in the 100 to 125°K region are impossible without shading.

The shade also protects the radiator from a direct view of the satellite antenna and solar panel, since these are warm surfaces and diffuse reflectors of solar energy.

A truncated ogive, or "wineglass," shape was chosen for the sunshade. It provides maximum shading for minimum size and weight. The internal surface is highly specular to minimize diffuse solar reflection toward the radiator. The shield is thermally isolated from other satellite structures to enable it to be as cold as possible, thus minimizing infrared radiant-heat input to the radiator, which is the largest single source of heat to that component.

Sunshade temperature is controlled by a circumferential radiator flange or lip on the outer edge of the sunshade. This lip is also covered with back-surface mirrors identical to those used on the radiator.

The sunshade is shown in Figure 5.2.3-12.

5.2.3.4.1.4 Support Design

The support mechanisms for both the radiator and sunshade are designed to provide good thermal isolation in orbit when these components have cooled, while providing good mechanical support during launch when they are still warm. The same type of support is used for both components. They are shown in Figure 5.2.3-2.

Basically, the orbit support consists of three spring-loaded balls resting in hardened steel sockets. This provides a minimum number of support points and minimum contact area at each point.

The launch support consists of circumferential contact around the outer edges of the radiator and sunshade. In orbit, the radiator and sunshade cool and contract away from the supporting members, breaking their contact.

5.2.3.4.2 Assembly

A principal advantage of the Aerojet radiator/sunshade design is the result of the feature of having the sunshade a separate component from the radiator. The entire experiment package can be assembled, aligned, and tested without the sunshade. Because of the critical nature of the sunshade surface, it must be protected. The Aerojet design allows it to be treated as a separate item until final integration with the ATS spacecraft.

5.2.3.4.3 Integration

The LCE package will be integrated with the ATS spacecraft in the following manner. The assembled package, without the sunshade, will be inserted into its berth in the ATS EVM and bolted into place. After alignment adjustments have been made, the sunshade will be assembled into place on the LCE. The protective covering over the sunshade need not be removed until this final integration operation.

5.2.3.4.4 Sunshade Shape

The size of the sunshade is determined by the diameter of the radiator; by the subtended angles to the highest point on the solar panel, and to the highest sun position (assuming the sun to be directly opposite the antenna/solar panel); and by the sunshade's interior shape. The radiator diameter (6.4 in.) is the greatest diameter that will allow the sunshade/radiator combination to fit in the required space volume. This volume is constrained by the following requirements:

- The radiator assembly must remain clear of the ATS/F-G solar panel launch support adapter
- It must not extend beyond the size of the LCE box's north face, 20 inches x 22 inches (Figure 5.2.3-4 defines the volume within which the radiator assembly must be contained)

The subtend angle for the sun's worst position is 23.5° at summer solstice, plus a 10° slew angle which the ATS/F-G could make; therefore, a total angle of 33.5° is required. The larger subtended angle made between the solar panel

and the antenna is obviously the solar panel (Figure 5.2.3-11). This angle is determined by the dimensions given in the G.E. drawing; the angle was found to be 51.3° .

A primary consideration in regard to the sunshade shape is the ability to manufacture the desired shape. With this in mind, it was decided to tilt the radiator/sunshade so that the sunshade could be a simple surface of revolution (Figure 5.2.3-12). For a symmetrical sunshade, the difference of $[180^\circ - (51.3 + 33.5)]$ must be bisected to determine the tilt angle. Thus, the radiator plus shade must be tilted 8.9° (Figure 5.2.3-13).

With the radiator tilted 8.9° and the center located on the optical axis, extreme rays to the sun and to the solar panel's uppermost point are shown in Figure 5.2.3-14. The shape of the inner surface of the sunshade is then drawn, and the intersection of the extreme rays and the sunshade inner surface defines the height of the sunshade and its largest inner diameter.

As stated earlier, the "wineglass" shape was chosen because it has the smallest weight and volume. Theoretically, the wineglass shape works in the following manner (Figure 5.2.3-15): all solar energy impinging on the interior surface at angle equal to 42.4° (the extreme ray angle) will be reflected specularly to a point at the radiator's lower edge, diametrically opposite the illuminated portion of the sunshade. However, to prevent a local hot spot in the shade, the curvature of the wineglass was altered to focus energy to a point several inches beyond the radiator's lower edge, in the radiator plane. The energy reflected from this focused zone on the sunshade interior is then be reflected directly to space.

To define the wineglass shape, the following formulas are employed:

$$\Delta y = -1/2\Delta\delta \quad (\text{Figure 5.2.3-16})$$

$$y = (X + 2R) \tan \delta$$

or

$$y + \Delta y = (X + \Delta X + 2R) \tan (\delta + \Delta\delta)$$

Solving for Δy gives:

$$\Delta y = -1/2 \left[\tan^{-1} \frac{Y + \Delta Y}{X + \Delta X + 2R} - \tan^{-1} \frac{Y}{X + 2R} \right]$$

This expression can be solved by finite differences from initial values for X_0 , Y_0 . A tabulated list of points are presented in Table 5.2.3-2. Since it is costly and difficult to machine and lap the surface described above, it was decided to replace the exact wineglass shape with a circular arc which would go through X_0 , Y_0 and X_1 , Y_1 (Figure 5.2.3-16) and have the same slope at X_0 , Y_0 as the wineglass. (Note the critical area for curvature is the first few inches of height above the radiator.)

Such a calculation was performed and led to the following results:

$$X' = -21.781 \text{ in.}$$

$$Y' = 8.507 \text{ in.}$$

$$R = 23.384 \text{ in.}$$

where X' and Y' are the center of the circular arc as measured from the coordinate system presented in Figure 5.2.3-16.

The area of the "wineglass" sunshade was determined by area integration (refer to Figure 5.2.3-17).

$$A = \int_0^{2\pi} \int_{\phi_1}^{\phi_2} R (R \sin \phi - X_0) d\phi d\theta$$

where

A = area, in.²

R = radius of curvature for ogival surface, in.

θ = polar angle, radians

ϕ = azimuth angle, radians

X_0 = distance of center line from center of ogival curvature, in.

Substituting

$$R = 23.38 \text{ in.}$$

$$X_0 = 18.58 \text{ in.}$$

$$\phi_1 = 69^\circ$$

$$\phi_2 = 87.1^\circ$$

an area = 198 in.² is obtained. This was required for the radiation interchange analyses which are described in following sections.

5.2.3.5 Radiator Analysis

All radiation interchange factors (B_{ij}) to the environment from the radiator and sunshade in the solar wavelength region and infrared wavelength region were determined by the Monte Carlo radiant interchange computer program used in conjunction with an IBM 360/65 computer. (B_{ij} factor represents the fraction of radiant energy leaving surface I that is absorbed on surface J, and it accounts for shading of one surface by another, both specular and diffuse interreflections, surface emittance characteristics, and the geometry of the problem.) The radiator was represented by a disk, the sunshade by a cone (because the wineglass shape is so shallow a cone is a good approximation), the sunshade radiator flange or lip by a disk, the antenna by a spherical cap, and the solar panel by a quadrilateral. The antenna was considered as an opaque surface in all Monte Carlo computer cases. Radiometric properties for the solar panel and antenna are presented in Table 5.2.3-3. The antenna and solar panel of the spacecraft were oriented in the computer program, as shown in Figure 5.2.3-11. The radiator and sunshade were tilted 8.9° away from the antenna solar panel, as would be the case in the flight item.

In order to accurately evaluate the amount of diffusely reflected solar energy from the sunshade interior to the radiator, the following approach was taken (the Monte Carlo computer program was used in this analysis). The shade was considered to be a diffuse body. The thermophysical properties of the coatings in the solar spectrum were used for both surfaces. The B_{ij} was obtained between the sunshade interior and the radiator. This B_{ij} was then used in the following formula:

$$Q_{RS} = S \gamma_D (1 - \alpha_s) A_T F_{SI}(\gamma) B_{ij}$$

where

Q_{RS} = diffusely reflected solar energy, watts

S = solar constant, 0.14 watts/cm²

γ_D = diffuse reflection fraction, 0.01

α_s = sunshade interior solar absorptance, 0.1

A_T = total sunshade interior area, 1283 cm²

$F_{SI}(\gamma)$ = solar shape factor (i.e., projected to total area ratio) as a function of orbit position (ρ) (see Table 5.2.3-4).
For $\rho = 180^\circ$, $F_{SI}(\rho) = 0.301$

B_{ij} = radiant interchange factor (0.00695)

Substitution of the above values yields:

$$Q_{RS} = 3.4 \text{ milliwatts}$$

Note: The solar intensity (S) was reduced by 25% for the orbit angles (ρ) of 0° and 30° , because the antenna blocks the sun. The sun is blocked by the antenna for angles from 0° to approximately 47.2° on either side of the subsolar point.

Reflected solar energy from the antenna and solar panel absorbed by the radiator was determined through the use of the Monte Carlo computer program. The solar panel and antenna were assumed to be diffuse reflectors of solar energy. To facilitate the efficient use of this computer program, rays were emitted diffusely from the radiator to the environment. The computer program gives the radiant interchange coefficient (B_{ij}) from the radiator to the other system elements. Reciprocity was then used to obtain the B_{ij} from the antenna, or solar panel, to the radiator. As an example consider the antenna:

$$\alpha_{si} B_{ij} A_i = \alpha_{sj} B_{ji} A_j$$

where

$$\alpha_{si} = \text{solar absorptance of the radiator} = 0.06$$

$$B_{ij} = \text{radiant interchange coefficient from the radiator to the antenna} = 0.00015$$

$$A_i = \text{total area of radiator} = 207 \text{ cm}^2$$

$$\alpha_{sj} = \text{solar absorptance of antenna} = 0.4$$

$$B_{ji} = \text{radiant interchange coefficient from the antenna to the radiator}$$

$$A_j = \text{total area of antenna} = 7.14 \times 10^5 \text{ cm}^2$$

Substitution into above formula yields

$$B_{ji} = 0.65 \times 10^{-7}$$

This result was then used in the following formula to find the heat rate to the radiator

$$Q = S (A_T) (1 - \alpha_s) B_{ji} \Omega$$

where

$$Q = \text{heat rate absorbed by the radiator}$$

$$S = \text{solar constant} = 0.14 \text{ watts/cm}^2$$

$$A_T = \text{projected area of antenna at } 0^\circ \text{ orbital position} = 6.57 \times 10^5 \text{ cm}^2$$

$$1 - \alpha_s = \text{reflected energy percentage} = 0.6$$

$$B_{ji} = \text{radiant interchange factor} = 0.65 \times 10^{-7}$$

$$\Omega = \text{fraction of absorbing area of antenna} = 0.25$$

Substitution in above formula yields

$$Q = 0.9 \text{ milliwatts}$$

Calculation of reflected solar energy from the solar panel was performed in a similar manner. Reflected solar energy is 0.07 mw for the spacecraft/earth position (ρ) of 180° . Both of these values were assumed to be a constant (although they vary with orbit position) because they are so small.

Infrared energy exchange between the radiator and the antenna, solar panel and sunshade were determined by the following formula:

$$Q = N_{ij} (T_A^4 - T_S^4)$$

where

Q = net heat exchange between surfaces (watts)

N_{ij} = radiation coefficients (watts/ $^\circ\text{K}^4$)

T_A = antenna temperature ($^\circ\text{K}$)

T_S = radiator temperature ($^\circ\text{K}$)

Defining N_{ij} :

$$N_{ij} = \sigma A_i \epsilon_i B_{ij}$$

A_i = radiator area (cm^2) (207 cm^2)

ϵ_i = radiator emissivity (see Table 5.2.3-3)

B_{ij} = radiant interchange coefficient determined by Monte Carlo computer program

σ = Stefan-Boltzmann constant, (watts/ cm^2K^4)
($.573 \times 10^{-11}$ watts/ cm^2K^4)

Radiation coefficients were first calculated, and then the heat exchange between bodies was determined in the orbit analysis. A typical calculation for the radiation coefficient between the radiator and the sunshade is:

$$N_{ij} = (.573 \times 10^{-11})(207)(.77)(.0207)$$

$$N_{ij} = 1.891 \times 10^{-11} \text{ watts}/^\circ\text{K}^4$$

A similar calculation was performed for the antenna and solar panel infrared exchange.

The antenna and solar panel are two heat-transfer boundary conditions upon which some assumptions were made as to properties and temperatures, since this information was not available at the time of the analysis. Radiometric properties for the solar panel and antenna are presented in Table 5.2.3-3. A simple heat balance was performed separately on the solar panel and antenna for different positions in orbit. Both spacecraft (S/C) parts were assumed to be isothermal and unaffected by the earth viewing module or each other. The temperature histories of both S/C parts are presented in Table 5.2.3-5. Blockage of the solar energy by the antenna was assumed to be 25%; in other words, 75% of the sun's energy is transmitted through the antenna.

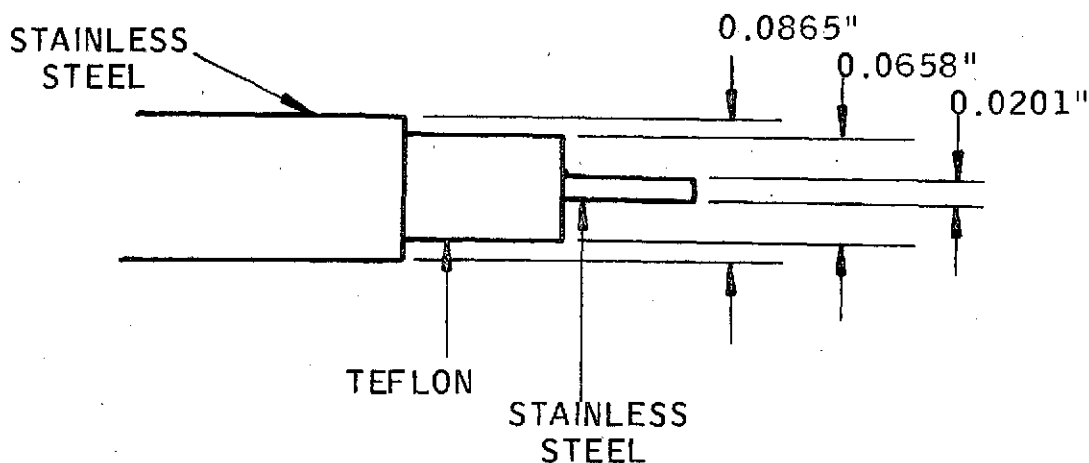
Detector bias power is 3 mw.

Total absorbed local oscillator power was assumed to be 20 mw. The rest of the incoming 85 milliwatts of local oscillator is reflected outside the germanium window by a reflecting conic surface (Figure 5.2.3-18). Details of the detector housing interface are shown in Figure 5.2.3-19. The cone angle (43.9°), shown in Figure 5.2.3-18, will reflect the incoming local oscillator beam ($f/\text{number} = 26$) across the active face of the detector to the diametrically opposite side of the cone, and then out of the system. The conic surface must have a low emissivity (e.g., gold $\epsilon \leq .03$) and must be highly specular ($\gamma > .98$). 30% of the local oscillator beam (25 mw) which is incident on the detector is absorbed. The other 17.5 mw is reflected diffusely; of this reflected energy 10 mw is absorbed in the housing and the rest reflected out. The smaller diameter edge of the reflecting cone should be as close to the active portion of the detector as is possible (within 0.0005"). The height and larger diameter are determined by the cone angle and the f/number of the local oscillator beam.

The mounting surface between the detector assembly and the radiator will have a 16 microinch finish and a flatness of 0.002 inches TIR. Temperature drop across the joint is expected to be 1°C or less for the expected bolt torques.

In the calculation of IR energy coming through the germanium window, it was assumed that all energy after getting through would be absorbed. It was assumed that the window would also act as a bandpass filter and allow only the 10.6μ energy $\pm 1.0\mu$ to pass through. The filter will reject energy from 2μ to 40μ except for the bandpass. The total energy absorbed is 2 mw.

Conduction of energy down the detector wire was calculated based on the following wire dimensions:



Pre-amplifier-Detector Coaxial Cable

A thermal conductivity (k) of $10 \text{ Btu/hr-ft-}^{\circ}\text{F}$ was used for stainless steel; for Teflon, a value $k = 0.12 \text{ Btu/hr-ft-}^{\circ}\text{F}$ was used. Total heat flow through the wire, assuming a 200°K temperature difference and a length of 12 in., was 20.6 mw.

A resistance-type temperature sensor will be mounted near the detector housing to monitor the housing's temperature. The heat leak down the two thermistor lead wires was calculated to be approximately 1 milliwatt. This calculation assumed a lead-wire length of 3 in., a wire outer diameter of 4 mils, and that the wire's material was stainless steel (thermal conductivity = $10 \text{ Btu/hr-ft-}^{\circ}\text{R}$).

Heat flow to the radiator through the mounting support had to be considered at two different times during the radiator's lifetime: first, during orbit acquisition, and second, during the orbit period. During orbit acquisition, the heat flow through the support must be reduced to allow the

radiator and the sunshade to cool down sufficiently in order to provide separation. A method which will provide adequate support during launch and yet permit the radiator and sunshield to cool down is shown in Figure 5.2.3-2. This simple means of minimizing heat flow is to reduce the contact area between the support and radiator or sunshade.

Serrations of the softer metal [i.e., the radiator (magnesium) or the sunshade (aluminum)], compared with serrations of the load support material (beryllium), is preferred by the Aerojet Structural Design Group.

In order to get the minimum area in contact, the worst spacecraft orientation was assumed (i.e., with the sun looking normal to the radiator). A heat balance was performed on the radiator and sunshade in conjunction with the information presented in Figure 5.2.3-20 to obtain the contact area percentage. (Interpretation of Figure 5.2.3-20 is as follows - consider the radiator as an example: for the radiator and support initially at 35°C, the radiator must cool to 13.6°C in order to relieve the preload and have a separation gap of 0.0005 inches.) Heat balance equations for the radiator and sunshade are:

$$\text{Radiator: } Q_{DS} + Q_{RS} + N_{R-S}(T_S^4 - T_R^4) + hA_c \eta_R (T_B - T_R) = N_{R-O} (T_R^4)$$

$$\text{Sunshade: } Q'_{DSI} + Q''_{DSI} + Q_{DSR} + hA_c \eta_S (T_B - T_S) = N_{S-O} (T_S^4) + N_{S-R} (T_S^4 - T_R^4)$$

where

$$Q_{DS} = \text{direct solar energy absorbed by radiator (1.74 watts)}$$

$$Q_{RS} = \text{reflected solar energy reflected by interior of sunshade absorbed by radiator (1.52 watts)}$$

$$N_{R-S} = \text{radiation coefficient from radiator to sunshade (1.9 x 10}^{-11} \text{ watts/}^\circ\text{K}^4\text{)}$$

$$N_{R-O} = \text{radiation coefficient from radiator to space (8.94 x 10}^{-11} \text{ watts/}^\circ\text{K}^4\text{)}$$

$$Q'_{DSI} = \text{direct solar energy on inside of sunshade which bounces once to radiator (3.09 watts)}$$

$$Q''_{DSI} = \text{direct solar on inside of sunshade which bounces twice or more to radiator (0.917 watts)}$$

- Q_{DSR} = direct solar energy on sunshade radiator (6.32 watts)
 N_{S-O} = radiation coefficient from shield to space; combines inside surface and radiator flange (3.47×10^{-9} watts/ $^{\circ}K^4$)
 N_{S-R} = same as N_{R-S} above
 h = contact coefficient (0.114 watts/ $cm^2^{\circ}K$)
 A_c = total contact area (54.6 cm^2)
 η_R = fraction of contact area of radiator
 η_S = fraction of contact area of sunshade
 T_B = support temperature (308 $^{\circ}K$, see Figure 5.2.3-20)
 T_S = sunshade temperature (287.3 $^{\circ}K$, see Figure 5.2.3-20)
 T_R = radiator temperature (287 $^{\circ}K$, see Figure 5.2.3-20)

This balance assumes that heat flow through low-conductance spring ball supports, heat flow through the superinsulation blankets, local oscillator heat dissipation, heat conduction through the coaxial cable and temperature sensor wire, and infrared and reflected solar energy from the antenna and solar panel are all small in comparison to the above and can be neglected. A steady-state solution was assumed because of the small time constants.

The above values were then substituted into the heat-balance equations. These equations were solved simultaneously by iteration until the solution for η_R and η_S converged.

The results are that the minimum area percent for the radiator is 2%, while for the sunshade, it is 10%; or in terms of the width of serration, the following formula can be used:

$$\eta_{A_T} = 2 \text{ NWL}$$

where

η = area fraction in contact

A_T = total area, in.² (the total contact area for the radiator or sunshade is 8.75 in.² for two support surfaces consisting of a 0.125 chamfer)

2 = number of mating surfaces

N = number of serrations (let $N = 36$, i.e., one every 10°)

W = width of serration (in. - to be calculated)

L = length of serration ($L = 0.176$ in.)

For the radiator

$$\eta = 0.02$$

Therefore

$$0.02 (8.75) = 2(36)(W)(0.176)$$

$$W = 0.0138 \approx 0.014 \text{ in.}$$

For the sunshade,

$$\eta = 0.10$$

Therefore

$$W = 0.070 \text{ in.}$$

The serrations can be offset by 5° between the two contact surfaces of either the radiator or sunshade.

During the orbit period, structural support will be provided by three stainless steel balls and springs (as shown in Figure 5.2.3-2). The socket for the balls will be serrated to provide a good thermal resistance. They and their mating surfaces must be very hard in order to minimize contact area. The conductance through the three-ball supports was calculated, using the following formulas:

$$C_o = 3 C_1$$

where

C_o = overall conductance (watts/°K)

C_1 = conductance for one ball support (watts/°K)

and

$$C_1 = \frac{C_B}{2}$$

where

C_B = conductance for support on one side of a ball (watts/°K)

Therefore

$$C_B = 3hA$$

where

h = contact coefficient (assume .0821 watts/cm²°K)

A = contact area for one of 3 support pads (cm²)

but

$$A = \frac{\pi d^2}{4} = \frac{\pi(5.8 \times 10^{-3})^2}{4} = 268 \times 10^{-6} \text{ cm}^2$$

$$C_B = 3(8.21 \times 10^{-2})(268 \times 10^{-6})$$

$$C_B = .663 \times 10^{-4} \text{ watts/°K}$$

or

$$C_o \cong 1 \times 10^{-4} \text{ watts/°K}$$

Heat flow through this type of support based on a conductance of 0.0001 watts/°K and a temperature difference of 180°K is 18 mw of thermal energy.

Preliminary structural analyses have been performed to verify that the radiator/sunshade system meets the flight requirements. The primary

structural requirement is that the detector/mixer alignment must be retained during orbital operation. The preliminary analysis is based on the temperature variations of the spacecraft and experiment ($20^{\circ}\text{C} = 15^{\circ}\text{C}$) which result in stresses greater than those resulting from the launch environment. Also, these stresses are lower than the micro yield strength (1-microinch offset yield strength) of the material which will preclude permanent deformation of the radiator and, thus, the detector/mixer alignment. Further analysis will be required to determine whether the three-point retention of the radiator is sufficient for the detector/mixer to remain in alignment. It is anticipated that there will be no problems because the operational loads are of considerably lesser magnitude. Details of the preliminary analyses are included in Appendix H.

Preliminary structural calculations have indicated that a natural frequency of the radiation cooler will be within the range of 300 ± 50 Hz, and that there is a potential amplification factor on the order of 5. In light of this, the engineering vibration tests will be performed on the mixer assembly during development to the levels presented in NASA Specification S-320-ATS-2B, with the following exception:

The qualification sinusoidal vibration spectrum should be increased to 60 g acceleration between 100 and 200 Hz, and to 25 g acceleration between 200 and 400 Hz (see Figure 5.2.3-21).

Note that the magnified effect of the sinusoidal vibration will be transmitted to the mixer assembly, mounted on the radiator, only if the spacecraft structure has an equivalent resonant frequency. It is believed that this is unlikely, but when the resonant frequency has been more closely determined, the information will be transmitted to NASA so that the spacecraft effect can be analyzed in depth to validate this. If the detailed analyses results in other modifications of the vibrational amplification transmitted to the mixer assembly, the vibration test exception noted above will be adjusted.

In addition, potential methods of damping the resonant frequency during launch are being investigated.

Heat conducted through the superinsulation blanket between the radiator and the S/C heat sink was calculated based on an in-situ effective

thermal conductivity ($k_{\text{eff}} = 2 \times 10^{-4}$ Btu/hr-ft- $^{\circ}$ R. Laboratory values for $k_{\text{eff}} = 2 \times 10^{-5}$ Btu/hr-ft- $^{\circ}$ F; however, the effectiveness of the blanket was decreased by a factor of 10 in order to account for blanket imperfections and radiation seals. A 7-in. effective diameter was assumed for the blanket and a temperature difference across the blanket of 200 $^{\circ}$ K was also assumed. The result is a 6-mw heat load on the radiator.

5.2.3.6 Sunshade Analysis

The exterior surface of the sunshade (Figure 5.2.3-13) is covered with a 1/4-in. blanket (i.e., 15 to 20 layers) of superinsulation (1/4-mil aluminized Mylar). The purpose of this blanket is to reduce the radiation effects of the spacecraft and of the sun. The outer layer of the blanket will be a 6-mil layer of aluminized Teflon (Teflon side facing outward). This outer layer will act as a second-surface mirror (i.e., a mirror with low solar absorptance and high infrared emittance) to reduce outer-surface blanket temperatures, and to protect the inner layers of the blanket from the degrading effects of the space environment. (Teflon has excellent outgassing characteristics and it is very stable in space.) Heat input to the shade, through the insulation blanket, was calculated for an in-situ blanket with an effective conductivity of ($k_{\text{eff}} = 2 \times 10^{-4}$ Btu/hr-ft 2 - $^{\circ}$ F; a total surface area of 1.63 ft 2 ; and a temperature difference of 240 $^{\circ}$ R. Heat input to the sunshade is 20 mw.

A high thermal resistance between the support and the sunshade is desired so that the sunshade's temperature is minimized. The support scheme for the sunshade is the same as for the radiator. Conductance values are the same (1×10^{-4} watts/ $^{\circ}$ K), because the same size support is used. The heat load to the sunshade via the supports is expected to be 12 mw for a 120 $^{\circ}$ K temperature difference.

The sunshade's structural material is 6061-T651 aluminum. Aluminum ($k = 99$ Btu/hr-ft- $^{\circ}$ R) was chosen for the following reasons: (1) it has a high strength to weight ratio; (2) it is readily available; (3) it has a high thermal conductivity; (4) electroless nickel can be readily applied to it; (refer to following explanation on coating finish); (5) it is low cost; (6) it can be machined readily; and (7) it has a high thermal coefficient of expansion. The

sunshade interior coating must be very specular; it must have a low solar absorptance and a low infrared emittance. One such coating is vapor-deposited aluminum on a electroless nickel substrate. Electroless nickel was chosen because it is a very hard metal which can be polished to the desired surface finish.

Discussions with Aerojet's Optical Coating Laboratory, the Aerojet Optical Design Group and Aerojet Manufacturing that, for an ensured high degree of specularity in the visible range, an internal surface ought to be ground and polished to a 60-40 scratch and dig tolerance (per AGC-STD-2040); no grayness or stain should be visible.

The vapor-deposited aluminum coating which is applied to the interior surface of shade, will meet the following requirements:

- Vapor deposition pressure will be $\leq 10^{-6}$ Torr
- Deposition rate will be greater than 1000 Å per sec, 600 to 1000 Å thick
- Aluminum will be applied in a single pass; aluminum purity to be > 99.99%
- Vapor incidence angle will be $< 30^\circ$
- The coating will be continuous with a bright, lustrous finish and a uniform, mirror-like specular appearance. The coating will be essentially free from yellow or blue discoloration, with no visible change in color. The coating will be free from streaks, windows, pinholes, blisters or other defects

A necessary piece of information for manufacturing is the waviness requirement for the inside surface of the sunshade. This information was obtained through the following argument. What deviation from the circular arc can the surface make so as to reflect the incoming rays (at the extreme ray angle) to the radiator edge, rather than some distance above the radiator? A simple geometrical calculation established the waviness height to be ≤ 0.002 in. per any 1.0-in. movement along the 23.384-in. radius circular arc.

The "wineglass" shape for the sunshade is designed to reflect all the solar energy impinging on the internal surface to an area approximately 1.5 in. in diameter diametrically opposite the illuminated interior, and approximately 1 in. to 1.5 in. above the radiator. A calculation was made to

determine if localized heating on such a small area could produce large temperature gradients in the sunshade itself. The solar heating was assumed to be uniformly distributed over a 1-in.-dia area. Heat was assumed to be conducted radially outward from this area. The sunshield thickness was assumed to be 0.09 in. The material thermal conductivity (k) is 99 Btu/hr-ft-°R. The temperature difference was calculated to be 10°F.

Reduction in the reflection of energy, from the edge (or lip) where the sunshade interior joins the sunshade radiator, is accomplished by extending the interior surface to the top of the back surfaced mirror (see Figure 5.2.3-12 for details). The top edge of this extension is rounded to reduce its influence on the radiator.

The total absorbed solar energy on the interior sunshade surface was approximated by use of the following formula:

$$Q_{DS} = n F_s(\rho) A_T S \alpha_s$$

where

Q_{DS} = solar energy absorbed by interior of sunshade (watts)

$n = 2$ (multiplication factor to account for 2 bounce system)

$F_s(\rho)$ = solar shape factor which is a function of orbital position (ρ) (Table 5.2.3-6)

A_T = total area of the interior of sunshade (cm^2) = 1283 cm^2

S = solar constant (watts/cm^2) = 0.14 watts/cm^2

α_s = solar absorptance of sunshade = 0.1

The solar shape factor is the ratio of projected area to total area for the interior of the sunshade. The solar shape factor was determined for seven orbital positions (Table 5.2.3-6) for the tilted sunshade. The Monte Carlo Radiant Interchange Computer Program was used to determine these values. The solar intensity (S) was reduced by 25% for the orbit angles (ρ) of 0° and 30°, because the antenna blocks the sun.

Reflected solar energy from the antenna and solar panel absorbed by the sunshade interior was also determined through the use of the Monte Carlo computer program. Calculations were performed in the same manner as for the radiator.

Reflected solar energy to the sunshade interior is: $Q = 0.053$ watts from the antenna, and $Q = 0.0063$ watts from the solar panel. Again, these values were held constant since they were so small.

The amount of direct solar energy absorbed by the sunshade radiator as a function of orbit position is presented in Table 5.2.3-7. Reflected solar energy from the spacecraft EVM is zero, because the sunshade radiator does not see it.

Reflected solar energy from the antenna is 0.0346 watts, while from the solar panel, it is 0.0054 watts.

5.3.2.6.1 Temperature Analysis For Sun Normal to Radiator

Temperatures were calculated for the radiator and sunshade when the sun rays are normal to the radiator (divergence of the sun's rays was neglected). These temperatures are a result of the heat balance on both the radiator and sunshade. Heat balance equations for the radiator and sunshade are:

$$\text{Radiator: } Q_{DS} + Q_{RS} + N_{R-S} (T_S^4 - T_R^4) = N_{R-O} (T_R^4)$$

$$\text{Sunshade: } Q'_{DSI} + Q''_{DSI} + Q_{DSR} = N_{S-O} (T_S^4) + N_{S-R} (T_S^4 - T_R^4)$$

where

Q_{DS} = direct solar energy absorbed by radiator, 1.74 watts

Q_{RS} = solar energy reflected by interior of sunshade absorbed by radiator, 1.52 watts

N_{R-S} = radiation coefficient from radiator to sunshade, 1.9×10^{-11} watts/ $^{\circ}\text{K}^4$

N_{R-O} = radiation coefficient from radiator to space, 8.94×10^{-11} watts/ $^{\circ}\text{K}^4$

Q'_{DSI} = direct solar energy on inside of sunshade which bounces once to radiator, 3.09 watts

Q''_{DSI} = direct solar on inside of sunshade which bounces twice or more to radiator, 0.917 watts

Q_{DSR} = direct solar energy on sunshade radiator, 6.32 watts

N_{S-O} = radiation coefficient from shade to space; combines inside surface and radiator flange, 3.47×10^{-9} watts/ $^{\circ}K^4$

N_{S-R} = same as N_{R-S} , above

This balance assumes that heat flow through low-conductance, spring-ball supports, heat flow through the superinsulation blankets, local oscillator heat inputs, conduction through coaxial cable and temperature sensor wires, infrared and reflected solar energy from antenna and solar panel are all small and can be neglected. A steady-state solution was assumed because of the small time constants.

The above values were then substituted into the heat balance equations. These equations were solved simultaneously by iteration until a solution for the temperatures converged. The results indicate that the maximum radiator temperature is $245^{\circ}K$ and the maximum sunshade temperature is $256^{\circ}K$. At these temperatures, the radiator and sunshade will not expand enough to make contact with the beryllium support.

5.2.3.6.2 Sunshield/Radiator Orbit Analysis

In order to determine the sunshade radiator width, temperature histories of the sunshade/radiator combination were made parametrically. A plot (shown in Figure 5.2.3-3) was made of the maximum and minimum radiator temperatures at the summer and winter solstices vs sunshade radiator lip width. The 3-in. width was chosen because it is also the maximum size lip that will fit in the allotted volume.

An orbit analysis was performed on the radiator/sunshade combination for two times of the year: summer solstice and winter solstice. These times of year were chosen because they represent warmest and coldest orbital inclinations. The temperatures and, thereby, the heat loads were approximately determined by a steady-state analysis for each point in orbit utilizing the steady-state computer program in conjunction with the IBM 360/65 computer.

This assumption is justifiable because of the low thermal masses and low rates of change. The spacecraft temperature was kept constant at 300°K. Temperature results were obtained for the 0° to 180° orbit positions.

Temperature history results for the radiator and sunshade at summer and winter solstice are presented in Figures 5.2.3-1 and -22, respectively. In addition, heat flow summary tables (Tables 5.2.3-8 and 5.2.3-9) for the radiator and sunshade are presented for the 180° orbital position. This position was chosen because the solar loads to sunshade and radiator are the largest. These tables allow a comparison of the heat loads on the radiator and sunshade.

5.2.3.7 Tests to be Conducted

In order to ensure that the design of the radiator/sunshade will work and the validity of the assumptions are verified, several tests are to be conducted to eliminate areas of uncertainty. These tests are:

1. Determine radiator and sunshade three ball support conductance (Section 5.3.3.1)
2. Verify that the sunshield and radiator will contract away from the support (Section 5.3.3.1)
3. Determine effective conductivity of superinsulation blanket for radiator (Section 5.3.3.1)
4. Ensure that the detector remains in the required position tolerances (Section 5.3.3.2)
5. Determine the temperature drop across the detector housing/radiator interface (Section 5.3.3.2)
6. Verify the sunshade interior contour and specularly (Section 5.3.3.3)
7. Determine the radiometric properties of the thermal control coatings and outer wrap of sunshade blanket used to regulate the heat transfer of the subassemblies (Section 5.3.3.4)

REFERENCES, SECTION 5.2.3

1. R. V. Annable et al., "A Day-Night High Resolution Infrared Radiometer Employing Two-Stage Radiant Cooling - Part I - Two-Stage Radiant Cooler." Contract NAS 5-10113 (final report), prepared by ITT Industrial Laboratories, Ft. Wayne, Ind. (ITTIL No. 1055) for NASA, Goddard Space Flight Center, Greenbelt, Maryland, 11 December 1967.
2. ITT Industrial Laboratories: "A Day-Night High Resolution Infrared Radiometer Employing Two-Stage Radiant Cooling - Part II - Breadboard Day-Night Radiometer," Contract NAS 5-10113 (final report), prepared by ITTIL for NASA, Goddard Space Flight Center, Greenbelt, Maryland, 28 December 1967.
3. F. Gabron and R. Merrian, "Design Study of Passive Detector Cooling Techniques," Contract NAS 5-21009 (final report), prepared by Arthur D. Little, Inc., Cambridge, Mass. for NASA, Goddard Space Flight Center, Greenbelt, Maryland, 29 August 1969 (C-71494).
4. "Radiation Cooler Design," XIII IR ADD-ON, Santa Barbara Research Center, Santa Barbara, Calif., 27 April 1970.
5. J. H. McElroy et al., "ATS-F Laser Communication Experiment Infrared Mixer and Radiation Cooler Subsystem," First Summary Design Report, Goddard Space Flight Center, Greenbelt, Maryland, April 1969. X-524-69-227.
6. S. H. Lin and E. M. Sparrow, "Radiant Interchange Among Curved Specularly Reflecting Surfaces - Application to Cylindrical and Conical Cavities," J. of Heat Transfer, May 1965, pp. 299-307.
7. "Design Techniques for Passive Radiative IR Detector Coolers." Proposal by Aerojet-General Corp. to Aeronautical Systems Division (AFSC), February 1969. AV(N)-69005.
8. N. Fuschillo, et al., "Radiation Cooled Cryostat," patent disclosure filed 17 June 1966, approved 21 January 1969.
9. J. S. Buller, "Radiation Cooler for Use in Space," patent disclosure filed 25 July 1966, approved 21 January 1969.
10. R. V. Annable, et al., "A Day-Night High Resolution Infrared Radiometer Employing Two-Stage Radiant Cooling," (1 October 1966 - 1 January 1967), Contract NAS 5-10113 (third quarterly report), prepared by ITTIL of Ft. Wayne, Ind. (ITT No. 67-1002) for NASA, Goddard Space Flight Center, Greenbelt, Maryland, 5 January 1967.

REFERENCES, SECTION 5.2.3 (cont.)

11. R. V. Annable et al., "A Day-Night High Resolution Infrared Radiometer Employing Two-Stage Radiant Cooling," (24 June 1966 - 1 October 1966), Contract NAS 5-10113, second quarterly report, prepared by ITT Industrial Laboratories, Ft. Wayne, Ind. (ITTIL No. 66-1051) for NASA, Goddard Space Flight Center, Greenbelt, Maryland, 15 October 1966.
12. P. C. Murray et al., "High Resolution Nighttime Cloud-Cover Radiometer," (April 1, 1966 to July 1, 1966), Contract NAS 5-668, Quarterly Report XIX, prepared by ITT Industrial Laboratories, Ft. Wayne, Ind., for Planetary Radiations Branch, Goddard Space Flight Center, Greenbelt, Maryland, 1 March 1967.
13. H. E. Bennett et al., "Infrared Reflectance of Evaporated Aluminum Film," J. of the Optical Society of America, Vol. 52, No. 11, pp. 1245-50, November 1962.
14. H. E. Bennett et al., "Infrared Reflectance of Aluminum Evaporated in Ultra-High Vacuum," J. of the Optical Society of America, Vol. 53, No. 9, pp. 1089-95, September 1963.
15. G. Hass et al., "Mirror Coatings for Low Visible and High Infrared Reflectance," Reprinted from J. of the Optical Society of America, Vol. 46, No. 1, pp. 31-35, January 1956.
16. G. Hass, et al.: Reflectance, Solar Absorptivity, and Thermal Emissivity of SiO₂-Coated Aluminum. Applied Optics, Vol. 8, No. 2, pp. 275-81, February 1969.
17. D. K. Edwards et al., "Spectral and Directional Thermal Radiation Characteristics of Selective Surfaces for Solar Collectors," Reprinted from Solar Energy, Vol. VI, No. 1, pp. 1-8, January 1962.
18. G. Hass and C. D. Salzberg, "Optical Properties of Silicon Monoxide in the Wavelength Region from 0.24 to 14.0 Microns," J. of the Optical Society of America, Vol. 44, No. 3, pp. 181-7, March 1954.
19. C. Hilsum, "Infrared Absorption of Thin Metal Films," J. of the Optical Society of America, Vol. 44, No. 3, pp. 188-91, March 1954.
20. W. B. Fussell et al., "A Dynamic Thermal Vacuum Technique for Measuring the Solar Absorption and Thermal Emittance of Spacecraft Coatings," Meas. of Thermal Radiation Properties of Solids, NASA SP-31, pp. 83-101.

REFERENCES, SECTION 5.2.3 (cont.)

21. "Enhanced Silver Coating," Specification No. 1020, Chromatix, Mountain View, Calif.
22. "Low Solar Absorptance and Emittance Surfaces Utilizing Vacuum Deposited Techniques," Report No. CR-73039, Contract NAS 2-3063, prepared by Lockheed Palo Alto Research Laboratory for NASA, Ames Research Center, Moffett Field, Calif. October 1966.
23. J. Cox and G. Hass, "Antireflection Coatings for Optical and Infrared Optical Materials," Physics of Thin Films, Vol. 2, pp. 239-303, 1964.
24. L. F. Drummeter and G. Hass, "Solar Absorptance and Thermal Emittance of Evaporated Coatings," Physics of Thin Films, Vol. 2, pp. 305-358, 1964.

TABLE 5.2.3-1

TYPICAL THERMAL CONTROL COATING RADIOMETRIC PROPERTIES

<u>Thermal Control Coating</u>	<u>Absorptance (α_s)⁽¹⁾</u>	<u>Total Hemispherical Emittance (ϵ)⁽²⁾</u>
Vapor Deposited Gold	0.20 <u>+0.02</u>	0.03 <u>+0.02</u>
Vapor Deposited Silver	0.05 <u>+0.02</u>	0.03 <u>+0.02</u>
Enhanced Vapor Deposited Silver	~ .04	0.03 <u>+0.02</u>
Back Surface Mirror	0.06 <u>+0.01</u>	0.80 <u>+0.02</u>
Vapor Deposited Aluminum	0.12 <u>+0.02</u> ⁽³⁾	0.03 <u>+0.02</u>

(1) α_s dependent upon metal film, substrate finish and deposition parameters.

(2) Emittance varies with dielectric thickness. Normal emittance lower than total hemispherical.

(3) A low value of 0.10 obtained for an optically lapped surface.

TABLE 5.2.3-2

POINTS TO DESCRIBE "WINE GLASS" SHAPE
 REFER TO FIGURE 5.2.3-16 FOR COORDINATE SYSTEM ORIGIN

X = 5.000000E-02	Y = 1.282436E-01
X = 9.999996E-02	Y = 2.592216E-01
X = 1.499999E-01	Y = 3.930657E-01
X = 1.999999E-01	Y = 5.299185E-01
X = 2.499998E-01	Y = 6.699351E-01
X = 2.999998E-01	Y = 8.132840E-01
X = 3.499997E-01	Y = 9.601490E-01
X = 3.999997E-01	Y = 1.110731E+00
X = 4.499996E-01	Y = 1.265253E+00
X = 4.999996E-01	Y = 1.423957E+00
X = 5.499995E-01	Y = 1.587116E+00
X = 5.999995E-01	Y = 1.755028E+00
X = 6.499994E-01	Y = 1.928031E+00
X = 6.999994E-01	Y = 2.106502E+00
X = 7.499993E-01	Y = 2.290866E+00
X = 7.999993E-01	Y = 2.481607E+00
X = 8.499992E-01	Y = 2.679278E+00
X = 8.999992E-01	Y = 2.884517E+00
X = 9.499991E-01	Y = 3.098065E+00
X = 9.999991E-01	Y = 3.320791E+00
X = 1.049998E+00	Y = 3.553726E+00
X = 1.099997E+00	Y = 3.798107E+00
X = 1.149996E+00	Y = 4.055440E+00
X = 1.199995E+00	Y = 4.327592E+00
X = 1.249995E+00	Y = 4.616916E+00
X = 1.299994E+00	Y = 4.926453E+00
X = 1.349993E+00	Y = 5.260249E+00
X = 1.399992E+00	Y = 5.623876E+00
X = 1.449992E+00	Y = 6.025379E+00
X = 1.499991E+00	Y = 6.477099E+00
X = 1.549990E+00	Y = 6.999675E+00
X = 1.599989E+00	Y = 7.632408E+00
X = 1.649989E+00	Y = 8.468520E+00
X = 1.699988E+00	Y = 9.862215E+00

Note: R = 4.5 inches - this defocuses the reflected sun's energy.

TABLE 5.2.3-3

RADIOMETRIC PROPERTIES OF THERMAL CONTROL SURFACES
WHICH AFFECT THE RADIATOR/SUNSHADE DESIGN

Surface Coating	Solar Absorptance (α_s)	Hemispherical Emittance (ϵ)	Specular Component of Reflection-Solar Wavelength Spectrum	Specular Component of Reflection-IR Wavelength Spectrum
Back Surface Mirrors ⁽¹⁾ (Radiator and Sunshade Radiator)	0.06	0.77 ⁽²⁾	0.95	0.0
Vapor Deposited Aluminum ⁽⁴⁾ (Sunshade Interior)	0.10	0.03	0.98	0.98
Solar Cells (Solar Panel)	0.71	0.81	0.0	0.0
Wire Mesh (Antenna)	0.4 ⁽³⁾	0.4 ⁽³⁾	0.0	0.0
White Paint (North Face EVM)	0.21	0.85	0.0	0.0

(1) Includes gaps in mirrors.

(2) At 100°K; 0.80 at ambient.

(3) Assumed values.

(4) Applied to an optically lapped surface.

TABLE 5.2.3-4

SOLAR SHAPE FACTOR AND DIFFUSELY REFLECTED SOLAR ENERGY
 ABSORBED ON THE RADIATOR VS ORBITAL POSITION

<u>ρ (deg)</u>	<u>$F_{SI}(\rho)$</u>	<u>Q_{RS} (watts)</u>
0	0.100	0.000845
30	0.110	0.000931
60	0.156	0.00176
90	0.211	0.00238
120	0.256	0.00288
150	0.300	0.00338
180	0.301	0.00339

ρ - orbital position (see Figure 5.2.3-10).

$F_{SI}(\rho)$ - solar shape factor for sunshade interior.

Q_{RS} - diffusely reflected solar energy absorbed on the radiator.

TABLE 5.2.3-5

TEMPERATURE OF ANTENNA AND SOLAR PANEL
FOR VARIOUS POSITIONS IN ORBIT - SOLSTICE

<u>ρ (deg)</u>	<u>Antenna Temperature (°K)</u>	<u>Solar Panel Temperature (°K)</u>
0	355	272
30	343	272
60	299	255
90	182	212
120	299	236
150	343	289
180	355	306

ρ - orbital position as defined in Figure 5.2.3-10

Assumptions:

- (1) Isothermal antenna and solar panel.
- (2) No influence from spacecraft EVM or each other.

TABLE 5.2.3-6

SUNSHADE SOLAR SHAPE FACTOR SUMMER SOLSTICE ORBIT

<u>ρ, deg</u>	<u>$F_s(\rho)$</u>	<u>Q_{DS}, watts</u>	<u>ρ, deg</u>	<u>$F_s(\rho)$</u>	<u>Q_{DS}, watts</u>
0	0.100	2.70	120	0.256	9.20
30	0.110	2.98	150	0.300	10.80
60	0.156	3.62	180	0.301	10.84
90	0.211	7.60			

TABLE 5.2.3-7

RADIATOR SOLAR SHAPE FACTOR SUMMER SOLSTICE ORBIT

<u>ρ, deg</u>	<u>$F_s(\rho)$</u>	<u>Q, watts</u>	<u>ρ, deg</u>	<u>$F_s(\rho)$</u>	<u>Q, watts</u>
0	0.191	1.42	120	0.520	3.85
30	0.220	1.63	150	0.600	4.45
60	0.301	2.23	180	0.630	4.66
90	0.410	2.94			

TABLE 5.2.3-8

RADIATOR HEAT LOADS AT 180° ORBITAL POSITION
SUMMER SOLSTICE

<u>Heat Source</u>	<u>Heat Load (milliwatts)</u>
Reflected Solar from Sunshade	3.39
Reflected Solar from Antenna	0.9
Reflected Solar from Solar Panel	0.07
IR from Sunshade	77.5
IR from Antenna	2.6
IR from Solar Panel	0.3
I ² R (Detector Bias)	3
Local Oscillator	20
Conduction Wire	22
IR from G _e Window	2.1
Mounting Support	18.0
Insulation Blanket	6.0
Wires: Temperature Sensor	2.0

TABLE 5.2.3-9

SUNSHADE HEAT LOADS AT 180° ORBITAL POSITION
SUMMER SOLSTICE

<u>Heat Source</u>	<u>Heat Load, watts</u>
Direct Solar	
Interior	10.84
S/S Radiator	4.66
Reflected Solar from Antenna	
Interior	0.053
S/S Radiator	0.0346
Reflected Solar from Solar Panel	
Interior	0.0063
S/S Radiator	0.0054
IR from Antenna	
Interior	0.029
S/S Radiator	0.154
IR from Solar Panel	
Interior	-0.0002
S/S Radiator	-0.001
Support Conduction	0.018
Insulation Blanket	0.020

- SUPER INSULATION OUTSIDE SHIELD
- THREE INCH SUNSHIELD RADIATOR
- SUNSHIELD RADIATOR COATED WITH BACK SURFACE MIRRORS
- "WINEGLASS" SHAPED INTERIOR

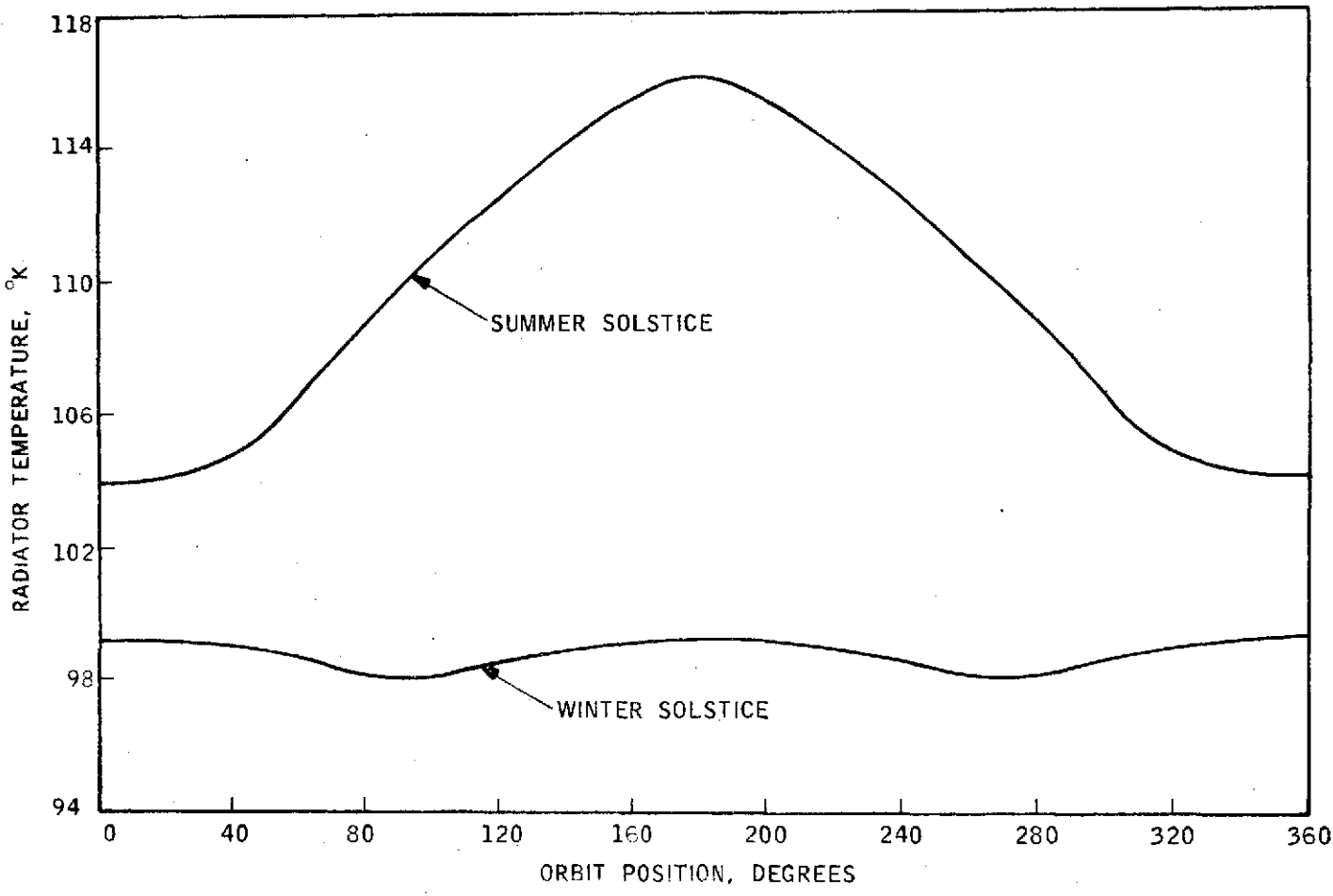


Figure 5.2.3-1

LCE RADIATOR TEMPERATURE HISTORY

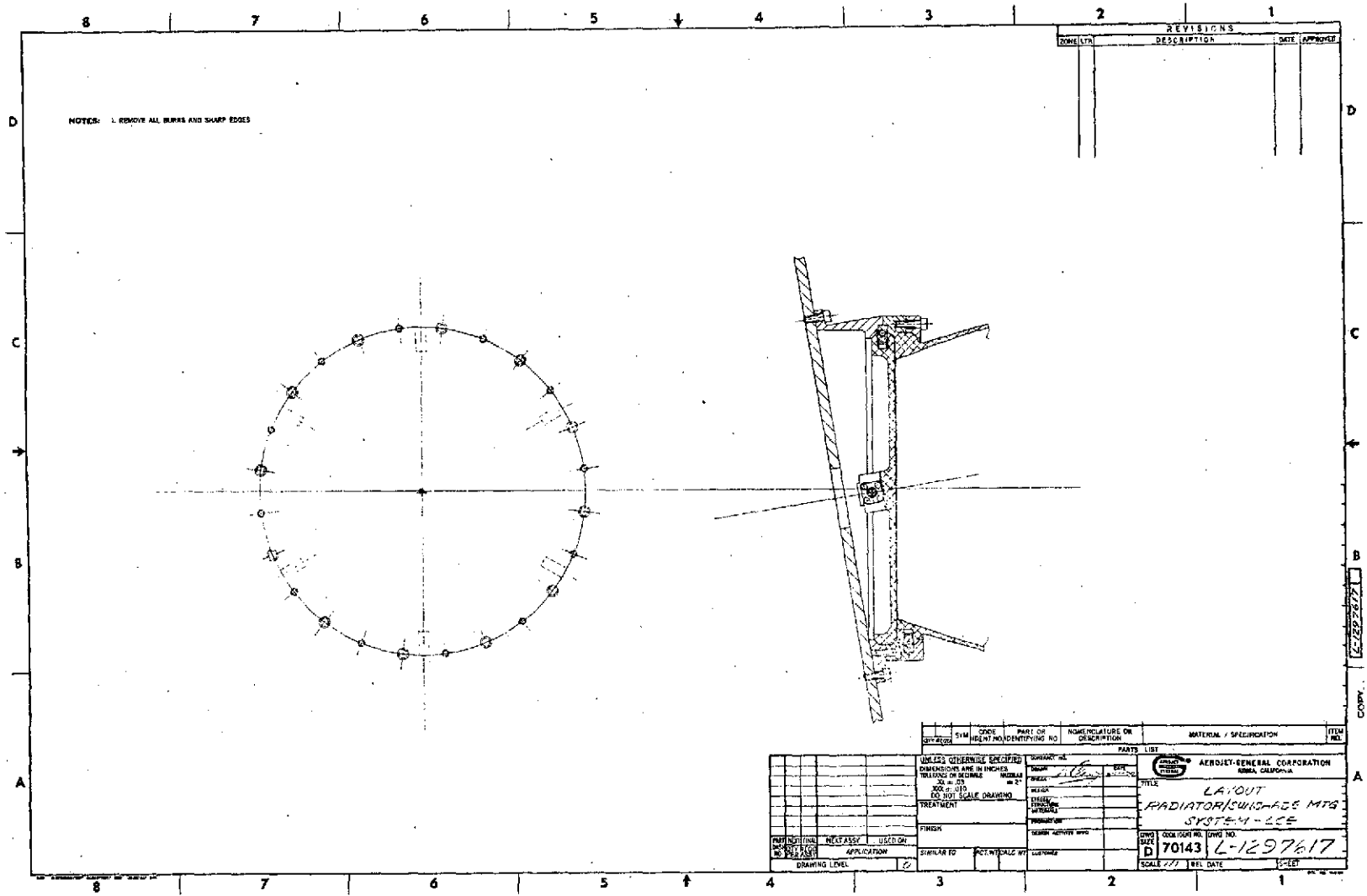
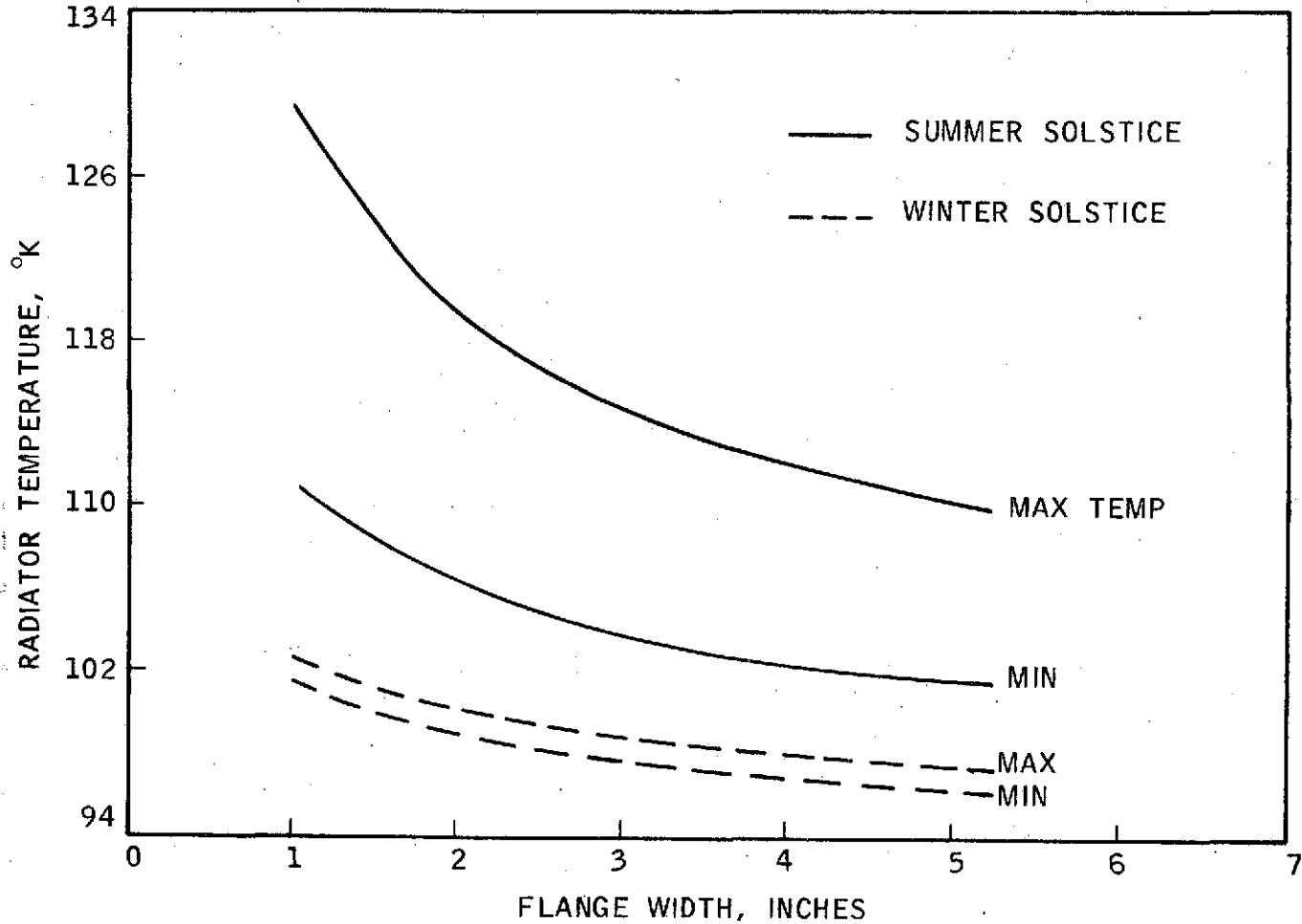


Figure 5.2.3-2

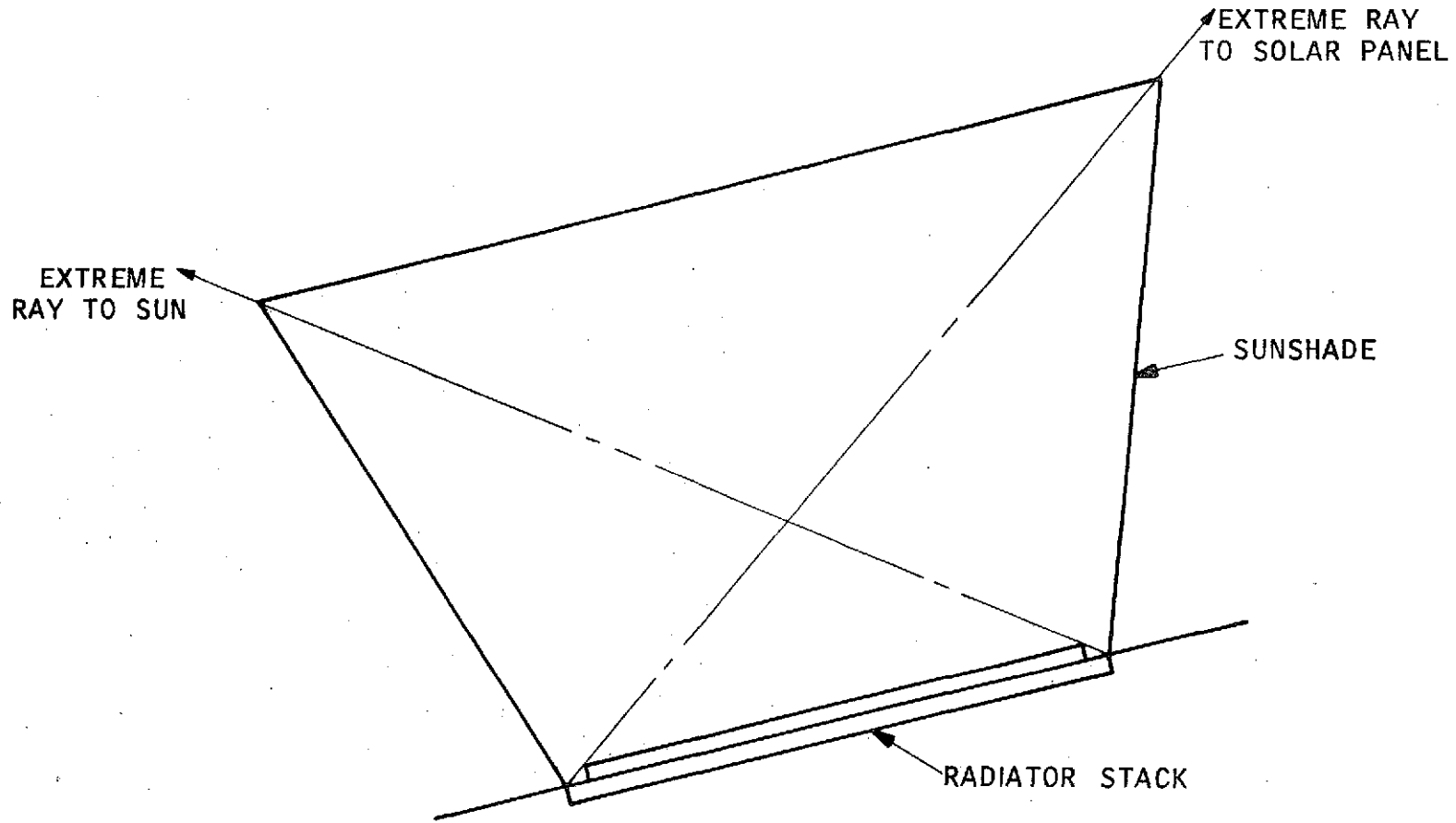
NOTE: "WINEGLASS" SHAPED INTERIOR SUPERINSULATION ON OUTSIDE SUNSHADE RADIATOR FLANGE COATED WITH BACK SURFACE MIRRORS.



LCE RADIATOR TEMPERATURE VS. SUNSHADE RADIATOR FLANGE WIDTH

Figure 5.2.3-3

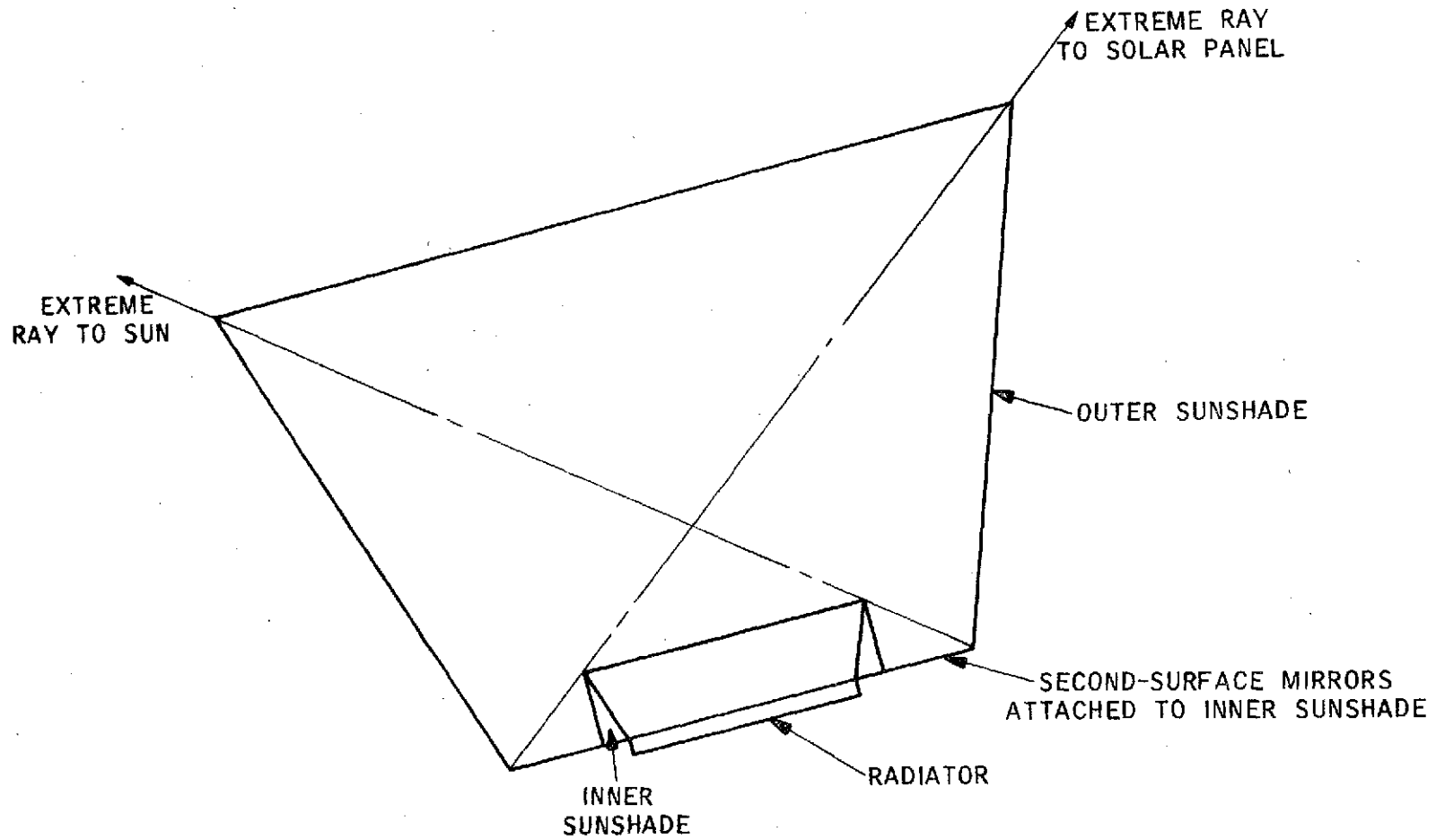
Report No. 4035, Vol. I, Part I



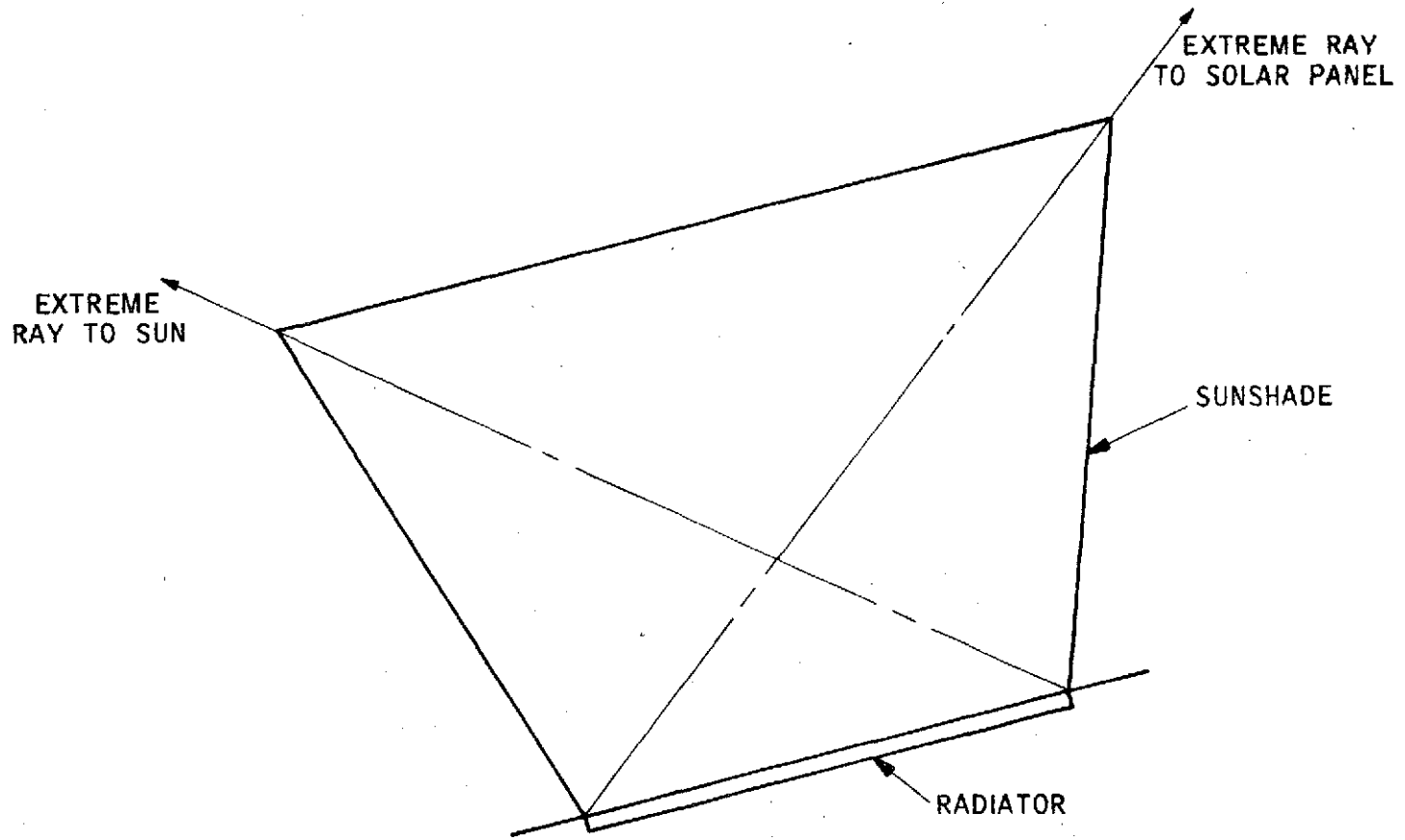
STACKED RADIATOR, ONE-STAGE SUNSHADE

Figure 5.2.3-4

Figure 5.2.3-5



ONE-STAGE RADIATOR, TWO-STAGE SUNSHADE



SINGLE RADIATOR, SINGLE SUNSHADE

Figure 5.2.3-6

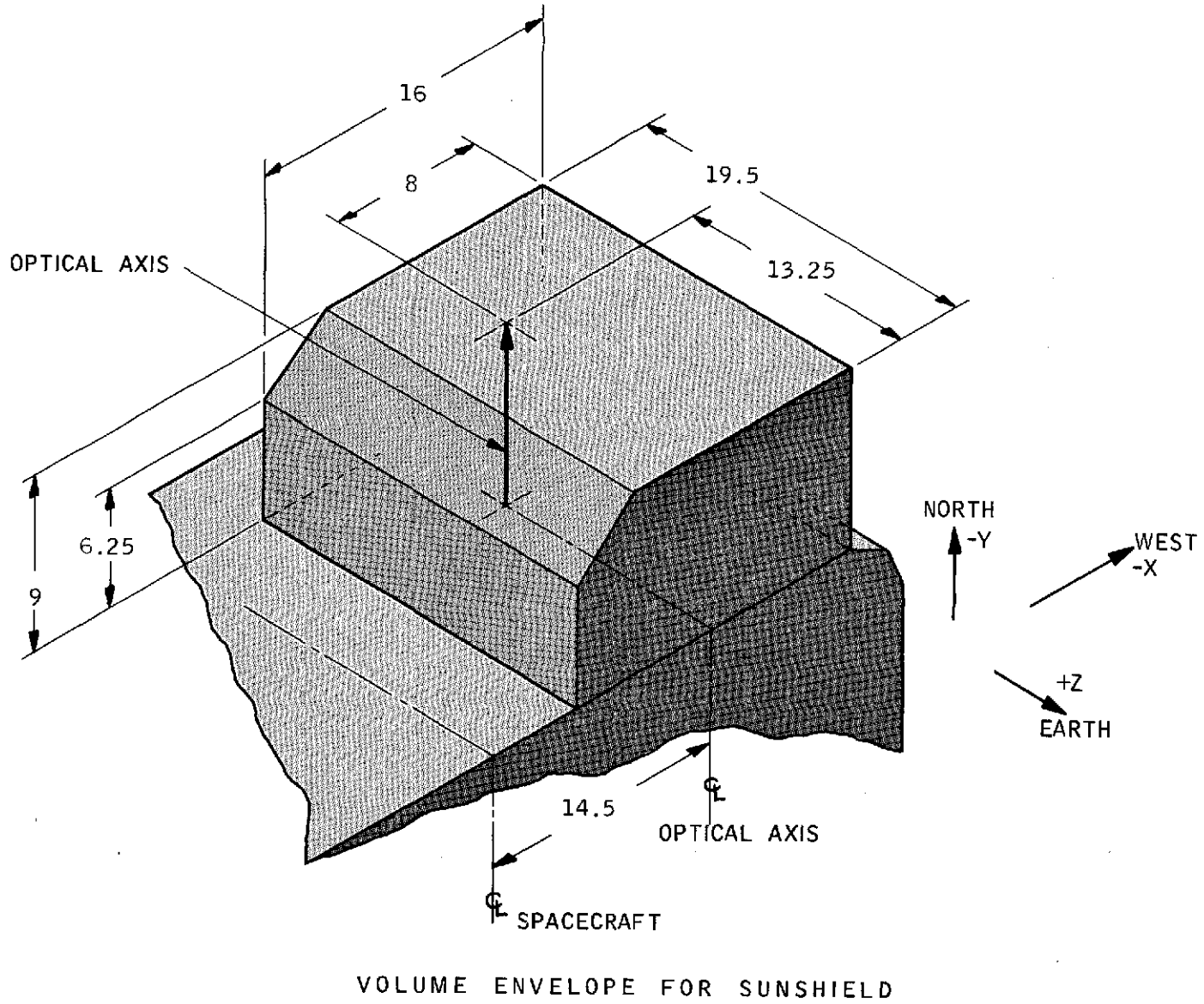
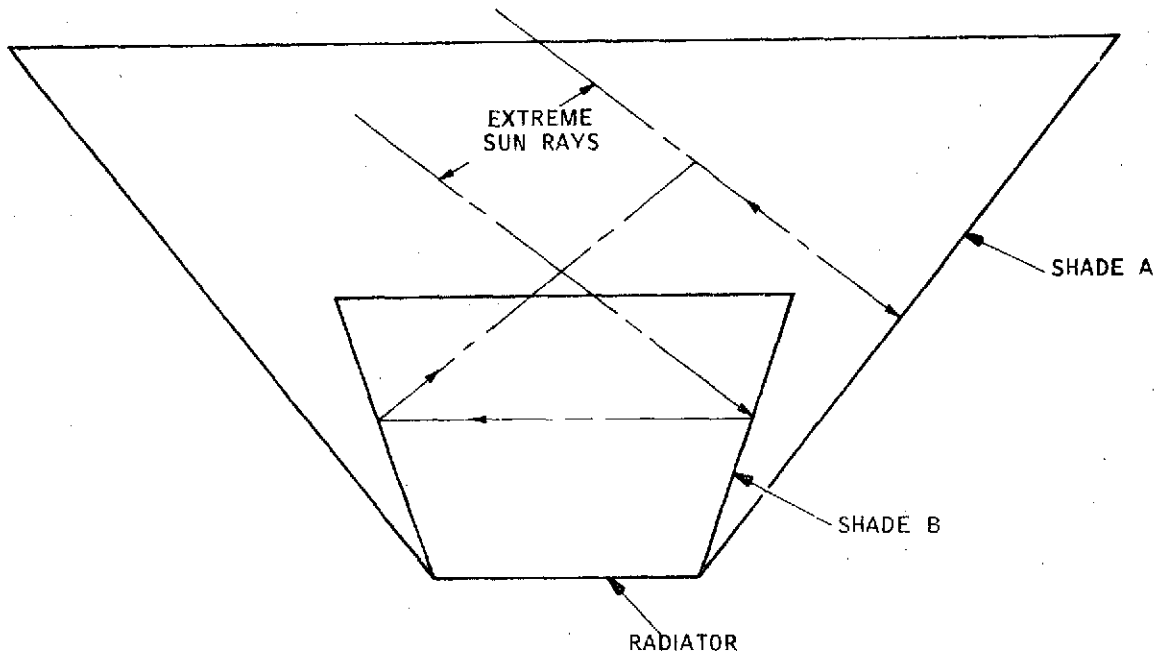
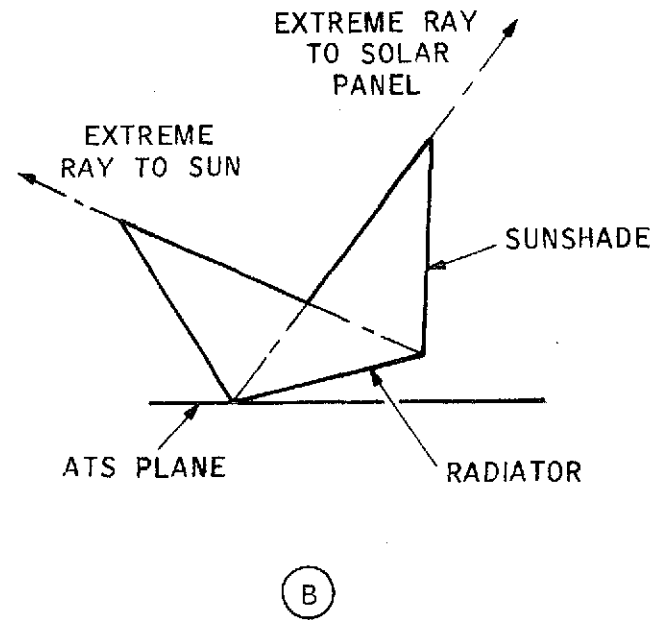
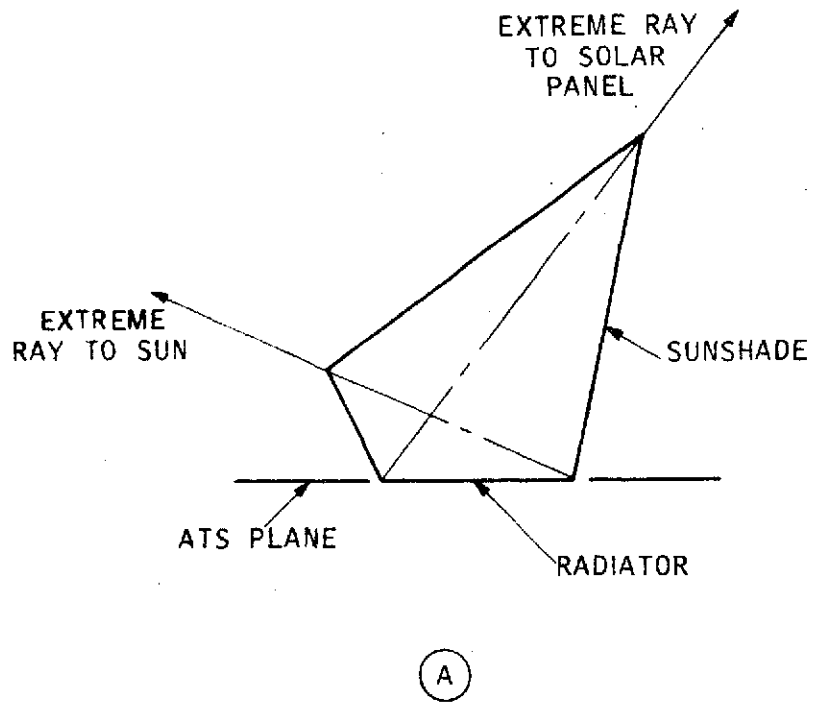


Figure 5.2.3-7



CONICAL SUNSHADE 1- AND 2- BOUNCE CONCEPTS

Figure 5.2.3-8



TWO METHODS OF SCARFING SUNSHADE

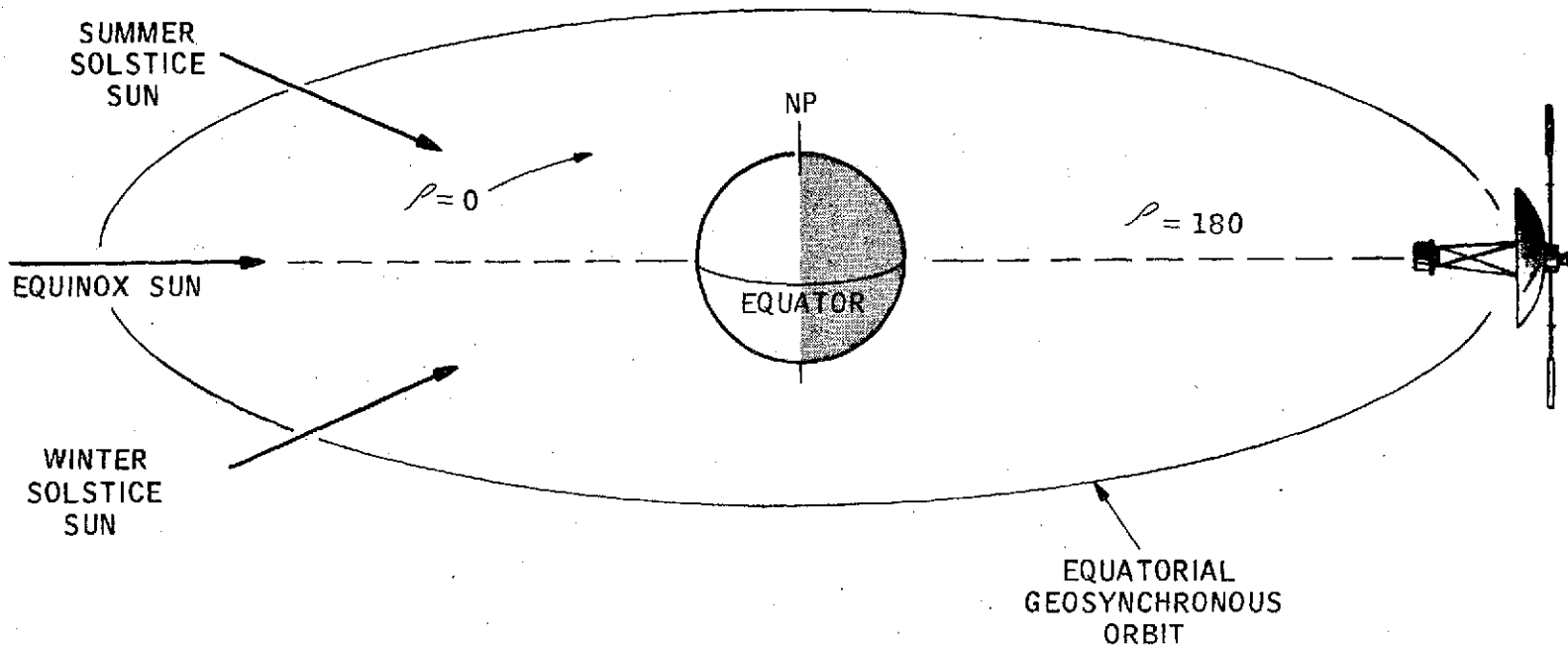
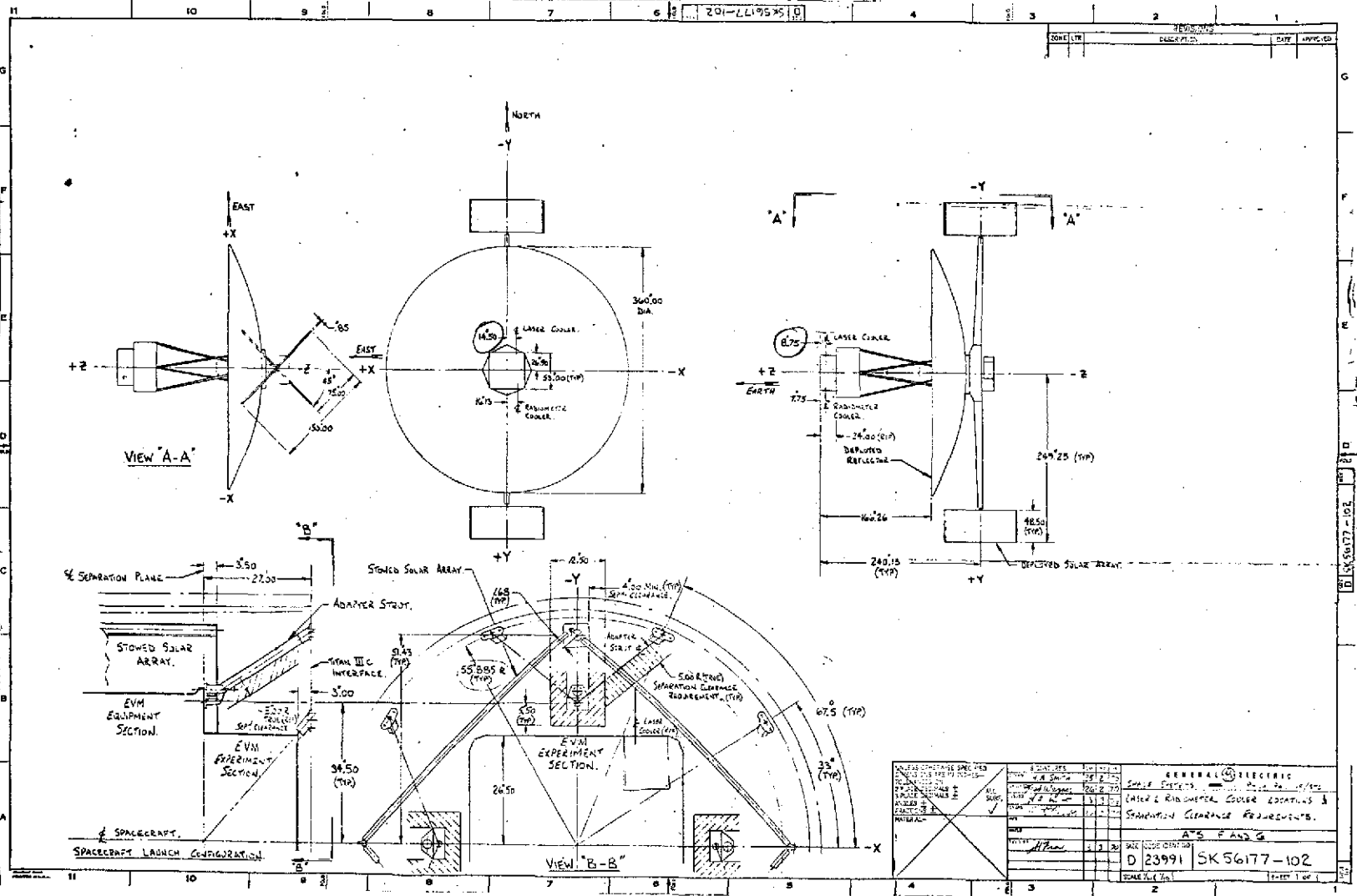


Figure 5.2.3-10

ATS/F-G SATELLITE - EARTH/SUN ORIENTATION

Figure 5.2.3-11



FOLDOUT FRAME 1

FOLDOUT FRAME 2

FOLDOUT FRAME 3

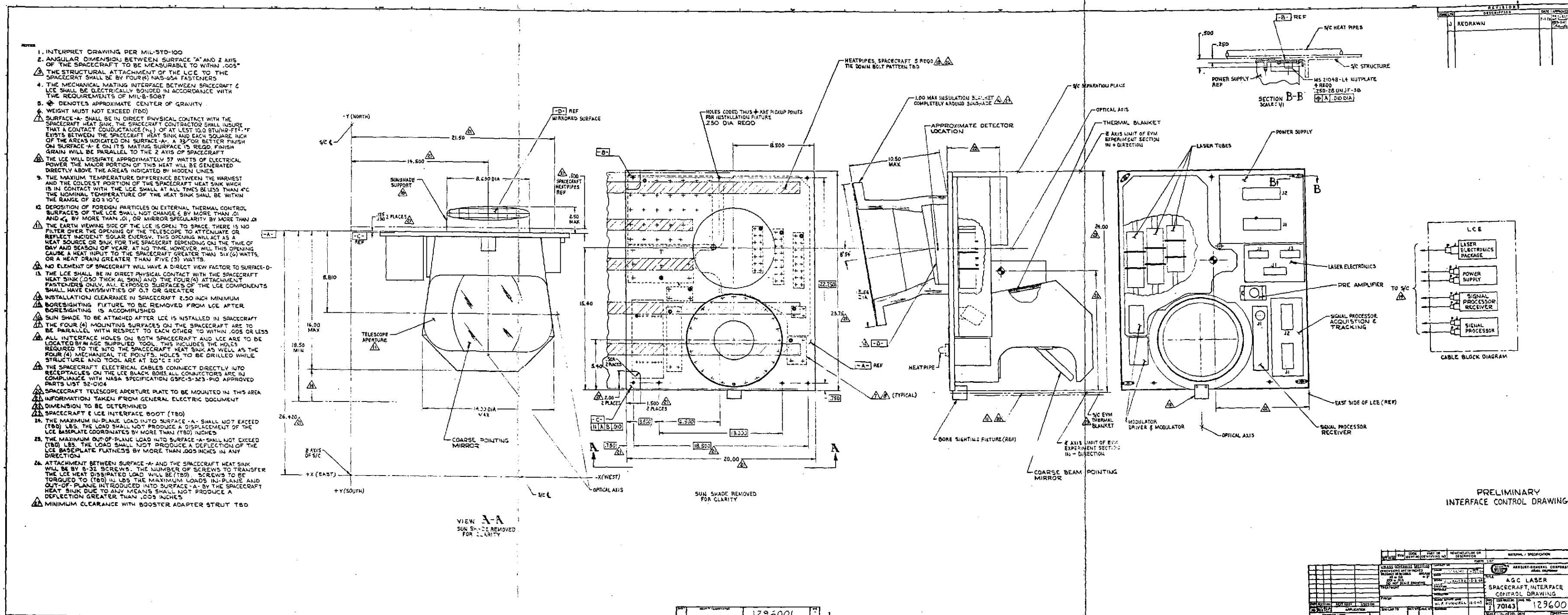
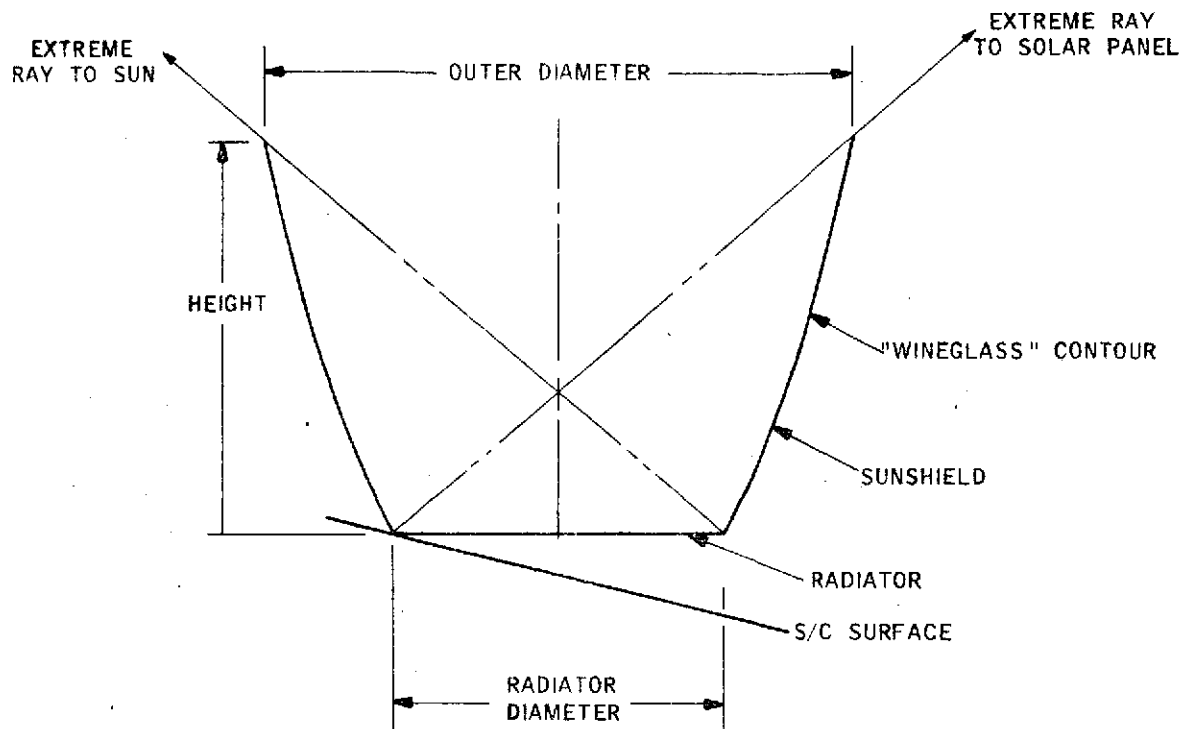


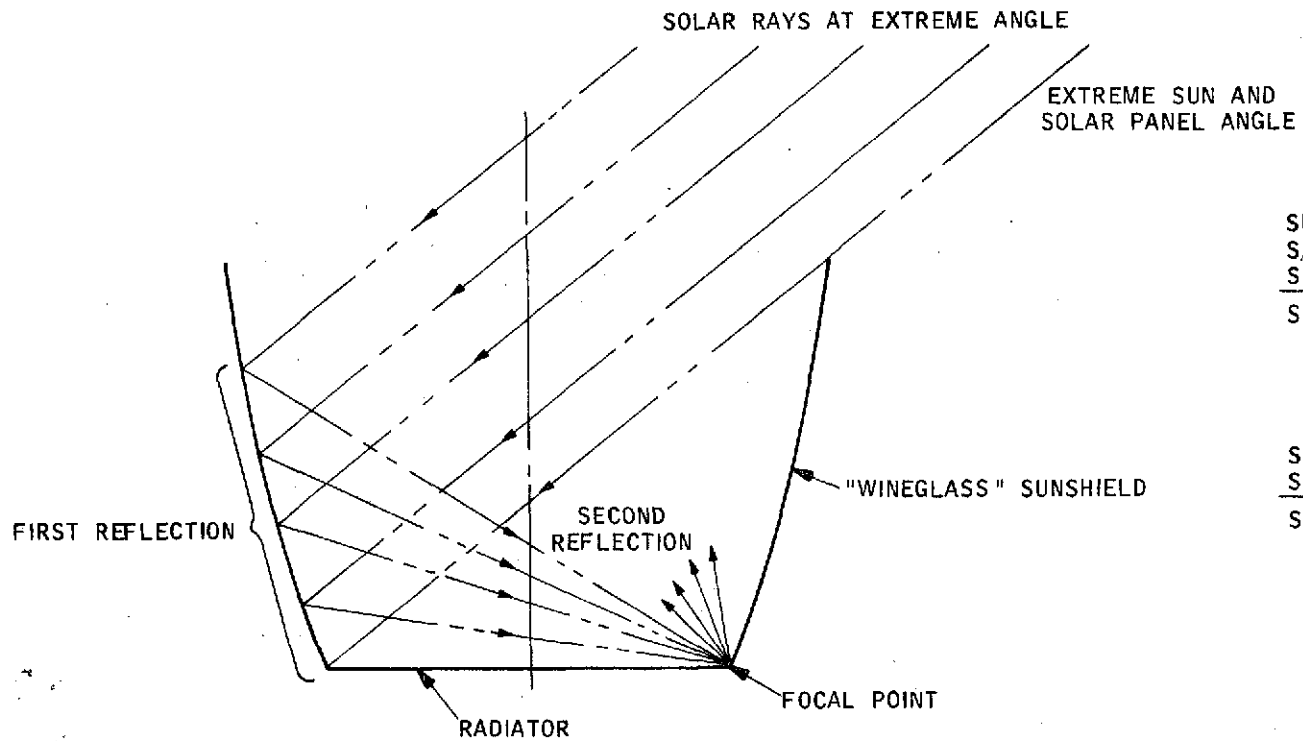
Figure 5.2.3-13



SKETCH OF RADIATOR AND SUNSHIELD TO DETERMINE
HEIGHT AND OUTER DIAMETER OF SUNSHIELD

Figure 5.2.3-14

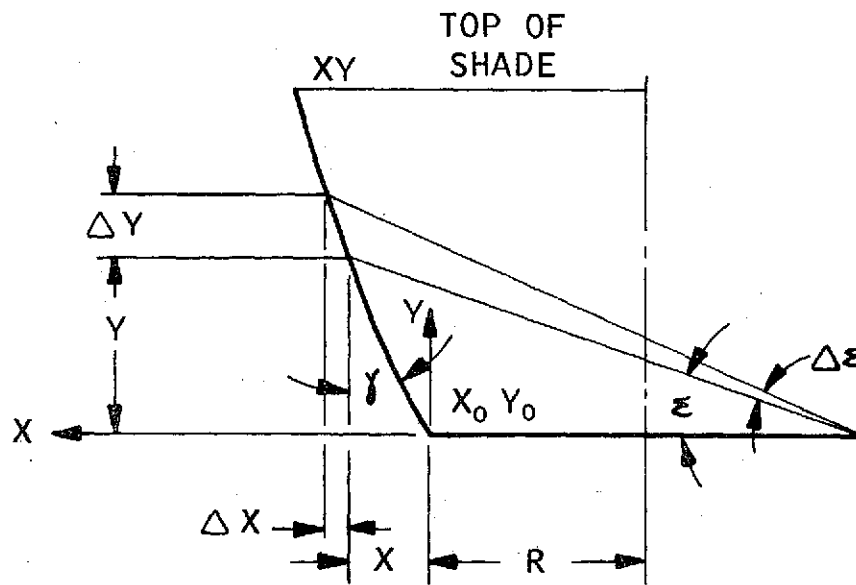
Figure 5.2.3-15



SUMMER SOLSTICE	23.5°
S/C SLEW	10.0°
SUNSHADE TILT	8.9°
<hr/>	<hr/>
SUN ANGLE	42.4°

SOLAR PANEL	51.3°
SUNSHADE TILT	8.9°
<hr/>	<hr/>
SOLAR PANEL ANGLE	42.4°

SCHEMATIC OF HOW "WINEGLASS" SURFACE REFLECTS ENERGY



Wineglass Shape

Figure 5.2.3-16.

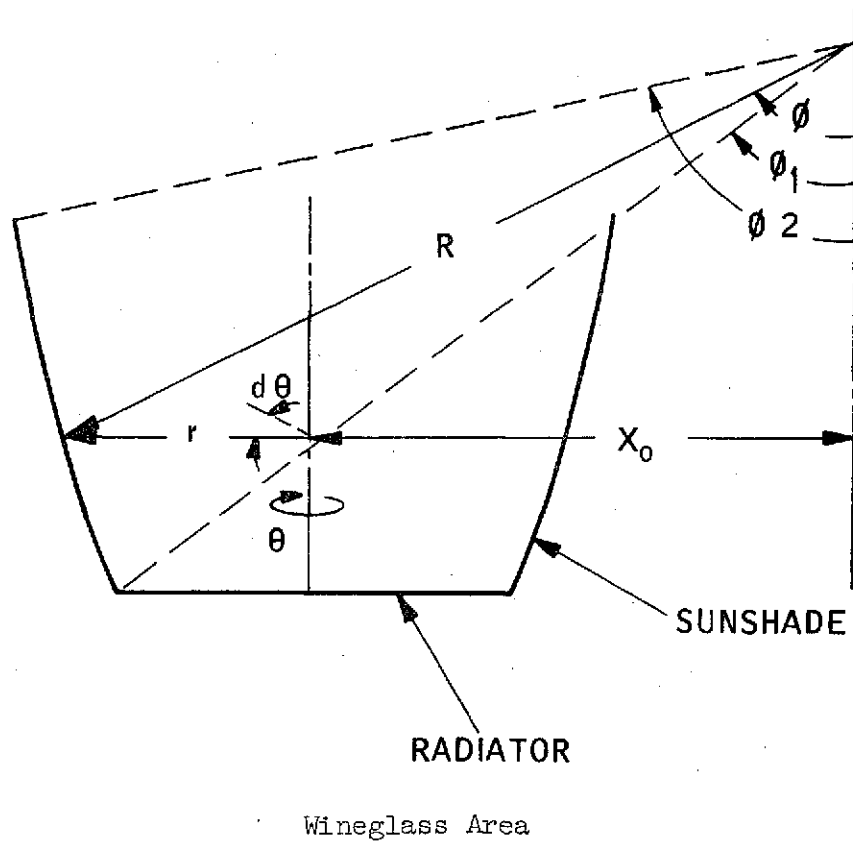
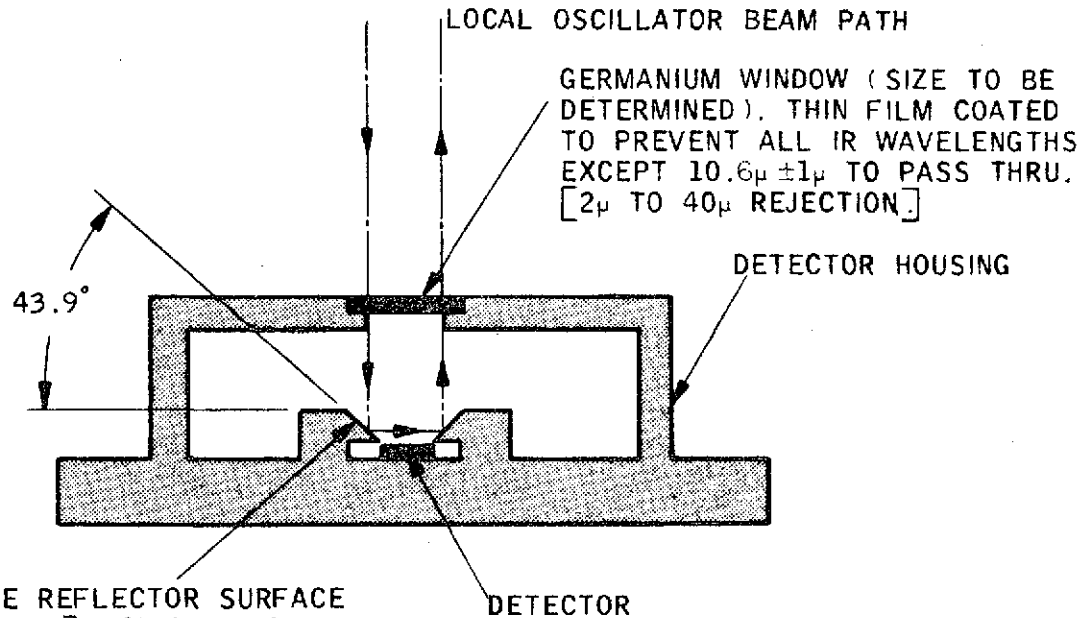


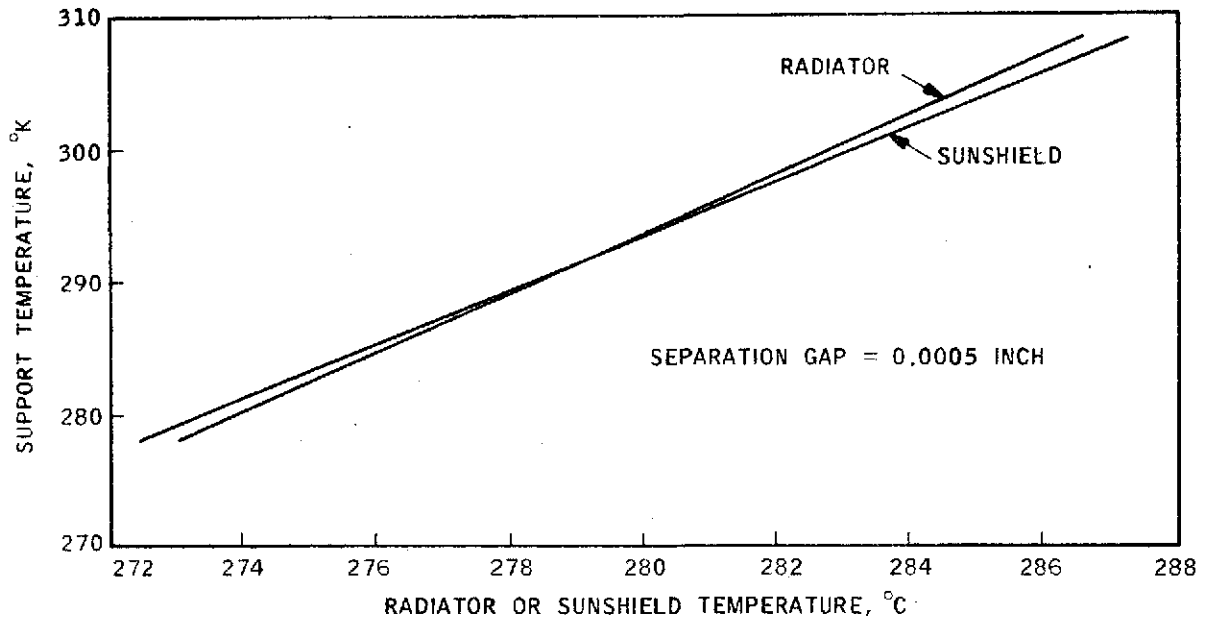
Figure 5.2.3-17



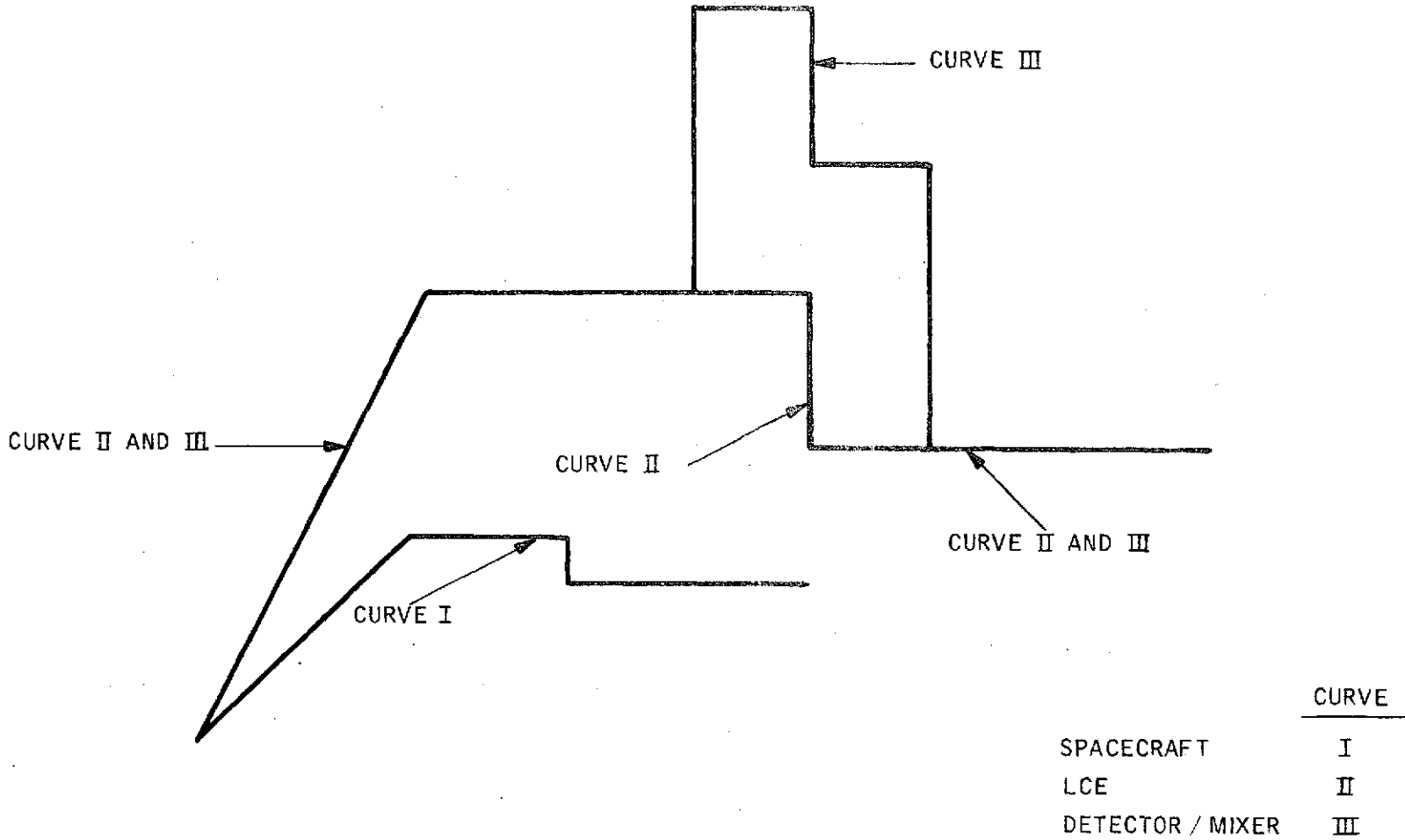
RIGHT CIRCULAR CONE REFLECTOR SURFACE [VAPOR DEPOSITED GOLD] HIGHLY SPECULAR (>98%) EMISSIVITY (ϵ) \leq .03. MINIMUM DIAMETER OF CONE SHOULD BE AS CLOSE TO UNMASKED DETECTOR AREA AS POSSIBLE (BOTH RADIALLY AS WELL AS LONGITUDINALLY).

GENERAL CONFIGURATION: RADIATOR DETECTOR HOUSING

Figure 5.2.3-18

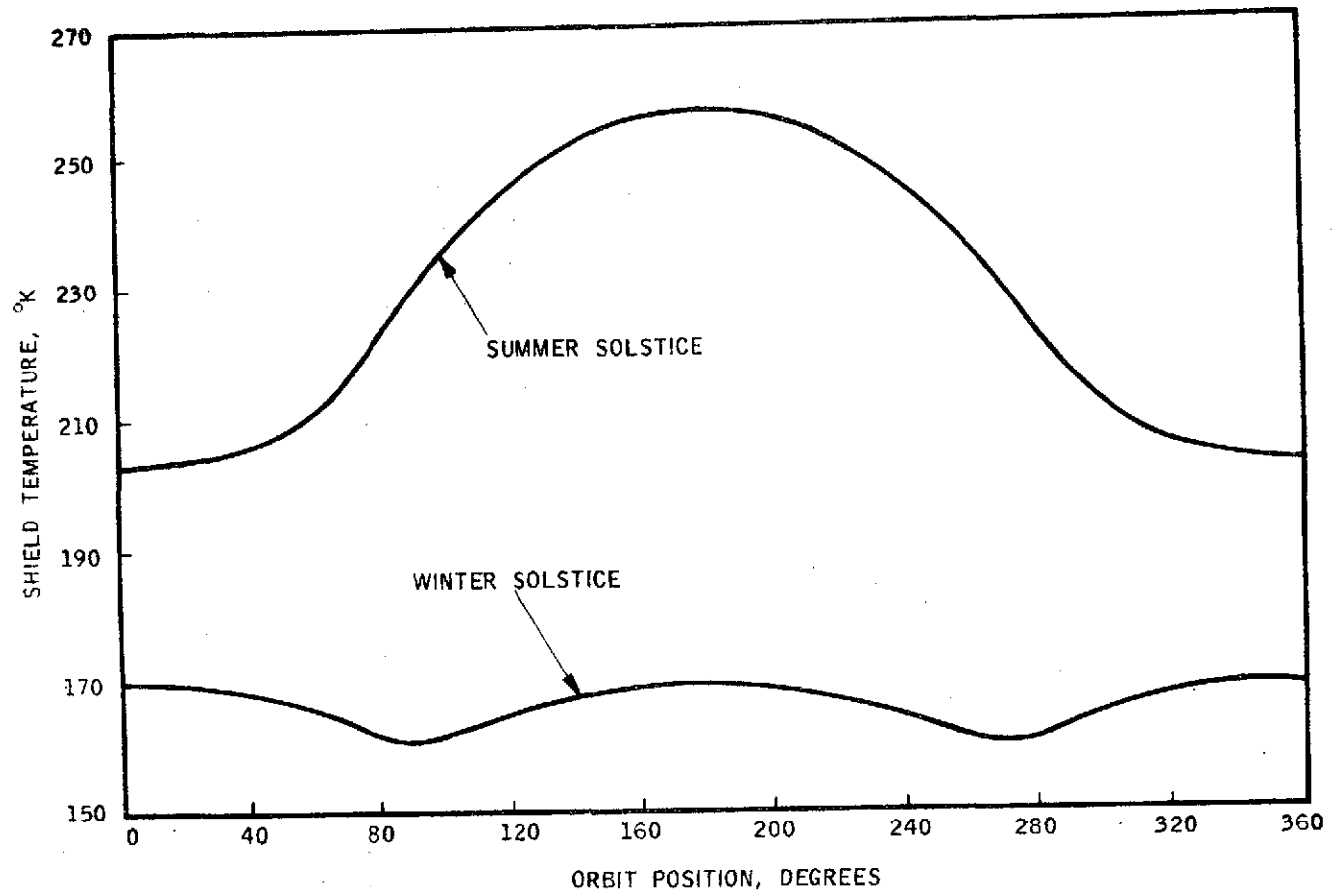


RADIATOR AND SUNSHIELD TEMPERATURES VS
SUPPORT TEMPERATURE TO GET 0.0005 INCH GAP SEPARATION



RELATIONSHIP OF SPACECRAFT, LCE DETECTOR / MIXER,
SINUSOIDAL QUALIFICATION VIBRATION LEVELS

- SUPERINSULATION OUTSIDE SHIELD
- THREE-INCH SUNSHIELD RADIATOR
- SUNSHIELD RADIATOR COATED WITH BACK SURFACE MIRRORS
- "WINEGLASS" SHAPED INTERIOR



LCE SUNSHADE TEMPERATURE HISTORY

Figure 5.2.3-22

5.2.4 Optical Heterodyne Receiver Subsystem

The Optical Heterodyne Receiver Subsystem (OHRS) is being designed and will be fabricated by Airborne Instrument Laboratories at Melville, New York, under subcontract to Aerojet-General Corporation. The OHRS is made up of a mixer, preamplifier, and processor. Functionally, the OHRS is divided into the following:

- Video and communications channel
- Tracking error channel
- Frequency error channel
- Mixer bias circuit
- Acquisition pulse channel
- Acquisition confirm channel

The acquisition pulse and acquisition confirm channels have only recently been added to the AIL subcontract. Therefore, their design has not reached the same maturity as other channel circuitry described in this report. In addition, Aerojet recently directed AIL to change the IF center frequency from 20 MHz to 30 MHz. This change was prompted by recent experimental results which verified that: (a) sufficiently wide laser operating line can be reliably achieved to permit offset of the local-oscillator operating frequency 30 MHz below the transmitter operating frequency (which is at the peak of the power-frequency profile); and, (b) (Hg,CD)Te mixers exhibit the required frequency response to operate efficiently at the 30 \pm 6 MHz frequency range.

The change to the 30-MHz IF center frequency considerably enhances the system performance in that:

- a. It permits the design of the filters which provide better amplitude and phase linearity thereby minimizing the distortion products
- b. The limiter action provides considerably wider separation between the IF spectrum and the second harmonic spectrum thereby minimizing this source of distortion
- c. The wider IF bandwidth permits higher peak frequency deviation (from 2.8 to 4.0 MHz) thereby resulting in a higher post-detection peak signal-to-noise ratio.

In addition, operating temperature of the mixer was changed from $100 \pm 5^{\circ}\text{K}$ to $110 \pm 15^{\circ}\text{K}$ in order to bring optimized mixer performance into alignment with the expected performance of the radiation cooler (see Section 5.2.3). Concurrently, the Noise Equivalent Power (NEP) was increased from 1×10^{-19} watts/Hz to 1.6×10^{-19} watts/Hz over the $110 \pm 15^{\circ}\text{K}$ range (with an anticipated attainable value of 1.35×10^{-19} watts/Hz and a design goal of 10^{-19} watt/Hz). The higher NEP is caused by degraded performance of the mixer at the highest temperature (125°K) anticipated during certain orbital segments. However, when the radiation cooler (and mixer) are at the anticipated nominal temperature of 110°K , a receiver NEP of 1.15×10^{-19} watts/Hz is expected.

Having implemented these changes at the time that this report was being prepared caused a certain amount of data overlap. The initial subsystem delivered for breadboard use will have a 20-MHz IF, while subsequent delivered subsystems will have a 30 MHz IF.

5.2.4.1 General Description of Optical Heterodyne Receiver Subsystem

The proposed Optical Receiver Subsystem (OHRS) (Figure 5.2.4-1) consists of:

- a. An infrared mixer assembly
- b. A preamplifier assembly
- c. Processing electronics.

The incident signal and local oscillator laser signals are offset by 30 MHz. The two laser beams are focused on a high-sensitivity infrared mixer element which provides an IF output centered at 30 MHz.

Tracking error information will be developed, using a conical scan with an axis through the center of the mixer element. If the conical scan is not centered, the OHRS will provide a modulation of the signal in which the amplitude and the phase (with respect to a reference) indicate the tracking error.

The cooled infrared mixer connects to a housing adaptor with coaxial connector output. A low-thermal-conductivity coaxial line connects the mixer output to the room-temperature IF preamplifier.

The receiver provides basically six outputs consisting of:

- a. Video signals
- b. Automatic frequency control (AFC) error signal
- c. East/west tracking error signal
- d. North/south tracking error signal
- e. Acquisition pulse
- f. Acquisition confirm signal.

Automatic gain control (agc) voltage and mixer bias current, which will be telemetered to provide indication of system operation, are not essential outputs.

It is convenient to categorize the receiver electronics for purposes of discussion into:

- a. Video and communications channel
- b. Tracking-error channel
- c. Frequency-error channel
- d. Mixer bias control
- e. Acquisition pulse channel
- f. Acquisition confirm channel.

The communications channel consists of all circuits needed to process the video and communications information in the experiment. It includes all the circuits from the IF preamplifier to the video buffer amplifier (Figure 5.2.4-1). The communications information is obtained by detecting the frequency modulation (FM) of the carrier in a wideband discriminator and amplifying in a video amplifier. In order to provide a receiver that can tolerate changing signal power levels without seriously affecting performance, the gain of the IF post-amplifier is automatically controlled by an agc detector and dc amplifier in a closed loop with the IF post-amplifier. This agc arrangement provides

nearly constant amplitude signals above the agc threshold. A limiter, which precedes the discriminator, provides additional amplitude control and reduction of amplitude changes that are faster than the response of the agc circuit (200 msec). The IF preamplifier (together with the infrared mixer) establishes the infrared receiver sensitivity. Various filters are used to establish the noise bandwidth and reduce harmonics or other distortion components and interference. An FM equalizer is used to compensate for phase distortion due to the nonlinearities of components in the receiver subsystem.

The tracking-error channel consists of circuits used to process the spatial tracking error signals and includes all the circuits after the IF post-amplifier from the bandpass filter to the two low-pass filters following the phase detectors. The band-pass filter establishes the noise bandwidth of the tracking-error channel prior to detection of the amplitude modulation on the carrier.

The orthogonal error components are produced (east/west and north/south) at the 100-Hz nutation frequency and are separated in the two phase-detectors following the audio amplifier. A band-pass filter tuned to the nutation frequency provides selectivity to reject undesired frequencies. The two tracking-error signals are then fed to the image motion compensator (IMC) which corrects the spatial error.

The frequency tracking error channel consists of circuits used to process the frequency tracking error and includes the low-pass filter and dc amplifier following the discriminator. An error signal is generated when the carrier and local oscillator frequencies are not separated by exactly the discriminator zero crossing frequency. The error voltage is proportional to the frequency error and provides a correction by means of the local oscillator laser. This automatic frequency control (afc) reduces frequency drifts and offset errors.

The mixer bias control contains the bias voltage regulator that provides the dc bias voltage for the infrared mixer.

The acquisition pulse channel consists of the circuits required to extract the received energy in noise (minimum signal-to-noise ratio of -18 db) as the scanning receiver beam is traversing the angular position at which the incoming energy is arriving. It consists of a matched filter (2 to 14 Hz at 3 db point), a threshold detector, and a shaping circuit to generate the acquisition pulse.

The acquisition-confirm channel is essentially the same as the tracking error channel except that it operates at 200 Hz. The presence of an output confirms the acquisition of the real station.

Implementation of the design necessary to meet the requirements of the OHRS will be discussed. The sections are divided into the infrared mixer design and the receiver electronics (includes preamplifier and processor assemblies).

5.2.4.2 Infrared Mixer Assembly

5.2.4.2.1 Receiver Noise Equivalent Power (NEP)

The receiver NEP, in watt/Hz, for a reverse-biased photovoltaic (Hg,Cd)Te mixer is expressed as

$$\frac{NEP}{B} = \frac{h\nu}{\eta} + \frac{k(T_M + T'_{IF})}{G} \quad (5.2.4-1)$$

where

B = IF bandwidth, Hz

$h\nu$ = photon noise

η = mixer quantum efficiency

k = Boltzmann's constant

T_M = mixer temperature

T'_{IF} = effective input noise temperature of receiver electronics, including coaxial line

G = available conversion gain of infrared mixer

The first term ($P_{\min} = \frac{h\nu}{\eta}$) in the above equation represents the quantum noise contribution. It is the minimum achievable NEP for a given mixer quantum efficiency. The second term $\left[k(T_M + T_{IF}')/G \right]$ represents the thermal noise of the system divided by the conversion gain of the infrared mixer.

This equation indicates that the NEP approaches P_{\min} asymptotically as the mixer conversion gain is increased. The mixer conversion gain increases linearly with absorbed local oscillator (LO) power. Figure 5.2.4-2 shows the expected variation of receiver NEP with LO power absorbed in the mixer. As can be seen, the receiver NEP is degraded when the applied LO power is low but changes very little when the LO power exceeds a threshold value for the particular mixer under test. Figure 5.2.4-3 shows measured NEP versus LO power incident on a reverse-biased, photovoltaic (PV) (Hg,Cd)Te mixer element.

For a measured quantum efficiency of 0.09, the measured NEP in Figure 5.2.4-3 is seen to approach P_{\min} asymptotically as the LO induced shot-noise begins to override the system thermal noise. The measured NEP was 7.2×10^{-19} w/Hz for an applied LO power of 0.50 milliwatt. For 2.0 mw of LO power, the NEP was 2.2×10^{-19} w/Hz, thus approaching the quantum-noise-limited value of P_{\min} . Using the measured results of Figure 5.2.4-3 ($P_{\min} = 2.08 \times 10^{-19}$ w/Hz, $T_M = 77K$ and $F_{IF} \sim 1.5$ db) the conversion mixer gain is -6.5 db. This result is reasonably close to the directly calculated conversion gain of -8.6 db.

While the mixer element used to obtain the data given in Figure 5.2.4-3 is not completely suitable for use in the LCE, it is representative of the type of detector to be used. The measured data on the above 9% quantum efficiency element was extrapolated to a mixer element having a 19% quantum efficiency. The resultant variation of NEP with LO power is shown in the dashed curve in Figure 5.2.4-3. The extrapolated curve shown in Figure 5.2.4-3 may be representative of the mixer performance in the LCE.

The mixer conversion gain varies directly with applied LO power as given by

$$G = \frac{(\eta q / h\nu)^2 P_{LO}}{2G_D \left[(1 + R_S G_D) + (f/f_c)^2 \right]} \quad (5.2.4-2)$$

where

R_S = series resistance of the mixer diode

f = IF frequency

f_c = mixer 3-db cutoff frequency

G_D = diode's small-signal shunt conductance (slope of I-V curve in reverse direction)

Sufficient LO power must be applied to the mixer element so that LO-excited shot-noise exceeds all other noise contributions in the optical receiver. Stated another way, the mixer conversion gain must be sufficient to minimize the receiver NEP.

For reverse-biased PV mixer, quantum-noise-limited operation is obtained when the local oscillator is sufficiently large so that

$$P_{LO} \gg \frac{2R (T_M + T_{IF}') G_D h\nu}{q^2 \eta} \quad (5.2.4-3)$$

where

G_D = diode small-signal shunt conductance

q = electron charge

When the terms on the left and right side of equation are equal, the thermal noise of the infrared mixer and IF amplifier degrade the receiver sensitivity by 3 db.

The LO-induced shot noise (and NEP) is expected to remain constant with frequency to 30 MHz and beyond as shown by the measured data in Figure 5.2.4-4.

The calculated variation of NEP with quantum efficiency is shown in Figure 5.2.4-5. Three curves are shown for the cases of degradation resulting from system thermal noise of 0, 10%, and 25% (see Equation 5.2.4-1). For a quantum efficiency of 20% and a 10% degradation in receiver sensitivity caused by thermal noise, the receiver NEP is approximately 10^{-19} watt/Hz. It is concluded that a quantum efficiency of 20% is required to meet the design objective of an NEP $\leq 10^{-19}$ watt/Hz. This type of receiver performance can be achieved over a narrow temperature range by proper selection of the mixer element and its operating parameters. The variation of quantum efficiency with temperature of a PV HgCdTe mixer having its peak response at $10.8 \mu\text{m}$ is shown in Figure 5.2.4-6. The quantum efficiency varies with temperature, since the detector material band-gap is temperature dependent. Selected mixer and operating parameters can be chosen to give wide temperature coverage with only slight degradation in receiver performance.

Figure 5.2.4-7 shows the measured NEP versus mixer temperature for a reverse-biased PV mixer. The NEP varied from 1.8 to only 2.4×10^{-19} watt/Hz for $V_B = -0.1$ volts for this particular element as the temperature varied from 77 to 130°K . Since the mixer quantum efficiency, reverse slope resistance and receiver thermal noise all vary with temperature, the infrared detector, dc bias, LO power and IF amplifier coupling network were carefully chosen to optimize the useful operating temperature range. In addition, the applied LO power was selected to give nearly quantum-noise-limited operation at the temperature extreme which exhibits the poorest receiver sensitivity. The measured receiver sensitivity for $V_B = -0.3$ volts is also shown in Figure 5.2.4-7 for comparison.

The present detector specification calls for infrared detectors whose parameters are optimized in the $100 \pm 5^\circ\text{K}$ temperature range. Minimum quantum efficiency will be 15%, with selected detectors expected to yield optimum efficiencies exceeding 20% in the $100 \pm 5^\circ\text{K}$ temperature range.

The minimum quantum efficiency vs mixer temperature for the basic specification and selected options is shown in Figure 5.2.4-8. Note that certain selected units from the deliverable detectors under the present subcontract can also meet the receiver performance levels of the Option A premium detectors (Figure 5.2.4-8). AIL has also obtained a quotation on Option B (Figure 5.2.4-8);

that is, two detectors with a minimum quantum efficiency of 13% over the 105 \pm 20°K range. Presently a mixer specification which fixes performance in the 110 \pm 15°K temperature range is being investigated.

In general, detector manufacturers measure Responsivity and Detectivity which are important parameters for incoherent detection applications. For coherent receiver applications, the principal mixer parameter is the quantum efficiency at the specified wavelength and operating temperature. The quantum efficiency is generally not measured by mixer manufacturers. This is presently being done at the mixer manufacturer (SAT) for mixer temperatures up to 130°K. The measured data for the best mixer element are shown in Figure 5.2.4-9 for wavelengths of 10.15, 10.6 and 11.3 microns. The measured quantum efficiency varied from 27.5% ($P_{\min} \sim 0.68 \times 10^{-19}$ w/Hz) at 80°K to a peak of $\eta = 31\%$ ($P_{\min} \sim 0.60 \times 10^{-19}$ w/Hz) at 90°K and then degraded to 12% ($P_{\min} \sim 1.55 \times 10^{-19}$ w/Hz) at 130°K. These data indicate the possibility of obtaining receiver sensitivities of 10^{-19} w/Hz over an extended temperature range. For optimum performance, the quantum efficiency peak at 10.6 micrometers should occur near the median operating temperature of the radiation cooler.

Note that measurements of detector uniformity, cutoff frequency, and 1/f noise were not made on the mixer element used to obtain the measurement data shown in Figure 5.2.4-9. Therefore, complete confidence as to the suitability of this mixer for the Optical Receiver Subsystem has not been fully established.

5.2.4.2.2 Selection of Receiver Parameters

This section summarizes the proposed design approach to attain the infrared sensitivity and power dissipation design goals for the Optical Receiver Subsystem. The following parameters having an impact on receiver sensitivity can be identified:

<u>Parameter</u>	<u>Interface</u>
T_M P_{LO}, P_{DC}	} Radiation cooler
η G_D, C, R_s f_c	} Detector subcontractor
T_{IF} Optimum source resistance	} Electronics

In addition, the coaxial cable between infrared mixer and the IF preamplifier has an important impact.

In arriving at the proposed design, the IF is the starting point, considering the post-amplifier maximum noise factor, preamplifier minimum gain, preamplifier maximum noise factor, and maximum coaxial cable loss to arrive at a minimum effective IF noise temperature, T_{IF}' , at the mixer output terminals.

Using the T_{IF}' and the maximum mixer physical temperature, T_M , and given the quantum efficiency, G_D and f_c , the required mixer conversion gain and local oscillator power for 10% thermal-noise contribution are calculated. The NEP is then obtained.

The results for two temperature are given in Table 5.2.4-1, which shows the projected receiver performance at the upper-mixer temperature extremes of 105°K (previous specification) and 125°K (new specification).

For temperatures in the 100 \pm 5°K range, a quantum efficiency of 20%, 3.6 mw of LO power incident on the mixer, a mixer gain of -3.9 db, and a reverse mixer dynamic resistance of 100 ohms, the calculated NEP meets the design objective of 10^{-19} watt/Hz. For the temperature conditions of 110 \pm 15°K, a quantum efficiency of 13%, at the temperature extremes, 6.25 mw of LO power incident on the mixer, a mixer gain of -5.5 db and a reverse dynamic resistance

of 100 ohms, the calculated NEP is 1.58×10^{-19} watt/Hz. This represents a degradation of 2 db in receiver sensitivity compared to the sensitivity calculated at 105°K. If the LO power applied to the mixer element is limited to 5 mw at 125°K, the conversion gain is reduced from -5.5 to -6.4 and the calculated NEP degrades to 1.62×10^{-19} watt/Hz.

The receiver sensitivity at 125°K is calculated for a quantum efficiency of 13%, based on mixers specified over the 105 \pm 20°K temperature range. For mixer elements specifically fabricated for quantum efficiency peaked in the 110 \pm 15°K range, it is anticipated that the NEP could be improved. This matter is presently under intensive investigation. Note that, even for a mixer with quantum efficiencies of 13% at the temperature range extremes, the quantum efficiency at temperatures between the extremes is higher (e.g., see Figure 5.2.4-9).

5.2.4.2.3 Coaxial Cable Design

A thermal interface exists, between the spaceborne radiation cooler and the IR mixer, through the coaxial cable which electrically connects the infrared mixer to the IF preamplifier. The temperature differential of 200°K along the coaxial cable (300°K at preamplifier and 100°K at mixer) presents a significant heat load to the radiation cooler.

In the design and selection of the coaxial cable, the following characteristics had to be considered in addition to thermal loading on the radiation cooler:

- Insertion loss at 30 MHz
- RFI immunity
- Basic mechanical strength and rigidity

A number of design tradeoffs were explored. For example, RFI immunity demands a continuous outer conductor cable jacket of high-electrical conductivity material, while thermal loading demands low thermal conductivity, thin material, construction - in direct opposition to the RFI requirement.

Experience and computations indicate that with a stainless steel coaxial cable, the above design considerations can be simultaneously satisfied. For example, using a steel coaxial cable 12 inches long with the dimensions shown below:

Outer diameter	.0865 in.
Dielectric diameter	.0658 in. (Teflon)
Center conductor diameter	.0201 in.

(Both the inner and outer conductors are stainless steel.)

The electrical loss is:

For the coaxial line,

$$\alpha_c = 13.6 \frac{\delta \mu}{\lambda} \frac{1}{b} \left(1 + \frac{b}{a}\right) \frac{\sqrt{\epsilon_1}}{\ln \frac{b}{a}} \text{ db/cm}$$

at 30 MHz, the skin depth, $\delta = .008 \text{ cm}$ (.00315 in.) and $\alpha_c = .0068 \text{ db/cm}$

Loss = .221 db for 32.5 cm (12.8 in.)

.207 db for 30.4 cm (11.95 in.)

while the thermal loss is:

Assuming the IF preamplifier at 300°K and the IR mixer at 100°K ,

$$Q = \frac{A}{L} \int \lambda dT$$

Cross section area, outer	.0159 cm ²
Cross section area, inner	<u>.0021 cm²</u>
Total	.018 cm ²

$$\int \lambda dT = 25.3 \text{ watts/cm}$$

Q = 15 mw for L = 30.4 cm (11.95-in.-long cable)

14 mw for L = 32.5 cm (12.8-in.-long cable)

A laboratory experiment was performed using coaxial cable UT-20-SS. The stainless steel outer conductor wall thickness was .0025 inch. In a 1-volt/meter field at 20 MHz, a -75 dbm signal was measured on the cable (one skin depth at 20 MHz = .0039 in., so that, for this case, the thickness of the outer jacket was less than 1 skin depth).

Although further testing will be required, it is believed that RFI protection to the level specified in MIL-STD-461 (-100 dbm) can be obtained using the proposed coaxial cable (.010-in. wall thickness, which is more than 3 skin depths) for the case of 30 MHz IF center frequency.

5.2.4.2.4 Effect of Coaxial Cable Losses on IF Noise Factor

RF losses in the coaxial cable between the infrared mixer and IF preamplifier must be carefully considered, since these losses can result in degradation of receiver sensitivity unless the receiver is properly designed. An approach to including this cable loss is to define an equivalent input noise temperature of the IF amplifier that includes the cable loss. This can be taken into account by means of the following equation:

$$T_e = (L-1) T_L + L T_{IF}$$

where

T_e = effective input IF noise temperature including cable loss

T_L = temperature of cable. The above expression assumes a constant or "effective" cable temperature, which we take here to be an average 200°K.

L = loss in the cable

T_{IF} = effective input noise temperature of the IF amplifier excluding cable loss

The above expression is plotted in Figure 5.2.4-10 for IF noise factors of 1.5, 1.7, and 2.0 db. For example, for a cable loss of 0.2 db ($L \sim 1.047$) and $T_{IF} = 139^{\circ}\text{K}$ ($F_{IF} = 1.7$ db), it can be calculated that $T_e \sim 155^{\circ}\text{K}$, which corresponds to a noise factor of 1.86 db. Thus, the 0.2 db cable loss causes the effective input noise factor of the IF amplifier to change from 1.7 to 1.86 db.

5.2.4.2.5 DC Bias Power Requirements

It is anticipated that the required dc bias power will not exceed 1 mw. This upper limit is calculated as follows: for a mixer with $G_D^{-1} = 100$ ohms, $V_B = -0.2$ volts, diode dark current $I_D = 1$ ma, and a photoinduced current as high as $I_O = 4$ ma, a dc bias power of 1 mw is calculated.

5.2.4.2.6 Mixer Subcontract

Airborne Instruments Laboratory has selected SAT Company to be the supplier of the IR mixer elements. The selection of the SAT is the result of a lengthy evaluation period of several manufacturer's mixers during last year. In March 1969, AIL issued an RFP for space qualified infrared mixers and invited responses from all major manufacturers of HgCdTe detectors. Three bids were received. Prior to this action, under the NASA head-start program, AIL evaluated photoconductive and photovoltaic mixers from various mixer manufacturers in an attempt to find a suitable 10.6-micron mixer element for the OHRS/LCE. The photovoltaic mixer purchased from SAT was the only mixer that exhibited efficient mixing up to 20 MHz. Note that the use of a reverse biased, photovoltaic mixer rather than a photoconductive mixer gives a potential 3 db improvement in receiver sensitivity for a given mixer quantum efficiency.

A fixed-price program was negotiated between AIL and SAT early in 1970 which included:

- Design qualification testing on two mixer elements
- Quantum efficiency specified over the $100 \pm 5^{\circ}\text{K}$ temperature range (presently, the mixers, the quantum efficiency of which is specified over $110 \pm 15^{\circ}\text{K}$, are being negotiated)
- Qualification testing of the mixer housing assembly
- Optimization of the location of the mixer element in the housing assembly to permit, if necessary, the incorporation of a redundant mixer element in the LCE

5.2.4.2.7 Mixer Housing

There are several critical interface areas in the design of the mixer housing:

a. Optically, it is the terminus of the optical subsystem telescope/mixer optical path. Therefore, the housing entrance window must have the diameter required to accept the received signal cone angle. Also, the window is an element in the optical path and, as such, must be included in the optical analysis.

b. The housing entrance window must filter out all IR wavelengths except 10.6 ± 0.5 microns. The rejected wavelength range is 2 to 40 microns. Energy coming through the bandpass is 2 mw. A further increase of 5 mw in energy absorbed beyond the 2 mw will result in an increase in mixer temperature of 1°K .

c. To provide uniform mixer illumination by the local oscillator and to allow for the mixer position tolerance of ± 0.005 in. (the extent of possible mixer position change as the radiation cooler is thermally decoupled while in space - see Section 5.2.3.1), the Airy disk of the local oscillator must be larger than the mixer diameter. The design of the radiation cooler assumes that the total local oscillator power deposited in the mixer and the housing is 22 mw. The total local oscillator power incident on the mixer and housing is 85 mw. Therefore, 63 mw must be rejected by reflection.

d. The surface finishes of the housing must be such that the background radiation is mostly reflected. Therefore, the surface coating of the exterior of the housing is specified to have an emissivity of $(e) \leq 0.05$. The mounting surface between the mixer assembly and the radiator should have a 16-microinch rms finish and a flatness of 0.0002 in. TIR. Temperature drop across the joint is expected to be 1°C , or less, for the expected bolt torques.

The development of a hermetically sealed mixer housing assembly, which will withstand the temperature shock as the mixer is cycled between 300°K and 77°K , will be one of the critical technical items of the subcontract. The housing assembly will be designed to successfully withstand 100 rapid cycles between nitrogen and ambient. Latest information from SAT indicates that housing assembly tests just completed showed 1000 cycles without degradation of

seal. Two approaches will be pursued through an entire qualification test cycle before the best approach is selected; the two proposed approaches are:

- A housing using an indium pre-form (Figure 5.2.4-11 for preliminary drawing)
- A housing using a Torr Seal sealant (Figure 5.2.4-12 for preliminary drawing)

A housing adapter will be used to couple IF output signal from the infrared detector to a coaxial cable. A preliminary design on the housing adapter is shown in Figure 5.2.4-13, which includes gasketing for good RFI shielding. The final housing adapter will be designed after the housing assembly design has been completed by the mixer subcontractor.

5.2.4.2.8 Frequency Response

As discussed in Section 5.2.4.2.6, the photovoltaic HgCdTe element is the only 10.6-micron intrinsic infrared photodetector which has been found to be suitable, at present, for use in the LCE at megahertz IF frequencies with low power dissipation.

Measurements on two photovoltaic HgCdTe mixers at 77°K showed a 3 db cutoff frequencies of 50 MHz, and greater than 60 MHz. The OHRS detector-purchase specification calls for a 2-db cutoff frequency of 50 MHz, minimum, at 100°K.

5.2.4.3 Receiver Electronics

The design of the receiver electronics includes the design of the four major elements of the receiver subsystem (video, tracking, AFC, and bias) and recently added functions (of acquisition and acquisition-confirm pulse). The two major receiver parameters are bandwidth and gain control. The first part of the discussion (Section 5.2.4.3.1) will center on the major considerations in the design tradeoffs of the subsystem elements and the receiver parameters. The second part of the discussion (Section 5.2.4.4.2) will be concerned with the performance of laboratory breadboards of various key circuits.

5.2.4.3.1 General System Design Considerations

Various system-design tradeoffs are possible in implementing a receiver system that provides the essential requirements of the OHRS. One of

the most important areas of tradeoff is in the selection of the IF and its bandwidth. With a higher IF, it is easier to provide filtering to separate video and IF, and the percentage bandwidth of the IF circuits becomes smaller. A smaller-percentage bandwidth eases IF filtering, reduces harmonic distortion in circuit elements, and improves the linearity of phase in the amplifiers and demodulation in the discriminator. The highest allowable IF is restricted by mixer bandwidth and laser tuning capabilities. Therefore, given the constraint of a maximum IF, the tradeoff must be between performance demands on various circuit elements, system performance (particularly video quality), and limitations of size, weight, and power. In the following paragraphs, this and other system design tradeoffs will be discussed.

5.2.4.3.1.1 Receiver Bandwidth

The receiver IF bandwidth is determined by tradeoffs between obtainable laser power profile and stability, information bandwidth desired, frequency deviation desired, and the amount of power available (RF and DC). Based on a detailed analysis of the above considerations, the receiver IF for the breadboard extends from 14.7 MHz to 25.3 MHz (20 MHz \pm 5.3 MHz), and the video bandwidth extends from 1.0 to 5.3 MHz. The IF bandwidth is defined by the Noise Bandwidth Filter since the IF amplifiers are quite broadband. This filter must be used prior to the limiter in order to restrict the noise entering the limiter so that signal-to-noise ratio is preserved. Although the channel filter (following the limiter) is sharper than the noise bandwidth filter, it is more rectangular because of the rejection required to signal harmonics.

The bandpass filter following the IF post-amplifier establishes the noise bandwidth in the tracking error channel. The present filter design calls for a 5-MHz bandwidth (17.5 MHz to 22.5 MHz, at 3-db points).

The video bandwidth is determined by tradeoffs between the desired signal quality, the modulator driver power requirements, and modulator limitations (low-frequency resonances). Based on these considerations, the video bandwidth in the breadboard extends from 1.0 to 5.3 MHz, with baseband translation to 0 to 4.3 MHz and de-emphasis being performed on the ground.

Recent investigations have shown that the laser power profile, the infrared mixer and the wideband discriminator can all be made to accommodate a higher IF. Since improved performance is possible with the IF at 30 MHz (Section 5.2.4.3.1.3.1), the breadboard unit will be modified for an IF of 30 MHz, and all future models will be directly made at 30 MHz. This increase in IF permits the bandwidth to be increased so that the IF will extend from 24 to 36 MHz and the video baseband will extend from 1 to 6 MHz. Future discussions will assume an IF of 30 MHz, unless it is specifically stated to be otherwise.

5.2.4.3.1.2 Automatic Gain Control

Automatic gain control is provided to limit the power level variations in the receiver electronics. It is desirable to have the agc threshold set at a power level corresponding to a signal below the minimum signal-to-noise ratio (S/N) of 23 db so that some degradation can be tolerated without seriously affecting system performance. It is also desirable to set the threshold at least 10 db above the noise level so that it is well defined. Thus, a threshold corresponding to a power level with a signal at a S/N of 17 db has been selected as a reasonable compromise, and this is where the threshold will be set (although adjustable) unless other factors dictate another choice.

Note that, during the acquisition mode, the signal levels will normally be considerably reduced and the S/N can be as low as -19 db. Under these conditions the signal level is not within range of the agc.

The dynamic range required of the agc in the communications mode is 10 db (from -66 dbm to -56 dbm at the mixer input). Over this range, it is very desirable to maintain a constant output level from the post-amplifier. The response time of the agc can be fairly slow since signal levels should change quite slowly in the communications mode. However, it is also important to define the characteristics of the tracking-error channel in the transition from the acquisition mode to the communications mode. During this transition, the signal level will suddenly increase (because of the narrowing of the laser beam) from a S/N of, typically, -14 db to +23 db, for a change of 37 db. Since the agc will take time to become operative, it is important that saturation recovery be fast and that the agc "attack" time be sufficient to obtain control, permit the gain to stabilize, and pass the tracking error signals before the beam drifts

off outside the spatial tracking range. To ensure that these conditions will be met, the tracking-error channel will be designed to recover from a 41-db signal-level change in less than 0.2 sec.

5.2.4.3.1.3 Video and Communications Channel

5.2.4.3.1.3.1 Receiver Sensitivity and Receiver Electronics Noise Factor

The OHRS receiver sensitivity is primarily determined by the infrared mixer (as discussed in Section 5.2.4.3), with a small contribution as a result of the receiver electronics noise factor and the coaxial cable connecting the mixer to the IF preamplifier. For this reason, and in order to prevent the sensitivity from being seriously degraded by a decrease in the local oscillator power, it is important to keep the receiver electronics noise factor (NF) as low as practicable. This is accomplished by a low noise factor on the IF preamplifier, a sufficiently high gain on the IF preamplifier (greater than 20 db), and a sufficiently low IF post-amplifier noise factor (less than 10 db). The combined gain of the IF preamplifier and the first IF post-amplifier will then be sufficiently high that all other noise contributions are negligible.

The noise factor of the receiver electronics can be described by the equation

$$F_r = F_1 + \frac{F_2 - 1}{G_1} \quad (5.2.4-4)$$

where

F_r = noise factor (ratio) of the receiver electronics

F_1 = noise factor (ratio) of the IF preamplifier

F_2 = noise factor (ratio) of the IF post-amplifier

G_1 = gain (ratio) of the IF preamplifier

The insertion loss of the noise bandwidth filter must also be included by adding its loss to the noise factor of the IF post-amplifier. The effect of varying G_1 and F_2 can be seen in Figure 5.2.4-14, in which it was assumed that $F_1 = 1.8$ db. To keep the overall NF below 2.0 db, with a gain of 21 db would have to keep the

second stage NF below 10 db. With a second stage NF of 13 db, the gain would have to be greater than 24 db. The preamplifier gain is designed for a nominal gain of 26 db and the second stage noise figure is designed for a NF of 8 db; this provides sufficient margin in both parameters.

The receiver electronics NF can also be dependent upon frequency. It can also be degraded by large variations in mixer source conductance if precautions are not taken. Proper selection of the IF transistor and careful matching to the optimum noise resistance are required to eliminate this degradation.

If the theoretical behavior of noise factor in transistorized IF amplifiers as a function of frequency is examined, it can be seen that, within a wide frequency range, there is a plateau of minimum F. Figure 5.2.4-15a illustrates the theoretical behavior, and Figure 3.2.4-15b shows the behavior for a typical transistor (2N3570) illustrating this broad plateau from 1 to 100 MHz. That this plateau is not very dependent upon source-resistance is shown by data on another transistor (2N4252) given in Figure 5.2.4-15c; in which a 2-to-1 change in source impedance hardly affects the broad plateau.

The theoretical equation for the noise factor of a transistor amplifier is:

$$NF = 1 + \frac{r'_b}{R_g} + \frac{r_e}{2R_g} + \frac{(R_g + r_e + r'_b)^2}{2R_g r_e h_{fb}} \left\{ \left[1 + (f/f_a)^2 \right] \left[\frac{h_{FB}}{h_{fb}} \left(1 + \frac{I_{CBO}}{I_c} \right) \right] - h_{fb} \right\} \quad (5.2.4-5)$$

where

- f_a = common-base alpha cutoff frequency
- h_{FB} = DC common-base short-circuit current gain
- h_{fb} = AC common-base short-circuit current gain
- I_c = collector current
- I_{CBO} = collector cutoff current (emitter open)
- r'_b = bulk resistance of base region
- r_e = emitter resistance
- R_g = generator resistance

The variation of NF with frequency arises because of the term f/f_a . That is, for the application of interest, it is only important to establish f_{CH} , the high-frequency noise corner, above the highest desired frequency of operation. This, in turn, means selecting a transistor with a high cutoff frequency compared to the operating frequency of 30 MHz. The transistors used in the design have cutoff frequencies of from 1.2 to 3.5 GHz.

The noise factor behavior versus source (or mixer) resistance depends somewhat upon the frequency of operation and the emitter current. Figure 5.2.4-16a shows such a measured plot where a variation of R_g from 1 to 10 kilohms produces about a 0.5-db change in F. This kind of insensitivity to R_g is possible if the frequency of operation is very small compared to the transistor cutoff frequency. It can be established that this is the case for the preamplifier design.

To examine this NF versus source resistance behavior in more detail, the equation 5.2.4-5 is normalized to obtain

$$\frac{NF}{NF_{min}} = 1 + \frac{\frac{1}{2} \left[\frac{R_g}{R_g(F_{opt})} + \frac{R_g(F_{opt})}{R_g} \right] - 1}{1 + K} \quad (5.2.4-6)$$

where

$$NF_{min} = 1 + \frac{K_1}{R_g} + \frac{(K_2 + R_g)^2 K_3}{R_g}$$

$$K = \frac{K_2 + \frac{1}{2K_3}}{R_g(F_{opt})}$$

$$K_1 = r'_b + \frac{r_e}{2}$$

$$K_2 = r'_b + r_e$$

$$K_3 = \frac{(1 - a_o) \left[1 + \left(\frac{f}{\sqrt{1 - a_o f_a}} \right)^2 \right]}{2a_o r_e}$$

and where a_o = the low-frequency, common-base current gain.

Equation (5.2.4-6) is plotted in Figure 5.2.4-16b for different values of K . Note that the larger values of K arise principally because of having an operating frequency f that is small compared to the transistor cutoff frequency f_a .

The mixer output impedance will be transformed to provide the optimum source resistance R_g to the IF amplifier for an average value of mixer resistance. For a transistor with $K = 1$, and a mixer output resistance variation of 1.33 to 1, the maximum F variation (for $K = 1$) is less than 0.3 db. For a mixer resistance variation of 2-to-1, the increase in frequencies in excess of 1 GHz will be used, and the signal frequency is 30 MHz, the curves for $K = 10$ are more appropriate. In this case, the increase in NF should be less than 0.2 db for an approximate 4-to-1 change in R_g .

5.2.4.3.1.3.2 Distortion

In order to provide a high-quality communications channel, several sources of distortion must be carefully minimized. These sources of distortion include:

- Degradation of S/N
- Nonlinear phase response
- Nonlinear demodulation
- Nonlinear post-detection gain
- Unfiltered harmonics, spurious responses, or interference
- a. Degradation of S/N

Degradation of S/N can occur by improper gain distribution in the IF stages, or by a low discriminator sensitivity and a high video amplifier noise factor (it is assumed that the system has been designed to

provide a satisfactory S/N with respect to such parameters as deviation, IF bandwidth, transmitter power, pre-emphasis, etc.).

In the LCE receiver, in which the dynamic range is only 10 db, the considerations associated with improper gain distribution are unimportant. However, because of the bandwidth of the discriminator, and the desire to conserve power, the discriminator sensitivity will be low (3×10^{-9} volts/Hz) and attention must be given to the video amplifier noise. The "front-end" noise at the output of the video amplifier can be calculated with the following equation

$$V_n = \frac{a_n \sqrt{2}}{A_c} \left[\frac{f_1^3}{3B_{IF}} \right]^{1/2} S_v \quad (5.2.4-7)$$

where

V_n = rms noise voltage at the output of the video amplifier

a_n = rms IF noise voltage

A_c = peak carrier amplitude in volts

f_1 = highest frequency in the baseband

B_{IF} = IF bandwidth in Hz

S_v = deviation sensitivity in volts/Hz

For the LCE receiver, the nominal C/N = 23 db, so that $A_c/A_n \sqrt{2} = \sqrt{200}/\sqrt{2} = 10$. Also, $B_{IF} = 12$ MHz, $S_v = 1$ volt for a 5 MHz deviation, and $f_1 = 6$ MHz, where all values are for a 30 MHz IF. Thus,

$$V_n = \left(\frac{1}{10} \right) \cdot \left[\frac{6^3 \times 10^{18}}{3 \times 12 \times 10^6} \right]^{1/2} \left(\frac{1}{5 \times 10^{-6}} \right)$$

≈ 50 mv rms

Now the video amplifier noise, with a noise figure of 10 db (from a source resistance of 100 ohms), a bandwidth of 6 MHz, and a gain of 37 db results in an output noise power of

$$\begin{aligned}
 P_n &= -174 \frac{\text{dbm}}{\text{Hz}} + 10 + 10 \log (6 \times 10^6) + 37 \\
 &\approx -64 \text{ dbm} \\
 &= 4 \times 10^{-10} \text{ watts}
 \end{aligned}$$

Then

$$\begin{aligned}
 V_n &= (4 \times 10^{-10} \times 10^2)^{1/2} \\
 &= 2 \times 10^{-4} \text{ volts} \\
 &= 0.2 \text{ mv}
 \end{aligned}$$

This video noise voltage is still quite low compared to the system noise of 50 mv, so that there will be no degradation of the output S/N. However, further efforts to improve the discriminator linearity, or to operate at a lower drive level will require a reduction in the video amplifier noise figure, or some degradation of S/N could occur.

b. Nonlinear Phase Response

Nonlinear phase characteristics in any component will result in signal distortion. The amplifying circuits (preamplifier, post-amplifier, and video amplifier) are all very broadband so that their phase characteristics will be very linear. However, the phase characteristics of the filters require equalization. Although the filters in the receiver could be designed to be broader than required, so that the most linear portion of its phase characteristics is used, they would become physically much larger and it is doubtful if the remaining nonlinearity would be acceptable in any case without equalization. Thus, the question of minimum size for a given performance becomes one of trading the number of poles in a filter for the number of poles in an equalizer.

Nonlinear phase characteristics are best described by the group-delay, or envelope-delay, distortion which can be represented by a truncated Taylor series:

$$t(f) = t_0 + K_1 f + K_2 f^2 + t_r(f) \quad (5.2.4-8)$$

The linear component of group delay distortion is K_1 and has units of seconds/Hz (often given as nanoseconds/MHz). The parabolic component of group delay distortion is given by K_2 which has units of seconds/Hz² (often given as nanoseconds/MHz²). The residual group-delay component is represented by $t_r(f)$, and is generally given as a peak-to-peak value in seconds (or nanoseconds).

The group delay requirements for the OHRS are as follows:

+0.7 nanosec/MHz slope

0.5 nanosec/MHz² parabolic

6.0 nanosec peak-to-peak ripple

Although this requirement can be achieved in the OHRS with proper design, it is not a trivial problem because of the lack of symmetry (see Figure 3.2.4-17) in the group delay characteristics in the IF filters. This lack of symmetry is related to the fact that the percentage bandwidth is large and the problem is even more severe (by about a factor of 2-to-1), if an IF of 20 MHz were employed (Figure 5.2.4-18). If the group-delay characteristics of the 30 MHz Noise Filter (Figure 5.2.4-19) and the 30 MHz Channel Filter (Figure 5.2.4-20), are considered, the result obtained is the combined characteristic shown in Figure 5.2.4-21. Solving for a polynomial to fit the curve of Figure 3-21c results in the following equation:

$$t(f) = 86.4 - 3.23 f_n + 0.734 f_n^2 + t_r(f_n) \quad (5.2.4-9)$$

where

$f_n = (f - 30)$, so that the frequency axis has been shifted to the IF of 30 MHz, and

f = frequency of interest in MHz

Note that the linear component of group delay K_1 is -3.23 nanosec/MHz. To permit a reasonable contribution to the delay distortion by other circuits within the LCE, the channel filter will be designed for lower group-delay distortion (Figure 5.2.4-21) by reducing the amount of rejection obtained in the

filter and in addition, the receiver will include an equalizer to reduce the delay distortion.

An equalizer would ordinarily provide at least one order of magnitude of improvement in at least the linear and parabolic coefficients. However, because of the lack of symmetry, the equalizer design becomes somewhat more difficult. Nevertheless, it is expected that the linear component can be reduced by a factor of 5, thereby meeting the requirements. Improvement in the parabolic and ripple components are not as readily predictable so that, although improvements are expected, the magnitude of improvement in each component is somewhat uncertain.

c. Nonlinear Demodulation

The receiver demodulator is a version of the Foster-Seeley discriminator. Two diode detectors are connected with opposite polarity, so that the output voltage is the difference between the outputs of the two detectors. Each detector has a resonant circuit associated with it. One of the tuned circuits is tuned above the center frequency and one is tuned below the center frequency, so that an S-shaped curve is generated with a zero-crossing at the center of the IF passband. By using a restricted portion of the curve between the peaks, various degrees of linearity can be obtained. The Q of the tuned circuits, and the separation of the tuned frequencies can be manipulated to control the width of the discriminator characteristic and the resultant linearity (for a more detailed analysis, see Appendix D).

In the discriminator design used in the OHRS, the peaks of the response must be widely separated (by about 29 MHz for either the 20 MHz or 30 MHz IF) to obtain very good (less than 3%) linearity over the region of interest. Although this response is only a static, or low-frequency characteristic, by keeping the video amplifier load very nearly constant as a function of frequency the discriminator characteristic should be preserved. The present design uses an emitter-follower buffer stage as the immediate load on the discriminator to present a fairly high and constant load. With this arrangement, the linearity is expected to be better than 3%.

The discriminator response is also sensitive to signal power level. With total power variations of a few db the most significant change is

in the discriminator sensitivity (volts/MHz) characteristic, not in its linearity. However, signal changes beyond a few db will cause the linearity to degrade. However, the receiver design will make use of an agc circuit and a limiter. Either of these circuits alone will hold the variation of signal level input to the discriminator to fractions of 1 db.

d. Nonlinear Post Detection Gain

Nonlinearities in video gain following the discriminator are another source of distortion. The amount of distortion introduced by an amplifier can be determined crudely on the basis of how close the maximum signal is to the amplifier's saturation power level (1-db compression). The present design calls for an output voltage of 1 volt peak-to-peak into 75 ohms (or approximately +2.2 dbm) from a video amplifier with a 1-db compression point of approximately +12 dbm. Operating with a signal that is about 10 db down from the 1-db compression point should produce 3rd order intermodulation products that are about 38 db down, harmonics that are about 25 db down, and 2nd order intermodulation products that are about 19 db down. If measurements show that the rules-of-thumb applied are correct, the power-handling capability of the video amplifier might have to be increased by about another 10 db because of 2nd-order intermodulation distortion.

The frequency response of the video amplifier goes well beyond the requirements, since it has a 3-db bandwidth of about 30 MHz. Over the 1- to 6-MHz video band, the amplifier is flat to better than 0.2 db.

e. Unfiltered Harmonics, Spurious Responses,
or Interference

Receiver nonlinearities, particularly those which result from the limiter, will produce harmonics - which, in turn, will produce distortion of the baseband video if these harmonics are not filtered prior to entering the wideband discriminator. Therefore, a band-limiting filter is required just before the discriminator to reject frequencies above 36 MHz. Unfortunately, the "corner" of the filter cannot be too close to 36 MHz, otherwise the group delay characteristic will begin to deteriorate. Thus, a compromise must be reached between the required rejection (or number of poles in the filter), the amount of equalization, and the allowable group delay distortion. With the five-pole

filter, shown in Figure 5.2.4-21, the rejection at $2(30-6) = 48$ MHz is about 25 db. Since harmonics in the limiter output are expected to be 6 to 10 db down, the total rejection should be 31 to 35 db. Because the discriminator is quite wide (the upper resonant frequency peak will be at about 44 MHz for an IF of 30 MHz), attenuation cannot be expected. Thus, the resultant rejection can be as low as 31 db (or 2.8%) for the extreme case of minimum rejection in the filter, maximum harmonics out of the limiter, with a signal that has frequency components out to the lower corner of the IF passband.

In order to keep the video response "flat" to at least 6 MHz, the discriminator circuit must pass signals well above 6 MHz, and so does not provide any appreciable attenuation to the IF signal. As a result, the signal which results from the IF "leakage" to the video amplifier is larger (by about 30 db) than the demodulated, or video, signal. Since the video amplifier has significant gain at the IF, if the IF leakage were not attenuated prior to the video amplifier, there would be significant intermodulation and possibly saturation in the video amplifier. To prevent intermodulation and possibly saturation, it would be necessary to provide at least 40 db of attenuation to the lowest frequency in the IF passband. This would make the leakage signal about 10-db below the desired signal. It then would be necessary to rely on a limited frequency response in other video components of the OHSR system to provide the additional attenuation. Although other video components will provide attenuation to frequencies below 24 MHz, it is believed that it is not advisable to depend upon this attenuation. Therefore, a video filter will be used before the video amplifier which has been designed to provide a minimum of 50 db of attenuation at 24 MHz. The calculated rejection for the filter design (Figure 5.2.4-22) is 68 db, which would make the IF leakage approximately 38 db below the video. Even though large rejection is obtained in the video filter, the delay distortion of the filter is negligible because it is a band-reject filter.

Nutation of the received signal to provide tracking error is not expected to produce any interference in the video channel. The nutation causes an amplitude modulation at the nutation frequency (100 Hz), which is removed by the limiter. In addition, the video bandwidth extends from 1 MHz to 5 MHz, so that the appearance of any 100-Hz component (or its harmonics) is well outside the video passband.

With regard to interference, at the present time, there are two areas of concern, which are:

- Coupling of HF signals within the frequency range of approximately 1 to 50 MHz, into the infrared mixer element, coaxial cable or IF preamplifier
- High-level signals in the video passband of 1 to 6 MHz, such as can be produced by the laser modulator, or other ATS-F experiments, coupling into any of the receiver circuits

With regard to the first area of concern, careful shielding will be provided for the mixer element, coaxial cable, and IF preamplifier to prevent signals in the frequency range of 1 to 50 MHz from saturating the IF preamplifier. The only signals in this frequency range within the LCE that might be strong enough to saturate the IF preamplifier are in the laser modulator with frequencies of 1 to 6 MHz. To saturate the preamplifier, a signal of approximately -35 dbm at the input is required. Since the case should provide about 80 db of shielding in this frequency range (limited by seam and gasket leakage), the interfering signal must produce a field that can induce greater than +45 dbm at the preamplifier location. Even the laser modulator will not produce signals of such a high level. Coupling into the cable between the mixer and the preamplifier will likewise be reduced by the cable shielding; this is discussed elsewhere in this report.

In addition to the above considerations, any signals in the IF passband must be attenuated below the noise level of the IF preamplifier so as not to degrade the signal. At the present time, there are no known sources of interference operating within the IF passband so that normal filtering and shielding will be adequate.

The second area of concern is a potential problem at the video amplifier, where the signal and interference are at the same frequency (IF filters will attenuate the video signal). The signal level at the video amplifier input is approximately -40 dbm. Since it is required that the interference be at least 30 db below the signal level, the induced signal must be no more than -70 dbm. With 80 db of shielding effectiveness, the field must be capable of producing +10 dbm, into a small wire or component with dimensions on the order of 1 cm at an impedance level of approximately 50 ohms. This would call for a

field of greater than 200 volts/meter which is clearly not going to be produced by any component within the LCE system.

Thus, at the present time, there are no interference conditions that can degrade the receiver performance. This discussion will be expanded in future design review documents and the question of potential interference will be in constant review.

5.2.4.3.1.4 Frequency Error Channel

This channel provides an error voltage by amplifying the output of the discriminator in a dc-coupled afc amplifier with a limited frequency response. Video signals will be present but the video signals will be above 1 MHz, so that no low-pass filter is needed ahead of the afc amplifier. The presence of video signals in the afc output could be troublesome. However, since afc channel-frequency response will be limited to about 10 kHz, the video components coming out of the afc amplifier will be quite small (as much as 90 db down). Since the afc error signal is derived from the same discriminator as is used in the video communications channel the circuit will be operative over a very large frequency range (greater than 29 MHz).

5.2.4.3.1.5 Tracking Error Channel

The tracking error channel requires phase detection of the amplitude and phase modulation produced by nutation. Since there are no video components below 1 MHz, there are no problems with interference between the video and the 100 Hz nutation frequency. The details of the overall tracking system requirements are given in the tracking system analysis (Appendix B).

5.2.4.3.1.6 Acquisition and Acquisition-Confirm Pulse Channels

The acquisition and acquisition-confirm pulse channel circuits are under preliminary design. The system requirements of these two channels are given in Appendix B.

5.2.4.3.2 Circuit Designs

The information in the following paragraphs contains highlights of the various circuit designs. It illustrates the performance capabilities of the breadboard circuits and points out where additional work may be required to obtain the desired performance or where problems may exist. At the present time,

no problem areas exist and the only areas where additional work is required are in:

- Reducing the IF preamplifier noise figure
- Determining the optimum tradeoffs between filter requirements, group-delay distortion, and equalizer capabilities
- Increasing the power output capability of the IF post-amplifier

None of these areas represent any technical difficulty, and these requirements can be resolved with proper attention to the engineering design.

All of the data are for circuit designs at an IF of 20 MHz. No technical problems are anticipated in realizing equal or better performance at 30 MHz.

5.2.4.3.2.1 IF Preamplifier

The important performance characteristic in the IF preamplifier is its noise figure. Since the resistance looking back into the infrared mixer will be greater than the optimum source resistance for the preamplifier, an input-matching network that does not narrow the bandwidth is required. Figure 5.2.4-23 shows noise-figure data as a function of source resistance for various matching networks. The noise figure can be optimized to approximately 2 db over a fairly broad range of source resistance. Noise figure measurements will be made with other transistors, and it is expected that the noise figure can be reduced to 1.5 db.

The nominal gain of the IF preamplifier is 26 db and is flat to within fractions of 1 db from 10 to 50 MHz.

5.2.4.3.2.2 Noise Bandwidth Filter

The noise bandwidth filter is a 3-pole filter with a bandwidth of 12 MHz at approximately 1/4 db, and a 3-db bandwidth of approximately 23 MHz. The equivalent noise bandwidth will be adequate if the carrier-to-noise ratio in a 12-MHz bandwidth is 23 db. The 3-db bandwidth is intentionally wide so that there will be negligible attenuation or group delay distortion in the IF pass-band.

5.2.4.3.2.3 IF Post-amplifier

Figure 5.2.4-24 shows the power output vs power input for the IF post-amplifier. The amplifier (which includes the agc circuit) has a nominal gain of 45 db, with an agc threshold set at approximately -50 dbm (this corresponds to S/N of about 17 db). Present work is directed at improving the amplifier so that the agc action is more abrupt and the output power is higher. Initial attempts to increase the output power have been marginal because the broad frequency response is degraded by the transformers.

5.2.4.3.2.4 Equalizer

An equalizer has been designed to reduce the group delay distortion of the receiver. The major part of the equalization will be to compensate for the delay distortion introduced by the channel filter. The remaining circuits in the receiver should not contribute any appreciable distortion.

5.2.4.3.2.5 Limiter

The breadboard limiter circuit at 20 MHz provides about 0.6 db of output change for an input variation of 10 db centered at an input power of 0 dbm (Figure 5.2.4-25). The previous design was for the IF post-amplifier to deliver -5 dbm to the limiter. At that level, the variation was similar but the phase linearity was not good enough.

Figure 5.2.4-26 shows the limiter frequency response. Although the response is very flat, it must be appreciated that the amplitude response of the amplifier driving the limiter diodes is lost in the limiting action. More significant information is contained in Figure 5.2.4-27 which shows the phase linearity of the limiter. Because of the linearity, the group-delay distortion will be quite small (less than 1 nanosec/MHz).

5.2.4.3.2.6 Channel Filter

The calculated characteristics of the 30 MHz channel filter have been shown before in Figure 5.2.4-21.

5.2.4.3.2.7 Discriminator

Figure 5.2.4-28 shows the discriminator linearity (the most important parameter) versus frequency. The linearity for an input power level

of 0 dbm is better than 2% over the entire IF passband. Similar linearity was obtained with earlier versions of this discriminator, but the earlier versions required a higher input power level. Figure 5.2.4-29 shows the performance of an early version that was optimized at +5 dbm. Note that very little degradation of linearity occurs when the input power level changes. This can be seen by observing the linearity of the curves for +4 dbm and +6 dbm, which is a change of ± 1 db from the nominal level. This is a larger change than is expected since the limiter and agc circuits are expected to hold the power level constant to less than ± 0.5 db. Although these measurements were performed on the discriminator that was optimized for a +5 dbm input level, the results should be the same for the final discriminator design.

The variation of discriminator linearity as a function of load impedance is shown in Figure 5.2.4-30 for the +5 dbm discriminator. Again, the results should be the same for either discriminator. Figure 5.2.4-30 shows that, while the linearity is not seriously affected by load impedance, the output voltage will decrease with decreasing load resistance. Therefore, it is more important that the load be independent of frequency than independent of time; that is, it is important that the input impedance to the video amplifier be constant with frequency up to the highest video frequency. The present design is expected to be constant at 1 kilohm, so that no problems are expected with load variation.

Measurements of the discriminator characteristic as a function of temperature have also been made and the effects are negligible over the temperature range of 10°C to 30°C. Additional measurements will be made over a wider temperature range when the 30-MHz discriminator is made.

5.2.4.3.2.8 Video Filter

The calculated response of the video filter was discussed earlier and is shown in Figure 5.2.4-22. The actual response is expected to be very nearly the same as the calculated response.

5.2.4.3.2.9 Video Amplifier

The video amplifier is flat within fractions of 1 db from 1 to 6 MHz. Its phase characteristic is quite linear from 1 to 6 MHz, and is shown in Figure 5.2.4-31.

The video amplifier can deliver 1 volt peak-to-peak into either 50 ohms or 75 ohms with about a 10-db margin. Figure 5.2.4-32 shows the output-power versus input-power characteristic for a 50-ohm load.

5.2.4.3.2.10 Acquisition Bandpass Filter

The acquisition bandpass filter for the 30-MHz IF will be a four-pole filter with a 4-MHz bandwidth at the 0.5-db points. The filter is of conventional design and has no special requirements.

5.2.4.3.2.11 AM Detector

The AM detector is straightforward. It will operate as a square-law detector for the low-level signals that will be experienced during acquisition.

5.2.4.3.2.12 Tuned Audio Amplifier

The selectivity characteristics of the tuned audio amplifier are shown in Figure 5.2.4-33. The amplifier is a twin-tee filter tuned to 100 Hz. The rejection to 200 Hz (the second harmonic) is approximately 10 db.

5.2.4.3.2.13 Phase Detectors

The phase detector output voltage versus percent amplitude modulation is shown in Figure 5.2.4-34. The data were taken with a signal of -45 dbm into the IF post-amplifier, which corresponds to a signal with a C/N of 19 db. The output voltage for a phase difference of 180 degrees is equal to the voltage for a phase difference of 360 degrees except for the algebraic sign. Varying the phase between 0 and 180 degrees causes the signal to change from negative to positive, with a minimum at 90 degrees.

5.2.4.3.2.14 Mixer Bias Control

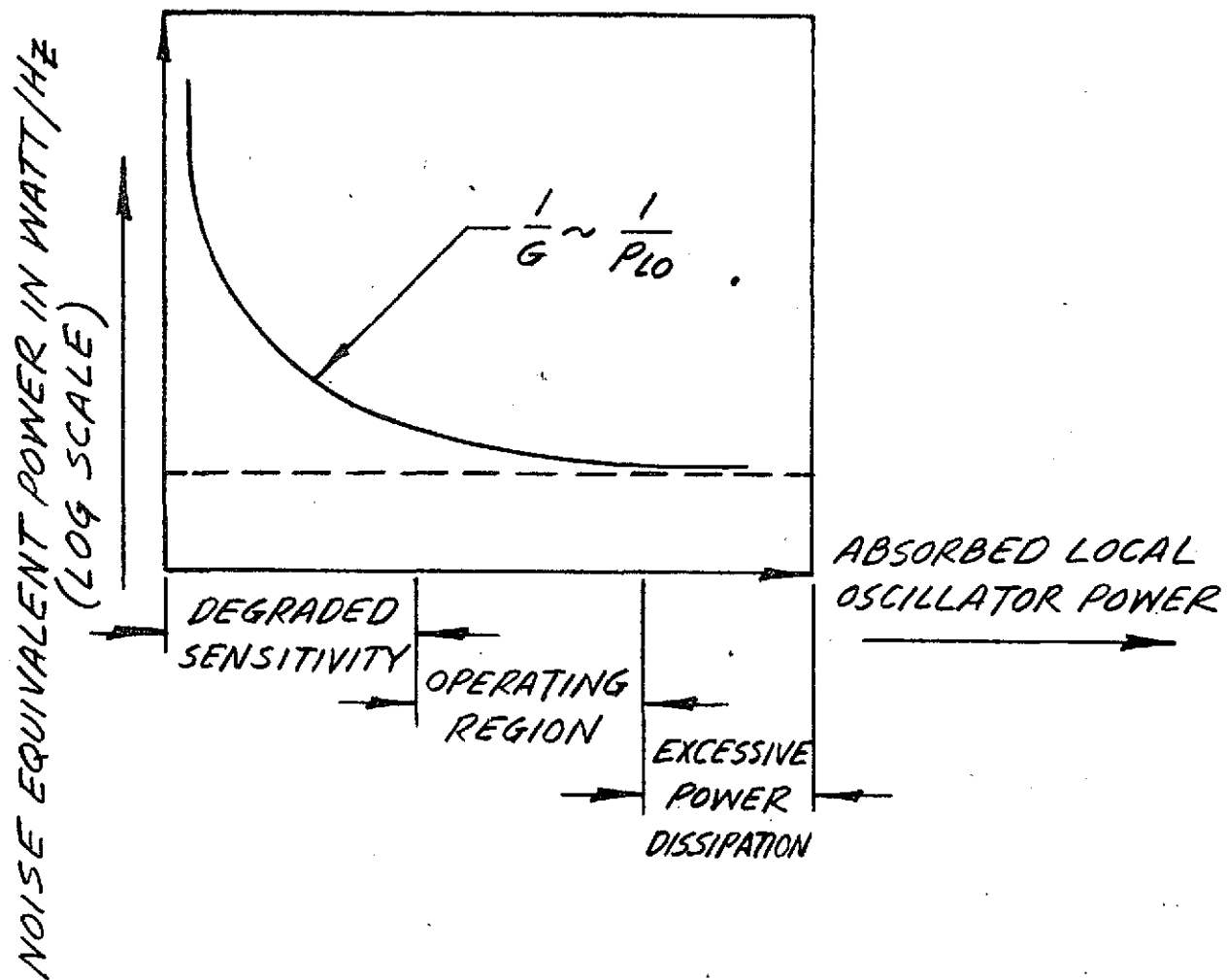
The mixer bias control circuit provides a regulated voltage to the mixer to maintain constant bias voltage. The output current is limited to prevent damage to the mixer. The characteristics of the circuit are shown in Figure 5.2.4-35. The normal region of operation is expected to be above 50 ohms and below 300 millivolts where the regulation is good.

TABLE 5.2.4-1

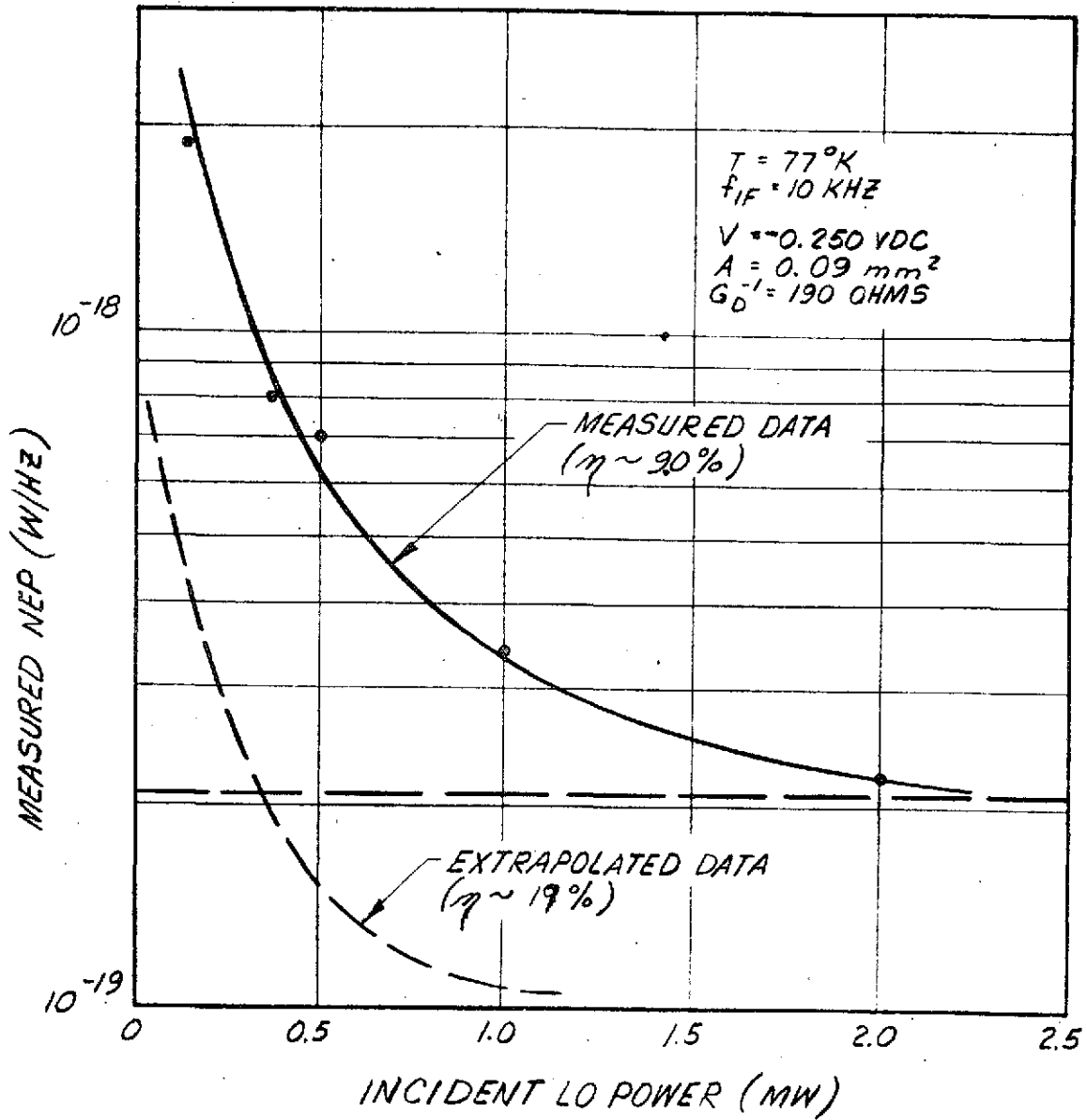
PROJECTED PERFORMANCE AT HIGH-TEMPERATURE LIMIT FOR
OHS FLIGHT AND GROUND MODELS

	Mixer Temperature	
	105 +5°K (Previous OHS Spec)	110 +15°K (OHS Spec)
Post-amplifier NF (db)	8	8
Post-amplifier temperature (°K)	1485	1485
Preamplifier gain (db)	26	26
Eff. post-amplifier noise temperature (°K)	3.7	3.7
Preamplifier NF (db)	1.8	1.8
Preamplifier noise temperature (°K)	148	148
Total IF noise temperature (°K)	151.7	151.7
Cable loss (db) $T_L \sim 200$ K	0.25	0.27
Effective IF noise temperature (T_{IF}) (°K)	172	174
Maximum mixer temperature (T_M) (°K)	105	125
($T_M + T_{IF}$) (°K)	277	299
Quantum efficiency (%)	20	13
P_{min} (w/Hz x 10^{-19})	.935	1.435
G_D^{-1} (ohms)	100	100
f/f_c	.54	.6
$f = (1 + (f/f_c)^2)^{-1}$.775	.735
P_{LO} (mw) (10% thermal degradation)	3.6	6.25
Mixer gain, G (db)	-3.9	-5.5
Thermal noise term (w/Hz x 10^{-19})	.0935	.144
NEP (w/Hz x 10^{-19})	1.03	1.58

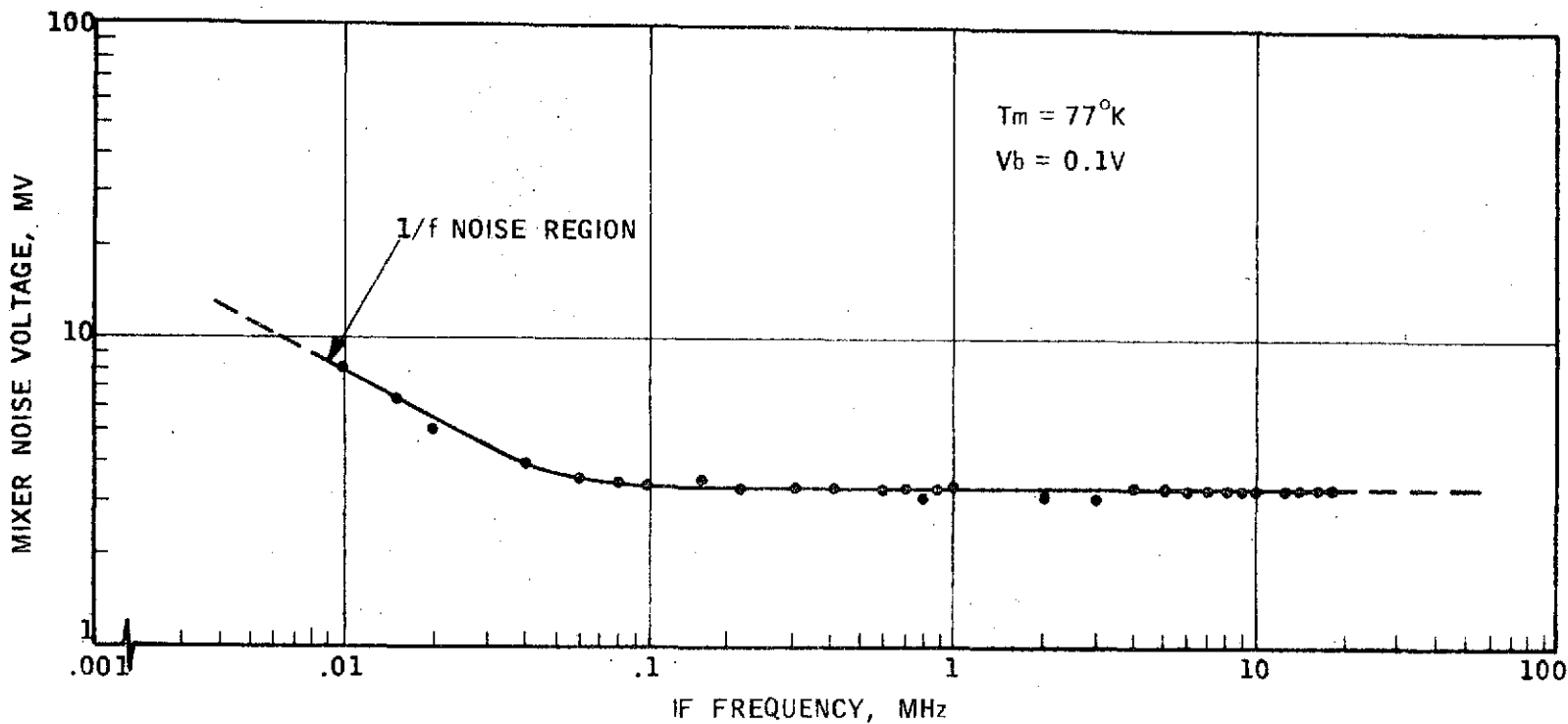
Table 5.2.4-1



Region of Optimum Mixer Operation

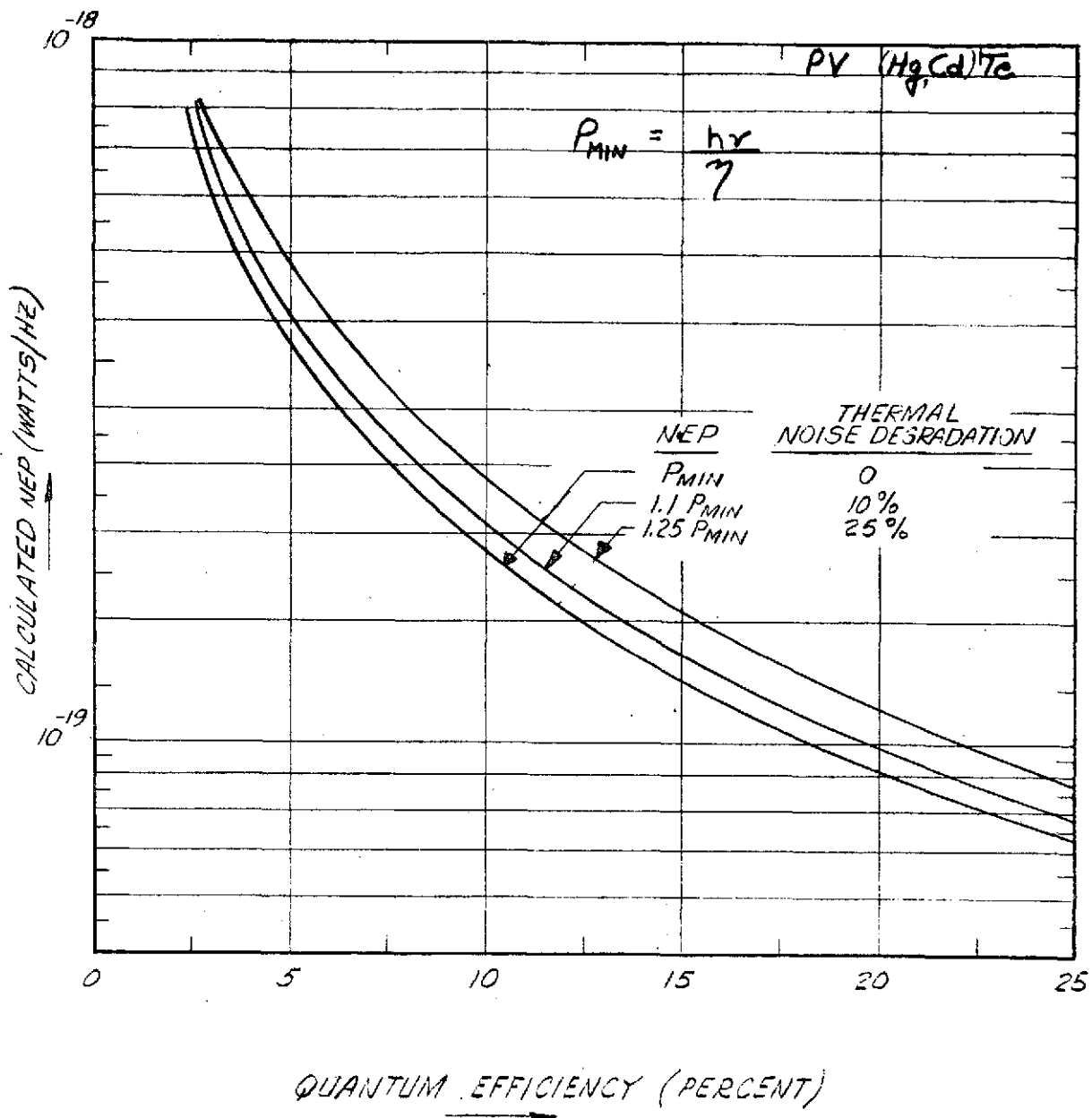


Measured & Extrapolated NEP vs LO Power
(Noise Measured at 300 KHz) in Photovaltaic (Hg, Cd) Te

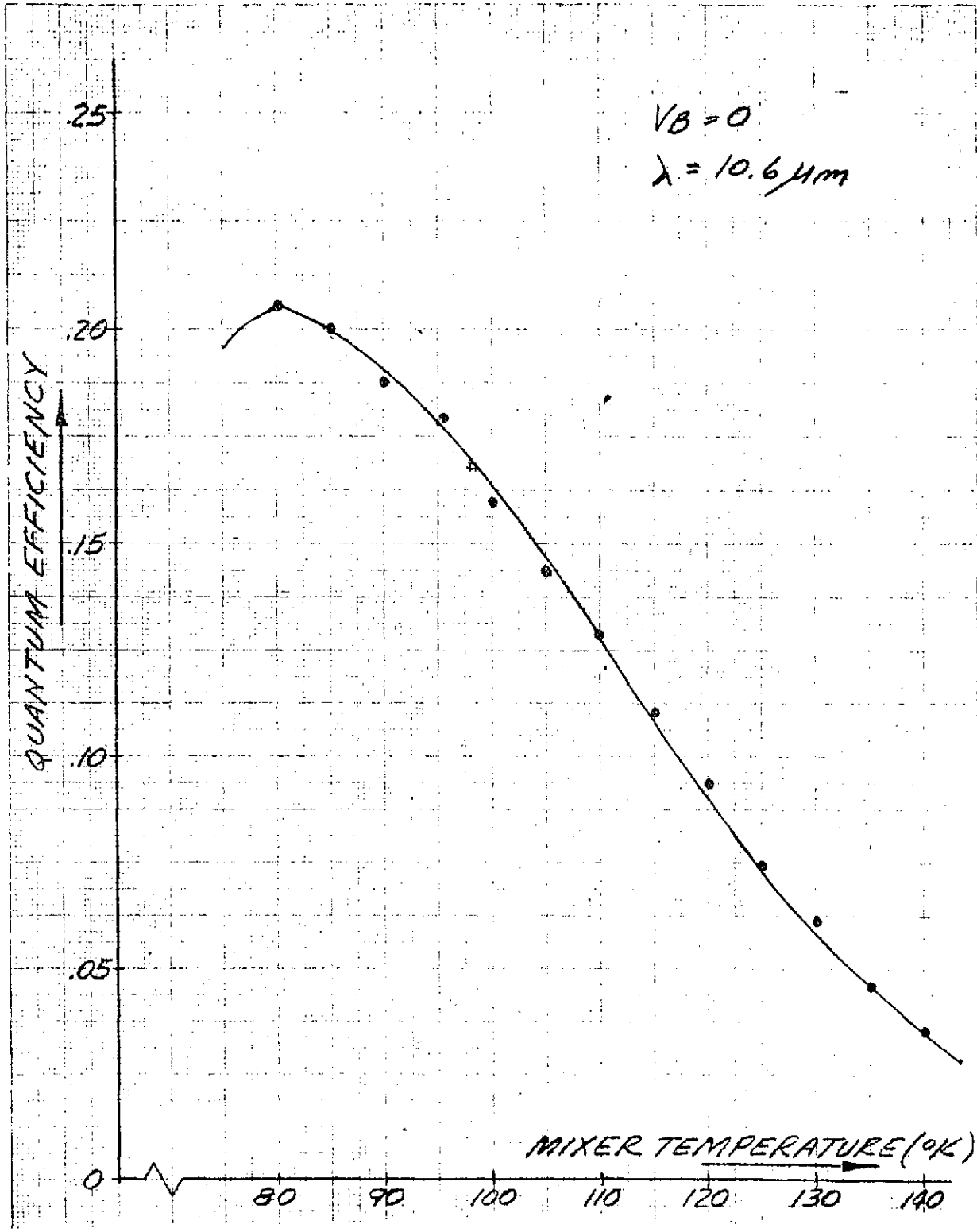


MIXER NOISE VOLTAGE VERSUS
IF FREQUENCY IN PHOTOVOLTAIC (Hg, Cd) Te

Figure 5.2.4 4

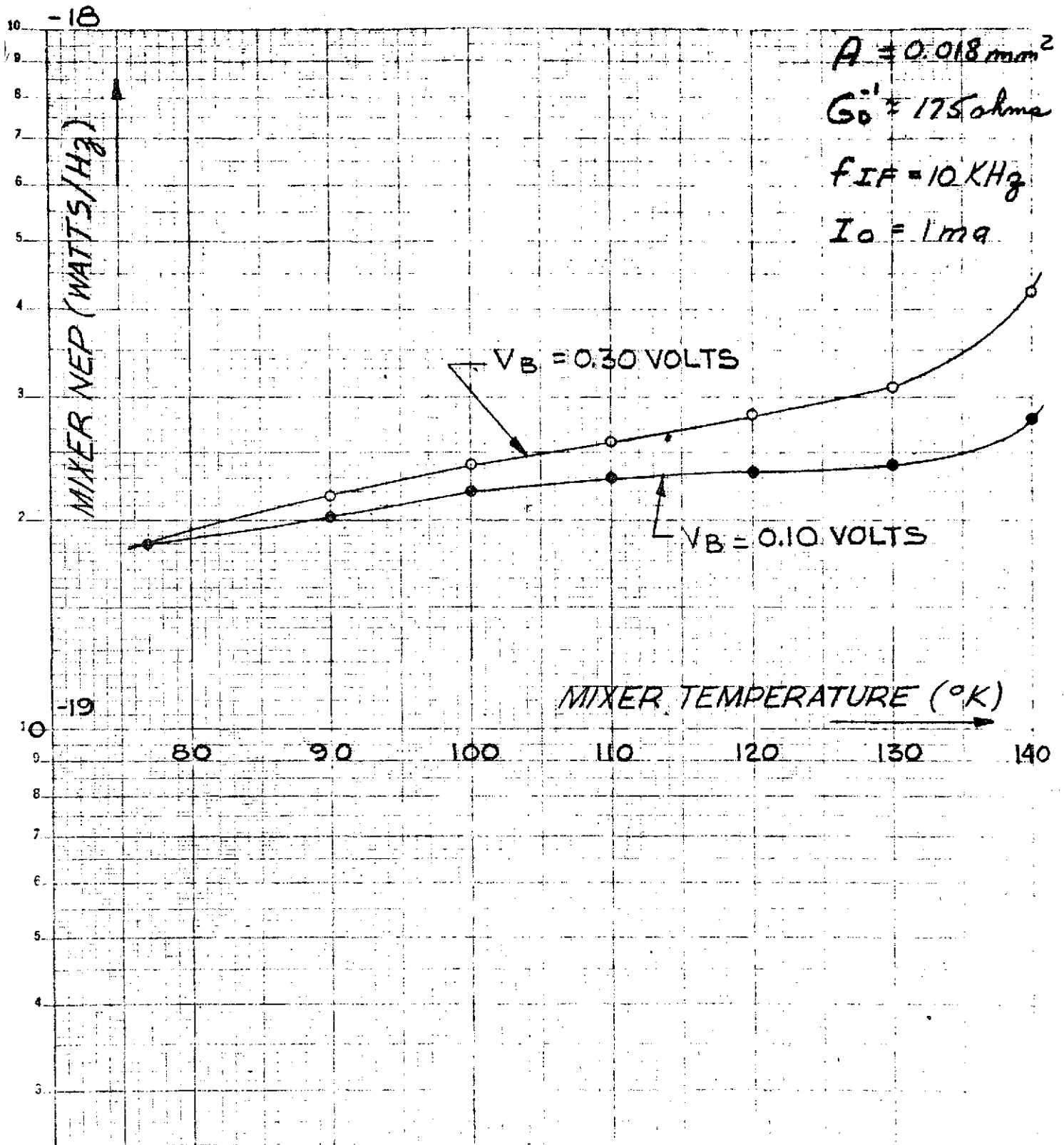


Calculated Quantum-Noise Limited Receiver Sensitivity vs Quantum Efficiency at 10.6 Microns



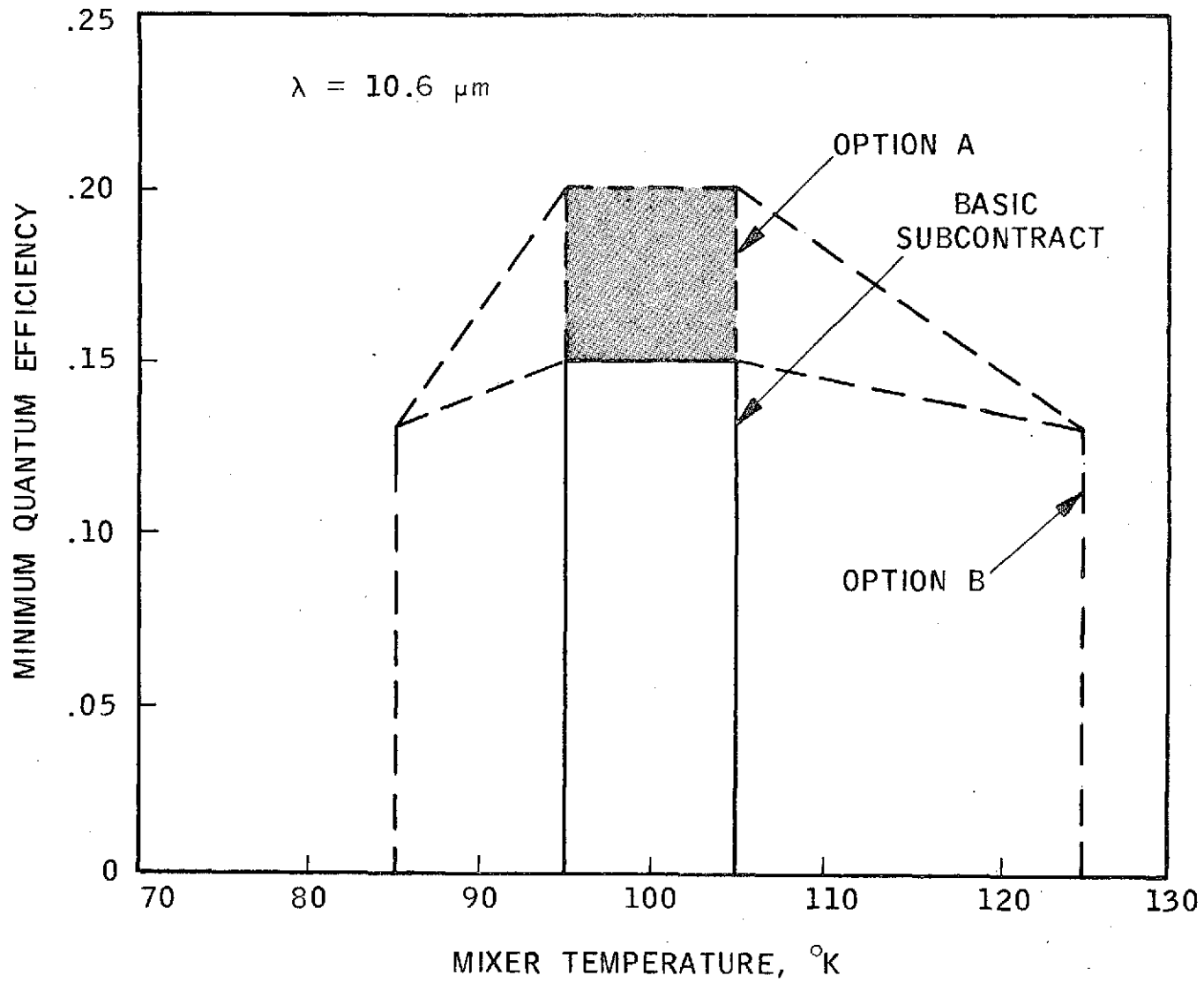
Quantum Efficiency Versus Temperature
in Photovoltaic (Hg, Cd) Te

Figure 5.2.4-6



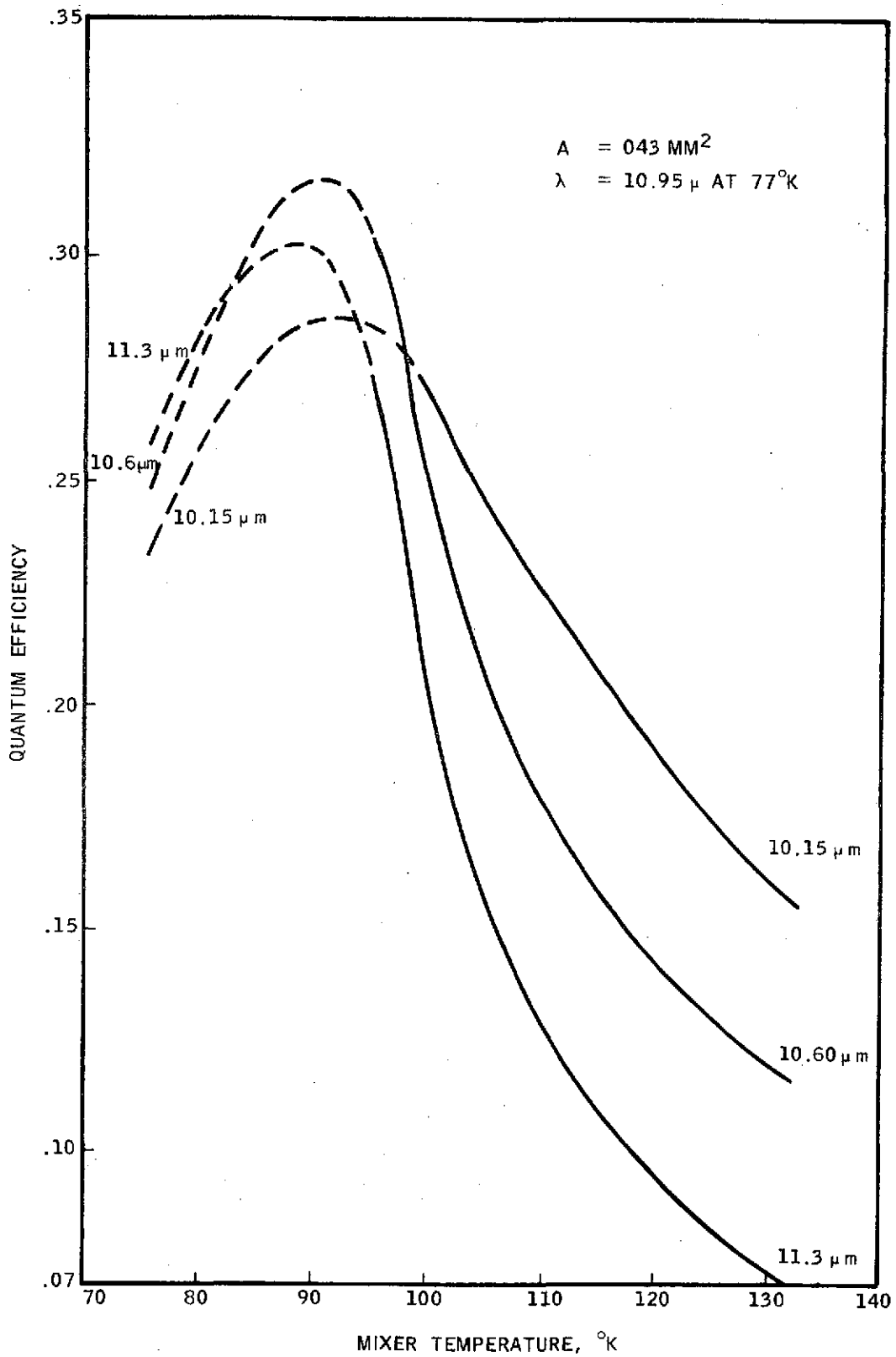
Noise Equivalent Power Versus Temperature in Photovoltaic (Hg, Cd) Te

Figure 5.2.4-7



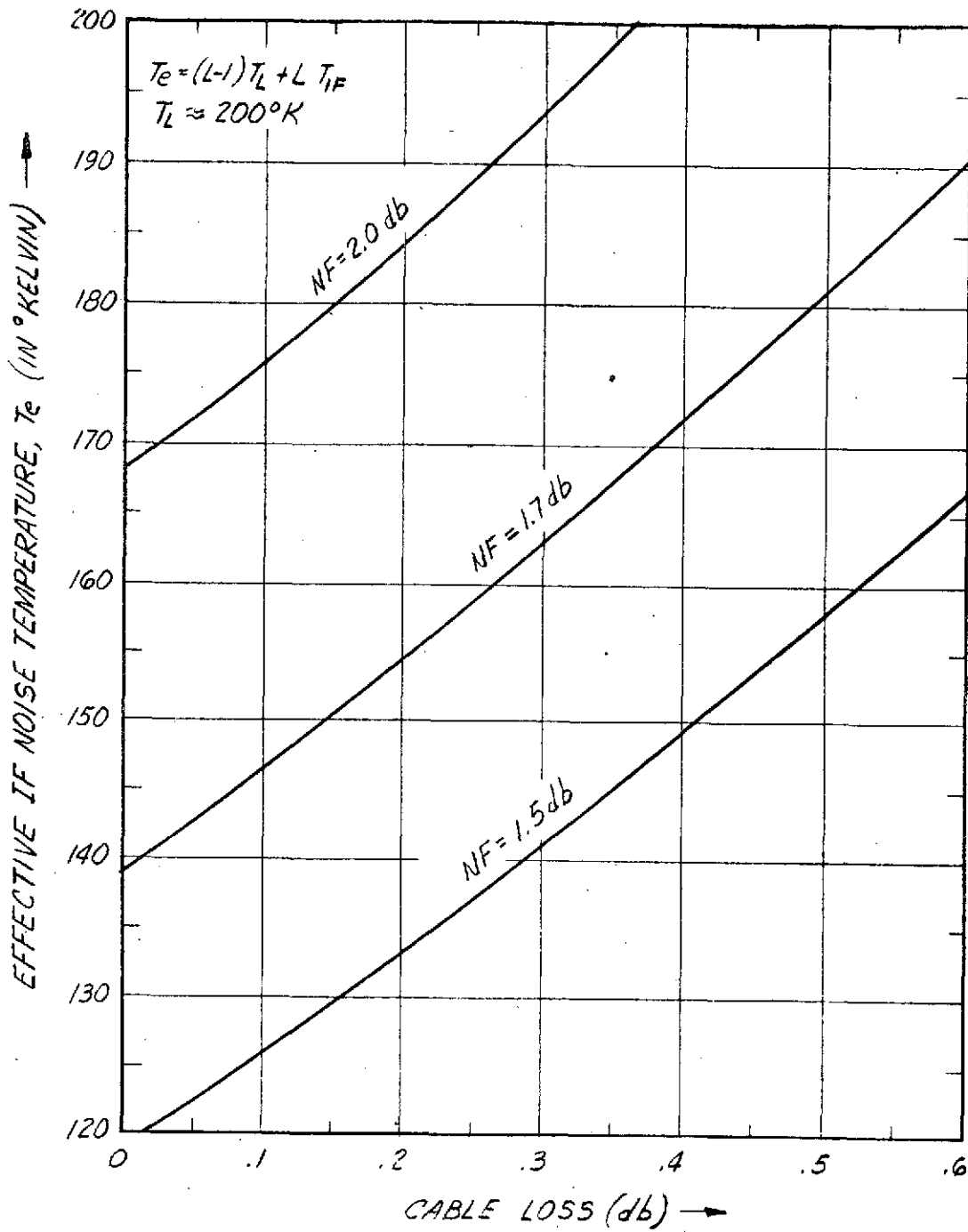
SUBCONTRACT MINIMUM QUANTUM EFFICIENCY
VS MIXER TEMPERATURE

Figure 5.2.4-8

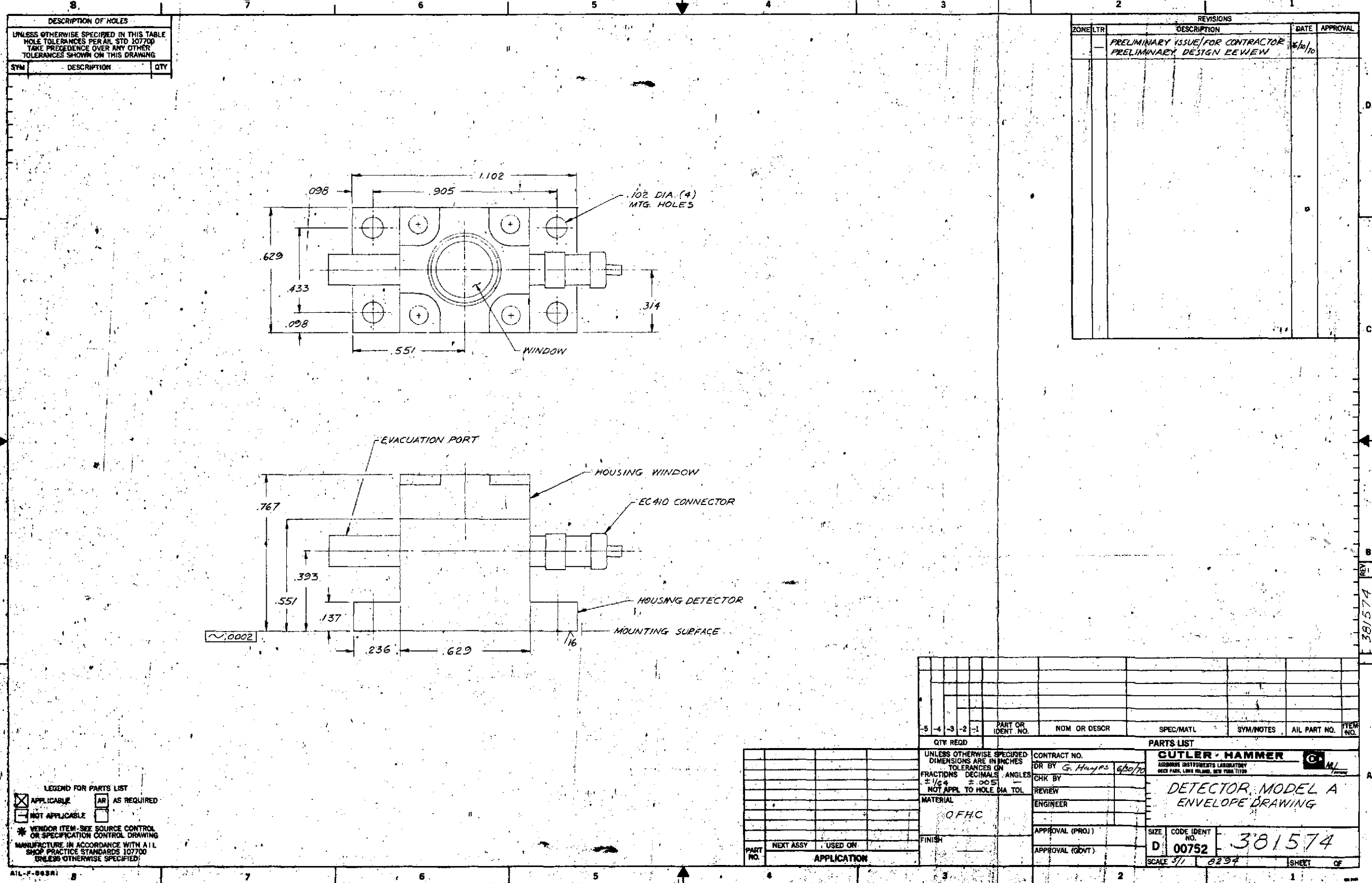


QUANTUM EFFICIENCY VS MIXER TEMPERATURE

Figure 5.2.4-9



Effective IF Noise Temperature vs Cable Loss



DESCRIPTION OF HOLES		
UNLESS OTHERWISE SPECIFIED IN THIS TABLE HOLE TOLERANCES PER AN. STD. 107700 TAKE PRECEDENCE OVER ANY OTHER TOLERANCES SHOWN ON THIS DRAWING		
SYM	DESCRIPTION	QTY

REVISIONS			
ZONE/LTR	DESCRIPTION	DATE	APPROVAL
	PRELIMINARY ISSUE FOR CONTRACTOR	6/20/70	
	PRELIMINARY DESIGN REVIEW		

LEGEND FOR PARTS LIST
 APPLICABLE AS REQUIRED
 NOT APPLICABLE AS REQUIRED
 * VENDOR ITEM - SEE SOURCE CONTROL OR SPECIFICATION CONTROL DRAWING
 MANUFACTURE IN ACCORDANCE WITH ALL SHOP PRACTICE STANDARDS 107700 UNLESS OTHERWISE SPECIFIED

QTY REQD	PART OR IDENT. NO.	NOM OR DESC	SPEC/MATL	SYM/NOTES	AIR PART NO.	ITEM NO.

UNLESS OTHERWISE SPECIFIED - DIMENSIONS ARE IN INCHES		CONTRACT NO.	
FRACTIONS	DECIMALS	DR BY	G. Hayes 6/20/70
ANGLES		CHK BY	
± 1/64	± .005	REVIEW	
NOT APPL TO HOLE DIA TOL		ENGINEER	
MATERIAL	OFHC	APPROVAL (PROJ)	
FINISH		APPROVAL (GOVT)	
APPLICATION		SIZE	D
		CODE IDENT NO.	00752
		SCALE	3/1 8294
		SHEET	381574

Figure 5.2.4-11

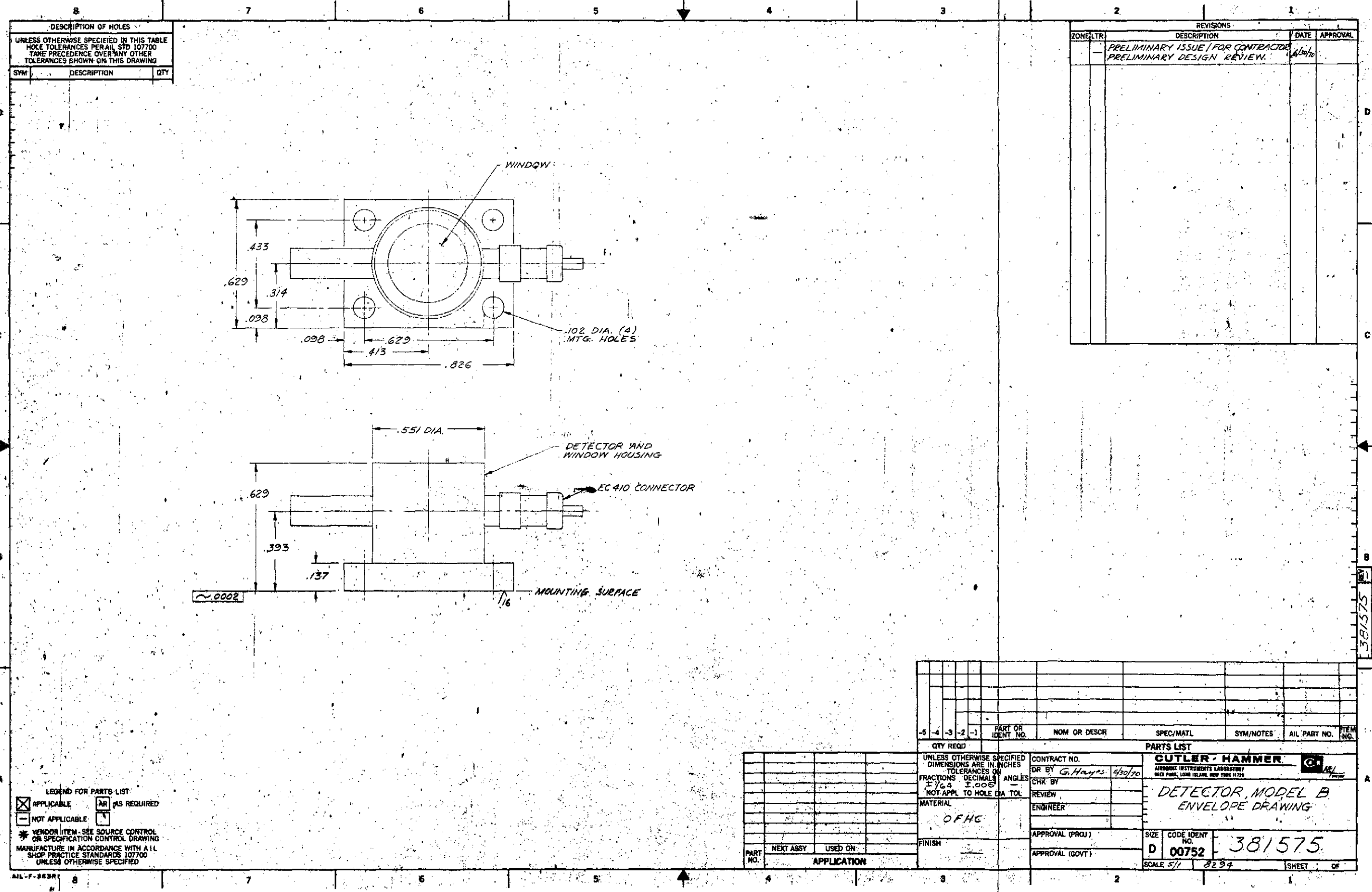
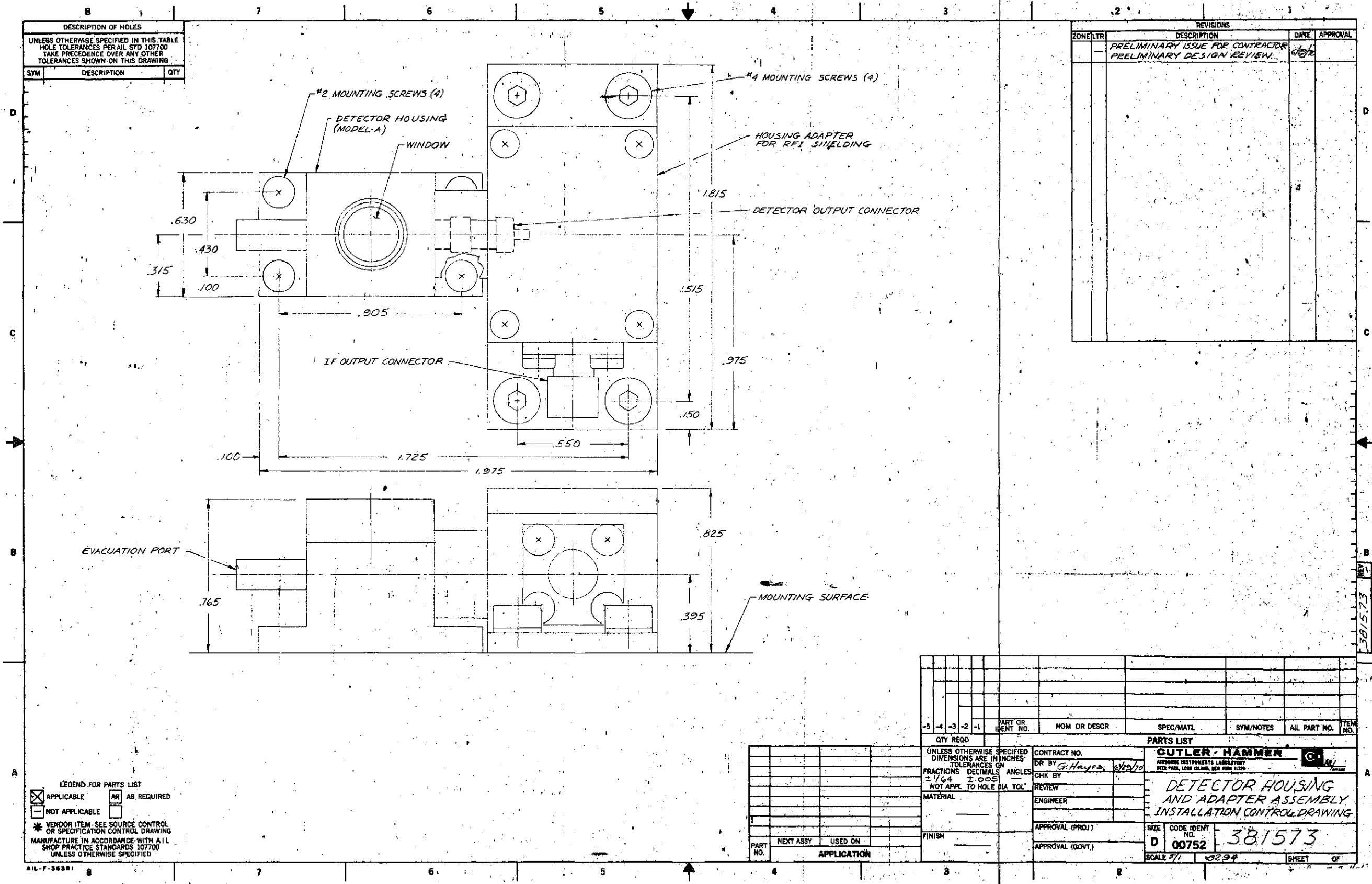


Figure 5.2.4-12



DESCRIPTION OF HOLES		
UNLESS OTHERWISE SPECIFIED IN THIS TABLE HOLE TOLERANCES PER MIL STD 107700 TAKE PRECEDENCE OVER ANY OTHER TOLERANCES SHOWN ON THIS DRAWING		
SYM	DESCRIPTION	QTY

REVISIONS			
ZONE/LTR	DESCRIPTION	DATE	APPROVAL
	PRELIMINARY ISSUE FOR CONTRACTOR PRELIMINARY DESIGN REVIEW	6/2/70	

LEGEND FOR PARTS LIST
 APPLICABLE AS REQUIRED
 NOT APPLICABLE AS REQUIRED
 * VENDOR ITEM - SEE SOURCE CONTROL OR SPECIFICATION CONTROL DRAWING
 MANUFACTURE IN ACCORDANCE WITH ALL SHOP PRACTICE STANDARDS 107700 UNLESS OTHERWISE SPECIFIED

QTY REQD	PART OR IDENT NO.	NOM OR DESCR	SPEC/MATL	SYM/NOTES	ALL PART NO.	ITEM NO.

UNLESS OTHERWISE SPECIFIED DIMENSIONS ARE IN INCHES		CONTRACT NO.	
FRACTIONS	DECIMALS	DR BY	G. Hayes
± 1/64	± .005	CHK BY	6/2/70
NOT APPL. TO HOLE DIA TOL.	ANGLES	REVIEW	
MATERIAL		ENGINEER	
FINISH		APPROVAL (PROJ)	
PART NO.		APPROVAL (GOVT)	
NEXT ASSY	USED ON	SIZE	CODE IDENT
APPLICATION		D	00752
		SCALE	3/1
			3294
		SHEET	OF

Figure 5.2.4-13

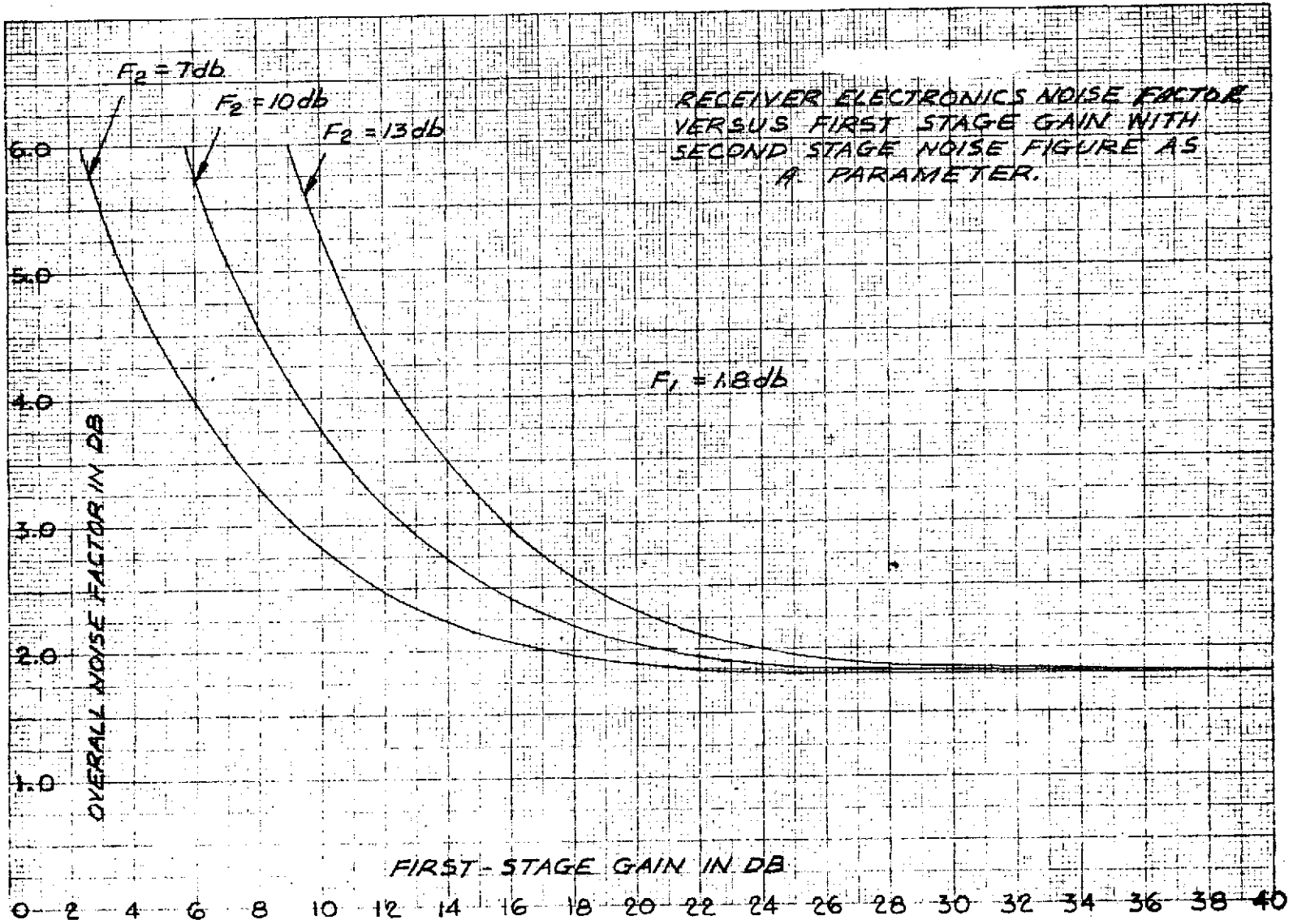
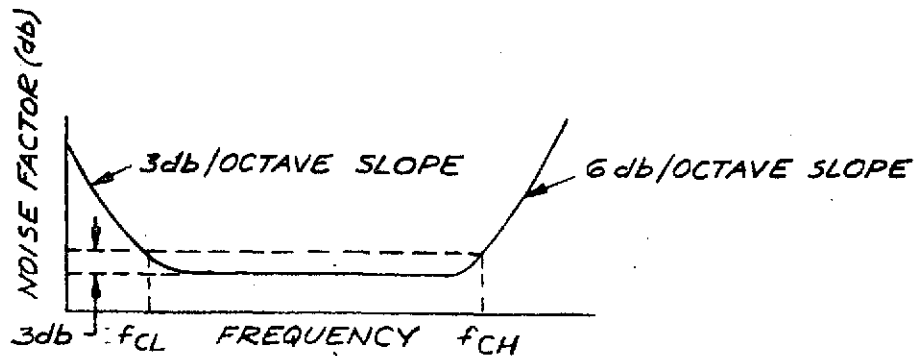
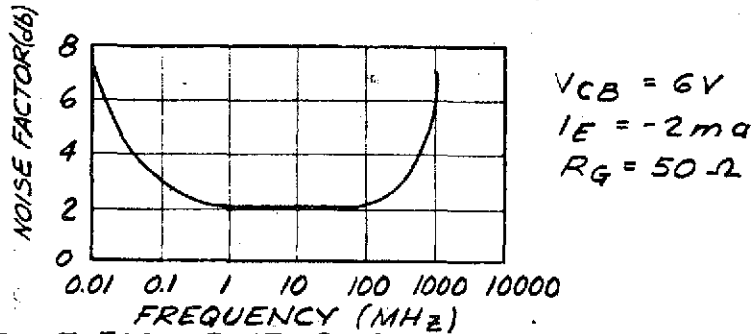


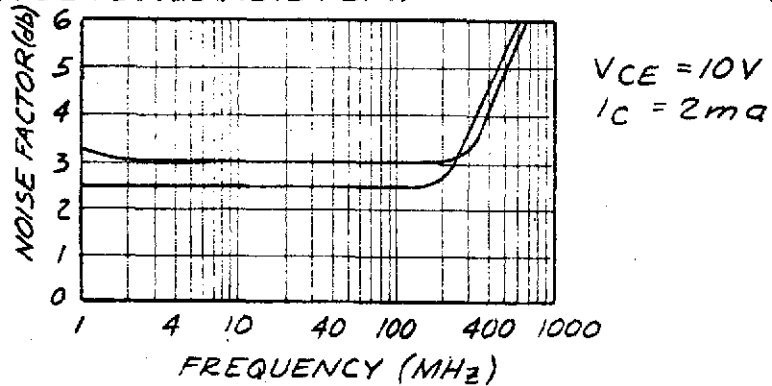
Figure 5.2.4-14



A. THEORETICAL BEHAVIOR OF NOISE FACTOR VERSUS FREQUENCY.



B. NOISE FACTOR VERSUS FREQUENCY FOR 2N3570 TRANSISTOR.



C. NOISE FACTOR VERSUS FREQUENCY FOR 2N4252 TRANSISTOR.

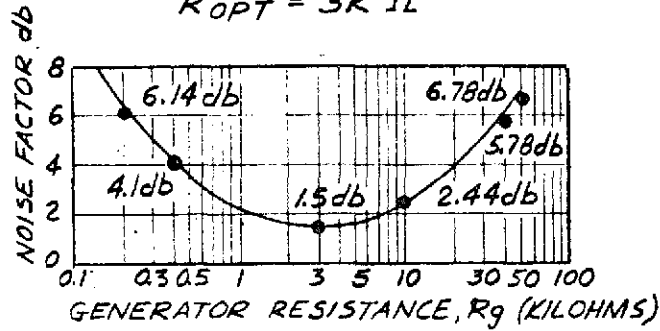
VARIATION OF AMPLIFIER NOISE FACTOR WITH IF FREQUENCY

• CALCULATED POINTS

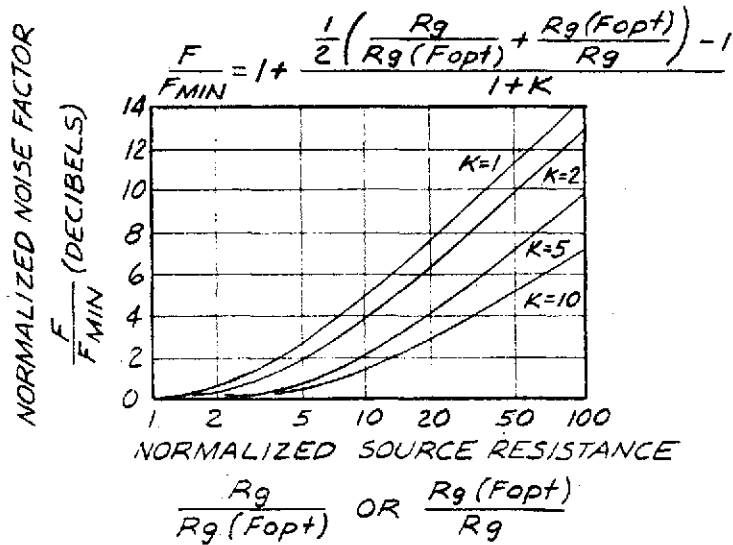
$I_C = 100 \mu \text{ AMP}$

$F_{\text{MIN}} = 1.5 \text{ db}$

$R_{\text{OPT}} = 3 \text{ K } \Omega$



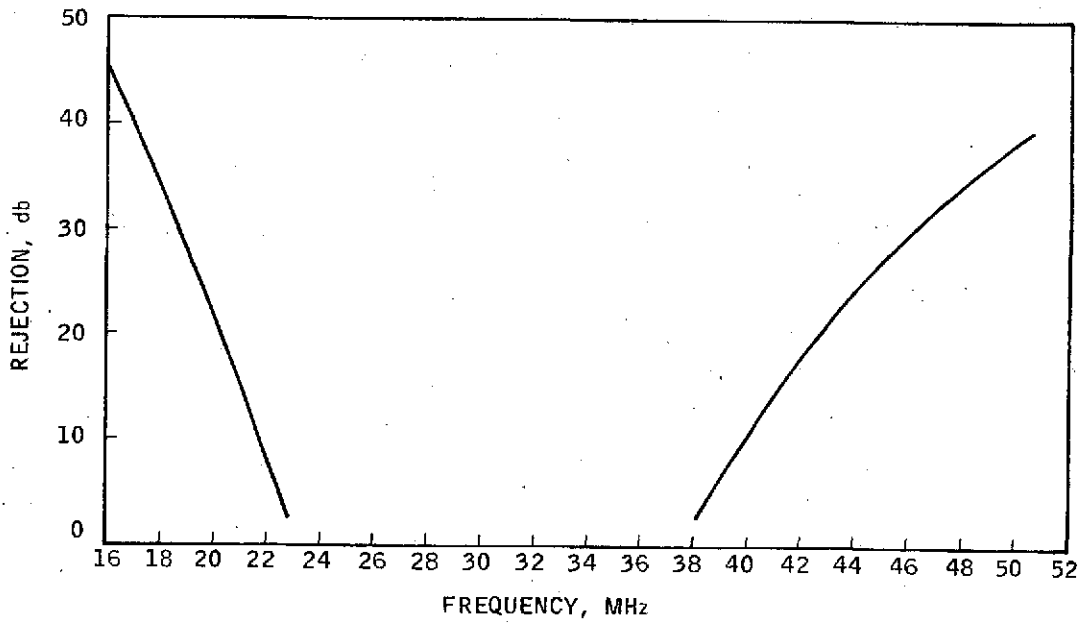
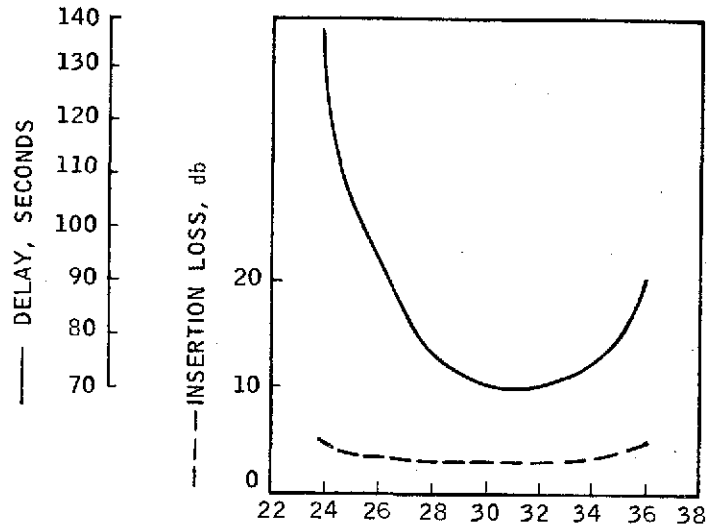
A. MEASURED VARIATION OF NF WITH SOURCE RESISTANCE FOR 2N930 TRANSISTOR.



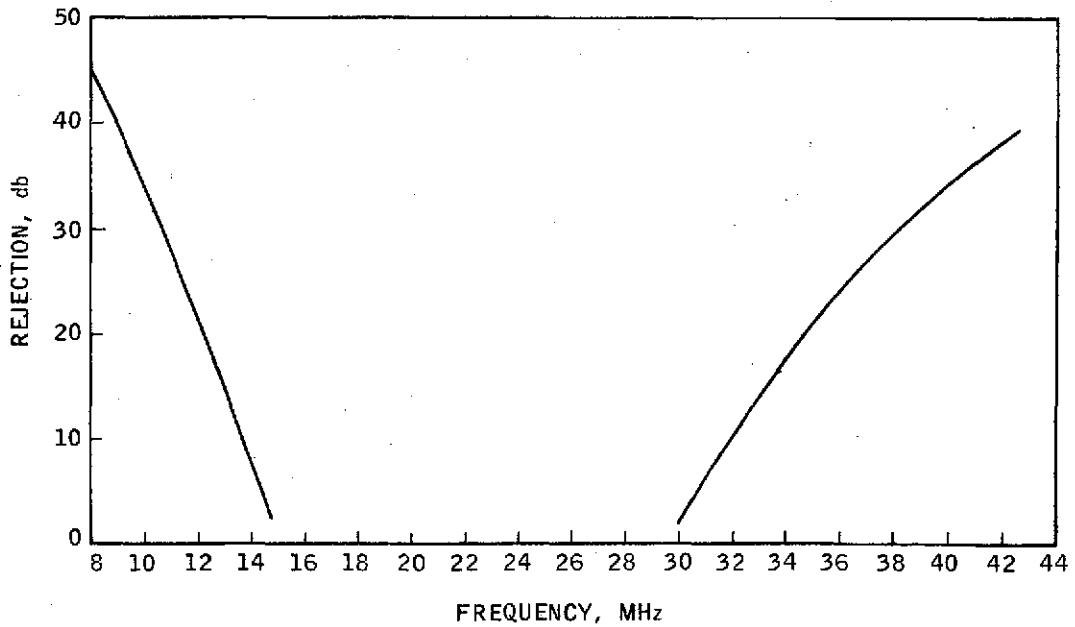
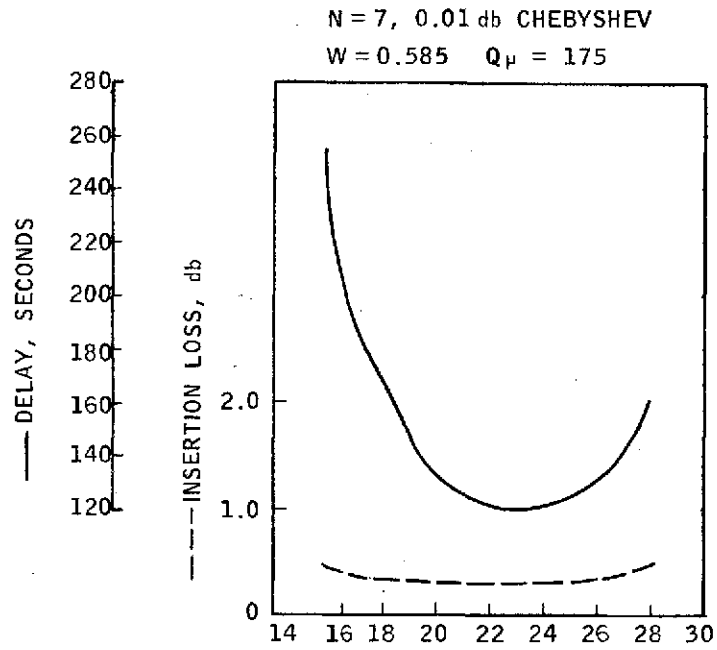
B. CALCULATED VARIATION OF IF NOISE FACTOR WITH SOURCE RESISTANCE.

VARIATION OF IF NOISE FACTOR WITH SOURCE RESISTANCE

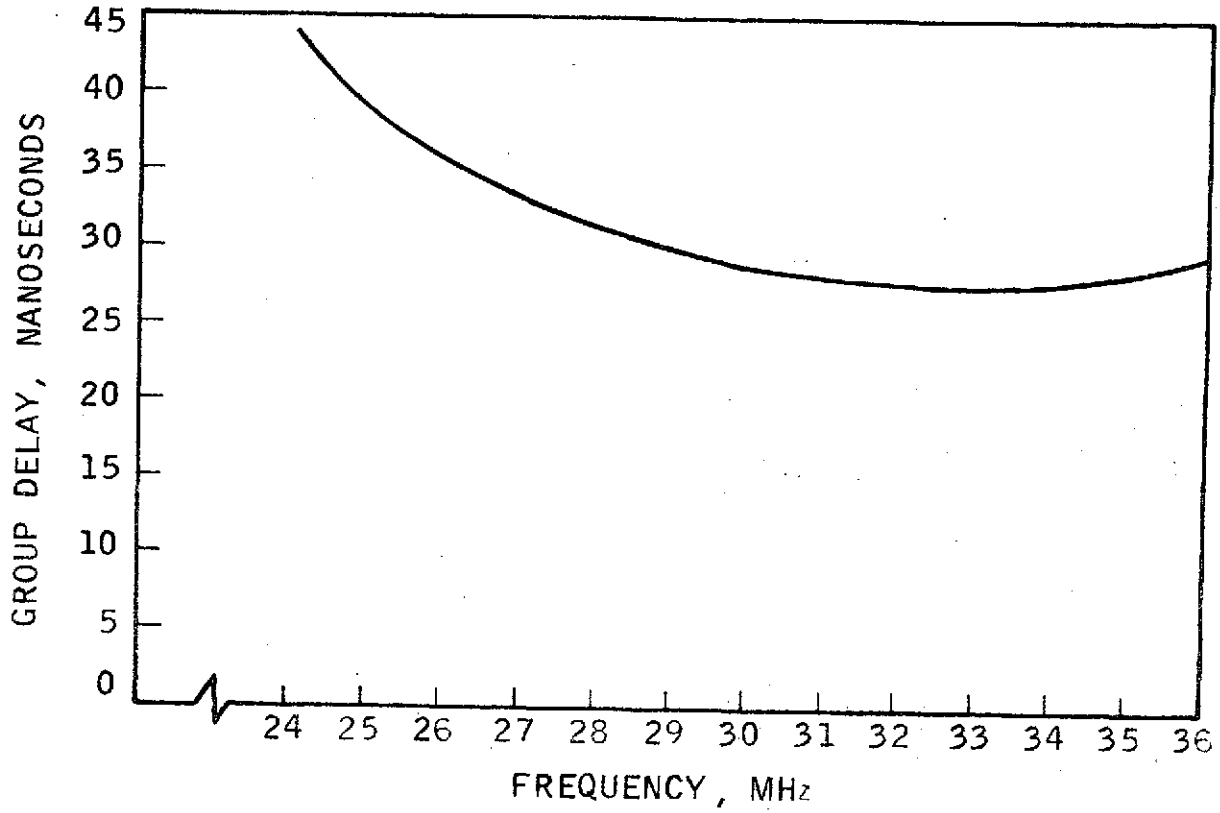
$N = 5, 0.01 \text{ db CHEBYSHEV}$
 $W = 0.415 \quad Q_{\mu} = 175$



CALCULATED RESPONSE OF 30 MHz CHANNEL FILTER
(HIGH REJECTION)



CALCULATED RESPONSE OF 20 MHz CHANNEL FILTER



CALCULATED GROUP DELAY VERSUS
FREQUENCY OF NOISE FILTER

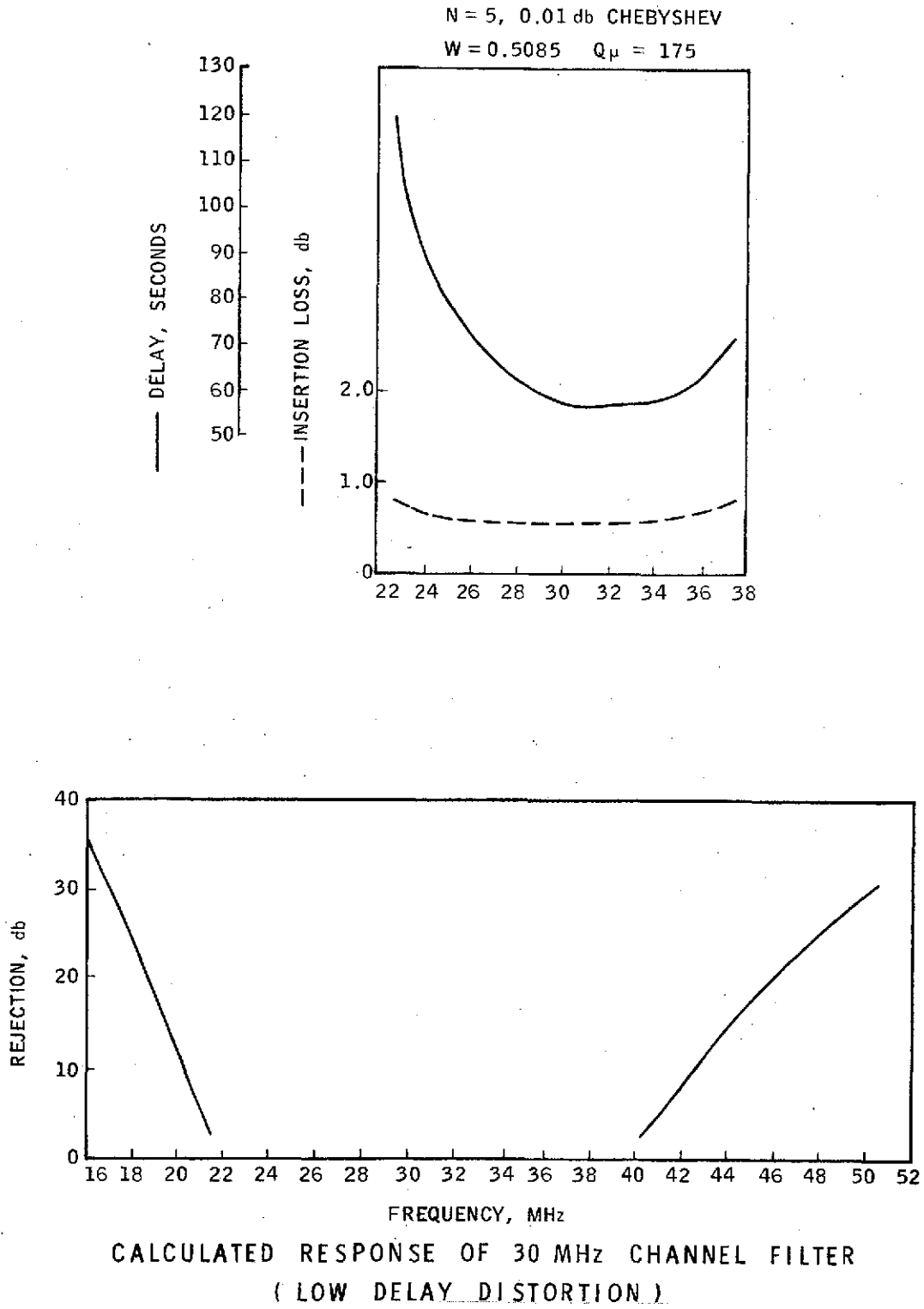
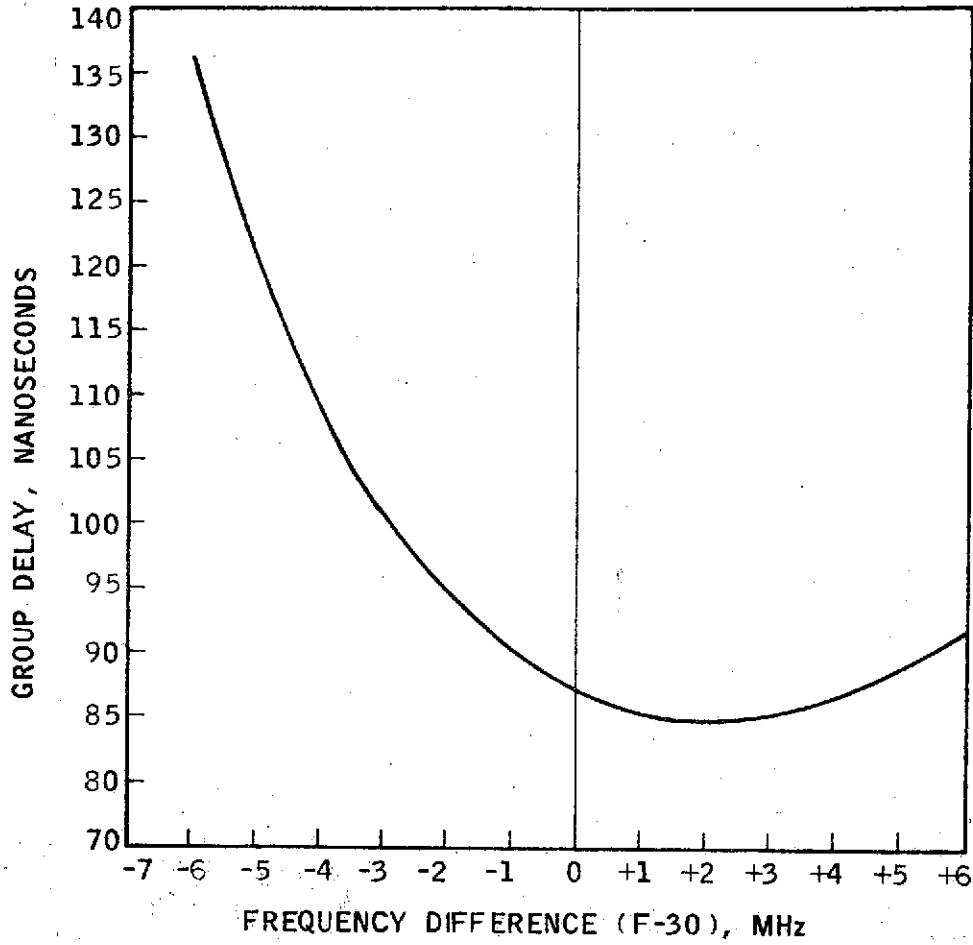


Figure 5.2.4-20

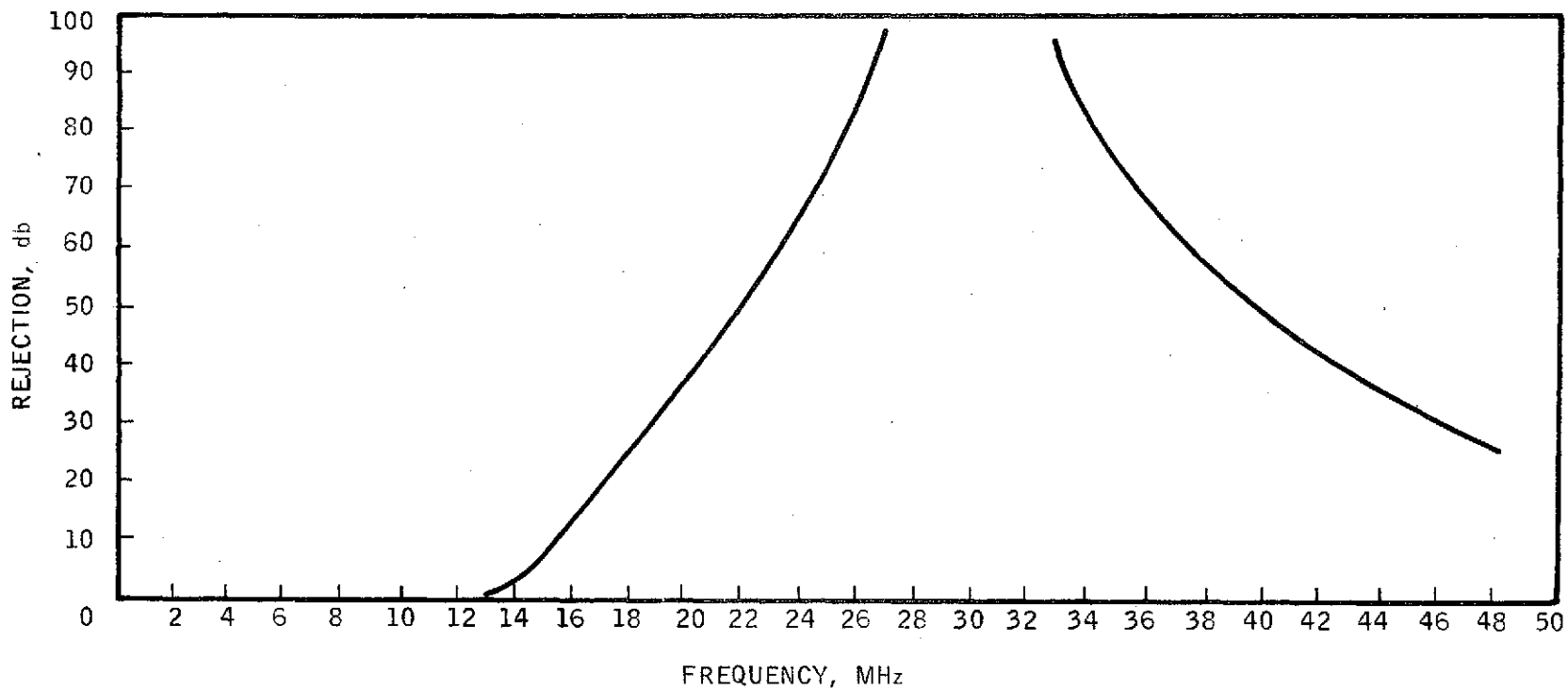


CALCULATED COMBINED GROUP DELAY VERSUS
FREQUENCY OF NOISE FILTER AND CHANNEL FILTER

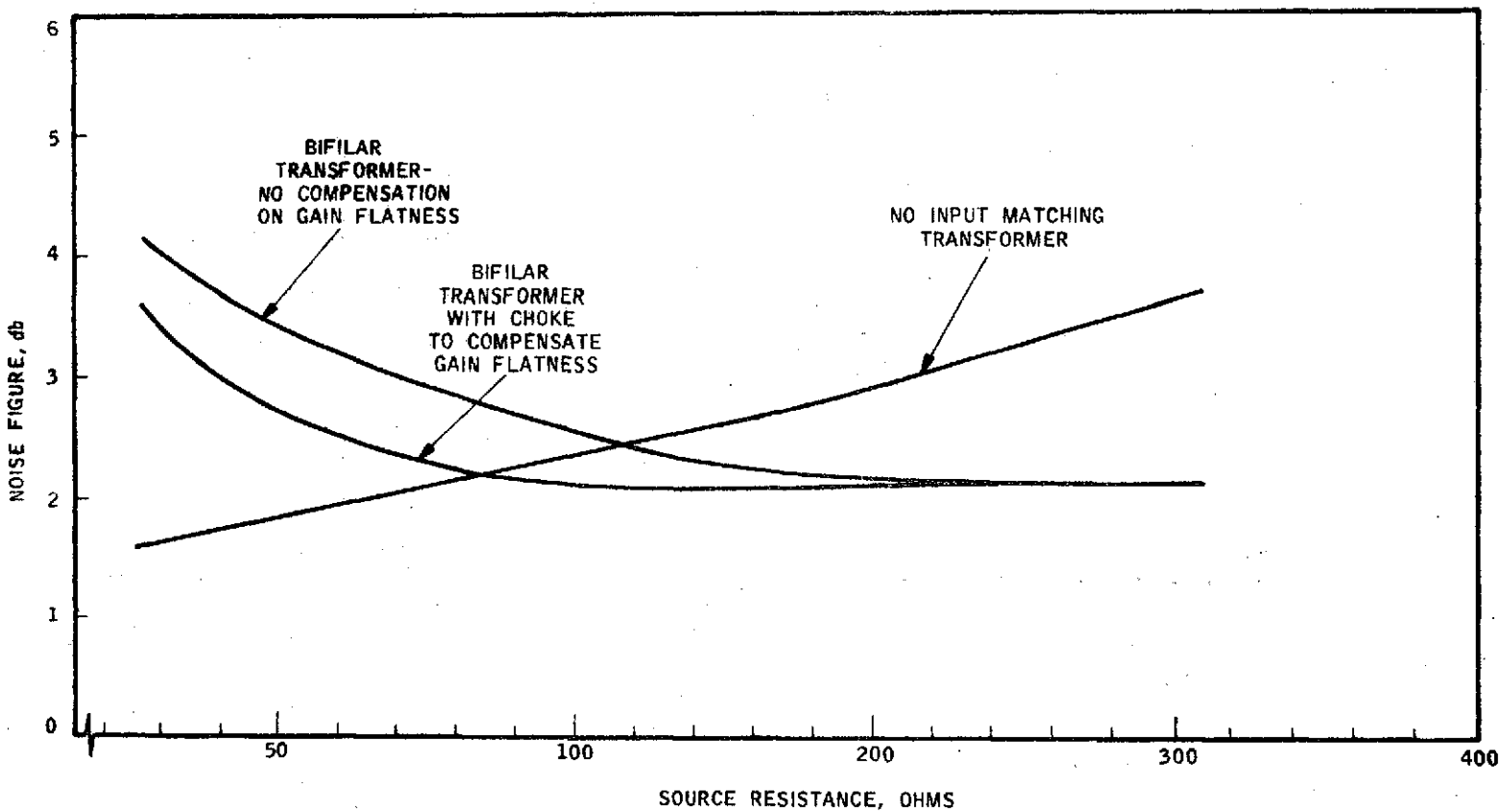
Figure 5.2.4-21

$N = 5, 0.01 \text{ db CHEBYSHEV}$

$W = 1.43 \quad Q_p = 175$



CALCULATED RESPONSE OF VIDEO FILTER



NOISE FIGURE OF IF PREAMPLIFIER FOR VARIOUS MATCHING CONDITIONS

Figure 5.2.4-23

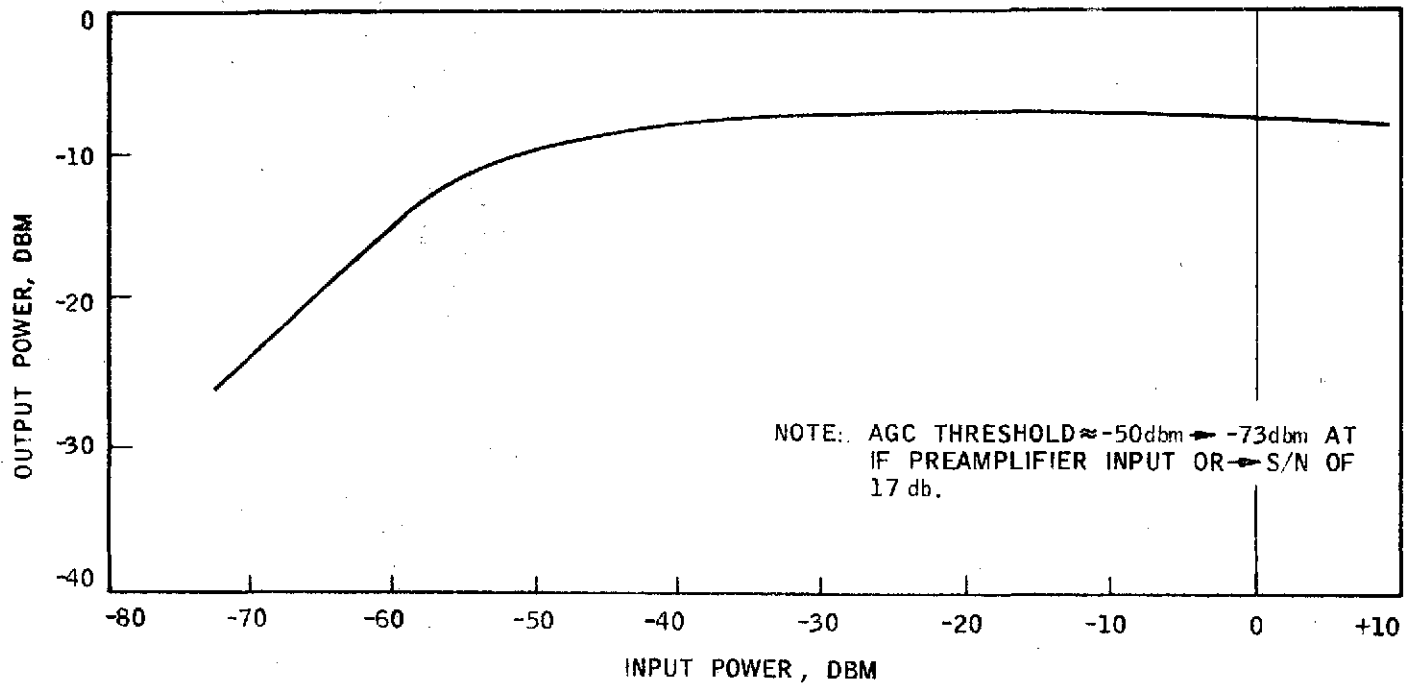
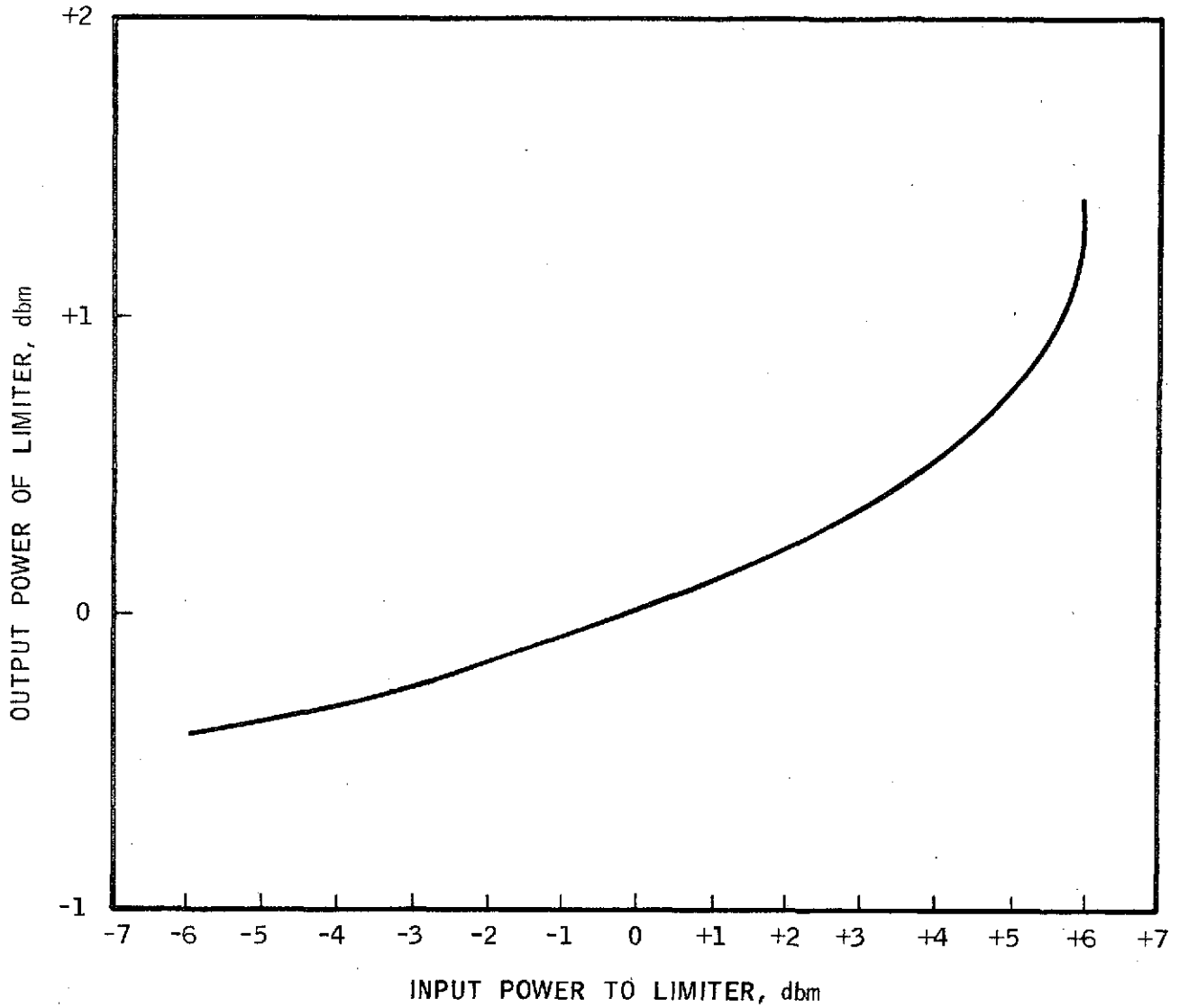
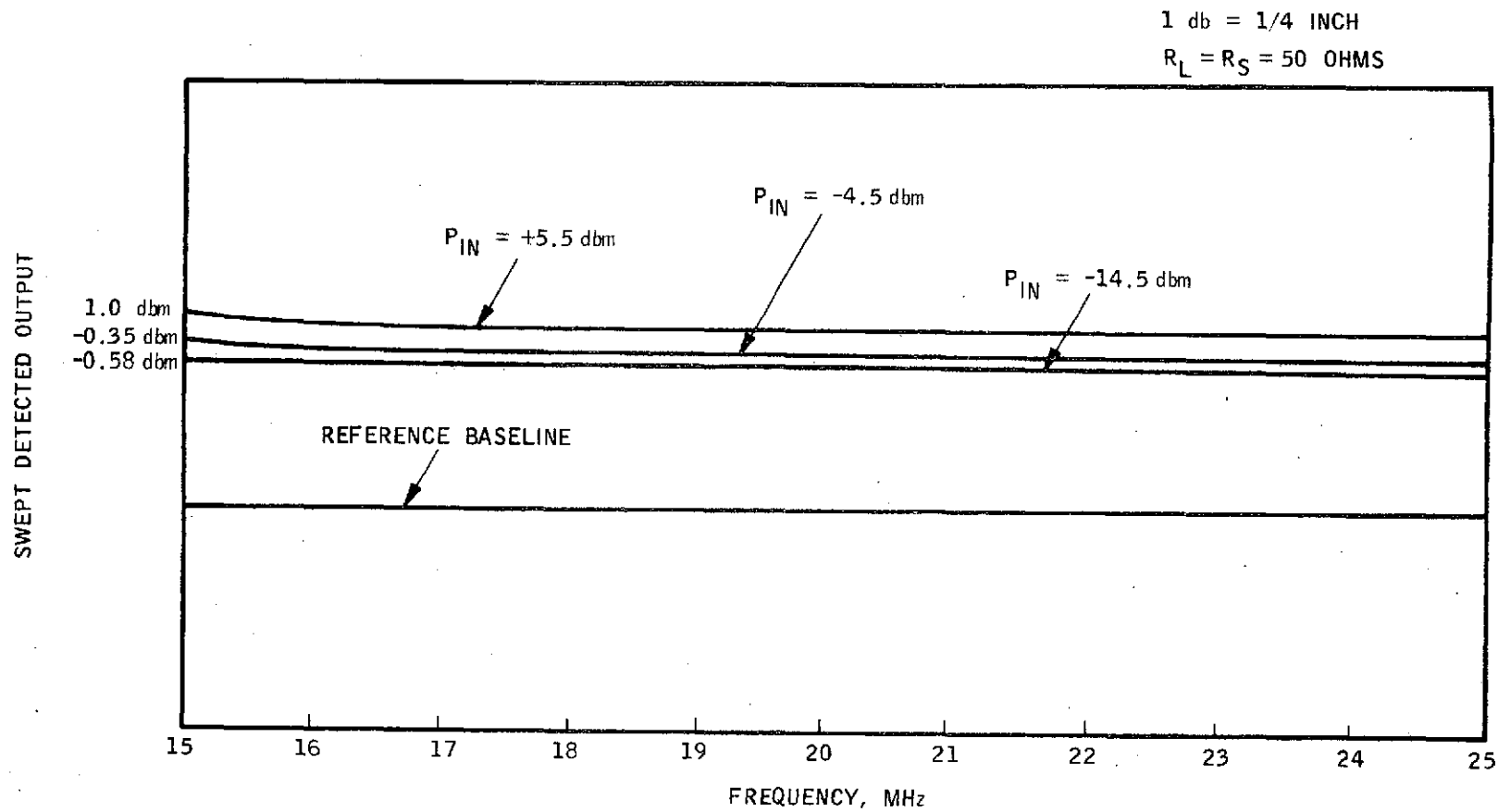


Figure 5.2.4-24

AGC CHARACTERISTICS OF IF AMPLIFIER, AGC DETECTOR,
AND DC AMPLIFIER IN CLOSED LOOP OPERATION

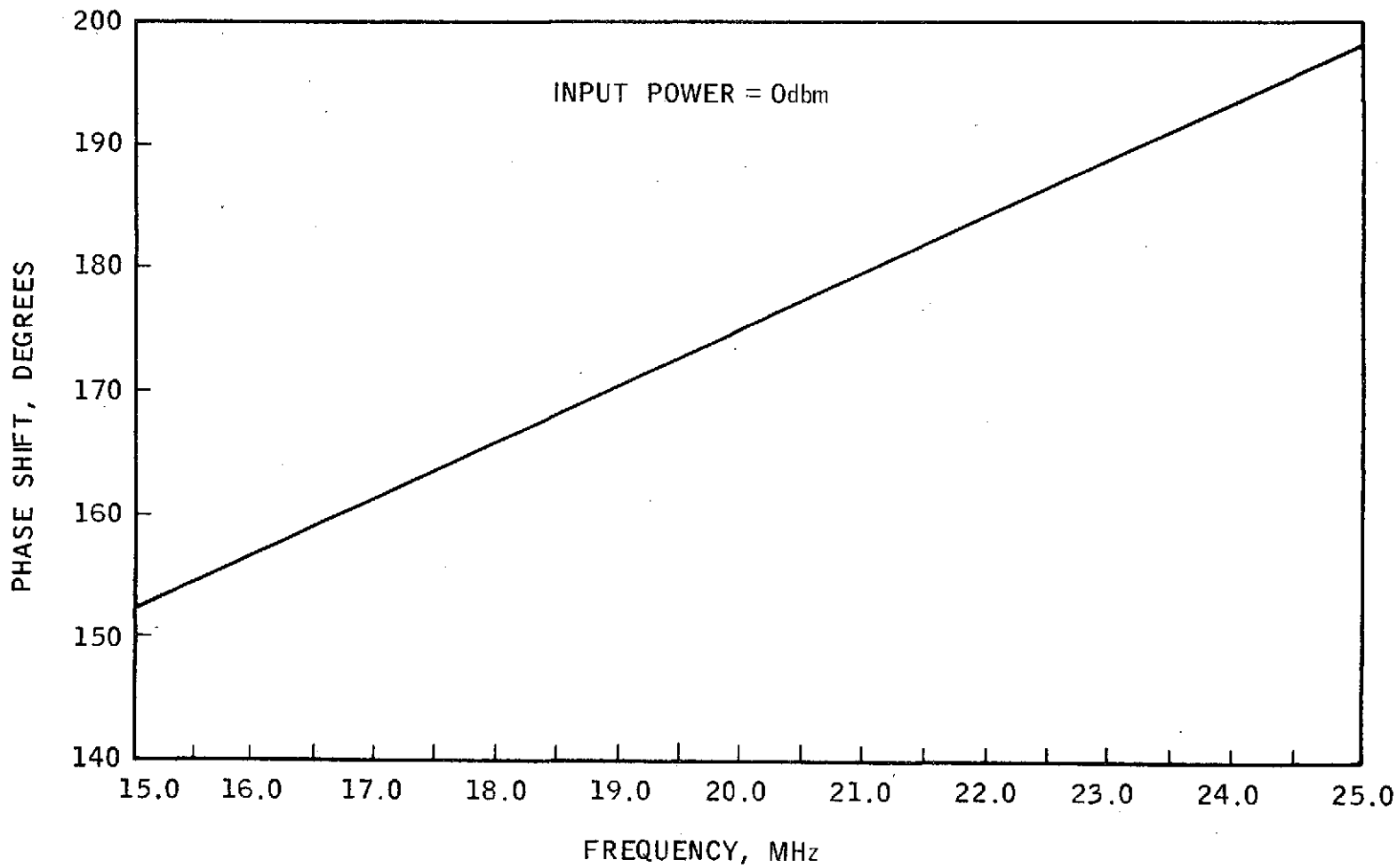


MEASURED POWER LIMITING CHARACTERISTICS OF 20 MHz LIMITER



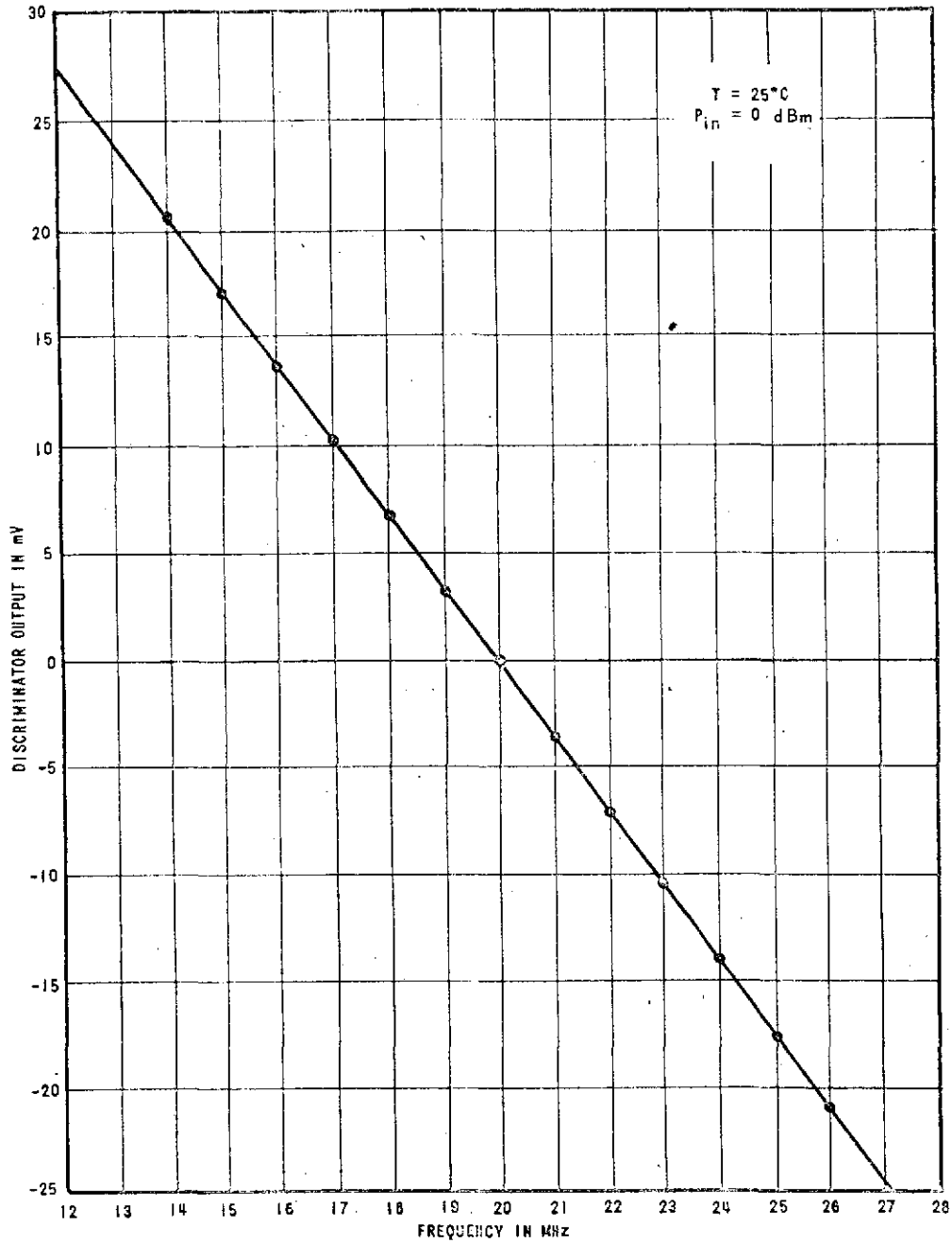
FREQUENCY RESPONSE OF LIMITER

Figure 5.2.4-26



PHASE SHIFT VS FREQUENCY OF LIMITER CIRCUIT

Figure 5.2 4-27



0-2012

Measured Discriminator Output Versus IF Frequency

Figure 5.2.4-28

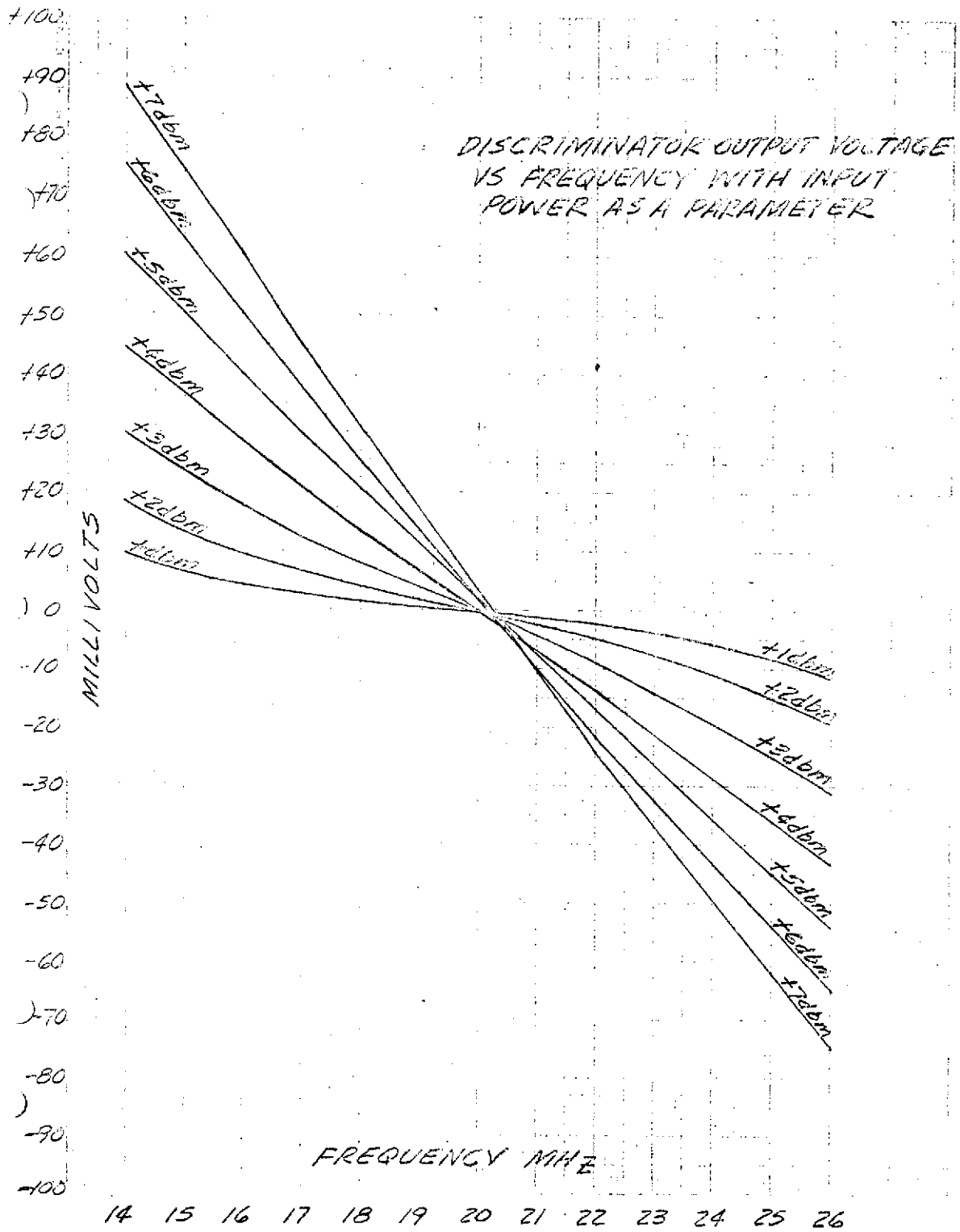


Figure 5.2.4-29

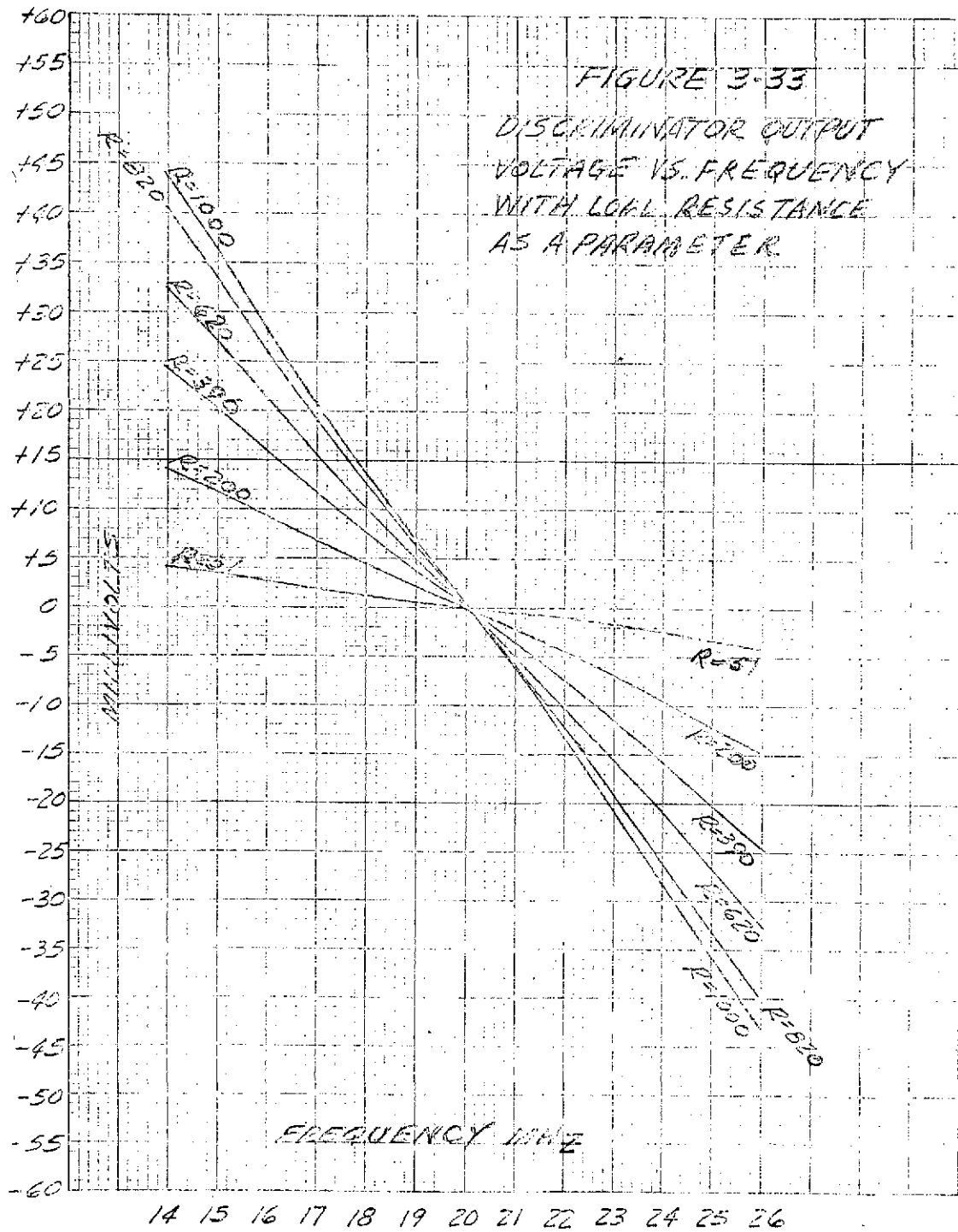
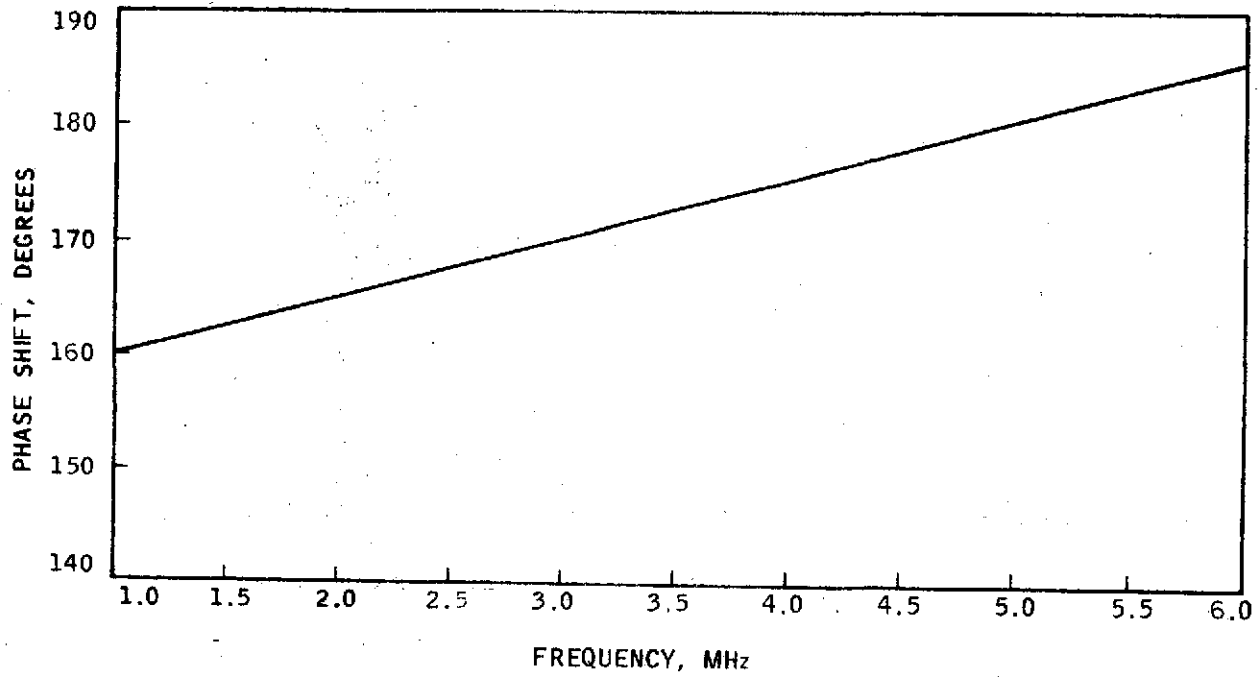
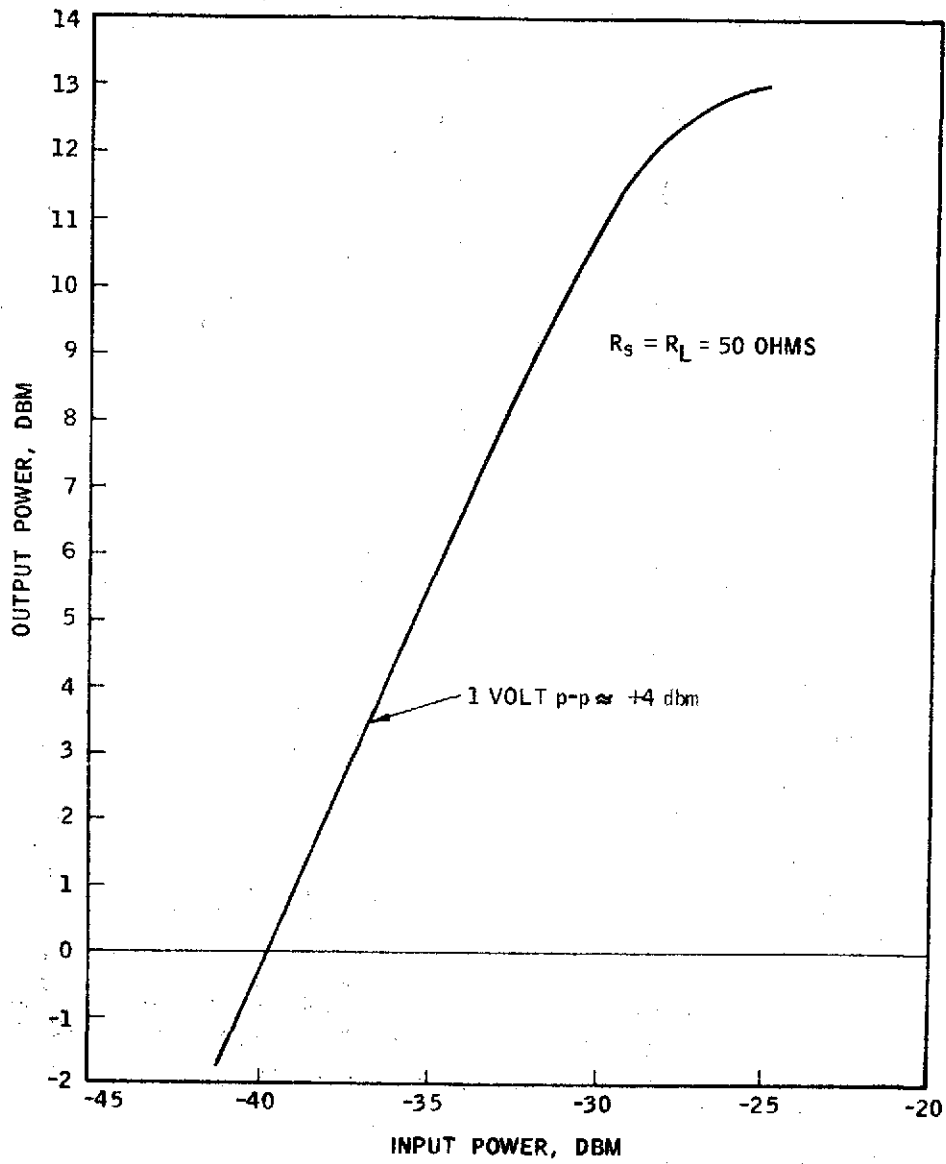


Figure 5.2.4-30



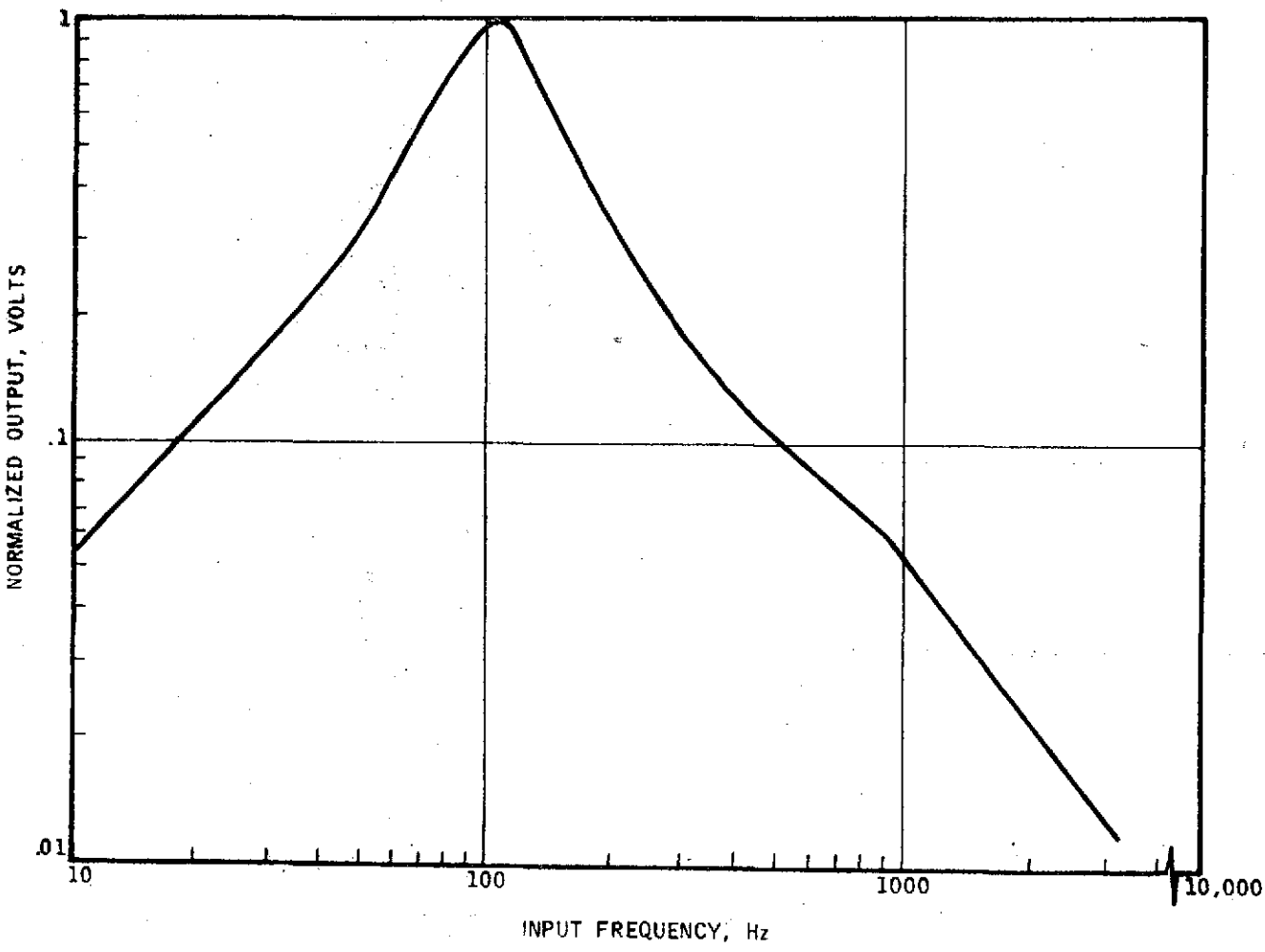
PHASE SHIFT—VS FREQUENCY OF VIDEO AMPLIFIER

Figure 5.2.4-31



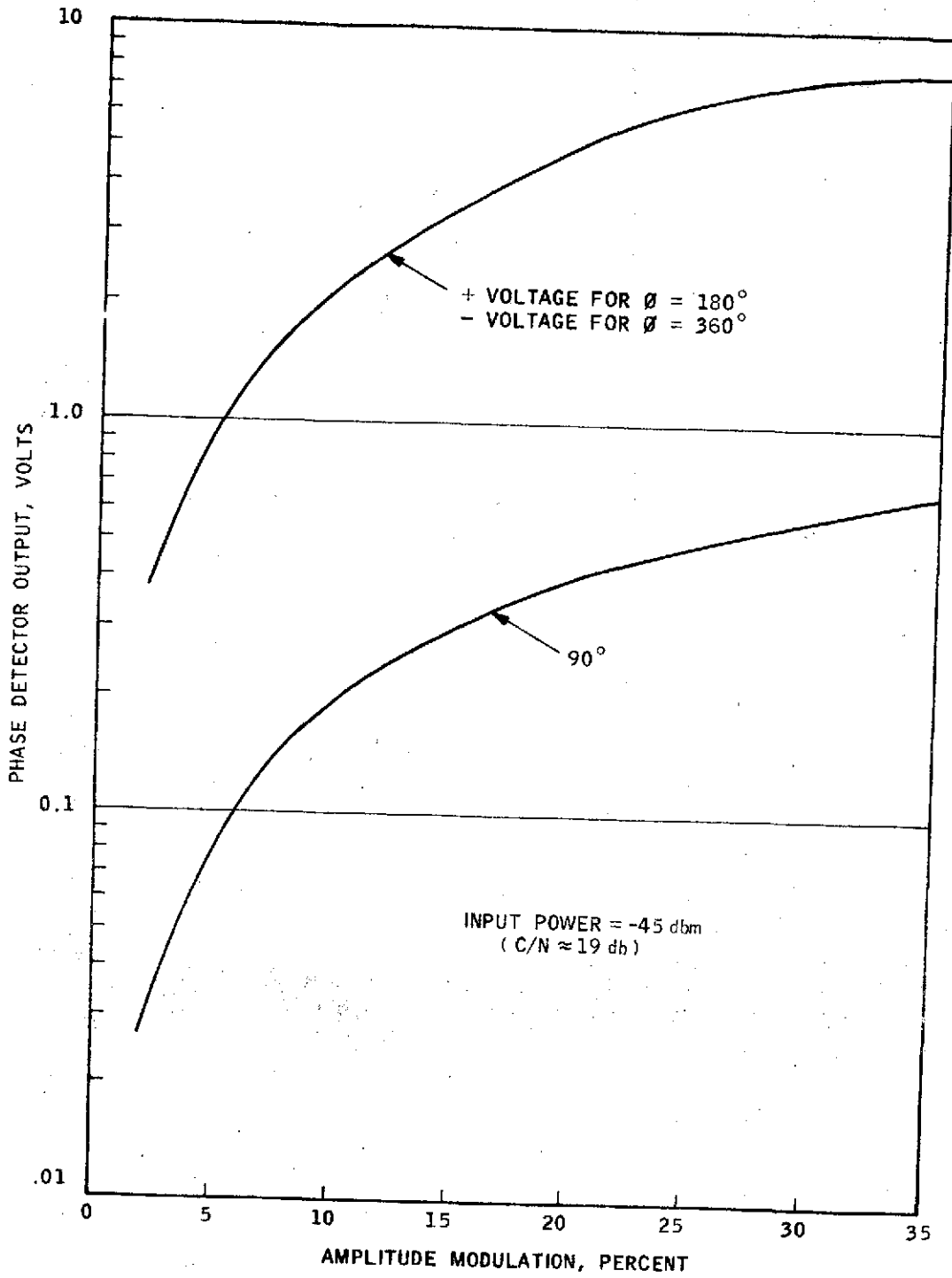
POWER OUTPUT CAPABILITY OF VIDEO AMPLIFIER

Figure 5.2.4-32



FREQUENCY RESPONSE OF TUNED AUDIO AMPLIFIER IN TRACKING ERROR CHANNEL

Figure 5.2.4-33



PHASE DETECTOR OUTPUT VOLTAGE VERSUS
PERCENT AMPLITUDE MODULATION

Figure 5.2.4-34

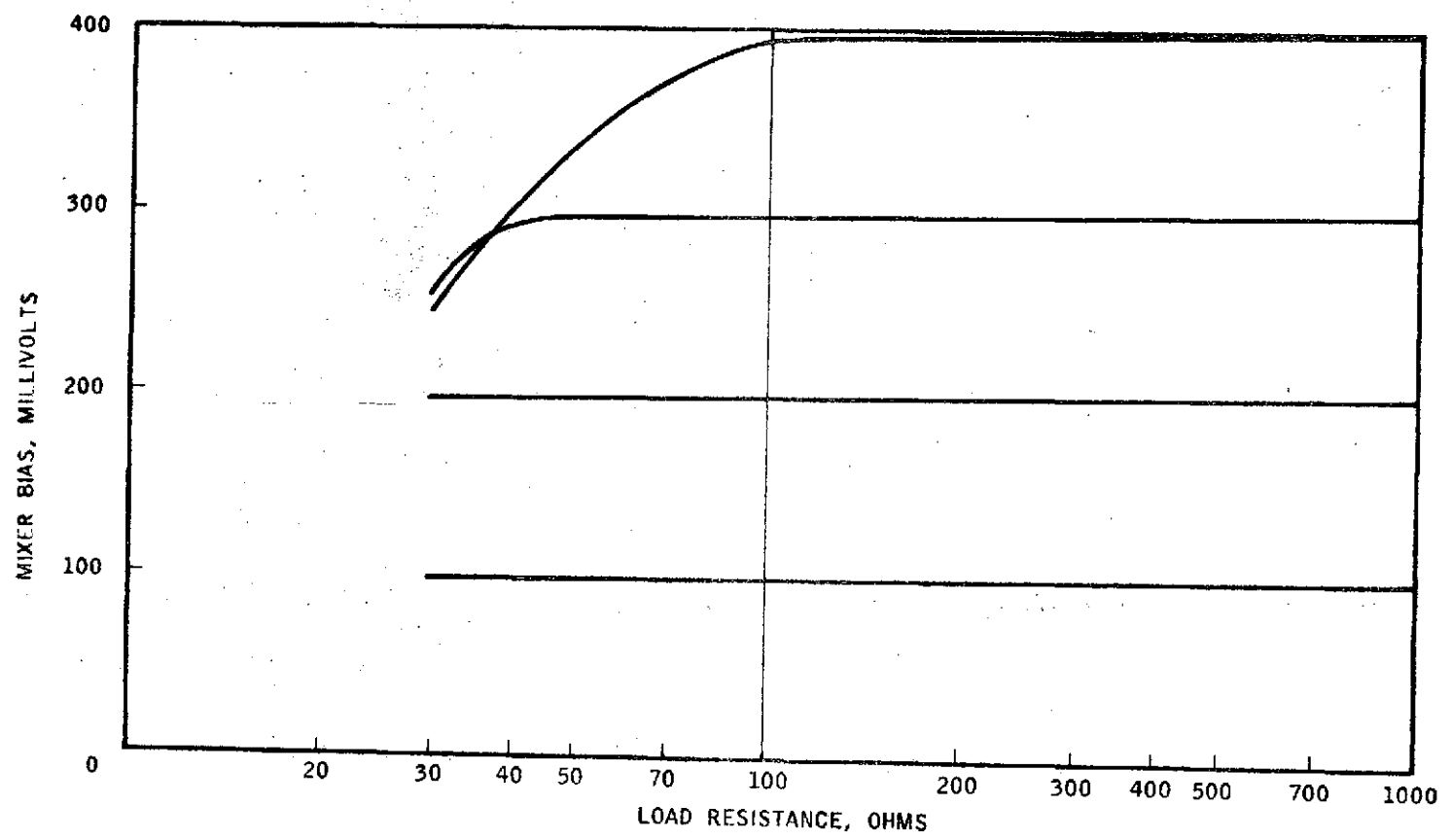


Figure 5.2.4-35

MIXER BIAS CIRCUIT CHARACTERISTICS

5.2.6 Power-Supply Subsystem

5.2.6.1 Requirements

The power-supply subsystem furnishes all electrical power to the LCE transceiver subsystems. It must provide current-regulated high voltage to the transmitter, local oscillator and backup lasers. The supplies for the transmitter and local oscillator must be redundant because of reliability considerations. In addition to providing these current regulated outputs, a high-voltage starting pulse circuit for each tube is required. The power-supply subsystem also supplies +12 volts, +5 volts and +225 volts for the processing and control circuitry. The detailed requirements for the power supply are contained in Aerojet Specification 20515. Table 5.2.6-1, which was taken from this specification, summarizes all of the output requirements. The most stringent performance requirements are applied to the high-voltage laser tube outputs, principally, the low-frequency ripple requirement and the efficiency requirement. Therefore, the following discussion will emphasize the high-voltage portion of the power supply.

5.2.6.2 Design Approaches Considered

The simplest method of obtaining a current source is to use a ballast resistance in series with the load. This approach is simple but has the disadvantage of being rather inefficient for high values of resistance and sensitive to primary power-line ripple for low values of ballast resistor. The minimum value of ballast resistor to obtain a positive load resistance is greater than 100K assuming a laser impedance of -100K. With this value, the ripple output of the supply must be extremely low since the load is almost 0 ohms. To alleviate this problem, higher values can be used but this reduces the power supply efficiency. Another approach considered was the use of a feedback loop around the high-voltage section, thus eliminating the ballast resistor. This approach requires a loop settling time in the order of 10 microseconds. It was considered that this settling time was not consistent with the characteristics of realizable transformers and the requirements for output filtering.

In order to optimize efficiency, improve input/output ripple rejection and reduce the dependence of the design on high-voltage transformer or laser characteristics, a design was conceived based on the use of active high-voltage current regulators and switching preregulators. This approach had the advantage that the effective output impedance of the current regulator can be very high and the overall efficiency can be optimized. The initial regulator design had an output impedance of greater than 5 megohms over the operating temperature range. It consisted of five cascaded Darlington circuits in a closed-loop system utilizing an operational amplifier to control the current. One of these regulators was connected in series with each laser anode. To optimize the overall efficiency of each high-voltage supply, a preregulator was added that receives its sense voltage from the output voltage section. This allows the voltage drop across the output to be minimized at each programmed current level. A switching regulator was used instead of a class A regulator to improve the efficiency.

The main disadvantage of this approach is the complexity of the circuitry required to withstand approximately 1800 volts in the event of a shorted output. To eliminate this problem without significantly increasing the sensitivity to low-frequency ripple, the 1800-volt current regulator has been replaced with a simple one-transistor regulator for each anode output. To further protect the regulator, two high-voltage outputs are being used with one regulator in each output return line. This change allows the transistor to operate within a maximum of 200 volts positive potential. In addition, a Zener diode is provided to limit the maximum collector-to-emitter voltage to 200 volts. To limit the maximum short-circuit current, a small ballast resistor (approximately 40K) has been added and high-voltage quadruplers have been designed to supply a limited amount of power.

This change has eliminated 18 transistors and two i.c. operational amplifiers from each supply, for a total reduction of 80 transistors and 10 i.c. amplifiers. This change has resulted in a reduction in the output impedance from greater than 5 megohms to approximately 500 kilohms; however, this reduction has been compensated by increasing the operating frequency of the converter to 20 kHz. The increased operating frequency has been possible

because of the use of a voltage quadrupler which has allowed the use of a lower voltage on the transformer secondary winding. The efficiency of the high-voltage supply has been reduced somewhat by this change but it is considered that the simplification and resulting improvement in reliability justifies this change.

It has been suggested by NASA that a closed-loop system utilizing an inductor for a ballast could satisfy the system requirements. The success of this system depends on limiting the amount of capacity in parallel with the laser to less than 2000 pf. This condition is satisfied by operating the converter at a higher frequency (> 20 kHz) thereby reducing the filter capacitor requirements.

This approach has two main disadvantages. The first is the extremely high ripple voltage on the high-voltage line, which will require additional shielding to prevent interference with other electronics. Another disadvantage is the lack of low-frequency ripple rejection. The design of the control loop must have a very fast response time to prevent low-frequency dither and it is questionable if it can be realized considering the gain/phase characteristic dictated by the tube shunt capacity limitation of 2000 pf and the low-frequency response of the high-voltage transformer. In regard to eliminating active components in the high-voltage section, this approach, as with the Aerojet present design, requires active components in the return line of the high-voltage supply.

5.2.6.3 Power-Supply Design Description

5.2.6.3.1 High-Voltage Circuit Design

Figure 5.2.6-1 shows a functional block diagram of the power supply. The function of each block is described below.

H.V. Preregulator

The preregulator provides three functions. It provides the necessary spacecraft command/power supply interface circuitry, and the means to control the voltage drop across the output current regulator to optimize the efficiency and provide approximately 35 db of primary power ripple rejection. This regulator utilizes pulse regulating techniques to minimize

losses. The switching frequency is approximately 40 kHz. The feedback sense voltage is generated by the voltage sense circuit.

Voltage Sense Circuit

The voltage sense circuitry senses the voltage drop across each of the two laser anode current regulators and generates a preregulator sense voltage that adjusts the output of the preregulator so that the average voltage drop across the two output current regulators is approximately 80 volts after the laser is ignited. To maintain good input/output isolation, current mode coupling is used between the input and output circuits. Any possible high-voltage discharge through this circuit is virtually eliminated by voltage limiting Zeners, current limiting resistors, and shielding of the current regulator.

Driver Oscillator

This square-wave oscillator generates the necessary drive voltage for the converter; a separate oscillator is used so that a non-saturating transformer can be used in the converter for higher efficiency.

Converter

The converter steps up the output voltage of the square wave oscillator to several hundred volts for the rectifier filter circuitry. The absolute voltage level that is generated will depend on which laser is being supplied. The transformer utilized in this design incorporates electrostatic shielding to prevent possible discharge from the high-voltage to the low-voltage section.

Rectifier Filter

Each of the two high-voltage outputs of the converter are rectified and filtered by a voltage quadrupler. Using a quadrupler reduces the transformer turns ratio making it possible to operate at a higher frequency. The tentative operating frequency is 20 kHz, well above the critical ripple current frequencies.

Current Regulators

Each quadrupler has a single transistor current regulator located in the ground side of the output. These current regulators are protected in case of a discharge by Zener diodes and a ballast resistor of approximately 40K which limits the peak current. This current regulator has an effective output impedance of 500K ohms and holds the current within 5% of its initial value from -25°C to +75°C.

Current Programmer

The current programmer allows the laser operating current to be changed to one of four predetermined levels by ground command. A counter is used in this programmer; therefore, several commands may be necessary to step the programmer to the desired current level.

Starting Circuit

The starting circuit provides a predetermined amount of energy to each laser anode every time an ON command is received. Isolation is provided between the two anode starting voltage outputs so that if one side of the laser ignites before the other side, the starting circuit will not be loaded down before ignition of the second side. If one side does not ignite with the application of the first ON command, additional ON commands can be provided to reapply the starting energy.

Redundant Switching

This circuit determines which of the redundant supplies is activated by switching on the base drive of the converter selected to operate. Succeeding ground commands will alternately command on each supply.

5.2.6.3.2 Low-Voltage Circuit Design

The preregulator for the low-voltage section is identical to the high-voltage preregulator. To minimize weight and insure high efficiency, the sense signal for the preregulator is derived from the 2.5-amp +5-volt output. By using this approach, the 5-volt line can be easily regulated without decreasing the efficiency with output regulators.

Driver Oscillator

As in the high-voltage supplies, this circuit generates the necessary drive voltage for the converter.

Converter

This is a saturating transformer converter which has isolated outputs for the $\pm 12V$, $+225V$, and $+5V$ output.

Rectifier Filter

Full-wave rectifiers are used to rectify all the outputs.

Output Regulator

Three series output regulators are used for the $\pm 12V$ and $+225V$ outputs. The only line variation that these regulators must operate over is that variation caused by the $+5V$ closed loop which is dictated mainly by transformer and $5V$ rectifier diode losses. Since this variation is small, approximately $\pm 5\%$, the series element drop can be minimized.

5.2.6.3.3 EMI Considerations

By incorporating separate input EMI filters for each supply section (low voltage, transmitter, LO and backup) fused on the primary power line side any possible interaction or interference between supply sections is eliminated.

The active current regulator makes the effective load equal to approximately $400K$. With an allowable $.08\%$ rms ripple current, the high-voltage output can have only $1.6V$ rms ripple for frequencies below 50 Hz. Reflecting this to the primary side reduces it to approximately 16 mV. With a preregulator input/output ripple rejection of 35 db, the allowable input ripple is approximately 600 mV pp which is considerably higher than the spacecraft power supply input ripple, but much lower than is specified in MIL-STD-461, which is 5% rms of the line or 3.6 VPP.

5.2.6.3.4 Efficiency

The overall efficiency of the supply (low- and high-voltage sections) has been calculated using ballast resistors, active current regulators

only, and active regulators with partial ballast resistors. These efficiency values are

High-Voltage current regulator	68%
150K ballast resistor	46%
Ballast/regulator (present design)	55.5%

5.2.6.3.5 Packaging

The package will consist of four subsections. Each section has five covered sides (see Figure 5.2.6-2). When the sections are bolted together, complete electrical isolation between supplies is obtained. This method of packaging was chosen mainly for its multiple heat-sinking surfaces, which are necessary when the mounting footprint is small. No interwiring between sections will be required since independent input EMI filters and command lines are utilized.

The high-voltage section of each high-voltage supply will be completely isolated from the low-voltage section by internal walls. The current regulators themselves will be enclosed in separate sections to protect them from high-voltage areas. The primary winding of each high-voltage transformer will be completely shielded from the high-voltage winding. To minimize the possibility of corona discharge, sharp edges will be eliminated and the high-voltage section will be completely encapsulated.

5.2.6.4.1 Potential Design Simplification

The high-voltage supplies can be considerably simplified by deleting the current programmer capabilities and the high-voltage sense circuitry. Detailed investigation of the requirement for current programmer capabilities has been performed in conjunction with the laser subsystem contractor and the results indicate that the requirement can be eliminated. This change is currently being incorporated into the power-supply specification. This change will also permit the deletion of the preregulator provided that the very low spacecraft power-supply ripple requirements, as specified in Section 5.4.3.1, are maintained. These deletions will reduce the component count in the transmitter and local oscillator by approximately 30%. In addition, the input/output isolation can be significantly increased. At the

present time, it is >10K. By sacrificing approximately 5% in efficiency, the high-voltage converters can be revised to a square-core oscillator, eliminating the need for a driver oscillator. These changes will eliminate approximately 12 modules, reducing fabrication and testing time. Detailed investigation of these potential modifications is being performed.

The low-voltage supply could be somewhat simplified by eliminating the preregulator. This change is considered undesirable, however, since the input/output isolation for the 5-volt line would be eliminated.

TABLE 5.2.6-1

POWER-SUPPLY POWER OUTPUT REQUIREMENTS

	Laser	Laser IO	Backup Laser	Nutator &	Low-Voltage Power Supply	
	Transmitter H.V. Current Regulator	H.V. Current Regulator	H.V. Current Power Supply	IMC Driver Power Supply	+12V	5V
Operating Current ^{8/} (milliamperes, dc)	4 ± 0.2 ^{1/}	5 ± 0.25 ^{1/}	4 ± 0.2 ^{1/}	1 to 25	100 to 235 ^{10/}	1500 to 2500
Operating Voltage ^{8/} (volts, dc)	2000 ± 100 ^{1/}	800 ± 50 ^{1/}	2000 ± 100 ^{1/}	225 ± 3.4 ^{1/}	$\pm 12 \pm 0.225$ ^{1/}	± 0.25 ^{1/}
Starting Voltage (volts)	5000 ± 1 ^{1/}	2600 ± 1 ^{1/}	5000 ± 1 ^{1/}	-	-	-
Ripple Current (max.) (0.5 to 50 Hz)	0.08% PP	0.08% PP	0.08% PP	-	-	-
(50 Hz to 1 Hz)	1% P-P	1% P-P	1% P-P	-	-	-
(1 kHz to 10 kHz)	3% P-P	3% P-P	3% P-P	-	-	-
Ripple Voltage (max.) (millivolts P-P)	-	-	-	150	15	00
(millivolts rms)	-	-	-	50	2	100
Load/Line Regulation ^{3/} (milliamperes, dc) ^{2/}	0.2 ^{2/}	0.0625 ^{4/}	0.2 ^{5/}	3400 ^{6/}	225 ^{6/}	250 ^{11/}
(millivolts, dc) (5 Hz to 50 kHz)						
Efficiency ^{7/}						
Temperature Coefficient (0 to 140°F)	.5%/°C	.5%/°C	.5%/°C	.1%/°C	.1%/°C	.1%/°C

^{1/} Initial tolerance.

^{2/} Line change $\pm 1\%$.

^{3/} Load change resulting in a 400-volt change in output voltage.

^{4/} Load change resulting in a 100-volt change in output voltage.

^{5/} Load change resulting in a 150-volt change in output voltage.

^{6/} Load ΔI of 50%.

^{7/} Overall efficiency shall be greater than 70% from 50% of full load to maximum rated load.

^{8/} To each of the tubes two anodes.

^{9/} Load impedance variation of $\pm 20\%$.

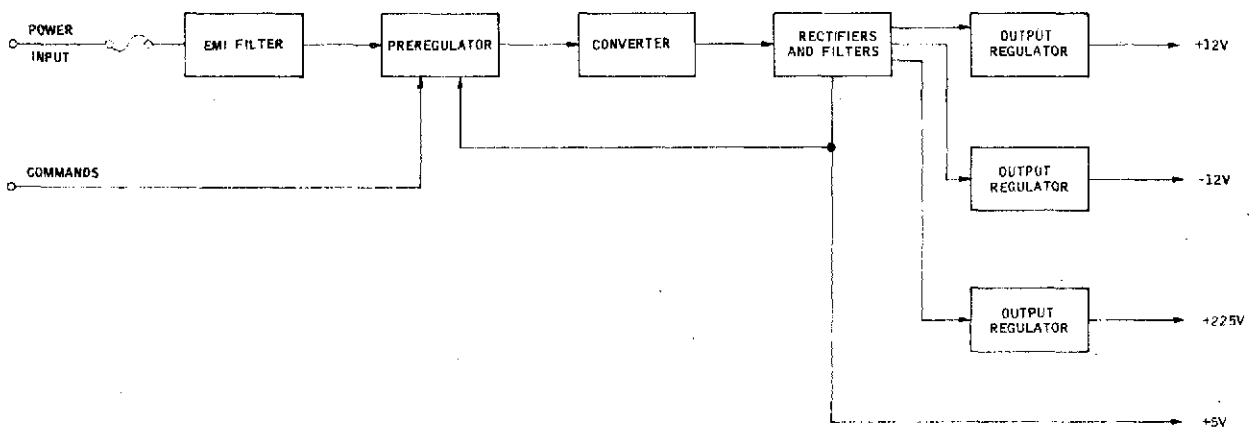
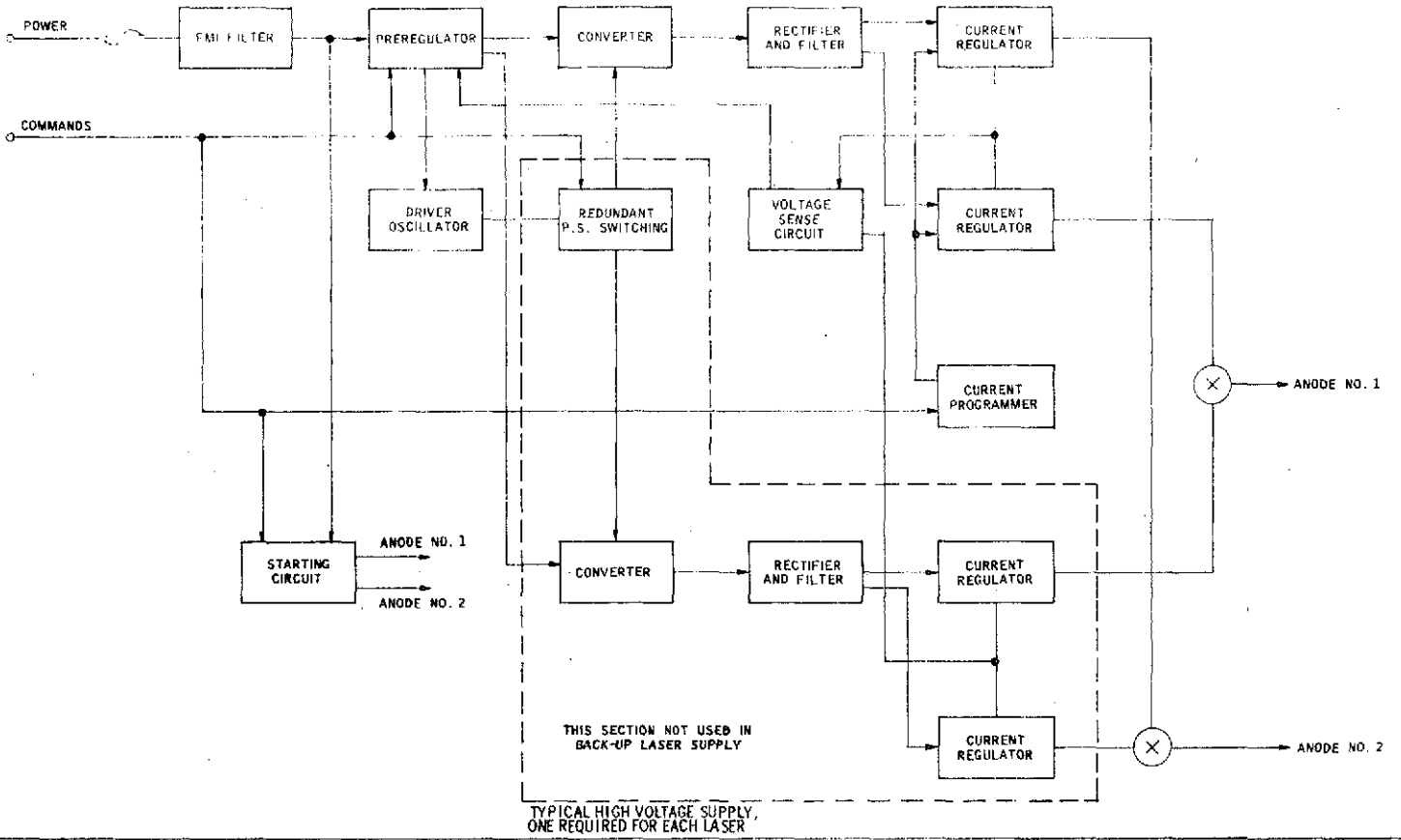
^{10/} Current required from each 12V source.

^{11/} Load ΔI of 30%.

Note: Cathodes of the laser tubes shall be operated near ground potential.

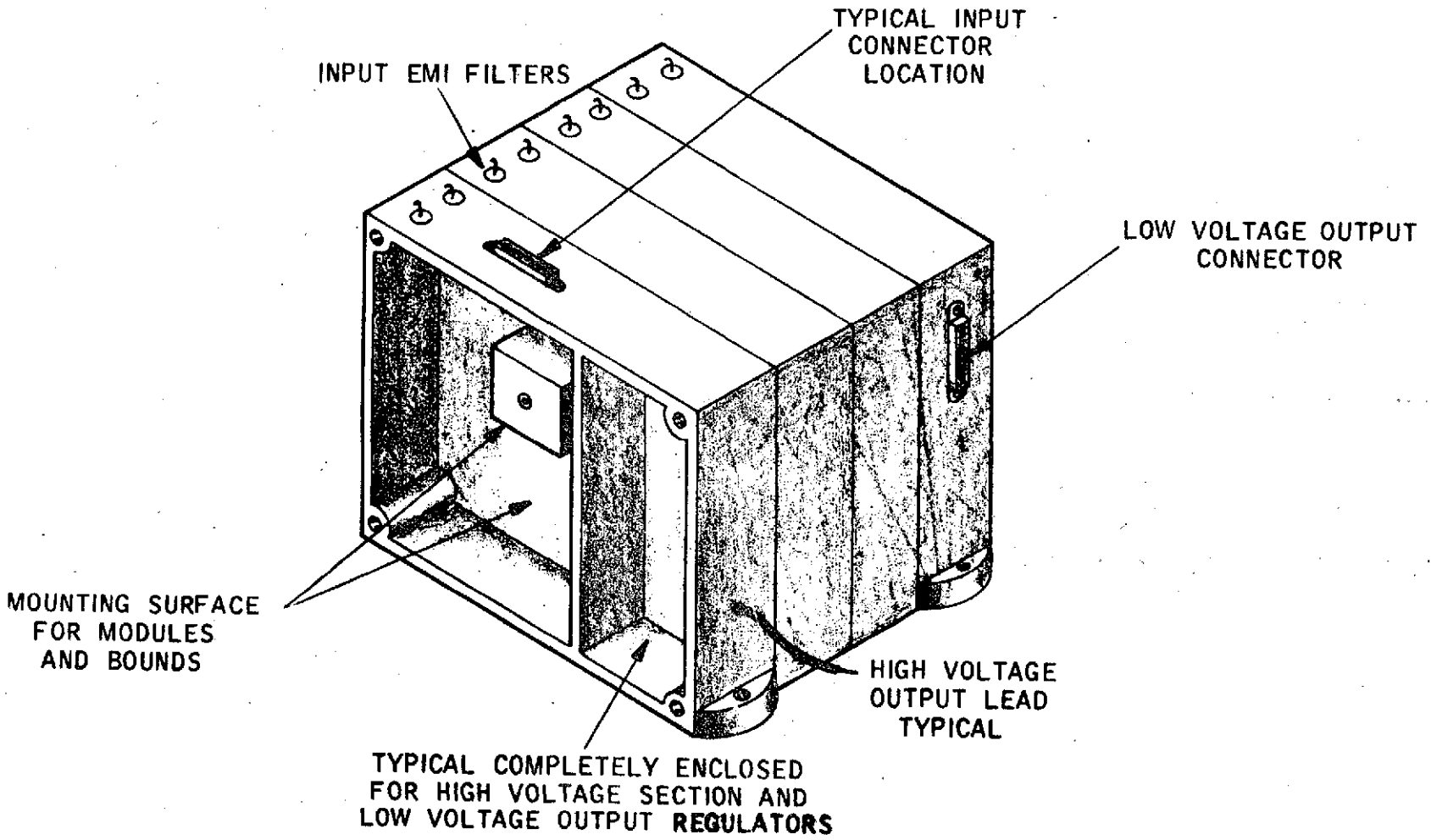
Table 5.2.6-1

Report No. 4033, Vol. I, Part 1



LCE POWER SUPPLY BLOCK DIAGRAM

Figure 5.2.6-1



PROPOSED L.C.E. POWER SUPPLY CONFIGURATION

Figure 5.2.6-2

5.2.7 Telemetry and Command Subsystem

The design requirements and signal characteristics of the telemetry and command subsystem for the LCE spacecraft transceiver are related intimately to the electrical interface with the spacecraft, through which these signals are routed. These LCE telemetry and command interface design requirements and characteristics are described in paragraphs 5.4.3.2 and 5.4.3.3, respectively.

5.3 TECHNICAL AREAS OF CONTINUING DEVELOPMENT

As described in the preceding sections, there were several technical areas that required investigation, further development and experimental and/or analytical resolving in order to insure a successful LCE Program. Also, as described in the preceding sections, investigations in all of these areas have resulted in a system design that, it is believed, (1) can be successfully fabricated and (2) will satisfy the LCE requirements.

Certain areas still require final resolving, although the analytical, experimental, and design efforts to date have resulted in a high confidence that the present solutions will satisfy the LCE requirements. In particular, these areas are (1) the laser tube, (2) the duplexer, and (3) the radiation cooler. Final development work is being performed in each of these areas and will continue until the solutions are proved. The development programs, along with some analysis and the basis for confidence, are described below.

5.3.1 Laser-Tube Development

A space-qualified CO₂ laser tube for the Laser Communication Experiment requires an operating life greater than 2,000 hours and a shelf life greater than 2 years. An operating life time of more than 10,000 hours has been demonstrated by Sylvania, using a CO₂ laser with a water-cooled quartz discharge tube, a large gas ballast, and self-heated nickel electrodes. However, no comparable life data are available for a space-qualified, conduction-cooled laser tube. One ceramic tube constructed under the head-start program for NASA (NAS 12-2021) has been operated over 1200 hours. The life of this tube was terminated when a small leak developed at one of the torr-sealed windows.

Therefore, in order to provide confidence that the laser-tube life requirements of the LCE program will be achieved, Aerojet has initiated a laser-tube development and life-test program at Sylvania. The objective of this program is to develop confidence in a final tube design which will meet the requirements of the LCE subsystem

The first part of the program has been completed. It consisted of an experimental phase to determine the most important life-limiting factors in the design of the laser tubes. The principal factor studied was the design of the cathode. This phase included experimental investigations of various cathode configurations, with particular attention given to the effects of sputtering. The next phase of the program will include the construction of six life-test tubes, each of slightly different design, reflecting the results of the design review held at the conclusion of the first phase of the program. These tubes will be operated on a life test for up to 3,000 hours.

The conclusion of this test will complete the basic life-test program. However, Aerojet has proposed the extension of the program to include the fabrication and testing of 12 additional transmitter tubes of the design found to be most successful in the preceding phase, plus six local-oscillator tubes. This extended life-test program will provide significant life-test data on the flight-configured tubes prior to delivery of the prototype laser subsystem and specific data to increase the confidence of achieving the laser subsystem reliability goals. Each of these phases will be described in greater detail in the following sections.

5.3.1.1 Life-Test Program, Experimental Phase

The experimental phase of the life-test program was designed to permit selection of the important life-limiting parameters involved in the operation of the LCE lasers. This phase of the program has nearly been completed, and the results to date are summarized below.

In order to measure cathode fall and voltage drop as a function of distance, an experimental discharge tube (shown in Figure 5.3.1-1) having a 4-mm ID was constructed with a movable anode and filled with a standard laser mix. The tube voltage at 5 ma current was measured as a function of anode-cathode separation. These data are shown in Figure 5.3.1-2. The figure shows a voltage slope of 180 V/cm, and a cathode fall voltage of approximately 350 v. This shows that very short tubes (less than a few centimeters anode-cathode separation) will have relatively low efficiency due to the large fraction of the input voltage dropped across the cathode.

A measurement of current density and cathode area for optimal filling of a coaxial cathode operating at 10 ma was next performed. For this test, a discharge tube (shown in Figure 5.3.1-3) with a large convex nickel cathode was constructed. The size of the glow region at the cathode was measured as a function of current. The current density was approximately constant at 4 ma/cm^2 . Therefore, 2.5 cm^2 , minimum, are required for 10 ma total current. As the gas pressure is reduced, the spot size increases, at the standard current of 10 ma, indicating that, as the tube ages and its pressure drops, more available cathode area is required. Appropriate cathode dimensions for the LCE transmitter laser are 7 mm in diameter and 11 mm minimum in length.

The next test was a measurement of pressure and partial pressure as a function of operating hours in small discharge tubes with nickel and platinum-coated nickel cathodes. Two 10-cm^3 discharge tubes were filled with a standard laser mix and operated at 10 ma. An additional non-discharge tube was also sealed to the partial-pressure sensing manifold as a reference. During operation, the pressure in both tubes fell to one-half the initial pressure in 90 hours. However, the CO_2 -to-He pressure ratio in the platinum-plus-nickel tube was 35% greater than in the pure nickel tube, although both tubes demonstrated a severe decline in CO_2 concentration, as shown in Figure 5.3.1-4. A 0.1-cc sampling valve was used to take gas from the tubes to an EAI residual gas analyzer and Baratron pressure gauge.

An additional test in process at the time of writing of this report involves the measurement of pressure and partial pressure in small discharge tubes of differing volumes. In this test, two discharge tubes and a reference volume will each be attached to a 0.1-cc sampling valve, as described above. However, here the volumes to be sampled will be 10 cc and 20 cc. Measurements will be made as before, and the difference in gas consumption for the two discharge tubes will be noted. An additional difference will be that these tubes will be operated at 8 ma rather than 10 ma to determine the effects of tube current. The cathode temperature resulting from this reduced current will be recorded and correlated with data from the previous experiment.

5.3.1.2 Life-Test Program, Test Phase

Information obtained during the experimental phase has been used to select six slightly different life-test lasers. The standard tube is defined as the experimental metal/ceramic laser used in this program, characterized by a 13-mm-long cathode, no additional gas ballast, and the standard gas mix. The standard gas mix is defined as 7 torr CO₂, 15 torr He, 7 torr N₂, 1 torr Xe and 0.1 torr H₂. The six tubes being constructed for the forthcoming life tests are listed below.

1. Standard tube
2. Standard tube with platinum-plated cathode
3. Same as Tube 2 with an additional 3 torr of CO₂
4. Same as Tube 2 with a 15-mm cathode
5. Same as Tube 4 with an additional 150 cc. of gas ballast
6. Same as Tube 5 with an additional 3 torr of CO₂

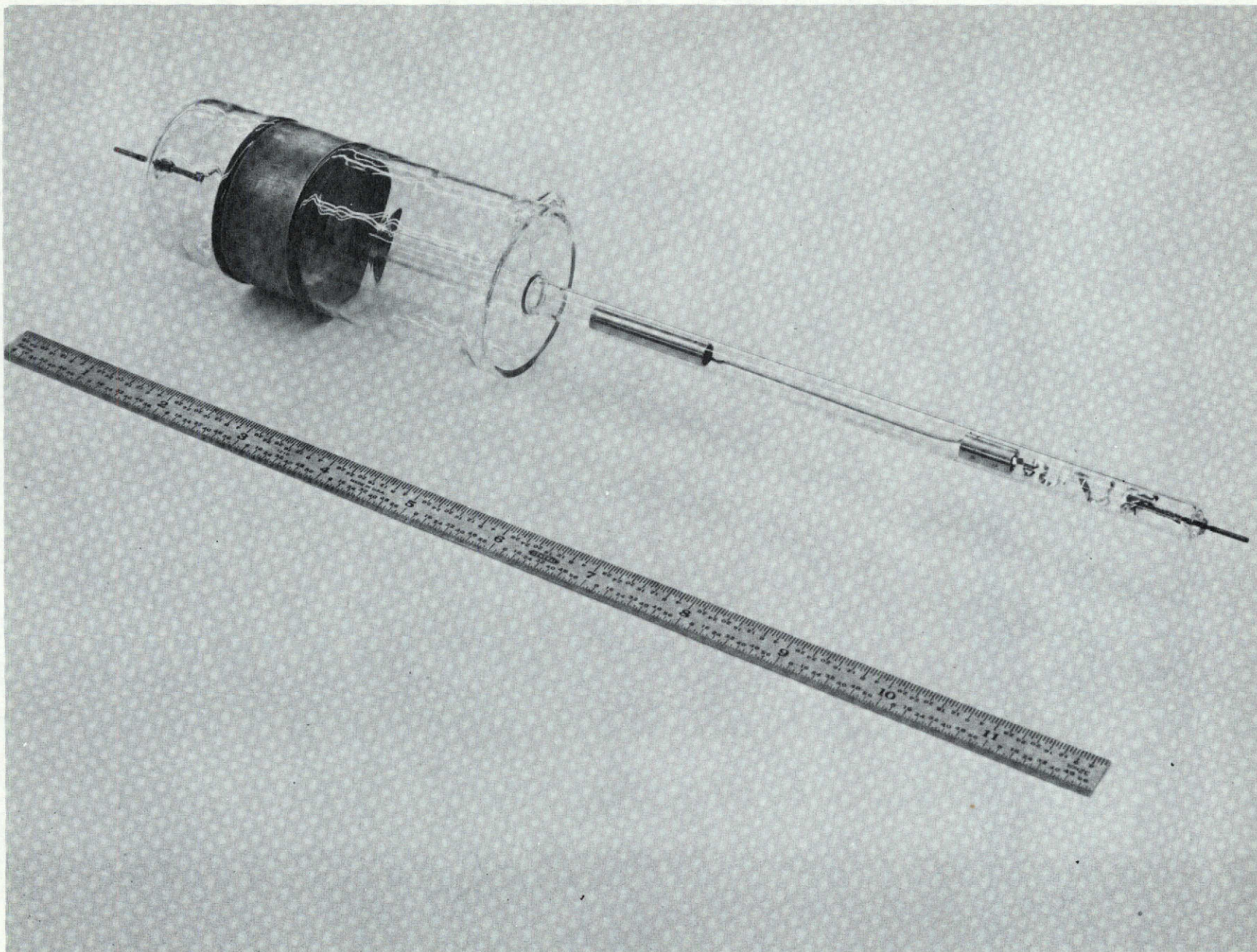
The 15-mm cathode allows for an extra 0.5 cm² of area for the discharge at the cathode when the pressure falls due to gas cleanup. This keeps the discharge from overflowing the cathode; i.e., it is kept in the normal glow region to reduce sputtering.

The six life-test tubes will be mounted to a common water-cooled aluminum baseplate. The observables to be monitored during the life test are voltage, current, output power and cathode temperature. The life-limiting factors of prime interest are gas cleanup, leaks, or defects in workmanship. The voltage-current characteristics of the tube will indicate any gross change in the total gas pressure. In addition, the gas pressure and composition will be reflected in a change in cathode temperature due to changes in the energy lost due to the cathode fall. The measurement of these factors throughout the life-test program will give valuable information which will allow us to predict the performance of the actual LCE tubes from data obtained during their initial 150 hour period of operation prior to delivery. The tube which performs most satisfactorily will be chosen for the final LCE design.

5.3.1.3 Extended Life-Test Program

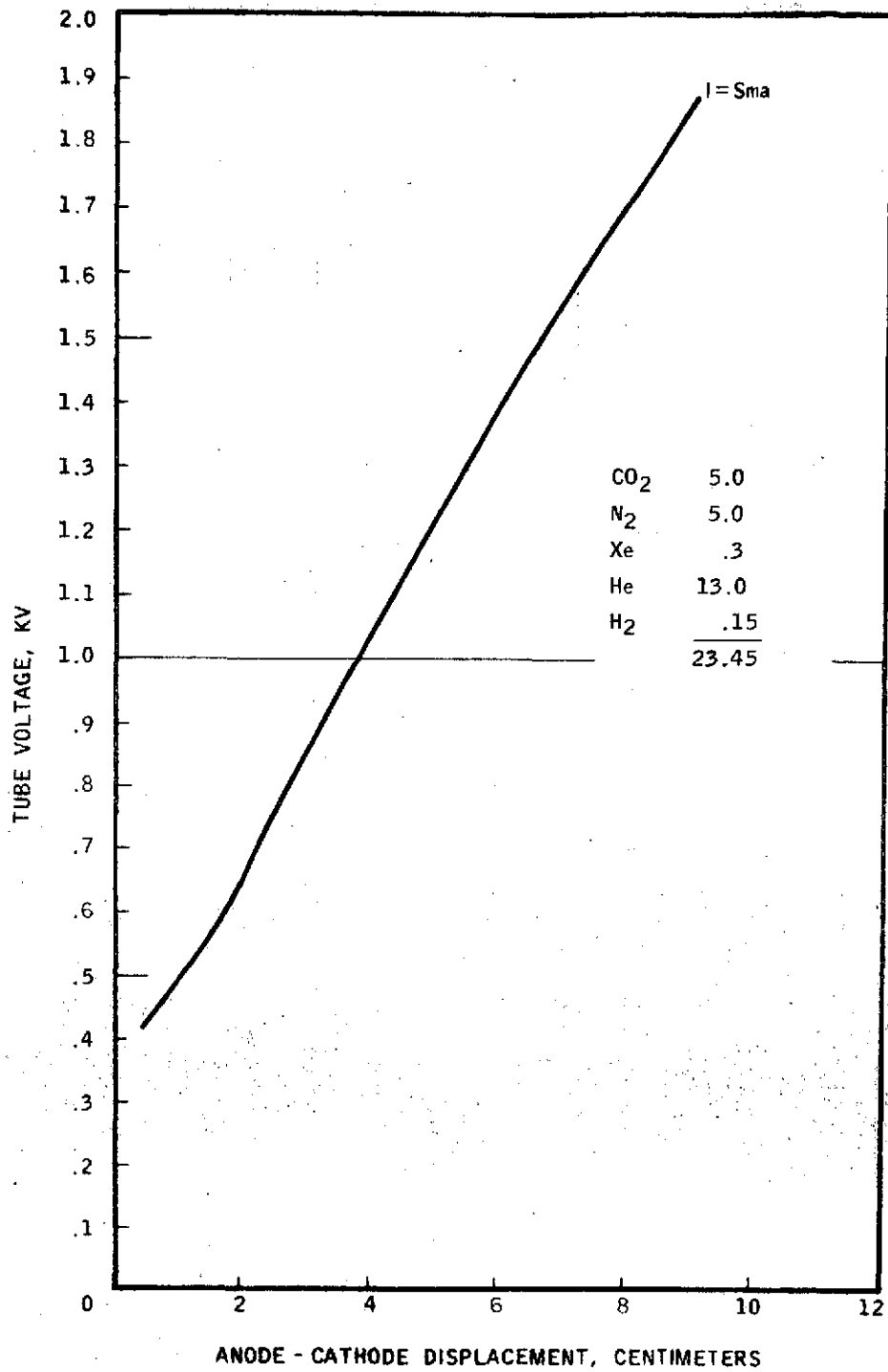
An extended program has been proposed, but not yet authorized by NASA GSFC. This program will include life testing of 12 tubes built to the most successful design of the six tubes described in the preceding paragraph, plus six tubes of the local-oscillator design. Each of these tubes would be placed on life test for a minimum of 2,000 and a maximum of 3,000 hours of operating time. The results of this test would greatly increase the life-test data available to the program and provide specific data which will be used to gain higher confidence in achieving the laser subsystem reliability goals. The schedule for the expanded program is shown in the lower half of Figure 5.3.1-5.

It is important to note that this program can provide significant information on the life of the 18 tubes prior to the delivery of the prototype from Sylvania, thus giving great confidence in the capability of the tubes prior to final qualification testing and fabrication of the flight system.



Experimental Discharge Tube with Variable Anode Position Capability

Figure 5.3.1-1



ANODE - CATHODE VOLTAGE VS. DISTANCE

Figure 5.3.1-2

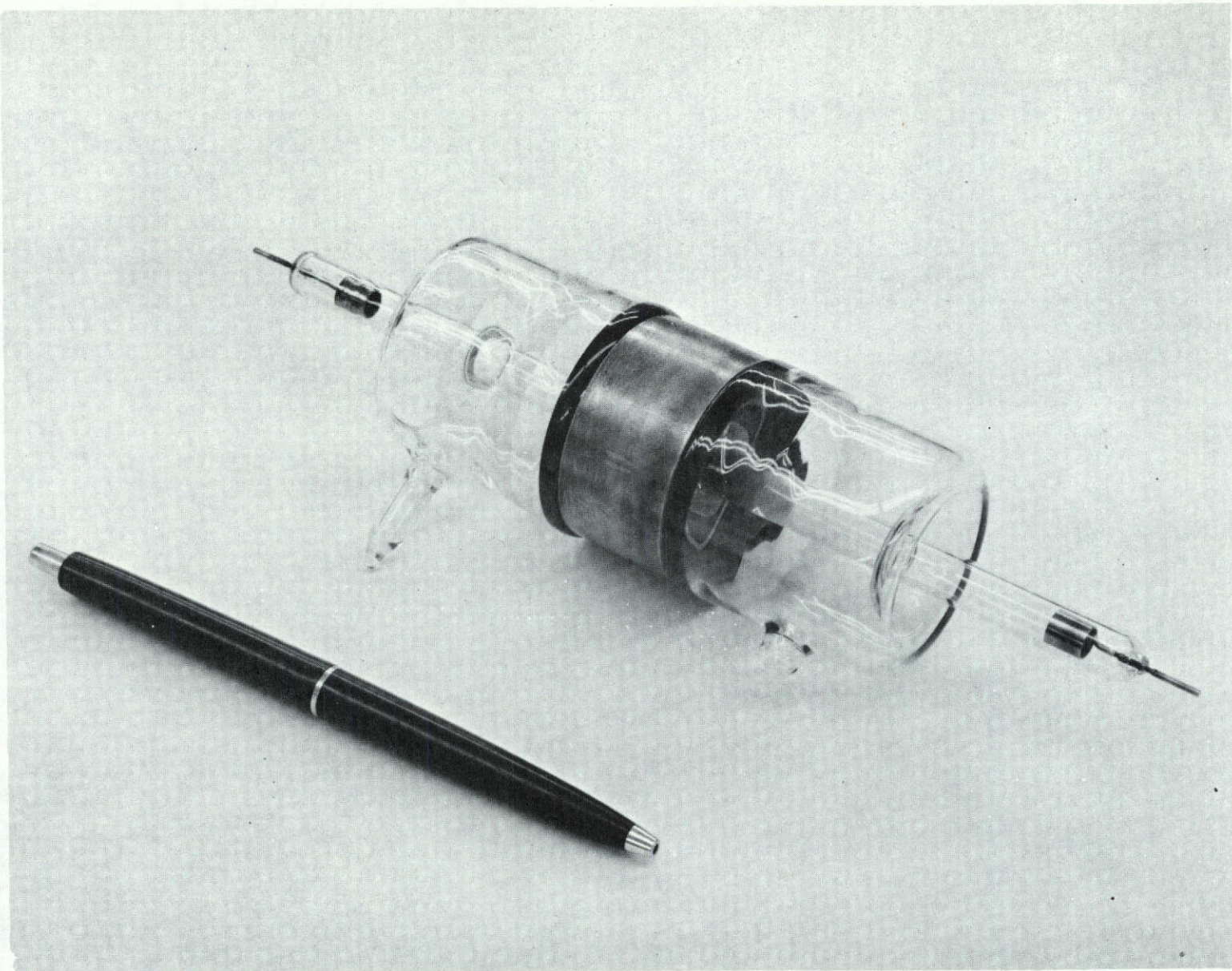
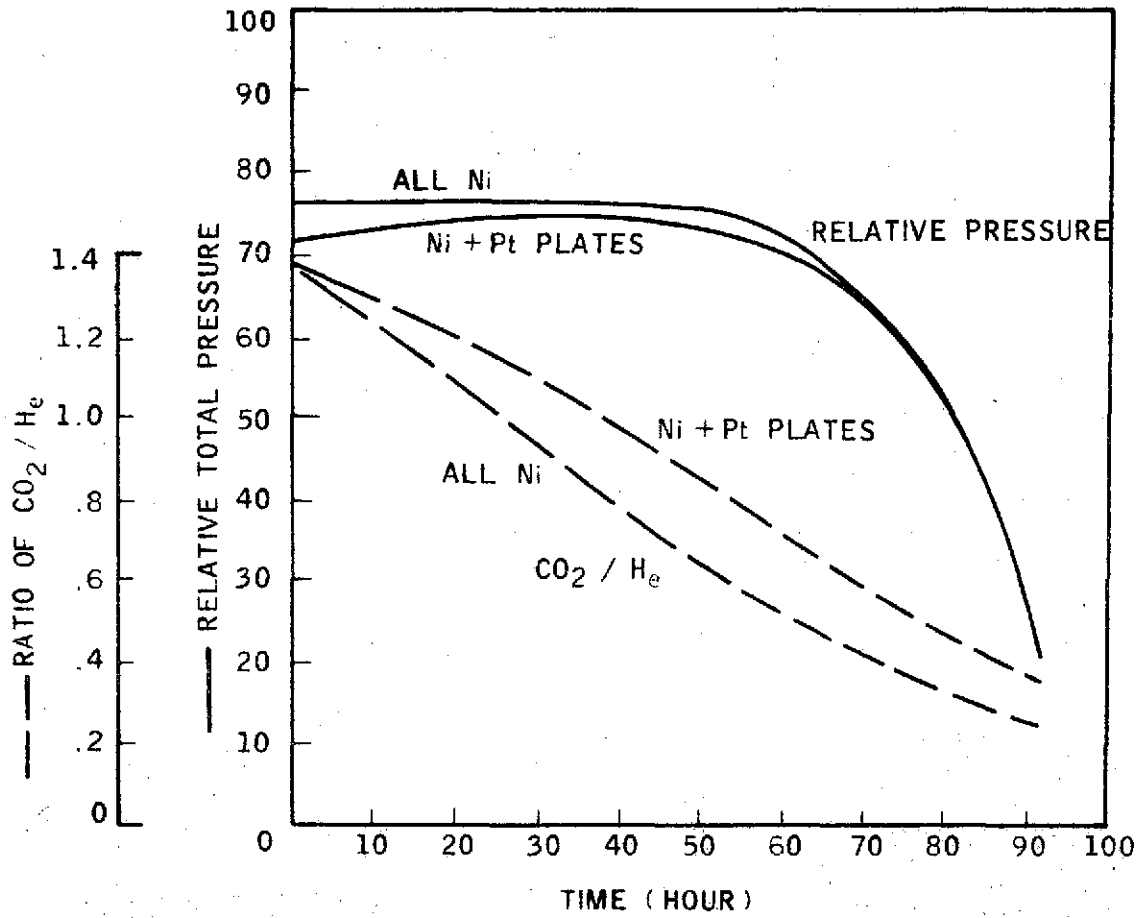


Figure 5.3.1-3

Experimental Discharge Tube Used to Measure Cathode Discharge Area

(4 MM ID AND 10 MA DISCHARGE CURRENT)



RELATIVE TOTAL PRESSURE VS TIME FOR Ni AND Ni + Pt PLATED DISCHARGE TUBES.

5.3.2 Duplexer

An efficient T/R switch is required to separate the transmit and receive optical paths. The straightforward technique of a simple beam splitter with some coding technique applied to the transmitter beams has been rejected in favor of more optimum methods. A wire grating polarizer, extrapolated from microwave and far IR devices, has been selected as the primary choice, and a polarizing interference filter for backup. Several other techniques have been considered, all of which appear to present more problems than fabrication of either the wire grid or the interference filter. The tradeoff considerations leading to selection of the separation mechanism and choice of polarizer are discussed. An analysis is presented to derive the specifications and fabrication techniques of the wire grid. Backup plans are discussed and a program plan for fabricating the wire grid is presented.

5.3.2.1 Separation Mechanism

The first basic tradeoff decision is related to the method of beam separation by polarization of P-line transitions closely spaced in frequency, or wavelength separation by transmitting in the 9.6- and 10.6-micron vibration-rotation transitions. The latter approach has the drawback that very few experimental measurements have been made on the 9.6-micron CO₂ laser. On the other hand, the power, gain and efficiency at 10.6 microns are well established. Qualitatively, it is known that the efficiency at 9.6 microns is about a factor of 2 below that at 10. (Ref. 1). As stated in the previous section, the worst possible duplexer entails a two-way loss about 4.5 db in excess of that allowed in the present link analysis (85% at each station). This is no worse than the 9.6/10.6 combination with wavelength filters, and does not require the investment of a large effort in developing the required new data base on 9.6-micron lasers. Therefore, separation by polarization has been selected. It will become evident in the following discussion that some development is also required to obtain an optimum polarizer. However, it appears that this effort is considerably less extensive than development of a new laser technology.

A search of optical component suppliers reveals that "off-the-shelf" IR polarizers are quite unsatisfactory for the LCE application. In general, these items are "pile-of-plates" reflection polarizers which are large, fairly

inefficient, and sometimes mechanically unstable. A review of the technical literature on polarization techniques (Refs. 2, 3, and 4, and references therein to further literature) leads to the following conclusions:

(a) Considering the overall requirements on optical and mechanical performance, the optimum polarizer is a wire grating supported on a Ge substrate.

(b) Since the requirements on a 10.6-micron wire grating polarizer are just beyond the capabilities of a supplier of standard components, a backup device is required in the event unexpected problems are encountered with fabrication of the wire grating.

(c) Refractive polarizers based on birefringence, thin-film/prism interfaces, and frustrated total internal reflection (FTIR) are decidedly less desirable than other techniques.

5.3.2.2 Wire-Grating Polarizer

The analysis of a wire-grating polarizer is presented below and in Appendix K, along with a proposed fabrication technique and technical references to substantiate anticipated performance of the grating and success of the fabrication technique.

5.3.2.2.1 Analysis

It was first noticed by H. Hertz that a wire grid used with electromagnetic radiation of wavelength equal to or greater than the grating spacing has the property of reflecting a wave whose E-field is parallel to the wires, and transmitting freely the perpendicularly polarized wave. Hertz's experiments were performed with microwaves, permitting the straightforward and easily controllable construction of "free-space" grating arrays, which can be directly compared with theory. At shorter wavelengths, more sophisticated techniques must be employed to produce a grating which results in strips of metal of known geometry, supported on a plane substrate, and thus amenable to comparison with the microwave theory.

The detailed analysis appears in Appendix K. The performance is a function of wavelength, λ , grating period, d , line width, a , angle of incidence, θ , and impedance matching $\lambda/4$ coating on the substrate. A schematic of the

wire-grating duplexer is given in Figure 5.3.2-1. Figure 5.3.2-2 corresponds to an unsupported (impedance-matched) substrate, and Figure 5.3.2-3 indicates the requirement for coating on Ge, and the desirability of coating other substrates. At $\lambda/d = 4$, the efficiency of the device is fairly insensitive to a/d , and theoretical performance exceeds the requirements of 5.2.1.6. (See Appendix K for further performance analysis and limitations of the theory.)

5.3.2.2.2 Fabrication Techniques

In order to establish a fabrication technique, the results of several technical articles are invoked. Bird and Parrish (Ref. 2) produced a wire grid supported on a plastic substrate which was a replica of a blazed diffraction grating with $d = .5$ micron. The "wires" were deposited on the substrate by "shadow casting" of the metal coating. That is, the substrate was held in the coating equipment so that the metal deposited preferentially on the tips of the blazed grooves. In spite of the fact that photomicrographs showed a highly irregular "wire" shape, and there was no quarterwave coating, results generally agreed with the predictions of this type of analysis. Young et al. (Ref. 3) ruled blazed grooves directly into Irtran 2 and 4 at $d = 1.6$ microns and achieved excellent polarization efficiency in the 8- to 14-micron region. Efforts to duplicate this technique on standard mechanical ruling engines have so far been unsuccessful. Preliminary analysis of alternate techniques appear very promising and results are expected shortly (see following sections).

Auton (Ref. 4) prepared wire-grid polarizers by masking and etching techniques. He worked in the far IR, 10-100 microns, and used polyethylene substrates. His results for $d = 10$ microns and $a = 4.2$ microns are reproduced in Figure 5.3.2-4. Accounting for the polyethylene transmission loss and experimental uncertainties, the results follow theory closely, particularly for $\lambda/d = 4$ and greater. Furthermore, the photomicrograph of the grating shows regular lines and spaces, which is required for application of the theoretical analysis.

Having established that λ/d should be 4 or 5 for a comfortable safety margin (see Appendix K), an easily fabricated photomask is just beyond practical limits. Sheridan (Ref. 5) has produced a blazed holographic grating

by exposing a photoresist layer coated on glass, and IBM (Ref. 6) has recently produced a grating coupler by interferometric exposure of a photoresist layer, resulting in a grating of "photoresist" strips of 0.7 microns.

Based on these results, the LCE duplexer will be fabricated by preparation of a Ge blank with ZnS quarter-wave coating (plus SiO thin-layer protective coating) 0.5- to 1-micron Al film, covered with a thin photoresist layer. The photoresist will be exposed with a two-beam interference pattern of 2- to 2.5-micron period in a standard holographic configuration. The exposed area will be etched, leaving the wire grating under the unexposed photoresist, which is subsequently removed. If the etching process is harmful to the coating, the grating will be formed by omitting the Al film and evaporatively coating over the exposed photoresist, thus reversing the positions of lines and spaces from the etching technique.

Discussions with Dr. Sheridan concerning this application of his technique provide a basis for a high level of confidence. He feels that the requirements and techniques are straightforward, and that he himself could fabricate such a grating in less than 1 month. However, Xerox does not accept contracts of this nature, but Dr. Sheridan will provide free consultation on the techniques required to apply and expose the photoresist. In addition to searching for a subcontractor, Aerojet will also pursue the possibility of fabricating the grating in-house, with consultation supplied by Dr. Sheridan. It is anticipated that the duplexer will be available within 2 months.

Although the analysis and proposed fabrication technique appear very favorable, alternative methods to produce a polarizer will also be pursued. The most attractive alternative is an interference filter with the following characteristics:

The passband is to be optimized for a 45° angle of incidence and peak transmission of a beam with an E-field vector parallel to the plane of incidence. The peak transmission of the orthogonal polarization is to be shifted in wavelength such that, within the passband, leakage at the orthogonally polarized wavelength is small enough to meet requirement No. 2, under section 5.3.2.1.

The advantage of this approach is fairly high efficiency and convenient mechanical configuration (again, merely a 45° component). Another advantage is rapid reaction time and quick repeats of fabrication with design modifications following measurements. (No long-lead items such as polished prisms with critical surfaces or ruled grating blanks.)

This component has not yet been designed, but preliminary indications are that the technique is feasible, and 70% transmission should result. This is sufficiently close to requirement for a backup device. In the event the supplier (Perkin-Elmer) fails to confirm his first indications, a Brewster-angle polarizer will be designed as an alternative backup. Available materials will be considered and a compromise made between efficiency and mechanical configuration.

5.3.2.3 Alternate Polarizers

Frustrated total internal reflection at an air space between two prisms has been considered. An analysis of the multiple reflections at the interface results in the following expressions for parallel and perpendicular polarizations:

$$\left(\frac{R}{T}\right)_{\text{para.}} = \frac{(n^2 - 1)^2 (n^2 \sin^2 \theta_o - \cos^2 \theta_o)}{4n^2 \cos^2 \theta_o (n^2 \sin^2 \theta_o - 1)} \sinh^2 \frac{2\pi d}{\lambda} \sqrt{n^2 \sin^2 \theta_o - 1}$$

$$\left(\frac{R}{T}\right)_{\text{perp.}} = \frac{(n^2 - 1)^2}{4n^2 \cos^2 \theta_o (n^2 \sin^2 \theta_o - 1)} \sinh^2 \frac{2\pi d}{\lambda} \sqrt{n^2 \sin^2 \theta_o - 1}$$

where

$$R = \frac{R/T}{1 + (R/T)}$$

R = reflectivity

T = transmissivity

n = refractive index of prism

θ_o = angle of incidence at surface of total reflection

d = air space between prisms

Figure 5.3.2-5 shows results for 90° NaCl prisms, $\theta_o = 45^\circ$, $n = 1.495$ at 10.6μ and for 90° Ge prisms, $\theta_o = 45^\circ$. It can be seen that the degree of polarization is inadequate in both cases. The Ge prisms might improve with larger angle of incidence, but then the geometry (already unsuitable) deteriorates further. FTIR polarizers have been eliminated for the following reasons: (1) inadequate polarization in simple cases, (2) extremely critical spacing requirements (air gap of $< .1\lambda$ for Ge, with rapid change of performance with d/λ), (3) awkward and bulky geometry, (4) materials problems, and (5) long lead time for evaluating new configuration.

Thin-film interfaces in multiple-prism geometries holding the films at Brewster angles have been considered qualitatively and summarily rejected on the following grounds: (1) awkward geometries, (2) large lateral beam displacement, (3) material availability problems, (4) critical tolerances on prism angles, (5) beam cross-section changes, (6) lack of suitable, space qualified interface cement (requires development program), (7) long-lead items, prism cutting and polishing, before evaluation can be made - no chance for modifications and fixes, and (8) four to six months before delivery of first item. Birefringent polarizers have not been seriously investigated because of (1) material availability problems, (2) interface cement problem, and (3) potential awkward geometries.

5.3.2.5 Wire-Grid Polarizer, Summary

Fabrication technique: exposure of photoresist layer on Ge substrate, $\lambda/4$ coated, followed by etching of predeposited Al film, or deposition of Al film over exposed photoresist; grating pattern produced interferometrically.

Preferable to mechanical ruling because:

- (a) Ge is more suitable substrate.
- (b) More control over shape and uniformity of wires.
- (c) Shadow casting of $\lambda/4$ coating over blazed grooves almost impossible, yet Figure 3 shows coating is desirable on almost any substrate.
- (d) Controlled wire shape means reliable comparison with microwave theory, which has been verified to 20 to 40 microns with similarly fabricated polarizer.

Report No. 4033, Vol. I, Part 1

- (e) 1- to 2.5-micron period is easy to achieve in holographic interference configuration.
- (f) Free consultation is available from expert in the field.
- (g) In-house microelectronics and coating facilities can handle blank preparation and chemical processing.
- (h) Many samples can be prepared without a long-lead item such as a master blank ruled on a diffraction grating ruling engine.
- (i) Efforts to date to produce a suitable ruled blank have yielded unsatisfactory results.

Specifications:

Size, Ge blank - 28 x 40 x 4.0 mm, polished flat to $1/4 \lambda$ visible light, with rms surface irregularities $< 1/4 \lambda$ visible light over the long dimension

Coating - $1/4 \lambda$ ZnS, overcoated with $< 1000 \text{ \AA}$ SiO₂

Wire material - Al (Au satisfactory)

Wire period - 1 to 2.5 microns $\pm 10\%$

Wire width - $1/2$ of period $\pm 10\%$

Wires to be parallel to 28 mm dimension

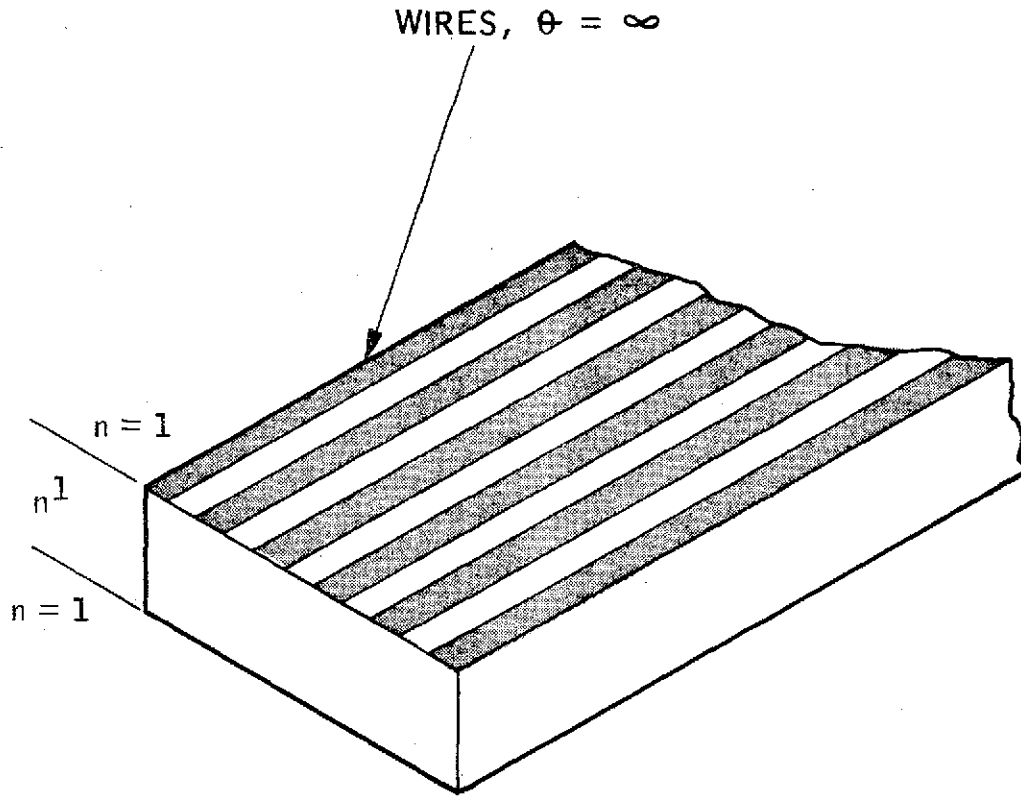
Irregularities and discontinuities in the grating should be small compared with 10 microns

Time to complete - 2 months or less

The efforts that are under way to fabricate the duplexer described above are shown in the program plan, Figure 5.3.2-6. This incorporates both of the parallel efforts in fabrication techniques that appear to be very promising noted above. Definitive results are expected by mid-August.

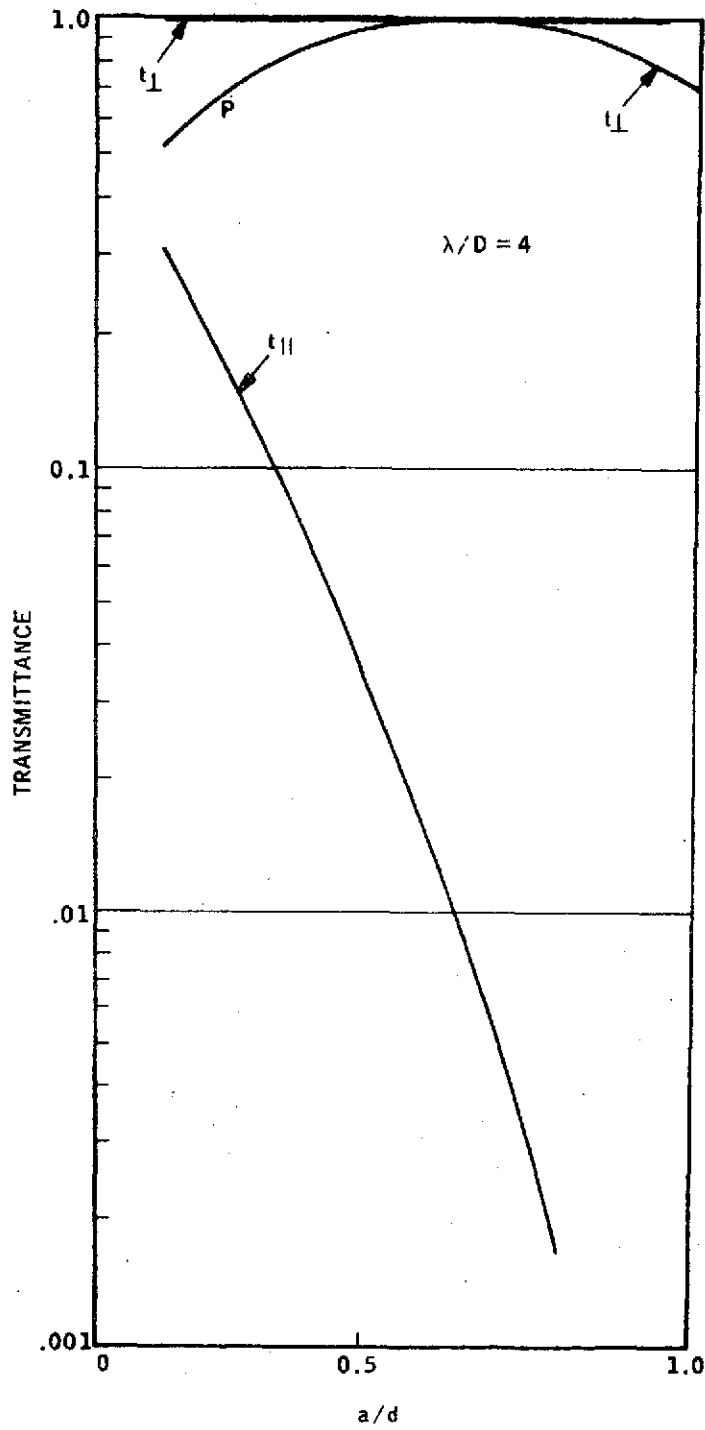
REFERENCES

1. P. K. Cheo, Private Communication.
2. G. R. Bird and M. Parish, J. Opt. Soc. Am., 50, 886 (1960).
3. J. B. Young, H. A. Graham, and E. W. Peterson, "Wire Grid Infrared Polarizer," Appl. Opt. 4, 1023 (1965).
4. J. P. Auton, "Infrared Transmission Polarizers by Photolithography," Appl. Opt. 6, 1023 (1967).
5. N. K. Sheridan, "Production of Blazed Holograms," Appl. Phys. Letters, 12, 316 (1968).
6. M. L. Dakss, L. Kuhn, P. F. Heidrich, and B. A. Scott, "A Grating Coupler for Efficient Excitation of Optical Guided Waves in Thin Films," IBM Research Preprint, 1 April 1970.

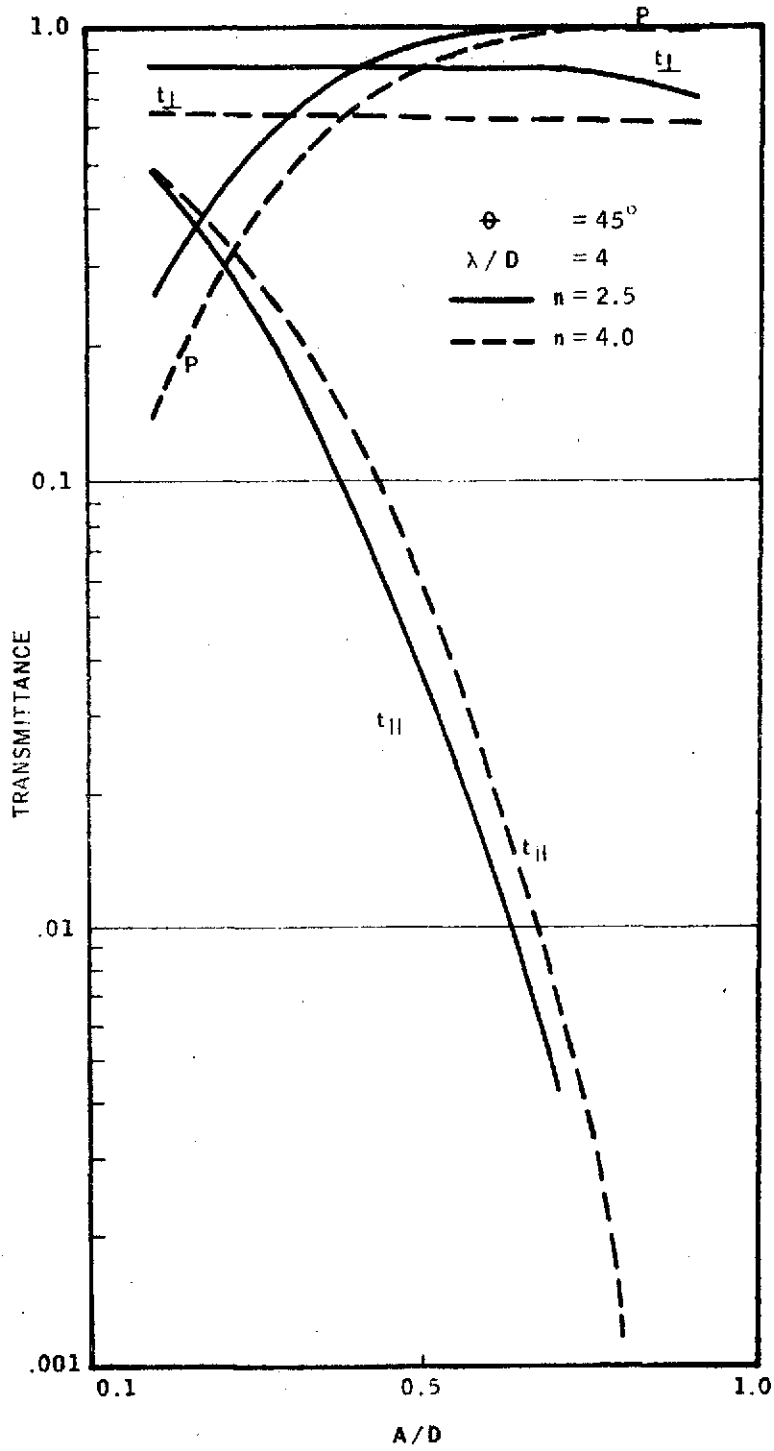


WIRE GRATING ON DIELECTRIC SUBSTRATE

Figure 5.3.2-1

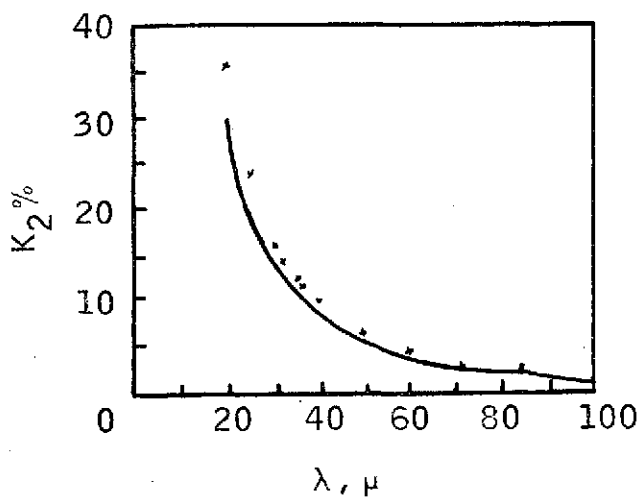
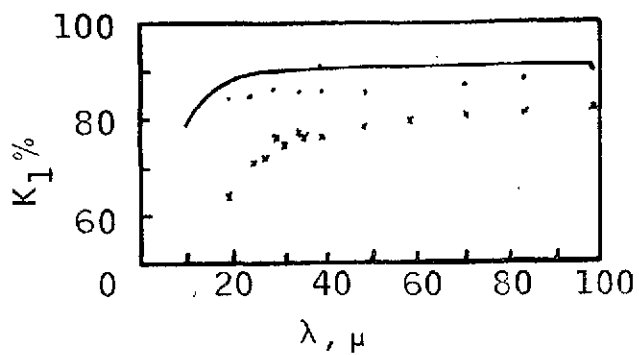


WIRE GRATING PERFORMANCE AT $\lambda/D = 4$



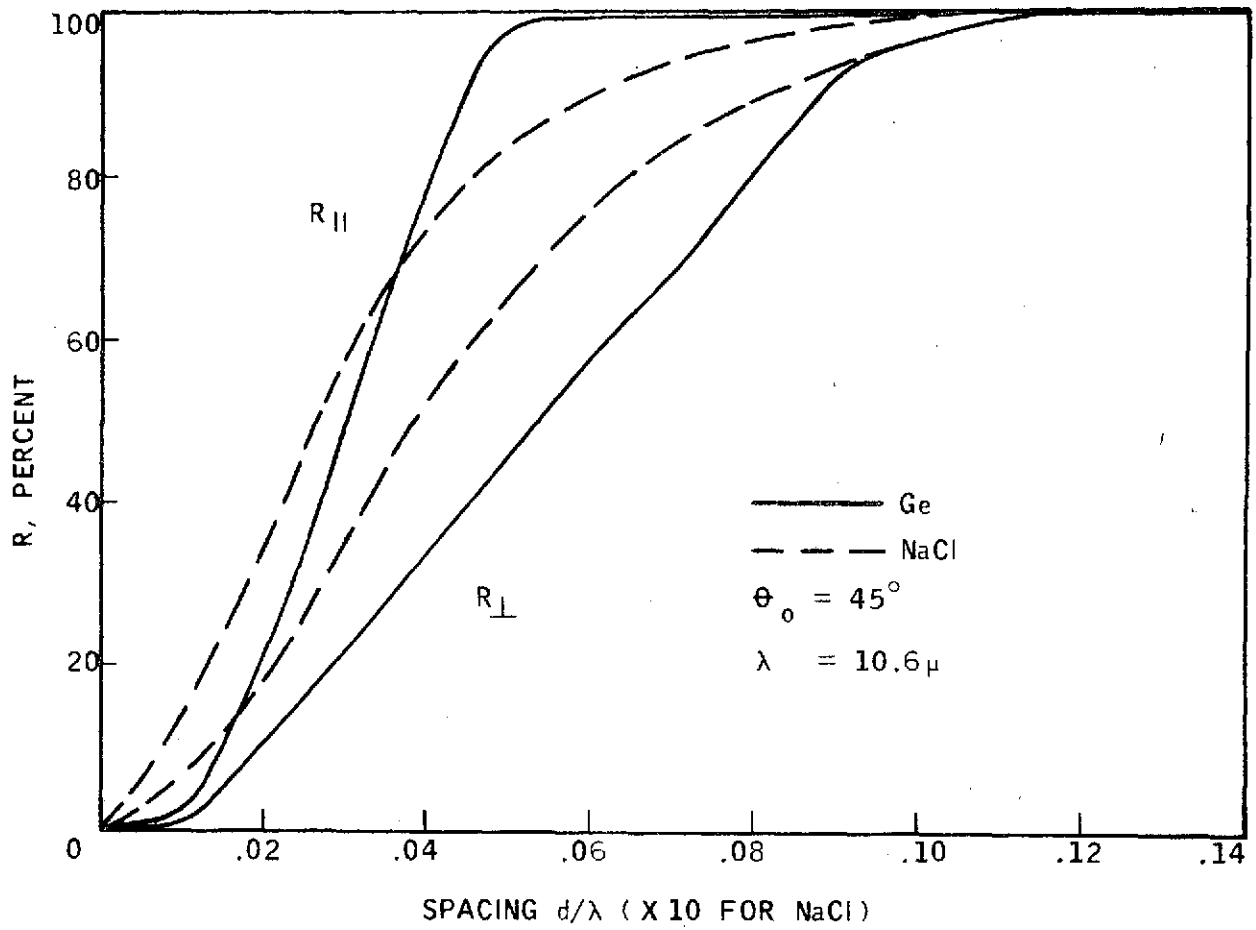
PERFORMANCE OF WIRE GRATING POLARIZER WITHOUT $\lambda/4$ COATING

Figure 5.3.2-3



TRANSMISSION OF A POLARIZER
ON A POLYETHYLENE SUBSTRATE

Figure 5.3.2-4



FTIR POLARIZERS

Figure 5.3.2-5

TASK / WEEK ENDING	7/10	7/17	7/24	7/31	8/7	8/14	8/21	8/28	9/4
WIRE GRID POLARIZER									
COMPLETE PERFORMANCE, ANALYSIS & SPECIFICATION OF WIRE GRID									
AGC EFFORT OR SUBCONTRACT DECISION									
WRITTEN SPECIFICATION AND TEST PLAN									
SUBSTRATE PREPARATION									
FABRICATION AND TEST									
MODIFICATIONS AND FINAL FABRICATION AND TEST - DUPLEXER AVAILABILITY									
INTERFERENCE FILTER									
ANALYSIS AND QUOTATION FROM PERKIN - ELMER									
LET SUBCONTRACT									
FABRICATION AND TEST									
MODIFICATIONS AND FINAL TEST									

Figure 5.3.2-6

DUPLEXER PROGRAM PLAN

5.3.3 Radiation Cooler

To assure successful performance of the ICE transceiver, the operating temperature of the mercury-cadmium-telluride (Hg.Cd)Te detector must be maintained between 95°K and 125°K throughout the operational portions of the orbital mission life of the experiment. A passive radiation cooler is used to obtain this low temperature. The design of such a cooler is essentially "state-of-the-art" so an extensive development and test effort will be carried out during the course of the program to insure early detection of unforeseen problems so that corrective actions can be taken to obtain successful and timely performance. There are four important areas in the design of the cooler that must be carefully examined during this effort to insure that the best system is being used and that it meets the mission requirements. These areas are:

1. The radiator and sunshade support design and its resulting thermal conductance
2. The detector position or alignment
3. The sunshade contour and specularity
4. The thermophysical properties of the coatings and insulations used to regulate the heat transfer of the subassemblies.

The table below lists the development test models and the tests to be performed on each. The details of these tests and their value to the overall design will be described in the sections which follow. A detailed discussion of the radiator cooler assembly function, requirements, and design is given in Section 5.2.3.

<u>TEST MODEL</u>	<u>TESTS TO BE PERFORMED</u>	<u>DESIGN AREA</u>
Structural Model	Vibration Thermal/Vacuum: Breakaway	Support Support
Dummy Support Assy	Thermal/Vacuum: Conductance	Support

<u>TEST MODEL</u>	<u>TESTS TO BE PERFORMED</u>	<u>DESIGN AREA</u>
Functional Test Model	Vibration Contour and Specularity Thermal/Vacuum: Detector Position Thermal/Vacuum: IR Transmission from Sunshade to Radiator	Support Sunshade Thermal Performance Alignment Coatings, Insulations

Note the extensive use of a structural model and dummy support assembly. Early fabrication of these items is possible since they do not require special surface coatings for radiation or a flight approved detector/mixer. The subsequently early testing of these articles will lead to timely solution of any design problems uncovered in the tests.

5.3.3.1 Radiator and Sunshade Support Design

When designing the supports for the radiator and sunshade, one must carefully review the requirements placed on them during each phase of the mission. During the launch and ascent portions of the mission, when there are large dynamic loads imposed on the system, the supports must be designed to securely restrain the radiator and sunshade so that excessive movements or accelerations do not damage any item in the cooler subassembly. This means that the radiator and sunshade must be in good structural contact with the LCE primary support structure. This generally connotes good thermal contact as well.

During the orbital phase of the mission, the dynamic loads imposed on the cooler subassembly are negligible. The supports which hold the radiator during launch are more than adequate from a structural/mechanical standpoint for the orbital design. However, the heat transfer through these supports would be excessive and satisfactory radiator temperatures would be unobtainable. Therefore, a different support mechanism must be used in orbit. This new support mechanism will provide the minimum required structural support for the radiator and sunshade to maintain detector alignment while keeping the heat leaks through the supports to a minimum. As a design goal, Aerojet will attempt to design supports that will securely hold the radiator and sunshade on orbit and conduct less than 20 mw to each of these items via the supports.

There are several techniques which have been successfully employed on various other spacecraft to remove supports not required after launch. These techniques, usually used on cryogenic subsystems, rely on the following mechanisms to free the supports:

1. Pin pullers
2. Explosive bolts
3. Differential thermal expansion

These and other release mechanisms will be examined in detail to ascertain which would be best for the LCE. At this time, the preferred candidate is the one that uses the differential thermal expansion of the materials of construction to obtain separation. The reason that this technique is preferred to the others is that it is an uncomplicated, passive system, requiring only temperature difference to operate. The pin-puller system requires electro/mechanical equipment whose weight and reliability are a disadvantage compared to the differential thermal expansion system. The explosive-bolt system has similar problems and there is also a contamination problem not encountered by the differential thermal expansion system. The validity of the present support approach will be proven early and conclusively by analysis and test of the structural model and dummy support model. Breakaway of the radiator and sunshade from the support mount will be verified in the structural model's thermal/vacuum test.

The structural model will also be tested in a vibration environment. The radiator, sunshade and mount, structural model will be structurally similar to the flight model. The purpose of the structural model tests is to determine, early in the program, any anomalies with the structural portion of the design. The vibration test will consist of a resonance search through the full frequency range (5 through 2000 Hz), with appropriate acceleration transducers attached to the test article to determine the response of the structure. Particular attention will be paid to the area of the simulated detector/mixer to determine maximum displacement differentials between the vibration fixture and the detector/mixer mount. This information will be directly applicable to the calculation of detector/mixer focus

and alignment. Of equal importance in this test, will be the search for possible detector/mixer resonant frequencies and their associated acceleration effects. Any such resonant frequencies will be found through measurement of accelerations of the simulated detector/mixer that is a part of the structural model. Should it be found that resonant frequencies create a problem, the required redesign to damp out excessive accelerations can be accomplished without adversely affecting downstream schedules due to the early problem discovery permitted by these timely structural model tests.

As stated earlier, the orbital supports must be designed to minimize heat leaks to the radiator and sunshade; a value less than 20 mw is a design goal. Several low-conductance support schemes have been developed for cryogenic vessels and other systems designed in the past. These support techniques include:

1. Tension wires
2. Monoballs
3. Centering pin
4. Spring-loaded ball supports

The tension-wire concept relies upon the technique of suspending the radiator and sunshade securely in place through use of wires that are maintained in tension. These wires will provide the only mounting-associated heat leak to the detector. The wires will be long, of small cross-section, and have low thermal conductivity to minimize the heat leak. Stainless steel is a primary wire candidate. An important tradeoff to be considered in the tension wire design is that improvements in thermal insulation capability, brought on by decreased cross-section and increased length, go counter to improvements in structural integrity.

The monoball support technique relies upon the use of three or more spheres attached to the component to be isolated. Each sphere sits in a transceiver-mounted race. Between the sphere and race is a teflon sheath. The advantages of this system are that it provides positive support while permitting thermal contraction of the isolated member. Its primary

disadvantage is that sizeable heat leaks will be sustained across the system's relatively large contact areas.

The centering pin concept has possible application in combination with virtually any orbital support plan and primarily deals with insuring meeting the mixer assembly positioning and alignment requirements. The center support would be comprised basically of a heat sink-attached pin fitted into a radiator-attached hole relatively near the radiator center. The pin would not touch the radiator while the radiator is warm and the positive launch support mechanism is acting. When the launch support system is removed, the radiator will contract as it cools. Should the radiator move out of focal plane alignment during launch support removal and/or radiator cooldown, the radiator would push against the centering pin. Thus, the pin would be providing an alignment restoration force as well as a positive stop to prevent excess misalignment. The primary disadvantage of such a system would be that it would create a small heat leak to the detector/mixer while acting. This system would, however, not be active should the primary support mechanisms (launch and orbital operation) operate as planned. An investigation of possible utilization of this mechanism is under way, primarily dealing with the added heat load, the structural requirements and the size and tolerances of the centering pin and hole.

At present, the spring-loaded ball support appears to be the most attractive support system. It provides positive support for detector alignment while allowing heat leakage across very small cross-sections. Thus, this system appears to provide the smallest heat leak of any of the above candidates. Early substantiation of this will be obtained by analysis and test of the dummy support assembly. The following test will be performed to insure the thermal adequacy of the design:

The dummy support assembly will be attached to an electrical heater and heat flowmeter (see Figure 5.3.3-1). The radiator and sunshade supports will be tested separately. The simulated radiator or sunshade (one will be tested then the other) will be coupled to a liquid-nitrogen or water-cooled heat sink whose temperature will be controlled so that the temperature of the radiator or sunshade is brought to the analytically

predicted value while the support mount is maintained near 300°K. By measuring the support temperature gradient and the corresponding heat flow, the conductance can be directly calculated. Radiant heat flow between the test article and its surroundings will be controlled passively using multi-layer insulation. When testing the support for conductance between the support mount and sunshade, radiant heat loss can be neglected as the support mount and sunshade will both be maintained near room temperature. All testing will be performed in a vacuum chamber evacuated to 10^{-5} Torr or less. An instrumentation list is presented in the following table:

<u>PARAMETER</u>	<u>TYPE</u>	<u>ACCURACY</u>
Support Mount Temp. #1	Cu-Con T/C	1°F ($\frac{1}{2}$ °C)
Support Mount Temp. #2	Cu-Con T/C	1°F ($\frac{1}{2}$ °C)
Radiator (Sunshade) Temp. #3	Cu-Con T/C	1°F ($\frac{1}{2}$ °C)
Radiator (Sunshade) Temp. #4	Cu-Con T/C	1°F ($\frac{1}{2}$ °C)
Heat Flowmeter EMF	Potentiometer	$\frac{1}{2}\%$
Heater EMF	Potentiometer	$\frac{1}{2}\%$
Heater Current	Potentiometer	$\frac{1}{2}\%$

The schedule for the development and testing of the support system is presented in Figure 5.3.3-2. This includes testing of the structural model and dummy support assembly. Note how early in the program the support design is tested. This is made possible through use of test articles that do not require special optical surfaces or use of a flight model detector/mixer.

5.3.3.2 Detector Position

During the functional test model (FTM) thermal/vacuum test, displacement of the detector focal plane will be measured in order to verify that the following focal plane alignment criteria are met:

<u>DIRECTION</u>	<u>MAGNITUDE</u>
Axial (ΔZ)	± 0.010 inch
Longitudinal ($\Delta X, \Delta Y$)	± 0.005 inch

Movement of the focal plane could result when the radiator is cooled below the radiator-support mount separation temperature, thus taking

the radiator out of contact with its support mount. This possibility, which might result in misalignment and poor system performance, can only be researched with a radiator/sunshade assembly test. The proposed test is described below:

The functional test model with a simulated detector/mixer assembly mounted on the radiator will be installed in a vacuum chamber with a liquid nitrogen cooled shroud. Instrumentation will include several copper versus constantan thermocouples and three linear velocity and displacement transducers (LVDT) attached to the simulated detector/mixer assembly. The instrumentation is described in the following table and illustrated on Figure 5.3.3-3.

<u>PARAMETER</u>	<u>TYPE*</u>	<u>ACCURACY**</u>
Radiator Temp.	Cu-Con T/C	1°F ($\frac{1}{2}$ °C)
Mixer Temp.	Cu-Con T/C	1°F ($\frac{1}{2}$ °C)
Sunshade Temp.	Cu-Con T/C	1°F ($\frac{1}{2}$ °C)
Support Mount Temp.	Cu-Con T/C	1°F ($\frac{1}{2}$ °C)
Heat Sink Temp.	Cu-Con T/C	1°F ($\frac{1}{2}$ °C)
Mixer Displacement ΔX	LVDT	0.0005 in.
Mixer Displacement ΔY	LVDT	0.0005 in.
Mixer Displacement ΔZ	LVDT	0.0005 in.

* Cu-Con T/C indicates a 36 AWG copper versus constantan thermocouple. LVDT indicates a linear motion transducer.

** The accuracy is estimated based on engineering test experience. All thermocouples will be calibrated.

In addition to the attachment of instrumentation to the test article, heaters will be bonded to the heat sink and sunshade to maintain them at the predicted orbital temperatures while the radiator is allowed to cool.

The data output from this test will be temperature and displacement versus time of the instrumented components, as indicated in the table above. The test schedule is included in Figure 5.3.3-4 which is the entire development and test program for the sunshade and radiator FTM up through delivery.

5.3.3.3 Sunshade Contour and Specularity

The slope or contour of the inner surface of the sunshade and its specularity are of prime importance to the success of the LCE transceiver's radiation cooler. Figure 5.2.3-12, presents the present design for the sunshade. This design evolved after an extensive analytical effort. It was demonstrated analytically that the shape of the wineglass sunshade could be described as a simple arc of a circle and therefore the sunshade was an ogival surface of revolution. In addition, analysis has indicated that the temperature of the detector will increase by 3°K for each 5 percent decrease in specularity.

Now that analysis has defined the requirements for the sunshade and the preliminary design is complete, a development and test program will be conducted to insure that the sunshade can be constructed to meet the requirements.

AGC mechanical design engineers, manufacturing and optical coating laboratory personnel will begin in July to develop techniques to machine and polish the sunshade. After the sunshade has been fabricated, the following test will be conducted to insure that its contour and specularity are within acceptable limits.

The FTM sunshade will be installed on an optical collimator test table so that it can be irradiated with collimated visible light at several angles about the shade's major axis. A radiometer will be placed in the radiator plane so that energy absorbed by the radiator will be indicated by the radiometer output.

Prior to testing, the collimated beam will be mapped with the radiometer to determine the total flux in the test volume. The flux absorbed by the radiometer with the shield in place will then be compared to the total flux known to be incident on the shield. The ratio of incident flux to absorbed flux is a measure of sunshade performance in the areas of contour and specularity. This test is included in the FTM schedule shown in Figure 5.3.3-4.

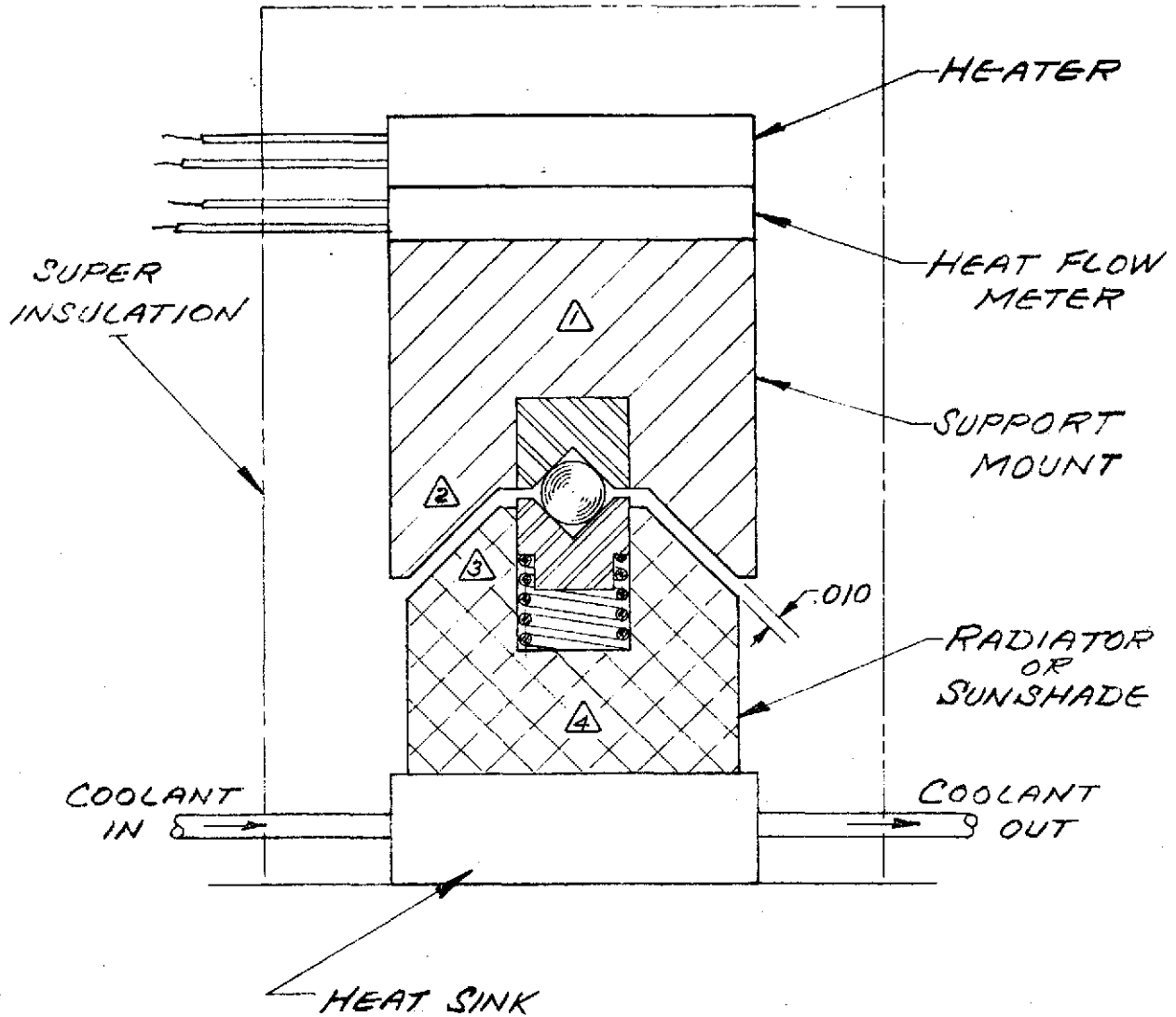
5.3.3.4 Thermophysical Property Testing

The thermophysical properties of critical thermal control coatings and insulations will be measured in a series of individual tests. These tests will produce results which can be entered into the analytic models of the cooler to reduce prediction uncertainties. The cooler will also be tested as a total assembly to obtain in-situ measurements of heat leaks within the system.

The IR emission from the sunshade to the radiator is the largest single heat load incident upon the radiator. Thus, verifying the exact magnitude of this heat load is of great importance. To accomplish this the test article, consisting of the heat sink, passive radiator and sunshade, and a simulated antenna and solar panel, will be installed in a thermal/vacuum test chamber. The test article will be instrumented with copper versus constantan thermocouples. Internal power dissipation will be simulated by heaters attached to the heat sink.

Testing will be conducted with the chamber evacuated to a pressure less than 10^{-5} Torr, and the chamber cryo-shroud cooled to a temperature less than 80°K. After the test article has reached a steady-state condition, temperature data will be recorded.

The reduced test data will be compared with previously predicted results to verify the validity of analytic techniques and to show that the radiator thermal performance is satisfactory. This thermal/vacuum test will be performed on the functional test model early in the program, then later repeated on the prototype, flight and flight spare models. The schedule for the FTM test is included in Figure 5.3.3-4.

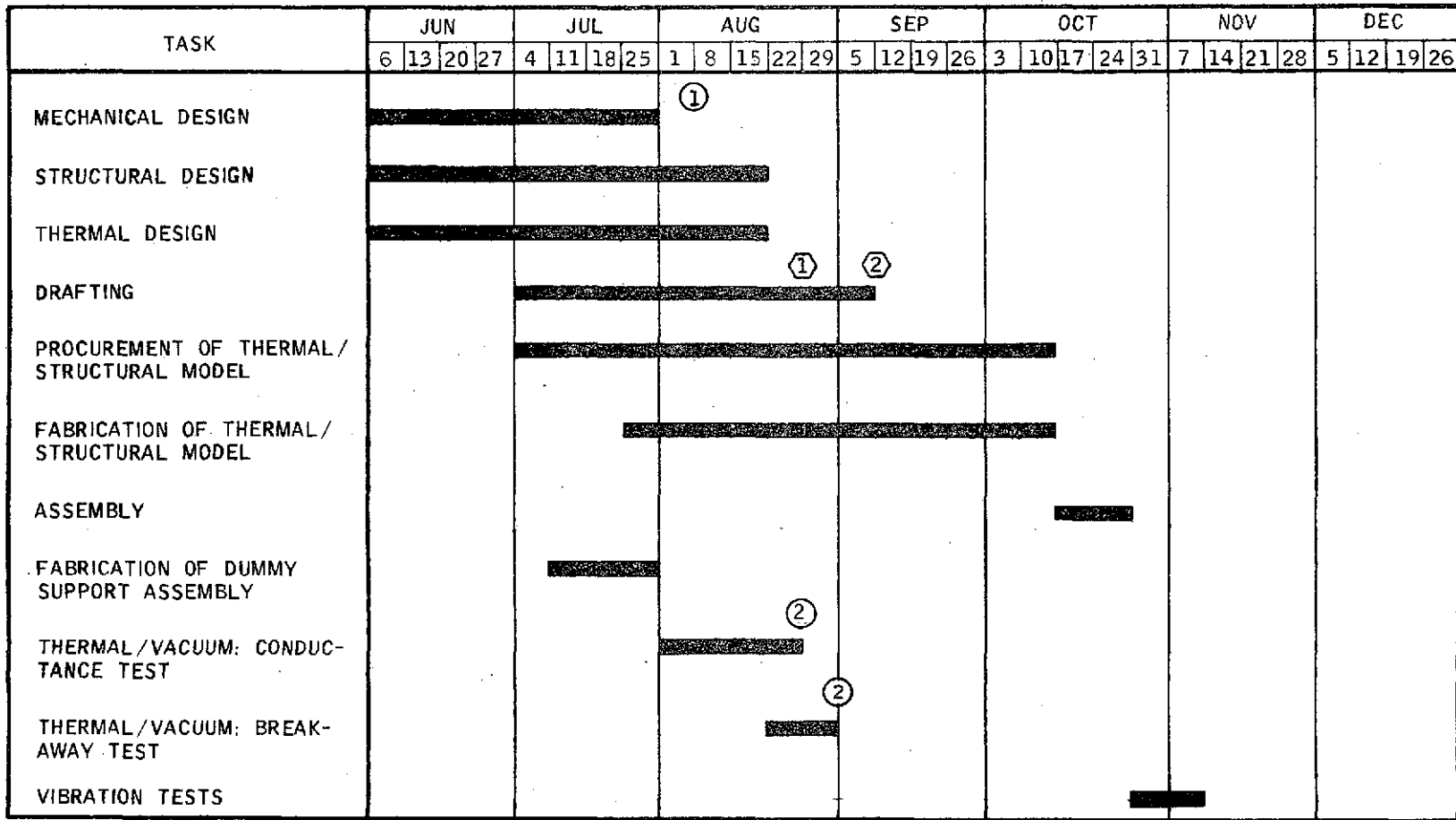


NOTE: Δ INDICATES LOCATION OF COPPER
VERSUS CONSTANTAN THERMOCOUPLES.

SUPPORT CONDUCTANCE
TEST SETUP
NO SCALE

SK-1297656
S.G. COON 7-7-70

Figure 5.3.3-1



① PRELIMINARY DESIGN COMPLETE - FIRST LAYOUT AVAILABLE.

① COMMENT PRINTS RELEASED.

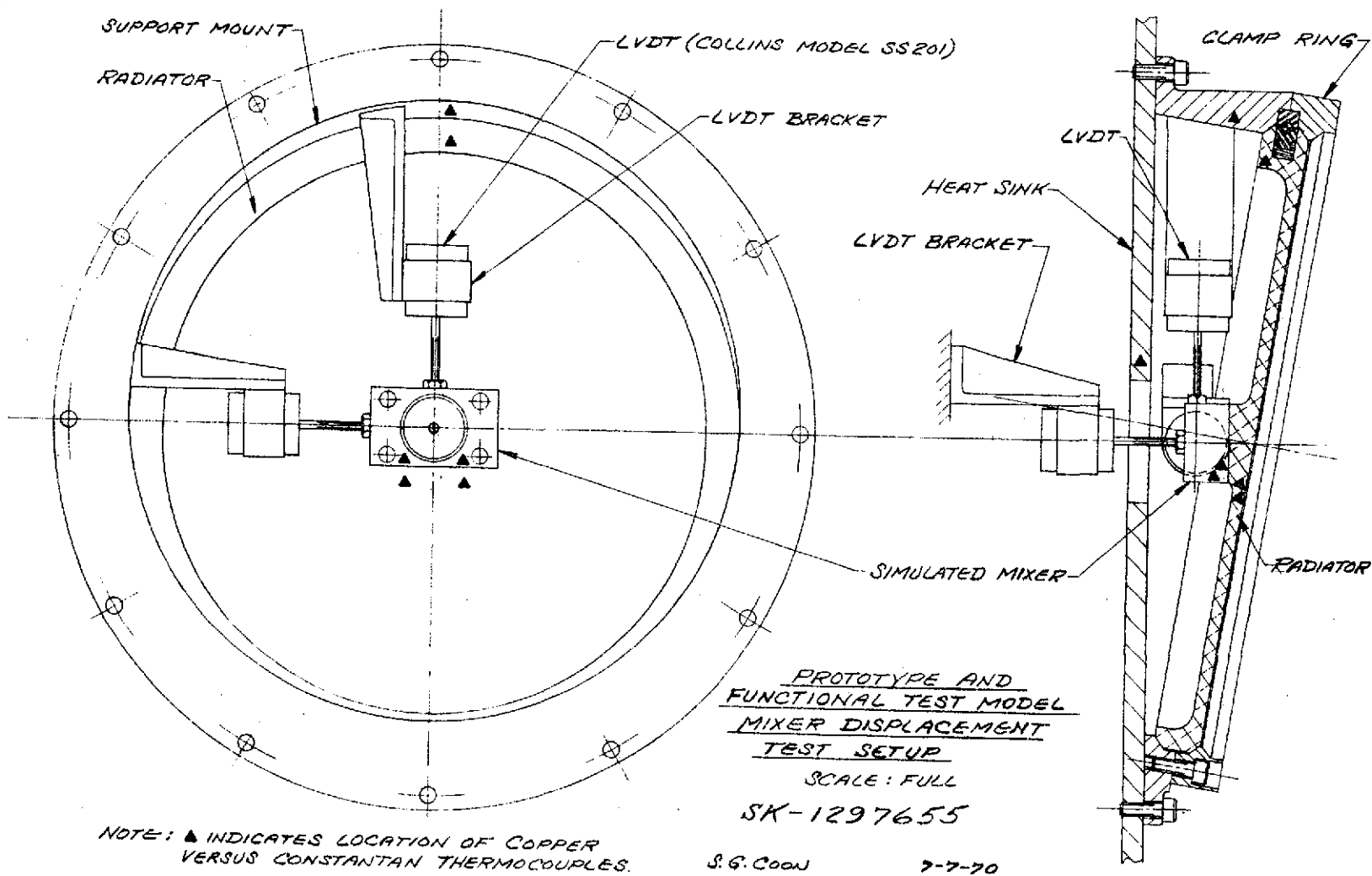
② INITIAL SUPPORT TESTS TO VERIFY DIFFERENTIAL EXPANSION CONCEPT WILL WORK ACCEPTABLY.

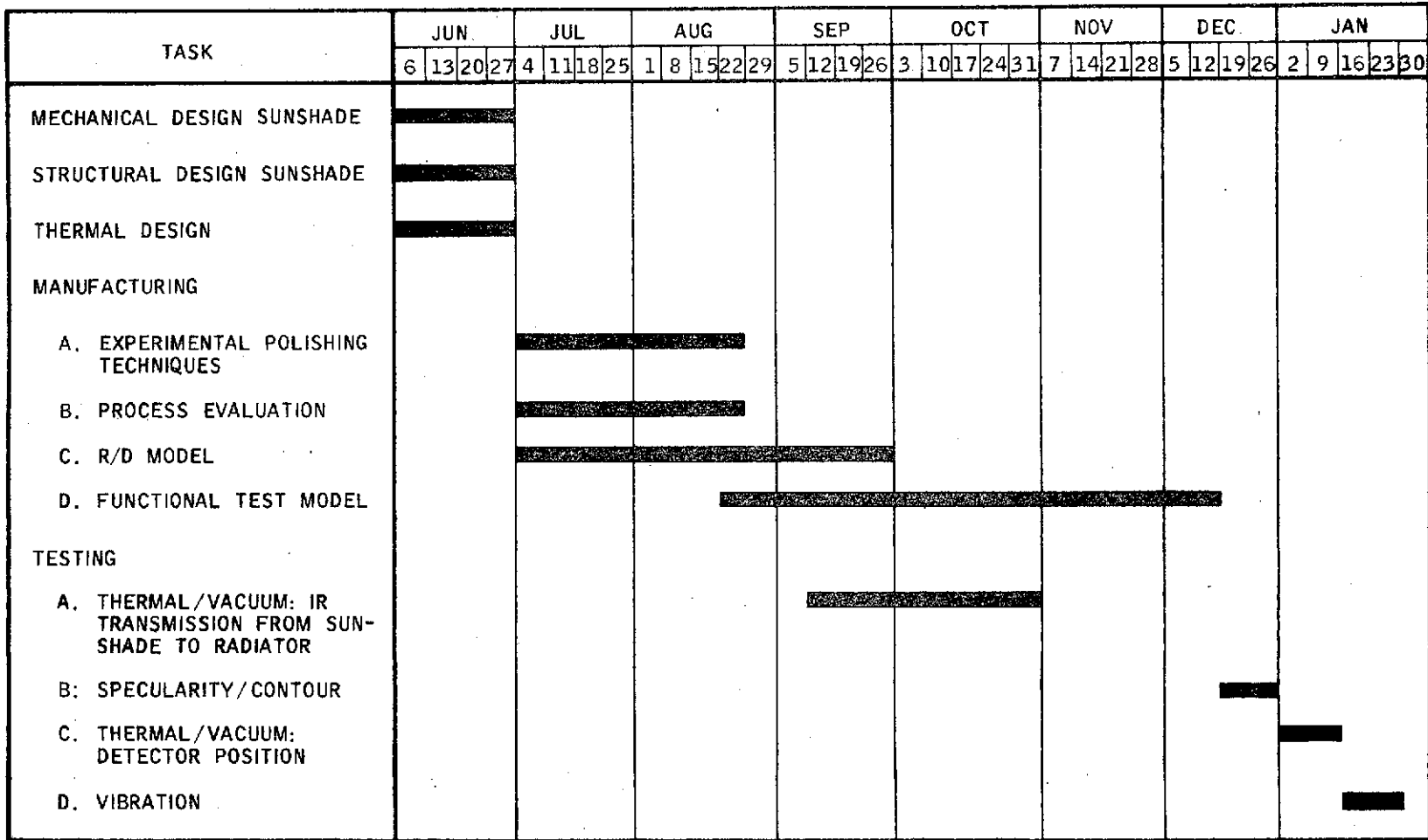
② ALL DETAIL DRAWINGS RELEASED.

RELEASE AND SUPPORT MECHANISMS--DEVELOPMENT SCHEDULE

Figure 5.3.3-2

Figure 5.3.3-3





SUNSHADE DEVELOPMENT / SYSTEM TESTING SCHEDULE

Figure 5.3.3-4

5.4. SPACECRAFT/EXPERIMENT INTERFACE

The physical interfaces between the LCE spacecraft transceiver and the spacecraft itself will now be considered. For this discussion, these interfaces are divided into five major types - mechanical, thermal, and electrical interfaces and EMI and environmental requirements. In all cases, the interfaces involve requirements and limitations imposed by the spacecraft design and the overall mission, as given in the ATS interface specification S-460-ATS-38. Other requirements and goals specific to the LCE design that affect the spacecraft capabilities are included in the LCE specification GSFC-S-524-P-4C.

The following discussion describes (1) the status of Aerojet efforts to tailor the LCE design to keep within these spacecraft interface constraints, and (2) the interface requirements which the LCE design imposes on the spacecraft. Based on preliminary interface discussions with ATS spacecraft project personnel, Aerojet believes that these latter requirements (in conjunction with S-460-ATS-38) provide a reasonable basis in arriving at a mutually acceptable definition of the spacecraft/LCE experiment interface. The only item which appears questionable at this time is the ability of the presently incorporated four-point mount to meet the stringent deflection requirement placed on the spacecraft/LCE mounting pads. This uncertainty can definitely be resolved by changing to a three-point mount (as discussed in section 5.2.1.9).

5.4.1 Mechanical Interface

The mechanical interface between the spacecraft and the LCE transceiver consists of four mating areas held together with bolts. The bolted supporting areas are the alignment and mechanical-stress-carrying interface between the experiment and the spacecraft.

5.4.1.1 Envelope

The space envelope of the spacecraft transceiver is defined by the latest revision of Aerojet's interface drawing No. 1296001, reproduced in Figure 5.4.1-1. The notes on this drawing provide additional details pertinent to the following discussions.

5.4.1.2 Location

The ATS-F spacecraft has an earth-viewing module which includes a north surface that is facing Polaris and the west surface is coincident with earth west. The south and east surfaces are opposite and parallel to the north and west surfaces. The LCE transceiver is located in the northwest corner of the earth-viewing module. The earth-viewing module location is necessary to allow laser communication to earth once the spacecraft is in orbit. The north surface is used because a passive radiator is necessary to cool the detector in the LCE transceiver, and the passive radiator must face an area of space in which the sun never appears. The location to the west side is required to prevent interference between the passive radiator sunshield and structural support members between the spacecraft and the rocket boosters.

The installation of the spacecraft transceiver is through the earth-viewing surface of the earth-viewing module. The passive radiator sunshield is removed and the transceiver is inserted through the earth-viewing surface of the module, and moved approximately 2 in. in a north direction until the mating mounting surfaces are in contact. The surfaces are then bolted together, and the sun shield and electrical connections can then be made.

5.4.1.3 Mounting Provisions

The transceiver is presently mounted to the spacecraft structure by four bolts, located as shown on Figure 5.4.1-1. Discussion of this four-bolt mounting approach as compared with a possibly more advantageous three-bolt configuration is included in para. 5.2.1.9.

The notes on Figure 5.4.1-1 that are important to the mechanical interface (particularly the LCE mounting) are discussed below. The notes more closely associated with the thermal interface are covered in Section 5.4.2.

Note 2: "Angular dimension between surface A and Z axis of the spacecraft to be measurable to within 0.005° ."

The LCE orientation to the spacecraft is not critical, since the LCE is capable of search, acquisition and tracking of an external source anywhere within the field of view of the LCE ($+40$ degrees in the east/west direction and $+8^\circ$ in the north/south direction). To use the relative orientation of the LCE for

attitude sensing of the spacecraft, however, requires a measurement of the angle between the spacecraft axis and the LCE field-of-view centerline. The degree of accuracy of measurement need not exceed the least resolvable angle of the coarse pointing mirror, which is 0.005° (one step of the stepper motor).

Note 6: "The weight must not exceed 70.0 lb."

The latest weight estimate information indicates an increase from a previously reported 53.1 lb. The increase is explained in para. 5.4.1.6.

Note 17: "The four(4) mounting surfaces on the spacecraft are to be parallel with respect to each other to within 0.005 inches or less."

With the present four-point mounting configuration, three of the mounting pads will determine the plane of the LCE base plate. Any misalignment of the fourth mounting pad will introduce stress and strain into the base plate. (Characteristics of the more favorable three-point mounting are considered in para. 5.2.1.9.) A strain capable of producing a misalignment of the laser tube relative to the resonant-cavity mirrors of 2.5 milliradians will reduce the laser power output by 3 decibels (or 50%), based on available data from the laser subcontractor. The 0.005-in. misalignment limitation is based on reducing the misalignment of the laser tube to $\frac{1}{2}$ milliradian or less.

Note 24: "The maximum in-plane load into surface A shall not exceed _____ lb. The load shall not produce a displacement of the LCE base plate flatness by more than 0.005 inches."

For the in-plane stiffness of the LCE base plate, it has been tentatively established that a deflection of greater than 0.005 in. may cause a loss in laser power which would be unacceptable.

Note 25: "The maximum out-of-plane load into surface A shall not exceed _____ lb. The load shall not produce a deflection of the LCE base plate flatness by more than 0.005 inches in any direction."

For the out-of-plane stiffness of the LCE base plate, it has been tentatively established that a deflection of more than 0.005 in. may cause a loss of laser power which would be unacceptable.

Note 26: "Attachment between surface A and the spacecraft heat sink will be by 8-32 screws. The number of screws to transfer the LCE heat dissipated load will be 114. Screws to be torqued to 17 in. lb. The maximum loads in-plane and out-of-plane introduced into surface A by the spacecraft heat sink due to any means shall not produce a deflection greater than 0.005 inches."

Based on test data, the above number of screws torqued to the above level are necessary to transmit the heat-dissipated load of 57 watts, the current predicted electrical load of the LCE. (See para. 5.4.3.)

5.4.1.4 Field-of-view and Alignment Requirements

The transceiver beam pointing mechanism can direct the optical axis of the system anywhere within a range of $\pm 40^\circ$ about the earth-viewing axis in the east-west direction and $\pm 8^\circ$ about the earth-viewing axis in the north-south direction. This dictates the location of the experiment on the earth-viewing side of the spacecraft with an unobstructed view corresponding to the 80° by 16° coverage described above. Because of the wide capability of the beam pointing mechanism, there is no critical alignment requirement because of the field of view.

The only requirement for alignment is due to thermal radiator considerations. The passive radiator sunshield has been designed, based upon our present knowledge of the spacecraft configuration, to prevent direct solar radiation or radiated or reflected energy from spacecraft elements from impinging on the passive radiator. The passive-radiator sunshield geometry is such that it provides a 0.5° excess amount of shielding. Thus, the alignment of the LCE field-of-view centerline with the spacecraft center line is not critical if it is within the 0.5° . Of course, any changes in spacecraft structure must be reviewed to assure that no structural element can have a direct view to within 0.5° of the thermal radiator. The misalignment must be measured for reasons explained in para. 5.4.1.5. The 0.5° alignment tolerance is well within manufacturing tolerances and can easily be held.

5.4.1.5 Alignment Measurement Requirements

The pointing and tracking capability of the spacecraft transceiver is better than 20 sec of arc, controlled by specifying tight backlash requirements for the stepper motor. The encoder resolution is $\pm .02$ degrees. The use of this fine pointing accuracy is restricted only by the ability to measure and maintain the alignment of the spacecraft axes relative to the axes in the north-south and east-west directions. The alignment of the LCE transceiver will be measurable by autocollimation from a removable mirror fixture, the alignment of which with the transceiver optical axis is known within the 20 sec of arc described above. This fixture, together with a means for accurately mounting it, will be provided by Aerojet.

5.4.1.6 Weight and Mass Properties

A mass-properties control program has been initiated for the LCE spacecraft transceiver. Early in the program a weight allotment was assigned to various subsystems and/or components which totaled 53.1 lb. As the design phase of the LCE program progresses, these allotted weights are being compared to the calculated or estimated component weights. Table 5.4.1.6 indicates the comparison of allotted to the presently estimated weight. There is a 16.5-lb increase over the original design allotted weight. An intensive effort has been initiated to investigate the weight increases and potential methods for weight reduction. The three prime targets for weight reduction are the primary structure and heat sink, the sunshade assembly, and the power supply units.

The primary structure and heat sink weight is estimated, based on a beryllium plate 0.25 in. thick. A potential weight reduction exists in this element once a better definition of the laser end-cavity alignment requirements and better spacecraft/LCE interface distortion allowables are obtained. The weight will be minimized through use of the NASTRAN computer program.

At present, it appears that it will be difficult to decrease the current weight of the sunshade because of the specular requirements, but the weight will be considered further during design. In order to achieve

the specularity requirement, the inside surface of the shade must have a surface finish similar to a highly polished mirror, which dictates the thickness of the shade.

For the power supply, efforts are being made to optimize the requirements and design. It is confidently felt that this optimization will result in a decreased weight for the supply.

TABLE 5.4.1-1

ALLOCATED AND ESTIMATED WEIGHTS

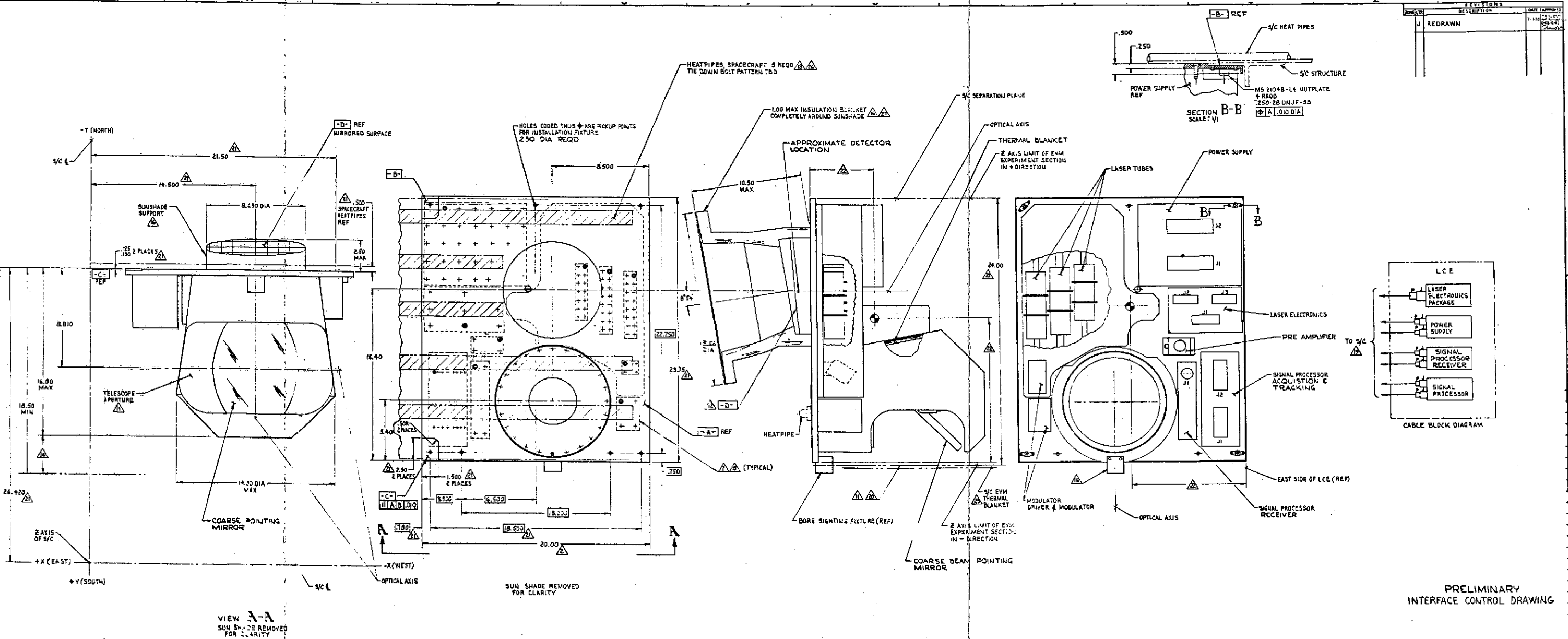
<u>P/N</u>	<u>Subsystem</u>	<u>Allocated Weight (lb)</u>	<u>Estimated Weight (lb)</u>
1295500-1	Installation Kit	53.07	69.60
1296220-1	Sunshade Assy	0.64	3.68
1296222-1	Thermal Blanket		0.15
1296000-1	LCE Assy	52.43	65.77
1296200-1	Primary Structure & Heat Sink	9.71	14.32
1296201-1	CPM & Tele Shroud Assy		1.29
1296240-1	Radiator/Support Stand Assy	4.23	4.23
1296250-1	Mirror Assy - CBP	5.57	6.02
1296275-1	Telescope Assy	2.53	2.53
1296400-1	Optical Processor Subassembly	9.64	7.21
	Local Oscillator Laser	0.40	1.395
	Transmitter Laser	0.44	1.553
	Standby Laser	0.44	1.553
	End Cavity Mirror No. 1	2.00	0.77
	End Cavity Mirror No. 2	2.00	0.77
	End Cavity Mirror No. 3	2.00	0.71
	Modulator & Driver	1.20	1.00
	Laser Electronics	0.26	5.00
	Signal Processing Electronics	4.31	3.92
	Power Supply Units	7.70	13.50

FOLDOUT FRAME 1

FOLDOUT FRAME 2

FOLDOUT FRAME 3

1. INTERPRET DRAWING PER MIL-STD-100
2. ANGULAR DIMENSION BETWEEN SURFACE 'A' AND Z AXIS OF THE SPACECRAFT TO BE MEASURABLE TO WITHIN .005°
3. THE STRUCTURAL ATTACHMENT OF THE LCE TO THE SPACECRAFT SHALL BE BY FOUR (4) NAS-634 FASTENERS
4. THE MECHANICAL MATING INTERFACE BETWEEN SPACECRAFT & LCE SHALL BE ELECTRICALLY BONDED IN ACCORDANCE WITH THE REQUIREMENTS OF MIL-B-5087
5. ⊕ DENOTES APPROXIMATE CENTER OF GRAVITY
6. WEIGHT MUST NOT EXCEED (TBD)
7. SURFACE 'A' SHALL BE IN DIRECT PHYSICAL CONTACT WITH THE SPACECRAFT HEAT SINK. THE SPACECRAFT CONTRACTOR SHALL INSURE THAT A CONTACT CONDUCTANCE (M²) OF AT LEAST 10.0 BTU/HR-FT²-°F EXISTS BETWEEN THE SPACECRAFT HEAT SINK AND EACH SQUARE INCH OF THE AREA INDICATED ON SURFACE 'A'. A 32 OR BETTER FINISH ON SURFACE 'A' ON ITS MATING SURFACE TO REQD FINISH GRAIN WILL BE PARALLEL TO THE Z AXIS OF SPACECRAFT
8. THE LCE WILL DISSIPATE APPROXIMATELY 57 WATTS OF ELECTRICAL POWER. THE MAJOR PORTION OF THIS HEAT WILL BE GENERATED DIRECTLY ABOVE THE AREAS INDICATED BY HIDDEN LINES
9. THE MAXIMUM TEMPERATURE DIFFERENCE BETWEEN THE WARMEST AND THE COLDEST PORTION OF THE SPACECRAFT HEAT SINK WHICH IS IN CONTACT WITH THE LCE SHALL AT ALL TIMES BE LESS THAN 4°C. THE NOMINAL TEMPERATURE OF THE HEAT SINK SHALL BE WITHIN THE RANGE OF 20 ± 10°C
10. DEPOSITION OF FOREIGN PARTICLES ON EXTERNAL THERMAL CONTROL SURFACES OF THE LCE SHALL NOT CHANGE ε BY MORE THAN .01 AND α BY MORE THAN .01, OR MIRROR SPOULDRY BY MORE THAN .01
11. THE EARTH VIEWING SIDE OF THE LCE IS OPEN TO SPACE. THERE IS NO FILTER OVER THE OPENING OF THE TELESCOPE TO ATTENUATE OR REFLECT INCIDENT SOLAR RADIATION. THIS OPENING WILL ACT AS A HEAT SOURCE OR SINK FOR THE SPACECRAFT DEPENDING ON THE TIME OF DAY AND SEASON OF YEAR. AT NO TIME HOWEVER WILL THIS OPENING CAUSE A HEAT INPUT TO THE SPACECRAFT GREATER THAN SIX (6) WATTS, OR A HEAT DRAIN GREATER THAN FIVE (5) WATTS.
12. NO ELEMENT OF SPACECRAFT WILL HAVE A DIRECT VIEW FACTOR TO SURFACE 'D'
13. THE LCE SHALL BE IN DIRECT PHYSICAL CONTACT WITH THE SPACECRAFT HEAT SINK (.050 THICK AL SKIN) AND THE FOUR (4) ATTACHMENT FASTENERS ONLY. ALL EXPOSED SURFACES OF THE LCE COMPONENTS SHALL HAVE EMISSIVITIES OF 0.7 OR GREATER
14. INSTALLATION CLEARANCE IN SPACECRAFT 2.50 INCH MINIMUM. BORESIGHTING FEATURE TO BE REMOVED FROM LCE AFTER BORESIGHTING IS ACCOMPLISHED
15. SUN SHADE TO BE ATTACHED AFTER LCE IS INSTALLED IN SPACECRAFT. THE FOUR (4) MOUNTING SURFACES ON THE SPACECRAFT ARE TO BE PARALLEL WITH RESPECT TO EACH OTHER TO WITHIN .005 OR LESS
16. ALL INTERFACE HOLES ON BOTH SPACECRAFT AND LCE ARE TO BE LOCATED BY AGC SUPPLIED TOOL. THIS INCLUDES THE HOLES REQUIRED TO TIE INTO THE SPACECRAFT HEAT SINK AS WELL AS THE FOUR (4) MECHANICAL TIE POINTS. HOLES TO BE DRILLED WHILE STRUCTURE AND TOOL ARE AT 20°C ± 10°
17. THE SPACECRAFT ELECTRICAL CABLES CONNECT DIRECTLY INTO RECEPTACLES ON THE LCE. BLACK BORE ALL CONNECTORS ARE IN COMPLIANCE WITH NASA SPECIFICATION 88FC-5-323-P10 APPROVED PARTS LIST 3E-0104
18. SPACECRAFT TELESCOPE APERTURE PLATE TO BE MOUNTED IN THIS AREA
19. INFORMATION TAKEN FROM GENERAL ELECTRIC DOCUMENT DIMENSION TO BE DETERMINED
20. SPACECRAFT & LCE INTERFACE BOOT (TBD)
21. THE MAXIMUM IN-PLANE LOAD INTO SURFACE 'A' SHALL NOT EXCEED (TBD) LBS. THE LOAD SHALL NOT PRODUCE A DISPLACEMENT OF THE LCE BASEPLATE COORDINATES BY MORE THAN (TBD) INCHES
22. THE MAXIMUM OUT-OF-PLANE LOAD INTO SURFACE 'A' SHALL NOT EXCEED (TBD) LBS. THE LOAD SHALL NOT PRODUCE A DEFLECTION OF THE LCE BASEPLATE FLATNESS BY MORE THAN .005 INCHES IN ANY DIRECTION
23. ATTACHMENT BETWEEN SURFACE 'A' AND THE SPACECRAFT HEAT SINK WILL BE BY 8-32 SCREWS. THE NUMBER OF SCREWS TO TRANSFER THE LCE HEAT DISSIPATED LOAD WILL BE (TBD). SCREWS TO BE TORQUED TO (TBD) IN LBS. THE MAXIMUM LOADS IN-PLANE AND OUT-OF-PLANE INTRODUCED INTO SURFACE 'A' BY THE SPACECRAFT HEAT SINK DUE TO ANY MEANS SHALL NOT PRODUCE A DEFLECTION GREATER THAN .005 INCHES
24. MINIMUM CLEARANCE WITH BOOSTER ADAPTER STRUT TBD



VIEW A-A
SUN SHADE REMOVED FOR CLARITY

PRELIMINARY
INTERFACE CONTROL DRAWING

1296001

REV	DESCRIPTION	DATE	BY	CHKD
1	REVISION			
2	REDRAWN			

PROJECT	AGC LASER SPACECRAFT INTERFACE CONTROL DRAWING
DESIGNER	
CHECKER	
DATE	
SCALE	
APP'D	
REVISED	
BY	
DATE	
REVISION	
DESCRIPTION	
DATE	
BY	
DATE	

Figure 5.4.1-1

5.4.2 Thermal Interface

The LCE spacecraft transceiver is mounted structurally to the north wall of the ATS at four locations. It is also in contact with the ATS on the north wall over the areas where the LCE beryllium heat sink is in direct contact with the ATS heat pipes. This latter contacting area is provided to permit sufficient ATS/LCE heat flow so that the spacecraft transceiver can be maintained at $20 \pm 10^{\circ}\text{C}$ under orbital conditions. There are no other physical contacts between the LCE and the spacecraft.

The maximum amount of thermal energy crossing from the LCE heat sink to the ATS heat pipes during normal laser operation at 28 volts will be 63.2 watts. This represents 57.2 watts of dissipated electrical power plus 6 watts of absorbed solar input to the telescope (should it be facing the sun). The maximum amount of thermal energy that will flow the other way is 5 watts. This is the maximum rate at which heat can escape to space through the telescope window. The LCE heat-sink/ATS heat-pipe energy transfer will be the only significant heat transfer occurring between the LCE and the ATS.

There are three spacecraft transceiver faces that are interior. Two of them face other experiments in the EVM. The third faces the equipment-module interior. Radiation across these three boundaries could be a source of LCE/ATS heat transfer, except that the ATS heat pipes will maintain the LCE transceiver at the same temperature as the other modules adjacent to the LCE.

The spacecraft transceiver is isolated from heat transfer to and from space by superinsulation on all uncovered areas of its three space-facing surfaces, except in two locations: the radiator/sunshade and the earth-facing window. The radiator/sunshade has been specifically designed to be effectively isolated from the rest of the transceiver. Thus, any thermal interchange between the radiator/sunshade and space has no effect on LCE/space thermal interchange. The earth-facing window allows a thermal interchange between the inside of the telescope assembly and space. Extensive analyses have been performed in this area utilizing an Aerojet Monte Carlo Program. The multi-bounce computer simulations include mirror geometries, locations, and surface properties, as well as the properties of the superinsulation that lines the

interior of the telescope assembly helmet. Details of the analysis, including assumptions and a discussion of tradeoffs that led to the present design, are included in Appendix C. The resulting extremes in energy transfer were found to be 6 watts into the LCE transceiver from space when the sun is looking directly in with rays normal to the earth-facing plane; and 5 watts out when this face is looking to space. The surface properties of each major telescope component have been selected with the solar input problem in mind.

During normal laser operation, the LCE electronics is presently scheduled to dissipate 57.2 watts of thermal energy. A listing of the specific amounts of power dissipated from each transceiver heat source that make up this total power is given in para. 5.4.3.1, along with the power dissipations under other operating modes.

The spacecraft/experiment interface control drawing, shown in Figure 5.4.1-1, includes several notes that are imposed in order to satisfy various thermal interface considerations. The text of each note and the need for including it are considered below. In general, these notes conform with the GSFC ATS F and G interface specification.

Note 7: "Surface A shall be in direct physical contact with the spacecraft heat sink. The spacecraft contractor shall insure that a contact conductance (h_c) of at least $40.0 \text{ Btu/hr-ft}^2\text{-}^\circ\text{F}$ exists between the spacecraft heat sink and each square inch of the areas indicated on surface A. A $\sqrt{32}$ or better surface finish on surface A and on mating surface is required. Finish grain will be parallel to the Z-axis of the spacecraft."

The thermal requirement here is that the contact between the LCE spacecraft transceiver heat sink and the ATS heat pipes be adequate for carrying the worst-case thermal load likely to cross that boundary. The specified surface finish, grain alignment, and contact areas are sufficient to satisfy this requirement.

Note 8: "The LCE will dissipate approximately 57 watts of electrical power. The major portion of this heat will be generated directly above the areas indicated by hidden lines."

The specific components from which this power is dissipated were delineated later in para. 5.4.3.1. All power dissipators that could be attached directly to the LCE transceiver beryllium heat sink have been so located in order to minimize thermal gradients.

Note 9: "The maximum temperature difference between the warmest and coldest portion of the spacecraft heat sink which is in contact with the LCE shall at all times be less than 4°C . The nominal temperature of the heat sink shall be within the range $20^{\circ}\text{C} \pm 10^{\circ}\text{C}$."

Placing an allowable maximum of 4°C on any heat-sink temperature gradient prevents the possibility of structural/optical distortion caused by differential thermal expansion of the base. Meeting the allowable 4°C is aided by proper selection of LCE heat-sink material, thickness, location with respect to power dissipators and to heat pipes, and heat-sink/heat-pipe contact conductance. Nominal heat-sink operating temperature limits of $20 \pm 10^{\circ}\text{C}$ are required by NASA. These limits assure a stable thermal platform from which to operate; they are met by the use of the ATS louver/heat pipe system.

Note 10: "Deposition of foreign particles on external thermal control surfaces of the LCE shall not change ϵ by more than .01 and α_s by more than .01, or mirror specularity by more than .01."

Observance of this note assures that no thermal control surface will be degraded to the extent that its function is significantly impaired.

Note 11: "The earth viewing side of the LCE is open to space. There is no filter over the opening of the telescope to attenuate or reflect incident solar energy. This opening will act as a heat source or heat sink for the spacecraft depending on the time of day and season of year. At no time, however, will this opening cause a heat input to the spacecraft greater than six (6) watts, or a heat drain greater than five (5) watts."

These values of maximum heat leak through the earth facing window were determined analytically using the Aerojet Monte Carlo program. A major assumption of this analysis was that the telescope interior would be completely covered with superinsulation, except for the mirror's reflecting surfaces. The details of the analysis are described in Appendix C.

Note 12: "No element of the spacecraft will have a direct view factor to surface -D-."

The purpose of this design requirement is to minimize the incident radiation to the radiator. Surface -D- is the space-viewing side of the radiator. The wineglass sunshade has been designed specifically so that the radiator does not have a direct view of the spacecraft nor any view of specular bounces from the spacecraft.

Note 13: "The LCE shall be in direct physical contact with the spacecraft heat sink (.050-in. thick aluminum skin) and the four (4) attachment fasteners only. All other surfaces within the EVM of the spacecraft which are viewed by the LCE shall be essentially adiabatic."

The purpose of this is to reiterate that the ATS spacecraft thermal control system is responsible for handling all LCE thermal loads directly through the LCE heat-sink attachment. The interior LCE transceiver faces are essentially adiabatic, by virtue of the LCE components being maintained at the same temperature as the components of the other EVM experiments.

Note 14: "Installation clearance in spacecraft 2.50 inch minimum."

This allows attachment of the radiator to the outside of the north wall heat sink prior to LCE transceiver integration with the spacecraft. Only the sunshade must be attached after the LCE has been installed in the spacecraft. The primary advantage of this is that the detector can be aligned better prior to spacecraft attachment than after, and the coaxial cable that connects the radiator-mounted detector to the preamp can be more easily installed prior to spacecraft installation.

Note 16: "Sunshade to be attached after LCE is installed in spacecraft."

There is no way around this, since the LCE is installed through the west face of the spacecraft while the sunshade must be attached to the north face of the LCE.

5.4.3 Electrical Interface

5.4.3.1 Power Requirements

The spacecraft transceiver will operate entirely from the EVM regulated DC bus. The characteristics of this supply as contained in Specification S-460-ATS-38 are summarized below:

Voltage	28.0±2%
Ripple	10 mv rms, maximum
Transient spikes	± 2v peak (energy 30 millijoules)
Conducted noise	10 mv pk, 0 to 15 kHz
Output impedance	0.1 ohm, 0 to 15 kHz

The necessary switching to activate or deactivate the equipment will be contained within the LCE power supply unit and will be controlled through the spacecraft command system.

Input current and power will be a function of the mode of operation, as defined in Table 5.4.3-1. In particular, during normal operating mode, the required power is 57.8 watts. The elements which make up the power budget and discussions of the potential ways in which this requirement will change and, in particular, decrease, are presented below.

5.4.3.1.1 Power Budget

The estimated power required for operation of the various elements of the LCE spacecraft transceiver, used in deriving Table 5.4.3-1, may be summarized as follows: The optical receiver requires 2.0 watts for operation while the laser startup and frequency control loops consume 4.9 watts; the signal processing subsystem requires 11.3 watts for operation; the transmitter laser uses 13.5 watts; the local oscillator laser 5 watts, and the backup laser 8.5 watts (when operating); the modulator and oven require a power input of 13.6 watts; power supply losses are estimated at 7.5 watts; and the mirror drive motors consume 2.0 watts (when running).

Reasons for increase of the power requirement over the original LCE spacecraft power estimate of about 30 watts fall into three categories:

- (1) increased power due to added functional capabilities, (2) power requirements for functions that were not included in the original estimate, and
- (3) original underestimation of the power required for certain functions.

The first category includes power for increased frequency offset for the local oscillator (3.6 watts) and increased peak frequency deviation in the modulator (4.7 watts). Both of these changes were incorporated after discussion with NASA personnel.

The original power estimate did not include allowances for power supply loss, encoder exciter lamp consumption, mirror motor drive requirements, PZT requirements, or modulator temperature control.

Present understanding of the design shows an original underestimation of the power required for the modulator driver and the signal processing subsystem.

Intensive efforts have been initiated to reduce the present power requirements. The possible modifications are discussed below.

5.4.3.1.2 Potential Changes in Power Consumption

There are potential changes in power consumption requirements for almost all of the budget elements, but most are expected to result in reduced power. These are discussed below.

- (1) The present Signal Processor design uses integrated circuits of high power consumption to achieve optimum performance. It is expected that low-power circuits will be available in the near future which provide similar operation. This change, if found feasible, offers a potential power reduction of 2.5 watts.

- (2) If the spacecraft transceiver can be operated without the need for continuous operation of the coarse pointing mirror position readout, the electronic circuitry and the encoder may be shut down with a power saving of 4.3 watts.

(3) The startup loops for the laser tubes operate continuously in the present design. The impact (~1 watt) and potential saving of including a mechanism for turning these off is being investigated.

(4) The power supply loss assumed an 80% efficiency. Present design results in an efficiency of 55-60%. An intensive redesign effort (See Section 5.2.6) is presently being performed. It is expected that a large simplification of the power supply design and a reduction in the power supply loss will result.

(5) Breadboard tests of the local oscillator have shown larger in-cavity losses than were originally anticipated, primarily due to the introduction of a grating in the cavity which was not optimized for the LCE operation. This resulted in a larger power requirement on the breadboard (10-20%, see Section 5.2.6). It is expected that this potential increase will be minimized by use of an optimized grating. In addition, a potential decrease of required local oscillator power (~2 watts) by extracting the output off the grating instead of through the mirror is being investigated.

(6) The breadboard tests of the transmitter have shown larger power requirements for the laser tube than were originally anticipated (10-20%, see Section 5.2.6). This was primarily due to unexpected in-cavity losses in the modulator crystal. This increased tube power can be eliminated by shortening the crystal, but there is a resulting increase in modulator power. A trade between tube power and modulator length and power is presently being performed to optimize the required power. The increased tube power can also be eliminated if future crystals exhibit absorption losses closer to the value expected.

5.4.3.2 Telemetry Requirements

5.4.3.2.1 Quantities

The LCE spacecraft-transceiver telemetered parameters and number of bits required to assure operation of the experiment are listed in Table 5.3.3-2. These are to be delivered on a real-time basis to the LCE operating console. All signals except the 22-bit coarse pointing mirror position channels will be presented at the ground station with an accuracy of $\pm 1\%$.

The mirror position channels need only be presented as binary bits ("0" or "1"). The spacecraft telemetry will give a read command to the experiment each time the 22 bits are to be read for transmission.

5.4.3.2.2 Signal Characteristics

All signals will nominally fall between 0 and +5 volts with respect to the experiment signal ground interface. Signals will be limited within the experiment so that the interface will not see more than 0.7 volts negative or more than 5.7 volts positive under any condition. All telemetry signals will be delivered from a source impedance of 1000 ohms or less.

5.4.3.3 Command Requirements

5.4.3.3.1 Functions

The LCE spacecraft transceiver functions which must be initiated by remote command are listed in Table 5.3.3-3, along with the associated data bits required. All commands are of the discrete, binary type except for those directing the coarse pointing mirror. Here three magnitude commands are required to provide azimuth and elevation orders to the necessary accuracy. A magnitude command shall consist of a nine-bit data word, a clock line for synchronization, an enable line to address the correct function for the elapsed time during which the nine bits are presented, and a separate discrete command for function execute. The remainder of the commands required are single discrete commands which must be capable of being repeated the required number of times to command the desired operation.

5.4.3.3.2 Signal Characteristics

All commands shall present a voltage of less than 0.5 for a "0" and more than 4.0 volts for a "1". The input of the command interface is a current source, and the spacecraft command source must be capable of supplying 2 milliamperes current sink while maintaining the "0" voltage limits.

5.4.3.4 Grounding Requirements

5.4.3.4.1 Power Grounds

The incoming spacecraft power return will not be grounded in the experiment. All internally converted power will be grounded to the experiment

heat sink/baseplate, as will all other housings and shields in the spacecraft transceiver.

5.4.3.4.2 Signal Grounds

Signal ground will be connected to power ground at the common point in the power supply. Throughout the rest of the experiment system, signal ground will be isolated from the frame and housings.

TABLE 5.4.3-1

LCE POWER DEMAND FOR VARIOUS MODES

Mode	Description	Power (at 28 v) watts
Startup	All subsystems on, as in normal operation; coarse-pointing mirror motors drive to selected position	59.8
Acquisition	Search system operating to acquire the remote station	57.8
Normal Operation	Operating in the track condition while transmitting and receiving the baseband signals	57.8
Backup	Backup laser replaces either the transmitter laser (for CW) or the local oscillator for normal operation	
Transmitter inoperative	No baseband transmission	40.7
IO inoperative	Normal operation	62.0
Standby	All electronic systems off, but modulator oven operating (always on when experiment power on)	2.8 max

TABLE 5.4.3-2

SPACECRAFT TRANSCEIVER TELEMETRY REQUIREMENTS

<u>Function</u>	<u>Channels</u>
Transmitter Current	1
Transmitter Voltage	2
Local Oscillator Current	1
Local Oscillator Voltage	2
Backup Laser Current	1
Backup Laser Voltage	2
Modulator Current	1
Local Oscillator Tuner Voltage	1
Backup Laser Tuner Voltage	1
Transmitter Power Output	1
Local Oscillator Power Output	1
Backup Laser Power Output	2
Analog Coarse Pointing Mirror Position	2
Digital Coarse Pointing Mirror Position	22
Image Motion Compensator Position (Coarse)	2
Image Motion Compensator Position (Fine)	2
Receiver AGC Voltage	1
Mixer Bias Current	1
AFC Error Output	1
Acquisition Threshold Voltage	1
Acquisition Conform Threshold Voltage	1
Nutator Bias Voltage	2
Laser Heat Sink Temperature	3
Modulator Temperature	1
Radiator Temperature	1
Sun Shield Temperature	1
Spare	<u>3</u>
	60

TABLE 5.4.3-3

SPACECRAFT TRANSCETIVER COMMAND REQUIREMENTS

<u>Function</u>	<u>Commands</u>
<u>Discrete</u>	
6 power supplies (on-off)	12
3 mirrors (in-out)	6
Passband selection	3
Laser current adjust	3
BU laser line selection	3
Receiver	2
Laser	1
Acquisition	1
Acquisition threshold	1
Beam alignment (nutator bias)	4
Acquisition confirm threshold	1
Spare	<u>4</u>
	41
<u>Magnitude</u>	
Coarse pointing mirror position	3 (9-bit words)

5.4.4 EMC Requirements

The GSFC specification for the LCE spacecraft transceiver calls, in paragraph 3.3.1.5, for listing all sources within the spacecraft transceiver generating RFI ($f > 1$ kHz) greater than 0 dbm, and for ripple feedback to the payload regulator of less than 150 millivolts as a design goal. The following discussion applies not only to these questions, but to the more general problem of LCE electromagnetic interference and techniques for its control.

5.4.4.1 Considerations

The following documents are being used as guides to accomplish EMC goals for the LCE spacecraft transceiver:

MIL-STD-461A	Electromagnetic Interference Characteristics Requirements for Equipment
MIL-STD-462	Electromagnetic Interference Characteristics, Measurement of
MIL-STD-463	Definitions and System of Units, Electromagnetic Interference Technology
MIL-B-5087 (ASG)	Bonding, Electrical, and Lightning Protection, for Aerospace Systems
MIL-C-5541A	Chemicals, Films, and Chemical Film Materials for Aluminum and Aluminum Alloys
AGC-20014	Coating, Corrosion Protective, for Magnesium, Magnesium Alloy, Application of

5.4.4.2 EMI Sources

5.4.4.2.1 Spacecraft

The main source of EMI from the spacecraft is radiation from the 2.3-GHz transmitter. The LCE is not directly susceptible to this frequency, but there is a possibility of induced currents causing rectification effects and effecting sensitive circuitry.

Conducted sources include the spacecraft power line, command lines, telemetry, and video cables. Power-line EMI will be controlled by filtering

and power-supply isolation. Control of the signal cable EMI will be effected by proper shielding and grounding.

5.4.4.2.2 LCE

There are two major sources of EMI in the LCE. The transmitter laser modulator requires a drive voltage of up to 200 volts peak-to-peak in the frequency range of 1 to 6 MHz. The second source is the laser high-voltage power supply.

Radiation from these sources will be minimized by RFI-tight shielding enclosures. Measurements will be made on the power-supply breadboard to determine the filtering required against conducted interference. The subcontractor responsible for detailed design of the laser subsystem, which contains the laser modulator, will be required to control his conducted and radiated interference and furnish proof of compliance.

There are no known sources of EMI in the LCE transceiver that are capable of producing any appreciable energy at 2.3 GHz that may interfere with the spacecraft RF receiver. The highest frequency signal with any significant power is contained in the laser modulator driver at 6 MHz. Since linearity is one of the prime design requirements of this circuit, no harmonics are generated. The LCE receiver subsystem contains a 30-MHz IF amplifier, but it processes low-level signals and by its very nature is well shielded.

5.4.4.3 Bonding Techniques

The following rules will be followed for LCE transceiver mechanical EMC design:

(1) All electronic enclosures will be electrically bonded to the baseplate. Conductive protective finishes on contacting surfaces are necessary to assure good electrical contact. Alodine 1200S, per MIL-C-5541, on aluminum and Iridite 15, per AGC-20014, on magnesium are being used for the W71 sensor project with success. Surface flatness required for thermal conductivity is adequate to assure good electrical conductivity. Bonding resistance will not be more than 2.5 milliohms, as a design goal, with an acceptance limit of 5 milliohms. The preceding comments apply also to spacecraft bonding.

(2) All other metallic structures such as optical elements that are mounted on an insulating surface will be bonded to the baseplate by a strap or jumper by the methods described in MIL-B-5087B, paragraph 3.4.

(3) The LCE transceiver will be provided with an overall metallic cover to prevent the entrance of RF energy. The cover will be bonded to the baseplate. RF gasketing material will be used at all joints to assure a tight seal.

5.4.4.4 Shielding and Cabling Considerations

Interconnecting cables and wires will be categorized; i.e., low level, power, video, etc. All wires will be cabled and routed only with wires and cables of the same category, and cables of the same category will be separated from all other cables by a minimum of 2 in. (except at a common connector). Where different cable categories are terminated in the same connector, grounded spare pins will be used for added isolation.

Shields of low-level, low-frequency circuit cables will be grounded at one end. Video and power cables will be grounded at both ends. In addition, all power cables will be twisted shielded pair.

5.4.4.5 EMC Tests

The MIL-STD-461A tests that have been selected to be performed on the FTM are listed in paragraph 7.3.37. The GSFC specification on conducted emissions will be adhered to. These tests were chosen on the basis of assuring compatibility of the LCE transceiver with itself and with the spacecraft. This list will be reviewed periodically during the program and changes made where necessary. Implementation of these tests will be set forth in the test plans and procedures.

5.4.4.6 EMC Summary

No great difficulty is anticipated in meeting the RFI requirements for the LCE spacecraft transceiver. This opinion is based on Aerojet experience with other applications of electro-optical equipment in spacecraft in which EMC techniques such as those discussed were successfully applied. The EMI levels at the spacecraft interface will be tabulated for the various LCE sources as part of the normal detail design process. It appears that the

ripple feedback to the payload regulator can be held below the specified maximum of 150 millivolts, except possibly for brief transients during infrequent LCE operations such as startup.

5.4.5 Design Environmental Requirements

The LCE spacecraft transceiver is being designed to the environmental requirements included in Specification AGC-20511, "Environmental Design Criteria and Test Levels for the Laser Communication Experiment and Associated Components."

5.5 FEASIBILITY OF INCLUDING LCE SYSTEM ON THE ATS-F SPACECRAFT

5.5.1 General Acceptability

From the information presented in the preceding sections, it is clear that the LCE is compatible with the interface requirements of the ATS-F spacecraft. Although the weight and power consumption of the LCE are higher than the design goals, they are both within the capability of the spacecraft. Furthermore, efforts to decrease both weight and power will be continued throughout the LCE design phase.

5.5.2 Installation and Handling

Installation of the LCE transceiver into the spacecraft does not appear to present any problems at this time. The experiment package with the radiator sun shield removed can be inserted into the spacecraft from the earth-viewing side, and then lifted onto its mounting pads on the north face of the EVM with the radiator projecting through a hole in the north side panel. The sun shield can be installed at a later time in order to minimize the exposure of its polished inner surface to handling and contamination.

There are no stringent requirements for alignment of the transceiver with the spacecraft. A tolerance of as much as 0.5° can be permitted. However once the unit is installed the alignment of a reference axis on the transceiver should be measured with respect to the spacecraft Z-axis to an accuracy of $\pm 0.005^{\circ}$ in order to permit pointing data from the LCE to be used to evaluate spacecraft attitude determination data. A removable alignment mirror will be supplied with the transceiver to facilitate this measurement.

In addition, care will be required in the design of the spacecraft mechanical and thermal interface to prevent deflection of the transceiver baseplate by the spacecraft during LCE operation.

Another area which will require close attention is the problem of maintaining the optical properties of the radiation cooler and sun shield. Means must be provided to protect the sun shield, in particular, from the time it is installed until the completion of the mission. During ground testing, the surfaces of the shield must be protected from handling and

airborne contaminants. Related to this, the surfaces must be protected from particles that may be shaken loose from nearby surfaces during the boost phase, and the surfaces must be protected from particles expelled from other portions of the satellite while in orbit (e.g., cesium ion engine, thrusters, etc.).

5.5.3 Launch Environment

The launch environment to which the LCE will be exposed is considered to be compatible with the system design as it is presently conceived. The design qualification test which will have the greatest influence on the structural design is the sinusoidal vibration test. If it appears from a preliminary low-level scan of the test spectrum that damage could result from high amplifications at resonant frequencies, NASA personnel will be contacted to determine if a reduction in input amplitude can be justified by spacecraft structural analysis at those specific frequencies. If such reductions are permitted, it may be possible to avoid damaging the test unit by an unrealistic test, and thus eliminate the consequent redesign and its attendant weight increase. Efforts are underway to determine potential resonant frequencies in the LCE structure and resultant amplifications so that investigation of spacecraft motion at these frequencies can be initiated.

5.5.4 Orbital Environment

The orbital environment does not appear to present any hazards to the operation of the experiment. However, information on vibration levels as a function of frequency within the spacecraft, caused by reaction wheels, solenoid valves, etc., is still needed to assure compatibility.

Care must also be taken that the LCE or other equipment within the spacecraft does not contain material which can outgas in a vacuum environment and condense on the cold radiator or mixer surfaces. Reports from other programs concerning the formation of frost on cooled detectors should be reviewed to determine if a cause and corrective action for this phenomenon has been determined so that this potential problem can be eliminated.

5.5.5 Cesium Ion Engine Considerations

Aerojet has made a detailed analysis of the possible effects of contamination from the cesium ion engine, which is also on the ATS-F spacecraft. This has been based primarily on the comprehensive report, HIT-399, "A Study of Cesium Exhaust from an Ion Engine and its Effect upon Several Spacecraft Components," prepared by Hittman Associates, Inc., for NASA on 26 June 1969. The HIT-399 report recommended that a proper biasing and shielding should be made to prevent cesium ions and neutrals from impairing the performance of an optical receiver. It is understood that proper actions will be taken by Dr. Robert Hunter of NASA in accordance with these recommendations. However, a careful review of the HIT-399 report reveals that there still exist a number of uncertainties which could have significant effects on the LCE program.

It is recognized that a direct view from the radiator opening to the ion engine nozzle must be avoided by a proper orientation of the ion engine with respect to the radiator and/or by a protective shield. However, no definite plan has been proposed as yet to achieve this. It is recommended that a detailed plan should be made for the installation of a shield to prevent any of the neutral Cs atoms from reaching the surfaces of the sun shade (in particular the inner surfaces) and the radiator.

According to the HIT-399 report, there will be more than one monolayer ($\sim 5 \overset{\circ}{\text{A}}$ thick) of Cs deposition over the radiator surface during the total proposed period (equivalent to 45 days) of the ion engine experiment. This estimation does not include diffusion and scattering of these neutral Cs atoms from directions other than direct line of sight. The report concluded that one to several monolayers of cesium would not cause any significant change in surface properties (emissivity, reflectivity, transmissivity and absorption) of the radiator, based on an older reference: (H. Ives and H. B. Briggs, J. Opt. Soc. Am. 27 395, 1937. It is thought that these old experimental results do not represent the physical properties of pure cesium films because of the oxidation and impurity contents in these films are very high due to inadequate high-vacuum techniques at that time.)

Dr. Cox of Fort Belvoir, estimates that a monolayer of pure Cs, when uniformly coated, can cause a significant change in the surface properties of the radiator. He believes that the reflectivity of Cs film can be as high as that of Au film in the infrared region. According to Figure IV-2 of the HIT-399 report, the transmittance of Cs film decreases rapidly with increasing wavelength. For a 500 Å thick film, the transmittance is about 5% at 1 micron and nearly zero at 1.3 microns. For longer wavelengths, no information on the optical properties are available. The surface temperature of the radiator is ~100°K, corresponding to a peak of blackbody radiation at about 30 microns. In this spectral region a very thin (~10 Å) layer of Cs film could cause a catastrophic change in both the transmittance and emittance of the radiator. Aerojet strongly recommends that a careful experimental study of the thermal and optical properties of thin (one to 10 monolayers) fresh Cs film should be conducted to resolve this problem.

The temperature of the radiator will be monitored as an indication of any adverse effects of Cs deposition. But this should only be considered as a gross monitor; it must be recognized that because of errors in the temperature measurement and the normal seasonal and orbital temperature variations, it may not be possible to recognize a temperature increase due to Cs deposition while it is still negligible. For this reason, it is necessary to implement the recommendations outlined above in order to develop a greater understanding of the problem.

It is to be hoped that this understanding will also provide a high degree of confidence that the Cs engine will not interfere with the operation of the LCE. Aerojet further recommends that the ion engine not be operated until a stable radiator-temperature history is obtained over several orbits. This may require greater than normal operation of the LCE during the early portion of the flight.

5.6 OPERATION UNDER NON-STANDARD CONDITIONS

There is a finite probability that the spacecraft will not achieve its planned orbit or its specified orbital characteristics. The resultant non-standard conditions will have a definite impact on LCE performance. The primary non-standard satellite conditions to be considered are (1) non-synchronous orbit, (2) spinning satellite, (3) excessive roll rate, and (4) improper inclination. The effect of each of these conditions on the operation of the LCE is discussed below.

It must be noted that for any of the experiment objectives to be achieved under adverse conditions, acquisition must be completed. The acquisition IF bandwidth is about 9 MHz at the half-power point, corresponding to a Doppler velocity component of 20M/sec. Attempting to acquire with a 3-db signal loss will severely reduce the acquisition probability. Furthermore, the nominal operating point about which the acquisition system parameters have been optimized would no longer exist, decreasing acquisition probability further. A detailed analysis for a particular non-standard condition must be performed in order to quantitatively determine the probability of acquisition.

Assuming acquisition has been achieved for a non-standard orbit, a Doppler velocity of $\sim 30\text{M/sec}$ can be tolerated with the heterodyne signal within the IF communication bandpass (12 MHz). Communication experiments could not be performed, but atmospheric measurements could be made by continuous recording of the Doppler signal. Higher orbits would reduce the 23-db C/N and lower orbits would increase this value.

If the satellite is spinning, the LCE will not be able to perform any of its operations.

If the roll rate exceeds the nominal value, acquisition will take longer, according to the discussions of Section 5.1.5. The probability is further decreased due to departing from the optimized operating point. A quantitative assessment again requires detailed analysis.

Report No. 4033, Vol. I, Part 1

Improper inclination would disturb the acquisition somewhat, assuming that the satellite could be found. After the two stations acquire and lock following some search operation, normal experiment operation would ensue.

5.7 ABILITY OF THE LCE SYSTEM TO PERFORM EXPERIMENTS

As stated in GSFC Specification, "10.6-Micron Laser Communications System Experiment for ATS-F," GSFC-S-524-P-46, dated January, 1969:

The fundamental objective of the Laser Communications Experiment is to ascertain the practicality of wideband communications between a spacecraft and a ground station and between two orbiting spacecraft using the 10.6 micron radiation from a carbon dioxide laser; and to establish the resulting efficiency that can be effected in terms of communication bandwidth per pound on the spacecraft. To this end, a number of related experiments, tests, and measurements will be performed.

A number of experiments, tests, and measurements are then listed, in addition to a presentation of overall system requirements. These are described in Section 3.0. The following sections deal directly with the listed items and describe the manner in which the LCE system design, presented in the preceding sections, satisfies these items.

It should be noted that these are not the only measurements that are expected to be taken during the course of the experiment. Further discussions will be presented in Volume II of the Design Study Report.

5.7.1 S/N Ratio as a Function of Atmospheric Parameters

It is expected that the atmosphere will affect both the intensity of the received signal and its angle of arrival.

The intensity variation (for a given zenith angle) will consist of slow fades and higher-frequency fluctuations. NASA data show that over a 15-km path the intensity varied a factor of 50 over a 24-hour period.* The higher-frequency fluctuations appear to extend up to 1-kHz frequency.

The slow fades will be measured by the automatic gain control (AGC) in the optical heterodyne receiver. The telemetry output of the AGC is

*Optical Space Communications, NASA SP-217.

designed to vary between 0 and 5 volts, corresponding to a carrier dynamic range of -72 dbm to -56 dbm, and has a frequency response from dc to 10 Hz at the 3-db point.

The high-frequency intensity measurement requires heterodyne AM receiver. Such a receiver is not presently included in the LCE, but Aerojet has submitted a proposal to NASA for incorporating one. Table 5.7-1 gives the technical highlights of the proposed AM receiver.

There are very little data available to determine expected fluctuations in the angle of arrival. Measurements performed at Marshall Space Flight Center using a He-Ne laser over a range of 3200 meters produced an rms deviation in angle of arrival of 1.3 $\widehat{\text{sec}}$ for a 5-in. receiver aperture.* Spectral analysis of the received fluctuations showed that power density fell to 10% of the dc spectral power density at 10 Hz, and to 1% at 100 Hz.

The position voltages of the image motion compensators of the tracking subsystem will be telemetered to earth. The tracking subsystem has a loop bandwidth of 5 Hz, and the response time is 0.11 sec (time to reach 80% of a step input). Therefore, slow variation of angle of arrival, together with the angular rotation of the spacecraft axes, will be measured. These data will have to be analyzed in order to separate spacecraft rotation from the angle-of-arrival data.

The ground-station transceiver systems will also produce data on the intensity fluctuation and the angle or arrival. Performance characteristics are identical to the spaceborne transceiver. The ambient motion of the earth as a result of the background seismic activity in the frequency range up to 5 Hz is expected to be 1 to 2 $\widehat{\text{sec}}$ rms. The high-frequency cultural noise will be decoupled in the ground station by proper foundation design.

To complete this experimental objective, data on atmospheric conditions will be required. As part of the ground station, the equipment shown on Table 5.7-2 will be provided to give in situ atmospheric data. Further,

* Ibid.

it is Aerojet's understanding that NASA will have an additional ground station (not part of the LCE contract to Aerojet) which will have AM receiving capability.

5.7.2 S/N as a Function of Receiver Aperture

The LCE transceiver has a fixed-diameter (7.75-in.) aperture. Therefore, measurement of S/N as a function of receiver aperture diameter cannot be performed by the LCE transceiver. This is recognized by the statement in the specification that this requirement is not applicable to the LCE transceiver.

5.7.3 S/N Ratio as a Function of Zenith Angle

The expected cloudless atmospheric transmission as a function of zenith angle is shown on Figure 5.7-1. From the figure it is seen that the variation is 3.25 db between zenith angles from 0° to 80°. The range of the AGC optical heterodyne receiver is 16 db, corresponding to carrier power input levels in the range from -72 to -56 dbm. Therefore, the automatic gain control will cover satisfactorily the expected variation of the S/N ratio as a function of the zenith angle. The corresponding AGC telemetry output level is 0 to 5 volts, with a tolerance of ±0.3 db. Of course, it is recognized that the satellite or the ground station must be moved in order to vary the zenith angle.

5.7.4 Space Background Noise (Sun, Stars, etc.)

As derived in Appendix B, the non-coherent background energy received by the optical heterodyne receiver system (OHRS) is given by

$$\sigma_b = \frac{Ed^3B}{2c} \quad (5.7-1)$$

where

σ_b = non-coherent energy received, watts

E = spectral radiance emittance, watts/m² of the background

d = radiation wavelength, meters (1.06 x 10⁻⁵ meters)

c = speed of light (3 x 10⁸ m/sec)

B = bandwidth of the receiver (12.0 MHz)

The ratio of the received background power (rms) to the receiver noise (rms) is given by

$$\frac{\sigma_b}{B(\text{NEP})} \quad (5.7-2)$$

where

NEP is the received noise equivalent power in watts/Hz (nominally 10^{-9} watts/Hz)

5.7.4.1 Direct Solar Energy

With a system optical bandpass of 1 micron and the assumption that the sun is a 6000°K blackbody, σ_b computes to be 2.6×10^{-13} watts. Therefore, the solar background to receiver noise ratio (henceforth called carrier-to-noise) is -6.6 db. Further, the carrier-to-noise ratio when communicating will be reduced by 0.9 db under worst conditions when the system is looking alternately at the sun and dark space.

5.7.4.2 Self-Emitted Energy From Earth

Self-emitted energy from earth received by the mixer can be calculated by Equation (5.7-1). The radiant emittance, E_λ , is $30.2 \text{ watts} \cdot \text{m}^{-2} \cdot \text{micron}^{-1}$ (as calculated in Appendix B) for $T = 300^\circ\text{K}$ and $\lambda = 10.6 \text{ microns}$. For a system with an optical bandpass of 1 micron, the radiant emittance E is $30.2 \text{ watt} \cdot \text{m}^{-2}$. Substitution of the appropriate numerical values into Equation (5.7-1) gives σ_b as 7.2×10^{-16} watts. This is 3 to 4 orders of magnitude lower than the receiver noise. Therefore, the carrier-to-noise ratio of the communication signal will remain essentially unchanged when the system is operating with the earth as background.

5.7.4.3 Self-Emitted Energy From The Moon

Self-emitted energy from the moon received by the mixer can be calculated by the method used to calculate energy received from earth. For $T = 250^\circ\text{K}$ and $\lambda = 10.6 \text{ microns}$, σ_b is 2.9×10^{-16} watts. Again, this is 3 to 4 orders of magnitude lower than the receiver noise, and the carrier-to-noise ratio of the communication signal will be essentially unchanged when the system is operating in the presence of the moon.

5.7.4.4 Energy From The Star

Under the Harvard system of star classification, the principal types of star spectra are designated by the letters B, A, F, G, K and M. Stars intermediate to these designations are designated by suffixed numbers from 0 to 9. The spectral classifications and star surface temperatures are listed in Table 5.7-3. The parameter $\frac{\sigma_b}{B(\text{NEP})}$ for each star classification can be calculated by the use of Equation (5.7-2), with

$$\frac{\sigma_b}{B(\text{NEP})} = \frac{Ed^3}{2c(\text{NEP})} \quad (5.7-3)$$

From the Planck radiation equation

$$E_\lambda = C_1 \lambda^{-5} \left[\exp \frac{C_2}{\lambda T} - 1 \right]^{-1} \quad (5.7-4)$$

where

E_λ = spectral radiant emittance, watt · m² · micron⁻¹

C_1 = 3.74 × 10⁸ watt · micron⁴ · m⁻²

C_2 = 1.44 × 10⁴ micron °K

λ = radiation wavelength, microns

T = source temperature, °K

For a system with an optical bandwidth of 1 micron, Equation (5.7-4) becomes

$$E = C_1 \lambda^{-5} \left[\exp \frac{C_2}{\lambda T} - 1 \right]^{-1} \text{ watt} \cdot \text{m}^{-2} \quad (5.7-5)$$

Substitution of Equation (5.7-5) into Equation (5.7-3) gives

$$\frac{\sigma_b}{B(\text{NEP})} = \frac{C_1 d^3}{2c \lambda^5 (\text{NEP}) \left[\exp \frac{C_2}{\lambda T} - 1 \right]} \quad (5.7-6)$$

Equations (5.7-6) and (5.7-1) were used to evaluate the numerical values of $\frac{\sigma_b}{B(\text{NEP})}$ and σ_b for each star classification. The results are tabulated in Table 5.7-3. In the calculation, it is assumed that the angular diameter of the stars is such that it covers the receiver's field-of-view. For stars that have smaller diameters, the energy received is reduced accordingly.

5.7.5 Laser Output Power as a Function of Total Elapsed Time and Operating Time in Space Environment

The output power of each laser will be measured using the thermistor infrared detectors. At the output of each laser is a beam splitter mirror which samples 1% of the laser output power for purposes of frequency tuning and power measurement of the lasers. The sampled beam illuminates a diffraction grating which is blazed to enhance the second-order reflection. This reflection is imaged on a thermistor so located that the focused energy falls on the thermistor when the frequency of the laser output is at the correct operating P-line. The voltage signal output from the thermistor will be amplified by a dc amplifier to a nominal voltage of 2.5 vdc for each laser power output at the beginning of the experiment, which will be telemetered to earth. The output sensitivities for the three lasers are

Transmitter	3.3 mV/mW
Backup	3.8 mV/mW
Local oscillator	31.2 mV/mW

As the laser outputs will decrease with total elapsed time and with operating time in the space environment, the dc output voltages will decrease proportionately. The total elapsed time and the operating time in a space environment will be known by logging the individual laser turn-on and turn-off command times.

5.7.6 Temperature and Noise Figure Of The Mixer/Radiation Cooler as a Function of Satellite Orientation and Time of Year

Measurement of the noise figure of the receiver requires the use of a calibrated noise source. The only such source is the sun. By pointing the system toward and away from the sun and telemetering the noise output at the video detector and noting the difference, the noise figure can be determined.

The carrier-to-noise ratio for heterodyne detection of blackbody radiation is derived in Appendix B as

$$\frac{\sigma_b}{B(\text{NEP})} = \frac{Ed^3}{2c(\text{NEP})}$$

where the parameters are defined under the 3.7.4.4 discussion

With the sun assumed to be a 6000°K blackbody, the variation of the carrier-to-noise ratio as a function of the NEP is shown in Figure 5.7-2.

An alternative method of measuring the noise figure of the receiver is to use the acquisition subsystem to scan the receiver beam across the search angle when the sun is in the field of view. As the receiver beam scans from the dark background to the bright solar disk, a signal is generated and the portion of the energy of the signal falling in the acquisition bandwidth appears at the output of the acquisition post-detection filter. The amplitude of this signal is determined by correlating the signal amplitude to the variable acquisition threshold levels.

The temperature of the mixer will be monitored by mounting a temperature sensor adjacent to the mixer assembly on the radiation cooler. Calibration of the sensor on earth will permit measurement of the mixer temperature to $\pm 0.5^\circ\text{K}$. The dynamic range of the sensor will be from 90 to 140°K.

5.7.7 Round-Trip and One-Way Data Compared to Reference Microwave Link

The laser communications link is designed to permit operation in the following modes:

- (a) Laser-up link/laser-down link
- (b) Laser-up link/microwave-down link simultaneously with microwave-up link/laser-down link
- (c) Laser-up link/laser-down link and microwave-down link

If the following symbols are assigned to define the data:

- (a) Laser-up link = Q(x)
- (b) Laser-down link = Q(y)

(c) Microwave-up link = $Q(z)$

(d) Microwave-down link = $Q(w)$

the following simultaneous equations can be set up:

$$F [Q(x) + Q(y)] = a$$

$$F [Q(x) + Q(z)] = b$$

$$F [Q(y) + Q(w)] = c$$

$$F [Q(z) + Q(w)] = d$$

where a, b, c, and d are sets of measured quantities. The solution of these equations will give round-trip and one-way data on the laser and microwave links. It is expected that the following parameters will be measured:

Digital-data error bit rates

Analog-data S/N ratio

Distortion products

5.7.8 Laser Frequency Stability in Space Environment

The transceiver is designed to permit mixing of the transmitter and backup laser outputs or the local oscillator and backup laser outputs at the mixer. These modes of operation are controlled by command to the spacecraft. In the transmitter mixing mode, the backup laser is set at 30 MHz below the transmitter laser output P-line peak. In the case of the local-oscillator mixing mode, the back-up laser operates at the peak of the LO P-line, so that the frequency separation in either case is 30 MHz.

The difference frequency is detected by the mixer and amplified by the OHRS receiver.

The output of the OHRS discriminator will be telemetered to earth.

The bandwidth is from zero to 10 kHz at the 3-db point. The slope of the output will be as follows:

Over frequency range 29.5 to 30.5 MHz, -5 to +5 volts

Over frequency range 29.5 to 27.5, -5 to -13 volts

Over frequency range 30.5 to 32.5 MHz, +5 to +13 volts

It is expected that the laser FM instabilities will have amplitudes within ± 0.5 MHz, primarily over the spectral region 0.1 to 1000 Hz.

Transmittal of these data to earth will require a wide-bandwidth telemetry channel.

5.7.9 Spacecraft Attitude Determination From Laser Data

Two sets of measurements will be possible. First, the position of the mirrors of the image motion compensator of the spaceborne transceiver with respect to the LCE reference axes (the positions of which with respect to spacecraft reference axes will, within a given tolerance, be known) will be telemetered to earth. This will give the relative attitude of the spacecraft with respect to angle of arrival of the laser signal. However, if the spacecraft is rotating around the direction of arrival of the laser signal, the position will be a function of the cosine angle between the incoming energy spatial polarization and the polarization of the local oscillator beam; this will have to be derived from communications-channel data. Since the polarities normally will be aligned, the sensitivity of this measurement will be very poor. Also, these data will include the variation in the angle of arrival of the signal due to atmospheric disturbances. Processing of the data will be required in order to separate spacecraft attitude variation from the laser-signal angle of arrival data.

Absolute measurement of the spacecraft attitude will be possible from knowledge of the direction of the ground-station-transmitted laser beam with respect to the ground station reference axes. By accounting for bending of the beam by the atmosphere, the nominal angle of arrival at the spacecraft can be predicted. With this information, the spaceborne transceiver IMC mirror position, and data from the spacecraft star tracker, the spacecraft absolute attitude will be calculable.

5.7.10 Modes of Operation

The LCE transceiver is designed to operate under the following modes:

- Atmospheric propagation experiment mode
- Two-way laser communications mode
- Down-link laser mode
- Data relay mode

The output of the spaceborne transceiver at the spacecraft interface will occupy a baseband range of 1.0 to 6.0 MHz.

5.7.11 Baseband Characteristics

At the ground transceiver/ground station interface, the following baseband signals will be accommodated:

- In the range from 30 Hz to 4.6 MHz
- In the range 1.0 to 6.0 MHz

At the spaceborne transceiver/spacecraft interface, the baseband signal in the range 1.0 to 6.0 MHz will be accommodated.

In the transmission of television, the following signal/noise and signal/distortion ratios have been calculated (Appendix A gives details) for various error sources:

<u>Error Source</u>	<u>Signal-to-Noise or Distortion</u>
Random noise	32.7 db
Transmission deviations	33.0 db
Phase effects	36.0 db
Amplitude effect	33.6 db
Modulator/demodulator linearity	36.0 db
Vestigial filters	27.0 db
Vestigial phase tracking error	<u>36.0 db</u>
Total	26.7 db

5.7.12 S/N Ratio and Flux Densities

The expected predetection carrier-to-noise ratio will be in the range from 24.6 to 25.5 db (Section 5.1.3 gives a detailed discussion) at the beginning of the experiment, and will drop to the range from 24.2 to 25.2 db (depending on laser temperature) at the end of 2 years. The post-detection peak signal-to-noise ratio will be 32.7 db if the carrier-to-noise ratio is 23 db. (see Appendix A for detailed discussion). The flux density at the earth at transmitter optical axis location will be 10^{-8} watt/meter² (see section 3.1.3 for detailed discussion).

TABLE 5.7-1

AM VIDEO CHANNEL PERFORMANCE SPECIFICATIONS

1.	<u>Receiver Video Output</u>															
	(a)	Level over 20 Hz to 5 MHz	1 volt peak-to-peak, ± 0.5 db													
	(b)	Impedance over 20 Hz to 5 MHz	75 ohms, unbalanced, with minimum return loss of 20 db													
2.	<u>Presampler</u>															
	(a)	Bandwidth	30 +6 MHz, consistent with video distortion and noise requirements													
	(b)	Input saturation	-40 dbm or greater													
3.	<u>Demodulation Characteristics</u>															
	(a)	Demodulation sense	Increase in positive potential for increase in carrier amplitude													
	(b)	Instantaneous bandwidth	Consistent with video distortion and noise requirements specified herein													
	(c)	Center frequency	30 MHz													
	(d)	Output sensitivity (over -72 dbm to -56 dbm carrier input power level at mixer window at 30% amplitude modulation and 20 Hz to 5.0 MHz envelope modulation frequencies)	Constant within ± 0.3 db													
	(e)	Baseband amplitude - frequency characteristics														
			<table border="1"> <thead> <tr> <th align="center">Reference Frequency</th> <th align="center">Design Group</th> <th align="center">Minimum Acceptable</th> </tr> </thead> <tbody> <tr> <td align="center">25 kHz</td> <td align="center">0 db</td> <td align="center">0 db</td> </tr> <tr> <td align="center">20 Hz to 840 kHz</td> <td align="center">± 0.1 db</td> <td align="center">± 0.25 db</td> </tr> <tr> <td align="center">840 kHz to 5.0 MHz</td> <td align="center">± 0.2 db</td> <td align="center">± 0.4 db</td> </tr> </tbody> </table>	Reference Frequency	Design Group	Minimum Acceptable	25 kHz	0 db	0 db	20 Hz to 840 kHz	± 0.1 db	± 0.25 db	840 kHz to 5.0 MHz	± 0.2 db	± 0.4 db	
Reference Frequency	Design Group	Minimum Acceptable														
25 kHz	0 db	0 db														
20 Hz to 840 kHz	± 0.1 db	± 0.25 db														
840 kHz to 5.0 MHz	± 0.2 db	± 0.4 db														
	(f)	Group delay over 10 MHz bandwidth	± 0.7 nanosec/MHz slope 0.5 nanosec/MHz ² parabolic 6.0 nanosec peak-to-peak ripple													
	(g)	Demodulation amplitude	A carrier amplitude modulated 30% shall produce a 1 volt ± 0.5 db peak-to-peak output signal													

Table 5.7-1
Sheet 1 of 2

Report No. 4035, Vol. I, Part 1

TABLE 5.7-1 (cont.)

4. Video Distortion and Noise

(a) Non-linearity distortion of the synchronizing signal Synchronizing pulses shall be between 0.29 \pm 0.02 volts

(b) Noise

Periodic noise (ratio of P-P picture signal amplitude to the P-P noise amplitude)

(1) Power supply hum 38 db
(Including the fundamental frequency and low harmonics)

(2) Single frequency noise between 1 KHz and 2 MHz 62 db

(3) Single-frequency noise between 2 and 5 MHz 46 db

(5) Automatic Gain Control

(a) Recovery time (for instantaneous carrier power level changes up to 41 db with respect to carrier to noise ratio (C/N) of -18 db to -6 db) Receiver AGC shall set the output power to its nominal level \pm 1 db within 0.2 seconds and pass amplitude modulation

(b) Telemetry output (corresponding to input carrier level -72 dbm to -56 dbm) Range 0 to 5 volts
Bandwidth: Zero to 10 Hz at 3 db point
Output Impedance: 1 Kohm or less

TABLE 5.7-2

CHARACTERISTICS OF WEATHER INSTRUMENTATION

<u>Wind Velocity</u>	<u>Wind Direction</u>	<u>Air Temp.</u>	<u>Relative Humidity</u>	<u>Barometric Pressure</u>	<u>Aerosol Content Analyzer</u>	<u>Digital Data Logger</u>
W101-dc Remote Recording Skyvane Weather Measure Corp.		Model T622A Temperature Weather Measure Corp.	Serdex Humidity Telemeter Bacharach Instrument Co.	B201 Barograph Weather Measure Corp.	Dust Counter, Model AP-P3 Weather Measure Corp.	Model M-731 Weather Measure Corp.
Range 1-200	0-360°	Sensor thermistor	Range, 0-100% RH	Sensor-14 cell-2-in.-dia aneroid	Particle size 0.3μ to 10μ	Data input analog
Sensitivity 0.2%	1° at winds 3-200 mph	Range, 40°F to +140 F	Accuracy rating, +3% RH between 15% and 90% RH at 32°F to 130°F	Sensitivity +0.3 milli-radian	Dynamic range 0.05 mg/cm ³ to 60 μg/cm ³ Accuracy +3%	No of channels, 20
Accuracy +1 mph below 25 mph; +5% above 25 mph	3°	Sensitivity 0.2% Accuracy 1°F of range Response time 30 sec for 60% resp. to a = t of 5°F	Response time, 10 sec to signal 86% of RH change with sensor exposed to moving air (800 ft/min velocity)	Accuracy +0.2% range Operating range, sea level to 12,000 ft Response time 0.1 sec		Resolution 0.1% Sampling rate 1 sec per channel Accuracy, 0.1% full scale +1 count Lock format ASCII or IBM 8 level code

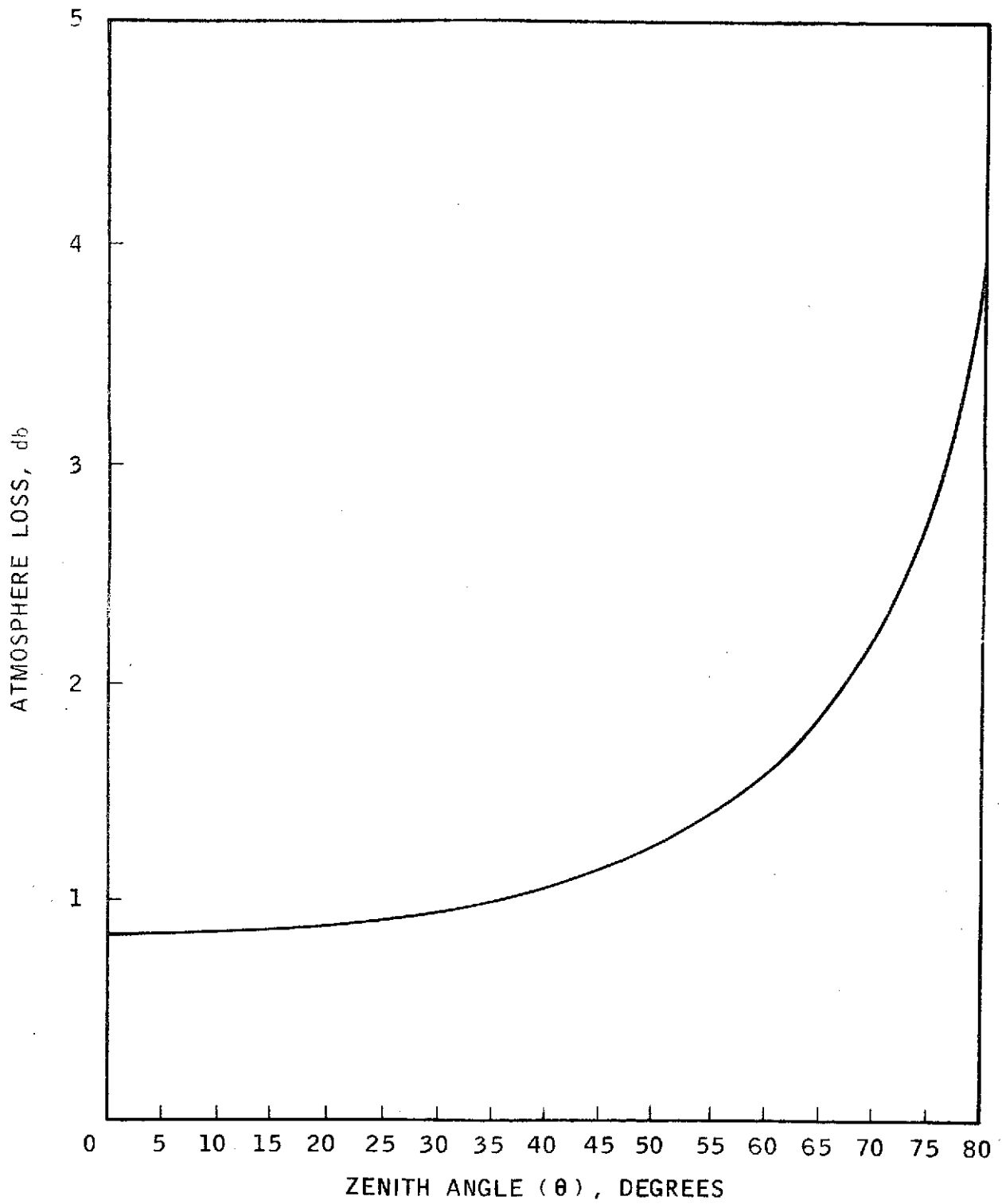
Table 5.7-2

Report No. 4033, Vol. I, Part 1

TABLE 5.7-3

STAR CARRIER-TO-NOISE RATIOS

<u>Spectral Classification</u>	<u>Surface Temperature, T (°K)</u>	$\frac{\sigma_b}{B(NEP)}$	σ_b (watts)
B-0	22,000	0.864	1.04×10^{-12}
A-0	11,000	0.421	5.05×10^{-13}
F-0	7,500	0.278	3.33×10^{-13}
G-0	6,000	0.218	2.61×10^{-13}
K-0	5,000	0.178	2.14×10^{-13}
M-0	3,500	0.117	1.40×10^{-13}



ATMOSPHERE LOSS VS ZENITH ANGLE

Figure 5.7-1

**6.0 EXPECTED LIFETIME
OF THE EXPERIMENT**

6.0 EXPECTED LIFETIME OF THE EXPERIMENT

6.1 SUMMARY

A reliability prediction model is presented for the LCE spacecraft transceiver, along with a reliability allocation. Reliability block diagrams, reliability prediction values, and reliability allocation values are presented for this initial prediction/allocation effort on the LCE proposed design. As the design develops, the reliability model, predictions, and allocations will be revised to reflect the effects of additional details and any changes. In addition, data from reliability engineering analyses and various tests will be used to improve reliability estimation.

The reliability information presented below is intended to provide a guide to reliability problem areas and to fruitful design tradeoff study areas, and to provide bases for reliability assessment during the evaluation phase. These data also furnish a background for the accomplishment of redundancy studies, and will facilitate test program planning and failure mode, effect, and criticality analyses.

The initial predicted LCE spacecraft-transceiver system reliability is 90.851%, as compared to the 90.00% required by contract. The bases for this predicted reliability are presented and discussed below.

6.2 RELIABILITY REQUIREMENTS

The LCE flight system (spacecraft-transceiver) requirement is 90% probability of an operational lifetime of 2 years on the ATS-F spacecraft, based upon an active operational time of 2000 hours, equally distributed between the 2 years. This requirement is contained in paragraph 4-1 of GSFC Specification GSFC-S-524-P-4C, dated January 1969.

6.3 RELIABILITY PREDICTIONS AND ALLOCATIONS

The predicted reliability for the LCE flight system at this preliminary-design stage is 90.851% probability of an operational lifetime of 2 years, with an active operational time of 2000 hours, equally distributed between the 2 years. This predicted reliability of 90.851% at this stage of

spacecraft-transceiver design exceeds the requirement of 90% by a comfortable margin, a favorable indication that the final detailed design will satisfy this requirement. Figure 6-1 shows the spacecraft transceiver reliability block diagram, prediction, and allocation for the system/subsystem level.

6.3.1 Criteria for Success

In this initial reliability prediction and allocation, the assumption is made that, for mission success, all parts in all subsystems must operate full time when the LCE spacecraft transceiver is turned on. The only exception is that the back-up laser subsystem is on standby as a replacement for the transmitter laser or for the local oscillator laser subassembly, should either one fail. The assumption that all parts must operate full time is considered very severe and pessimistic with regard to predicted reliability. It has become apparent that there are a number of component and subassemblies which will not have to operate full time when the LCE system is turned on, depending on the experiment mode. Aerojet plans to apportion the 2000-hour LCE operating time among the various experiment modes as follows:

<u>Mode</u>	<u>Percent of Operating Time</u>
Atmospheric propagation experiment	50
2-Way laser communication	25
Down-link laser	15
Data relay	10

This preliminary apportionment was selected after discussion with NASA personnel. The initial reliability analysis herein is based on operation in the predominant atmospheric-propagation-experiment mode. This tends to be optimistic, since the modulator will not be in use for the required CW laser function. Predictions and allocations for the other modes are planned for the future, along with further consideration of (1) the related component and piece-part duty cycles, and of (2) criteria definition and predictions for overall LCE mission success.

6.3.2 Definitions of Prediction and Allocation

The present reliability prediction provides an estimate of the reliability inherent in the current LCE preliminary design in order to establish the reliability feasibility.

The present reliability allocation is basically a reliability budget based upon the target reliability of 90% for the LCE flight-system mission. The reliability allocation provides a reliability goal or objective for each assembly and subassembly.

Both the reliability prediction and the reliability allocation for the spacecraft transceiver are based upon the following factors:

- a. The use of generic (or application) failure rates for components
- b. Application of failure-rate multipliers (K factors) which reflect environmental conditions during the mission
- c. Operating times for the system missions
- d. Standby or nonoperating failure rates
- e. Judgments of project designers and engineers
- f. Reliability information from similar components or assemblies used in comparable environments.

The effect of duty cycles on assemblies and components will be determined at the next stage of development, and the reliability allocation will ultimately be refined to include the following considerations:

- a. The criticality of each item and its function to the system and mission
- b. The capability for achieving improvement in item failure rates
- c. The capability for maintenance and repair of non-flight LCE items.

6.3.3 Reliability Block Diagram

The reliability block diagrams (Figures 6-1 through 6-6) are patterned after the LCE spacecraft transceiver block diagram of Figure 5.1.1-1.

The diagram contains each of the subsystems shown there. The functional nature of the LCE transceiver is such that an exponential distribution of failure times is assumed, and the following series reliability mathematical model is applicable at the system/subsystem level:

$$R_{LCE} = R_A \times R_O \times R_L \times R_R \times R_V \times R_T \times R_P$$

R_{LCE} = Reliability of LCE transceiver

R_A = Reliability of Acquisition and tracking subsystem

R_O = Reliability of Optical subsystem

R_L = Reliability of Laser subsystem

R_R = Reliability of Receiver subsystem

R_V = Reliability of Video switching subsystem

R_T = Reliability of Telemetry and command subsystem

R_P = Reliability of Power supply subsystem

Figures 6-1 through 6-6 show the reliability block diagrams, mathematical models, predictions and allocations for the LCE spacecraft transceiver, acquisition and tracking subsystem, optical subsystem, laser subsystem, receiver subsystem and power supply subsystem. The degree of definition of the component parts in the remaining subsystems precludes preparation of detailed block diagrams/predictions/allocations at this design stage.

Moderately detailed lists of electronic parts were available only for the Acquisition and Tracking Subsystem and for the High-Voltage Power Supply. For the Receiver Subsystem, AIL provided predicted and allocated failure rates for 24 subassemblies of the receiver in their Design Study Report. For the laser subsystem, Sylvania has provided a reliability prediction. The data from both subcontractors are incorporated into this document.

6.3.4 Comparison of Predicted versus Allocated Reliabilities

The allocated reliability for subsystems reflects the reliability budget for lower-level assemblies, which provides a 90% reliability for the LCE spacecraft transceiver. The comparison of predicted versus allocated reliabilities (Figure 6-1) is summarized in the following table:

	<u>Reliability</u>	
	<u>Allocated</u>	<u>Predicted</u>
Acquisition and tracking	95.843%	96.631%
Optical	99.738%	99.698%
Laser	98.000%	98.001%
Receiver	98.000%	98.461%
Video switching	99.930%	99.920%
Telemetry and command	99.077%	98.935%
Power supply	99.014%	98.861%
Total spacecraft transceiver	90.000%	90.851%

It is seen that predicted reliability is better by 0.851% than the allocated reliability for the LCE spacecraft transceiver.

6.3.5 Potential Changes in Reliability Values

The minor divergences of predicted versus allocated reliability for the optical, video-switching, telemetry and command, and power-supply subsystems can readily be rectified as the design matures. It is expected that minor circuit simplification and the reduction of parts quantities, along with additional part application derating, will collectively reduce predicted failure rates.

A redesign effort is under way to improve reliability of the high-voltage power supply. The new design will use simplified circuits with significantly fewer parts. A specific example is that ten current-regulating transistors on the high-voltage side are being reduced to one current-regulating transistor on the ground-voltage side. A different form of redundancy is also being considered which, together with further derating, will also increase reliability.

The laser tube will undergo a life test and development program designed to determine and eliminate potential failure modes, to determine the best tube design, and to demonstrate acceptable life characteristics. In addition, a proposal for an extended laser-tube life-test program (see Section 5.3.1) has been submitted to NASA which will significantly add to these functions and will definitively determine the tube reliability and life characteristics. It is expected that this overall program will improve the tube and its design on a continual basis and that the allocated reliability requirement will be met.

The laser subsystem was predicted by Sylvania to have a reliability of .98001, through use of generic electronic parts failure rates and by allocation to the laser tubes of the balance of the failure rate necessary to provide 98% reliability for the laser subsystem. The Sylvania calculation was based upon a 2000-hour mission time and an environmental K factor of 1.0. The mission is actually composed of three intervals under varying environments, as shown in paragraphs 6.3.8 and 6.3.9. Sylvania allocated the laser-tube failure rate at 28,500 failures per 10^9 hours. The tube rate had to be proportionately decreased to an equivalent of 15,975 failures per 10^9 hours for the full 2-year mission (including standby time) and for differing mission environments. It is confidently expected that this failure rate can be achieved and exceeded with present technology. Obtaining a laser-tube life of more than 2000 hours is thought to be the greater problem. The current tube evaluation and life-test program is expected to result in a low laser-tube failure rate and a tube life much longer than the 2000-hour operating life requirement.

As the LCE receiver matures to its final configuration, there is high confidence that its predicted reliability will exceed its allotment by a significant margin. Although no reliability deficiencies are foreseen, the H_d-Cd-Te detector element and its housing will receive intensive investigation and will be qualified as a unit before incorporation into the receiver subsystem.

6.3.6 Example of Subsystem Prediction/Allocation Data

The reliability prediction for the acquisition and tracking subsystem (Figure 6-2) is based upon a detailed parts list for which failure-rate data were obtainable. The cumulative failure rates by subsystem, the predicted and allocated reliabilities, and the allocated failure rates are as follows:

<u>Subassemblies</u>	<u>Predicted Failure Rate per 10⁹ Hours</u>	<u>Predicted Reliability</u>	<u>Allocated Failure Rate per 10⁹ Hours</u>	<u>Allocated Reliability</u>
Coarse mirror and drive (mechanical-optical)	2411.	99.144%	2988.	98.940%
Feedback encoders/mirror drive (electronics)	4080.	98.554%	5054.	98.213%
Search-pattern generator and acquisition control	1516.	99.460%	1879.	99.332%
IMC driver	304.	99.892%	378.	99.865%
Nutator driver	1032.	99.632%	1279.	99.545%
Nutation signal generator	259.	99.908%	322.	99.885%
Acquisition and tracking subsystem	9606.	96.631%	11900.	95.843%

The reliability of a given assembly is calculated, conventionally, as

$$R = e^{-\lambda Kt}$$

where

λ is the failure rate of the given assembly

K represents the environmental multipliers

t represents the mission times.

The values for K and t are presented in paragraph 6.3.8.

6.3.7 Failure Rates and Parts Lists

The failure rates used in the LCE spacecraft transceiver prediction, when a detailed parts list was available, were taken whenever possible from the document "ATS 'Hi-Rel' Parts List Failure Rates," January 12, 1970. Other failure rates used were for established reliability (ER) and JAN TX parts which comply with NASA approved parts, per

GSFC Preferred Parts List Number PPL-10, or

GSFC Spacecraft Approved Parts List, Number S2-0104.

Other failure rates were obtained (1) from breadboard test results of the LCE image motion compensator, (2) from life test results on motors identical to the LCE flip mirror motors, and (3) from FARADA (the Failure Rate Data Program handbook, SP 63-470) on the stepper motor and on the gear drive for the coarse pointing mirror. The standby failure rate of the back-up laser is assumed to be 10% of the operating failure rate.

Sylvania laser subsystem failure rates are based upon a 42°C operating temperature; rates for the remaining subsystems are based on a 50°C operating temperature. The latter is a conservative estimate associated with a 25°C nominal spacecraft heat-sink temperature and a 5°C total computed rise through the mounting to the transceiver modules and from the modules to the components.

6.3.8 Environmental Multiplier and Mission Time

The environmental K factors and time intervals used in calculating the reliabilities are as follows:

<u>Phase</u>	<u>Environmental K Factor</u>	<u>Time Interval</u>
Boost	80	1/5 hour
Orbit operate	1	2,000 hours
Orbit standby	0.1	15,520 hours
	Total	2 years

6.3.9 Derived Reliability Equation for Flight Mission

$R = e^{-\lambda Kt}$ is the conventional expression for the exponential reliability function, reference MIL-STD-757

where

λ is the cumulated failure rate for the LCE flight system

K is the pertinent environmental factor

t is mission time.

For the LCE flight mission:

$$R_{(\text{mission})} = R_{(\text{boost})} \times R_{(\text{orbit operate})} \times R_{(\text{orbit standby})}$$

$$R_{(\text{mission})} = e^{-\lambda(80)(1/5)} \times e^{-\lambda(1)(2000)} \times e^{-\lambda(0.1)(15,520)}$$

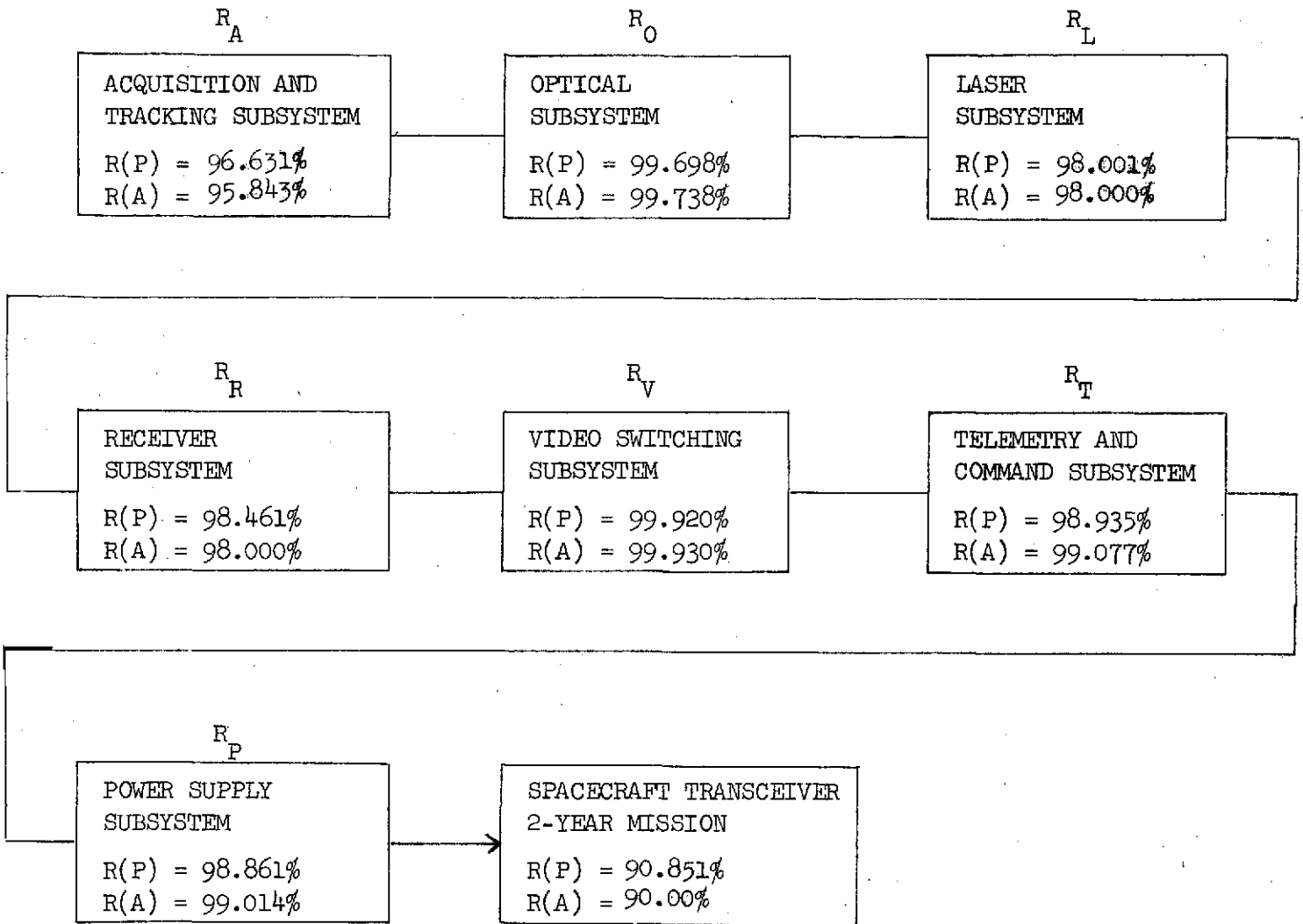
$$R_{(\text{mission})} = e^{-16\lambda} \times e^{-2000\lambda} \times e^{-1552\lambda}$$

$$R_{(\text{mission})} = e^{-3568\lambda} = \text{Mission Reliability Equation}$$

6.3.10 Sources of Failure-Rate Data

<u>Sources of Failure-Rate Data</u>	<u>Failure-Rate Data Sources</u>
Acquisition and tracking	ATS*, FARADA
Optical	ATS*, IMC Breadboard Result, W71 Tests of Flip-Mirror Motor
Laser	ATS*, Sylvania Reliability Program Plan, FARADA
Receiver	Airborne Instrument Laboratory
Video switching	ATS*
Telemetry and command	ATS*
Power supply	ATS*, W71 FIVLD Low-Voltage Power Supply Reliability Prediction

*"ATS 'Hi-Rel' Parts List Failure Rates," January 12, 1970.



RELIABILITY MATHEMATICAL MODEL:

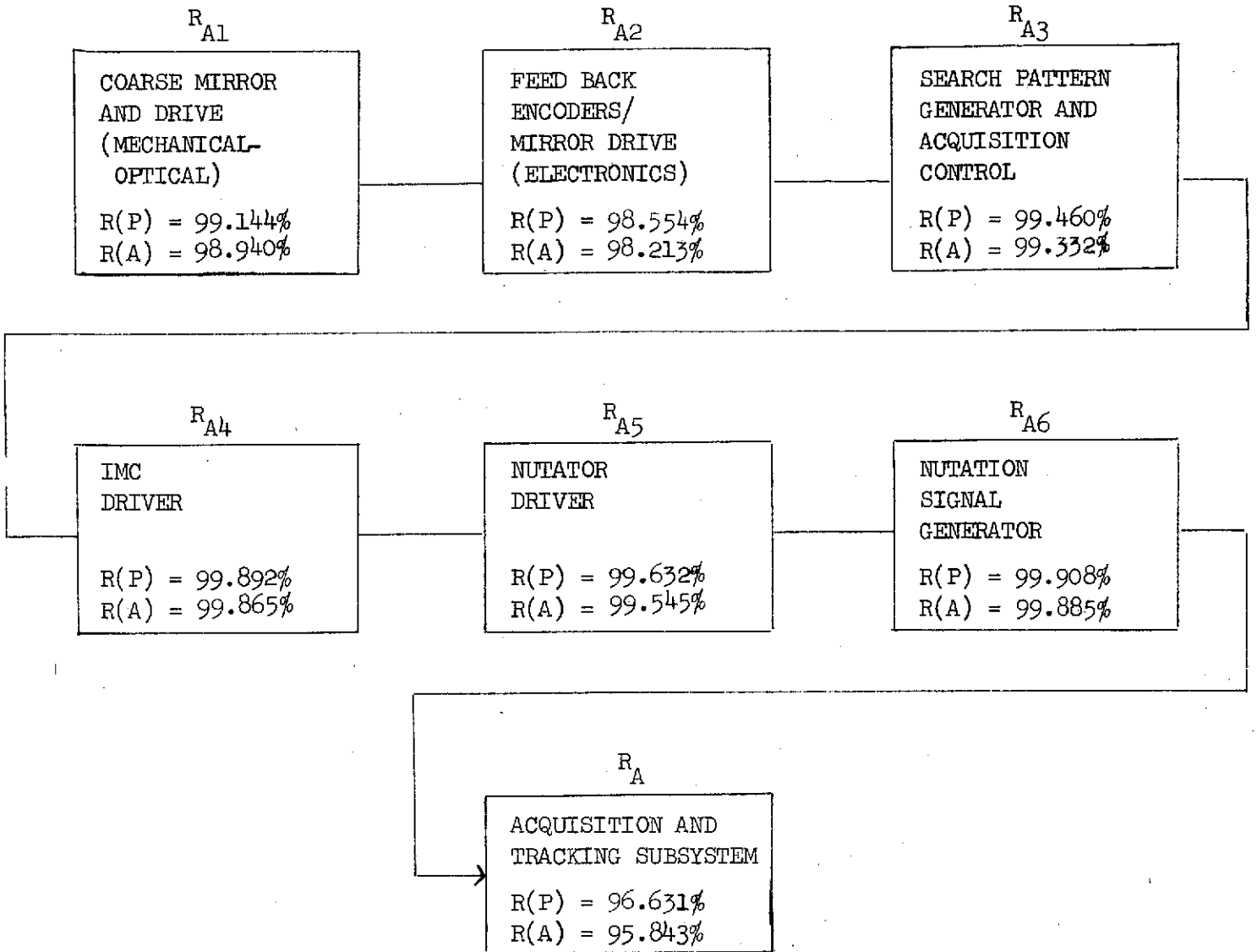
$$R_{LCE} = R_A \times R_O \times R_L \times R_R \times R_V \times R_T \times R_P = 90.851\% \text{ PREDICTED MISSION RELIABILITY}$$

R(P) = PREDICTED RELIABILITY

R(A) = ALLOCATED RELIABILITY

Reliability Diagram, LCE Spacecraft Transceiver

Figure 6-1



RELIABILITY MATHEMATICAL MODEL:

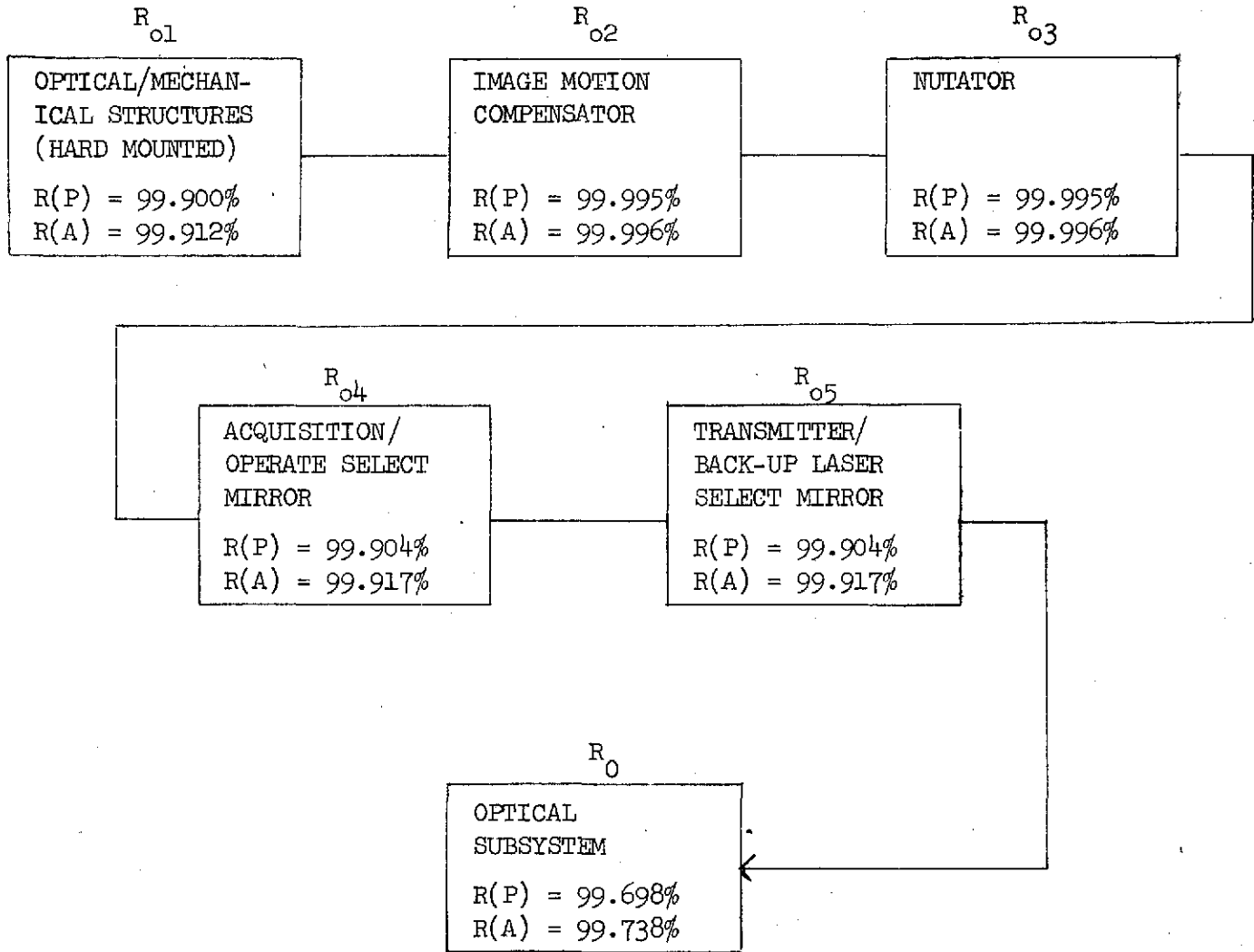
$$R_A = R_{A1} \times R_{A2} \times R_{A3} \times R_{A4} \times R_{A5} \times R_{A6} = 96.631\% \text{ PREDICTED MISSION RELIABILITY}$$

R(P) = PREDICTED RELIABILITY

R(A) = ALLOCATED RELIABILITY

Reliability Diagram, Acquisition and Tracking Subsystem

Figure 6-2



RELIABILITY MATHEMATICAL MODEL:

$$R_0 = R_{01} \times R_{02} \times R_{03} \times R_{04} \times R_{05} = 99.698\% \text{ PREDICTED MISSION RELIABILITY}$$

R(P) = PREDICTED RELIABILITY

R(A) = ALLOCATED RELIABILITY

Reliability Diagram, Optical Subsystem

Figure 6-3

Definitions of symbols on Figure 6-4 for reliability mathematical model of laser subsystem:

$$R \text{ LASER SUBSYSTEM} = R(AC) + R(ACS;t) R(AB;T-t) + R(ACS;t) R(CB;T-t)$$

where

$R(AC)$ is probability of no failure of the transmitter or local oscillator.

$R(ACS;t)$ is probability of no failures of the three lasers to time t , with the backup laser in standby until time t and operable at time t .

$R(AB;T-t)$ is probability of no failure of the transmitter and backup laser from time t to T . The local oscillator failed at time t .

$R(CB;T-t)$ is probability of no failure of the local oscillator and the backup laser from time t to T . The transmitter failed at time t .

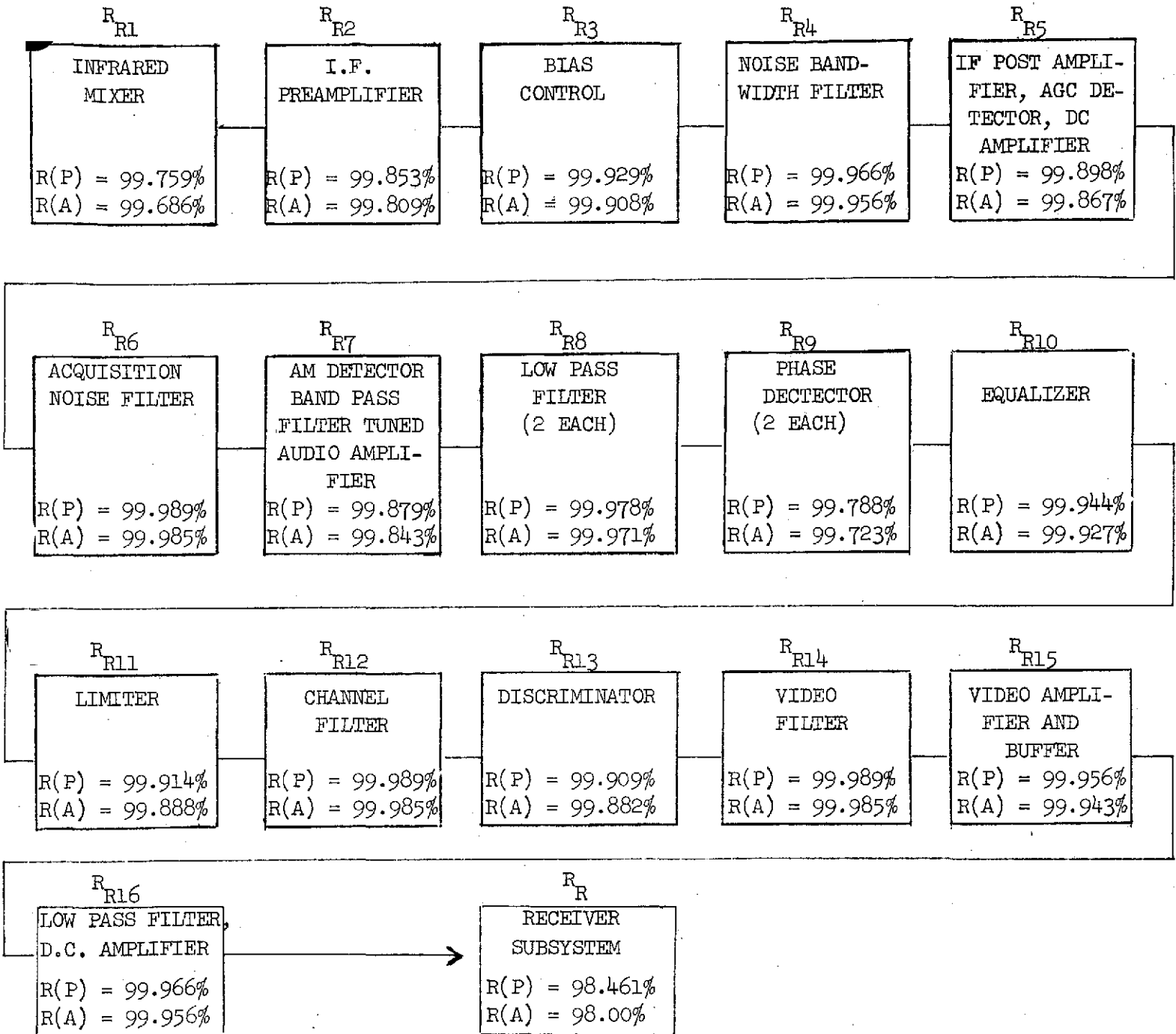
A is transmitter laser

B is backup laser

C is local oscillator laser

S is backup laser in standby

T is mission time



Reliability Mathematical Model:

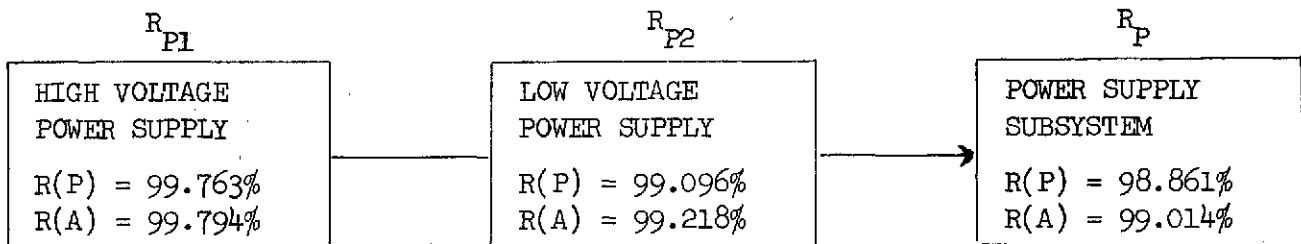
$$R_R = R_{R1} \times R_{R2} \times R_{R3} \times R_{R4} \times R_{R5} \times R_{R6} \times R_{R7} \times R_{R8} \times R_{R9} \times R_{R10} \times R_{R11} \times R_{R12} \times$$

$$R_{R13} \times R_{R14} \times R_{R15} \times R_{R16} = 98.461\% \text{ PREDICTED MISSION RELIABILITY}$$

R(P) = Predicted Reliability

R(A) = Allocated Reliability

Reliability Diagram, Receiver Subsystem



RELIABILITY MATHEMATICAL MODEL:

$$R_P = R_{P1} \times R_{P2} = 98.861\% \text{ PREDICTED MISSION RELIABILITY}$$

$R(P)$ = PREDICTED RELIABILITY

$R(A)$ = ALLOCATED RELIABILITY

Reliability Diagram, Power Supply Subsystem

7.0 TEST PLAN

7.0 TEST PLAN

The tests that will be performed during the LCE program are outlined and described below. This section includes (a) discussions of the purpose of the testing of each of the transceiver models, (b) flow charts for the tests to be performed on each of the models, including the tests at the subcontractor level, (c) descriptions of the test setups, (d) descriptions of the environmental and functional tests called out on the flow charts, (e) a summary table that indexes the tests to be performed and the models on which they will be performed, and (f) a summary table listing the functional and environmental tests to be performed on each model and the assembly level or levels at which they will be performed. In addition, Section 7.1 summarizes critical development/testing milestones during the program.

The test program, which includes informal engineering functional and environmental tests and formal qualification and acceptance tests, is intended to uncover problem areas and to prove out the designs at the earliest possible date. In addition to those described, engineering tests will be performed on items for which unforeseen potential problems may arise during the program.

A detailed test plan and test procedures, which will include qualification and flight acceptance testing at Aerojet, AIL, and Sylvania and testing at the integration contractor's plant and at the launch site, will be submitted at a future date.

7.1 TEST FLOW CHARTS

The primary test objectives for each of the LCE models are described briefly below, with reference to detailed flow charts. Charts are provided for the breadboard, functional test model (FTM), prototype, and flight units, as well as for the receiver and laser subsystems. Also covered are developmental tests that will be performed to prove the functional performance and environmental integrity of various critical parts of the LCE transceiver.

7.1.1 Breadboard Testing

Breadboard testing will be undertaken to verify the validity of design concepts and to determine the parameters for use in further optimization of system design. It will be performed under ambient, laboratory conditions.

Figure 7-1 presents a flow chart for tests of the breadboard transceiver at Aerojet. The blocks there give paragraph numbers of the applicable test descriptions in Section 7.3.

7.1.2 FTM Testing

The FTM will be fabricated as close to the flight-model design as is possible at that stage of development. It will be used to prove the performance capability, environmental integrity, and interface compatibility of the LCE transceiver and to aid in early identification of potential problems that may prevent the prototype from passing qualification tests. The FTM testing, including tests at the subsystem and assembly level, will be directed toward satisfying those objectives. In particular, qualification-level environmental testing will be performed at any level of hardware assembly that might be considered to be sensitive to that environment.

Figure 7-2 presents a flow chart for tests to be performed on the FTM transceiver at Aerojet. The blocks identify paragraph numbers of the applicable test descriptions in Section 7.3.

7.1.3 Prototype Testing

The prototype model will be identical to the flight model, and the prototype testing is planned to qualify the flight design at the system level. In addition, the coarse pointing mirror and gimbal subassembly, the laser subsystem, and the receiver subsystem will be qualified at their respective levels of assembly. Tests will also be performed at various levels of hardware assembly to assure the performance of the assembled system.

Figure 7-3 presents a flow chart for tests to be performed on the prototype transceiver at Aerojet. The blocks give paragraph numbers of the applicable test descriptions in Section 7.3.

7.1.4 Flight-Model Testing

The test program for the flight model is planned to provide flight acceptance testing at the system level. Tests will also be performed at various levels of hardware assembly to assure the performance of the assembled system.

Figure 7-4 presents a flow chart for tests to be performed on the flight transceiver at Aerojet. The blocks identify paragraph numbers of the applicable test descriptions in Section 7.3.

7.1.5 Laser-Subsystem Testing

Approaches similar to those reflected above will apply to laser-subsystem testing. As an example, a typical test sequence to be performed by Sylvania at various hardware levels during FTM development is shown in Figure 7-5, which covers only the laser transmitter of the subsystem. The local oscillator and backup laser will be tested identically, with the exception of the modulator assembly. Figure 7-5 is keyed to indicate the other models on which a particular test will be performed.

Functional testing of the various subassemblies will include only the tests required to provide engineering confidence in the basic design and fabrication. During early evaluation, for example, the functional tests of the laser tubes will be limited to power output and mode measurements. The same measurements will be made during thermal vacuum and after vibration. Full functional testing (frequency stability, beam size, collimation modulator linearity, etc.) will not be performed until after all the subassemblies are integrated. Before each laser subsystem is shipped to Aerojet, full acceptance testing will be performed at the subcontractor's facility in accordance with Specification AGC 20187.

7.1.6 Receiver-Subsystem Testing

Approaches similar to those reflected above will also apply to the receiver-subsystem testing. Figure 7-6 illustrates the AIL program for receiver-subsystem tests at various hardware levels during FTM development. This scheme will be used for all receiver-subsystem models, and Figure 7-6 is keyed

keyed to indicate the models on which a particular test will be performed. The functional testing of subsystems is planned to provide engineering confidence in the basic design and fabrication. Infrared measurements will be limited to NEP and bias power. The electronic measurements will be made to provide engineering confidence in the four electronic channels (IF, video, acquisition, and AFC). Before each receiver subsystem is shipped to Aerojet, full acceptance testing will be performed at the subcontractor's facility in accordance with Specification AGC 20186.

7.1.7 Development Testing

Development tests of many of the functional concepts and engineering designs, for early verification of transceiver performance and integrity, are of particular importance to the LCE program. Many will be performed during the fabrication and testing of the various transceiver models, but additional important tests will be conducted during development and on special assembly models such as the structural model of the radiation cooler.

7.1.8 Development and/or Testing Milestones

Table 7-1 lists key development and/or testing milestones and the points in the program at which they will be demonstrated. As the table shows, tests are performed in order to uncover problem areas and verify the designs and performance at the earliest possible dates.

7.2 TEST SETUPS

Certain test setups are described briefly in this section as background for the test descriptions presented in Section 7.3.

7.2.1 Test Setup No. 1

Test Setup No. 1, shown in Figure 7-7, will be used for

- a. Alignment of transmitted and received beams
- b. Measurement of received and far-field transmitted-beam antenna patterns
- c. Dynamic and static acquisition and tracking tests
- d. NEP measurements.

Pinholes mounted on x-y slides will be placed at the focal point of the parabolic mirror on either side of the beam-splitter by autocollimation techniques. A detector behind one of the pinholes will measure the far-field intensity distribution of the beam transmitted from the transceiver.

A diverger lens, along with attenuators and a stable laboratory laser, will be placed behind the second pinhole to act as a source for the receiver. The effective f/number of the diverger lens will be chosen to be much smaller than the effective f/number of the parabolic mirror in order to provide a relatively uniform intensity across the transceiver-telescope aperture. A received beam with a Gaussian intensity distribution across the telescope aperture would not produce the correct Airy disc pattern at the mixer. The deflection-plate assembly will consist of a thick parallel plate of germanium, mounted in a gimbal. It will be used to deflect the beam angles through the parabolic mirror approximately ± 50 arc sec for dynamic acquisition and tracking.

7.2.2 Test Setups No. 2 and 3

Setups No. 2 and 3, shown in Figures 7-8 and 7-9, will be used for closed-loop testing of the communication link on the breadboard model. Closed-loop testing will be required, because a second transceiver will not be available at the time. Both the transmitter and local oscillator lasers will have to be tuned to the same line.

Setup No. 2 will use an aluminum mirror to deflect the transmitted beam into an absorber in order to reduce backscattering into the receiver by the other components of the setup. Two apertures in the aluminum mirror will allow contrarotating beams to circulate through the attenuators and quarter-wave plate. The quarter-wave plate will change the polarization of the transmitted beam from linear to circular, so that some of the circulated beam will have polarization in the receiver orientation.

Setup No. 3 will be similar to Setup No. 2, except that the aluminum mirror will have one aperture. A hollow corner cube retroreflector will be used to reflect the beam back through the aperture to the receiver. The retroreflector should induce enough elliptical polarization into the reflected beam for detection by the receiver.

7.2.3 Test Setup No. 4

Setup No. 4, shown in Figure 7-10, will be used for functional testing of the modulator and the transmitter, local oscillator, and backup

lasers after assembly on a Cervit baseplate at Aerojet. The test laser will be heterodyned with a stable laboratory laser. The IF frequency output from the detector will be fed into either a spectrum analyzer, IF amplifier, and discriminator, or the receiver video-channel electronics. Various signal sources and measurement electronics will be added to the setup as required for the individual tests.

7.2.4 Test Setup No. 5

Setup No. 5, shown in Figure 7-11, will be used for

- a. Acquisition and tracking tests
- b. Two-way communication-link functional tests
- c. NEP measurements.

It is similar to Setup No. 1 except that the stable laboratory laser and detector assemblies will be replaced by the breadboard transceiver. The transceiver telescope will be removed, and its function will be performed by the diverger lens and parabolic mirror. This approach will provide a uniform intensity across the telescope of the test transceiver for the reasons discussed in paragraph 7.2.1.

7.3 TEST DESCRIPTIONS

The environmental and functional tests to be performed at the various levels of transceiver assembly are described briefly below. The test descriptions are referred to in the accompanying flow diagrams by paragraph number.

7.3.1 Miscellaneous Optical Parts

The deflection mirrors, beam splitters, lenses, power meters, gratings, narrow-band filter, and optical mounts are not considered development items, and will not be subjected to special environmental or functional tests. Receiving or manufacturing inspection will be performed to ensure that these parts conform to their specifications or drawings.

7.3.2 Flip-Mirror Vibration and Functional Testing

The flip-mirror assembly will be mounted on a vibration-test fixture. The mirror alignment at the mechanical stops will be set and measured relative to a fixed reference on the test fixture. The flip-mirror assembly, as mounted on the test fixture, will then be subjected to a qualification-level vibration test in accordance with Specification AGC 20511, with the mirror stowed in its launch position. After vibration, mirror alignment at the mechanical stops will be measured relative to the fixed reference on the test fixture. This measurement will be compared with the one made before the vibration test.

7.3.3 Duplexer Distortion and Efficiency Testing

The wavefront distortion in the beams transmitted and reflected from the duplexer will be measured by placing the duplexer in a Mach-Zehnder interferometer. The interferometer will be illuminated with a CO₂ laser beam having the proper polarization orientation for the transmitted and reflected modes of operation. A small-aperture detector will scan the output beam from the interferometer to measure its intensity distribution.

Duplexer transmittance and reflectance will be determined by comparing the power of the incident beam with the power of the transmitted and reflected beams of the correct polarization orientation.

7.3.4 IMC and Nutator Engineering Testing

Engineering tests will be performed to evaluate the important operating parameters of the nutator. They will include measurements of

- a. Deflection angles of each axis at the mechanical stops
- b. Deflection response as a function of driving frequency
- c. Deflection linearity
- d. Deflection angle as a function of driving voltage (deflection factor)
- e. Hysteresis induced by the bimorph element.

7.3.5 IMC and Nutator Vibration Testing

The IMC and nutator will be mounted on a vibration-test fixture. Mirror alignment in the null position (zero volts input) will be measured relative to a fixed reference on the test fixture. The unit, as mounted on the test fixture, will be subjected to a qualification-level vibration test in accordance with Specification AGC 20511. After vibration, mirror alignment in the null position will be measured relative to the fixed reference on the test fixture. This measurement will be compared with the one made before the vibration test.

7.3.6 IMC and Nutator Temperature Testing

The IMC and nutator will be mounted on a temperature-test fixture, and the null alignment and deflection factor will be measured at -5 and +40°C.

7.3.7 Telescope Alignment and Aberration Testing

The telescope will be aligned and tested for aberrations on a laser unequal-path interferometer. Because the telescope has all-reflective (achromatic) optics, the tests can be performed with a helium-neon laser source. The breadboard telescope will be aligned and tested by the vendor.

7.3.8 Coarse-Pointing-Mirror-Assembly Functional Testing

The functional tests listed below will be performed on the coarse pointing mirror and gimbal assembly. A special electronic package will be used to supply the required electrical inputs and to read the output signals.

a. Deflection Limits: The deflection limits of the coarse pointing mirror will be measured in east-west and north-south directions.

b. Pointing Rate: The command pointing rate will be computed with data collected from the shaft-encoder outputs, as the assembly responds to pointing-command inputs.

c. Angular Positioning: The angular-positioning accuracy of the coarse pointing mirror will be measured by mounting a special mirror-test fixture on the gimbal and using autocollimation techniques.

7.3.9 Receiver Functional Testing

The functional tests summarized below will be conducted on the video channel of the receiver to check its performance in order to ascertain that no damage was sustained during shipping. They will be performed with an FM test modulator, bypassing the optical detector in the receiver. The modulator will be special test equipment capable of simulating an FM signal at the IF frequency to test the receiver electronics.

a. Baseband Amplitude, Frequency Characteristics: This test will be conducted to check the overall performance of the video channel. A video-test signal covering this band will be inserted into the FM test modulator and the video output will be checked on the waveform monitor.

b. Periodic Noise: Periodic noise will be measured by terminating the input to the test modulator with the proper load, and noting the receiver output displayed on the waveform monitor.

7.3.10 Laser Signature Testing

The output signature of the transmitter and backup lasers will be recorded for incremental changes in the cavity length around the nominal cavity design length. To determine the signature, the cavity length will be scanned over a half-wavelength by placing a linear ramp voltage on the piezoelectric-transducer mirror element; the laser output will be observed with a fast detector and an oscilloscope. (This test will be performed only if Sylvania information suggests the possibility of line competition that reduces the bandwidth to less than acceptable limits on a particular line.)

7.3.11 Laser Functional Testing

After the automatic line-selection devices (gratings and power meters) have been installed and aligned, the laser functional tests summarized below will be performed on the transmitter, local oscillator, and backup lasers to ensure that the lasers are properly reassembled at Aerojet. Test Setup No. 4, shown in Figure 7-10, will be used for most of these tests.

a. Start-Up Operation: Automatic start-up loops will be monitored.

b. Mode: The TEM₀₀ mode will be checked by noting the absence of mode beating in a spectrum analyzer when the test laser is heterodyned against a stable laboratory laser. The intensity distribution will also be checked with a thermographic screen.

c. Power Output: The total power output will be measured with a power meter.

d. Polarization: The polarization angle will be measured with a Brewster-angle germanium plate.

e. Output-Power Beamwidth: The intensity distribution in the output beam will be measured near the laser output and in the far-field by scanning a pin-hole and detector across the beam. The beam diameter between the 0.367 relative-power points and the beam collimation will be determined from these data.

f. Operating Line: The operating line will be measured with a grating monochrometer.

g. Operating-Line Width and Power-Frequency Profile: The line width and profile will be measured by splitting the output beam into a power meter and into a heterodyne setup and spectrum analyzer. The power output will be measured as the operating frequency of the laser is tuned across the line.

h. Operating Frequency (Transmitter and Backup Laser): The operating-frequency long-term stability and dither peak-to-peak frequency deviation will be measured by heterodyne techniques. The test laser will be dither-stabilized to line center. The stable laboratory laser will be tuned to operate open loop at 30 MHz below line center. The heterodyned output will be fed into a 30-MHz discriminator. The discriminator output will be fed into (1) a low-pass filter and recorder to measure long-term frequency stability, and (2) a bandpass filter centered at the dither frequency and oscilloscope to measure the dither peak-to-peak deviation frequency.

i. Operating Frequency (Local Oscillator and Backup Lasers): The operating frequency will be measured by heterodyne techniques. A stable laboratory laser will be dither-stabilized to line center. The test laser will be tuned to operate at 30 MHz below line center by an AFC loop controlled

by a 30-MHz discriminator. The discriminator output will be fed into a low-pass filter and recorder to measure the long-term frequency stability.

j. Frequency Uncertainty During Acquisition (Local Oscillator and Backup Lasers): The frequency uncertainty will be measured by heterodyne techniques. A stable laboratory laser will be dither-stabilized to line center. The test laser will be tuned to operate at 30 MHz below line center by the acquisition-mode laser electronics. The output from a 30-MHz discriminator will be fed into a low-pass filter and a recorder to measure the frequency uncertainty for a minimum of 5 minutes.

k. Frequency Stability: This measurement will be made by heterodyne techniques. The test laser, stabilized at its operating frequency, will be operated at a 30-MHz difference frequency. The output from a 30-MHz discriminator will be fed into one of three bandpass filters. The output from the 0.1 to 5-Hz filter will be fed into a recorder converted to root-mean-square (rms) values. The output from the 5-Hz-to-800-kHz and the 800-kHz-to-6-MHz filters will be measured with an rms voltmeter. The 5-Hz-to-800-kHz filter will have a notch at the dither frequency.

l. Amplitude Stability: The output power from the laser will be directed onto a detector, whose output will be fed through a 5 to 45-Hz bandpass filter to an rms voltmeter, which will read the rms voltage caused by fluctuations of the laser-output power. The detector voltage corresponding to the average laser-output power will be measured on an oscilloscope by chopping the laser beam. The percentage of rms power fluctuations will be computed by dividing the rms-voltmeter reading by the oscilloscope reading and multiplying by 100.

m. Power Input: The power input to the laser tubes will be calculated from measurements of the operating current and voltage of the tubes.

7.3.12 Modulator Functional Testing

The functional tests listed below will be conducted on the laser modulator to ensure that the transmitter laser is operating properly. They will be performed with a heterodyne setup and an optical receiver, as shown in Figure 7-10.

a. Baseband Amplitude-Frequency Characteristics: These characteristics will be measured by injecting a video-test signal covering the band into the modulator driver, and noting the receiver output displayed on the waveform monitor.

b. Modulator/Driver Sensitivity: A 1-volt peak-to-peak signal will be applied to the modulator/driver, and the receiver output will be measured with the spectrum analyzer for maximum frequency deviation using the side-band-amplitude Bessel-function technique.

c. Periodic Noise: This measurement will be made by terminating the input to the modulator driver with a proper load, and noting the receiver output displayed on the waveform monitor.

7.3.13 Transmitter and Backup Laser Beam Alignment

The test setup shown in Figure 7-7 will be used to align the backup laser beam to the transmitter beam in the far field of the transceiver for both the acquisition and the tracking modes. Alignment will be accomplished by measuring and superimposing the intensity distributions of the transmitter and backup laser beams at the focal point of the parabolic mirror. The measured far-field antenna patterns for both laser beams in the acquisition and tracking modes will be compared with computer values to determine if the beams are diffraction-limited.

7.3.14 Transmitted-Beam and Received-Beam Alignment

The test setup shown in Figure 7-7 will be used to align the received beam at the mixer with the transmitted beam in the far field of the transceiver. The far field of the transmitted beam will be centered on the pinhole and detector at the focal point of the parabolic mirror. The received beam from the laboratory laser source will be centered on the mixer by optimizing the nonheterodyned mixer output for a chopped signal beam.

The transmitted far-field antenna pattern from the breadboard transceiver will be measured and compared with computed values to determine if the beam is diffraction-limited.

7.3.15 Alignment of Local Oscillator and Backup Laser Beams and Received Beam

The test setup shown in Figure 7-7 will be used to align the local oscillator and backup laser beams to the received beam at the mixer. The received beam from the laboratory laser source will be centered on the mixer as in paragraph 7.3.14. The local oscillator laser and backup laser beams will each be centered on the mixer by optimizing the heterodyne output signal. A backup laser has not been incorporated into the breadboard transceiver. The receiver antenna pattern will be measured by scanning the received beam across the mixer with the IMC.

7.3.16 Coarse-Beam-Pointing-Circuit Functional Testing

The coarse beam pointing circuit (consisting of command registers, shaft-position registers, a comparator, motor driving circuitry, and an IMC position-error detector) will be functionally tested by the Electronic Engineering group.

7.3.17 Search Pattern Circuit Functional Testing

The search pattern circuits (consisting of a clock, a clock and command gate, a line-width counter, a frame-width counter, and rest-gate, line, and frame-width D/A converters, a line-width integrator, and auxiliary circuitry) will be functionally tested by the Electronic Engineering group.

7.3.18 Acquisition Control Circuit Functional Testing

This circuit (consisting of circuitry required to generate internal control and command functions, and an acquisition-threshold-signal generator) will be functionally tested by the Electronic Engineering group.

7.3.19 IMC Driver Circuit Functional Testing

This circuit (consisting of drivers for the east-west and north-south axes of the image-motion compensator) will be functionally tested by the Electronic Engineering group.

7.3.20 Tracking Circuit Functional Testing

The tracking circuit (consisting of a nutator and threshold signal generator, and nutator drivers) will be functionally tested for operation in the acquisition and normal tracking modes by the Electronic Engineering group.

7.3.21 Command Distribution Circuit Functional Testing

This circuit will be tested for all functional operations by the Electronic Engineering group.

7.3.22 Telemetry-Data-Conditioning-Circuit Functional Testing

The telemetry data conditioning circuit will be tested for all functional operations by the Electronic Engineering group.

7.3.23 Video Switch Functional Testing

The video switch will be functionally tested for all required operations - i.e., cross-strapping within the transceiver and between the transceiver and the spacecraft microwave-communication system.

7.3.24 Signal Conditioning Package Functional Testing

This testing will be performed to check the functional characteristics of all the circuits integrated into the signal conditioning package. The extent of the functional testing at this level will depend on the availability of test points of each individual circuit in this configuration. The testing will be planned and performed by the Electronic Engineering group.

7.3.25 Signal-Conditioning-Package Storage-and-Operating-Temperature Testing

A combined storage and operating temperature test in accordance with Specification AGC 20511 will be performed on the signal conditioning package. During storage temperature cycling, functional tests in accordance with paragraph 7.3.24 will be performed with the unit stabilized at the operating-temperature extremes.

7.3.26 Power Supply Functional Testing

The power supply will be tested for all functional-operation requirements by the Electronic Engineering group, which will prepare a detailed test plan.

7.3.27 Power-Supply Storage-and-Operating-Temperature Testing

A combined storage-and-operating-temperature test will be performed on the power supply. During storage-temperature cycling, functional tests will be performed in accordance with paragraph 7.3.26 at operating-temperature extremes.

7.3.28 Power-Supply Vacuum Testing

A vacuum test will be performed on the power supply to ensure the proper operation of this unit in a space environment. Functional tests in accordance with paragraph 7.3.26 will be performed on the power supply during the vacuum test.

7.3.29 Radiation-Cooler Thermal-Balance Testing

The radiation cooler (consisting of the heat sink, passive radiator and shield, and a simulated antenna) will be installed in a thermal-vacuum test chamber. The test article will be instrumented with thermocouples to monitor temperatures at various locations. Internal power dissipation will be simulated by heaters attached to the heat sink.

Testing will be conducted with the chamber evacuated to a pressure below 10^{-5} torr, and with the chamber cryo-shroud cooled to a temperature below 90°K . Temperature data will be recorded after the test article has reached a steady-state condition.

The reduced test data will be compared with previously predicted results to verify the validity of analytical techniques and to verify that the thermal performance of the radiator is satisfactory.

7.3.30 Radiation-Cooler-Shield Energy-Control Testing

A passive radiator and shield assembly will be installed on the J104 collimator test table for irradiation with collimated visible light at several angles about the shield's major axis. The EMF output of a radiometer placed under the radiator will indicate the energy absorbed by the radiator.

Before testing, the test plane will be mapped with the radiometer to determine the total flux in the test volume. The flux absorbed by the

radiometer, with the radiator and shield in place, will then be compared with the total flux known to be incident on the radiator/shield assembly. The ratio of absorbed flux to incident flux is a measure of radiator/shield performance.

7.3.31 Radiation Cooler Vibration Testing

The cooler will be subjected to a qualification-level vibration test in accordance with Specification AGC 20511.

7.3.32 Radiation-Cooler Thermal-Balance Testing

The thermal-balance test discussed in paragraph 7.3.29 will be repeated after the vibration test to check the performance of the radiation cooler.

7.3.33 System Weight and Center of Gravity

After all subsystems are integrated into the final transceiver-system configuration, the package will be weighed and the center of gravity of the package will be determined.

7.3.34 System EMC Testing

The following selected EMC tests from MIL-STD-461A will be performed on transceiver system: CE01, CE02, CE03, CE04, CS01, CS02, CS06, RE01, RE02, RS01, and RS03. They were chosen to assure the compatibility of the LCE transceiver with itself and with the spacecraft.

7.3.35 System Functional Testing

The functional tests summarized below will be performed on the transceiver system under ambient, laboratory conditions in order to establish a reference baseline of data. The test setups shown in Figures 7-7, 7-8, and 7-9 will be used for the breadboard transceiver. The setups shown in Figures 7-7 and 7-11 will be used for the FTM, prototype, and flight transceivers. The tests associated with the coarse pointing mirror assembly will not be performed on the breadboard transceiver, because it does not include this assembly.

a. Startup Loops: The startup and frequency stabilization of the laser subsystem will be functionally tested using appropriate commands.

- b. Power Measurement: The total prime power consumption will be measured.
- c. Coarse Pointing Mirror Functional Test: Commands will be fed into the coarse pointing mirror to position it to various angles. The shaft-encoder outputs will be checked to verify these angles.
- d. Acquisition: The acquisition-limit angles relative to this telescope axis in east-west and north-south directions will be measured. The minimum carrier threshold power at which the transceiver can acquire will be measured. Dynamic-acquisition tests over small angular ranges will be performed with a deflection-plate assembly (see Figure 7-7).
- e. Tracking: Transmitted and received beam alignments will be checked during tracking. A dynamic-tracking test, including the coarse-pointing-mirror correction to zero the IMC driver voltage, will be conducted to check all tracking functions of the transceiver. This test will be performed with a deflection-plate assembly (see Figure 7-7).
- f. Baseband Amplitude-Frequency Characteristics: These characteristics will be measured by injecting a video-test signal covering the band into the modulator driver, and noting the output of the receiver displayed on the waveform monitor.
- g. Nonlinearity Distortion: The nonlinearity distortion of the synchronizing signal will be measured. A video-test signal (CCIR No. 3) will be applied to the video input of the modulator driver, the receiver output will be displayed on a waveform monitor, and the amplitude of the synchronizing pulse will be measured.
- h. Modulation Sense: The black-to-white transition in the output video signal will be checked for correspondence to the input video signal.
- i. Envelope Delay Distortion: This test will be performed to check that the envelope delay distortion is within the specified limits. A group delay test set will be used to make point-by-point measurements on a complete communication link.

j. Periodic Noise: The signal-to-periodic-noise ratio will be measured in the communication link. The periodic noise will be measured on the waveform monitor with the video input of modulator driver terminated with a proper load.

k. NEP Measurement: A setup such as shown in Figure 7-7 or 7-11 will be used to measure system NEP. The laser beam will be chopped so that the signal can be distinguished from noise. The mixer output will be fed into the receiver electronics. The signal-to-noise ratio will be measured at the IF-amplifier output. The test will be conducted starting with a high signal-to-noise ratio, and the laser beam from the test source will be attenuated in increments until the noise and the signal can no longer be differentiated at the output. The signal power at this point represents the NEP of the system.

l. Telemetry Functional Test: All telemetry outputs will be functionally tested. This test will not be performed on the breadboard transceiver.

m. Command Functional Test: The transceiver will be tested for all command operations. This test will not be performed on the breadboard transceiver.

7.3.36 System Storage Temperature Testing

The complete prototype transceiver system will be subjected to a storage temperature test in accordance with Specification AGC 20511.

7.3.37 Selected System Functional Testing

The functional tests listed below (selected from the tests described in paragraph 7.3.35) will be performed on the transceiver system under laboratory ambient conditions in order to check the performance after each environmental test.

a. Startup Loops: The startup and frequency stabilization loops and switching functions of the laser subsystem will be functionally tested with appropriate commands.

b. Power Measurement: The total prime power consumption will be measured.

c. Acquisition and Tracking: These functions will be checked for normal operation.

d. Baseband Amplitude-Frequency Characteristics: These characteristics will be checked by injecting a video test signal covering the band into the modulator driver and noting the receiver output displayed on the waveform monitor.

7.3.38 System Vibration Testing

The FTM and prototype transceiver systems and the flight transceiver system will be subjected to qualification-level and flight-acceptance-level vibration tests, respectively, in accordance with Specification AGC 20511.

7.3.39 System Acceleration Testing

The prototype transceiver system will be subjected to an acceleration test in accordance with Specification AGC 20511.

7.3.40 System Thermal-Vacuum and Thermal-Balance Testing

The FTM and prototype transceiver systems and the flight transceiver system will be subjected to qualification-level and flight-acceptance-level thermal-vacuum tests respectively in accordance with Specification AGC 20511. A thermal-balance test in accordance with Specification AGC 20511 will be combined with the thermal-vacuum tests performed on each transceiver system. During these environmental tests, a complete system functional test, as described in paragraph 7.3.35, will be performed to check for proper operation.

7.3.41 Final System Functional Testing

The final testing of the transceiver system will be a repeat of the system functional testing under laboratory ambient conditions as described in paragraph 7.3.35. The results will be compared with the initial test results to determine if any performance degradation resulted from environmental testing.

7.3.42 Coarse-Pointing-Mirror-Assembly (Qualification Unit) Functional Testing

The qualification unit of the coarse-pointing-mirror assembly (consisting of north-south and east-west gimbals, gear boxes, stepping motors,

shaft position encoders, and the mirror) will be function-tested under laboratory ambient conditions as summarized below. A special electronic package will be used to supply the required electrical inputs and to read the output signals.

a. Deflection Limits: The deflection limits of the coarse pointing mirror will be measured in east-west and north-south directions.

b. Pointing Rate: The command pointing rate will be computed from data collected from shaft-encoder outputs as the assembly responds to the pointing-command inputs.

c. Angular Positioning: The angular-positioning accuracy of the coarse pointing mirror will be measured by mounting a special mirror-test fixture on the gimbal and using autocollimation techniques.

7.3.43 Coarse-Pointing-Mirror Storage-Temperature Testing

The assembly will be subjected to a storage temperature test in accordance with Specification AGC 20511.

7.3.44 Coarse-Pointing-Mirror Functional Testing

The functional testing described in paragraph 7.3.42 will be performed on each coarse pointing mirror in order to check its performance after each environmental test.

7.3.45 Coarse-Pointing-Mirror Vibration Testing

The assembly will be subjected to a qualification-level vibration test in accordance with Specification AGC 20511.

7.3.46 Coarse-Pointing-Mirror Thermal-Vacuum Testing

A long-term thermal-vacuum test of the coarse pointing mirror will be performed in accordance with Specification AGC 20511. Its duration will be determined on the basis of reliability data. The unit will be operated periodically to perform all required functions and will be tested in accordance with paragraph 7.3.42. The purpose is to ensure proper operation in a space environment during the useful lifetime.

7.3.47 Final Coarse-Pointing-Mirror Functional Testing

The final testing of the coarse-pointing-mirror-assembly qualification unit will be a repeat of the functional testing under laboratory ambient conditions as described in paragraph 7.3.42. The results will be compared with the initial test results to determine if any performance degradation resulted from the environmental testing.

7.4 SUMMARY

Tables 7-2 and 7-3 summarize the testing scheme for the LCE transceiver models.

Table 7-2 provides an index for all tests described in Section 7.3 that will be performed on the different transceiver models as indicated in test flow charts.

Table 7-3 shows the functional and environmental tests that will be performed on each transceiver model and the assembly level or levels at which they will be performed. It illustrates the sequence of tests at the various hardware levels through the different transceiver models that will be performed in order to ensure a high probability of successful flight-transceiver operation in space. The arrows drawn in this table imply a successful test at the subsystem or system level indicates that all parts and assemblies at the lower levels performed satisfactorily.

Report No. 4033, Vol. I, Part 1

TABLE
KEY PROGRAM TEST MILESTONES

ITEM	DESCRIPTION
Breadboard Testing	Verifies the validity of the design concepts and determines the parameters for use in further optimization of system design. <u>System level testing in conjunction with approval of the design report, will serve as the basis for FTM assembly.</u> Several functional design concepts will be verified during subsystem level testing.
Functional Test Model Testing	Serves to prove the performance capability, environmental integrity, and interface compatibility of the LCE transceiver and to aid in early identification of potential problems that may prevent the prototype from passing qualification tests. The FTM will be fabricated as close to the flight-model design as is possible at that stage of development. <u>System level testing will be the basis for prototype and flight model assembly.</u> Several function and environmental design concepts will be verified during subsystem-assembly level testing.
Prototype Testing	Qualifies the flight model design. Several of the subsystems will be qualified before system assembly.

FUNCTION	TESTING PERIOD
<u>Laser Startup and Stabilization</u>	
Demonstrate startup operation and automatic line selection	Breadboard Subsystem*/System Tests
Demonstrate Amplitude and frequency stability	Breadboard* (Invar baseplate) and FTM Subsystem/System Tests (CERVIT baseplate)
<u>Acquisition and Tracking</u>	
Demonstrate IMC and nutator performance	Breadboard Subsystem*/System Tests
Demonstrate course pointing, mirror performance	FTM Subsystem/System Tests
Demonstrate acquisition and tracking subsystem performance	Breadboard System Tests
<u>Communications</u>	
Achieve required transmitter and local oscillator power output	FTM Subsystem/System Tests
Determine transmitted and received antenna patterns	Breadboard and FTM System Tests (Telescope design changed from Breadboard to FTM)
Demonstrate modulator performance	Breadboard* and FTM Subsystem/System Tests (Modulator design may change from Breadboard to FTM)
Demonstrate receiver sensitivity	FTM Subsystem/System Tests
Demonstrate receiver performance	Breadboard* System Tests
<u>Radiation Cooler Performance & Environmental Effects</u>	
Demonstrate Ability to Withstand Vibration	Development Tests on Structural Model of Radiation Cooler and during FTM System Tests
Demonstrate Cooling Performance in Thermal Vacuum	Development Tests on Structural Model (comparison to predicted values for rough sunshield surface) and during FTM Subsystem Tests
<u>Laser Performance & Environmental/Life Effects</u>	
Achieve required transmitter, local oscillator, and backup Laser efficiencies	FTM Subsystem/System Tests
Achieve 2000 hours life on ceramic laser tube	Basic Laser Tube Life Test Program performed in conjunction with FTM development
Demonstrate experimentally lifetime reliability of flight configured laser tubes	Extended Laser Tube Life Test Program (proposed) performed in conjunction with FTM development and completed prior to Prototype System delivery
Demonstrate ability of laser tubes to withstand vibration	Breadboard development tests*, Basic Laser Tube Life Test Program and FTM System tests
<u>Mixer Performance and Environmental Effects</u>	
Demonstrate ability of mixer to withstand vibration	Development tests performed in conjunction with FTM development and during FTM Subsystem/ System Tests
Achieve required NEM over operating temperature range	Development tests performed in conjunction with FTM and prototype development and during Prototype Subsystem/System Tests.
<u>Additional Environmental/Life Effects</u>	
Demonstrate ability to maintain alignment	FTM Subsystem/System Tests
Demonstrate coarse pointing mirror assembly ability to withstand vibration and vacuum life performance	Assembly qualification level and life tests to be performed in conjunction with FTM development and completed prior to Prototype Subsystem delivery

*Completed

TABLE 7-2

TESTING INDEX

Para- graph	Type	Bread- board	FIM	Proto- type	Flight
7.3.1	Miscellaneous optical parts - inspection		x	x	x
7.3.2	Flip-mirror vibration and functional testing		x		
7.3.3	Duplexer distortion and efficiency testing	x			
7.3.4	IMC and nutator engineering testing	x	x	x	x
7.3.5	IMC and nutator vibration testing		x		
7.3.6	IMC and nutator temperature testing	x	x		
7.3.7	Telescope alignment and aberration testing		x	x	x
7.3.8	Coarse-pointing-mirror-assembly functional testing		x	x	x
7.3.9	Receiver functional testing		x	x	x
7.3.10	Laser signature testing		x	x	x
7.3.11	Laser functional testing		x	x	x
7.3.12	Modulator functional testing		x	x	x
7.3.13	Transmitter and backup laser beam alignment		x	x	x
7.3.14	Transmitted-beam and received-beam alignment	x	x	x	x
7.3.15	Alignment of local oscillator and backup laser beams and received beam	x	x	x	x
7.3.16	Coarse-beam-pointing-circuit functional testing		x	x	x
7.3.17	Search pattern circuit functional testing	x	x	x	x
7.3.18	Acquisition control circuit functional testing	x	x	x	x
7.3.19	IMC driver circuit functional testing	x	x	x	x
7.3.20	Tracking circuit functional testing	x	x	x	x
7.3.21	Command distribution circuit functional testing		x	x	x

TABLE 7-2 (cont.)

Para- graph	Type	Bread- board	FIM	Proto- type	Flight
7.3.22	Telemetry-data-conditioning-circuit functional testing		x	x	x
7.3.23	Video switch functional testing		x	x	x
7.3.24	Signal conditioning package functional testing	x	x	x	x
7.3.25	Signal-conditioning-package storage-and-operating-temperature testing		x		
7.3.26	Power supply functional testing		x	x	x
7.3.27	Power-supply storage-and-operating-temperature testing		x		
7.3.28	Power supply vacuum testing		x	x	x
7.3.29	Radiation-cooler thermal-balance testing		x		
7.3.30	Radiation-cooler-shield energy-control testing		x		
7.3.31	Radiation cooler vibration testing		x		
7.3.32	Radiation-cooler thermal-balance testing		x		
7.3.33	System weight and center of gravity		x	x	x
7.3.34	System EMC testing		x		
7.3.35	System functional testing	x	x	x	x
7.3.36	System storage temperature testing			x	
7.3.37	Selected system functional testing		x	x	x
7.3.38	System vibration testing		x	x	x
7.3.39	System acceleration testing			x	
7.3.40	System thermal-vacuum and thermal-balance testing		x	x	x
7.3.41	Final system functional testing		x	x	x
7.3.42	Coarse-pointing-mirror-assembly (qualification unit) functional testing		x		
7.3.43	Coarse-pointing-mirror storage-temperature testing		x		
7.3.44	Coarse-pointing-mirror functional testing		x		
7.3.45	Coarse-pointing-mirror vibration testing		x		
7.3.46	Coarse-pointing-mirror thermal-vacuum testing		x		
7.3.47	Final coarse-pointing-mirror functional testing		x		

TABLE 7-3
LCE TRANSMITTER MODELS, TEST SEQUENCE LOGIC

Functional Unit	Breadboard				FTM				Prototype				Flight			
	Part Or Subassembly	Assembly	Subsystem	System	Part Or Subassembly	Assembly	Subsystem	System	Part Or Subassembly	Assembly	Subsystem	System	Part Or Subassembly	Assembly	Subsystem	System
<u>Opto-Mechanical Subsystem</u>							F	F,V1,TV1 T2			F	F,T1,T2,V1 A,TV1			F	F,V2,T2, TV2
Misc. Optical Parts																
Flip Mirror Assemblies						F,V1										
Duplexer					F											
Mutator and IMC		P,T2		F		F,V1,T2				F						
Telescope		SP		F		F				F						
Course Pointing Mirror Assy.						F				F						
Laser Base Plate																
Thermal Structural Base Plate				F												
<u>Acquisition and Tracking Subsystem</u>							F,T1,T2	F,F,V1,TV1 T2		F	F	F,T1,T2,V1 A,TV1				F,V2,T2, TV2
Course Pointing Circuit																
Search Pattern Circuit		F	F	F												
Acquisition Control Circuit		F	F	F												
IMC Driver Circuit		F	F	F												
Tracking Circuit		F	F	F												
Command Distribution Circuit																
Telemetry Data Conditioning																
Video Switching Circuit																
Harness																
Mechanical Structure																
<u>Power Supply Subsystem</u>							F1,T1,T2	F,F,T2,V1, TV1			F,TV1	F,T1,T2 F1,A,TV1			F,TV2	F,V2,T2, TV2
<u>Radiation Cooler Subsystem</u>							TV1,F,V1	F,T2,V1 TV1				F,V1,A,TV1 T1,T2				F,V2,T2, TV2
<u>Course Pointing Mirror Assy. Qualification Unit</u>						F,T1,V1 TV1										

Table 7-3, Sheet 1 of 2

Report No. 4035, Vol. I, Part I

TABLE 7-5 (cont.)

Functional Unit	Breadboard				FIM				Prototype				Flight			
	Part Or Subassembly	Assembly	Subsystem	System	Part Or Subassembly	Assembly	Subsystem	System	Part Or Subassembly	Assembly	Subsystem	System	Part Or Subassembly	Assembly	Subsystem	System
Laser Subsystem (All Tests Performed at Sylvania)			F				Q				Q				Q	
Electronics Assembly		F			F,R,V1,				F				F			
a. TX-startup and AFC Electronics	F	↓			F,T2				F				F			
b. LD-startup and AFC Electronics	F	↓			F,T2				F				F			
c. BU-startup and AFC Electronics	F	↓			F,T2				F				F			
Laser Assembly		V3				F,T2										
a. Laser tubes	F	↓			F,T2				F				F			
b. Modulator and Driver	F	↓			F,T2				F				F			
c. Mirrors & mounts	F	↓			F,T2				F				F			
Laser Subsystem (Tests Performed at Aerojet)				F			F	E,F,V1,TV1,T2			F	F,T2,TV1,A,TV1			F	F,T2,TV1,T2
Receiver Subsystem (All Tests Performed by AIL)			F,T2				Q				Q				Q	
Receiver Electronics		F,T2				F,R,V1,TV1			F				F			
a. IF Preamp. and Bias Control	F,T2	↓			F,T2				F				F			
b. IF Channel	F,T2	↓			F,T2				F				F			
c. Video Channel	F,T2	↓			F,T2				F				F			
d. Acquisition Channel	F,T2	↓			F,T2				F				F			
e. Laser Frequency Error Channel	F,T2	↓			F,T2				F				F			
TR-Mixer Assembly						F,T1,V1			F,T1	Q					Q	
Receiver Subsystem (Tests Performed at Aerojet)				F			F	E,F,V1,TV1,T2			F	F,T1,T2,TV1,A,TV1			F	F,V2,TV2,T2

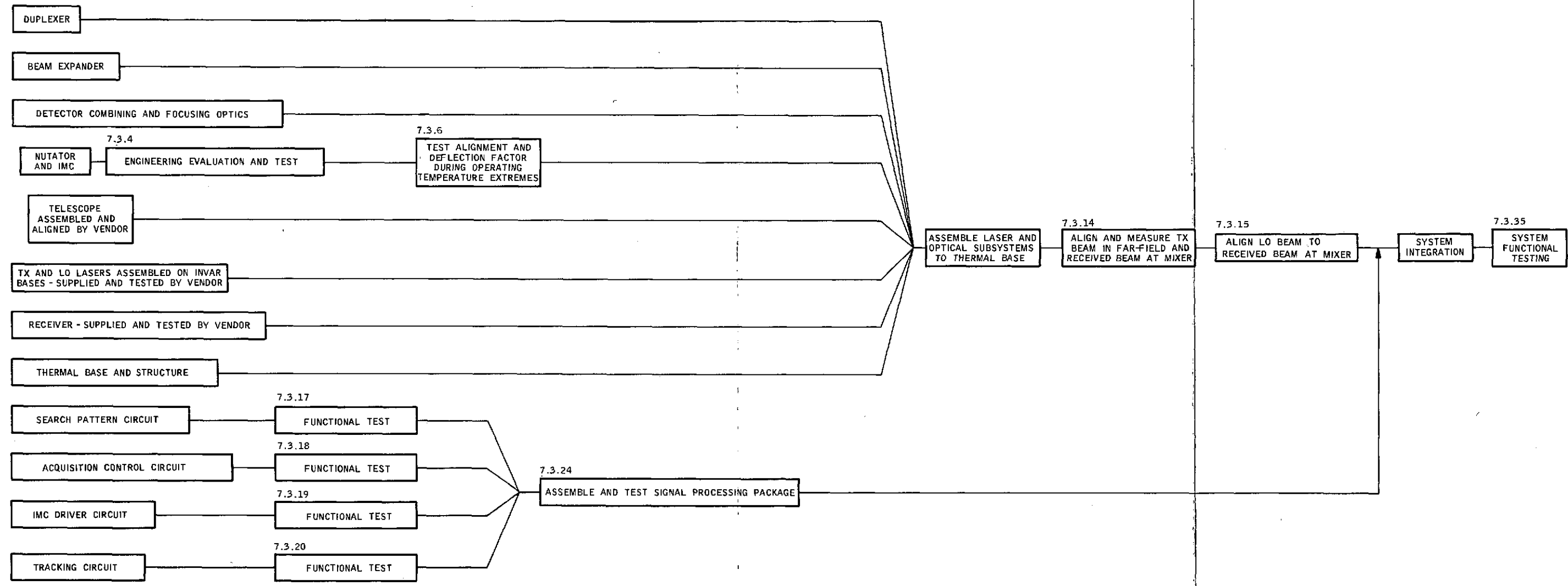
Legend:

- A - Acceleration Test per Spec AGC-20511
- E - EMC Tests per Spec AGC-20511
- F - Functional Test
- Q - Acceptance Testing Performed by Vendor per AGC Specification
- SF - Functionally Tested by Supplier
- T1 - Storage Temperature Test per Spec AGC-20511
- T2 - Operating Temperature Test per Spec AGC-20511

- T3 - Test Performed at Max Operating Temperature per Spec AGC-20511
- V1 - Design Qualification Vibration Test Level I per Spec AGC-20511
- V2 - Flight Acceptance Vibration Test Level II & III per Spec AGC-20511
- V3 - Vibration Test Performed on "Road Start" Laser Assembly
- TV1 - Design Qualification Thermal Balance & Thermal Vacuum Test Level I per Spec AGC-20511
- TV2 - Flight Acceptance Thermal Balance & Thermal Vacuum Test Level II per Spec AGC-20511

FOLDOUT FRAME

FOLDOUT FRAME 2



83511.70-1687

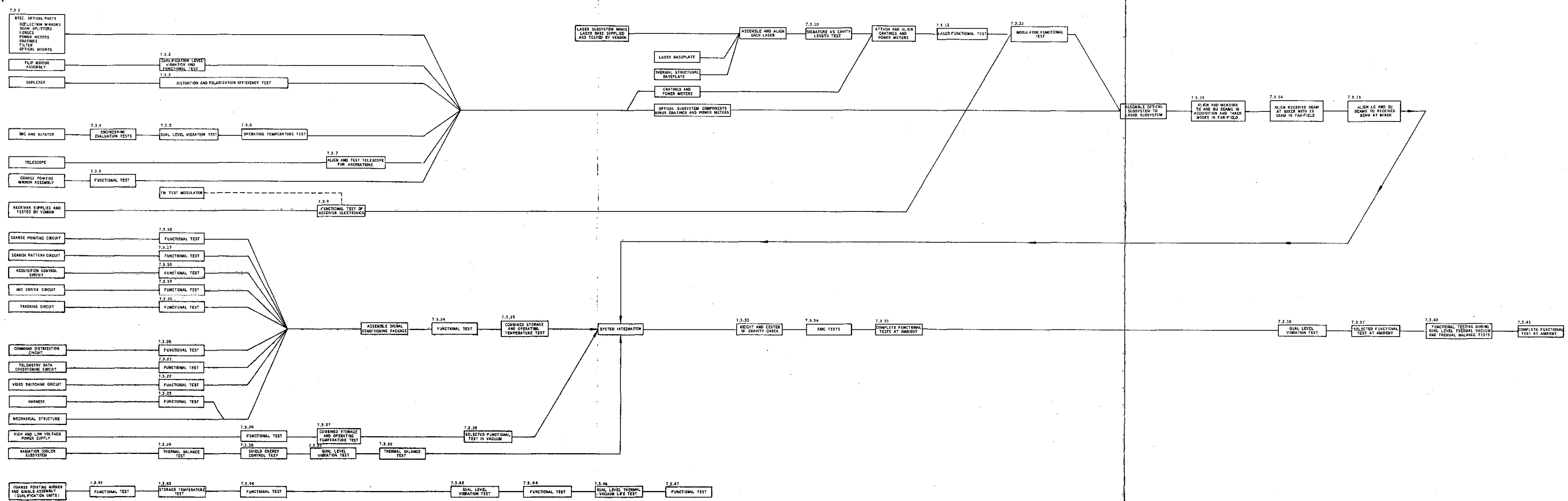
Breadboard Test Chart

Figure 7-1

FOLDOUT FRAME 1

FOLDOUT FRAME 2

FOLDOUT FRAME 3

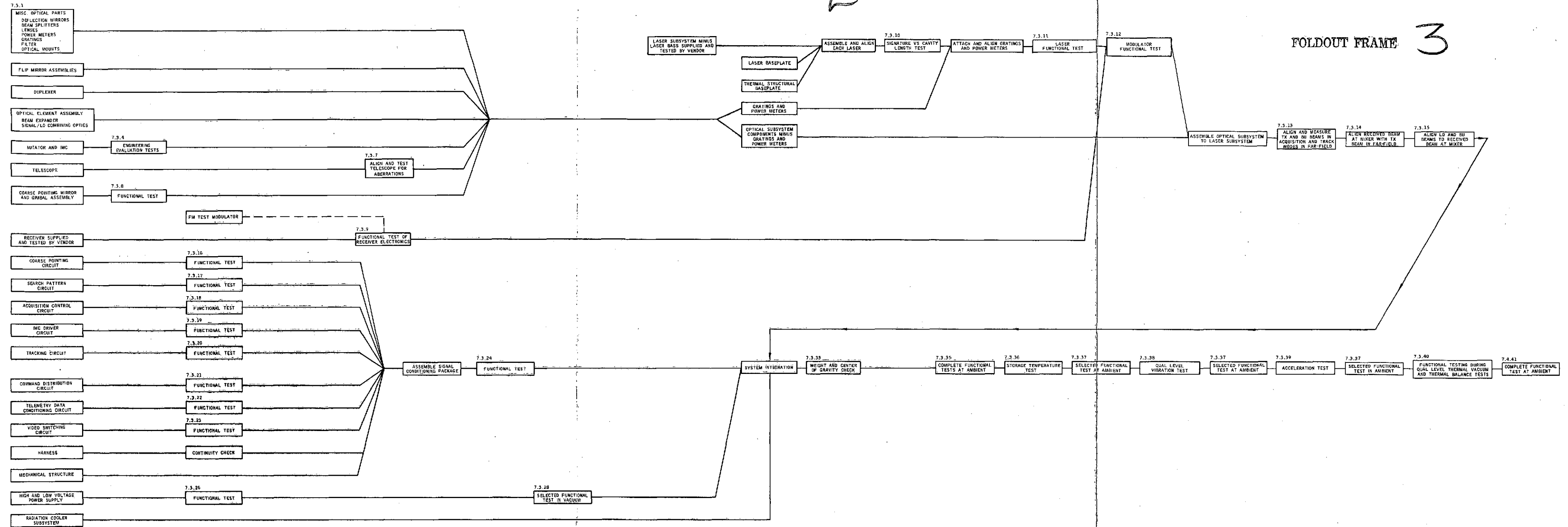


FIM TEST CHART

8511:79-1088

FIM Test Flow Chart

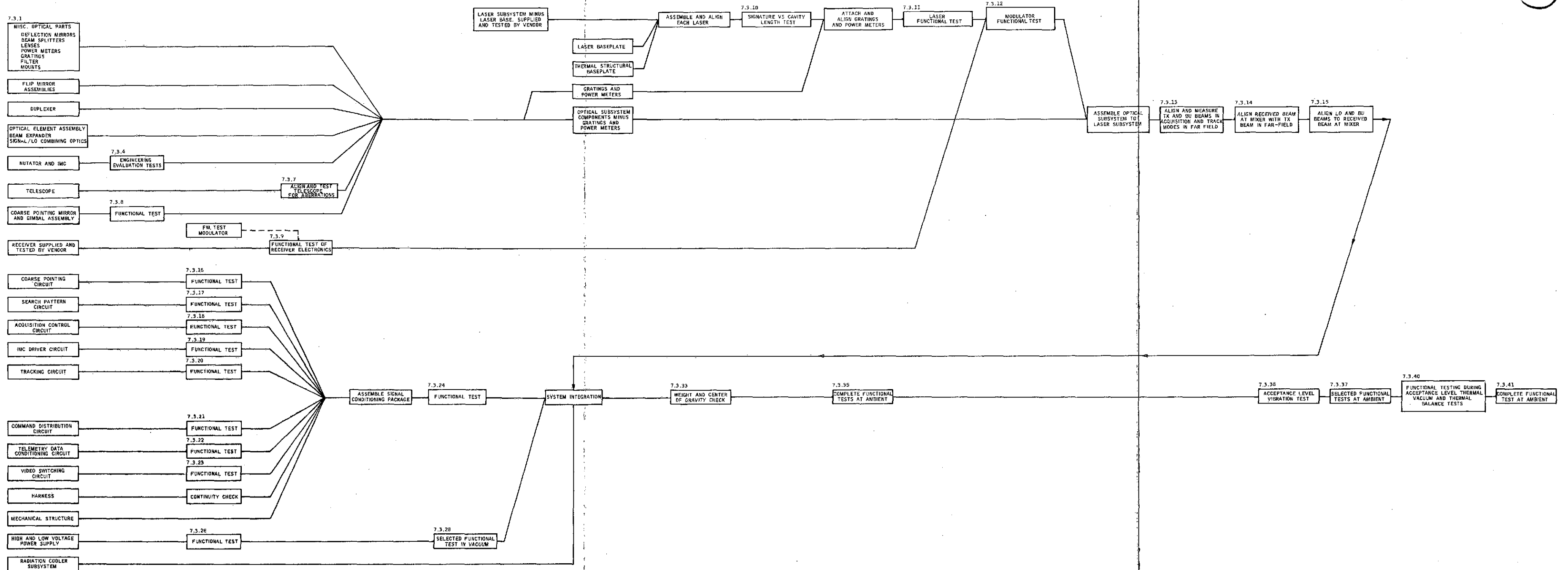
Figure 7-2



PROTOTYPE TEST CHART

Prototype Test Flow Chart

Figure 7-3

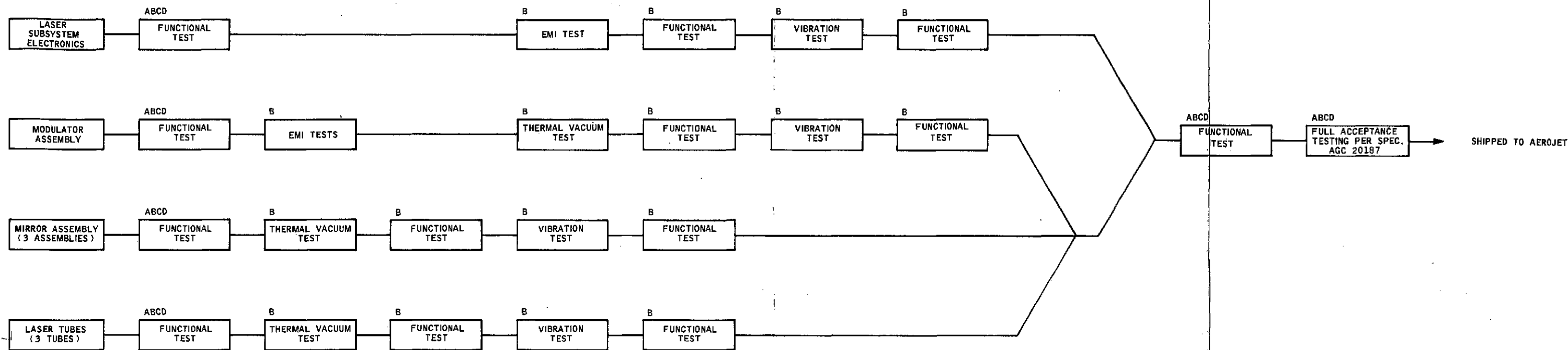


FLIGHT TEST CHART

Flight Test Flow Chart

Figure 7-4

2



BREADBOARD TRANSCEIVER - A
 FTM TRANSCEIVER - B
 PROTOTYPE TRANSCEIVER - C
 FLIGHT TRANSCEIVER - D

NOTE: ONLY LASER TRANSMITTER IS SHOWN HERE AS A TYPICAL MODEL; LOCAL OSCILLATOR AND BACKUP LASER WILL BE TESTED SIMILARLY WITH AN EXCEPTION OF MODULATOR ASSEMBLY.

LASER SUBSYSTEM TESTING AT SYLVANIA

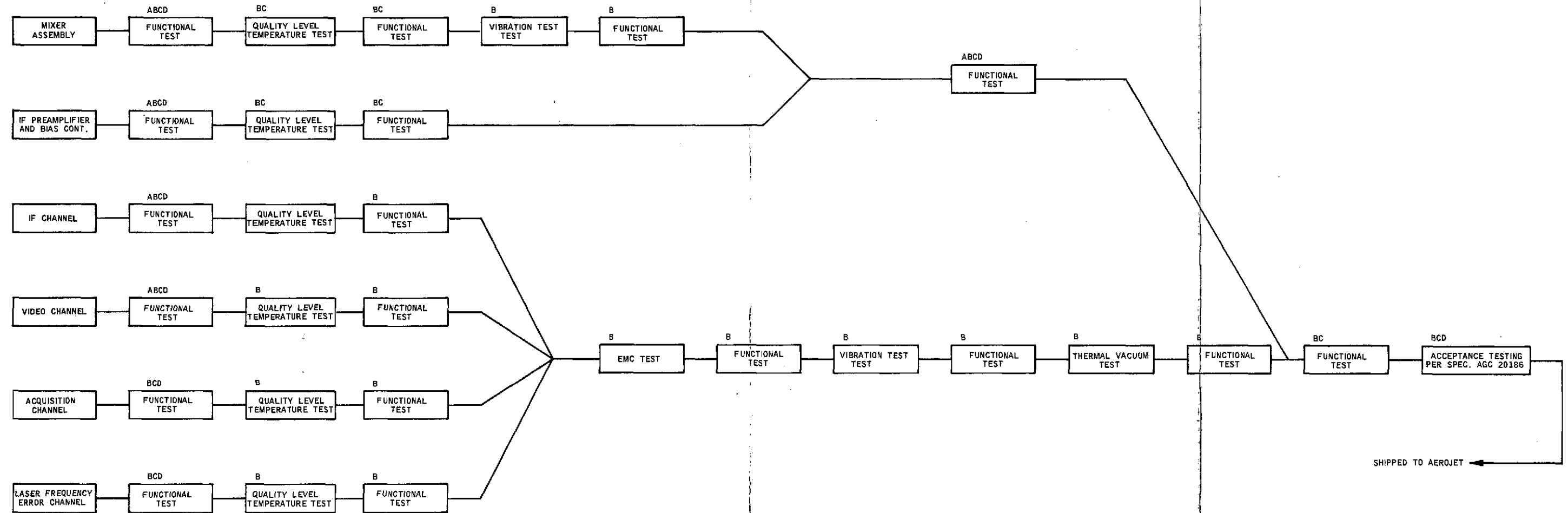
B3511:70-1809

Figure 7-5

FOLDOUT FRAME 1

FOLDOUT FRAME 2

2



- BREADBOARD TRANSCIEVER - A
- FTM TRANSCIEVER - B
- PROTOTYPE TRANSCIEVER - C
- FLIGHT TRANSCIEVER - D

RECEIVER SUBSYSTEM TESTING AT ALL

C3511:70-1810

Figure 7-6

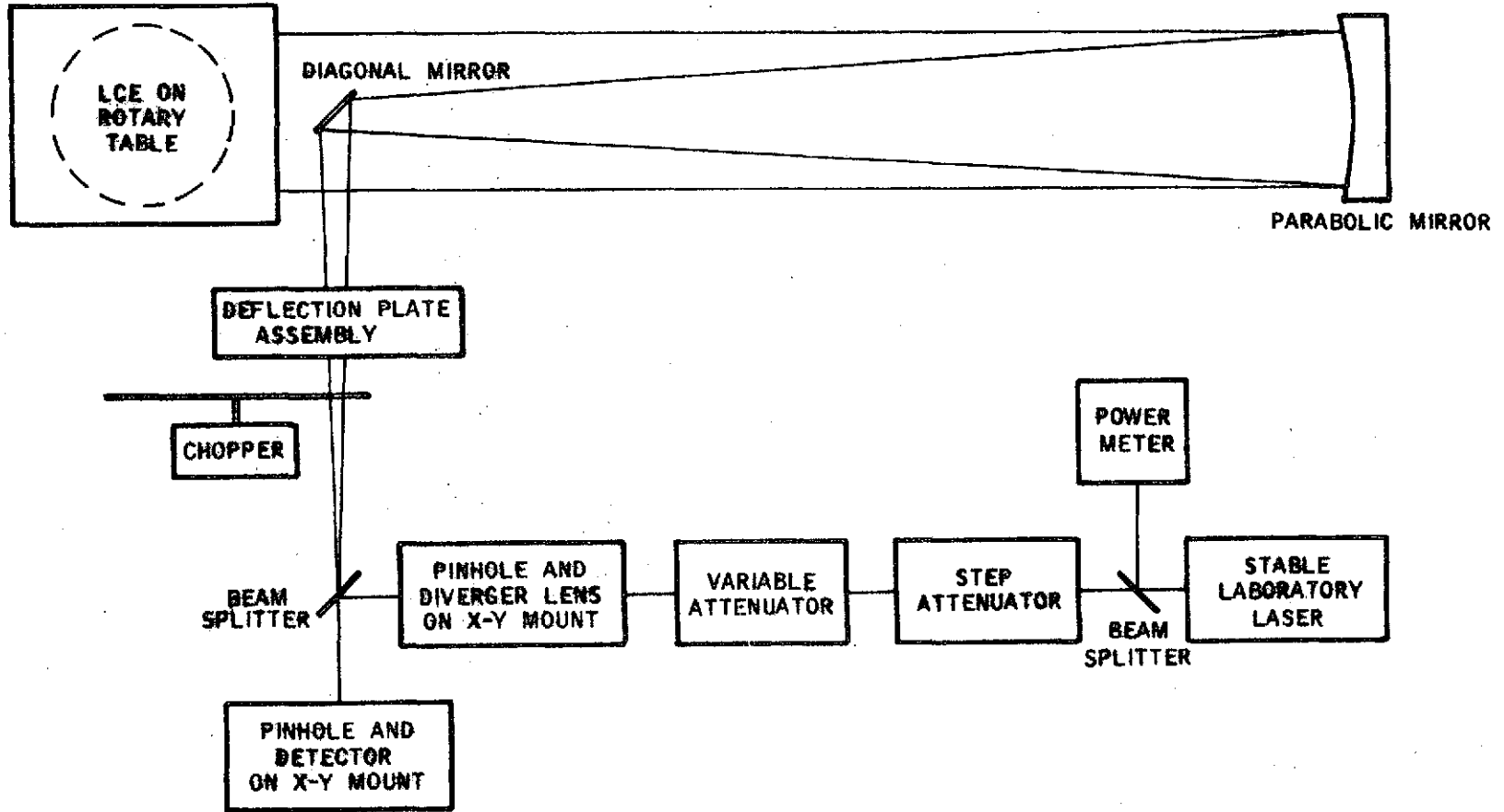
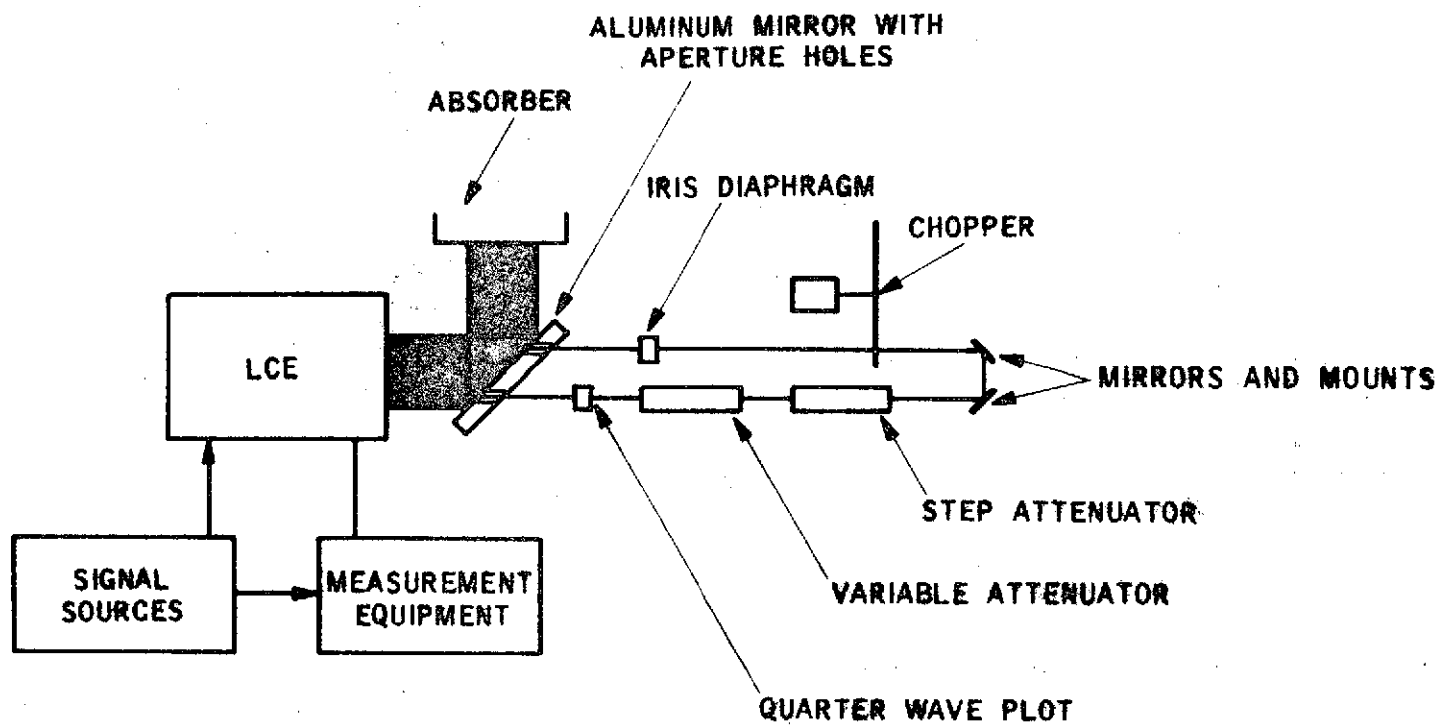


Figure 7-7

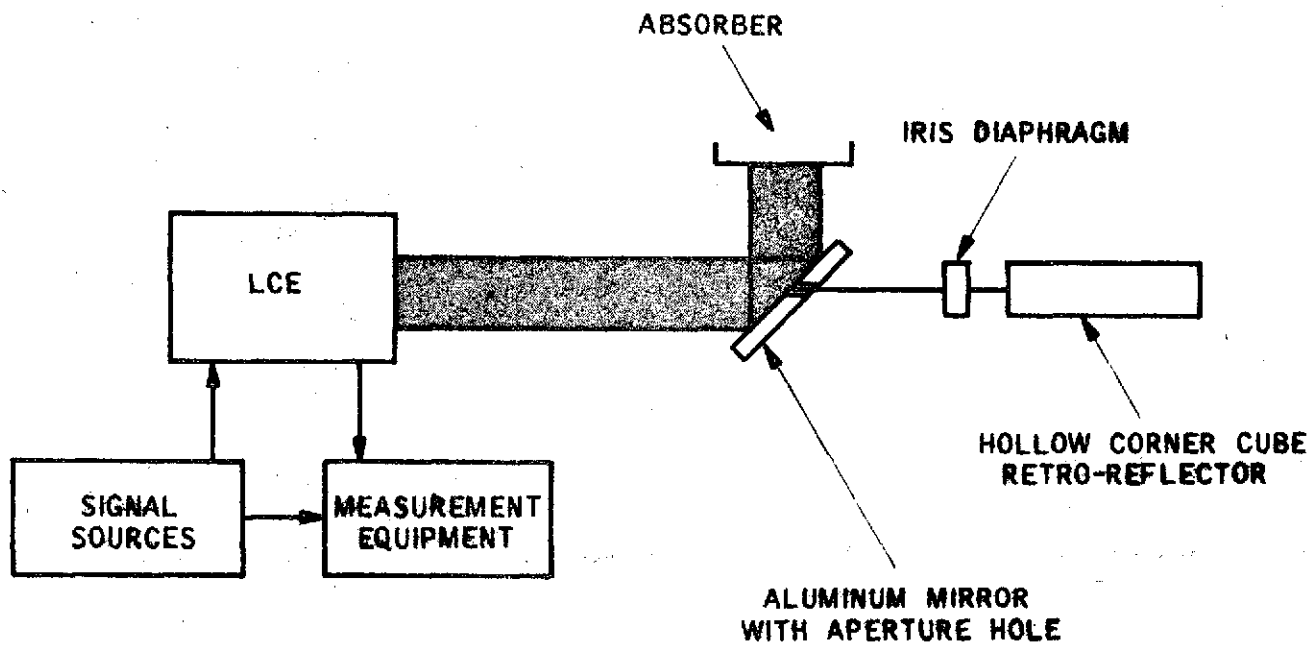
TEST SETUP NO. 1



TEST SETUP NO. 2

Figure 7-8

Figure 7-9



TEST SETUP NO. 3

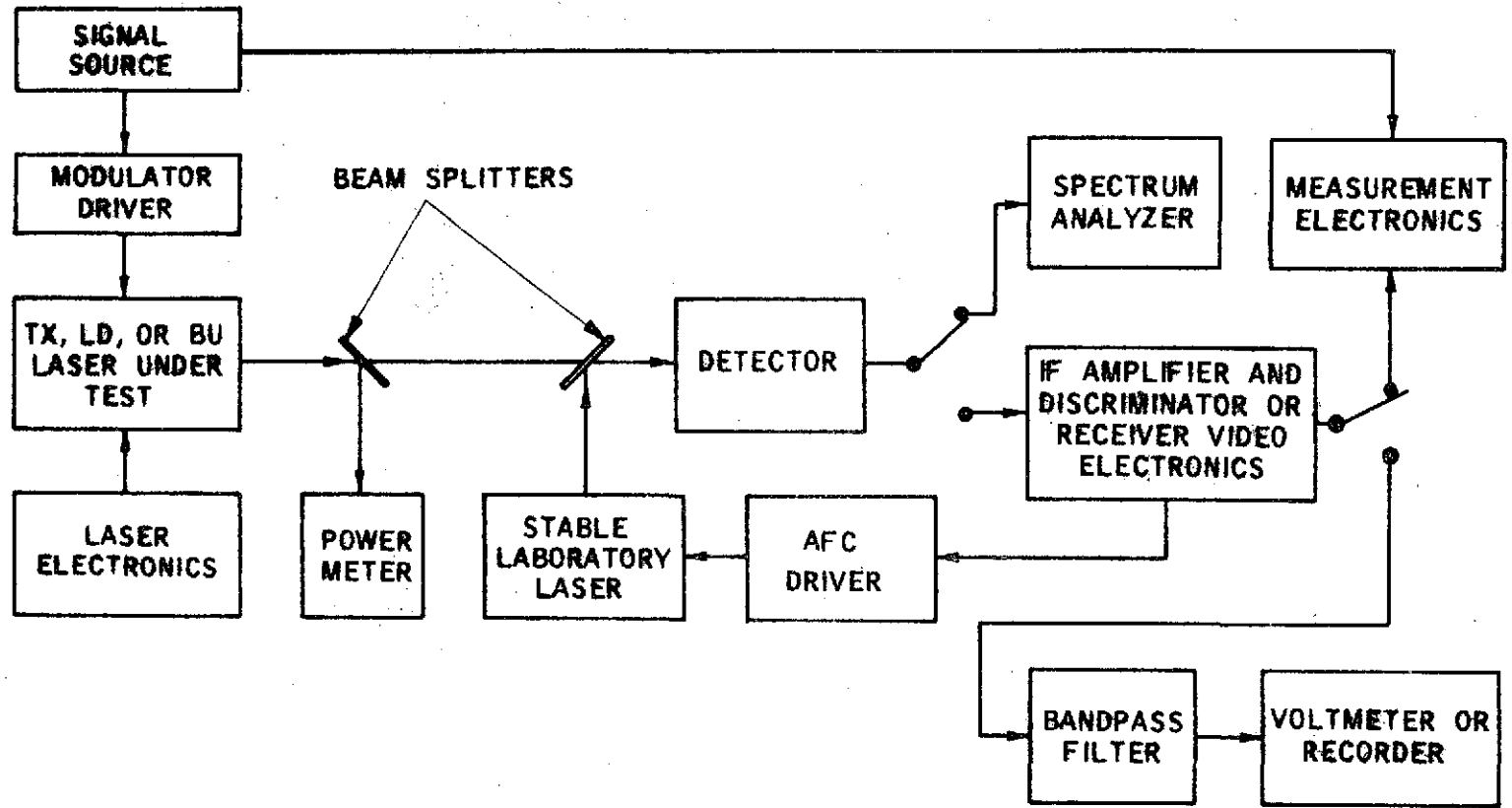
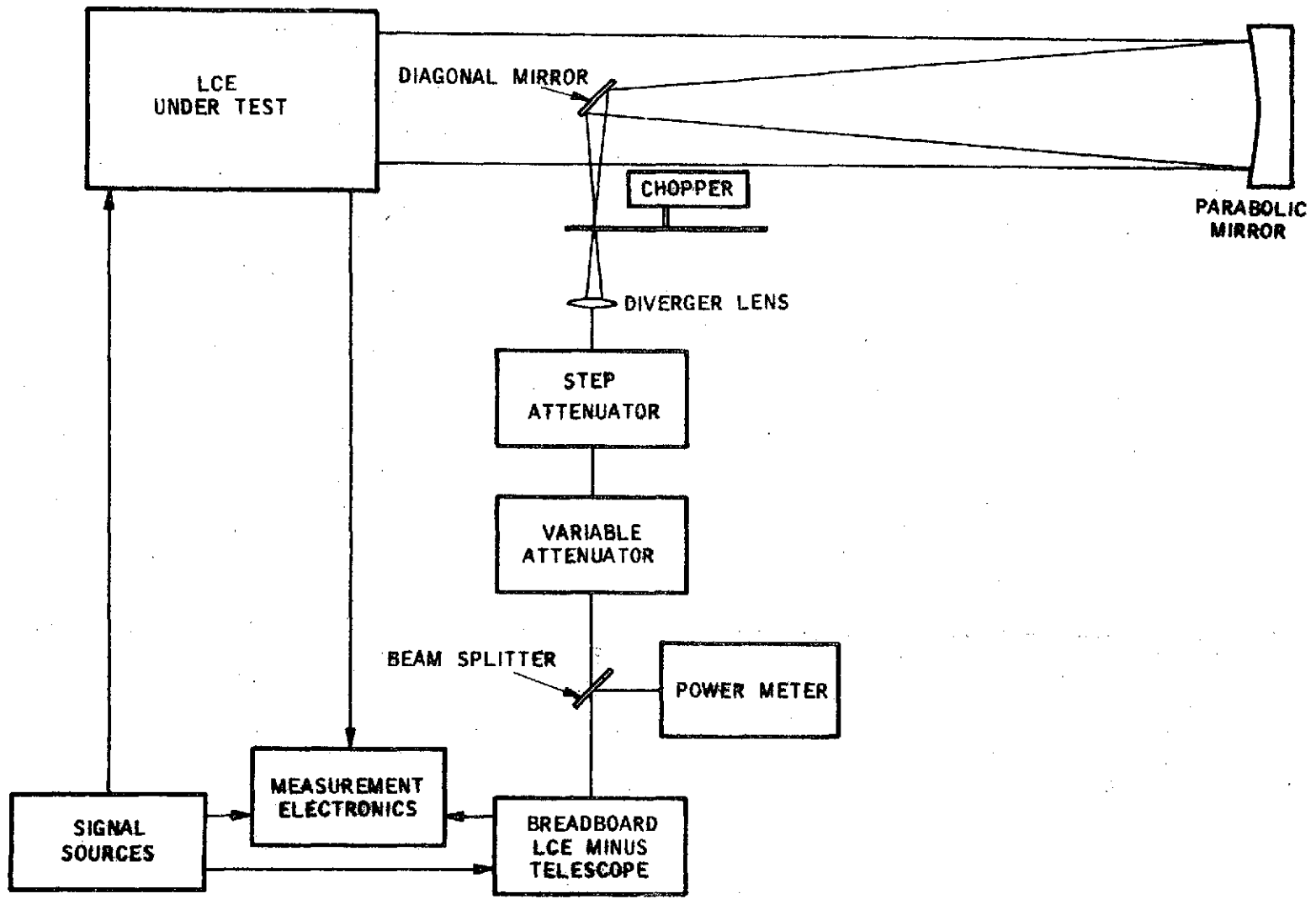


Figure 7-10

TEST SETUP NO. 4



TEST SETUP NO. 5

Figure 7-11